MULTIDISCIPLINARY LOESS GEOHAZARD INVESTIGATIONS

EDITED BY: Fanyu Zhang, Gonghui Wang, Mark Allen and Yueren Xu
PUBLISHED IN: Frontiers in Earth Science

frontiers Research Topics

frontiers

ISSN 1664-8714
ISBN 978-2-88976-765-6
DOI 10.3389/978-2-88976-765-6

About Frontiers

Frontiers is more than just an open-access publisher of scholarly articles: it is a pioneering approach to the world of academia, radically improving the way scholarly research is managed. The grand vision of Frontiers is a world where all people have an equal opportunity to seek, share and generate knowledge. Frontiers provides immediate and permanent online open access to all its publications, but this alone is not enough to realize our grand goals.

Frontiers Journal Series

The Frontiers Journal Series is a multi-tier and interdisciplinary set of open-access, online journals, promising a paradigm shift from the current review, selection and dissemination processes in academic publishing. All Frontiers journals are driven by researchers for researchers; therefore, they constitute a service to the scholarly community. At the same time, the Frontiers Journal Series operates on a revolutionary invention, the tiered publishing system, initially addressing specific communities of scholars, and gradually climbing up to broader public understanding, thus serving the interests of the lay society, too.

Dedication to Quality

Each Frontiers article is a landmark of the highest quality, thanks to genuinely collaborative interactions between authors and review editors, who include some of the world's best academicians. Research must be certified by peers before entering a stream of knowledge that may eventually reach the public - and shape society; therefore, Frontiers only applies the most rigorous and unbiased reviews.
Frontiers revolutionizes research publishing by freely delivering the most outstanding research, evaluated with no bias from both the academic and social point of view. By applying the most advanced information technologies, Frontiers is catapulting scholarly publishing into a new generation.

What are Frontiers Research Topics?

Frontiers Research Topics are very popular trademarks of the Frontiers Journals Series: they are collections of at least ten articles, all centered on a particular subject. With their unique mix of varied contributions from Original Research to Review Articles, Frontiers Research Topics unify the most influential researchers, the latest key findings and historical advances in a hot research area! Find out more on how to host your own Frontiers Research Topic or contribute to one as an author by contacting the Frontiers Editorial Office: frontiersin.org/about/contact

MULTIDISCIPLINARY LOESS GEOHAZARD INVESTIGATIONS

Topic Editors:
Fanyu Zhang, Lanzhou University, China
Gonghui Wang, Kyoto University, Japan
Mark Allen, Durham University, United Kingdom
Yueren Xu, China Earthquake Administration, China

Citation: Zhang, F., Wang, G., Allen, M., Xu, Y., eds. (2022). Multidisciplinary Loess Geohazard Investigations. Lausanne: Frontiers Media SA.
doi: 10.3389/978-2-88976-765-6

Table of Contents

frontiers | Frontiers in Earth Science

EDITORIAL
published: 16 May 2022
doi: 10.3389/feart.2022.884610

Editorial: Multidisciplinary Loess Geohazard Investigations

Fanyu Zhang[1]*, *Gonghui Wang*[2], *Mark B. Allen*[3] and *Yueren Xu*[4]*

[1]MOE Key Laboratory of Mechanics on Disaster and Environment in Western China, Department of Geological Engineering, Lanzhou University, Lanzhou, China, [2]Disaster Prevention Research Institute, Kyoto University, Uji, Japan, [3]Department of Earth Sciences, Durham University, Durham, United Kingdom, [4]Key Laboratory of Earthquake Prediction, Institute of Earthquake Forecasting, China Earthquake Administration, Beijing, China

Keywords: loess, geohazards, multidisciplinary investigations, mitigations, China

Editorial on the Research Topic

Multidisciplinary Loess Geohazard Investigations

INTRODUCTION

Loess geohazards are among the most catastrophic geological processes, causing severe casualties, serious economic losses, and massive eco-environment destructions. Because loess is a surficial loose deposit with exceptional water sensitivity and representative metastable structure, it is very prevalent to instability during wetting under loading. It has received particular attention to the loess behaviors and loess geohazards in the last few decades.

There are several research topics worth mentioning here. In 1988, a special issue titled "Loess geotechnology" was published in Engineering Geology (Lutenegger, 1988). In 2001, Derbyshire, (2001) gave a systematic summary of geological hazards in Chinese loess terrain. In 2018, Engineering Geology published another special issue titled "Loess engineering properties and loess geohazards" (Peng et al., 2018). Recently, loess geohazards research, for example, landslide, subsidence, and erosion, brought about a new focus on mega engineering projects in the Chinese Loess Plateau (CLP) (Li et al., 2014; Juang et al., 2019; Zhang et al., 2019; Hu et al., 2021). While the previous studies have improved the understanding of loess engineering properties and loess geohazards, they are inherently complex due to loess unique properites. So, further investigations will be needed to understand loess geohazards for hazard mitigation, especially with progress of climate changes and human activities.

This Research Topic aimed at widening the knowledges on the loess geohazards emphasizing interdisciplinary contributions. The issue currently includes 23 papers on the dynamic mechanism of loess geohazards, multi-scale analysis of loess mechanical behaviors, and new method of loess geohazards mitigation. The papers are from several fields across engineering geology, geotechnical engineering, geomorphology. All contributions to this Research Topic focus on one or more of the research areas highlighted above, evidenced below by reference to the designated areas' letters.

DYNAMICAL MECHANISM OF LOESS GEOHAZARDS

This thematic issue utilizes different techniques to investigate and analyze various types of loess geohazards, such as natural landslide, cave, and surficial erosion, and ground subsidence, check dam break, gully head incision related to the engineering projects. These contributions pay close attention

OPEN ACCESS

Edited by:
Candan Gokceoglu,
Hacettepe University, Turkey

Reviewed by:
Nejan Huvaj,
Middle East Technical University, Turkey
Hakan Ahmet Nefeslioglu,
Eskisehir Technical University, Turkey

***Correspondence:**
Fanyu Zhang
zhangfy@lzu.edu.cn
Yueren Xu
xuyr@ief.ac.cn

Specialty section:
This article was submitted to Geohazards and Georisks, a section of the journal Frontiers in Earth Science

Received: *26 February 2022*
Accepted: *07 March 2022*
Published: *16 May 2022*

Citation:
Zhang F, Wang G, Allen MB and Xu Y (2022) Editorial: Multidisciplinary Loess Geohazard Investigations. Front. Earth Sci. 10:884610. doi: 10.3389/feart.2022.884610

to the evolution of the natural loess geohazards, aiming to understand their dynamical mechanisms and their relation with the engineering projects.

Concerning the natural loess geohazards, Ma et al. conducted flume tests aiming to understand the initiation mechanism of rainfall-triggered loess mudflows in the CLP. They found two global and local liquefaction failure models with the same retrogressive sliding close to the slope toe. Mao et al. used low-cost UAVs photogrammetry and terrestrial laser scanner (TLS) to produce the digital surface model (DSM) data for geomorphic change detection of the landslide. They provided also offered a novel perspective and technical scheme for evaluating unmanned aerial vehicle (UAV) data for geological hazard surveys. Geng et al. studied the interaction between animal burrowing and loess cave formation in the CLP by *in-situ* measurement and UAV image analysis. This field evidence shows that the formation and expansion of loess caves can dictate the distribution of active areas of biotic disturbance and that both biotic and abiotic processes exist in the distinct "topographic niches". Huang et al. analyzed the GNSS monitoring data using an adaptive sliding-window method, and the improved algorithm successfully extracte loess landslide deformation features on the Heifangtai, China. Chao et al. explained the failure mechanism of loss slope triggered by the Minxian-Zhangxian earthquake, and they speculated that this failure is cominbed effects ground water and ground shaking. Ma et al. reported piping-induced the break of the loess dam of a reservoir in the CLP. In addition, Lyu et al. performed a special focus on the landslide hazard that occurred in geoheritage.

In the loess geohazards arose from the engineering projects, through adopting a large-scale vibration table test, Deng et al. studied the seismic response of a water transmission pipeline across a fault zone. They observed that the dynamic responses are amplified significantly by the fault zone and the hanging wall and provided reasonable seismic design parameters for the detailed project. Zhu et al. used flume to mimic the failure models of the earthen check dam in the "Gully Land Consolidation" project. They found that water seepage triggered the progressive failure of the dam, leading to the slope slide and overtopping. Liu et al. evaluated the effectiveness of engineering measures in gully-head stabilization and loess-platform protection (GSLP) in the typical Dongzhiyuan area in the CLP.

MULTI-SCALE ANALYSIS OF LOESS MECHANICAL BEHAVIORS

This thematic section contains nine papers to the study of loess mechanical behaviors. They rely on experimental results with focus on the application in different loess geohazards and the analysis of well-constrained different loess strata.

Here the mechanical creep behaviors of the loess samples gained particular concerns. Li et al. studied the creep behavior of intact loess (Q_3) followed unloading paths experimentally, and proposed a modified Burgers model to compare the test data. Their results elucidate the possible mechanisms of the progressive failure of loess slopes due to excavation in high-fill projects. Liu et al. conducted the experimental study on the creep characteristics of saturated loess (Q_2), and used the Burgers model to mimic the experimental test data and *in-situ* monitoring deformation. They present two models of the brittle shear failure and progressive failure, which contribute to explaining the flow failure of the deep-buried loess tunnel along with the ground collapse above the tunnel.

The other seven papers discuss the effect of micro-and macro-structures on the shear and compression behaviors of the loess samples. Dong et al. studied the angle of repose of the loess (Q_3) using the fixed funnel methods. They analyze the different mechanisms in four kinds of microscopic contact structures and suggest speculating the formation process of the loess slope system. Zhu et al. developed an empirical shear model of the interface between the loess (Q_3) and red clay based on a series of modified direct shearing experiments. Their results suggest that the mechanical properties of the geological interface have a significant influence on the failure of loess landslides developed on the tertiary Hipparion red clay. Zhang et al. examined the compression behavior of undisturbed and compacted loess (Q_3) using a modified oedometer by controlling total suction and injected solutions. They illustrate that undisturbed loess has more slight changes in void ratio than compacted loess, which guides the mega land creation project in Lanzhou New Area. Gu et al. studied the effect of sulfate on the aggregation of clay particles in loess (Q_3), and analyzed the relation between microstructure and mechanical properties. Rong et al. and Guan et al. studied the tensile strength of loess (Q_2), stiff and soft rocks using five different test methods. They found that the inner hole fracturing and horizontal compression tests have distinct advantages. Liu et al. examined the effect of shear velocity and water content on residual strengths of slip zone taken from Middle Pleistocene loess (Q_2) using a drained ring shear apparatus, and compared the strength differences in the single-stage and multi-stage shear tests.

Almost all these contributions try to use microstructures to explain loess mechanical behaviors. There is no doubt that there is an inherent link between macroscopic properties and microscopic characteristics. Nevertheless, building this kind of quantitative relation is vital to the physical mechanism of loess mechanical behaviors.

STABILIZED METHODS OF LOESS GEOHAZARDS MITIGATION

The loess performance improved through various stabilization methods are the study subjects of the three papers, aiming to develop new strategies for different loess geohazards mitigation. Kong et al. analyzed the geotechnical and physicochemical changes in loess (Q_3) caused by nano-SiO_2 pile migration. These authors find that loess preformation improvement is a physical structure modification rather than chemical stabilization leading to an increase in collapse resistance. Zhang et al. developed a cross-linked polymer soil stabilizer for loess hillslope conservation on the CLP. The results from indoor tests and field practices show that the stabilizer effectively

improves the stability of the loess slope and, consequently decreases soil erosion and vegetation growth. Wang et al. studied the mesoscopic characteristics and performance evaluation of loess (Q_3) treated by different improvement technologies. The results present that chemical additive (i.e., fly ash and cement) and compound improvement methods (dynamic compaction + chemical additive) are more efficient than physically dynamic compaction methods to eliminate the earthquake subsidence.

All three contributions also used the multi-scale viewpoint to analyze the changes in the mechanical properties and microstructures of those treated loess samples. Still, there is also lacking bridging multi-scale linkages. In addition, these suggested stabilized methods still need to be verified for more comprehensive practical application.

PERSPECTIVES

In conclusion, this Research Topic provided multidisciplinary loess geohazard Investigations, focusing on relevant geological engineering, geotechnical engineering, geomorphology. Emphasizing the research on the nature, state, behavior of loess could contribute to the future mitigation of the loess geohazards. Nevertheless, incredible challenges on the loess geohazard need more attention following the abrupt extreme weather and the mega engineering project. Then, the following aspects are provided as references for loess geohazard mitigation.

1) Bridging multi-scale analysis to better understand the progress mechanisms of the loess geohazards. Here, microscopic characteristics benefit to explain the physical mechanisms, while mesoscopic or/and macroscopic behaviors prefer to predict the dynamical processes.
2) Building multiple physical field observation systems of loess geohazards to accurately early warning and precisely real-time forecast. Here, the combination of mechanism-driven and data-driven models should be given further attention to local and regional case studies.
3) Seeking eco-friendly and cost-effectively remediation materials and technologies for loess performance improvement and loess geohazard mitigation. Here, this probably requires more attention to the assessment framework in embodied energy and carbon dioxide emissions of ground improvement works to green, low-carbon, and sustainable development.

AUTHOR CONTRIBUTIONS

All authors listed have made a substantial, direct, and intellectual contribution to the work and approved it for publication.

FUNDING

This study was supported by the National Natural Science Foundation of China (No. 41927806), and the Fundamental Research Funds for the Central Universities (No. lzujbky-2021-ct04), and Education Science and Technology Innovation Project of Gansu Province (grant no. 2021A-008).

ACKNOWLEDGMENTS

We deeply thank all the authors and reviewers who have participated in this Research Topic.

REFERENCES

Derbyshire, E. (2001). Geological Hazards in Loess Terrain, with Particular Reference to the Loess Regions of China. *Earth-Science Rev.* 54, 231–260. doi:10.1016/s0012-8252(01)00050-2

Hu, X., Xue, L., Yu, Y., Guo, S., Cui, Y., Li, Y., et al. (2021). Remote Sensing Characterization of Mountain Excavation and City Construction in Loess Plateau. *Geophys. Res. Lett.* 48, e2021GL095230. doi:10.1029/2021gl095230

Juang, C. H., Dijkstra, T., Wasowski, J., and Meng, X. (2019). Loess Geohazards Research in China: Advances and Challenges for Mega Engineering Projects. *Eng. Geol.* 251, 1–10. doi:10.1016/j.enggeo.2019.01.019

Li, P., Qian, H., and Wu, J. (2014). Environment: Accelerate Research on Land Creation. *Nature* 510, 29–31. doi:10.1038/510029a

Lutenegger, A. J. (1988). Preface. *Eng. Geol.* 25, 101. doi:10.1016/0013-7952(88)90021-x

Peng, J., Qi, S., Williams, A., and Dijkstra, T. A. (2018). Preface to the Special Issue on "Loess Engineering Properties and Loess Geohazards". *Eng. Geol.* 236, 1–3. doi:10.1016/j.enggeo.2017.11.017

Zhang, F., Yan, B., Feng, X., Lan, H., Kang, C., Lin, X., et al. (2019). A Rapid Loess Mudflow Triggered by the Check Dam Failure in a Bulldoze Mountain Area, Lanzhou, China. *Landslides* 16, 1981–1992. doi:10.1007/s10346-019-01219-2

Conflict of Interest: The authors declare that the research was conducted in the absence of any commercial or financial relationships that could be construed as a potential conflict of interest.

frontiers in Earth Science

ORIGINAL RESEARCH
published: 20 September 2021
doi: 10.3389/feart.2021.744864

Creep Behavior of Intact Loess Followed Unloading Paths

Zhenxiao Li, Jiading Wang and Dengfei Zhang*

State Key Laboratory of Continental Dynamics, Department of Geology, Northwest University, Xi'an, China

Several high-fill projects are carried out on the Loess Plateau, China, accompanying the progressive failure of slopes due to excavation. The compelling need requires a deep understanding of variation in the creeping behaviors of intact loess exposed to unloading. A series of creep tests of intact loess were performed under two separated unloading paths: decrease in confining pressure at constant deviator stress and decrease in confining pressure at axial stress. The results demonstrated that axial deformation followed the first unloading path always appears as compression while the three forms of axial deformation followed the second path, depending on the applied axial stress level. At a low unloading stress level, the elongation of axial deformation was observed. At a relatively unloading stress level, the axial deformation of the soil experienced the first elongation and then compression. At a high unloading stress level, the axial deformation appeared as compression, and finally, failure occurred with the increase of the unloading stress level. The failure approach index was introduced to use as the criterion for the loess to transform from stable to accelerated creeping. Finally, a modified Burgers model was proposed to characterize the creeping behavior of intact loess followed unloading paths. There was a good comparison between the calculated and measured data of the soil that establishes the rationality and validity of the proposed model.

Keywords: creep behaviors, unloading paths, failure approach index, constitutive model, intact loess

OPEN ACCESS

Edited by:
Fanyu Zhang,
Lanzhou University, China

Reviewed by:
Zhiwei Zhou,
University of Chinese Academy of Sciences, China
Rubén Galindo,
Polytechnic University of Madrid, Spain

****Correspondence:***
Jiading Wang
wangjiading029@163.com

Specialty section:
This article was submitted to Geohazards and Georisks, a section of the journal Frontiers in Earth Science

Received: *21 July 2021*
Accepted: *25 August 2021*
Published: *20 September 2021*

Citation:
Li Z, Wang J and Zhang D (2021) Creep Behavior of Intact Loess Followed Unloading Paths. Front. Earth Sci. 9:744864. doi: 10.3389/feart.2021.744864

INTRODUCTION

In recent years, with the rapid economic development, many engineering construction activities have been carried out in the Loess Plateau area, accompanied by a large number of loess slopes subjected to excavation and high-fill projects. Due to the unique physical properties of loess, once improperly disposed of, engineering accidents and damage to the local ecological environment can quickly occur. When soils are subjected to long-term loading, creep deformation increases over time, posing a safety hazard to the actual project. Therefore, the study of creep deformation of loess has tremendous significance for the construction of loess projects. With the rapid development of economic construction, it is necessary to broaden its development space, and then the project of gully control and land construction has been carried out in Yan'an New Area, China. Yan'an New Area is divided into three parts: the North District, the East District, and the West District (**Figure 1**). The total amount of excavation and filling in the first phase of the construction project in the north district is 363×106 m^3, and the maximum filling height is 100 m. Due to the difference between the original loess on its sides and bottom and the compacted fill in the middle and upper part, the soil is very easy to produce deformation under the rainfall and long duration loading, which causes foundation deformation and uneven settlement. It is beneficial to alleviate the shortage of land reserve resources in the urban area and is also conducive to protecting the revolutionary sites in the

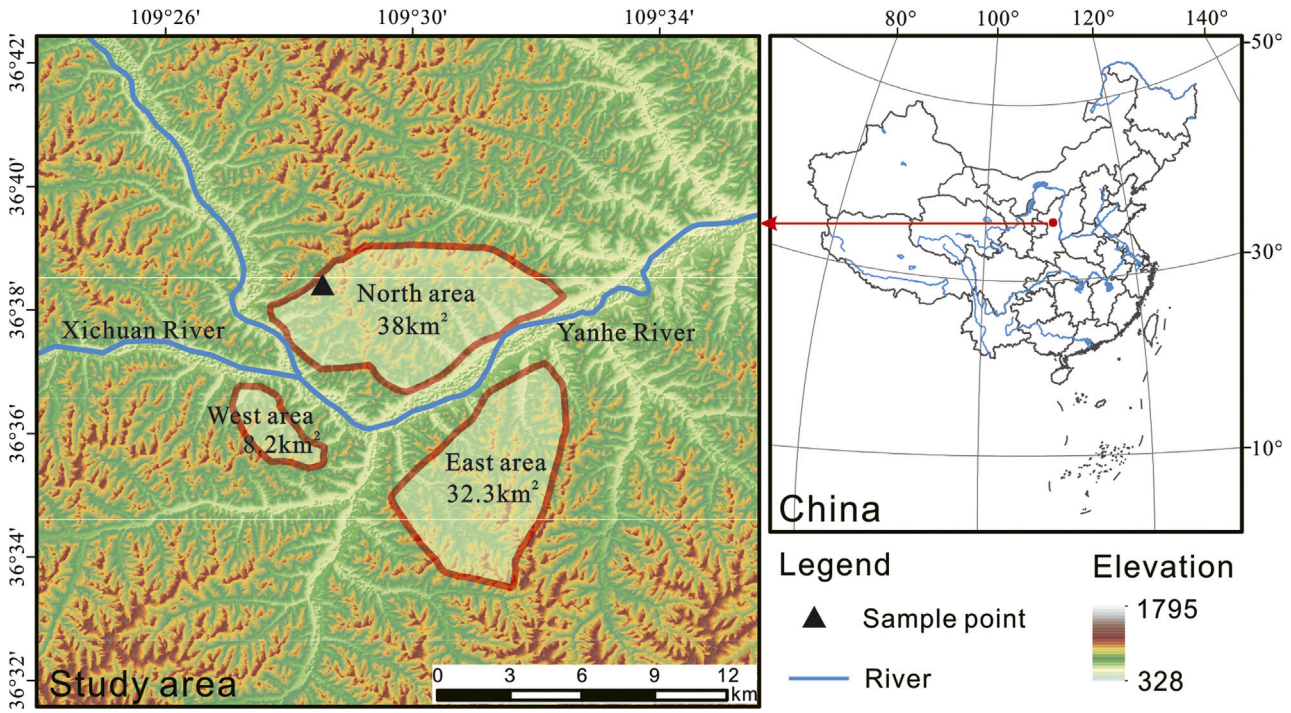

FIGURE 1 | Study area and location of soil samples.

old urban area, promoting the development of the tourism industry, stimulating the healthy and sustainable growth of the economy, and improving the living environment.

Yan'an City is located in the north-central part of the Loess Plateau and belongs to the hilly and gully area of the Loess Plateau. Quaternary Aeolian loess is exposed in the area, mainly loess hills and gullies. The terrain in the area is high in the west and low in the east, with some uplifts in the central part and relatively large ups and downs in the north relative to the south. The geomorphology can be divided into the valley stage area and the loess beam area according to the geomorphic unit. Landforms can be divided into river landforms and loess landforms according to their genesis, and loess landforms can be subdivided into loess erosion landforms, submerged landforms, gravity landforms, and accumulation landforms. Due to the uplift of the stratum (Late Pleistocene-Holocene) in the Loess Plateau, more water systems and valleys were formed, and the erosion effect of water flow (tracing erosion, lateral erosion, and down erosion) continued to reshape the landform, leading to forming a comprehensive landscape with undulating terrain and ravines.

The excavation process is also the unloading process of the soil, and its deformation characteristics have unique laws. The traditional soil mechanics theory uses conventional triaxial test (loading test) parameters to calculate the slope deformation. This stress path is completely different for the slope excavation unloading stress path and cannot truly reflect the unloading process of the slope excavation. For example, due to excavation, some parts of the surrounding stratum have stress relaxation and rebound deformation, while other parts have stress concentration and compression or shear deformation, which changes the pore density. Due to the complexity of the problem, the current experimental research and theoretical analysis on the deformation and failure mechanism of the soil under unloading are not perfect. Therefore, it is necessary to strengthen the research on the unloading characteristics of the soil, a more comprehensive understanding of the deformation and failure mechanism of the soil under unloading state, providing the theoretical basis and reasonable calculation parameters for the calculation of soil deformation under unloading.

During slope excavation, the stress paths of the soil at different parts of the slope are completely different. In order to correctly simulate the stress path in excavation engineering, several kinds of typical stress paths are abstracted from the soil at different parts of the slope during the excavation process, carrying out unloading tests that simulate the slope excavation process. And there are relatively few studies on the creep behavior of soil under the unloading path. For excavated slopes, the unloading path is more consistent with the actual working conditions, and the creep behavior of the soil under the unloading path should be studied. In order to accurately simulate the change of the soil stress path during the slope excavation process, the drainage conditions during the test must first be determined. The slope excavation project should adopt a fast excavation method, the water in the outer soil body will not be discharged, and it is approximately regarded as an undrained process.

Excavation of slope is a typical excavation unloading problem. In slope excavation, the soil will exhibit different mechanical properties when it goes through different unloading paths from the same stress state. Therefore, it is necessary to carry out a creep test of soil under different unloading stress paths. In recent years, through long-term monitoring of landslides and other data, most landslides have creeping behavior (Sasaki et al., 2000; Mansour et al., 2011; Di Maio et al., 2013, 2015; Wen and Jiang, 2017). As creep accumulates in the soil of the most sensitive slip zone of the landslide, it may eventually trigger a large-scale slip of the slope under the action of external factors (Pytharouli and Stiros, 2010). It is recognized that the recent human casualties and property damage in loess areas are closely related to the creep behavior of landslides (Sun et al., 2016; Palmer, 2017). The porous structure and well-developed vertical cracks of loess contribute to the unique creep properties of loess (Tan and Yang, 1988; Derbyshire, 2001; Zhang et al., 2014; Zhou et al., 2014; Peng et al., 2015; Xu and Coop, 2016; Xu et al., 2018). Many researchers have analyzed the creep behavior of soils. Xin et al. (2016) conducted a kinematic analysis of large-scale landslides on the Loess Plateau in Baoji, China, and concluded that creep movements in the slip zone predispose to landslides. Yates et al. (2018) conducted a statistical analysis of landslides caused by loess creep in Canterbury, New Zealand, and found that loess landslides with creep behavior are mainly controlled by the liquid behavior of saturated loess, potential failure surfaces, and seasonal wetting/drying cycles. Wang et al. (2020) analyzed the creep behavior of loess at different water contents and proposed a modified Burgers model that accurately describes the accelerated creep stage curves. Xie et al. (2018) found that the creep behavior of loess is closely related to microstructural changes. Among them, elemental models are widely used in loess soils. Zhou et al. (2016) conducted creep tests under different confining pressure and temperature conditions and established a rate-dependent constitutive model for frozen loess. Tang et al. (2020) conducted triaxial creep tests using a rheological triaxial test apparatus and proposed a dual-element creep model to describe the creep process of loess. Zhu et al. (2014) investigated the creep properties of red-layer slip zone soils under different vertical loading and water content conditions through direct shear creep tests. In addition, many scholars have also achieved many results in the experimental study of the creep behavior of different geotechnical materials (LO PRESTI, 1996; Gasc-Barbier et al., 2004; Fabre and Pellet, 2006; Wang et al., 2014, 2015; Ye et al., 2015; Yu et al., 2015; Zheng et al., 2015). Although scholars have studied the strength of loess extensively, research on the creep properties of loess has been relatively limited. The progress of creep test on loess is mainly based on loading principal stress in steps under constant confining pressure. There is rarely research on unloading confining pressure creep test under different stress paths, while for the actual engineering construction of filling and excavation process, the surrounding soil is in the state of cyclic unloading and loading relative to the stress state before mining.

The mechanical properties of soils under unloading stress paths from different perspectives have been analyzed. Li and Kong (2019) analyzed the creep properties of Nanyang expansive soil under different levels of deviator stress by unloading creep tests and proposed a nonlinear four-element model to describe the creep deformation of soil. Yang et al. (2020) conducted an undrained unloading test to analyze the effects of different unloading stress paths and unloading rates on the mechanical properties of the Tianjin blowing soil and proposed a prediction formula for soil damage strength considering these two factors. Mei et al. (2010) pointed out that the shear strength parameters of the soil under different unloading paths were significantly different. Zhen et al. (2008). analyzed the stress-strain curve of clay soil, based on triaxial unloading tests under K_0 consolidation undrained and pointed out that its initial tangential modulus is proportional to the soil consolidation perimeter pressure.

Furthermore, some researchers have also constructed creep models based on empirical, yielding surfaces, and damage effects (Sivasithamparam et al., 2015; Chang et al., 2020). For loess, creep models have been proposed, based on the results of triaxial creep tests and theoretical analysis (Li et al., 2011), and there are four creep models, including Cam–Clay model, Duncan–Chang model, Kelvin model, and Burgers model (Graham et al., 2001; Liu and Carter, 2002; Nguyen et al., 2011; Wan et al., 2011). Among these creep models, the Burgers model is widely used to describe the creep behavior of various rocks and soils due to its intuitive concept, clear parameters and physical implications, and simple calculations. However, in the Burgers model, the deformation of the loess followed unloading paths is generally not considered, and the compelling need requires a modified Burgers model to characterize the creeping behavior of the loess followed unloading paths.

The objectives of this work are to understand the creep behavior of intact loess followed the unloading path. The unloading creep tests with constant principal stress and deviator stress are carried out on undisturbed Malan loess. The creep deformation characteristics of the undisturbed Malan loess under the two stress paths were analyzed. The failure approach index was introduced to evaluate the degree of soil damage during the unloading creep test. An improved Burgers model was proposed by connecting a nonlinear dashpot element in series with the Burgers model and combining the functional relationship between the viscoelastic modulus and creep behavior.

Sample and Test Methods

Sample Preparation

The loess specimen was taken from the construction site of Yan'an New Area, which belongs to the late Pleistocene loess (Q_3, Malan loess), and the coordinates of the sampling point are N36°45′13.5″, E109°11′4.2″. To prevent the soil from being affected by the external environment (frost, rainfall, sunshine), excavate 0.5 m horizontally before sampling, and avoid disturbing the soil. After removal, soil samples were marked top-bottom, then quickly sealed by wrapping with cling film, and subsequently wrapped with bubble film to avoid soil disturbance during transportation. Soil samples were placed in a dry and ventilated place after being transported back to the room to avoid direct sunlight.

TABLE 1 | Physical and mechanical properties of soil in the study area.

Water content ω/%	Density ρ/(g/cm^3)	Specific gravity G_s	Liquid limit ω_L/%	Plastic limit ω_P/%	Cohesion c/kPa	Internal friction angle φ/(°)	Uniaxial tensile strength q_u/kPa
15.0	1.54	2.72	29.2	18.6	28.87	18.99	8.0

TABLE 2 | Loading and unloading programs.

Sample number	σ_1-σ_3/kPa	σ_3/kPa
UC-1	150	400→300→200→100→50→25
UC-2	125	400→300→200→100→50→25
UC-3	100	400→300→200→100→50→25→0
	σ_1/kPa	σ_3/kPa
UC-4	500	400→350→300→250→200→150
UC-5	450	400→350→300→250→200→150→125
UC-6	400	400→350→300→250→200→150→125
	σ_3/kPa	σ_1/kPa
LC-1	0	50→75→100→125
LC-2	100	200→250→300→350
LC-3	200	400→450→500→550→600→650→700

The liquid limit of the soil was 27.9%, and the plastic limit was 18.6%, as determined by the LG-100D combined liquid-plastic limit tester. Using the compaction test, the optimum moisture content and maximum dry density of loess in the study area were measured as 16.3% and 1.82 g/cm^3, respectively (**Table 1**).

Testing Programs

The three groups of the creep tests were performed by following unloading paths to investigate the creep behavior of intact loess. The first groups involved unloading the confining pressure in steps with constant deviator stress. The mean net stress is $(\sigma_1 + 2\sigma_3)/3$, deviator stress is $\sigma_1-\sigma_3$, σ_1 is principal stress, and $\sigma_3$is confining pressure. The test results were used to investigate the creep characteristics under unloading the confining pressure in steps. the unloading creep samples were identified as UC-X. Therefore, three intact specimens (UC-1, UC-2, and UC-3) are kept under different constant deviator stress ($\sigma_1-\sigma_3$=150, 125, and 100 kPa) and carry out the creep test under the same unloading path. The stress paths of UC1-3 are shown in **Table 2**. Meanwhile, the relationship of mean net stress and deviator stress are shown in **Figure 2A**. For the second experiment, three intact specimens (UC-4, UC-5, and UC-6) are kept under different constant principal stress (σ_1=500, 450, and 400 kPa) through the same unloading confining pressure in steps to investigate creep characteristics of intact loess with constant principal stress. The third test is comparative, the loading creep samples were identified as LC-X, and three intact specimens (LC-1, LC-2, and LC-3) are kept under different constant confining pressure (σ_3=0, 100, and 200 kPa), loading the principal pressure in steps, used to compare with the former two sets of unloading path experiments and compare the loading and unloading of two different types of stress paths creep deformation characteristics. The stress paths of LC-1–3 are shown in **Table 2**.

Testing Method

The equipment selected for this creep test is the FSR-20 triaxial creep meter for unsaturated soil. The instrument mainly consists of a pressurization system, data acquisition system, and air compressor. The maximum axial load that the equipment can provide is 2,000 kPa, the maximum pore air pressure is 500kPa, the maximum axial deformation that can be measured is 18 mm,

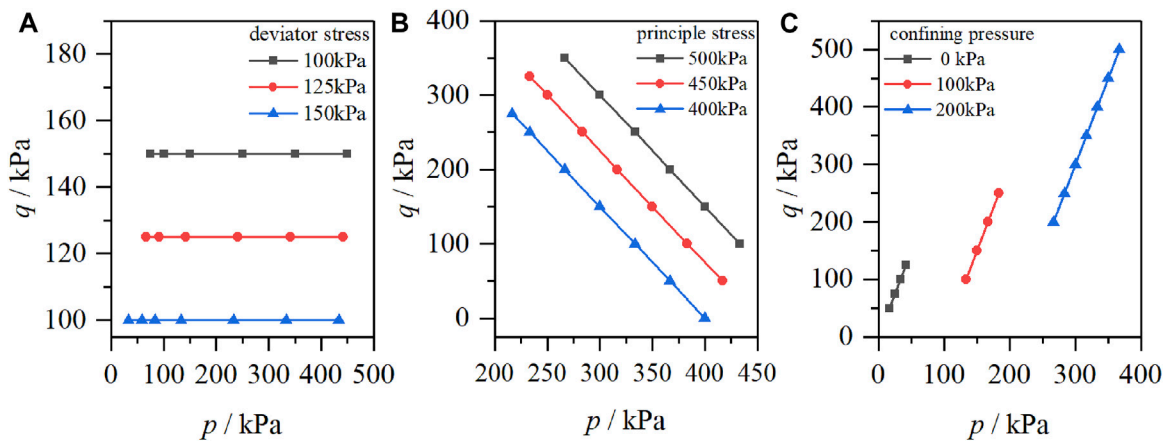

FIGURE 2 | Stress path of the testing program.

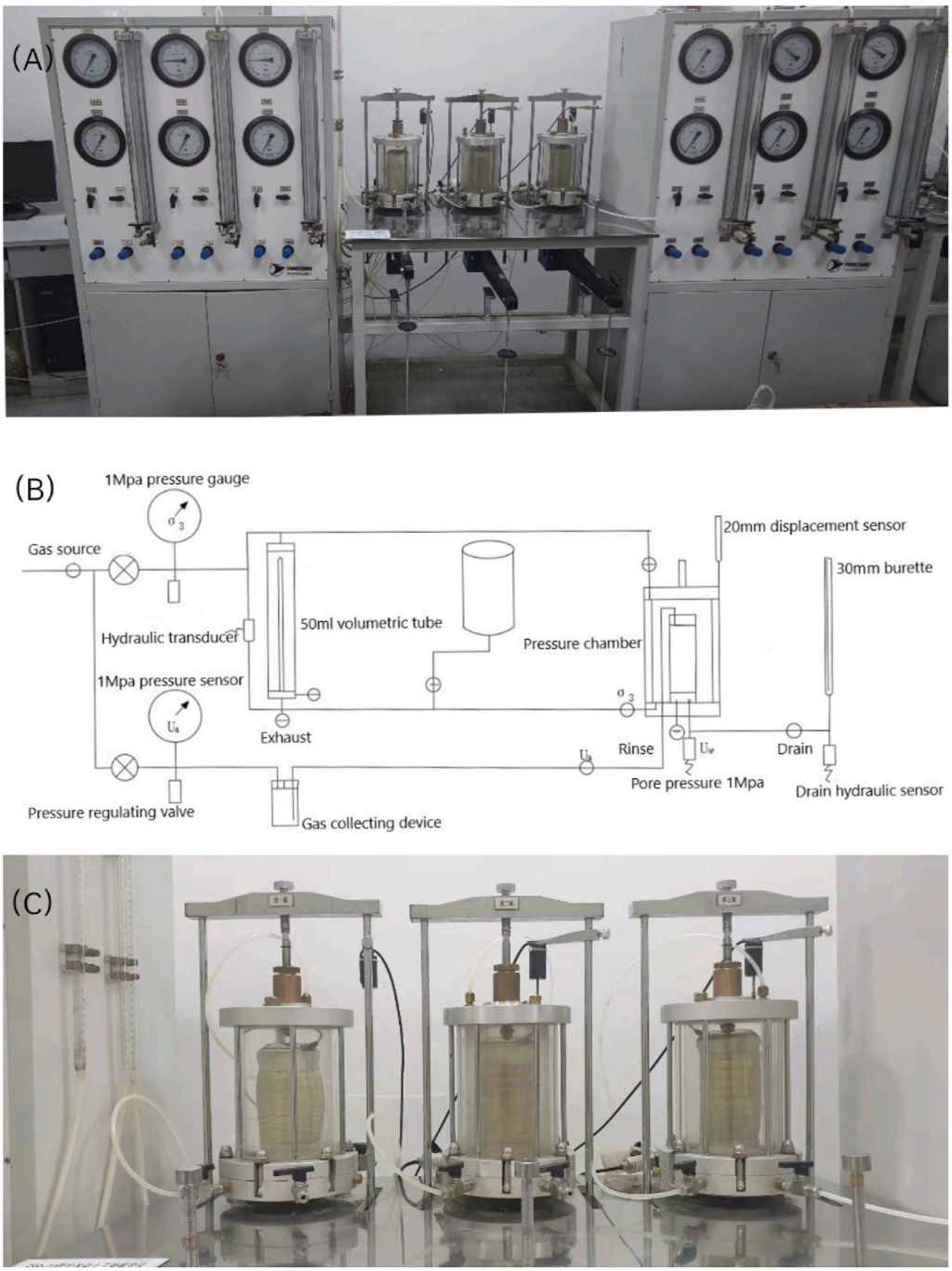

FIGURE 3 | (A) FSR-20 Unsaturated Soil Triaxial Creep Apparatus. **(B)** Schematic diagram of creep apparatus. **(C)** Creep experiment.

and the volume deformation is 50 cm^3. For the preparation of undisturbed loess triaxial creep type samples: take out the cling film-wrapped loess original soil sample, determine the upper and lower position of the soil sample, cut it flat and place it in the triaxial chipper, and cut the soil sample into a cylinder of 61.8 mm diameter (**Figure 3**).

The unloading stress path of slope excavation can be generally simplified into three paths (**Figure 4**). The first unloading path is the stretching path, and it can be considered that the horizontal load decreases while the vertical load remains unchanged under the limit condition; the second unloading path is a triaxial shearing path, which shows that the horizontal and vertical loads are unloaded at the same time, and it can be considered that the partial stress remains unloaded under the limit condition; the third unloading path is the direct shearing path, which corresponds to the bottom area in **Figure 4** and can be

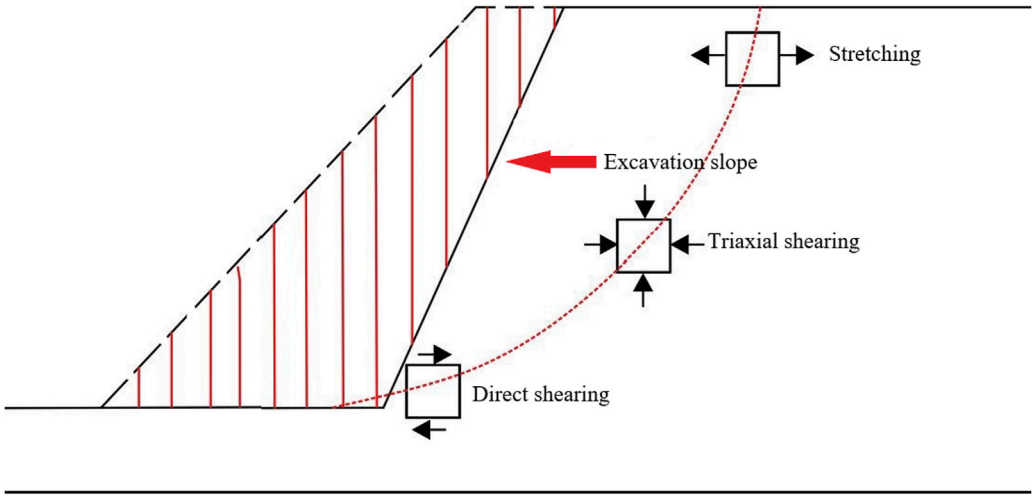

FIGURE 4 | Sketch map of unloading stress paths.

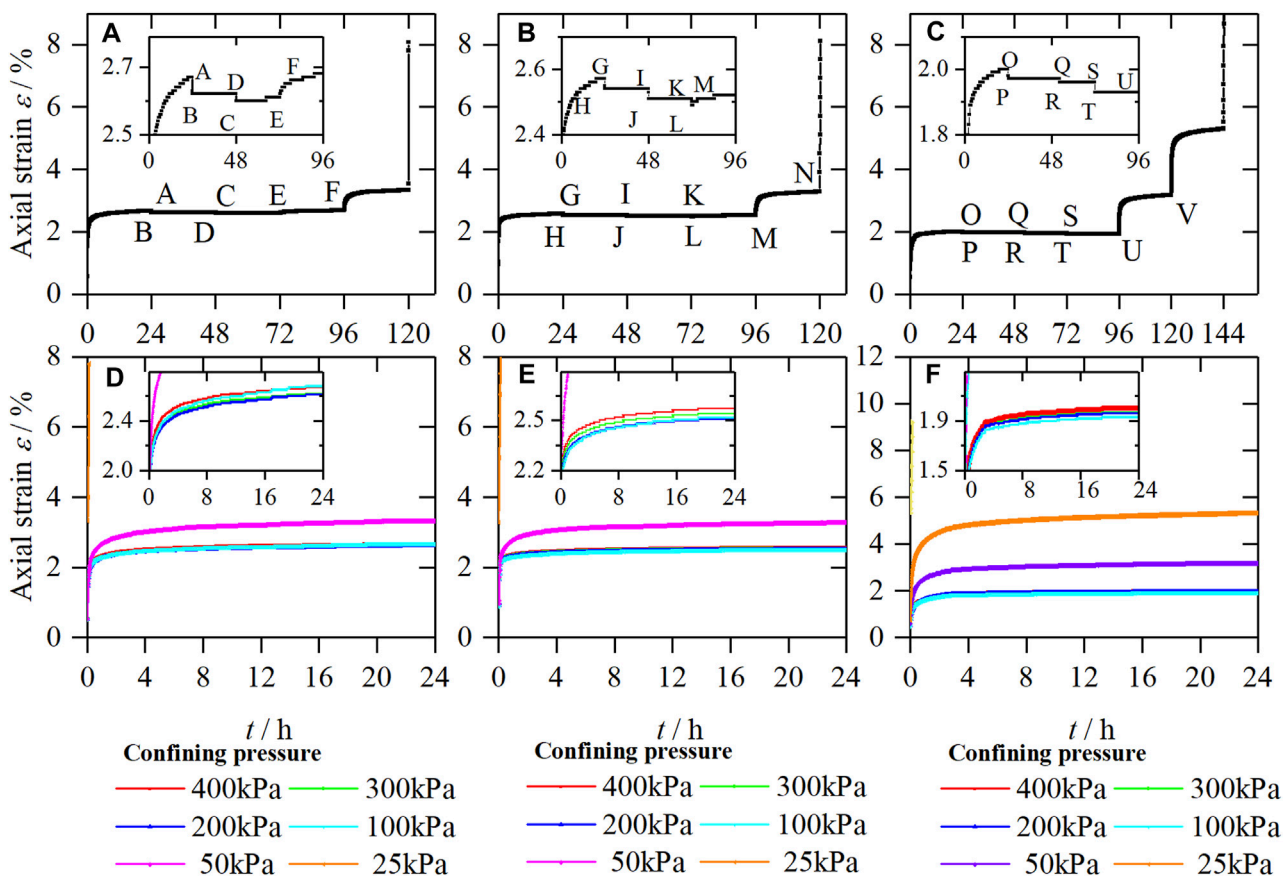

FIGURE 5 | Strain-time curves of samples, **(A)** UC-1, **(B)** UC-2, **(C)** UC-3, and creep curves of samples, **(D)** UC-1, **(E)** UC-2, **(F)** UC-3.

considered as vertical unloading and transverse unloading. Comprehensive existing research, most of the current research on unloading characteristics is based on direct shearing path, and the reduction of vertical load while the lateral load remains unchanged generally does not cause damage to the soil, so this article focuses on zone stretching and triaxial shearing path.

Testing Results

Unloading the Confining Pressure in Steps With Constant Deviator Stress

Assuming that the soil is mainly deformed in elasticity at the beginning of unloading, the deformation law of the axial strain of the soil during the unloading process can be analyzed according to the linear elasticity theory. For the first type of triaxial creep test with constant deviator stress, the axial strain ε_1 of the soil can be expressed by **Eq. 1**:

$$\boldsymbol{\varepsilon}_1 = \frac{1}{\boldsymbol{E}}\left[\boldsymbol{\sigma}_1 - 2\boldsymbol{\mu}\boldsymbol{\sigma}_3\right] = \frac{1}{\boldsymbol{E}}\left[(\boldsymbol{\sigma}_1 - \boldsymbol{\sigma}_3) + (1 - 2\boldsymbol{\mu})\boldsymbol{\sigma}_3\right]. \quad (1)$$

According to the generalized Hooke's law, as the unloading stress level increases (the confining pressure σ_3 decreases), the axial strain will decreases (shown as axial elongation), expressed as the way of change of section AB and section DC in **Figure 5A**.

Figures 5A–C show the strain-time curves of deviator stress under the control of 150, 125, and 100 kPa, respectively. **Figures 5D–F** are obtained according to the Boltzmann superposition principle. As can be seen from **Figure 4**, the axial strain variation of unloading confining pressure in steps under different deviator stresses is similar, which is manifested in three forms of deformation. As shown in **Figures 5A,D**, the variation of axial strain is slight at the initial unloading stage, the confining pressure is gradually unloaded from 400 kPa to 300 kPa, and the axial strain decreases (shown as axial elongation, corresponding to the ABD section in **Figure 5A**, which is the same as the above analysis results based on the generalized Hooke's law. When the confining pressure is unloaded from 300 kPa to 200 kPa, the axial strain decreases at the moment of unloading (shown as axial elongation) and gradually increases over time (axial compression, corresponding to the DCE section in **Figure 5A**). When the confining pressure is unloaded from 100 kPa to 50 kPa, the axial strain increases significantly (shown as axial compression, corresponding to the EF section in **Figure 5A**), and noticeable creep occurs. With the further increase of unloading stress level, the soil samples show an accelerated creep stage, and the soil is damaged.

By comparing **Figures 5A–C**, it can be seen that the unloading stress points of soil under the above three deformation forms are different under different deviator stresses. The curve segments ABD, GHIJK, and OPQRSTU showed axial elongation deformation; the curve segments DCE and KLM showed axial elongation deformation followed by axial compression deformation; and the curve segments EF, MN, and UV showed axial compression deformation. When the deviator stress is 100 kPa, the second deformation form does not appear, and the axial elongation deformation is directly transformed into axial compression deformation.

The reason for the above phenomenon is that, at the initial stage of unloading the confining pressure, the soil can be considered to be in an elastic deformation stage, which corresponds to the first deformation form (axial extension) mentioned above; as the level of unloading stress increases, tiny cracks appear inside the soil, and the deformation of the soil gradually changes from elastic deformation to plastic deformation, which corresponds to the second form of deformation (first axial extension and then axial compression); with the further increase of the unloading stress level, the internal micro-cracks of the soil are penetrated, and the deformation of the soil is mainly plastic deformation, which corresponds to the third form of deformation (axial compression).

Unloading the Confining Pressure in Steps With Constant Principal Stress

Refer to the analysis in the previous section, assuming that the soil is mainly elastically deformed in the initial stage of unloading, so the deformation law of the axial strain of the soil during the unloading confining pressure can be analyzed according to the linear elasticity theory. For the second type of triaxial creep test with constant principal stress, the axial strain ε_1 of the soil can be expressed by **Eq. 2**:

$$\boldsymbol{\varepsilon}_1 = \frac{1}{\boldsymbol{E}}\left[\boldsymbol{\sigma}_1 - 2\boldsymbol{\mu}\boldsymbol{\sigma}_3\right] \quad (2)$$

According to the generalized Hooke's law, as the unloading stress level increases (the confining pressure decreases), the axial strain increases (shown as axial compression).

Figures 6A–C show the strain-time curves when the first principal stress is controlled at 500kPa, 450 kPa, and 400 kPa, respectively. **Figures 6D,E,F** are obtained according to the Boltzmann superposition principle. It can be seen from **Figure 6** that the axial strain of the unloading confining pressure under different σ_1 conditions is similar. With the increase of the unloading confining pressure stress level, the axial strain of the soil gradually increases, which is the same as the above analysis results based on the generalized Hooke's law. In AC, GJ and NP sections, the increase of deformation within 24 h is same, showing a linear characteristic of $\Delta\varepsilon$ and $\Delta\sigma_3$ when unloading the same confining pressure, while in CF, JM and PS sections, the increase of deformation within 24 h is obviously increased when unloading the same confining pressure. The characteristics of $\Delta\varepsilon$ and $\Delta\sigma_3$ are nonlinear. It shows that the creep deformation of soil changes from elastic to plastic with the increase of unloading stress level.

Analyzing the above reasons, it can be seen that removing the confining pressure σ_3 while maintaining σ_1 is equivalent to imposing tensile stress σ_3 on the basis of the original stress conditions (shown as a decrease in confining pressure). This situation is likely to cause tensile fractures in the soil along the confining pressure direction, which is macroscopically manifested as axial compression and lateral bulging of the soil. At the initial stage of unloading confining pressure, it can be approximately considered that the soil is in an elastic deformation stage. As the stress level of unloading confining pressure increases, the internal damage of the soil continues to accumulate. When it develops to a certain degree, the internal micro-cracks of the soil can penetrate, soil deformation changes from mainly elastic deformation to

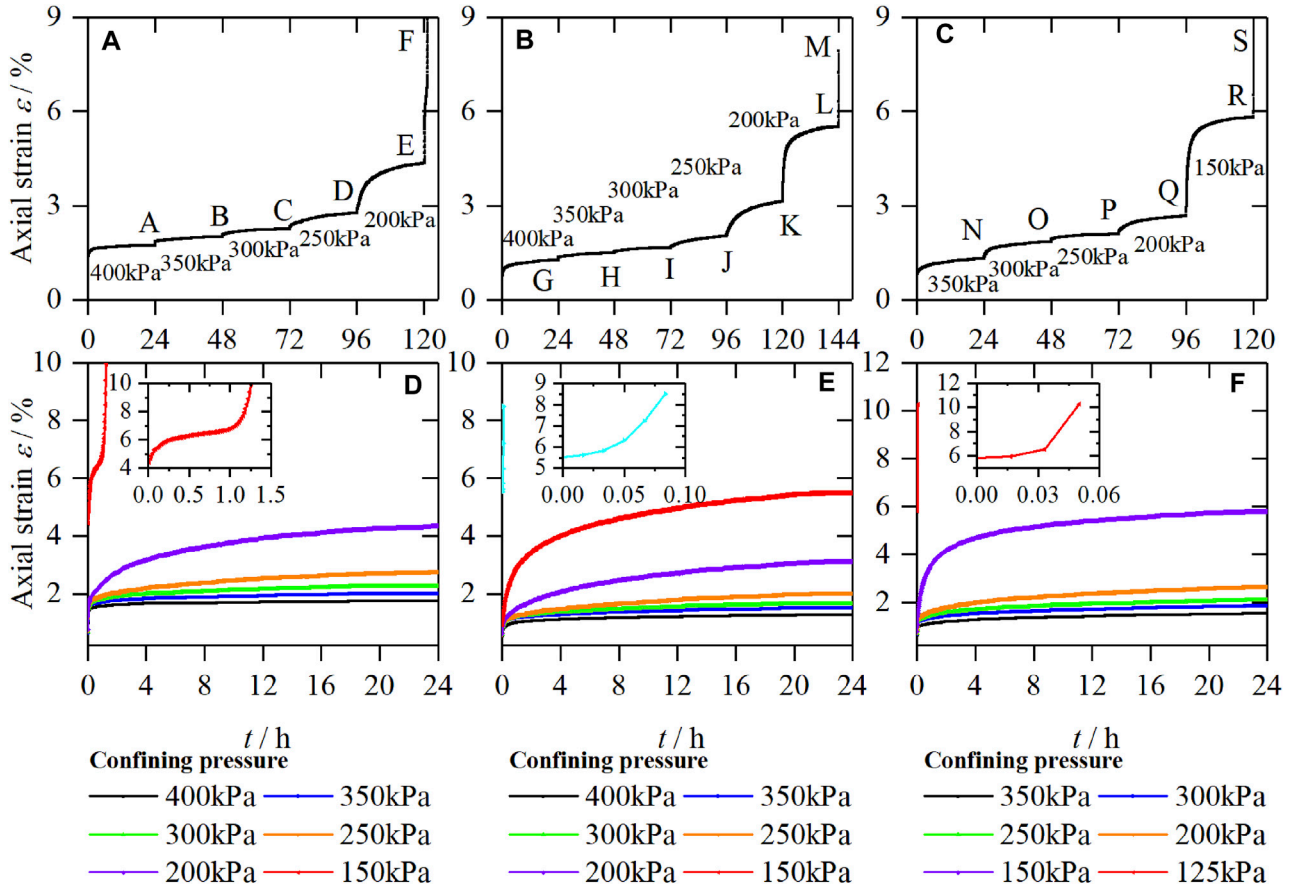

FIGURE 6 | Strain-time curves of samples, **(A)** UC-4 **(B)** UC-5, **(C)** UC-6, and creep curves of samples, **(D)** UC-4, **(E)** UC-5, **(F)** UC-6.

mainly plastic deformation, deformation increases rapidly, and when the deformation accumulates to a certain level, soil damage occurs.

Loading the Principal Pressure in Steps With Constant confining Pressure

Under different confining pressures and different deviator stress, the creep curves of loess all show prominent creep deformation characteristics: first is instantaneous deformation, then deformation at the decaying creep stage, and the deformation at the stable creep stage. The loess is dominated by instantaneous deformation under the deficient deviator stress level (generally the first deviator stress level). The instantaneous deformation of the soil occurs at the moment of loading, and with the increase of time, a tiny creep deformation occurs. With the increase of time, the creep deformation rate gradually decreases, and approaching zero, the creep curve shows the decay type. Under a higher deviator stress level, the loess first produces instantaneous deformation. As time increases, its creep deformation rate decreases, gradually approaching a specific value greater than zero, and the creep curve presents a steady flow type. Under high deviator stress levels, the deformation rate of loess increases rapidly, and the soil is damaged. Under the same confining pressure, the greater the deviator stress, the greater the instantaneous deformation of loess, the more severe the creep deformation, and the more significant the creep effect. Increasing deviator stress under constant confining pressure, referring to the analysis in the former section, and assuming that the soil is predominantly deformed elastically at the beginning of loading, the deformation pattern of the axial strain in the soil during the increase of the first principal stress can be analyzed according to the theory of linear elasticity (**Figure 7**).

RESULTS ANALYSIS

By analyzing the test curves, when keeping the principal stress and the deviator stress constant, the creep test law of soil unloading confining pressure is different. Unloading the confining pressure in steps with constant principal stress, the axial deformation shows an increasing trend (manifested as axial compression). Unloading the confining pressure in steps with constant deviator stress, when the unloading stress level is low, the axial deformation will show a decreasing trend (shown as axial elongation); while the unloading stress level is high, it will first decrease and then increase (shown as the first axial

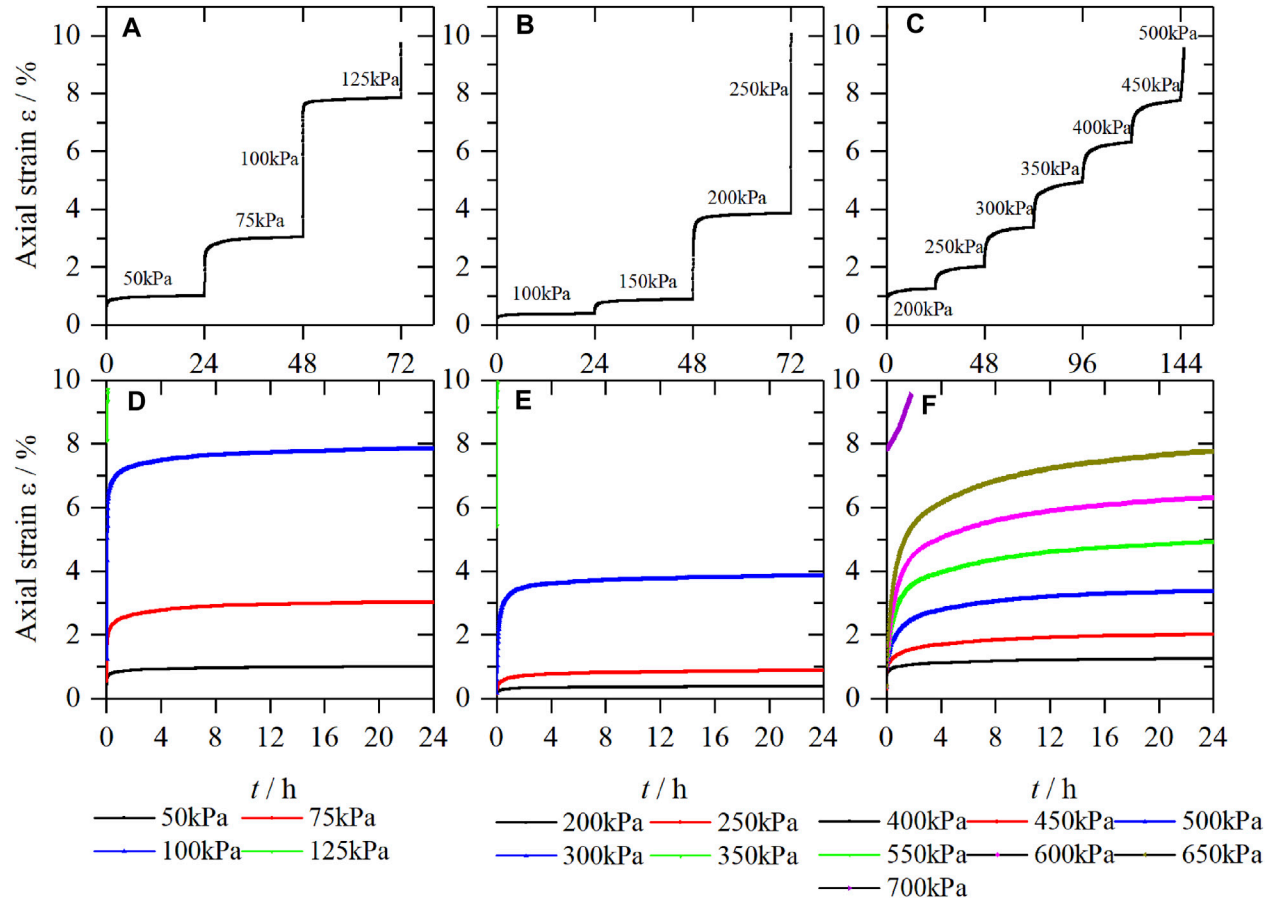

FIGURE 7 | Strain-time curves of samples, **(A)** LC-1 **(B)** LC-2, **(C)** LC-3, and creep curves of samples, **(D)** LC-1, **(E)** LC-2, **(F)** LC-3.

elongation and then axial compression). When the loading stress level is higher, it shows an increasing trend (shown as axial compression).

Both unloading methods will damage the soil, but their stress paths are not the same. Unloading the confining pressure in steps with constant principal stress, the axial deformation of the soil has been increasing and the change rule is obvious, which is suitable for studying the unloading creep characteristics of the soil. Unloading the confining pressure in steps while keeping the deviator stress constant, according to the different unloading levels, the variation law of axial deformation presents three forms. The transition stress state points of the first deformation form (axial elongation) and the second deformation form (axial elongation followed by axial compression) can be used to distinguish the elastic deformation from the plastic deformation.

In order to describe the dangerous degree of the stress state of the soil under different stress loading paths, this article analyzes the damage proximity based on the Mohr-Coulomb strength criterion, where the parameters are as shown in **Eqs 5–9**:

$$R = Min\left(\frac{d_1}{D_1}, \frac{d_2}{D_2}\right), \tag{3}$$

$$D_1 = \frac{\frac{1}{2}(\sigma_1 + \sigma_3)tan\varphi + c}{\sqrt{tan^2\varphi + 1}}, \tag{4}$$

$$d_1 = \frac{\frac{1}{2}(\sigma_1 + \sigma_3)tan\varphi + c}{\sqrt{tan^2\varphi + 1}} - \frac{\sigma_1 - \sigma_3}{2}, \tag{5}$$

$$D_2 = \sigma_L + \frac{\sigma_1 + \sigma_3}{2}, \tag{6}$$

$$d_2 = \sigma_L + \sigma_3. \tag{7}$$

The failure approach index R refers to the state function of soil material damage, and its value range is (0, 1). When R=0, the stress point is on the yield surface, and the soil yields; when R=1, the stress point is in a three-dimensional isostatic stress state, which is relatively safe.

The creep test curves of UC-1, UC-2, and UC-3 are analyzed by the failure approach index. **Figure 8A** shows the failure approach analysis of each soil sample under different stress states. Comparing **Figure 5** and **Figure 8A**, it can be seen that when R > 0.4, unloading the confining pressure in steps while keeping the deviator stress constant will only cause the soil to

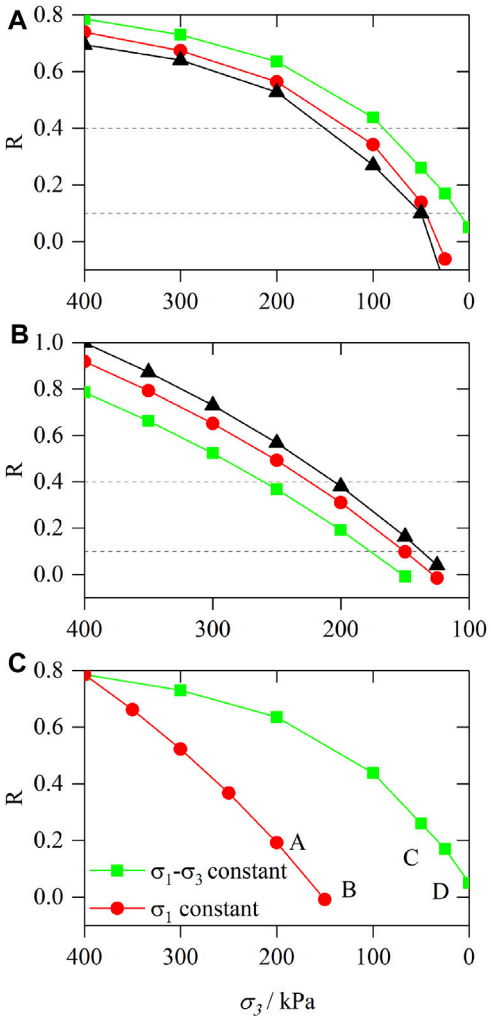

FIGURE 8 | (A) Comparison of R under different deviator stress. **(B)** Comparison of R under different principal stress. **(C)** Comparison of R in different stress paths.

produce axial tension; when 0.1 < R < 0.4, the soil has obvious creep deformation; when R < 0.1, the soil has an accelerated creep stage, the axial deformation of the soil increases rapidly, and the soil is damaged. Similarly, the creep test curves of UC-4, UC-5, and UC-6 are analyzed by the failure approach index. Comparing **Figure 6** and **Figure 8B**, it can be seen that when R > 0.4, the confining pressure is removed while principal stress remains unchanged, and only a small axial deformation is generated in the soil. When 0.1 < R < 0.4, the axial deformation of soil increases obviously. When R < 0.1, the soil shows accelerated creep stage.

Based on the above analysis, it can be seen that when R < 0.4, the soil gradually changes from elastic deformation to plastic deformation; when R < 0.1, the soil enters the accelerated creep stage. Therefore, the failure approach index R = 0.4 can be used as the critical value to distinguish between elastic deformation and plastic deformation; use R = 0.1 as the critical value to distinguish the stable creep stage and accelerated creep stage of the soil.

DISCUSSION

This study found that the creep characteristics of soil are different under different stress paths. When principal stress is constant, the deviator stress increases gradually under unloading confining pressure, and the soil exhibits prominent creep characteristics, which is consistent with the creep behavior of soil under the stress path of increasing deviator stress in steps when confining pressure is constant; however, when deviator stress is constant, the soil exhibits different creep characteristics under unloading confining pressure. The reason is that when the unloading stress level is low, the stress state of the soil is far away from the Mohr-Coulomb failure surface. At this time, the application of deviator stress only causes the relative dislocation among the soil particles, and the internal structure of the soil is reorganized and balanced, so when the unloading stress is low, the soil only shows axial elongation; with the increase of the unloading stress, the stress state of the soil gradually approaches the Mohr-Coulomb failure surface. At this time, the lateral limit of the soil decreases, and the soil particles are easy to move around, resulting in tiny cracks in the soil. The macroscopic performance is lateral swelling and axial compression, so when the unloading stress is high, the soil will be firstly elongated and then compressed. With the further increase of the unloading stress level, the internal cracks of the soil are penetrated, and the axial deformation rapidly increases, which leads to the destruction of the soil. Therefore, when the unloading stress level is higher, the soil directly shows axial compression.

With the gradual increase of the axial strain caused by unloading, it is accompanied by the adjustment of the soil structure. Microcracks are weak structural planes in loess, and the unloading effect causes loess to have a tendency to expand along the cracks, and the cracked planes are softened, resulting in a certain deformation of the soil along with the cracked planes, and serious damage to the integrity of the soil sample. Under the same axial strain, the existence of cracks magnifies the unloading damage effect at the same axial strain. In the same way, When the principal stress remains and unloading the confining pressure, due to the simultaneous axial and radial action, microcrack generation and expansion are stronger than other stress paths, and damage and degradation effects are relatively enhanced.

Figure 8C shows the comparison of the closeness of soil damage under two stress paths ($\sigma_1 - \sigma_3$=100 kPa, σ_3=400 kPa under unloading confining pressure stress path and σ_1=500 kPa, σ_3=400 kPa under unloading confining pressure stress path), when the principal stress σ_1 and the deviator stress $\sigma_1 - \sigma_3$ are kept constant, the failure approach index R gradually approaches 0; as the confining pressure decreases, it will gradually approach the yield surface. When the initial confining pressure is equal to the unloading confining pressure, the failure approach index R of unloading confining pressure when the principal stress σ_1 is constant is smaller than that when the deviator stress $\sigma_1 - \sigma_3$ is constant, indicating that the unloading confining pressure path when σ_1 is constant can lead to soil sample failure more quickly. It shows that, in the actual slope engineering, the soil pressure value under this stress path is close to the active soil pressure under the condition of small lateral deformation. If the horizontal displacement of the retaining wall cannot be effectively controlled, this part of the soil is easy to appear Slip damage.

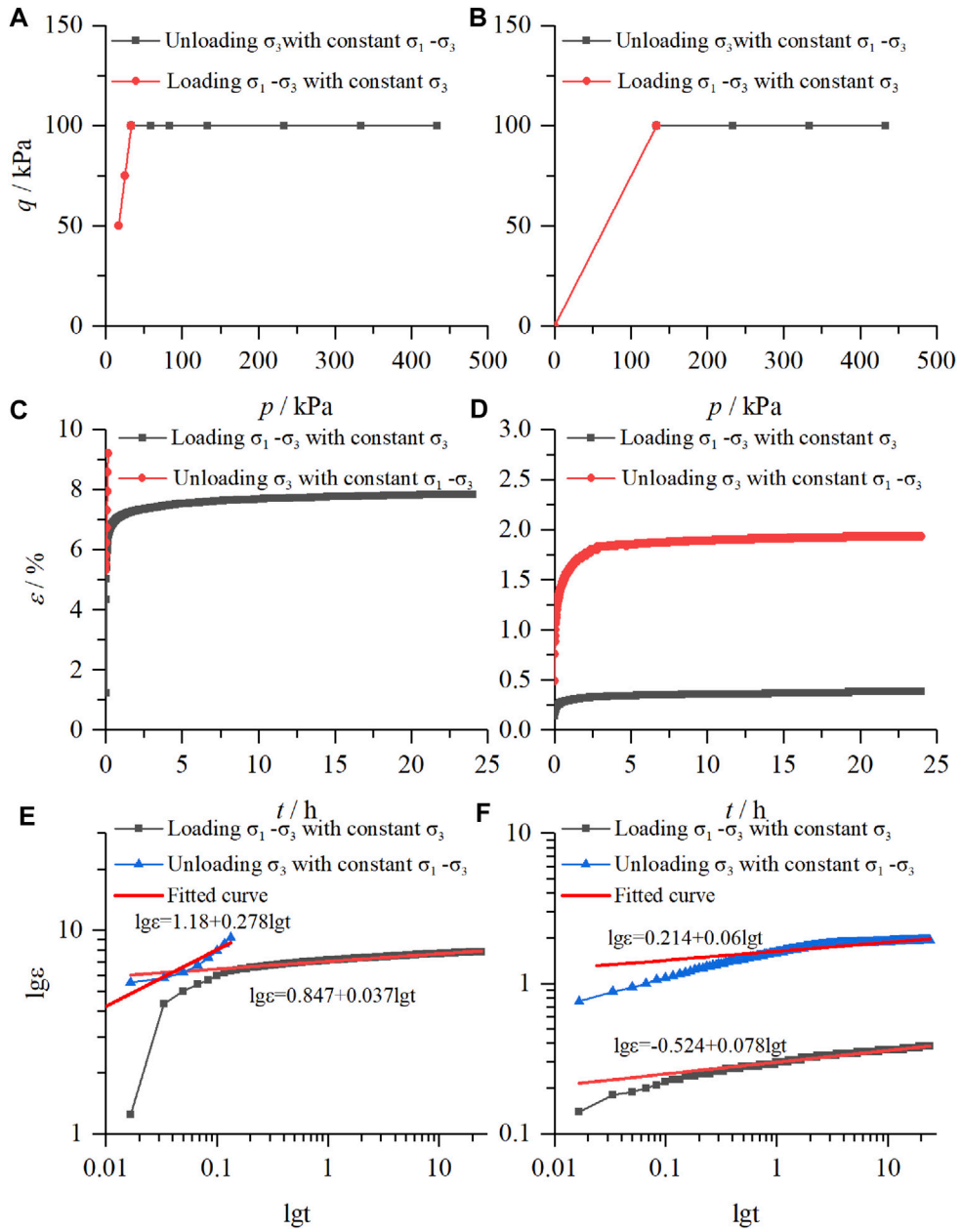

FIGURE 9 | Comparison of unloading the confining pressure in steps with constant deviator stress and loading the deviator stress in steps with constant confining pressure, **(A) (B)** the relationship of mean net stress and deviator stress, **(C) (D)** strain-time curves, **(E) (F)** double logarithmic curves of strain time.

The path of unloading confining pressure stress with constant principal stress can be considered as stepwise increasing deviator stress is superimposed on the stress path of unloading confining pressure with constant deviator stress, and the removed confining pressure $\Delta\sigma_3$=50 kPa is equal to the additional applied deviator stress $\Delta\sigma_1 - \sigma_3$=50 kPa; UC-3 stress path is superimposed on UC-4 stress path, which further indicates that the unloading confining pressure path can lead to soil sample failure more quickly when σ_1 is constant. The additional applied deviator stress $\Delta\sigma_1 - \sigma_3$=50 kPa has a more significant impact on the axial deformation than the unloaded confining pressure $\Delta\sigma_3$=50 kPa, so when σ_1 is constant, the stress path of the progressively unloaded confining pressure always shows axial compression.

Comparative Analysis of Different Stress Paths for Loading

The loading and unloading experiments under different stress paths are unloading the confining pressure with constant deviator stress and loading the deviator stress with constant confining

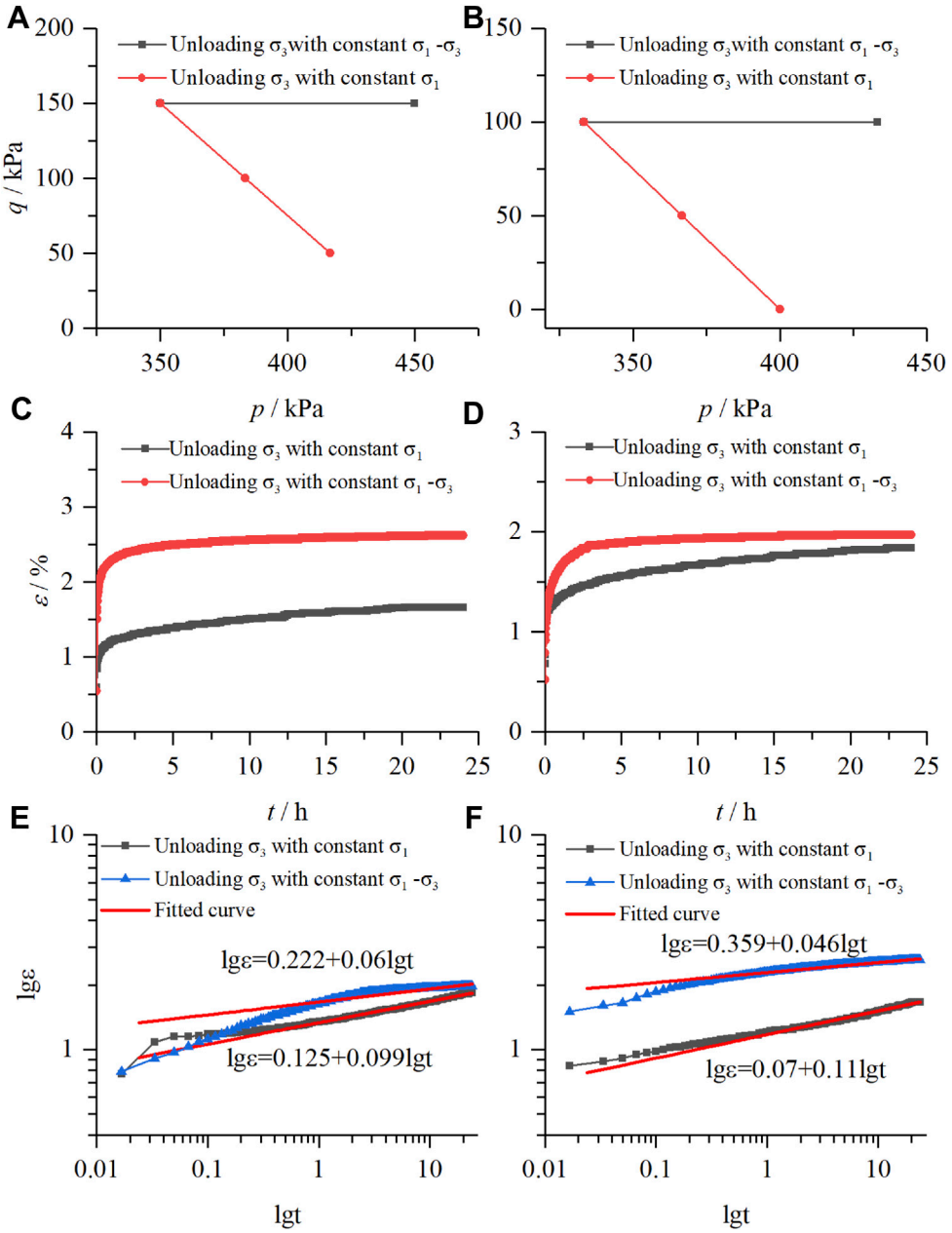

FIGURE 10 | Comparison of unloading the confining pressure in steps with constant deviator stress and unloading the confining pressure in steps with constant principal stress, **(A) (B)** the relationship of mean net stress and deviator stress, **(C) (D)** strain-time curves, **(E) (F)** double logarithmic curves of strain time.

stress. Align the following three comparisons: the relationship of mean net stress and deviator stress, strain-time curves, and double logarithmic curves of strain time. Observe the law of curve change and draw the following conclusions.

Comparing the curves under different stress paths, it can be seen that the strain-time curve is obviously non-linear; the shape of the curve is roughly similar before the soil is damaged, showing an attenuation stable type (hyperbolic type). From the strain-time diagrams of the two stress paths when the soil sample reaches the confining pressure of 0 kPa and the axial pressure of 100 kPa (**Figures 8E**, **9C**), it can be seen that unloading the confining pressure in steps with constant deviator pressure will destroy first compared to loading deviator pressure in steps with constant confining pressure. Meanwhile, from the strain-time diagrams of the two stress paths when the soil sample reaches the confining pressure of 400 kPa and the deviator stress of 100 kPa (**Figures 8F**, **9D**, it can be seen that loading the axial pressure with constant confining pressure will cause more deformation. This is because the soil has accumulated a certain deformation in the case of deviator pressure of 100 kPa and confining pressure of 400 kPa. It

shows that in the stress path of unloading the confining pressure with constant deviator stress, the deformation is not as obvious as in the stress path of increasing the deviator pressure with constant confining pressure, due to the accumulation of internal damage, loading (unloading) to the same stress state, and unloading the confining pressure state of the soil damage required for the minor deviator stress.

Meanwhile, use the same method to compare the unloading experiments of the following two stress paths: unloading the confining pressure with constant deviator stress and principal stress. The following conclusions can be drawn from comparing the relationship of mean net stress and deviator stress, strain-time curves, and double logarithmic curves of strain time.

Form the strain-time diagrams of the two stress paths when the soil sample reaches the confining pressure of 300kPa and the principal stress of 450 kPa (**Figures 9E**, **10C**, the curve shows that the deformation of unloading confining pressure with constant deviator stress is immense; meanwhile, the following steady-state creep rate is low, it is due to the fact that the unloading confining pressure with constant deviator stress has accumulated a certain amount of deformation in the initial state, and the creep deformation is evident in this case. The curves (**Figures 9F**, **10D**) reach another final stress via the same stress path (σ_3=300 kPa σ_1=400 kPa) showing similar results; unloading the confining pressure in steps with constant deviator stress has large deformation. Meanwhile, it has a lower steady-state creep rate.

Constitutive Model

Analysis of the results of the unloading confining pressure in steps creeping test with constant principal stress shows the following:

1) At each stress level, the soil sample produces instantaneous strain, and the value increases with enhancing the unloading stress level.
2) When the unloading level is low, the soil sample goes through the decay creep phase and the stable creep phase (its stable creep rate is close to 0).
3) When the unloading stress level is high, the soil goes through the decay creep phase and the stabilization creep phase and then enters the accelerated creep phase; eventually, the soil is destroyed.

The complete creep curve of soil sample includes decay creep phase, stable creep phase, and accelerated creep phase; Burgers model can describe the decay creep phase and stable creep phase of soil well. However, because the elements in the Burgers model are linear elements, the accelerated creep phase of the soil cannot be described. The whole process of creep deformation is the process of gradual cracking and damage accumulation inside the soil until the crack propagation is destroyed. Therefore, a parameter can be introduced to characterize the microstructure change of the soil due to irreversible deformation until failure. Considering that the stress-strain relationship often loses its one-to-one correspondence after the soil enters the nonlinear characteristic, and the creep deformation of the soil is irreversible, the strain parameter can be chosen to indicate whether the soil enters the accelerated creep phase and a nonlinear accelerated dashpot Liu et al. (2018) is introduced to describe the deformation of the soil in the accelerated creep phase, as shown in **Figure 11A**. The stress-triggered means, the nonlinear viscous pot is rigid when the strain generated by the model is less than ε_t, and the pot does not function at this time; the nonlinear viscous pot is triggered when the model generates the strain more significant than ε_t. Let η_{nl} be the viscosity coefficient of the nonlinear accelerated viscous pot, and define the intrinsic relationship of the nonlinear viscous pot as

$$\begin{cases} \sigma = \dfrac{\eta_{nl}\dot{\varepsilon}_{nl}}{nt^{n-1}} & (\varepsilon \geq \varepsilon_t) \\ \varepsilon_{nl} = 0 & (\varepsilon < \varepsilon_t) \end{cases}, \tag{8}$$

where η_{nl} is the viscosity coefficient of the nonlinear accelerated viscous pot, t is time, and n is the rheological coefficient.

Based on the previous analysis on the failure approach index of soil, when R < 0.1, the soil enters the accelerated creep stage. Therefore, classify whether the soil enters the accelerated creep stage according to R.

Based on the above analysis, the improved Burgers component model for the loading creep process of the high-fill loess in this area is shown in **Figure 11B**, and the total strain and differential form of the constitutive equation of this model can be expressed as follows:

1) when $R \geq 0.1$, $\varepsilon < \varepsilon_t, \varepsilon(t) = \varepsilon_e(t) + \varepsilon_v(t) + \varepsilon_{ve}(t)$, the differential form of the constitutive equation is

$$\ddot{\varepsilon} + \frac{E_2}{\eta_2}\dot{\varepsilon} = \frac{1}{E_1}\ddot{\sigma} + \left(\frac{1}{\eta_1} + \frac{1}{\eta_2} + \frac{E_2}{E_1\eta_2}\right)\dot{\sigma} + \frac{E_2}{\eta_1\eta_2}\sigma. \tag{9}$$

2) When $R < 0.1$, $\varepsilon \geq \varepsilon_t, \varepsilon(t) = \varepsilon_e(t) + \varepsilon_v(t) + \varepsilon_{ve}(t) + \varepsilon_{nl}(t)$, the differential form of the constitutive equation is

$$\ddot{\varepsilon} + \frac{E_2}{\eta_2}\dot{\varepsilon} = \frac{1}{E_1}\ddot{\sigma} + \left(\frac{1}{\eta_1} + \frac{1}{\eta_3} + \frac{E_2}{E_1\eta_2} + \frac{nt^{n-1}}{\eta_3}\right)\dot{\sigma} + \left(\frac{E_2}{\eta_1\eta_2} + \frac{E_2 nt^{n-1}}{\eta_2\eta_3} + \frac{n(n-1)t^{n-2}}{\eta_3}\right)\sigma. \tag{10}$$

Under the action of constant stress σ_0, the solution is obtained:

1) When $R \geq 0.1, \varepsilon < \varepsilon_t$. Referring to (Yang, et al., 2011) research on nonlinear rheological models shows that the initial conditions are $\sigma = \sigma_0, \varepsilon(0) = \frac{\sigma_0}{E_1}, \varepsilon'(0) = 0$, and the Laplace transform of **Eq. 11** yields the following equation:

$$\tilde{\varepsilon}(s) = \tilde{\varepsilon}_e(s) + \tilde{\varepsilon}_v(s) + \tilde{\varepsilon}_{ve}(s) = \frac{\sigma_0}{E_1 s} + \frac{\sigma_0}{(E_1 + \eta_1 s)s} + \frac{\sigma_0}{\eta_3 s^2}. \tag{11}$$

2) When $R < 0.1, \varepsilon < \varepsilon_t$, the initial conditions are $\sigma = \sigma_0, \varepsilon(0) = \frac{\sigma_0}{E_1}, \varepsilon'(0) = 0$, and the Laplace transform of **Eq. 12** yields the following equation:

$$\tilde{\varepsilon}(s) = \tilde{\varepsilon}_e(s) + \tilde{\varepsilon}_v(s) + \tilde{\varepsilon}_{ve}(s) = \frac{\sigma_0}{E_1 s} + \frac{\sigma_0}{(E_1 + \eta_1 s)s} + \frac{\sigma_0}{\eta_3 s^2}. \tag{12}$$

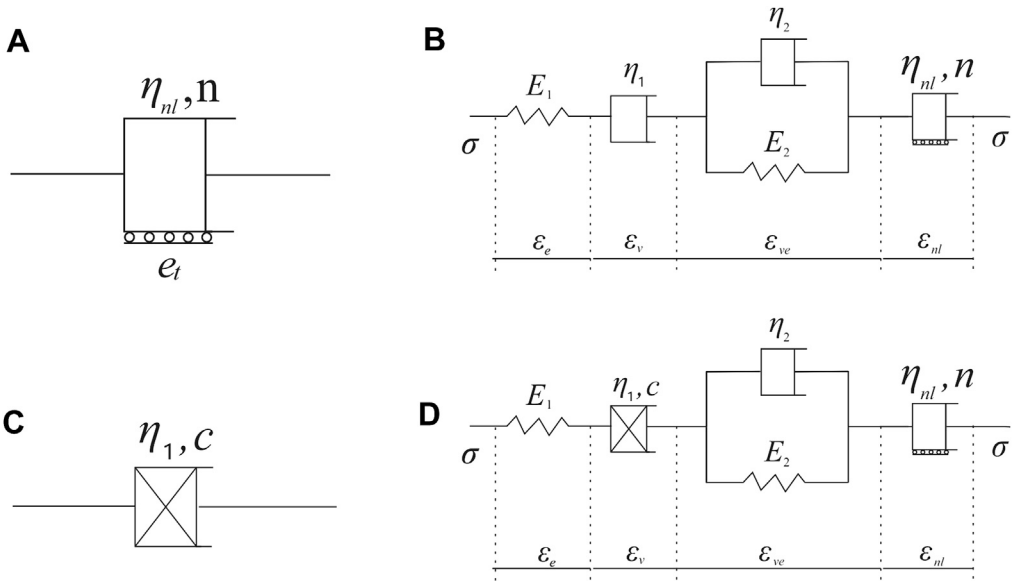

FIGURE 11 | (A) Nonlinear accelerated dashpot. **(B)** Improved Burgers component model. **(C)** Nonlinear accelerated dashpot. **(D)** Improved Burgers component model.

3) When $R < 0.1$ $\varepsilon \geq \varepsilon_t$, the initial conditions are $\sigma = \sigma_0, \varepsilon(0) = \frac{\sigma_0}{E_1}, \varepsilon'(0) = 0$, and the Laplace transform of **Eq. 11** yields the following equation:

$$\widetilde{\varepsilon}(s) = \widetilde{\varepsilon}_e(s) + \widetilde{\varepsilon}_v(s) + \widetilde{\varepsilon}_{ve}(s) = \frac{\sigma_0}{E_1 s} + \frac{\sigma_0}{(E_1 + \eta_1 s)s} + \frac{\sigma_0}{\eta_3 s^2} + \frac{\sigma_0 n!}{\eta_{nl} s^{n+1}}. \tag{13}$$

Carry out Laplace inverse transformation on **Eqs 13–15** to obtain the creep constitutive equation:

$$\varepsilon(t) = \begin{cases} \frac{\sigma_0}{E_1} + \frac{\sigma_0}{\eta_1} t + \frac{\sigma_0}{E_2}\left[1 - \exp\left(-\frac{E_2}{\eta_2} t\right)\right] & (R \geq 0.1 \text{且} \varepsilon < \varepsilon_t) \\ \frac{\sigma_0}{E_1} + \frac{\sigma_0}{\eta_1} t + \frac{\sigma_0}{E_2}\left[1 - \exp\left(-\frac{E_2}{\eta_2} t\right)\right] & (R \geq 0.1 \text{且} \varepsilon < \varepsilon_t) \\ \frac{\sigma_0}{E_1} + \frac{\sigma_0}{\eta_1} t + \frac{\sigma_0}{E_2}\left[1 - \exp\left(-\frac{E_2}{\eta_2} t\right)\right] + \frac{\sigma_0}{\eta_{nl}} \tau^n & (R < 0.1 \text{且} \varepsilon \geq \varepsilon_t) \end{cases}. \tag{14}$$

$\tau = t - t|_{\varepsilon=\varepsilon_a}, t|_{\varepsilon=\varepsilon_a}$ is the moment when the soil is about to enter the accelerated creep phase.

According to the research on the viscosity coefficient in soil creep, the viscosity coefficient is the attenuation function of stress and an increasing function of time. The nonlinear formula of the viscosity coefficient is

$$\eta(\sigma, t) = \eta_1 t^c \sigma^{c-1}. \tag{15}$$

η_1 is the initial viscosity coefficient and c is the material parameter.

Figure 1(C) is the constitutive equation shown by the nonlinear viscous element constructed by the above formula.

$$\sigma = \eta(\sigma, t)\dot{\varepsilon} = \eta_1 t^c \sigma^{c-1}\dot{\varepsilon}. \tag{16}$$

In order to avoid mathematical problems on the derivation of nonlinear creep model from former research Xia et al. (2011), the above equation can be obtained:

$$\varepsilon_v = \frac{\sigma^{2-c}}{\eta_1(1-c)} t^{1-c}. \tag{17}$$

The nonlinear dashpot element is used to replace the ε_v part of the series dashpot element, as shown in **Figure 11D**. The creep constitutive equation in this article is

$$\varepsilon(t) = \begin{cases} \frac{\sigma_0}{E_1} + \frac{\sigma^{2-c}}{\eta_1(1-c)} t^{1-c} + \frac{\sigma_0}{E_2}\left[1 - \exp\left(-\frac{E_2}{\eta_2} t\right)\right] & (R \geq 0.1 \text{且} \varepsilon < \varepsilon_t) \\ \frac{\sigma_0}{E_1} + \frac{\sigma^{2-c}}{\eta_1(1-c)} t^{1-c} + \frac{\sigma_0}{E_2}\left[1 - \exp\left(-\frac{E_2}{\eta_2} t\right)\right] & (R \geq 0.1 \text{且} \varepsilon < \varepsilon_t) \\ \frac{\sigma_0}{E_1} + \frac{\sigma^{2-c}}{\eta_1(1-c)} t^{1-c} + \frac{\sigma_0}{E_2}\left[1 - \exp\left(-\frac{E_2}{\eta_2} t\right)\right] + \frac{\sigma_0}{\eta_{nl}} \tau^n & (R < 0.1 \text{且} \varepsilon \geq \varepsilon_t) \end{cases}. \tag{18}$$

Fit the creep test curves under the four stress states of A, B, C, and D in **Figure 8A**, **Figure 12** is the fitting results under different stress paths, and **Table 3** is fitting parameters.

The fitted results in **Figure 12** and the fitted data in **Table 3** show that the theoretical values of the improved Burgers model are in good agreement with the experimental results. It not only fully reflects the instantaneous elastic deformation of the soil after loading but also reflects the initial creep of the first stage and the stable creep of the second stage; especially, the model overcoming the traditional linear element model cannot describe the difficulty of the accelerated creep stage, and the deformation of the accelerated creep stage of the soil is successfully fitted. The result is significantly better than the traditional Burgers model. Since accelerated creep is the key stage of slope failure

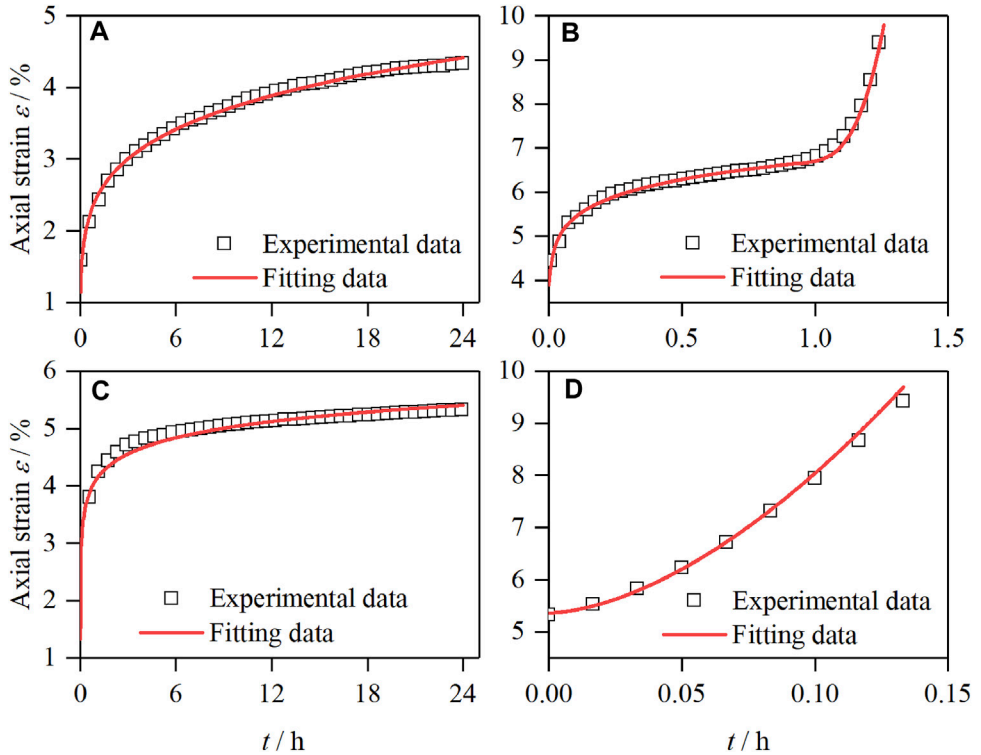

FIGURE 12 | Fitting curve of unloading confining pressure in steps with constant principal stress. **(A)** Stress state at point A. **(B)** Stress state at point B. **(C)** Stress state at point C. **(D)** Stress state at point D.

TABLE 3 | Fitting parameters.

	σ_1 (kPa)	σ_3 (kPa)	E_1(kPa)	E_2(kPa)	η_1(kPa·h)	η_2(kPa·h)	c	η_{nl}(kPa·h)	t_s (s)	n	R^2
A	500	200	192.3	112.5	61,772.5	518.8	0.917	—	—	—	0.97
B	500	150	89.7	178.3	5,932.2	6,322.1	0.632	2.17	0.92	3.5	0.99
C	125	25	83.3	62.3	55,429.3	518.8	0.851	—	—	—	0.96
D	100	0	18.86	153.1	4,913.1	6,322.1	0.753	18.87	0	17.6	0.97

prediction, the successful description of the accelerated creep stage by this model shows that it has a certain guiding significance for slope failure prediction.

CONCLUSION

In this article, the undisturbed Malan loess from Yan'an is taken as the research subject, and the unloading creep tests are carried out to analyze the creep deformation characteristics of undisturbed Malan loess under different stress paths by progressively unloading confining pressure in steps under constant principal stress and constant deviator stress; the conclusions are as follows:

1) Under the two unloading stress paths, the axial deformation of soil is different. Under constant σ_1 confining pressure unloading, the axial deformation always shows compression. The axial deformation of unloading confining pressure under constant deviator stress shows three forms: when the unloading stress level is low, the axial deformation is expressed as elongation, and when the unloading stress level is high, it is expressed as axial elongation first and then axial compression. When the load stress level is higher, it appears as axial compression. It shows that, with the increase of the unloading level, the soil gradually changes from elastic deformation to plastic deformation and finally fails.
2) By introducing the concept of the failure approach index, the stress state of the soil under the two unloading stress paths and the degree of near failure of the soil can be well described. The failure approach index R=0.4 can be used as the critical value for distinguishing between elastic deformation and plastic deformation, and R=0.1 is used as the critical value for

distinguishing between the stable creep stage and the accelerated creep stage of the soil.

3) By comparing the failure approach index of the soil under the two stress states, it is found that the failure approach index R of unloading confining pressure when the principal stress σ_1 is kept constant decreases faster than when the deviator stress $\sigma_1 - \sigma_3$ is kept constant. It shows that the path of unloading confining pressure can cause soil sample damage faster when σ_1 is kept constant.
4) The Burgers model is widely used to describe the creep behavior of soils due to its intuitive concept, clear parameters, physical implications, and simple calculations. By connecting a nonlinear dashpot element in series with the Burgers model and combining the functional relationship between the viscoelastic modulus and creep behavior. It can be concluded that the improved Burgers model proposed in this article has higher relevant results and can more accurately describe the creep characteristics under different unloading stress paths by comparing the modeling results to the testing results.

DATA AVAILABILITY STATEMENT

The original contributions presented in the study are included in the article/Supplementary Material; further inquiries can be directed to the corresponding author.

AUTHOR CONTRIBUTIONS

ZL is responsible for experimental design and conduct and article writing. JW and DZ are responsible for providing theoretical guidance and article revision.

FUNDING

This research was supported by the National Natural Science Foundation of China (grant numbers 42027806 and 41630639) and the National Key Research and Development Plan (grant number 2018YFC1504703).

REFERENCES

Chang, Z., Gao, H., Huang, F., Chen, J., Huang, J., and Guo, Z. (2020). Study on the Creep Behaviours and the Improved Burgers Model of a Loess Landslide Considering Matric Suction. *Nat. Hazards* 103, 1479–1497. doi:10.1007/s11069-020-04046-0

Derbyshire, E. (2001). Geological Hazards in Loess Terrain, with Particular Reference to the Loess Regions of China. *Earth-Science Rev.* 54, 231–260. doi:10.1016/S0012-8252(01)00050-2

Di Maio, C., Scaringi, G., and Vassallo, R. (2015). Residual Strength and Creep Behaviour on the Slip Surface of Specimens of a Landslide in marine Origin clay Shales: Influence of Pore Fluid Composition. *Landslides* 12, 657–667. doi:10.1007/s10346-014-0511-z

Di Maio, C., Vassallo, R., and Vallario, M. (2013). Plastic and Viscous Shear Displacements of a Deep and Very Slow Landslide in Stiff clay Formation. *Eng. Geology.* 162, 53–66. doi:10.1016/j.enggeo.2013.05.003

Fabre, G., and Pellet, F. (2006). Creep and Time-dependent Damage in Argillaceous Rocks. *Int. J. Rock Mech. Mining Sci.* 43, 950–960. doi:10.1016/j.ijrmms.2006.02.004

Gasc-Barbier, M., Chanchole, S., and Bérest, P. (2004). Creep Behavior of Bure Clayey Rock. *Appl. Clay Sci.* 26, 449–458. doi:10.1016/j.clay.2003.12.030

Graham, J., Tanaka, N., Crilly, T., and Alfaro, M. (2001). Modified Cam-Clay Modelling of Temperature Effects in Clays. *Can. Geotech. J.* 38, 608–621. doi:10.1139/t00-125

Li, D.-W., Fan, J.-H., and Wang, R.-H. (2011). Research on Visco-Elastic-Plastic Creep Model of Artificially Frozen Soil under High Confining Pressures. *Cold Regions Sci. Technology* 65, 219–225. doi:10.1016/j.coldregions.2010.08.006

Li, J. J., and Kong, L. W. (2019). Creep Properties of Expansive Soil under Unloading Stress and its Nonlinear Constitutive Model. *Rock Soil Mech.* 40, 3465–3473. doi:10.16285/j.rsm.2018.2306

Liu, K. Y., Xue, Y. T., and Zhou, H. (2018). Study on 3D Nonlinear Visco-Elastic -plastic Creep Constitutive Model with Parameter Unsteady of Soft Rock Based on Improved Bingham Model. *Rock Soil Mech.* 39, 4157–4164. doi:10.16285/j.rsm.2017.0572：

Liu, M. D., and Carter, J. P. (2002). A Structured Cam Clay Model. *Can. Geotech. J.* 39, 1313–1332. doi:10.1139/t02-069

Lo Presti, D. C. F. (1996). Rate and Creep Effect on the Stiffness of Soils. *Measuring And Modeling Time Dependent Soil Behavior. Geotech. Spec. Publ.* 61, 166–180.

Mansour, M. F., Morgenstern, N. R., and Martin, C. D. (2011). Expected Damage from Displacement of Slow-Moving Slides. *Landslides* 8, 117–131. doi:10.1007/s10346-010-0227-7

Mei, G. X., Chen, H., Lu, T. H., and Yin, Z. Z. (2010). Research on Lateral Stress-Strain Relation on Side of Foundation Pit with Lateral Unloading. *Chin. J. Rock Mech. Eng.* 29, 3108–3112.

Nguyen, S. T., Dormieux, L., Pape, Y. L., and Sanahuja, J. (2011). A Burger Model for the Effective Behavior of a Microcracked Viscoelastic Solid. *Int. J. Damage Mech.* 20, 1116–1129. doi:10.1177/1056789510395554

Palmer, J. (2017). Creeping Earth Could Hold Secret to Deadly Landslides. *Nature* 548, 384–386. doi:10.1038/548384a

Peng, J., Fan, Z., Wu, D., Zhuang, J., Dai, F., Chen, W., et al. (2015). Heavy Rainfall Triggered Loess-Mudstone Landslide and Subsequent Debris Flow in Tianshui, China. *Eng. Geology.* 186, 79–90. doi:10.1016/j.enggeo.2014.08.015

Pytharouli, S. i., and Stiros, S. c. (2010). Kinematics and Rheology of a Major Landslide Based on Signal Analysis. *Géotechnique* 60, 207–222. doi:10.1680/geot.8.P.049

Sasaki, Y., Fujii, A., and Asai, K. (2000). "Soil Creep Process and its Role in Debris Slide Generation-Field Measurements on the north Side of Tsukuba Mountain in Japan," in *In* Developments In Geotechnical Engineering *Engineering Geological Advances in Japan for the New Millennium*. Editors Y. Kanaori, K. Tanaka, and M. Chigira (Elsevier), 199–219. doi:10.1016/S0165-1250(00)80017-6

Sivasithamparam, N., Karstunen, M., and Bonnier, P. (2015). Modelling Creep Behaviour of Anisotropic Soft Soils. *Comput. Geotechnics* 69, 46–57. doi:10.1016/j.compgeo.2015.04.015

Sun, M., Tang, H., Wang, M., Shan, Z., and Hu, X. (2016). Creep Behavior of Slip Zone Soil of the Majiagou Landslide in the Three Gorges Area. *Environ. Earth Sci.* 75, 1199. doi:10.1007/s12665-016-6002-x

Tan, R. Y., and Yang, C. H. (1988). Structural Responses of Underground Pipelines to Dynamic Loadings. *Mech. Structures Machines* 16, 103–122. doi:10.1080/08905458808960255

Tang, H., Duan, Z., Wang, D., and Dang, Q. (2020). Experimental Investigation of Creep Behavior of Loess under Different Moisture Contents. *Bull. Eng. Geol. Environ.* 79, 411–422. doi:10.1007/s10064-019-01545-8

Wan, L. H., Cao, P., Huang, Y. H., Wang, Y. X., and Zhang, X. Y. (2011). Creep Test of Hard Rock and Modified Generalized Kelvin Creep Model. *Amm* 90-93, 626–632. doi:10.4028/www.scientific.net/AMM10.4028/www.scientific.net/amm.90-93.626

Wang, G., Zhang, L., Zhang, Y., and Ding, G. (2014). Experimental Investigations of the Creep-Damage-Rupture Behaviour of Rock Salt. *Int. J. Rock Mech. Mining Sci.* 66, 181–187. doi:10.1016/j.ijrmms.2013.12.013

Wang, J.-a., Wang, Y.-x., Cao, Q.-j., Ju, Y., and Mao, L.-t. (2015). Behavior of Microcontacts in Rock Joints under Direct Shear Creep Loading. *Int. J. Rock Mech. Mining Sci.* 78, 217–229. doi:10.1016/j.ijrmms.2015.05.002

Wang, X., Wang, J., Zhan, H., Li, P., Qiu, H., and Hu, S. (2020). Moisture Content Effect on the Creep Behavior of Loess for the Catastrophic Baqiao Landslide. *CATENA* 187, 104371. doi:10.1016/j.catena.2019.104371

Wen, B.-P., and Jiang, X.-Z. (2017). Effect of Gravel Content on Creep Behavior of Clayey Soil at Residual State: Implication for its Role in Slow-Moving Landslides. *Landslides* 14, 559–576. doi:10.1007/s10346-016-0709-3

Xia, C. C., Jin, L., and Guo, R. (2011). Nonlinear Theoretical Rheological Model for Rock a Review and Some Problems. *Chin. J. Rock Mech. Eng.* 30, 454–463.

Xie, X., Qi, S., Zhao, F., and Wang, D. (2018). Creep Behavior and the Microstructural Evolution of Loess-like Soil from Xi'an Area, China. *Eng. Geology.* 236, 43–59. doi:10.1016/j.enggeo.2017.11.003

Xin, P., Liang, C., Wu, S., Liu, Z., Shi, J., and Wang, T. (2016). Kinematic Characteristics and Dynamic Mechanisms of Large-Scale Landslides in a Loess Plateau: a Case Study for the north Bank of the Baoji Stream Segment of the Wei River, China. *Bull. Eng. Geol. Environ.* 75, 659–671. doi:10.1007/s10064-015-0824-8

Xu, L., and Coop, M. R. (2016). Influence of Structure on the Behavior of a Saturated Clayey Loess. *Can. Geotech. J.* 53, 1026–1037. doi:10.1139/cgj-2015-0200

Xu, L., Coop, M. R., Zhang, M., and Wang, G. (2018). The Mechanics of a Saturated Silty Loess and Implications for Landslides. *Eng. Geology.* 236, 29–42. doi:10.1016/j.enggeo.2017.02.021

Yang, A. W., Yang, S. K., and Zhang, Z. D. (2020). Experimental Study of Mechanical Properties of Dredger Fill under Different Unloading Rates and Stress Paths. *Rock Soil Mech.* 41, 2891–2900+2912. doi:10.16285/j.rsm.2019.1992

Yang, W. D., Zhang, Q. Y., and Chen, F. (2011). Research on Nonlinear Rheological Model of Debase and Treatment for Creep Loading History. *Chin. J. Rock Mech. Eng.* 30, 1405–1413.

Yates, K., Fenton, C. H., and Bell, D. H. (2018). A Review of the Geotechnical Characteristics of Loess and Loess-Derived Soils from Canterbury, South Island, New Zealand. *Eng. Geology.* 236, 11–21. doi:10.1016/j.enggeo.2017.08.001

Ye, G.-l., Nishimura, T., and Zhang, F. (2015). Experimental Study on Shear and Creep Behaviour of green Tuff at High Temperatures. *Int. J. Rock Mech. Mining Sci.* 79, 19–28. doi:10.1016/j.ijrmms.2015.08.005

Yu, H. D., Chen, W. Z., Gong, Z., Tan, X. J., Ma, Y. S., Li, X. L., et al. (2015). Creep Behavior of Boom clay. *Int. J. Rock Mech. Mining Sci.* 76, 256–264. doi:10.1016/j.ijrmms.2015.03.009

Zhang, F., Wang, G., Kamai, T., and Chen, W. (2014). Effect of Pore-Water Chemistry on Undrained Shear Behaviour of Saturated Loess. *Q. J. Eng. Geology. Hydrogeology* 47, 201–210. doi:10.1144/qjegh2013-085

Zhen, G., Yan, Z. X., Lei, H. Y., and Wang, P. (2008). Experimental Studies on Unloading Deformation Properties of Silty clay of First marine Layer in Tianjin Urban Area. *Rock Soil Mech.* 5, 1237–1242. doi:10.16285/j.rsm.2008.05.058

Zheng, H., Feng, X.-T., and Hao, X.-j. (2015). A Creep Model for Weakly Consolidated Porous sandstone Including Volumetric Creep. *Int. J. Rock Mech. Mining Sci.* 78, 99–107. doi:10.1016/j.ijrmms.2015.04.021

Zhou, Y. F., Tham, L. G., Yan, R. W. M., and Xu, L. (2014). The Mechanism of Soil Failures along Cracks Subjected to Water Infiltration. *Comput. Geotechnics* 55, 330–341. doi:10.1016/j.compgeo.2013.09.009

Zhou, Z., Ma, W., Zhang, S., Du, H., Mu, Y., and Li, G. (2016). Multiaxial Creep of Frozen Loess. *Mech. Mater.* 95, 172–191. doi:10.1016/j.mechmat.2015.11.020

Zhu, F., Duan, Z. Y., Wu, Z. Y., Wu, Y. Q., Li, T. L., and Cai, Y. D. (2014). Experimental Study on Direct Shear Creep Characteristics and Long-Term Strength of Red Layer Sliding Zone Soil in Southern Hunan. *Adv. Mater. Res.* 842, 782–787. doi:10.4028/www.scientific.net/AMR

Conflict of Interest: The authors declare that the research was conducted in the absence of any commercial or financial relationships that could be construed as a potential conflict of interest.

frontiers in Earth Science

ORIGINAL RESEARCH
published: 12 October 2021
doi: 10.3389/feart.2021.724678

Flume Tests to Investigate the Initiation Mechanism of Loess Mudflows on the Chinese Loess Plateau

Penghui Ma, Jianqi Zhuang, Xinghua Zhu, Yuxiang Cheng and Cong Liu*

College of Geological Engineering and Surveying of Chang'an University/Key Laboratory of Western China Mineral Resources and Geological Engineering, Xi'an, China

Loess has a strong water sensitivity, so loess landslides often transform into loess mudflows when water is added on the Chinese Loess Plateau, which results in high casualties and property loss of the Chinese government. In this study, a series of flume tests were designed to study the initiation of loess mudflows. The results reveal that the initiation modes of loess mudflows include large-scale mudflow and retrogressive toe sliding (Type A), and small-scale mudflow and retrogressive toe sliding (Type B). A model was used to analyze the test results that describe the effects of water flow on the potential for hillslope failure and liquefaction. It was found that the soil accumulation was unconditionally stable before a loess mudflow was formed, but as the rainfall continued, the water gradually infiltrated the soil, and the soil accumulation changed from unconditionally stable to unconditionally unstable. Thus, this led to different initiation modes during the tests. For Type A, the water preferentially infiltrated into the area with an uneven density and a large amount of water accumulated. The pore water pressure increased quickly and could not dissipate in time, so the loess liquefied. As the liquefaction area continued to expand and became larger, Type A occurred. Relatively speaking, Type B occurs in soil accumulations with relatively uniform densities. These results provide a certain scientific reference for the study of loess mudflows.

Keywords: flume tests, loess mudflow, loess liquefaction, initiation modes, unconditionally stable, unconditionally unstable

OPEN ACCESS

Edited by:
Fanyu Zhang,
Lanzhou University, China

Reviewed by:
Shenghua Cui,
Chengdu University of Technology, China
Zhao Duan,
Xi'an University of Science and Technology, China

****Correspondence:***
Jianqi Zhuang
jqzhuang@chd.edu.cn

Specialty section:
This article was submitted to Geohazards and Georisks, a section of the journal Frontiers in Earth Science

Received: *14 June 2021*
Accepted: *28 September 2021*
Published: *12 October 2021*

Citation:
Ma P, Zhuang J, Zhu X, Cheng Y and Liu C (2021) Flume Tests to Investigate the Initiation Mechanism of Loess Mudflows on the Chinese Loess Plateau. Front. Earth Sci. 9:724678. doi: 10.3389/feart.2021.724678

INTRODUCTION

Loess is widely distributed over about 6.3×105 km^2 in China (Liu, 1985; Ma et al., 2019a). At present, loess landslides occur frequently in the loess area in China. Field investigations have revealed that from 1950 to 1992, a total of 14,109 loess landslides occurred on the Chinese Loess Plateau, with a distribution density of greater than 6/km^2 (Zhuang and Peng, 2014). The loess landslides in Shanxi Province account for about one third of the landslides on the Chinese Loess Plateau, causing huge casualties and property loss of the Chinese government (Zhou et al., 2002; Peng et al., 2019).

Loess mudflows are a special type of landslide. There are many joints exposed on the surface of loess, and its structure is loose and porous. The strength of natural dry loess is very high, and it has a good uprightness. However, loess is prone to collapse, softening, and even deformation as its water content increases, and water is the most important inducing factor of loess geohazards (Xu et al.,

2013; Zhang et al., 2013; Fan et al., 2017; Peng et al., 2018; Pu et al., 2021), In addition, as with sand, loess can also undergo liquefaction. A high pore water pressure can be produced quickly and will not dissipated in a short time period, and thus, the soil's strength drops quickly, and the soil body liquefies and flows like water (Pei et al., 2017; Peng et al., 2018; Ma et al., 2019b). Therefore, sometimes, loess landslides can transform into loess mudflows due to liquefaction of the loess. At present, loess mudflows occur frequently on the Chinese Loess Plateau, and they have become the most catastrophic and influential loess disaster (Zhang et al., 2019).

Compared with traditional loess landslides, loess mudflows exhibit fluid movement, so a loess mudflow has a greater mobility and a wider accumulation range, leading to greater danger (Leng et al., 2018; Zha et al., 2019). A large number of field investigations have shown that the motion characteristics of loess mudflows mainly include the following aspects. 1) The flow distance is long. According to the statistics of landslide movement distance on the Heifangtai Platform, Gansu Province, China, the average apparent friction angle of the loess landslides is 0.53. However, once a loess landslide is transformed into a mudflow, its average apparent friction angle is about 0.3 (Peng et al., 2018; Ma et al., 2019a). The statistics of the loess landslides on the Jingyang South Platform show that once a loess landslide transforms into a loess mudflow, the average apparent friction angle is 0.185, or about 10.5°, which is close to the critical apparent friction angle (10°) of loess landslide caused by the liquefaction of loess (Ma et al., 2019a). Thus, the movement distance of a loess mudflow is far greater than that of a traditional loess landslide. 2) The movement speed is large (Peng et al., 2015). According to the statistics of loess mudflows in Tianshui City, China, in the movement of a loess landslide, once the loess experiences liquefaction and transforms into a loess mudflow, its movement speed will increase sharply, and the maximum speed will reach about 8 m/s. For example, a large landslide occurred on Salle Mountain, Gansu Province, China, in 1983, and then, it transformed into a mudflow. The maximum peak velocity was about 15 m/s, and the velocity was very high, i.e., much higher than that of a loess landslide (Zhang et al., 2002; Kang et al., 2018). Therefore, ascertaining the initiation mechanisms of loess mudflows has great significance for geohazards prevention and mitigation on the Loess Plateau.

As the most disastrous geological hazard on the Chinese Loess Plateau, the initiation mechanisms of loess mudflows have been seldom been studied over the years when investigating loess geological hazards in China. Based on the initiation characteristics of the loess mudflows on the Chinese Loess Plateau, in this study relevant flume tests were designed to investigate the modes and initiation mechanisms of loess mudflows in order to provide a scientific basis for scientific research on loess mudflows.

Loess Mudflows on the Chinese Loess Plateau

The Loess Plateau has evolved landforms, including loess platforms, beams, and hills (Loess yuan, Liang, and Mao in Chinese) (Liu, 1985; Ma et al., 2019a). Generally speaking, loess mudflows often occur in loess gullies and on the edges of loess platforms (Yuan et al., 2015; Peng et al., 2019).

For the loess mudflows in gullies, the gully is generally steep in the upper reaches of the channel. The upstream area is relatively open and has a wide catchment area, which is conducive to the collection of mudflow sources. **Figure 1** shows a loess mudflow that occurred near Dagou Village in Tianshui City, China, in 2013. The sliding body quickly transformed into a loess mudflow during the movement process. The flow distance was more than 1 km, and it destroyed more than 10 houses in the village (**Figure 1A**). Field investigations revealed that the gully was V-shaped with a large channel gradient. The slope on both sides of the ditch was steep, with a gradient of 35–50°, which provided a potential source for the loess mudflow (**Figures 1A–C**). According to the meteorological data, heavy rainfall occurred before the loess mudflow. Due to the infiltration of a large amount of rainwater, the debris started to form a loess mudflow. The loess mudflow entrained a large amount of loose deposits on the surface of the channel throughout the entire movement process, causing the scale of the mudflow to increase continuously (**Figure 1**) (Peng et al., 2015).

Loess mudflows that occur on the edges of loess platforms always require the landslide substrate is always flat, which is suitable for loess mudflow moving with a high speed (Peng et al., 2018; Ma et al., 2019b). The Jingyang South Platform and the Heifangtai Platform are both typical platforms in China. There are many sites which observed slides multiple times in these two platforms. Lots of previous landsliding materials deposits at the foot of the slope, which would trigger a loess mudflow when a large amount of water infiltrate into the materials. For example, a loess mudflow occurred in Jiangliu Village in the Jingyang South Platform on March 8, 2016. The volume of the sliding body was only about 2.0 × 104 m3. However, the deposits turned loess mudflow like water with a sliding distance reached 260 m in a very short time. Another example, a loess mudflow occurred near Chenjia Village on the Heifangtai Platform, Gansu Province. Three loess mudflows occurred at the same location in 2015. These mudflows were all characterized by high-speeds, long runout distances, and liquefaction (**Figure 2**).

Flume Tests

Flume Instrumentation

Flume tests were designed to study the initiation modes and mechanisms of loess mudflows. The flume used in the tests was 4 m long, 0.4 m wide, and 0.8 m deep. Both sides of the flume are constructed of tempered glass, which allows for observations of the entire initiation process of the loess mudflow. The bottom of the flume is equipped with a rough steel plate. The slope angle of the flume can be adjusted between 6° and 35°, which is sufficient for the experimental research requirements. The rainfall system can automatically lift and move to control its position and height. A voltage pump was installed in the rainfall system, which can automatically control the rainfall intensity, and the effective area of the rainfall can reach 150 × 50 cm2. Pore pressure sensors and

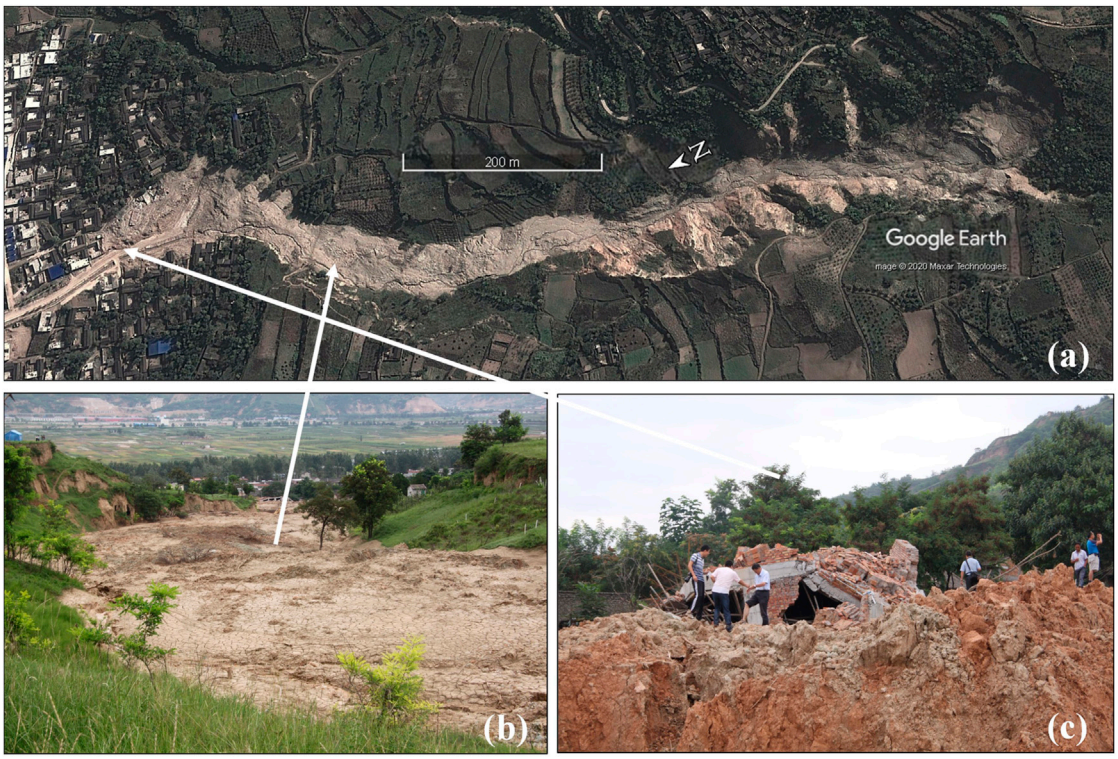

FIGURE 1 | A loess mudflow that occurred near Dagou Village, Tianshui City, China. **(A)** View of the entire loess mudflow; **(B)** Accumulation characteristics; **(C)** House destruction.

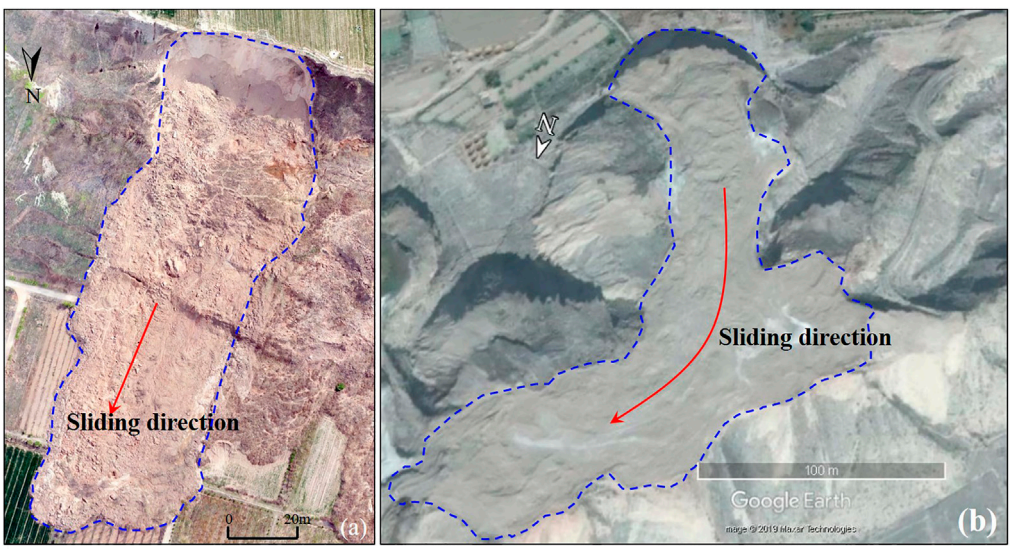

FIGURE 2 | The characteristics of loess mudflows on loess platforms. **(A)** A loess mudflow that occurred near Jiangliu Village on March 9, 2016 on the South Jingyang Platform in Xi'an, China; **(B)** A loess mudflow occurred near Chenjia Village in 2015 on the Heifangtai Platform, Gansu.

water content sensors were arranged for the tests. The water content sensors were model-5TE produced by the American Decagon Company (**Figure 3**). The pore pressure sensors were produced by the Tianjin Aoyou Xingtong Company, China, with a measuring range of 0–50 kPa. The specific layout of the soil sensors is shown in **Figure 4**.

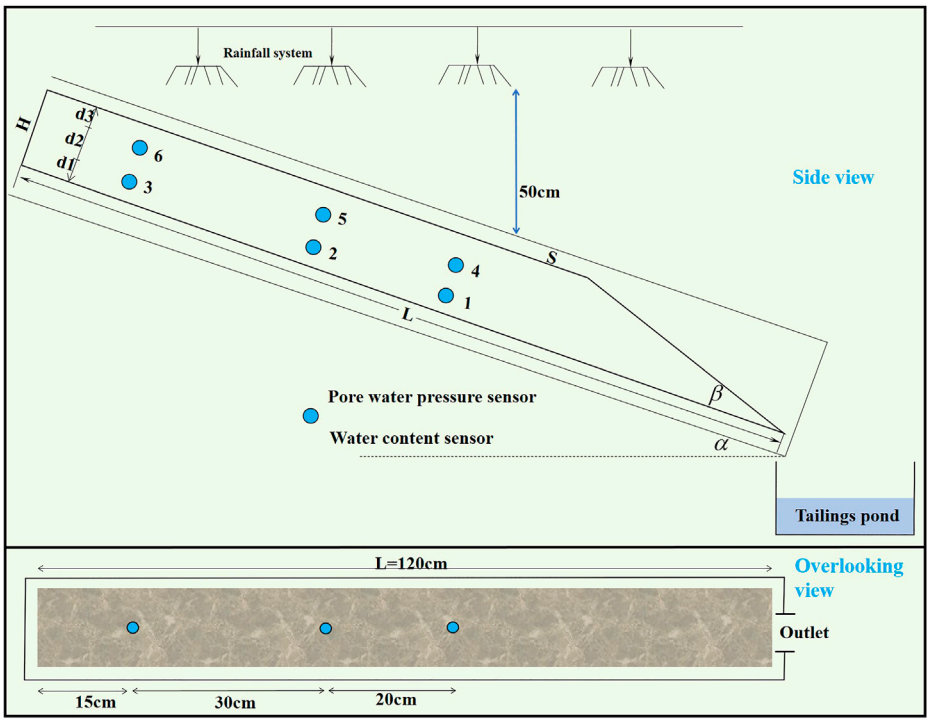

FIGURE 3 | A sketch of the flume and its hydrological equipment.

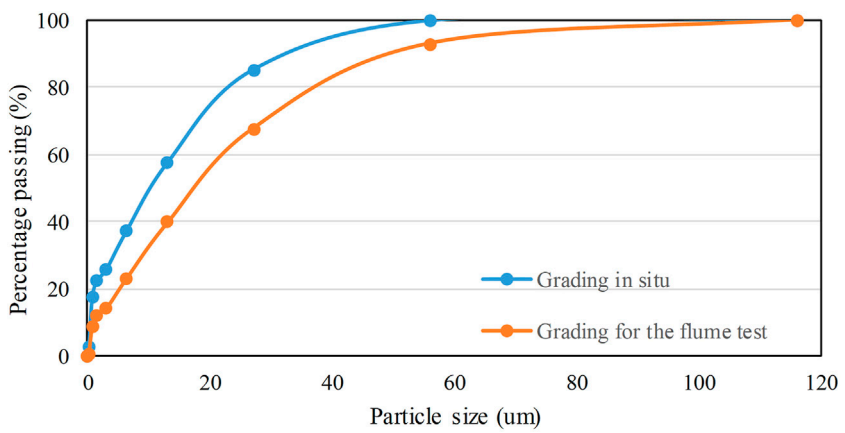

FIGURE 4 | The grading of the *in situ* soil and the material used for the flume test.

Experimental Procedure

A series of different tests were set up by controlling the slope angle and rain intensity. We investigated the types of loess mudflows that occur on the Loess Plateau. The critical rain intensity on the Chinese Loess Plateau is mostly 100–220 mm/h, so the rainfall intensity in the tests was controlled between 100 and 220 mm/h (Peng et al., 2015) (**Table 1**). Because the South Jingyang Platform is one of the areas in China in which loess mudflows frequently occur, soil from the South Jingyang Platform was selected for the tests. Before the tests, the soil particles with diameters of >5 cm were eliminated. The particle size of the test soil and the particle size of the actual soil are shown in **Figure 4**. In the situ soil, particles less than 50 μm in diameter accounted for 98%, while those less than 75 μm in diameter accounted for 100%. In the material used for the flume test, particles less than 50 μm in diameter accounted for 90%, while those less than 75 μm in diameter accounted for 97%. They are relatively consistent, so the soil can be tested. According to statistics, the average apparent friction angle of loess mudflow on the South Platform is 0.185, or about 10.5°, and the average apparent friction angle of loess mudflow on the South Platform is 0.3, or about 17° (Peng et al., 2018; Ma et al., 2019b), so the slope angle of the accumulation was controlled

TABLE 1 | An overview of the tests.

Railfall (mm/h)	Slope (°)	H (cm)	L (cm)	d1 (cm)	d2 (cm)	Failure mode
120	10°	12	120	2	5	Type A
105	13°	12	120	2	5	
210	15°	15	120	5	5	Type B
185	16°	11	120	2	5	
186	17°	11	120	2	5	
158	18°	11	120	2	5	
189	19°	12	120	2	5	

TABLE 2 | Parameter values of the materials.

Dried bulk density (g/cm^3)	Friction angle (°)	Cohesion (kPa)	Hydrological conductivity (m/h)	Initial water content (%)
1.50–1.70	26.4	38.3	0.042	17.5–24.0

TABLE 3 | Summarized failure modes.

Type a	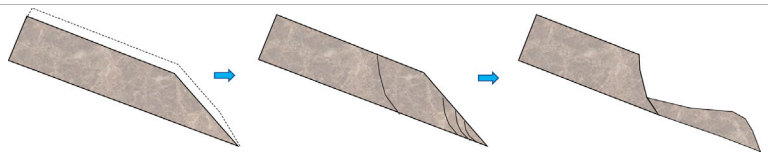	Large-scale mudflow and retrogressive toe sliding
Type B	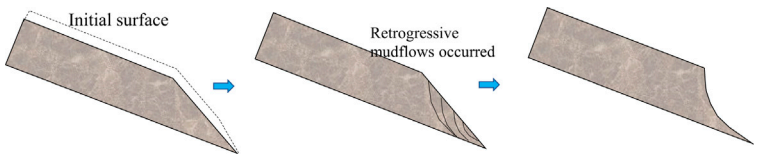	Small-scale mudflow and retrogressive toe sliding

between 10° and 20°. Before a test was carried out, it was necessary to test the roughness of the bottom of the flume and confirm whether it was necessary to increase the roughness in order to reduce the influence of the bottom boundary effect on the tests. According to the Manning formula, the roughness coefficient of the flume test was calculated to be 0.055 (Zhu et al., 2020). The loess used in the experiment has a higher silt and clay content, about 30%. Thus, there was no need to increase the roughness of the flume's bottom during the tests (**Table 1**).

A total of seven sets of experiments were designed to study the initiation processes of loess mudflows. In the actual soil accumulation process, it is difficult to achieve homogenous parameters. Therefore, the dried bulk density of the seven groups of tests were controlled between 1.50 g/cm^3 and 1.70 g/cm^3. The water content of the seven sets of tests was controlled between 17.5 and 24.0%. In addition, the basic mechanical parameters of the soil were tested using relevant related geotechnical tests (**Table 2**). Altogether six pore water pressure sensors and six water content sensors were arranged in the soil accumulation (**Figure 3**). Before a test was carried out, the sensors and rainfall intensity were calibrated accurately.

RESULTS AND DISCUSSION

By analyzing the video and data results of the seven groups of tests, it was found that there are two different initiation modes: large-scale mudflow and retrogressive toe sliding, and small-scale mudflow and retrogressive toe sliding.

Large-Scale Mudflow and Retrogressive Toe Sliding

Type A. When the test began, the water started to infiltrate gradually. Because the loess structure was loose and the initial volumetric water content of the loess was low, almost all of the rainfall infiltrated into the soil. The soil particles began to shrink and the porosity began to decrease. The soil accumulation underwent overall collapse and subsidence. The thickness of the soil in the toe part of the accumulation was thinner than that in other areas, so the water quickly penetrated to the bottom of the soil. The volumetric water content of the soil began to increase, and a small amount of sliding occurred at the toe part of the accumulation. The small amount of sliding at the toe part led

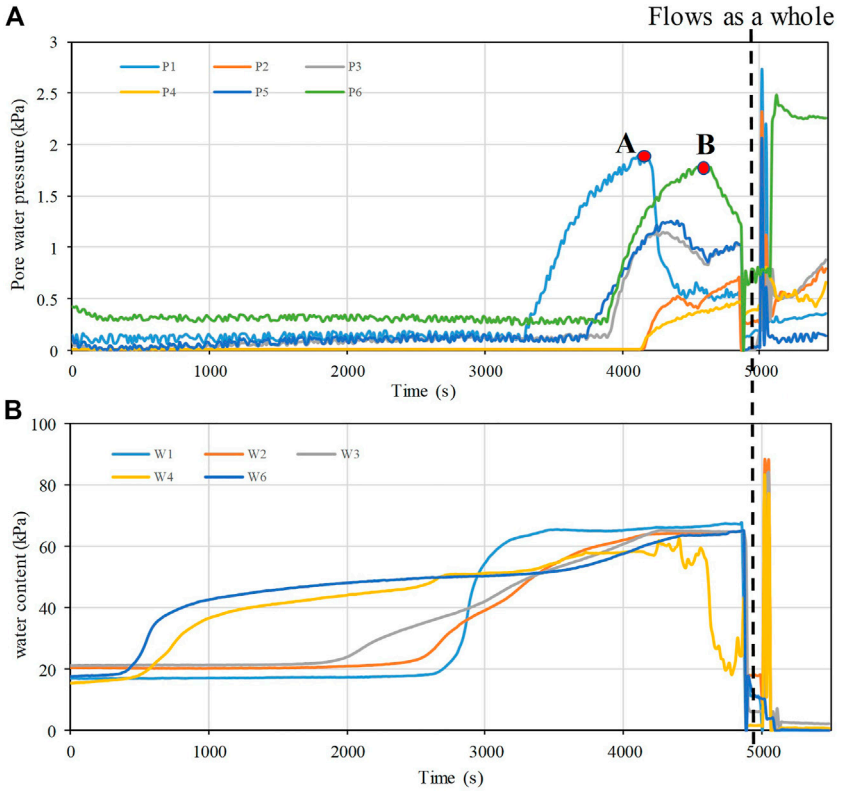

FIGURE 5 | Variations in pore water pressure and water content with time in the flume test with a slope angle of 13°. **(A)** Pore water pressure; **(B)** Water content. Small-scale mudflow and retrogressive toe sliding.

to further loss of the accumulation's support, and retrogressive compound loess mudflows constantly occurred at the toe part of the soil accumulation. As the rainfall continued to infiltrate into the soil, the soil accumulation underwent shear deformation as a whole and a potential shear zone began to form. Then, a loess mudflow (large scale) occurred (**Table 3**).

The variations in the water content and pore water pressure of the soil in the test with a slope angle of 13° are shown in **Figure 5**. At 458 s, the volumetric water content at position six began to increase first. Then, the volumetric water content at position four began to increase at 488 s. The water contents at these two positions exceeded 40% of the original water content in a short time, and then, they began to increase slowly. The water content at position three began to increase at 1950 s, and the water content at position two began to increase at 2,580 s. The increase rate of the water content at these two positions was slow and then increased to the peak value. Comparatively speaking, the water content at position one began to increase at 2,670 s, rapidly increased to the peak value, and rapidly exceeded 60 percent of the original water content. Because position one is located at the bottom of the toe part of the soil accumulation, the rainfall infiltrated at position four in the shallow part of the soil accumulation first. The surrounding soil began to loosen, and then, the seepage channel began to expand, so the water quickly infiltrated vertically, which led to a rapid increase in the water content at position 1. This process led to the occurrence of a slide at the toe part of the soil accumulation. We observe the change in the pore water pressure. Before 3,200 s, although the water content of the soil increased greatly, the pore water pressure did not change at position 1. The pore water pressure increased rapidly until 3,200 s, reached a peak value of 1.8 kPa at 4,200 s (Point A in **Figure 5**), and then began to decrease sharply. The total pressure before sliding was $\sigma = \rho g h \approx 1.7 \times 10 \times 0.1$ kPa ~ 1.7 kPa (**Table.2**). At this time, the pore water pressure exceeded the total pressure in the original accumulation state of the soil. The soil structure was completely destroyed and the effective stress was completely lost, resulting in retrogressive shallow compound sliding of the front edge of the accumulation body. Then, a similar mutation occurred at position 6, cracks formed in the surface of the soil accumulation at position 6, and a potential shear zone began to form at position 6 (Point B in **Figure 5**). Soon after, the pore water pressure increased sharply at positions 2, 3, 4, and 5 and reached the peak value, and it remained at this value for a period of time. At 4,800 s, the water contents at every position all began to decrease sharply, the pore water pressure also began to decrease sharply, and a large-scale loess mudflow occurred (**Figure 5**).

Type B. First all, as the rainfall continued, the wetting peak during the water infiltration into the soil accumulation gradually moved downward, so the volumetric water content of the soil increased. Then, the soil began to shrink, and the soil accumulation underwent overall collapse and subsidence. When the water recharge was greater than the infiltration rate of the soil, surface runoff formed and the slope's surface was

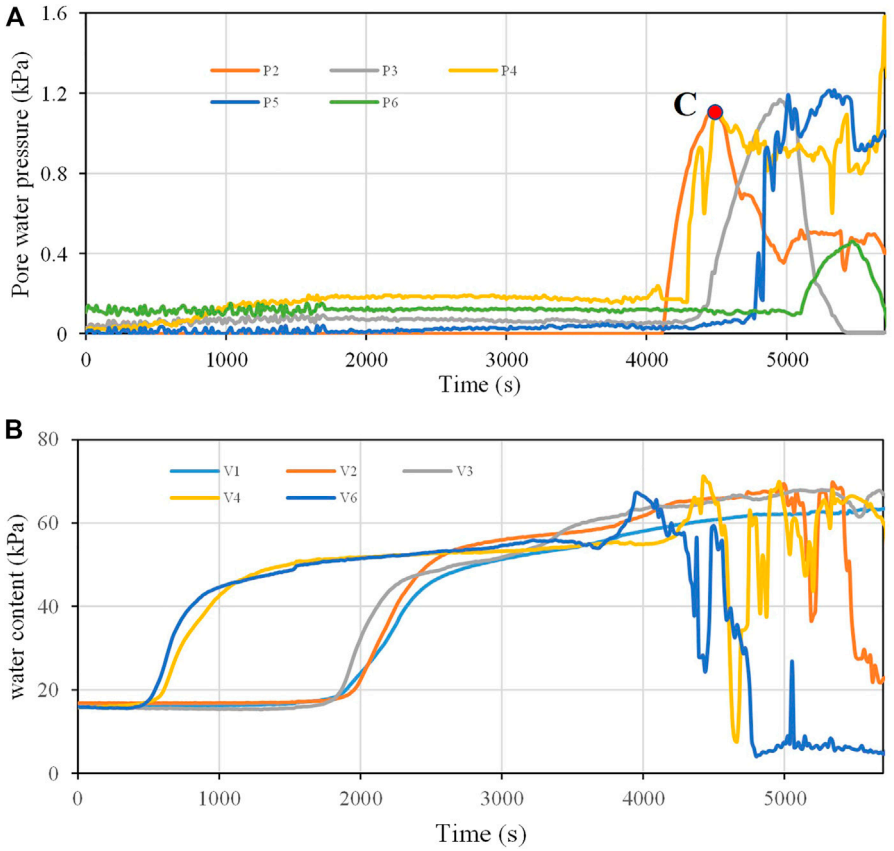

FIGURE 6 | Variations in pore water pressure and water content with time in the flume test with a slope angle of 15°. **(A)** Pore water pressure; **(B)** Water content. Discussion of the initiation mechanisms of loess mudflows.

continuously eroded. As a large amount of water accumulated in the toe part of the slope, the volumetric water content of the soil at the toe part of the slope increased, the pore water pressure of the soil began to increase, and retrogressive shallow composite sliding occurred in the toe part. Then, the soil accumulation began to generate retrogressive mudflows around a position. There was no large-scale mudflow throughout the entire experiment. The scale of the loess mudflow was less than the scale of Type A. Moreover, because of the continuous sliding, several sensors were moved and the sensor positions changed, Therefore, some of the volumetric water content and pore water pressure sensor data may not match (such as P5) (**Figure 6**). Overall, the pore water pressure of each location exhibited a sudden increase. This shows that the loess liquefied during the initiation of the loess mudflow.

The initiation mode of the test with a slope angle of 15° was Type B (**Table 3**). **Figure 6** shows the variations in the volumetric water content and pore water pressure in the soil accumulation. At 480 s, the water content at shallow positions four and six began to increase. At 1,500 s, the volumetric water content reached 50%. As the rainfall continued, the water constantly infiltrated, In the first 1,800 s, the water contents at deep positions 1, 2, and three began to increase, and the water contents increased to >50% at 3,000 s. The soil was nearly saturated. At the same time, there was no response in the pore water pressure before 4,000 s. After 4,000 s, the pore water pressure at every location began to increase suddenly. Then, the soil began to liquefy (Point C in **Figure 5**). Later, retrogressive shallow compound sliding occurred.

The seven sets of tests were conducted under different rainfall intensities and slope angles. First, we analyzed the variations in the seepage field in the different tests to compare the effects of the rainfall intensity and slope angle on the initiation processes of the loess mudflows. The test with slope angle of 13° and the lowest rainfall intensity and the test a slope angle of 15° and the largest rainfall intensity were selected, and then, the test with a slope angle of 17° and a moderate rainfall intensity was selected for comparison (**Table 1**). The changes in the seepage fields before the first sliding event in each group of tests were selected for analysis. According to the change in the pore water pressure at each location, the streamline of the slope was drawn (**Figure 7**). It can be seen that the infiltration direction of the water in each group of experiments was almost vertical, and the horizontal infiltration was much smaller. The rainfall intensity in the test with a slope angle of 13° was 120 mm/h, and the rainfall intensity in the test with a slope angle of 16° was 185 mm/h. However, the rainfall intensity had little effect on the initiation timings of the first sliding events, which occurred at 4,700 s and 4,300 s, respectively. This may be because the rainfall intensities in all of the experiments in this paper are rainstorm levels, which exceed the permeability

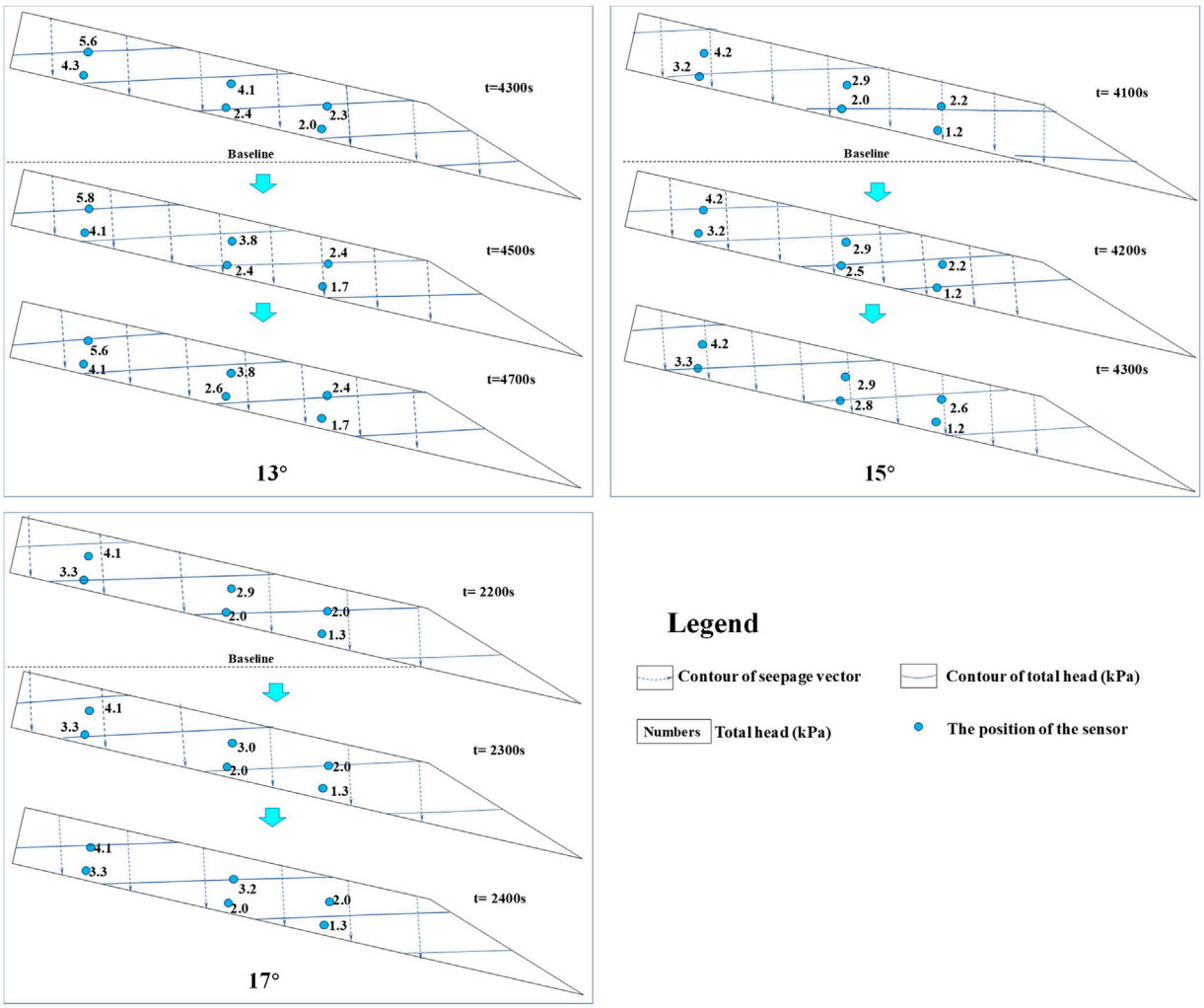

FIGURE 7 | Distribution of the seepage field in the flume tests (the slope angle was respectively 13°, 15°and 17°).

coefficient of loess. Therefore, the rainfall intensity had little effect on the infiltration time, and only the slope angle had a significant influence on the initiation time of the first sliding event in a series of experiments (**Figure 7**). This may be because increasing the slope angle increased the sliding force of the accumulation slope, and after rainfall infiltration, as the volumetric water content of the soil increased, the stability coefficient decreased, and then, a loess mudflow occurred.

Iverson and Major (1986) investigated the effect of groundwater flow on the potential for hillslope failure and liquefaction based on a novel limit-equilibrium analysis of infinite slopes with steady, uniform Darcian seepage with an arbitrary magnitude and direction. Normalization of the limit-equilibrium solution shows that three dimensionless parameters completely govern the Coulomb failure potential of a saturated infinite homogeneous hillslope (**Figure 8A**). These results indicate that three dimensionless parameters completely govern the Coulomb failure of the slope, including the ratio of the force magnitude of the seepage to the force magnitude of the gravitational body. The angle is $\theta - \phi$, where θ is the surface slope angle and ϕ is the angle of the internal friction of the soil; and the angle is $\lambda + \phi$, where λ is the angle of the seepage vector measured with respect to an outward-directed surface-normal vector (**Figure 8A**). A failure domain, which illustrates intriguing possibilities for the initiation of flowing mass movements, is also shown in the bottom right corner of **Figure 8B**.

The angles of the soil accumulation selected in the tests was 10°–20°. The internal angle ϕ of the soil was 26.4° (**Table 2**). Because the infiltration direction in the seven groups of tests was almost vertical (**Figure 7**), the range of λ was 160°–170°, the range of $\theta - \phi$ was −16° to −6°, and the range of $\lambda + \phi$ was 186°–196°. As can be seen, the soil accumulation in the seven sets of tests was in a unconditionally stable original state (blue box in **Figure 8B**). As the infiltration progressed, the internal friction angle of the soil changed with time. Moreover, since loess is a type of clay silt, the changes in the cohesion should be considered. It is difficult to quantify the changes in the cohesion of loess, Sassa (1984) proposed the concept of the apparent friction angle based on the concept of liquefaction. This formula was proposed based on

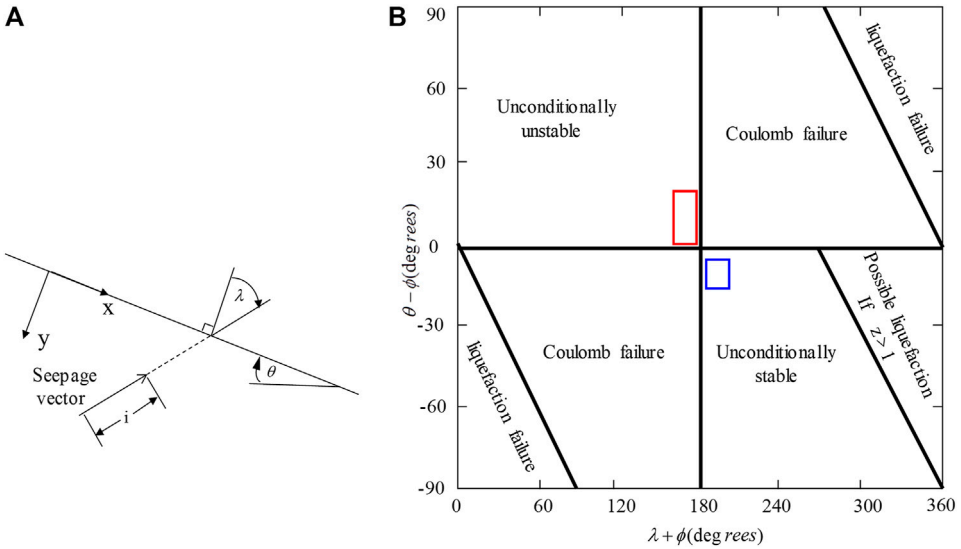

FIGURE 8 | Distribution of the domains that exhibit a preferred slope failure mode. **(A)** Definition of the seepage vector magnitude and direction; **(B)** The tests' failure mode.

FIGURE 9 | Failure process in the experiment with a slope angle of 17°.

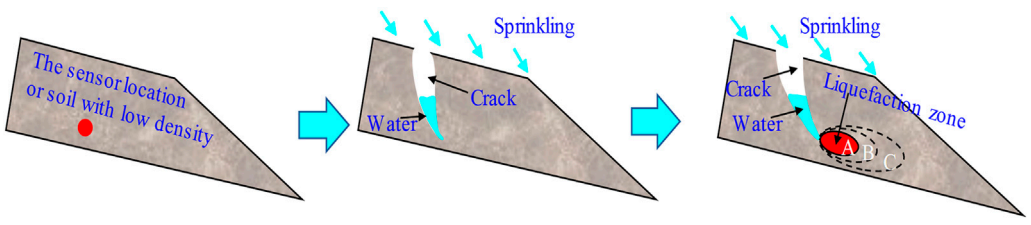

FIGURE 10 | The initiation process of the loess mudflows in the tests with slope angles of 10° and 13°.

the effective stress principle, and it uses the apparent friction angle to quantify the change in the state of the soil when the soil is liquefied.

$$\tan \phi_a = \frac{\sigma - \mu}{\sigma} \tan \phi. \quad (1)$$

In the seven sets of tests, as the pore water pressure increased, the pore water pressure came close to the total stress σ several times (**Figures 5**, **6**), so the range of ϕ was 0°–10° before the loess mudflow was initiated, the range of $\theta - \phi_a$ was −0° to 10°, and the range of $\lambda + \phi_a$ was 160–180°. At this time, the soil accumulation in the seven sets of tests was in unconditionally unstable (red box in **Figure 8B**). Therefore, as the rainfall continued, the water flow gradually entered the soil, and the soil accumulation changed from unconditionally stable to unconditionally unstable. This led to the different initiation modes observed during the tests.

Although loess has a loose structure, its infiltration rate is far less than that of sand. The deep sensor positions (4, 5, and 6) were about 8 cm away from the ground. The infiltration rate of the soil was only 0.042 m/h (**Table 2**). The infiltration of the water was mainly vertical infiltration. It would take at least 2 h for the water content of the deep sensor positions (4, 5, 6) to begin to respond under the condition of homogeneous infiltration. However, the water content of the deep positions in the seven groups of tests basically responded within 3,000 s, i.e., less than 2 h (**Figures 5**, **6**). This indicates that advantageous infiltration occurred during the water infiltration process, which led to a reduction in the time required for the water to reach the deep positions. The viewpoint of dominant infiltration in loess has long been described by many scholars (Xu et al., 2013; Ma et al., 2019a; Zhuang et al., 2020). In the experiments described in this paper, the advantage infiltration mainly occurred in two locations. 1) The soil was looser in the sensor layout area, with a larger porosity than in the other parts of the soil accumulation, which was beneficial to water infiltration. For example, in the test with a slope angle of 17°, positions one and three provided advantageous infiltration channels. Thus, water infiltration occurred in these positions first (**Figure 9**). 2) In the process of stacking the soil in the models, it is inevitable that there will be some areas with uneven density, resulting in places with a larger porosity that easily conduct water. As the rainfall continued, the infiltration into the homogeneous soil was limited, and a large amount of water flowed into the sensor location or area with a lower density, which caused the volumetric water content of the soil to increase. In addition, due to the water sensitivity of loess, the loess shrank when it encountered the water, its strength decreased, and the area continued to expand, forming a crack. As the infiltration of the water continued, when the water content of the soil had nearly reached the saturated water content, the water accumulated in this area, and the pore water could not dissipate in time. The pore water pressure increased rapidly, and the soil was liquefied in a small area (**Figure 10A**). As the rainfall continued, the water storage capacity increased and the local liquefied soil flowed, causing the liquefaction area to continue to spread and become larger (**Figures 10B,C**). Thus, the unstable area of the accumulation increased until the driving force was greater than the resistance of the slope, at which point a loess mudflow (large scale) occurred (**Figure 10**).

CONCLUSION

Loess mudflows occur frequently on the Chinese Loess Plateau, resulting huge casualties and property damage. In this study, a series of flume tests were designed by controlling the slope angle between 10° and 20° to study the initiation mechanism of loess mudflows. The following conclusions were drawn from the results of the experiments.

1) There are two initiation modes when the slope angle of the soil accumulation is 10°–20°. For slopes of 10–13°, the mode is large-scale mudflow and retrogressive toe sliding (Type A); and for slopes of 14–19°, the mode is small-scale mudflow and retrogressive toe sliding (Type B).
2) Based on the distribution of the domains that exhibit the preferential slope failure mode proposed by Iverson and Major (1986), the soil accumulation was unconditionally stable before a loess mudflow was formed. However, as the rainfall continued, the water gradually entered the soil, and the soil accumulation changed from unconditionally stable to unconditionally unstable, which led to different initiation modes for the loess mudflows during the tests.
3) The water preferentially infiltrated into the areas with uneven densities and a large amount of water accumulated. The pore water pressure quickly increased and could not dissipate in time, so the loess liquefied. As the liquefaction area continued to spread and became larger, the soil accumulation underwent shear deformation as a whole and a potential shear zone began to form. Then, a loess mudflow (large scale) occurred. Relatively speaking, Type B occurred in the tests in which the soil accumulation had a relatively uniform density. Lei, 2001.

DATA AVAILABILITY STATEMENT

The original contributions presented in the study are included in the article/Supplementary Material, further inquiries can be directed to the corresponding author.

AUTHOR CONTRIBUTIONS

This paper represents a result of collaborative teamwork. PM and XZ designed the tests. JZ, YC and CL guided the laboratory experiments and conducted the field observation. JZ and PM prepared the original manuscript. All of the authors contributed equally to this work.

FUNDING

This work was financially supported by the Program of National Natural Science Foundation of China (42090053, 42107198, 42041006, 41790441).

REFERENCES

Fan, X., Xu, Q., Scaringi, G., Li, S., and Peng, D. (2017). A Chemo-Mechanical Insight into the Failure Mechanism of Frequently Occurred Landslides in the Loess Plateau, Gansu Province, China. *Eng. Geology.* 228, 337–345. doi:10.1016/j.enggeo.2017.09.003

Iverson, R. M., and Major, J. J. (1986). Groundwater Seepage Vectors and the Potential for Hillslope Failure and Debris Flow Mobilization. *Water Resour. Res.* 22, 1543–1548. doi:10.1029/wr022i011p01543

Kang, C., Zhang, F., Pan, F., Peng, J., and Wu, W. (2018). Characteristics and Dynamic Runout Analyses of 1983 Saleshan Landslide. *Eng. Geology.* 243, 181–195. doi:10.1016/j.enggeo.2018.07.006

Lei, X. Y. (2001). *Geo-hazards in Loess Plateau and Human Activity*. Beijing, China: Science Press.

Leng, Y., Peng, J., Wang, Q., Meng, Z., and Huang, W. (2018). A Fluidized Landslide Occurred in the Loess Plateau: a Study on Loess Landslide in South Jingyang Tableland. *Eng. Geology.* 236, 129–136. doi:10.1016/j.enggeo.2017.05.006

Liu, T. S. (1985). *Loess and the Environment*. Beijing, China: Science Press. (in Chinese).

Ma, P. H., Peng, J. B., Wang, Q. Y., Zhuang, J. Q., and Zhang, F. Y. (2019a). The Mechanisms of a Loess Landslide Triggered by Diversion-Based Irrigation: a Case Study of the South Jingyang Platform, China. *Bull. Eng. Geology. Environ.* 78, 4945–4963. doi:10.1007/s10064-019-01467-5

Ma, P., Peng, J., Wang, Q., Duan, Z., Meng, Z., and Jianqi, Z. (2019b). Loess Landslides on the South Jingyang Platform in Shaanxi Province, China. *Q. J. Eng. Geology. Hydrogeology* 52 (4), 547–556. doi:10.1144/qjegh2018-115

Pei, X., Zhang, X., Guo, B., Wang, G., and Zhang, F. (2017). Experimental Case Study of Seismically Induced Loess Liquefaction and Landslide. *Eng. Geology.* 223, 23–30. doi:10.1016/j.enggeo.2017.03.016

Peng, D., Xu, Q., Liu, F., He, Y., Zhang, S., Qi, X., et al. (2018). Distribution and Failure Modes of the Landslides in Heitai Terrace, China. *Eng. Geology.* 236 (26), 97–110. doi:10.1016/j.enggeo.2017.09.016

Peng, J., Fan, Z., Wu, D., Zhuang, J., Dai, F., Chen, W., et al. (2015). Heavy Rainfall Triggered Loess-Mudstone Landslide and Subsequent Debris Flow in Tianshui, China. *Eng. Geology.* 186 (2), 79–90. doi:10.1016/j.enggeo.2014.08.015

Peng, J., Ma, P., Wang, Q., Zhu, X., Zhang, F., Tong, X., et al. (2018). Interaction between Landsliding Materials and the Underlying Erodible Bed in a Loess Flowslide. *Eng. Geology.* 234, 38–49. doi:10.1016/j.enggeo.2018.01.001

Peng, J., Wang, S., Wang, Q., Zhuang, J., Huang, W., Zhu, X., et al. (2019). Distribution and Genetic Types of Loess Landslides in China. *J. Asian earth Sci.* 170, 329–350. doi:10.1016/j.jseaes.2018.11.015

Pu, X., Wan, L., and Wang, P. (2021). Initiation Mechanism of Mudflow-like Loess Landslide Induced by the Combined Effect of Earthquakes and Rainfall. *Nat. Hazards* 105, 3079–3097. doi:10.1007/s11069-020-04442-6

Sassa, K., The Mechanism Starting Liquefied Landslides and Debris Flows." in Proceedings of the 4th International Symposium on Landslides, Toronto, Canada, Sept 1984, 2, 349–354.

Xu, L., Dai, F. C., Tu, X. B., Javed, I., Woodard, M. J., Jin, Y. L., et al. (2013). Occurrence of Landsliding on Slopes where Flowsliding Had Previously Occurred: an Investigation in a Loess Platform, north-west China. *Catena* 104, 195–209. doi:10.1016/j.catena.2012.11.010

Yuan, B., Chen, W., Tang, Y., Li, J., and Yang, Q. (2015). Experimental Study on Gully-Shaped Mud Flow in the Loess Area. *Environ. Earth Sci.* 74 (1), 759–769. doi:10.1007/s12665-015-4080-9

Zha, X., Huang, C., Pang, J., Li, Y., Liu, J., Cuan, Y., et al. (2019). Sedimentary Records of Holocene Palaeo-Mudflow Events in Tianshui basin of the Western Loess Plateau, China. *Quat. Int.* 521, 129–137. doi:10.1016/j.quaint.2019.06.027

Zhang, F., Wang, G., Kamai, T., Chen, W., Zhang, D., and Yang, J. (2013). Undrained Shear Behavior of Loess Saturated with Different Concentrations of Sodium Chloride Solution. *Eng. Geology.* 155 (6), 69–79. doi:10.1016/j.enggeo.2012.12.018

Zhang, F., Yan, B., Feng, X., Lan, H., Kang, C., Lin, X., et al. (2019). A Rapid Loess Mudflow Triggered by the Check Dam Failure in a Bulldoze Mountain Area, Lanzhou, China. *Landslides* 16 (10), 1981–1992. doi:10.1007/s10346-019-01219-2

Zhang, Z.-Y., Chen, S.-M., and Tao, L.-J. (2002). "1983 Sale Mountain Landslide, Gansu Province, China," in *Catastrophic Landslides, Geological Society of America*. Editors SG. Evans and JV. DeGraff Colorado, US: Reviews in Engineering Geology, XV, 149–164. doi:10.1130/reg15-p149

Zhou, J. X., Zhu, C. Y., Zheng, J. M., Wang, X. H., and Liu, Z. H. (2002). Landslide Disaster in the Loess Area of China. *J. For. Res.* 13 (2), 157–161. doi:10.1007/bf02857244

Zhu, X., Peng, J., Liu, B., Jiang, C., and Guo, J. (2020). Influence of Textural Properties on the Failure Mode and Process of Landslide Dams. *Eng. Geology.* 271, 105613. doi:10.1016/j.enggeo.2020.105613

Zhuang, J. Q., and Peng, J. B. (2014). A Coupled Slope Cutting-A Prolonged Rainfall-Induced Loess Landslide: a 17 October 2011 Case Study. *Bull. Eng. Geol. Environ.* 73 (4), 997–1011. doi:10.1007/s10064-014-0645-1

Zhuang, J., Peng, J., and Zhu, Y. (2020). Study of the Effects of clay Content on Loess Slope Failure Mode and Loess Strength. *Bull. Eng. Geol. Environ.* 80, 1999–2009. doi:10.1007/s10064-020-02055-8

Conflict of Interest: The authors declare that the research was conducted in the absence of any commercial or financial relationships that could be construed as a potential conflict of interest.

frontiers in Earth Science

ORIGINAL RESEARCH
published: 14 October 2021
doi: 10.3389/feart.2021.771316

A Cross-Linked Polymer Soil Stabilizer for Hillslope Conservation on the Loess Plateau

Xiaochao Zhang[1,2], *Yujian Zhong*[1,2]*, *Xiangjun Pei*[1,2] and *Yuying Duan*[1]

[1]State Key Laboratory of Geological Disaster Prevention and Environmental Protection, Chengdu University of Technology, Chengdu, China, [2]State Environmental Protection Key Laboratory of Synergetic Control and Joint Remediation for Soil and Water Pollution, School of Ecological and Environmental Sciences, Chengdu University of Technology, Chengdu, China

The soil of the Loess Plateau is highly susceptible to erosion due to its distinct loess structure with poor water stability and disintegrates easily. Previous research has focused on improving soil strength without considering stability and ecological performance. Comprehensive improvements may be achieved by cross-linked polymers (CLPs), but their effect on loess structure remains unclear. In the present study, we investigate CLPs as a new organic soil stabilizer to improve soil aggregate stability. To determine the effect of CLPs on the stabilization of loess, a series of indoor tests was conducted to assess unconfined compressive strength, water stability, soil-water characteristics, and plant height. The stabilization mechanism was analyzed by comparing the microstructure, mineral composition, and features of functional groups of loess before and after treatment. The results showed that, compared with untreated loess, the unconfined compressive strength and anti-disintegration property of treated loess were significantly increased. The water retention capacity was improved, and the germination rate and growth of plants were promoted. Microscopic analysis showed that the use of CLPs did form new minerals in the loess or change the functional groups, rather, CLPs improved the microstructure, reduced the total volume of pores, and increased the degree of soil compaction. Field tests showed that the erosion of loess hillsides was effectively controlled by CLPs. Under the same erosive conditions, the slope surface treated with CLPs was more intact than the untreated slope surface. Our findings provide new strategies regarding the application of CLPs as soil stabilizers to control loess erosion and promote vegetation restoration.

Keywords: cross-linked polymer, soil stabilizer, loess, erosion control, curing mechanism, mechanical property

OPEN ACCESS

Edited by:
Fanyu Zhang,
Lanzhou University, China

Reviewed by:
Tongwei Zhang,
Lanzhou University, China
Fangzhou Liu,
University of Alberta, Canada

***Correspondence:**
Yujian Zhong
zhongyujian@stu.cdut.edu.cn

Specialty section:
This article was submitted to Geohazards and Georisks, a section of the journal Frontiers in Earth Science

Received: *06 September 2021*
Accepted: *30 September 2021*
Published: *14 October 2021*

Citation:
Zhang X, Zhong Y, Pei X and Duan Y (2021) A Cross-Linked Polymer Soil Stabilizer for Hillslope Conservation on the Loess Plateau. Front. Earth Sci. 9:771316. doi: 10.3389/feart.2021.771316

1 INTRODUCTION

Loess is rich in calcium and soluble salts; its structure is loose, cementation is weak, and large pores and vertical joints develop. Under rainfall or irrigation, the integrity and stability of loess without vegetation cover are easily damaged, which may cause various disasters, such as collapse, landslide, and debris flow (Peng et al., 2018; Feng et al., 2020). With more intensive construction on the Loess

Abbreviations: CLPs, cross-linked polymers (stabilizer); CMC, carboxymethylcellulose; FTIR, Fourier-transform infrared; PAM, polyacrylamide; SWCC, soil-water characteristic curve; SEM, scanning electron microscopy; UCS, unconfined compressive strength; XRD, X-ray diffraction

Plateau, exposed slopes have been produced, causing serious soil erosion (Hu et al., 2020; Wu et al., 2020).

The factors influencing soil erosion on loess slopes can be summarized into four categories: rainfall, soil erodibility, topography, and slope surface cover (Liu et al., 2019). By reducing the slope (Zhao et al., 2015; Li et al., 2019) and setting buffer steps (Duan et al., 2021a; Wen et al., 2021), we can effectively reduce the kinetic energy of runoff and control rill erosion (Wei et al., 2007; Fu et al., 2009; Zhao et al., 2013; Tang et al., 2020). For slope surface cover, erosion control can be achieved by, for example, planting trees and grass (Chen et al., 2018; Yan et al., 2021) or laying artificial turf (Li et al., 2020). However, there remain challenges associated with implementing these physical measures, such as large engineering volume, complicated construction, and incomplete erosion control. Furthermore, such measures mainly strengthen the macroscopic structure of the slope, but they fail to alter the soil properties. For the problem of loess erosion, the microstructure of loess can be fundamentally improved by stabilizers to improve soil stability.

Soil stabilizers can be divided into calcium-based stabilizers and non-calcium-based stabilizers according to composition (Behnood, 2018; Jalal et al., 2020). Studies have shown that calcium-based stabilizers, such as lime (James, 2020), gypsum (Ahmeda and Issa, 2014), fly ash (Xu et al., 2019; Yoobanpot et al., 2020), cement (Choobbasti and Kutanaei, 2017), and ground granulated blast furnace slag (GGBFS) (Keramatikerman et al., 2016), significantly enhance the compressive and shear strength. Indeed, this kind of stabilizer offers an effective measure to increase the bearing capacity of foundations. However, the abovementioned techniques are inapplicable to soil conservation, since such measures cause excessive hardening of the soil. Moreover, the use of traditional calcium-based stabilizers in soil stabilization projects leads to ecological damage, including the consumption of energy and resources, increasing pH, and high CO_2 emissions. Non-calcium-based soil stabilizers are more suitable for controlling hillslope erosion owing to their lower concentration and stability strength. Such stabilizers have achieved soil reinforcement (Zhang T. et al., 2020), improved the degree of compaction (Kushwaha et al., 2018; Mohammad and Eris, 2020), and increased soil aggregation (Ghasemzadeh and Modiri, 2020), which manifests as an increase in mechanical strength. Some non-calcium-based stabilizers can alter the form and distribution of water in soil (Chandler et al., 2017), thereby reducing soil erodibility. Indoor and outdoor rainfall simulation experiments have demonstrated the feasibility of using non-calcium-based stabilizers to prevent or control erosion (Song et al., 2019; Krainiukov et al., 2020). Different non-calcium-based stabilizers have different benefits in terms of seed germination, seedling growth, and long-term plant growth (Liu et al., 2011; Chang et al., 2015; Yang et al., 2019).

Loess is more susceptible to erosion than many other soils, resulting in lower vegetation coverage and fragile ecological environments on the Loess Plateau. For the effective use of soil stabilizers to control loess hillslope erosion, the overall performance must be considered, including soil stability, plant compatibility, and water-retention capacity. Most previous research focused on optimizing soil strength, and there remains a lack of more comprehensive research considering stability and ecological performance. Such comprehensive improvements may be achieved by grafting with a polyacrylamide (PAM), containing amide groups, and carboxymethylcellulose (CMC), containing several hydroxyl groups. Both CMC and PAM can effectively stabilize the soil while improving the water-retention capacity (Ozan et al., 2018). CMC is used as agricultural water retention additive, which can improve soil water retention capacity, but its solution viscosity is limited due to low molecular weight. PAM can make up for the lack of viscosity because of the larger molecular weight. The high viscosity solution formed by PAM solution due to flocculation and high molecular weight can effectively stabilize the soil. By crosslinking and polymerization, the viscosity increases with the increase of molecular weight, and has the excellent water retention performance of CMC. In the present study, a new type of dual CLP was synthesized using the abovementioned method. The application benefits of this new curing agent in loess erosion control were evaluated comprehensively.

2 MATERIALS AND METHODS

To determine whether CLPs improve the engineering performance of loess, the unconfined compressive strength (UCS), disintegration, and soil-water characteristic curve (SWCC) were determined, and a pot experiment was carried out on untreated and CLP-treated loess. To explain the stabilization mechanism, the effects of CLPs on loess particles, pore characteristics, mineral composition, and functional groups were studied through scanning electron microscopy (SEM), X-ray diffraction (XRD), and Fourier-transform infrared spectra (FTIR).

2.1 Materials

The loess used in this study was obtained from a land excavation slope in Yanan, Shaanxi Province, China. The coordinates of the sampling point are 109°19′25″ E and 36°36′00″ N. The sampling site is shown in **Figure 1**. Owing to rainfall and soil erosion on both sides of the drainage ditch, many erosive rills were formed on the hillside, and collapse was evident. The physical properties of loess were: natural water content, 12.77%; soil natural density, 1.6 g cm^{-3}; plastic limit, 17.4%; liquid limit, 28.9%; optimum water content, 18%; maximum dry unit weight, 1.77 g cm^{-3}; plasticity index, 11.5. Moreover, the particle size distribution is presented in **Figure 2**. As per the Chinese Soil Classification System, the soil was classified as silty clay.

CLPs are cross-linked copolymers synthesized by grafting PAM with CMC, and the preparation reaction formula is shown in **Figure 3A**. First, 10 g of CMC and 1 g of PAM were added to 200 and 100 ml of ultrapure water, respectively. Then, the two solutions were heated in a water bath at 80°C. Next, we added 40 ml of CMC solution, 10 ml of PAM solution, and 50 ml of distilled water to the flask and used ammonium persulfate as the initiator for graft copolymerization. To ensure the full progress of the cross-linking reaction, the solution was stirred for 2 h to obtain CLPs. The FTIR spectrum of the CLPs is shown in **Figure 3B**. There were numerous absorption peaks in the

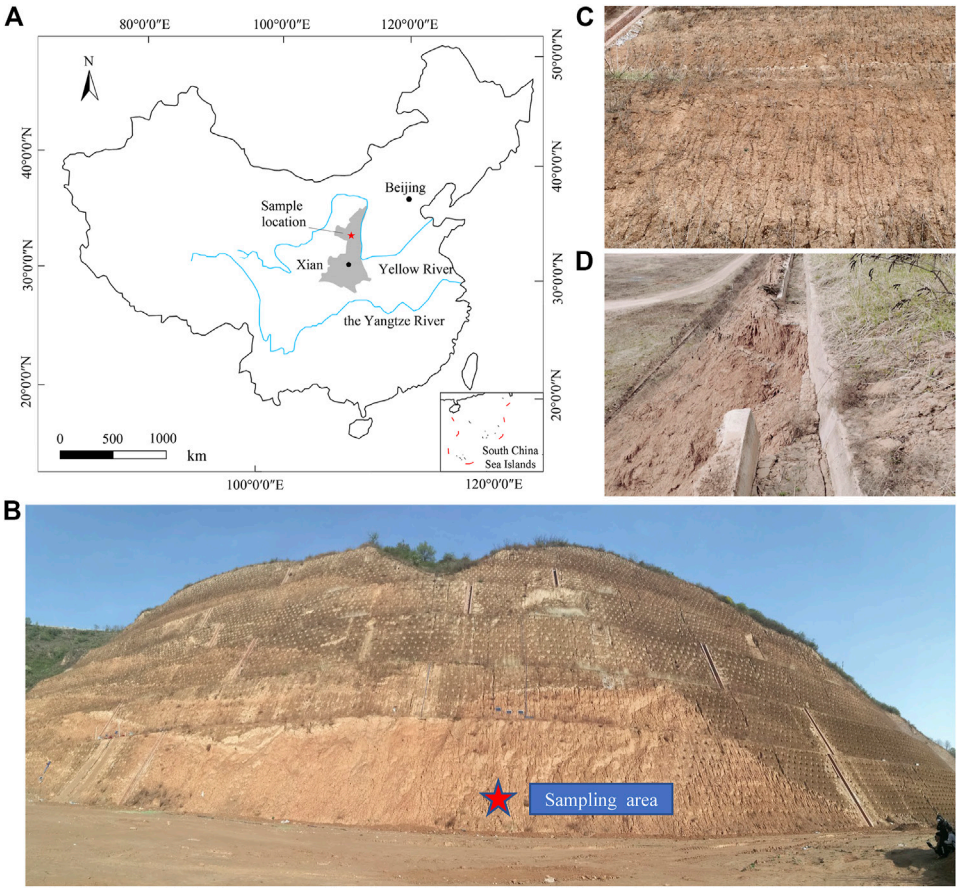

FIGURE 1 | Soil erosion on loess hillslope and sample location. **(A)** Geographical location of the sampling area; **(B)** panoramic image of the sampling area; **(C)** erosion gully on the hillslope; **(D)** drain collapsed owing to water erosion.

CLPs, including OH stretching vibration (3,400 cm^{-1}), CH_2 asymmetric stretching vibration (2,945 cm^{-1}), -CH_2- bending vibration (1,459 cm^{-1}), C=O stretching vibration (1,735 cm^{-1}), O–C–C antisymmetric stretching vibration (1,272 cm^{-1}), symmetrical CO deformation (1,146 cm^{-1}), and aromatic ring CH twisting vibration (669 cm^{-1}). All absorption peaks at these positions are caused by the characteristic functional groups in CMC and PAM. The CLPs are in the form of a transparent amorphous liquid, and their basic parameters were: concentration, 2.0%; pH 6.8–7.2; viscosity, 25 m Pa s; density, 1.1 g cm^{-3}; boiling point, 100°C.

2.2 Sample Preparation

The collected loess was dried and sieved through a 2-mm sieve. Then, the CLPs were diluted to 0% (water), 0.4, 0.8, 1.2, 1.6, and 2.0% (undiluted). We took the diluent of 18% of the dry weight of loess and stirred it to obtain the stable loess of CLPs. Stable loess with different CLPs concentrations was obtained by adjusting the concentration of CLPs solution. According to the dry density of 1.5 g cm^{-3} (85% of the maximum dry density), layering and compaction in the standard sample preparation mold were carried out so that the sample was uniform. The UCS mold was a cylinder with a diameter of 50 mm and a height of 100 mm. The SWCC mold was a ring cutter with a diameter of 61.8 mm and a height of 20 mm. The disintegration test mold was a cylinder with a diameter of 61.8 mm and a height of 40 mm. Following the unconfined compressive test, the samples were required for SEM. The UCS samples were demolded for testing after curing for 3, 7, 14, and 28 days. Other samples were demolded for testing after curing for 14 days.

2.3 Test Methods

2.3.1 Unconfined Compressive Strength Test

The UCS test was carried out according to the Chinese Standard for Soil Test Method (GB/T 50,123, 2019) using strain-controlled unconfined compression apparatus (YYW-2, Ningxi Soil Instrument Co., Ltd, China) at a loading rate of 2.4 mm/min. The relationship curve between axial stress (σ) and axial strain (ε) was drawn, and the peak stress (σf) on the curve was taken as the UCS. When the peak stress on the curve was not evident, the axial stress corresponding to 15% of the axial strain was taken as the UCS.

2.3.2 Disintegration Test

The disintegration test was carried out by the static water measure method. Into a beaker, we placed 1,500 ml of water and the prepared disintegration sample m_0. The state of the sample was recorded at

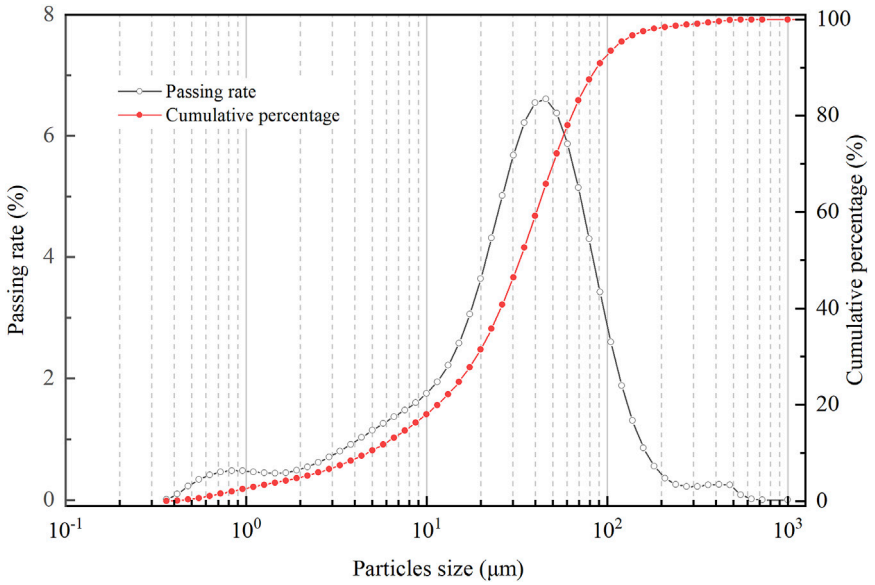

FIGURE 2 | Particle-size distribution curves of loess.

2 s, 10 s, 1, 10, 60 min, and 24 h. After 24 h, the beaker was placed for 12 h to precipitate the residual samples, absorb the supernatant, and air dry to obtain the sample. Then, the samples were cooled to 25°C for sieving, the soil mass in each particle size range was recorded, and the stability index was calculated using **Eq. 1** (Zhang et al., 2020).

$$K = \frac{\sum_{n=1}^{11}[10m_n \times (n-1)]}{m_0} \quad (1)$$

where K is the stability index with a value of 0–100; the range of n is 1–11; and m_n corresponds to sieved particle sizes of 0–1, 1–2, 2–5, 5–10, 10–20, 20–30, 30–40, 40–50, 50–60, 60–61.8, and 61.8 mm (initial size).

2.3.3 Soil-Water Characteristic Curve Test

The SWCC test was carried out with a 1D-SDSWCC pressure plate extractor (Earth Products China Ltd, China). The dehumidification curve was used to characterize the SWCC. The sample was fully saturated before the test and then placed on a porous ceramic plate for testing. The suction range of the instrument was 1–1,500 kPa. The suction of the matrix was loaded by the "axis translation technique". The reference of negative pore water pressure was translated from the standard atmospheric pressure to the final pressure of the loading chamber. By increasing the pore gas pressure, matrix suction was applied to the sample to force the soil water to seep out, and the drainage volume of the soil was measured to obtain the matrix suction–volume water content relationship curve. Since the dehydration process of cohesive soil is relatively slow, loess treated with 1.6% CLPs and untreated loess were selected for the experiment.

The van Genuchten model (van Genuchten, 1980) was used to obtain the air entry value, dehumidification rate, residual water content, and other parameters of treated and untreated loess. The formula is as follows:

$$\theta_w = \theta_r + \frac{(\theta_s - \theta_r)}{[1 + (a \times \varphi)^n]\left(1 - \frac{1}{n}\right)} \quad (2)$$

where θ_w is the volumetric water content; θ_s and θ_r are the saturated and residual volumetric water content (%), respectively; φ is the matrix suction (kPa); a is the air entry value (kPa); and n is affected by soil pore characteristics, which is a parameter related to the dehydration rate of the soil for high air entry values.

2.3.4 Pot Experiment

To explore the effect of CLPs on plant growth, a pot experiment was conducted. The experimental subjects comprised one control (CLP concentration of 0%) and three CLP treatment groups (CLP concentration of 0.8, 1.6, or 2.0%). Alfalfa was selected for the experiments as this plant was often used for slope protection and cultivation in loess areas. We placed 4 kg of loess soil in 12 pots (three treatments plus the control with three replicates) of 24 cm diameter and 20 cm height, and then sowed 100 selected seeds into each pot. Each pot was sown with 100-selected seeds, covered with approximately 1 cm of soil, covered with plastic wrap, and placed in a greenhouse for cultivation. The indoor cultivation temperature, relative humidity, and light period were controlled at 25°C, 60%, and 16 h, respectively. Once the plants had developed three-petaled leaves, the germination rate of alfalfa was calculated. In order to ensure sufficient space and nutrients in the pot, 50 seedlings were selected. Control the same number of seedlings to confirm that the difference in soil water content and plant growth is not caused by the inconsistent number of seedlings. Five hundred milliliters of pure water was supplied every 2 days. In the first 4 weeks after germination, alfalfa plant height was measured weekly. Meanwhile, to study the health of

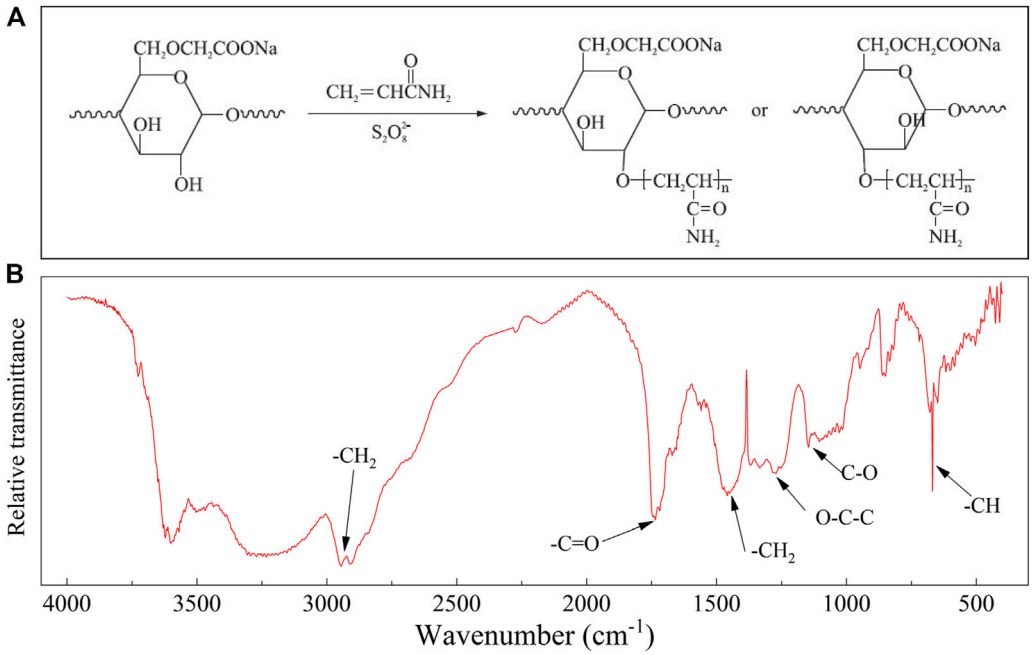

FIGURE 3 | (A) Reaction formula for preparing cross-linked polymers (CLPs); **(B)** Fourier-transform infrared reflection spectrogram of CLPs.

the plants under adverse conditions, the water content of potted plants in each group was controlled to be the same. Then, the humidifier was turned off and watering was stopped. The drought stress treatment was carried out to the sixth week for measuring soil water content. After rehydration, we continued to monitor the plant height indicator after 8, 10, and 12 weeks.

2.3.5 Scanning Electron Microscopy Test

The microstructure of soil treated with CLPs at different concentrations was analyzed by scanning electron microscopy SEM. A Prisma E scanning electron microscope (Thermo Fisher Scientific, Waltham, Massachusetts, United States) was used. The samples were plated with a thin layer of gold before testing to avoid the accumulation of electric charges on the surface of the samples. Using image processing techniques, we vectorized the SEM images of soil microstructure, and the pore structure characteristics were quantitatively analyzed. The process included 1) preprocessing, 2) binarization, 3) rasterization, 4) vectorization, 5) measuring the perimeter and area, and 6) calculating the surface void ratio according to the following formula.

$$e_m = S_n/(S - S_n) \times 100\% \quad (3)$$

where e_m is the surface void ratio (the ratio of the pore area to the area of the soil particles in the two-dimensional image); and S_n and S are the total areas of the pore polygons in the image and the total area of the image in the same statistical range, respectively.

2.3.6 Field Test

Through the field test, the role of CLPs in the prevention and control of loess hillslope erosion was evaluated. The loess sampling site was an engineering excavation hillslope with a slope of 50–55°. Two test plots (13 m long; 5 m wide) were established. Both slopes were sown, and the selected grass species were alfalfa, tall fescue, ryegrass, and bluegrass. The CLP diluent, loess, and seeds were mixed uniformly and then spread for sowing. Firstly, 15 kg of 1.6% CLPs was added to every 100 kg of loess on the treated slope surface, and the same amount of water was added to the untreated slope surface. Then, 50 g of mixed grass seeds was added. After being evenly combined, the mixture was sprayed on the slope. The field test procedures were as follows: 1) The vegetation and topsoil were removed, and the slope surface was leveled by compaction. 2) Three-dimensional nets were laid on the modified slope and fixed with pegs. 3) The loess, seeds, and CLP diluent (or pure water for the untreated slope) were mixed according to the above proportions and then evenly spread on the slope (90 kg mixed mud per square meter was paved with a thickness of 5 cm). 4) The plastic film was removed 2 weeks later, and the plots were watered every 3 days after curing. Finally, the erosional features on the slopes were observed and compared.

3 RESULTS

3.1 Effect of CLPs on Unconfined Compressive Strength

Figure 4A–D shows the stress–strain relationship of samples with different CLP concentrations for each curing period. Compared with the untreated samples, the σ_f of the treated samples notably increased, while **Figures 4E,F** shows the change trend in the UCS of samples treated with different

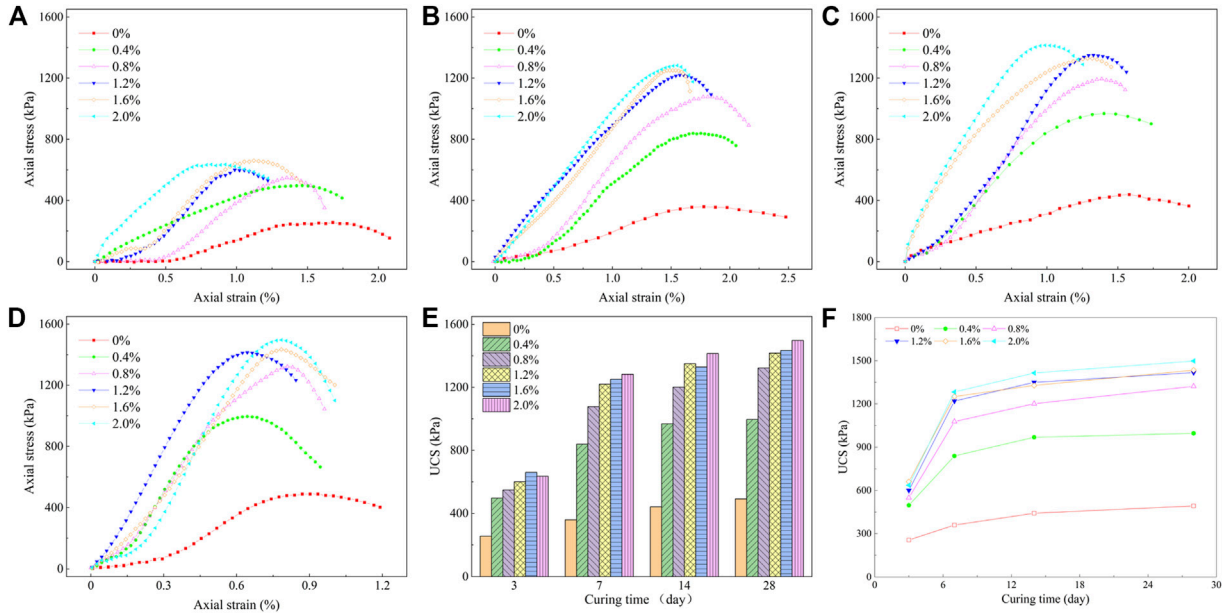

FIGURE 4 | (A–D) Stress–strain curves of cross-linked polymer-treated loess curing for 3, 7, 14, and 28 days **(E–F)** Unconfined compressive strength of cross-linked polymer-treated loess at different curing times.

concentrations of CLP with curing time. The σ_f of the CLP-treated samples was significantly higher than that of the untreated samples. As the concentration of CLP increased, the σ_f of the samples exhibited an increasing trend. Comparing the UCS of samples with different CLP concentrations in the same period, at 3 days, the strength slightly increased with the increase in material content, and at 7 days, the UCS of each sample showed an increasing trend with the increase in CLP concentration. After 28 days, the σ_f of the 2.0% CLP-treated samples was 1,497.84 kPa, which was 3.04 times that of the untreated samples (491.97 kPa). However, with the continuous increase in CLPs, the σ_f of soil tended to gradually stabilize. Compared with 2.0% CLPs, the application of 1.2% CLPs increased strength by more than 90% in each curing period. Therefore, considering the cost and strength, the optimal concentration range of CLPs was 1.2–1.6%.

3.2 Effect of CLPs on Disintegration

Table 1 and **Figure 5** illustrate the disintegration of samples treated with different concentrations of CLPs after soaking for 24 h. According to the disintegration failure mode and disintegration products, the untreated loess immediately and strongly bubbled and collapsed after being soaked in water and completely disintegrated within 1 min leaving scaly fragments and powder, and the water became turbid. In the loess samples reinforced with 0.4 and 0.8% CLPs, cracks appeared initially after being immersed in water and further expanded over time; the loess completely disintegrated after soaking for 10 min. The disintegration mode was layered spalling accompanied by a massive slump, and the final disintegration product was a muddy mixture of thick scales and granular fragments. The loess samples treated with 1.2% CLPs had to be soaked for 10 min before cracks appeared and did not completely disintegrate until 1 h. The final disintegration product was thick soil. The loess samples treated with >1.6% CLPs remained intact. Therefore, the addition of CLPs significantly improved the anti-disintegration property of loess.

Improvements in the anti-disintegration property of loess can be quantitatively evaluated using the stability index. The stability index results of the samples treated with CLPs are shown in **Figure 6**. When the concentration of CLPs was 0, 0.4, 0.8, 1.2, 1.6, and 2.0%, the stability index was 0, 3.85, 9.57, 20.28, 88.06, and 100, respectively. When the CLP concentration was <1.6%, the anti-disintegration property sharply increased. At CLP concentration of 1.6%, the stability index slowly increased, indicating increased stability in the loess. After loess samples treated with 2.0% CLPs were soaked for 24 h, their stability index reached 100%.

3.3 Effect of CLPs on Soil Water Retention

The relationship between the matrix suction and volumetric water content of treated and untreated loess was characterized by the SWCC (**Figure 7**). The SWCC of both treated and untreated loess were consistent with the VG model. However, the SWCC of the treated loess trended to the upper right compared with the untreated loess, that is, under the same matrix suction, the treated loess had a higher volumetric water content than the untreated loess. These results are in line with previous findings (Eyo et al., 2020; Zhai et al., 2020). White et al. (1970) and Vanapalli et al. (1999) suggested that the SWCC can be divided into three stages namely boundary effect, transition, and unsaturated. Combined with the fitting parameters of every stage obtained from the VG model, the hillslope of the transition

TABLE 1 | Disintegration of loess under different cross-linked polymer (CLP) concentrations.

CLP concentration (%)	Disintegration experimental phenomenon					
	2 s	10 s	1 min	10 min	60 min	24 h
0	Bubbly	Cracked	Disintegrated and Turbid	——	——	——
0.4	Bubbly	——	Cracked	Disintegrated	——	——
0.8	Bubbly	——	Cracked	Disintegrated	——	——
1.2	Bubbly	——	——	Cracked	Disintegrated	——
1.6	Bubbly	——	——	——	——	——
2.0	Bubbly	——	——	——	——	——

—— indicates no significant changes were observed.

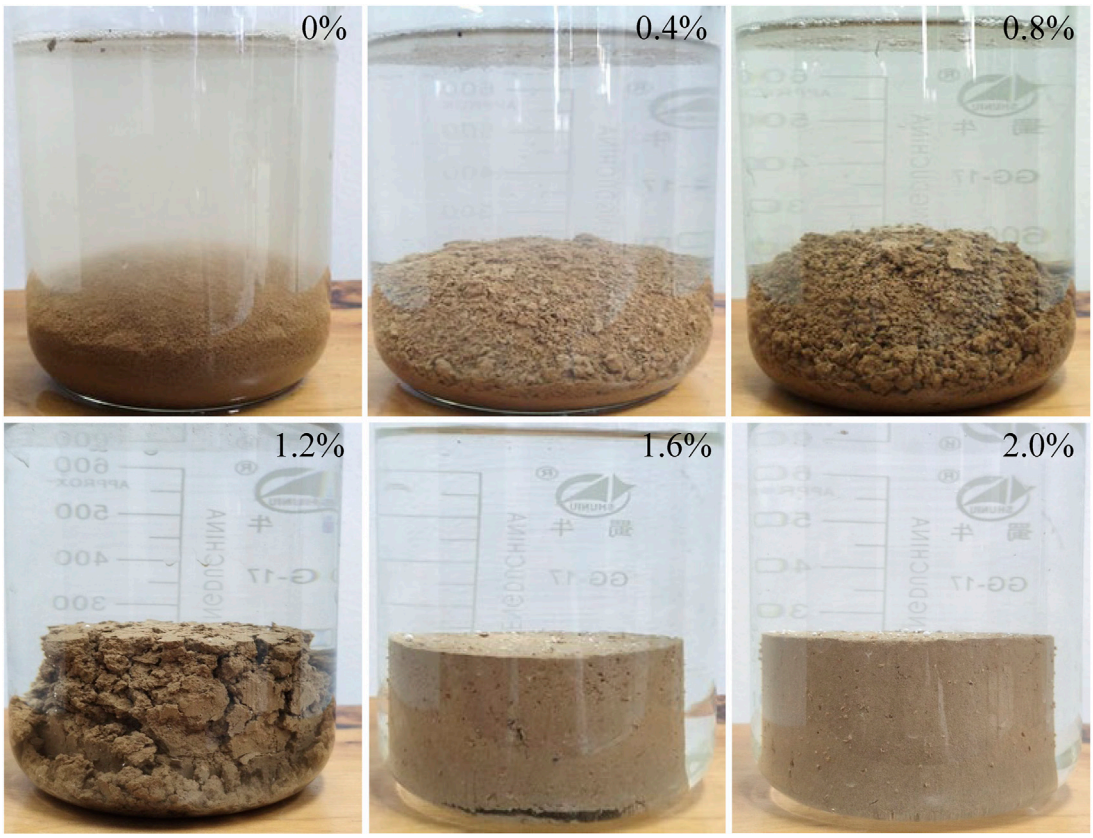

FIGURE 5 | Samples treated with different cross-linked polymer (CLP) concentrations following immersion for 24 h.

stage, saturated volumetric water content, air entry value, dehumidification rate, and residual water content of loess can be obtained (**Table 2**). Following this, the effect of CLPs on soil water retention was analyzed. In the boundary effect stage, the soil was saturated, and only free water driven by gravity was discharged. The saturated volumetric water content of treated loess was 54.24% and that of untreated loess was 43.25%, indicating that CLPs considerably improved the saturated volumetric water content of loess. With the gradual increase in matrix suction, the capillary water in the pores was gradually discharged due to its inability to resist the applied matrix suction. The critical value of matrix suction is referred to as the air-entry value. The air-entry value of the treated loess (6.26 kPa) exceeded that of the untreated loess (5.16 kPa), indicating that CLPs improved the capillary water holding capacity of loess. After the matrix suction exceeded the air-entry value, the transitional stage began, during which the changes in the SWCC were even more considerable. The absolute value of the tangent slope of the transition stage is defined as the dehumidification rate, which represents the strength of the capillary force in the soil against the loss of external forces. The dehumidification rate of treated loess was 0.31 and that of untreated loess was 0.74. This result indicated that increased matrix suction made it more difficult for the capillary water of the treated loess to discharge, thereby, strengthening the water retention capacity. The suction continued to increase and

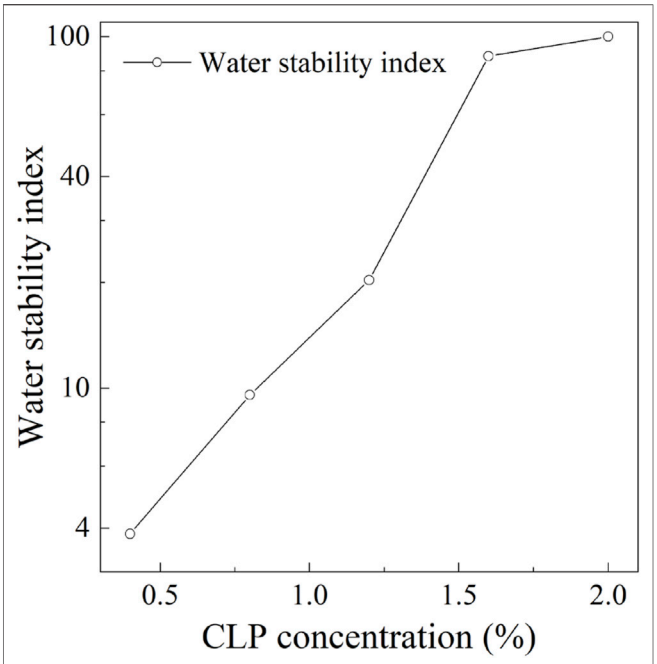

FIGURE 6 | Anti-disintegration index of samples treated with different concentrations of cross-linked polymers (CLPs).

reached the unsaturated stage. With increased suction, the water content stopped decreasing, and the residual water content of treated loess significantly increased compared with that of untreated loess. Calculating the effective water content (field water content minus residual water content) showed that the effective water content of treated loess was higher than that of untreated loess.

3.4 Effect of CLPs on Plant Growth Characteristics

The water content of potted loess was measured after 2 weeks of drought stress (**Figure 8A**). Under the same initial water content and culture conditions, the water content of potted loess treated with CLP concentrations of 0, 0.8, 1.6, and 2.0% was 4.34, 4.97, 5.38, and 5.73%, respectively. This result indicated that when CLP concentration increased, the water content of the potted loess also increased. The loess with treated CLPs had an improved water retention capacity owing to the presence of hydrophilic functional groups. This, in turn, enhanced the infiltration of water into loess particles.

After sowing for 3 days, the germination rate of the seeds in each pot was calculated (**Figure 8A**). The germination rate of untreated seeds was 65%, and that of seeds treated with 0.8, 1.6, and 2.0% CLPs was 66, 67, and 69%, respectively, indicating that CLPs did not adversely affect the germination rate. After 28 days, the average plant height was measured, as shown in **Figures 8B,C**. The plants grew well, and evident differences in plant height were observed after 3 weeks. As the concentration of CLP increased, plant height also increased, indicating that CLPs promoted plant growth to some extent. Treated loess exhibited less water evaporation, therefore, more water was available to promote plant growth. After 12 weeks, the alfalfa taproots in loess treated with 2.0% CLPs were significantly more developed and thicker than those in untreated loess. These findings suggest that the application of CLPs did not inhibit plant development and

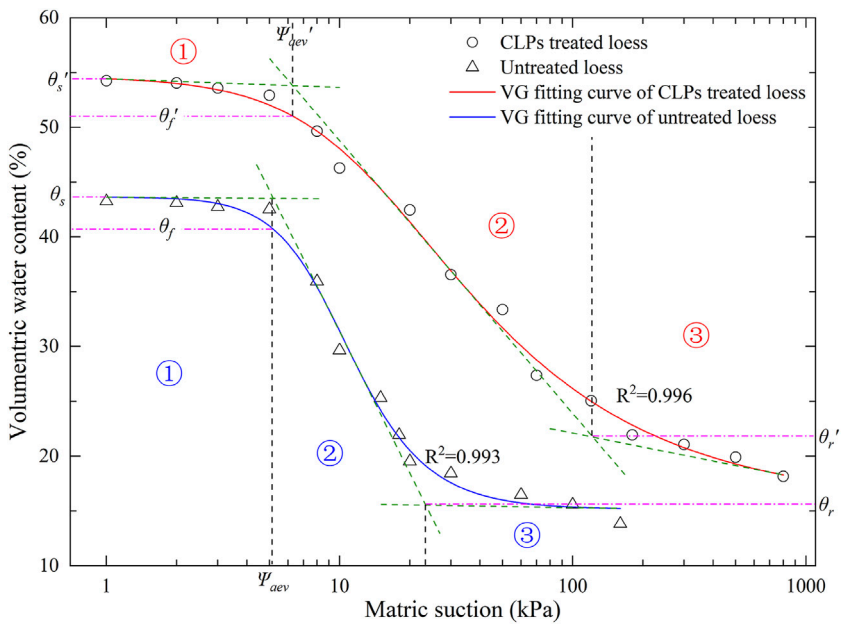

FIGURE 7 | Soil-water characteristic curve of treated and untreated loess. Regions ①, ②, and ③ represent the boundary (gravity water loss area), transition (capillary water loss area), and residual (combined water loss area) stages, respectively (White et al., 1970; Vanapalli et al., 1999).

TABLE 2 | Soil-water characteristic parameters of treated and untreated loess.

CLP concentration (%)	Saturated water content (%)	Field capacity (%)	Entry air value (kPa)	Dehumidification rate (%)	Residual water content (%)	Effective water content (%)
0	43.25	40.76	5.16	0.31	15.54	25.33
1.6	54.24	51.02	6.26	0.74	21.74	29.32

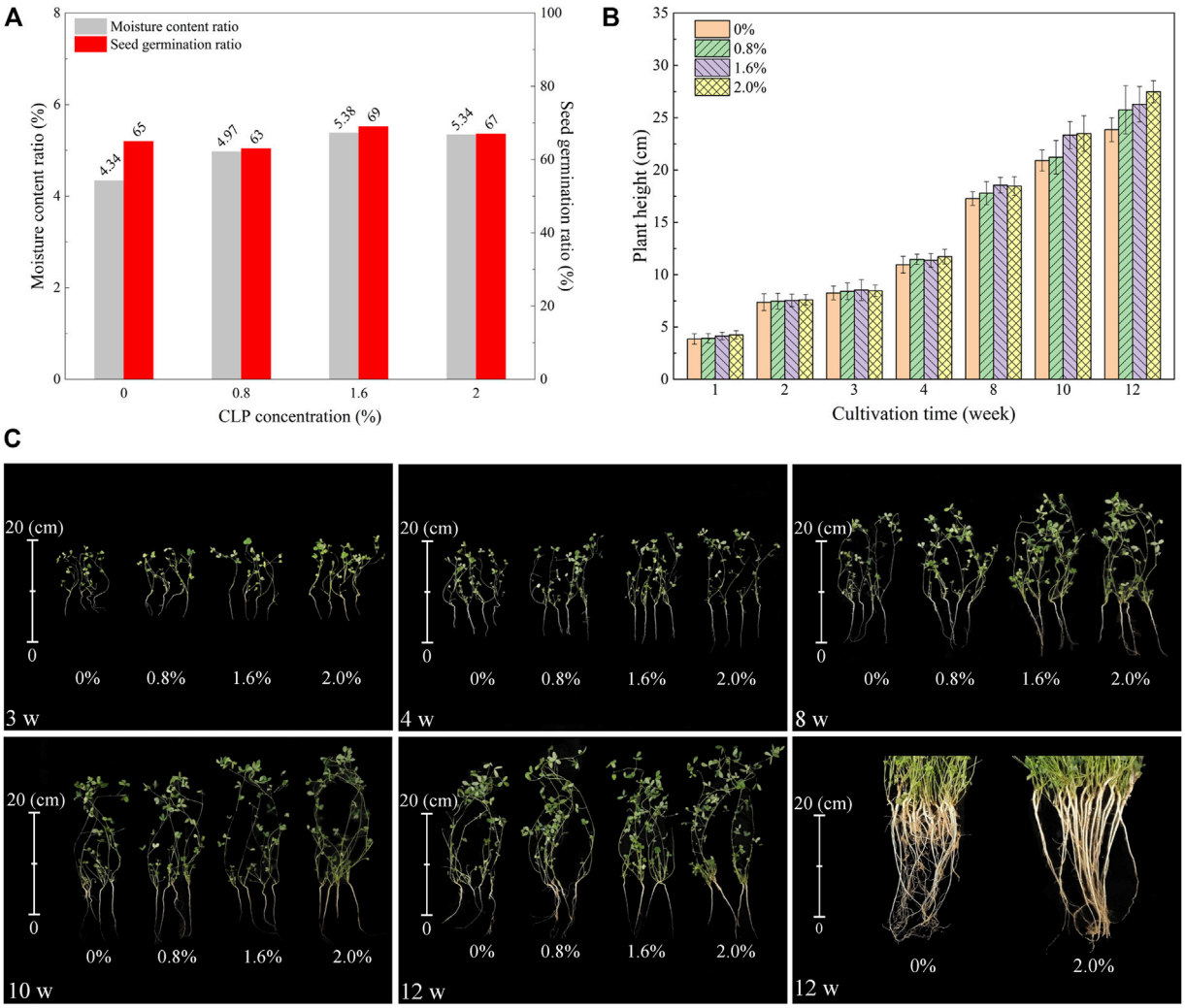

FIGURE 8 | (A) Water content ratio of potted loess treated with different cross-linked polymer (CLP) concentrations after drought stress, and its seed germination ratio 3 days after sowing. **(B)** Plant height of potted plants treated with different cross-linked polymer concentrations over time. **(C)** Potted plants treated with different cross-linked polymer (CLP) concentrations over time.

actually promoted plant growth. Therefore, CLPs can be combined with vegetation to better control loess slope erosion.

3.5 Effect of CLPs on Soil Microstructure

3.5.1 Particle Skeleton Structure

The scanning electron micrographs (1,000× magnification) of the untreated and treated loess are shown in **Figure 9A**. The boundaries between the different sized particles and small debris of untreated loess can be observed in **Figure 9A** (0%). The loess particles were mainly in point contact, and intergranular pores were developed. Furthermore, the structure of the loess particles was loose and easily destroyed. This was not the case for the treated loess (**Figure 9A**). After the CLPs were added, they adsorbed small soil particles and connected and wrapped large particles. The boundary of the particles was blurred, and the contact mode was mainly that of inlaid contacts. The contact area between the particles increased, changing from point contact to surface contact.

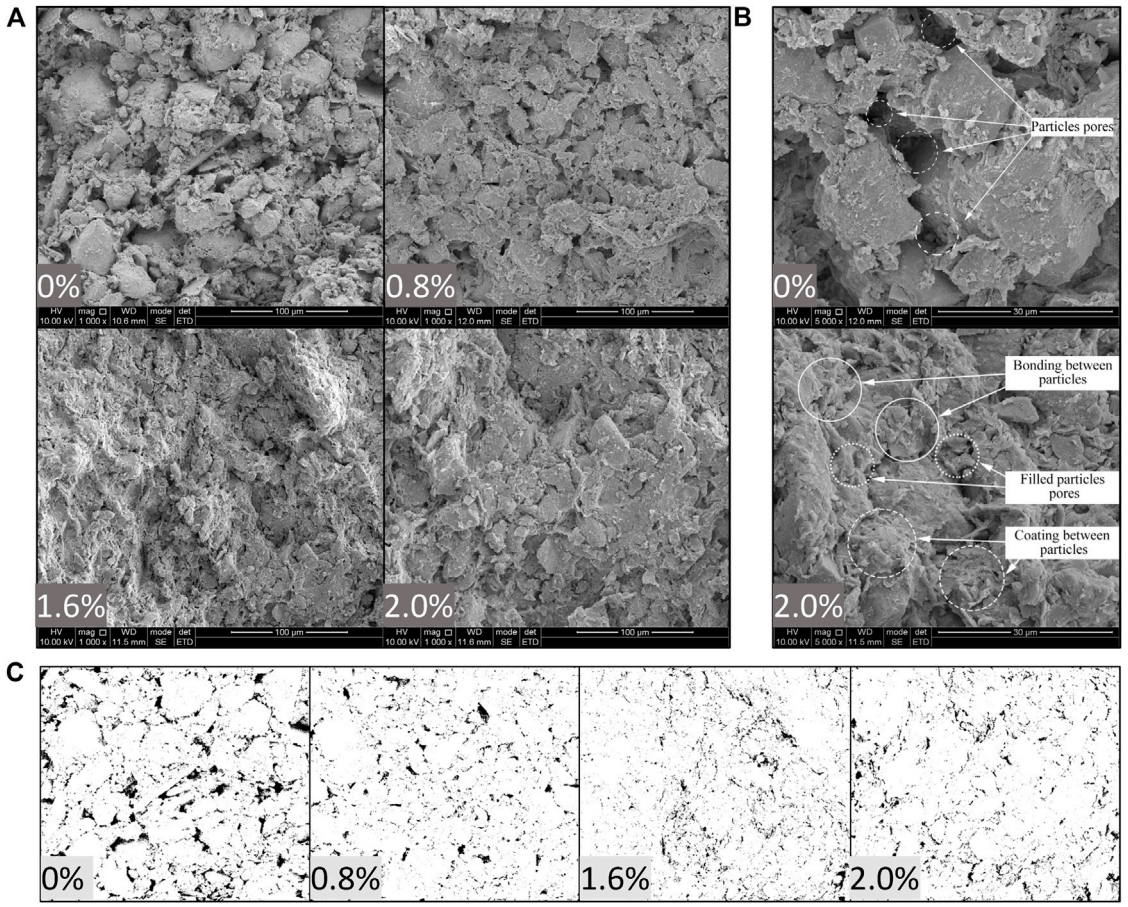

FIGURE 9 | Scanning electron micrographs of untreated and cross-linked polymer (CLP)-treated loess samples after 28 days curing at 1,000× magnification: **(A)** untreated loess; **(B)** 0.8% CLP-treated loess; **(C)** 1.6% CLP-treated loess; and **(D)** 2.0% CLP-treated loess. And 5,000× magnification: **(E)** untreated loess; and **(F)** 2.0% CLP-treated loess after curing for 28 days.

The magnification was further increased to 5,000× (**Figure 9B**). The untreated soil had clear particle boundaries, smooth surfaces, and evident interparticle pores. Following CLP addition, the pores were significantly reduced, and the structure was more compact. The soil particles were wrapped layer by layer by a flocculent or flaky substance, blurring the particle boundaries. One part of the CLPs was combined with particle debris and filled the large pores, while the other part was wrapped on the surface of soil particles and adhered to particle debris. Through these two actions, more soil particles were bonded to form larger aggregates, leading to increased compaction of the soil structure and further improving the structural stability.

3.5.2 Pore Structure Analysis

The binarized scanning electron micrographs is shown in **Figure 9C**. The pore data were classified according to Lei (1988) and Zhang L. et al. (2020), as shown in **Table 3**. The cumulative distribution curve showed that the pore diameter decreased with increasing CLP concentration (**Figure 10A**). The number and total area of various pores in treated loess were measured (**Figures 10B,C**). The treated and untreated loess had a similar number of pores, and both were dominated by small pores with few large and medium pores. As the CLP concentration increased, the number of micropores first decreased and then increased. The number of small pores remained basically unchanged, whereas the number of large and medium pores exhibited a downward trend. The total pore area of untreated loess mainly comprised large and medium pores, whereas the treated loess mainly comprised medium and small pores. With the increased CLP concentration, the total area of small pores showed little change, whereas the total area of large and medium pores significantly decreased. This result indicated that the CLPs changed the soil structure mainly by affecting the area of large and medium pores. The stabilizer wrapped the soil particles and filled the pores; therefore, the total pore area and total porosity were significantly reduced.

4 DISCUSSION

4.1 Stabilization Mechanism of Solidified Loess

The mechanisms underlaying soil stabilization vary and can be divided into physical, chemical, and biological processes. Physical

TABLE 3 | Number of pores and surface porosity of treated loess with different cross-linked polymer (CLP) concentrations.

Pore type CLP concentration (%)	Macropore D ≥ 32 μm	Mesopore 8 μm ≤ D < 32 μm	Small pore 2 μm ≤ D < 8 μm	Micropore D < 2 μm	Surface porosity ratio (%)
0	20	168	769	2,353	19.09
0.8	5	112	549	1,554	7.60
1.6	0	126	644	1,542	6.88
2.0	2	77	747	2092	5.22

D indicates the diameter.

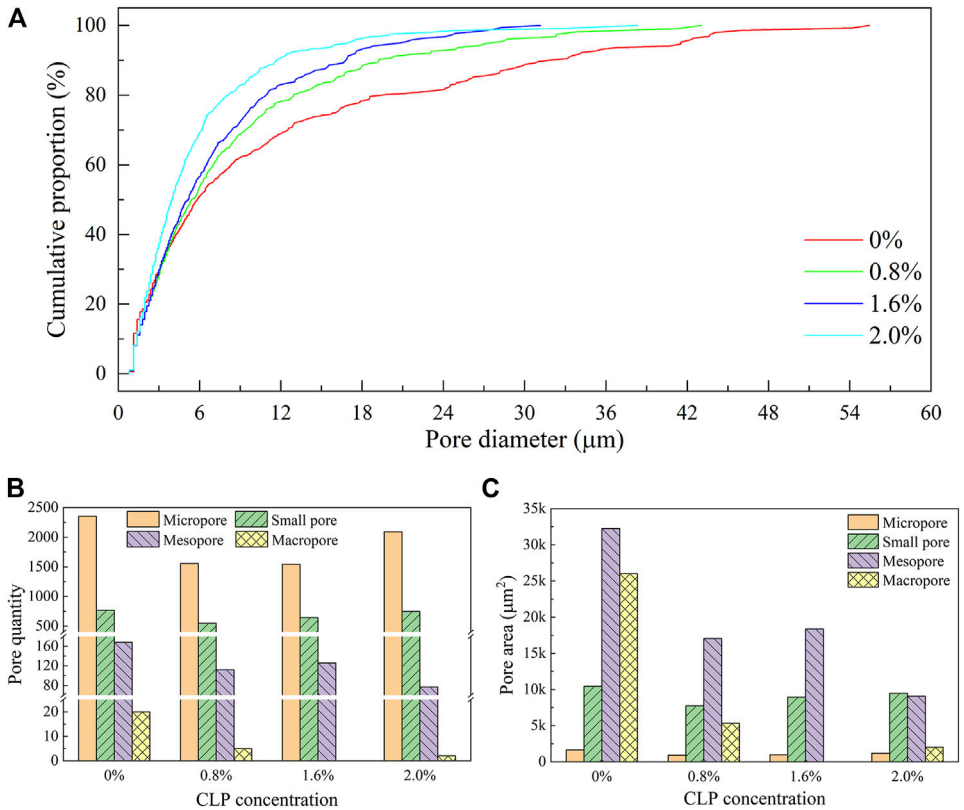

FIGURE 10 | (A) Cumulative pore distribution percentage of loess treated with different cross-linked polymer concentrations. Pore quantity **(B)** and total area **(C)** of loess treated different cross-linked polymer (CLP) concentrations.

processes include fiber reinforcement (Chebbi et al., 2020), filling, bonding, and wrapping (Ghasemzadeh and Modiri, 2020). Chemical processes include calcification, chemical bonding, hydrogen bonding, and ion exchange (Tingle et al., 2007; Dehghan et al., 2019; Zhang et al., 2019). Biological processes include microbially induced calcium carbonate precipitation (Wang et al., 2019) and enzyme-catalyzed reactions (Chandler et al., 2017). CLPs are formed by cross-linking carboxymethyl cellulose and polyacrylamide.

Traditional soil stabilizers, such as lime, cement, and fly ash, generate hydrated calcium silicate, calcium carbonate, and other products through calcification reactions, which cause evident changes in mineral composition (Choobbasti and Kutanaei, 2017; Al-mashhadani et al., 2018; James, 2020). Conversely, CLPs are formed through polymer cross-linking and lack a calcium source for the calcification reaction. Thus, their stabilization mechanism differs from that of calcium-based stabilizers. This was demonstrated by the XRD results of different CLPs used to stabilize loess (**Figure 11A**). Before and after enhancement, the peak group, position, and intensity of the diffraction pattern were basically the same. This result indicated that CLPs differed from calcium-based stabilizers and did not produce new compounds that affected soil crystallization. These findings are consistent with those of Liu et al. (2020) and Zhang et al. (2016). CLPs contain hydrophilic functional groups, such as -OH, -COOH, and -NH_2, leading to changes in the functional groups of treated loess. According to the infrared spectra of treated loess (**Figure 11B**), the asymmetric stretching vibration of

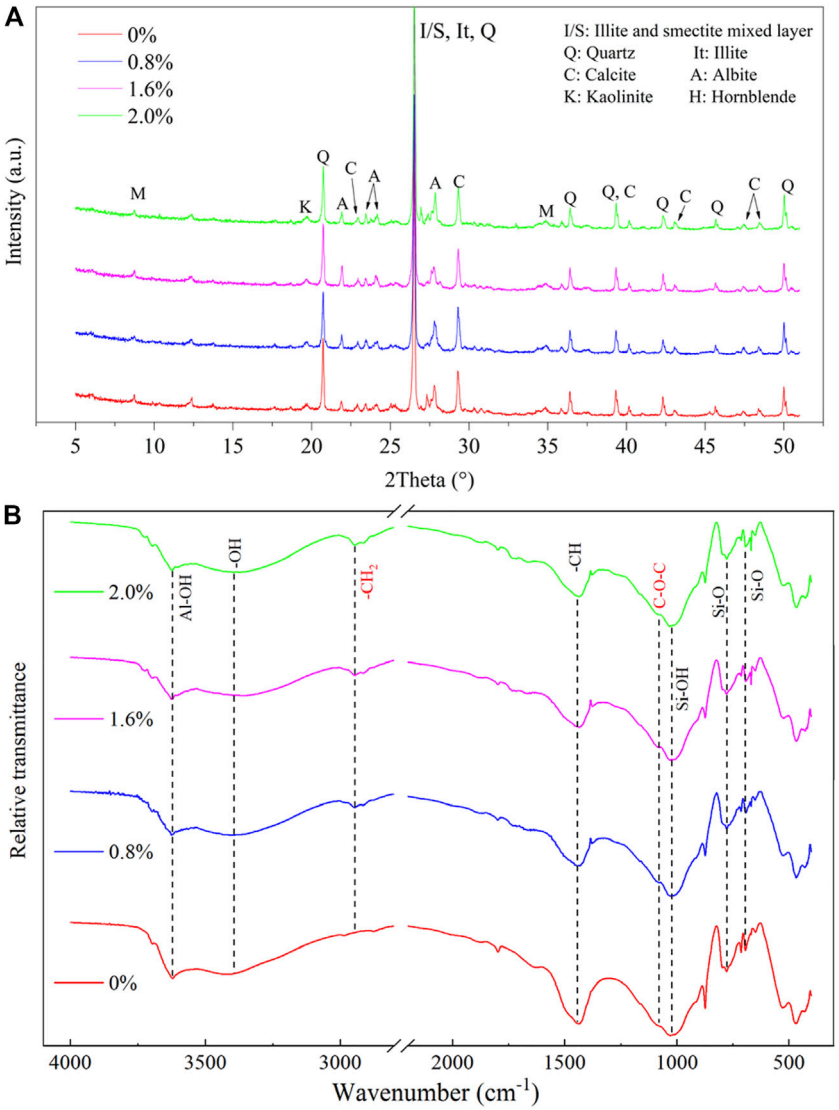

FIGURE 11 | (A) X-ray diffraction patterns of loess treated with different cross-linked polymer concentrations. **(B)** Fourier-transform infrared reflection spectrogram of loess treated with different cross-linked polymer concentrations.

-CH_2- was added at 2,945 cm^{-1}. This indicated that aliphatic hydrocarbon methylene groups were added to the treated loess, corresponding to the macromolecular backbone of CLPs. Simultaneously, the C–O symmetrical deformation peak at 1,125 cm^{-1} of the treated loess was more prominent, indicating the addition of an ether bond. These new functional groups were also found in the infrared spectra of the corresponding CLPs. This result indicated that CLPs were not completely hydrolyzed after being introduced into loess, and they still existed as long chains of macromolecules.

Based on our and previous results, the CLP stabilization mechanism could be described as the superposition of physical and chemical effects. The process included the following steps: 1) After the CLPs were mixed with the soil, they dissociated and released a large amount of free H+, which was exchanged with the metal cations in the soil particles. In response, the thickness of the water film of the electric double layer was weakened, and the soil particles were arranged more closely, enhancing the mechanical properties. The particle structure, as observed through SEM, also supported this conclusion. Additionally, the dissociated H+ could combine with elements such as O and N in loess minerals and organic matter to form hydrogen bonds and enhance the stability of the soil (Latifi et al., 2017). 2) After the mixed treated loess lost water, the CLPs formed a gel to fill the soil pores. The gaps between the particles adsorbed, wrapped, and bound soil particles to form an overall three-dimensional spatial network structure, which was more stable. This alteration also reduced the large and medium pores and the total pore area, which further improved the soil stability (Bu et al., 2019). When CLPs were added to the soil, the gel formed by its curing was filled with particles, altering the microstructure of the soil. Moreover, CLPs contain abundant hydrophilic groups. Combined, these factors could contribute to an increase in the bound water and

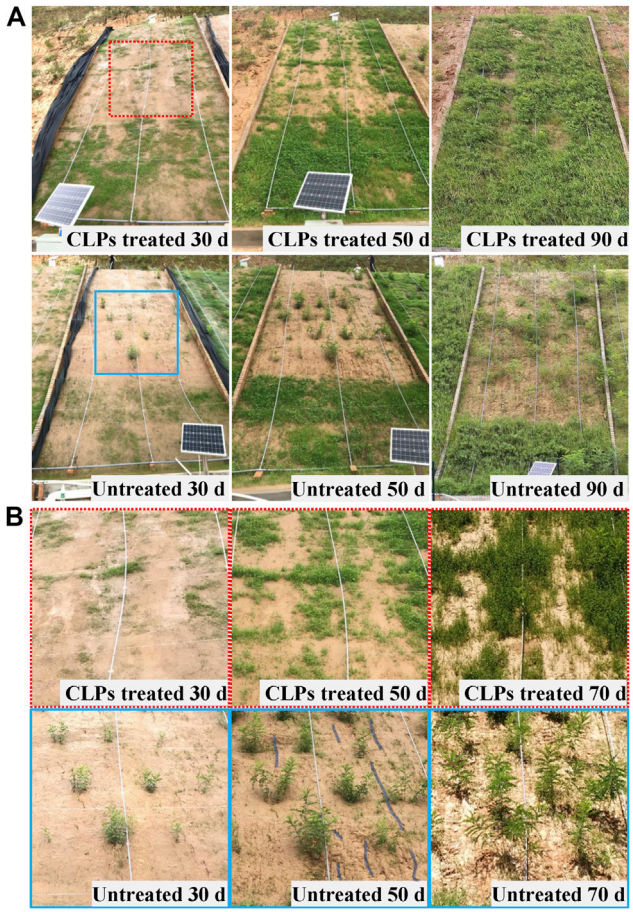

FIGURE 12 | Untreated and cross-linked polymer (CLP)-treated loess hillslopes in the field test over time. **(A)** Overview and **(B)** close-up of slopes.

capillary water content of treated loess and enhance its water retention capacity. This contribution was manifested by an increase in the effective water content and residual water content of the treated loess and a decrease in the dehumidification rate.

4.2 Application

Details of the slope surface in the field test are illustrated in **Figure 12**. Owing to the impact of rainfall erosion, some seeds were washed down, cracks appeared after 30 days, and there was more vegetation coverage in the lower part of the slope than in the upper part. This phenomenon was more evident on the untreated slope, indicating that the application of CLPs reduced soil erosion. The images after 50 days showed that increasing erosion rills appeared on the untreated slope under rainfall and irrigation conditions. However, the vegetation coverage on the treated slope significantly increased, with no significant erosion occurred. After 70 days, rill erosion further developed into flaky denudation on the untreated slope, and the surface layer peeled off, forming scaly erosion. Meanwhile, the treated loess remained basically intact. After 90 days, the untreated slope continued to deteriorate. The upper part of the untreated slope was not effectively protected by the vegetation, increasing the erosion. The worsened erosion led to vegetation deterioration, which further increased the erosion. However, the surface of the treated slope was mostly covered by vegetation forming a barrier on the surface, and the splash erosion caused by raindrops was alleviated. Therefore, the field tests showed that treating slope loess with CLPs was an effective and feasible measure for controlling soil erosion and restoring vegetation. In addition, the CLP material was used in very small quantities, achieving significant results at a concentration of only 1.6%, at a cost of only 34 USD per ton soil-binder mixture.

5 CONCLUSION

Herein, we proposed a method for alleviating the erosion of loess slopes by stabilizing them with double cross-linked polymers. Our main conclusions are as follows:

1) CLPs can significantly increase the UCS of loess. The strength increases with the increase in CLP concentration and curing time. The UCS of loess treated with 2.0% CLPs (1,497.84 kPa) was 3.04 times that of untreated loess (491.97 kPa). The optimal concentration range for CLP application is 1.2–2.0%, and the optimal curing time range is 7–14 days.
2) CLPs can improve the anti-disintegration property of loess. With an increase in CLP concentration, the stability index of loess was greatly increased, and the 1.6% CLP treatment showed the best anti-disintegration effect considering cost and benefit.
3) The SWCC index showed a higher saturated effective water content and lower dehumidification rate in treated loess compared with that in untreated loess. The treated loess showed a better ability to hold and retain water than untreated loess.
4) CLPs can reduce water evaporation from potted loess without inhibiting the germination rate of plant seeds. Under long-term conditions, CLPs can significantly promote plant growth due to their water retention capacity.
5) XRD, FTIR, and SEM showed that CLPs did not affect the mineral composition of loess nor did they cause major changes in the functional groups. However, the particles were more closely connected, and the contact mode changed. Thus, the porosity was reduced, and many pores were filled with gel and debris. CLPs stabilized loess through ion exchange, hydrogen bonding, and packing and filling.
6) CLPs not only improve the strength and disintegration resistance of loess but also have high water retention. Field tests showed that compared with untreated loess slopes, the slopes treated with CLPs had reduced soil erosion, which promoted vegetation recovery.
7) As a new type of soil stabilizer, CLPs have the following advantages: 1) They can be configured into a solution at normal atmospheric temperature (15–20°C) and can be diluted to varying degrees. 2) They can be solidified at normal atmospheric temperature with high strength. 3) The concentration of CLP stock solution is only 2.0%, the amount of CMC and PAM needed is small, and the cost/performance ratio is high.

DATA AVAILABILITY STATEMENT

The raw data supporting the conclusion of this article will be made available by the authors, without undue reservation.

AUTHOR CONTRIBUTIONS

XZ: Conceptualization, Formal analysis, Data curation, Writing—review and editing, Methodology, Supervision. YZ: Writing—original draft, Writing—review and editing, Formal analysis, Visualization, Investigation. XP: Methodology, Writing—review and editing, Supervision, Resources, Funding acquisition. YD: Writing—review and editing, Visualization, Data curation.

FUNDING

This study was partially supported by the Major Program of the National Natural Science Foundation of China (Grant No. 41790445), the National Science Fund for Distinguished Young Scholars of China (Grant No. 41702335), and the National Key Research and Development Project (2018YFC1504702).

REFERENCES

Ahmed, A., and Issa, U. H. (2014). Stability of Soft clay Soil Stabilised with Recycled gypsum in a Wet Environment. *Soils and Foundations* 54, 405–416. doi:10.1016/j.sandf.2014.04.009

Al-mashhadani, M. M., Canpolat, O., Aygörmez, Y., Uysal, M., and Erdem, S. (2018). Mechanical and Microstructural Characterization of Fiber Reinforced Fly Ash Based Geopolymer Composites. *Construction Building Mater.* 167, 505–513. doi:10.1016/j.conbuildmat.2018.02.061

Behnood, A. (2018). Soil and clay Stabilization with Calcium- and Non-calcium-based Additives: A State-Of-The-Art Review of Challenges, Approaches and Techniques. *Transportation Geotechnics* 17, 14–32. doi:10.1016/j.trgeo.2018.08.002

Bu, F., Liu, J., Bai, Y., Prasanna Kanungo, D., Song, Z., Kong, F., et al. (2019). Effects of the Preparation Conditions and Reinforcement Mechanism of Polyvinyl Acetate Soil Stabilizer. *Polymers* 11, 506–520. doi:10.3390/polym11030506

Chandler, N., Palson, J., and Burns, T. (2017). Capillary Rise experiment to Assess Effectiveness of an Enzyme Soil Stabilizer. *Can. Geotech. J.* 54, 1509–1517. doi:10.1139/cgj-2016-0511

Chang, I., Prasidhi, A. K., Im, J., Shin, H.-D., and Cho, G.-C. (2015). Soil Treatment Using Microbial Biopolymers for Anti-desertification Purposes. *Geoderma* 253-254, 39–47. doi:10.1016/j.geoderma.2015.04.006

Chebbi, M., Guiras, H., and Jamei, M. (2020). Tensile Behaviour Analysis of Compacted Clayey Soil Reinforced with Natural and Synthetic Fibers: Effect of Initial Compaction Conditions. *Eur. J. Environ. Civil Eng.* 24, 354–380. doi:10.1080/19648189.2017.1384762

Chen, H., Zhang, X., Abla, M., Lü, D., Yan, R., Ren, Q., et al. (2018). Effects of Vegetation and Rainfall Types on Surface Runoff and Soil Erosion on Steep Slopes on the Loess Plateau, China. *Catena* 170, 141–149. doi:10.1016/j.catena.2018.06.006

Choobbasti, A. J., and Kutanaei, S. S. (2017). Microstructure Characteristics of Cement-Stabilized sandy Soil Using Nanosilica. *J. Rock Mech. Geotechnical Eng.* 9, 981–988. doi:10.1016/j.jrmge.2017.03.015

Dehghan, H., Tabarsa, A., Latifi, N., and Bagheri, Y. (2019). Use of Xanthan and Guar Gums in Soil Strengthening. *Clean. Techn Environ. Pol.* 21, 155–165. doi:10.1007/s10098-018-1625-0

Duan, J., Liu, Y.-J., Tang, C.-J., Shi, Z.-H., and Yang, J. (2021a). Efficacy of Orchard Terrace Measures to Minimize Water Erosion Caused by Extreme Rainfall in the Hilly Region of China: Long-Term Continuous *In Situ* Observations. *J. Environ. Manage.* 278, 111537. doi:10.1016/j.jenvman.2020.111537

Eyo, E. U., Ng'ambi, S., and Abbey, S. J. (2020). An Overview of Soil-Water Characteristic Curves of Stabilised Soils and Their Influential Factors. *J. King Saud Univ. - Eng. Sci.* doi:10.1016/j.jksues.2020.07.013

Feng, L., Lin, H., Zhang, M., Guo, L., Jin, Z., and Liu, X. (2020). Development and Evolution of Loess Vertical Joints on the Chinese Loess Plateau at Different Spatiotemporal Scales. *Eng. Geology.* 265, 105372. doi:10.1016/j.enggeo.2019.105372

Fu, B.-J., Wang, Y.-F., Lu, Y.-H., He, C.-S., Chen, L.-D., and Song, C.-J. (2009). The Effects of Land-Use Combinations on Soil Erosion: a Case Study in the Loess Plateau of China. *Prog. Phys. Geogr. Earth Environ.* 33, 793–804. doi:10.1177/0309133309350264

Ghasemzadeh, H., and Modiri, F. (2020). Application of Novel Persian Gum Hydrocolloid in Soil Stabilization. *Carbohydr. Polym.* 246, 116639. doi:10.1016/j.carbpol.2020.116639

Hu, S., Qiu, H., Wang, N., Cui, Y., Wang, J., Wang, X., et al. (2020). The Influence of Loess Cave Development upon Landslides and Geomorphologic Evolution: A Case Study from the Northwest Loess Plateau, China. *Geomorphology* 359, 107167. doi:10.1016/j.geomorph.2020.107167

Jalal, F. E., Xu, Y., Jamhiri, B., and Memon, S. A. (2020). On the Recent Trends in Expansive Soil Stabilization Using Calcium-Based Stabilizer Materials (CSMs): a Comprehensive Review. *Adv. Mater. Sci. Eng.* 2020, 1–23. doi:10.1155/2020/1510969

James, J. (2020). Sugarcane Press Mud Modification of Expansive Soil Stabilized at Optimum Lime Content: Strength, Mineralogy and Microstructural Investigation. *J. Rock Mech. Geotechnical Eng.* 12, 395–402. doi:10.1016/j.jrmge.2019.10.005

Keramatikerman, M., Chegenizadeh, A., and Nikraz, H. (2016). Effect of GGBFS and Lime Binders on the Engineering Properties of clay. *Appl. Clay Sci.* 132-133, 722–730. doi:10.1016/j.clay.2016.08.029

Krainiukov, A., Liu, J., Kravchenko, E., and Chang, D. (2020). Performance of Silty Sand Reinforced with Aqueous Solution of Polyvinyl Alcohol Subjected to Freeze-Thaw Cycles. *Cold Regions Sci. Techn.* 174, 103054. doi:10.1016/j.coldregions.2020.103054

Kushwaha, S. S., Kishan, D., and Dindorkar, N. (2018). Stabilization of Expansive Soil Using Eko Soil Enzyme for Highway Embankment. *Mater. Today Proc.* 5, 19667–19679. doi:10.1016/j.matpr.2018.06.329

Latifi, N., Suksun, H., Meehan, C., Abd Majid, Z., Tahir, M. M., and Mohamad, E. T. (2017). Improvement of Problematic Soils with Biopolymer-An Environmentally Friendly Soil Stabilizer. *J. Mater. Civil Eng.* 29, 1–11. doi:10.1061/(ASCE)MT.1943-5533.0001706

Lei, X. (1988). The Types of Loess Pores in China and Their Relationship with Collapsibility. *Sci. Chin. (Ser. B).* 31, 1398–1411. doi:10.1360/zb1987-17-12-1309

Li, M., Zhang, X., Yang, Z., Yang, T., and Pei, X. (2020). The Rainfall Erosion Mechanism of High and Steep Slopes in Loess Tablelands Based on Experimental Methods and Optimized Control Measures. *Bull. Eng. Geol. Environ.* 79, 4671–4681. doi:10.1007/s10064-020-01854-3

Li, T., Zhao, L., Duan, H., Yang, Y., Wang, Y., and Wu, F. (2019). Exploring the Interaction of Surface Roughness and Slope Gradient in Controlling Rates of Soil Loss from Sloping farmland on the Loess Plateau of China. *Hydrological Process.* 34, 339–354. doi:10.1002/hyp.13588

Liu, G., Hu, F., Zheng, F., and Zhang, Q. (2019). Effects and Mechanisms of Erosion Control Techniques on Stairstep Cut-Slopes. *Sci. Total Environ.* 656, 307–315. doi:10.1016/j.scitotenv.2018.11.385

Liu, J., Shi, B., Jiang, H., Huang, H., Wang, G., and Kamai, T. (2011). Research on the Stabilization Treatment of clay Slope Topsoil by Organic Polymer Soil Stabilizer. *Eng. Geology.* 117, 114–120. doi:10.1016/j.enggeo.2010.10.011

Liu, Y., Zheng, W., Wang, Q., Cao, C., Chang, M., and Rocchi, I. (2020). Evaluating Sulfur-free Lignin as a Sustainable Additive for Soil Improvement against Frost Resistance. *J. Clean. Prod.* 251, 119504. doi:10.1016/j.jclepro.2019.119504

Özen, İ., Okyay, G., and Ulaş, A. (2018). Coating of Nonwovens with Potassium Nitrate Containing Carboxymethyl Cellulose for Efficient Water and

Fertilizer Management. *Cellulose* 25, 1527–1538. doi:10.1007/s10570-018-1655-0

Peng, J., Sun, P., Igwe, O., and Li, X. a. (2018). Loess Caves, a Special Kind of Geohazard on Loess Plateau, Northwestern China. *Eng. Geology.* 236, 79–88. doi:10.1016/j.enggeo.2017.08.012

Reza Golhashem, M., and Uygar, E. (2020). Volume Change and Compressive Strength of an Alluvial Soil Stabilized with Butyl Acrylate and Styrene. *Construction Building Mater.* 255, 119352. doi:10.1016/j.conbuildmat.2020.119352

Song, Z., Liu, J., Bai, Y., Wei, J., Li, D., Wang, Q., et al. (2019). Laboratory and Field Experiments on the Effect of Vinyl Acetate Polymer-Reinforced Soil. *Appl. Sci.* 9, 208–222. doi:10.3390/app9010208

Tang, B., Jiao, J., Zhang, Y., Chen, Y., Wang, N., and Bai, L. (2020). The Magnitude of Soil Erosion on Hillslopes with Different Land Use Patterns under an Extreme Rainstorm on the Northern Loess Plateau, China. *Soil Tillage Res.* 204, 104716. doi:10.1016/j.still.2020.104716

Tingle, J. S., Newman, J. K., Larson, S. L., Weiss, C. A., and Rushing, J. F. (2007). Stabilization Mechanisms of Nontraditional Additives. *Transportation Res. Rec.* 1989-2, 59–67. doi:10.3141/1989-49

van Genuchten, M. T. (1980). A Closed-form Equation for Predicting the Hydraulic Conductivity of Unsaturated Soils. *Soil Sci. Soc. America J.* 44, 892–898. doi:10.2136/sssaj1980.03615995004400050002x

Vanapalli, S. K., Fredlund, D. G., and Pufahl, D. E. (1999). The Influence of Soil Structure and Stress History on the Soil-Water Characteristics of a Compacted till. *Géotechnique* 49, 143–159. doi:10.1680/geot.1999.49.2.143

Wang, Y., Soga, K., Dejong, J. T., and Kabla, A. J. (2019). A Microfluidic Chip and its Use in Characterising the Particle-Scale Behaviour of Microbial-Induced Calcium Carbonate Precipitation (MICP). *Géotechnique* 69, 1086–1094. doi:10.1680/jgeot.18.P.031

Wei, W., Chen, L., Fu, B., Huang, Z., Wu, D., and Gui, L. (2007). The Effect of Land Uses and Rainfall Regimes on Runoff and Soil Erosion in the Semi-arid Loess Hilly Area, China. *J. Hydrol.* 335, 247–258. doi:10.1016/j.jhydrol.2006.11.016

Wen, Y., Kasielke, T., Li, H., Zhang, B., and Zepp, H. (2021). May Agricultural Terraces Induce Gully Erosion? A Case Study from the Black Soil Region of Northeast China. *Sci. Total Environ.* 750, 141715. doi:10.1016/j.scitotenv.2020.141715

White, N. F., Duke, H. R., Sunada, D. K., and Corey, A. T. (1970). Physics of Desaturation in Porous Materials. *J. Irrig. Drain. Div.* 96, 165–191. doi:10.1061/JRCEA4.0000716

Wu, Z.-j., Zhao, D.-y., Che, A.-l., Chen, D.-w., and Liang, C. (2020). Dynamic Response Characteristics and Failure Mode of Slopes on the Loess Tableland Using a Shaking-Table Model Test. *Landslides* 17, 1561–1575. doi:10.1007/s10346-020-01373-y

Xu, H., Miao, J., Chen, P., Zhan, L., and Wang, Y.-z. (2019). Chemical and Geotechnical Properties of Solidified/stabilized MSWI Fly Ash Disposed at a Landfill in China. *Eng. Geology.* 255, 59–68. doi:10.1016/j.enggeo.2019.04.019

Yan, Y., Zhen, H., Zhai, X., Li, J., Hu, W., Ding, C., et al. (2021). The Role of Vegetation on Earth Bunds in Mitigating Soil Erosion in Mollisols Region of Northeast China. *Catena* 196, 104927. doi:10.1016/j.catena.2020.104927

Yang, Q.-w., Pei, X.-j., and Huang, R.-q. (2019). Impact of Polymer Mixtures on the Stabilization and Erosion Control of Silty Sand Slope. *J. Mt. Sci.* 16, 470–485. doi:10.1007/s11629-018-4905-6

Yoobanpot, N., Jamsawang, P., Poorahong, H., Jongpradist, P., and Likitlersuang, S. (2020). Multiscale Laboratory Investigation of the Mechanical and Microstructural Properties of Dredged Sediments Stabilized with Cement and Fly Ash. *Eng. Geology.* 267, 105491. doi:10.1016/j.enggeo.2020.105491

Zhai, Q., Rahardjo, H., Satyanaga, A., and Dai, G. (2020). Estimation of the Soil-Water Characteristic Curve from the Grain Size Distribution of Coarse-Grained Soils. *Eng. Geology.* 267, 105502. doi:10.1016/j.enggeo.2020.105502

Zhang, L., Qi, S., Ma, L., Guo, S., Li, Z., Li, G., et al. (2020b). Three-dimensional Pore Characterization of Intact Loess and Compacted Loess with Micron Scale Computed Tomography and Mercury Intrusion Porosimetry. *Sci. Rep.* 10, 8511. doi:10.1038/s41598-020-65302-8

Zhang, T., Cai, G., Liu, S., and Puppala, A. J. (2016). Engineering Properties and Microstructural Characteristics of Foundation silt Stabilized by Lignin-Based Industrial By-Product. *KSCE J. Civ. Eng.* 20, 2725–2736. doi:10.1007/s12205-016-1325-4

Zhang, T., Yang, Y.-L., and Liu, S.-Y. (2020a). Application of Biomass By-Product Lignin Stabilized Soils as Sustainable Geomaterials: A Review. *Sci. Total Environ.* 728, 138830. doi:10.1016/j.scitotenv.2020.138830

Zhang, Z., Gao, W., Zhang, Z., Xiao-yu, T., and Jun, W. (2020). Evolution of Particle Disintegration of Red sandstone Using Weibull Distribution. *Rock Soil Mech.* 41, 877–885. doi:10.16285/j.rsm.2019.0926

Zhang, Z., Zhang, H., Zhang, J., and Chai, M. (2019). Effectiveness of Ionic Polymer Soil Stabilizers on Warm Frozen Soil. *KSCE J. Civ. Eng.* 23, 2867–2876. doi:10.1007/s12205-019-0561-9

Zhao, G., Mu, X., Wen, Z., Wang, F., and Gao, P. (2013). Soil Erosion, Conservation, and Eco-Environment Changes in the Loess Plateau of China. *Land Degrad. Develop.* 24, 499–510. doi:10.1002/ldr.2246

Zhao, Q., Li, D., Zhuo, M., Guo, T., Liao, Y., and Xie, Z. (2015). Effects of Rainfall Intensity and Slope Gradient on Erosion Characteristics of the Red Soil Slope. *Stoch Environ. Res. Risk Assess.* 29, 609–621. doi:10.1007/s00477-014-0896-1

Conflict of Interest: The authors declare that the research was conducted in the absence of any commercial or financial relationships that could be construed as a potential conflict of interest.

Publisher's Note: All claims expressed in this article are solely those of the authors and do not necessarily represent those of their affiliated organizations, or those of the publisher, the editors and the reviewers. Any product that may be evaluated in this article, or claim that may be made by its manufacturer, is not guaranteed or endorsed by the publisher.

frontiers in Earth Science

ORIGINAL RESEARCH
published: 15 November 2021
doi: 10.3389/feart.2021.747317

Multi-Scale Analysis of Geotechnical and Physicochemical Changes in Loess Caused by Nano-SiO_2 Pile Migration

Ran Kong, Lei Gao, Wenqing Zhao and Bo Zhao*

Department of Geology and Jewelry, Lanzhou Resourses and Environment Voc-Tech College, Lanzhou, China

Understanding property changes in soil improvement using a new technique is critical for enhancing engineering activity. However, little is known about nano-SiO_2 pile-induced changes in soil properties due to its excellent properties as an alternative new additive material. This study aims to examine the changes in properties of loess stabilized with nano-SiO_2 pile after curing for 28 days. Using samples taken from four desired radii (i.e., 5, 10 15, and 20 cm), we tested their mineralogical, structural, physicochemical, and index properties and analyzed the relationship of these properties to strengthen the link between microscopic characteristics and macroscopic behaviors. We then discussed the mechanism of the changes in the treated loess properties. The test results show that nano-SiO_2 pile induced a physical structure modification in the treated loess and, consequently, an isotropic process with coarser particles due to crystallinity. This resulted in a solidification process in loess with nano-SiO_2 pile, causing a decrease in water content and void ratio as well as an increase in natural density, thereby improving its mechanical strength. Meanwhile, the specific surface area (SSA)and cation exchange capacity (CEC) of treated loess were smaller than those of original loess, and there were slight changes in chemical properties. The disintegration rate of treated loess decrease compared with the original loess. The interactional relationship of the microscopic and macroscopic observation was facilitated to better understand the mechanism of changes in nano-SiO_2 pile-treated loess properties. This finding reveals that nano-SiO_2 pile has the potential as an alternative stabilized technique in loess improvement due to its obvious performance improvement and slight chemical changes.

Keywords: loess, nano-SiO_2 pile, nanoparticle migration, multi-scale analysis, stabilization

OPEN ACCESS

Edited by:
Gonghui Wang,
Kyoto University, Japan

Reviewed by:
Jin Liu,
Hohai University, China
Yao Jiang,
Institute of Mountain Hazards and Environment (CAS), China

****Correspondence:***
Ran Kong
kongran413@163.com

Specialty section:
This article was submitted to Geohazards and Georisks, a section of the journal Frontiers in Earth Science

Received: *26 July 2021*
Accepted: *27 August 2021*
Published: *15 November 2021*

Citation:
Kong R, Gao L, Zhao W and Zhao B (2021) Multi-Scale Analysis of Geotechnical and Physicochemical Changes in Loess Caused by Nano-SiO_2 Pile Migration. Front. Earth Sci. 9:747317. doi: 10.3389/feart.2021.747317

INTRODUCTION

A large number of highways and railways have been constructed in China's loess area. Meanwhile, urbanization promotes the significant scale of land creation projects by cutting hilltops and then filling valleys (Zhang and Wang, 2018). However, loess also easily collapses and experiences subsidence through wetting and loading. Hence, it is important to improve its performance in engineering projects (Zhang et al., 2018a; Kong et al., 2018).

Considerable research has explored ways to improve loess performance using various stabilizing treatment techniques, but much of this effort has focused on changes in the properties of the treated

loess by mixing different chemical additives (Zia and Fox, 2000; Tchakalova and Todorov, 2008; Sariosseiri and Muhunthan, 2009; Arrua et al., 2010; Metelková et al., 2012; Zhang et al., 2017; Zhang et al., 2018a; Haeri et al., 2019). Generally, these chemical additives, such as lime, fly ash, and cement, are added into the loess in order to modify its physical, chemical, structural, and mineral properties, thereby improving its geotechnical performance. Efforts have also sought to use alternative new materials, such as nano-SiO_2, to replace the generally used chemical additives in loess performance improvement (Ren and Hu, 2014; Kong et al., 2018; Tabarsa et al., 2018). Such research demonstrated that the nano-SiO_2 particle has potential as a cost-effective and eco-friendly stabilized agent for loess improvement. In addition, a few studies have examined the pile treatment technique for loess improvement (Dolgikh, 1966; Tystovich et al., 1971; Pei et al., 2015). The still widely used agents of stabilized piles are chemical additives, such as lime and fly ash (Tystovich et al., 1971; Pei et al., 2015). In developed sites, pile treatment techniques are more practical than mixing treatment methods (Pei et al., 2015). Hence, using a stabilization treatment technique that can be easily applied in various contexts is important for soil improvement. Another area of research interest is seeking alternative new materials to replace the traditional chemical additives for eco-friendly and cost-effective purposes.

Pile treatment techniques have been used to improve the slope, Earth embankment, and clay soils (Rogers and Glendinning, 1997; Rajasekaran and Narasimha Rao, 2002; Larsson et al., 2005; Barker et al., 2006, 2007; Gallagher et al., 2007; Saoudi et al., 2013; Abiodun and Nalbantoglu, 2014; Helle et al., 2017; Selvakumar and Soundara, 2019). According to the nature of the stabilizing agent, pile treatment techniques can be divided into two different types. The first type is for chemical piles, which are generally filled by lime, fly ash, cement, and salt additives (Rogers and Glendinning, 1997; Larsson et al., 2005; Barker et al., 2006, 2007; Pei et al., 2015; Quang and Chai, 2015; Helle et al., 2017). The improvement mechanism of chemical pile-treated soils is mainly attributed to ion migration, which generates a chemical reaction with the surrounding soil. The second type is for physical piles, which are currently made up of stone or colloidal silica grout without a chemical reaction with neighboring soil (Gallagher et al., 2007; Saoudi et al., 2013). The reinforced effect of the stone pile comes from its own mechanical properties Saoudi et al. (2013), Castro (2017), while stabilization from colloidal silica can also be attributed to silica nanoparticle migration (Gallagher et al., 2007). On the whole, chemical piles are still more generally practiced in soil improvement, but the interest in physical piles such as silica nanoparticle has increased due to its eco-friendly characteristics and effectively stabilized effects.

The purpose of this study is to examine the changes in properties of loess stabilized with nano-SiO_2 pile. We treated loess with nano-SiO_2 pile and cured it for 28 days. The treated loess was subsequently sampled at four radial distances from the pile (i.e., 5, 10, 15, and 20 cm). We examined their mineralogical, structural, physicochemical, disintegrated, and index properties, and then analyzed the relationship of these properties to define the link between microscopic characteristics and macroscopic behaviors. Ultimately, we discussed the mechanism of the changes in the treated loess properties.

MATERIALS AND METHODS

Tested Samples

The sample used in this study was taken from the Malan loess in Lanzhou City, Gansu Province, China. Nano-SiO_2 used as the treated pile is commercially available with a mean aggregate size of 20 μm. Their basic properties are provided in **Table 1**.

Sample Preparation

We used Pei *et al.*'s Pei et al. (2015) procedure for sample preparation. First, using a plastic hammer, large clods and aggregations were broken into homogeneously sized particles that could pass through a sieve with a 1 mm aperture. Second, to achieve the original water content of 15%, distilled water was added to oven-dried loess and thoroughly mixed by hand. The wet loess was then sealed and stored for 24 h at room temperature before packing. The more uniformly distributed loess was placed in the test tank (45 cm × 45 cm × 30 cm) with a polyvinyl chloride (PVC) tube (5 cm internal diameter) using the moist tamping method. To get a consistent density, the samples were tamped with 10 layers, and each layer was designed to have 1.73 g/cm^3 of wet density.

Distilled water was added to the dry nano-SiO_2 to achieve 15% water content by weight. To minimize the aggregation as much as possible, a glass stirring rod was used to stir in the mixture. The mixture was quickly poured into the pre-positioned PVC tube to form the stabilized nano-SiO_2 pile (measuring 5 cm in diameter and 10 cm in length). The PVC tube was gradually pulled out as each layer was tamped.

The loess with the nano-SiO_2 pile in the middle of was cured for 28 days at room temperature. After curing, the samples were collected using a unique cutting ring (2.8 cm diameter and 1.5 cm height) at the desired radius (i.e., 5, 10, 15, and 20 cm) from the periphery of the nano-SiO_2 pile (**Figure 1**). The physicochemical and structural properties of these samples were then defined. Meanwhile, the mechanical test was conducted on the desired

TABLE 1 | Basic properties of loess and nano-SiO_2 used in this study.

Loess	**Value**
Specific gravity (Gs)	2.71
Liquid limit (%)	28.25
Plastic limit (%)	16.46
Plasticity index (%)	11.79
Specific surface area (m^2/g)	27.50
Mean particle size (mm)	0.021
Uniformity coefficient	2.72
Coefficient of curvature	1.05
Nano-SiO_2	
Diameter (nm)	30
Mean aggregated size (μm)	20
Purity (%)	≥99.8
Density (g/cm^3)	<0.15
Specific surface area (m^2/g)	300
Color	White

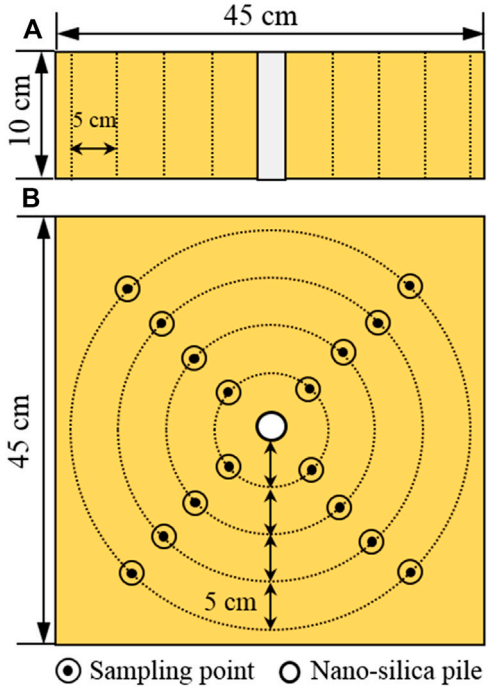

FIGURE 1 | Experimental arrangement and sampling point.

radii at another depth. In the limited test tank, the radial sampling pattern facilitated examination of the nano-SiO_2 migration-induced changes in the properties of the samples, as observed in the loess with lime and fly ash piles (Pei et al., 2015). It should be noted that the sampling has not been conducted in vertical profile, because the limited size of test tank is difficult to take multiple undisturbed samples in the depth of 10 cm.

Sample Tests

Mineralogical Tests

To examine the mineralogical changes after the curing, X-ray diffraction (XRD) techniques were performed on the original and treated loess, which was collected from the specified radial point. All samples were scanned using a Philips PW 3710 X-ray diffractometer with Cu-Kα radiation. Data were recorded from 5 to 45 at a rate of 0.05°2θ/s per step. Meanwhile, a thermogravimetric analysis, including mass loss (TG) and its derivative (DTG), was performed up to 1,000°C in oven-dried samples, at a ramp of 10°C/min on a Perkin-Elmer Instrument, Waltham, MA. In this thermogravimetric test, 10 mg of sample was filled into the instrument.

Structural Tests

The macro-texture and micro-structure of the original and treated loess were examined. The macroscopic particle size distributions of these samples were determined using the sieve and sedimentation methods (ASTMD422-63, 2007). The micro-morphology and micro-size were observed on the representative samples after metallization with gold powder using a JSM-5600 LV Scanning Electron Microscope (SEM).

The slake test has been recommended to assess the aggregation or cementation of soil treated by stabilization agents Pei et al. (2015), due to directly visual structure stability. The slake test was performed on each desired radius. Cylindrical samples were prepared after the oven-dry test. The four samples on each desired radius were simultaneously soaked in the plate, and water completely covered them. Their stability was recorded accompaning the time by camera. Complete disintegration was indicated by no further breakage of samples. The disintegration rate was calculated by dry weigt of the samples divided by the completely disintegrated time.

Index Property Tests

Hardness value was determined using an Equotip hardness tester (Piccolo). Previous research has sought to assess the strength of loess stabilized with lime and fly ash piles (Pei et al., 2015). This study found the Equotip to be a convenient quantitative tool for assessing the changes in strength and stiffness of tread soils due to its ease of use and rapid outcomes. This study used the Equotip hardness test on a newly planed soil surface after obtaining the cutting ring samples, which allowed for rapid and multiple measurements at the desired radius. The hardness value was determined as the average value of 30 measurements along each desired radius from the nano-Sio_2 pile edge.

Density and water contents are two of the most commonly determined properties in characterizing the engineering behavior of soil. The preferred test method for the laboratory determination of the moisture content is the oven drying method. Density and water contents are determined as the reduction in the mass of the test specimen after oven drying. The specimens, cut using a circular ring of iron, were 2.8 cm in diameter and 1.5 cm in height at each desired radial point. All specimens were weighed, recorded, and then oven dried at 105°C for 24 h. The mass of the dry sample was recorded. The density and water contents were subsequently calculated, and the average value was used in the analysis.

Liquid and plastic limits were measured using the fall cone test following the Chinese standard procedures GB/T50123 (1999), which define the liquid and plastic limits for penetration as 17 and 2 mm, respectively. The tested samples were taken along each desired radius.

Physicochemical Tests

The total SSA and CEC of the samples were measured using a methylene blue spot test method. The test procedure for determining the total SSA of soil was described by Santamarina *et al.* (2002), and its CEC was calculated using the formula suggested by Çokça and Birand (1993). Chemical properties were measured using a water quality monitor, including pH, total dissolved solids (TDS), electrical conductivity (CE), and oxidation-reduction potential (ORP) of extracts from 1:5 soil to water.

RESULTS AND ANALYSES

Changes in Mineralogical Composition

XRD Diffractograms

The results of the XRD of the original loess and loess treated with nano-SiO_2 pile at different radial distances are shown in **Figure 2**.

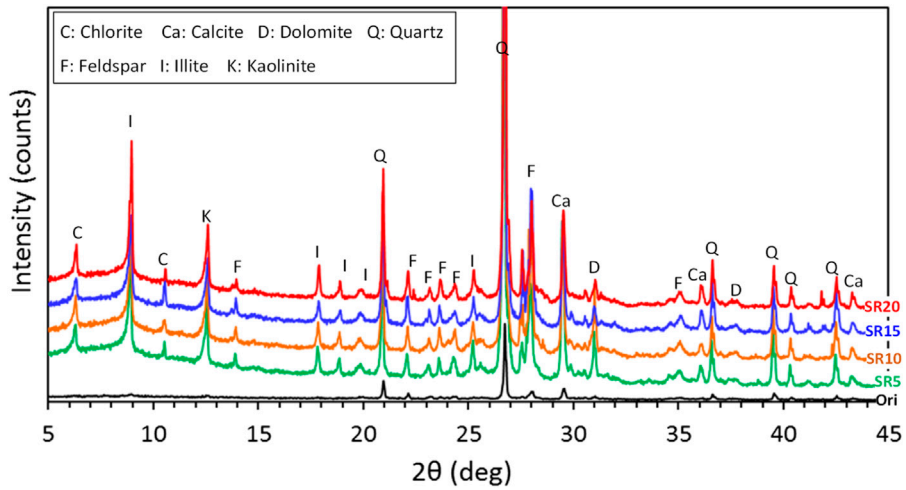

FIGURE 2 | X-ray diffractions of original loess and treated loess at different radial distances from the nano-SiO_2 pile.

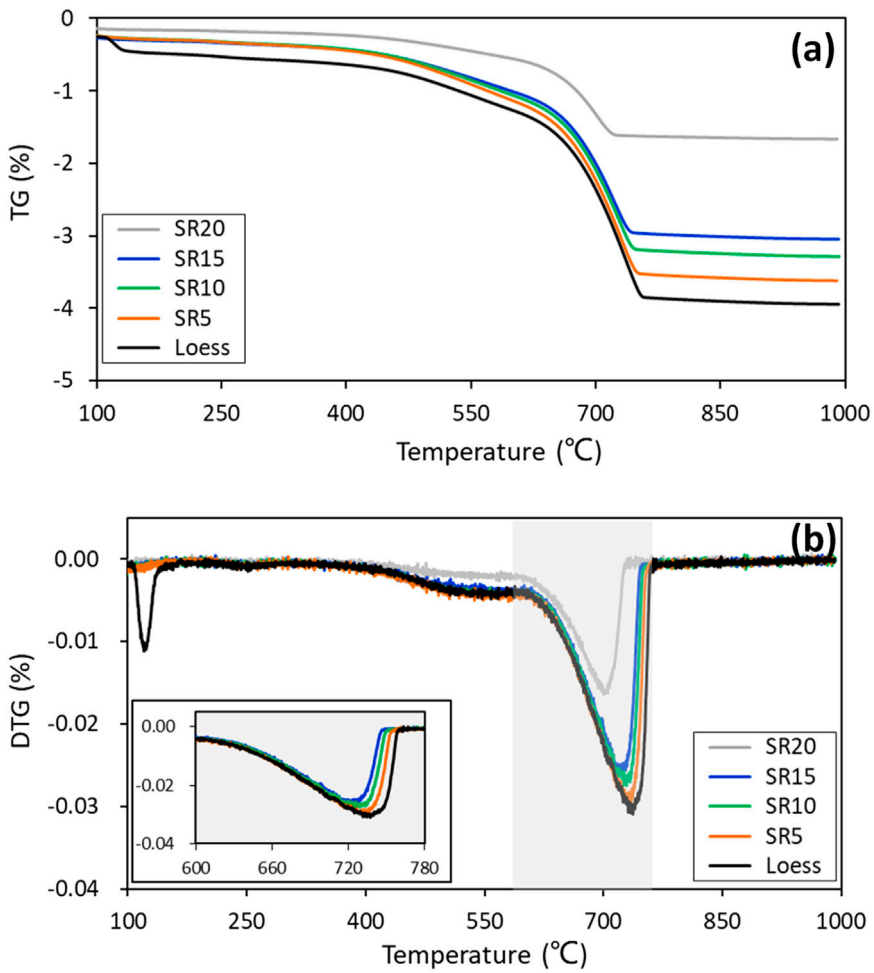

FIGURE 3 | TG-DTG curves of original loess and treated loess at different radial distances from the nano-SiO_2 pile.

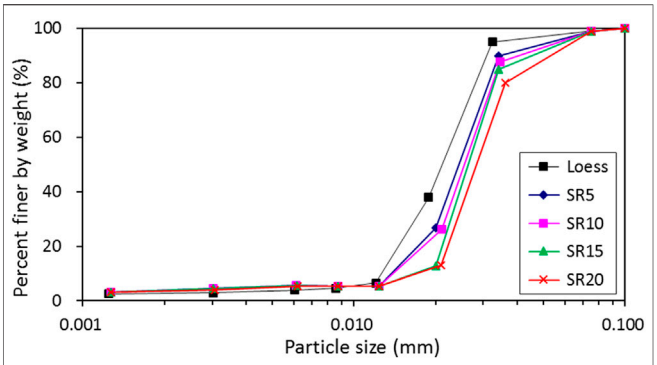

FIGURE 4 | Particle size curves of original loess and treated loess at different radial distances from the nano-SiO_2 pile.

Based on the XRD diffractograms, there is no new reflection; only intensity is enhanced. Sharp changes occurred in intensity and full width in all treated loess, and the crystalline structure seemed to be quite insensitive after nano-SiO_2 mitigation into loess around the pile. Generally, the changes in reflection shape can be related to a structural adjustment that fabric tends to become more isotropic due to the increase in crystallinity (Choquette et al., 1987; Souli et al., 2013). Thus, only physical structure modification exists while lacking the chemical reaction (Kong et al., 2018). Meanwhile, a slight difference occurred in the mixture of nano-SiO_2 added into the loess; the intensity and full width indicated only slight enhancement in XRD diffractograms (Kong et al., 2018). As a whole, the physical structure modification shows that an isotropic process occurred due to the increase of crystallinity.

TG-DTA Curves

The TG-DTA results of this study are presented in **Figure 3**. Among these results, the TG-DTA curves indicated two noticeable changes in two temperature domains. The first significant drop finished at about 150°C, corresponding to the loss of absorbed water in treated the loess. The second striking change occurred in the temperature range from 600°C to 780°C. The samples influenced by nano-SiO_2 migration showed relatively lower and narrower peaks with lesser mass loss, and the turning point of the curves shifted toward a slightly lower temperature. In the first domain, the loss of the absorbed water of original loess is related to the absorption of migrated nano-SiO_2 due to its large surface area and high activity. Menwhile, it is striking compared to the changes in the second domain. Previous studies have found that more hydration products causing denser structure can produce taller and wider peaks (Wu et al., 2016), and the shift in the turning point toward a lower temperature is derived from a more stable stage for materials (Galindo et al., 2015). Hence, the apparent changes in the second domain contributed to the generation of a more stable structure. Meanwhile, a looser structure existed in the sample with a more significant distance from the nano-SiO_2 pile. These findings also support the XRD results.

Changes in Texture and Structure

Macro-Texture From Particle Size Curves

The particle size curves of original loess and loess treated with nano-SiO_2 pile are shown in **Figure 4**. The macrostructure changes suggest a slight increase in the coarse fraction in the treated loess, with samples farther from the nano-SiO_2 pile becoming coarser. As a whole, the loess influenced by the nano-SiO_2 pile has a higher uniformity coefficient than that of the original loess. This finding also supports the idea that the loess involves an isotropic process with coarser particles due to crystallinity.

Micro-structure From SEM Micrographs

The SEM micrographs of the loess at 5 and 20 cm radial distances from the nano-SiO_2 pile are shown in **Figure 5**. The microstructure of the samples closer to the nano-SiO_2 pile is denser and more filling, with a more homogeneous state (**Figure 5A**), whereas that of the farther example is a looser and larger void space, with greater aggregation and more contact (**Figure 5B**). This result can be attributed to the degree of nano-SiO_2 migration into the loess. When the loess is close to the nano-SiO_2 pile, the degree of its migration is high; as a result, the nano-SiO_2 filled the pores and adhered to the soil particles (**Figure 5A**). Meanwhile, low nano-SiO_2 migration occurred in the loess farther from the pile. The few nano-SiO_2 particles mainly adhered to the surface of the soil particles, strengthening the bonding, while also filling the pores between particles. These created a bridge effect to link together soil particles as greater aggregates with larger void space (**Figure 5B**). The observation from microstructures effectively explains the changes in the particle size curve of the samples at a different radial distance from the nano-SiO_2 pile.

Aggregate Structure Stability From Disintegration

Figure 6 shows the disintegration characteristics of treated loess at different radial distances from the nano-SiO_2 pile with soaking time, and **Figure 7** shows disintegration rate of treated loess at different radial distances from the nano-SiO_2 pile. It can be seen that the disintegration rate of the treated loess has an obvious decrease acomparing with original loess, and that the disintegration rate of the treated loess increased with with increasing radius from the piles (**Figures 6**, **7**). These trends are matched with the denser packing from micro-structure observation, as shown in **Figure 5**. These results reveal that that the treated loess with the nano-SiO_2 pile have stronger cementation of aggregates, leading to more stable structure between aggregates.

Changes in Index Properties

Basic State From Water Content, Density, and Void Ratio

The changes in water content, natural density, and void ratio of treated loess with different radial distances from the nano-SiO_2 pile are shown in **Figure 8**. As indicated, the water content of loess treated with the nano-SiO_2 pile is lower than that of the original loess (**Figure 8A**), while the natural density of the treated loess is noticeably greater than the original one (**Figure 8B**). As a result,

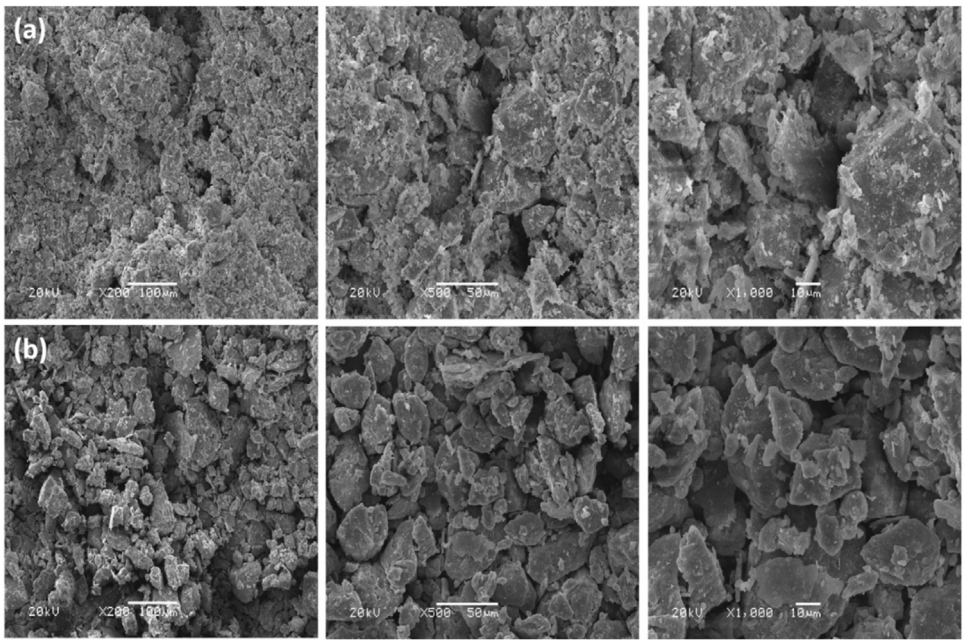

FIGURE 5 | SEM images of treated loess with a nano-SiO_2 pile at different amplification factors: **(A)** 5 cm radius from the pile; **(B)** 20 cm radius from the pile.

the void ratio of the treated loess is strikingly low compared to that of the original loess (**Figure 8C**). On the other hand, as shown in **Figure 8**, when the treated loess is closer to the nano-SiO_2 pile, the decrease in water content and the void ratio are stronger, and the increase in natural density tapers off as radial distance from the pile increases. Consequently, the loess treated with the nano-SiO_2 pile becomes dryer and denser, essentially producing a solidification process—namely, the water is removed and the densification also occurs in the treated loess (Zhang et al., 2018a). These state changes in the treated loess can attribute to the nano-SiO_2 migration, which has dual roles during the progress. Two direct effects involve adsorption and filling due to the special properties of nano-SiO_2, and one indirect derivative effect is the generation of tighter bonding between aggregates or particles. Meanwhile, the stronger effects in the treated loess are closer to the nano-SiO_2 pile.

The changes in the Atterberg limit of treated loess at different radial distances from the nano-SiO_2 pile are shown in **Figure 9**. As shown, the nano-SiO_2 migration has almost no effects on liquid limit, plastic limit, or plasticity index. This may be because the treated loess has no essential change in composition, with modification of only its structure and state. The results indirectly support that this is lacking for chemical reactions.

Mechanical Strength From Hardness Value

The changes in the hardness of treated loess at different radial distances from the nano-SiO_2 pile are shown in **Figure 10**. The hardness of the treated loess decreases as the radius from the nano-SiO_2 pile increases, but the hardness values is greater than that of loess treated with the lime and fly ash piles (Pei et al., 2015). In addition, no similar radial cracks occurred in the loess stabilized with the lime pile. This means that there should have a greater mechanical strength in the loess stabilized with the nano-SiO_2 pile than in the untreated loess. The increase in the mechanical strength is related to the nano-SiO_2 migration, which results in structure and state modification of the treated loess. Hence, the mechanical improvement is attributed to the coarsening effect and solidification process of the treated loess (i.e., large aggregate formation) as well as the dryer and denser state with more contact, smaller void space and more stable structure (as shown in **Figures 4**–**8**). Furthermore, the weakening strength improvement depends on the degree of nano-SiO_2 migration as the radius from the pile increases.

Changes in Physicochemical Properties

Particle or Aggregate Surface Properties From SSA and CEC

The changes in SSA and CEC of treated loess at different radial distances from the nano-SiO_2 pile are shown in **Figure 11**. Both SSA and CEC increase as the radial distance from the nano-SiO_2 pile increases, but all measurements are smaller than the original loess ones. The decrease in SSA and CEC is due to the formation of large aggregates due to the nano-SiO_2 migration. Nevertheless, their increasing trends seem to contradict the results of the particle size distribution (**Figure 4**). However, the increase in SSA and CEC with increasing radial distance from the nano-SiO_2 pile is a reasonable expectation. The total SSA and CEC depend not only on the particle size of a soil, but also on the structure of the soil (Zhang et al., 2018b). Previous research has found that the formation of larger aggregate clusters can result in a larger void space (Zhang et al., 2013). As observed in microstructural images (**Figure 5**), the treated loess farther from the nano-SiO_2 pile showed a larger void space in the greater aggregates. Hence, the

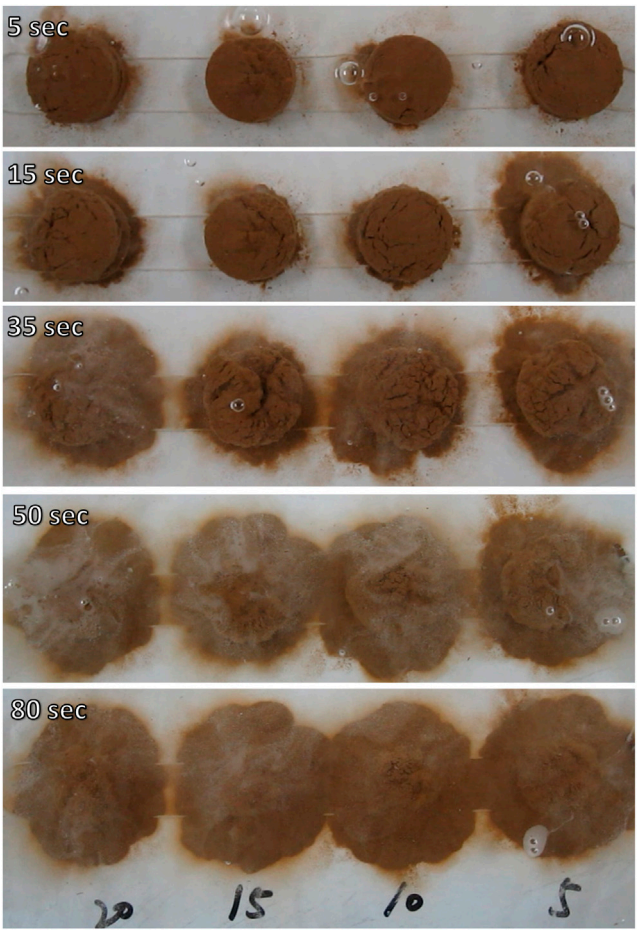

FIGURE 6 | Disintegration characteristics of treated loess at different radial distances from the nano-SiO_2 pile.

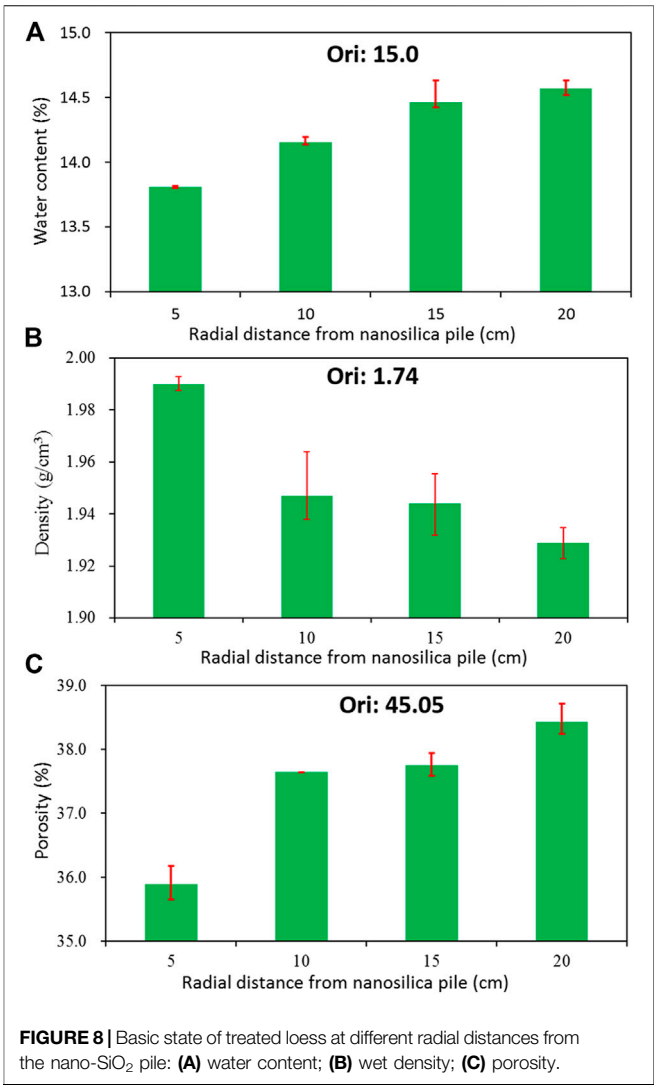

FIGURE 8 | Basic state of treated loess at different radial distances from the nano-SiO_2 pile: **(A)** water content; **(B)** wet density; **(C)** porosity.

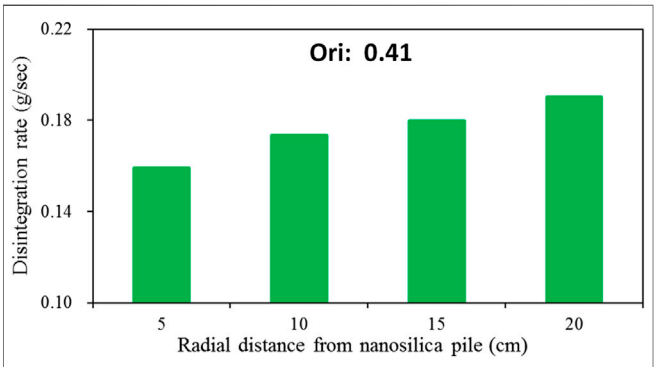

FIGURE 7 | Disintegration rate of treated loess at different radial distances from the nano-SiO_2 pile.

higher SSA and CEC of the farther treated loess could be attributed to a larger surface contact area due to its structure modification.

Soil Chemical Properties From EC, TDS, pH, and ORP

The changes in chemical properties (i.e., EC, TDS, pH, and ORP) of treated loess at different radial distances from the nano-SiO_2 pile are shown in **Figure 12**. As a whole, the EC and TDS of the treated loess with radial distance from the nano-SiO_2 pile, and their pH and ORP, accordingly decrease with increasing radius. It should be noted that the EC and TDS of the treated loess at radii of 5 and 10 cm are very slightly lower compared to the original loess, and the values at radii of 15 and 20 cm are also slightly higher compared to the original loess. The pH and ORP of the treated loess are overall lower than those of the original loess. This trend clearly shows the effect of nano-SiO_2 migration into loess, causing the changes in chemical properties due to the high activity and small size of the nano-SiO_2 particle. The very slight changes in chemical properties illustrate that the loess treated with nano-SiO_2 can keep an almost constant chemical environment. Thus, the nano-SiO_2 particle has the potential to act as an eco-friendly stabilized additive in loess improvement.

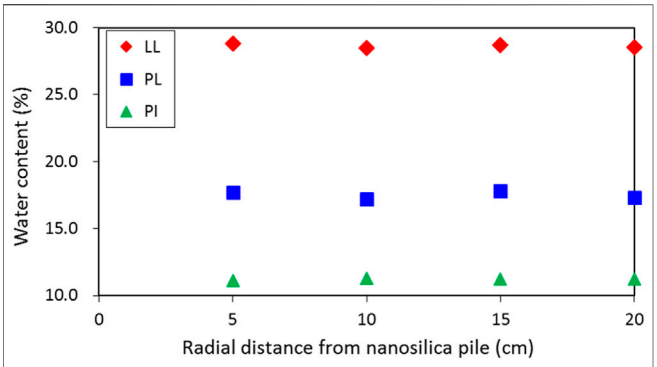

FIGURE 9 | Atterberg limits of treated loess at different radial distances from the nano-SiO_2 pile.

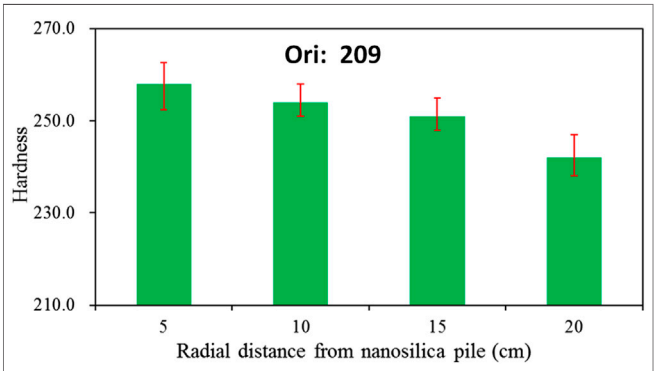

FIGURE 10 | Hardness value of treated loess at different radial distances from the nano-SiO_2 pile.

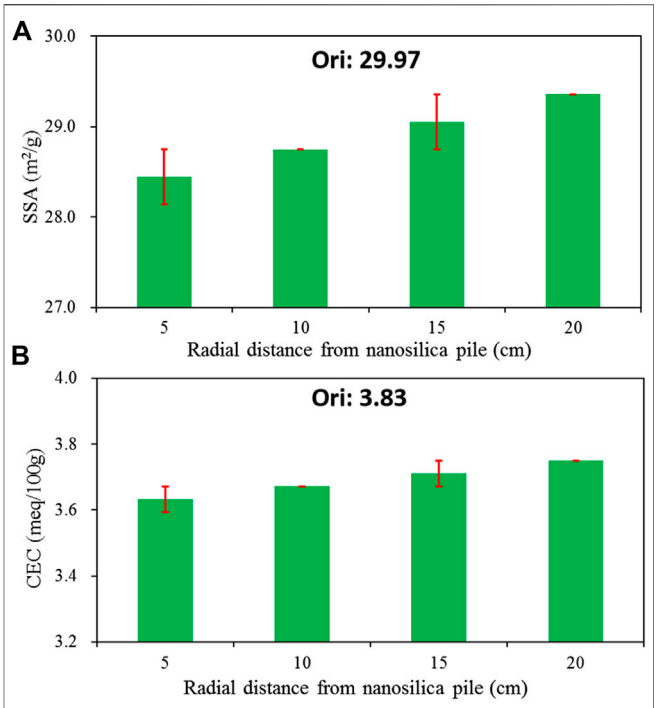

FIGURE 11 | Specific surface area **(SSA)** and cation exchange capacity **(CEC)** of treated loess at different radial distances from the nano-SiO_2 pile.

DISCUSSION

Nano-SiO_2 Migration-Induced Changes in Loess Properties

The results presented herein confirm that the nano-SiO_2 migration modifies the properties of the nano-SiO_2 pile treated loess. The structural, mechanical, physicochemical, and index properties all change, but the mineral composition experiences no noticeable change. In the previous studies, these have also no observable compositon modification to different nano-particles treated clay, silt and sands, even longer curing periods (Taha and Taha, 2012; Choo et al., 2015; Kong et al., 2018). Meanwhile, the very slight changes in EC and TDS can support the unobservable compositon modification. This is due to the fact that the chemical properties have close links to the mineral compositions. However, the particle coating, cemention between aggregates, more uniform aggregate formation have contributed to the physcial structure modification, which responsible for the changes in mechanical, physicochemical, and index properties (Kong et al., 2018; Kong et al., 2019). Hence, the changes in the treated loess properties are related to the physical structure modification rather than a chemical reaction.

It is interesting to note that the same initial water content existed between the loess and nano-SiO_2, which prevented the generation of the pore water pressure gradient. Here should mainly be adsorption force and capillary force. The nano-SiO_2 migration would be attributed to its dispersion because many previous studies have proved that nanoparticles are easily dispersed in various media (Li et al., 2004; Yao et al., 2005; Gallagher et al., 2007; Hendraningrat and Torsæter, 2015). Research using nano-SiO_2-treated concrete also found that large contents can seriously inhibit the uniform dispersion of nanoparticles (Li, 2004). Meanwhile, the dispersion can contributed to the special particle features, i.e. extremely small particle size and extremely great surface area, and correspondingly strong surface energy. It is should to noted that the density and water content of nano-SiO_2 migrated loess are different in that of nano-SiO_2 mixed loess. Theos treated loess by mixing nano-SiO_2 has slight decrese in water content and density (Kong et al., 2018). This may be relative with their reaction progress, but there still has a need to do a further study. As the difference of the stabilizing treatment techniques has important influence on its practial appilcation and availability. Aa a whole, a small amount of nano-SiO_2 particles migrating from the pile into loess may facilitate improving loess performance, and thus it has potential as a new treatment technique for soil improvement.

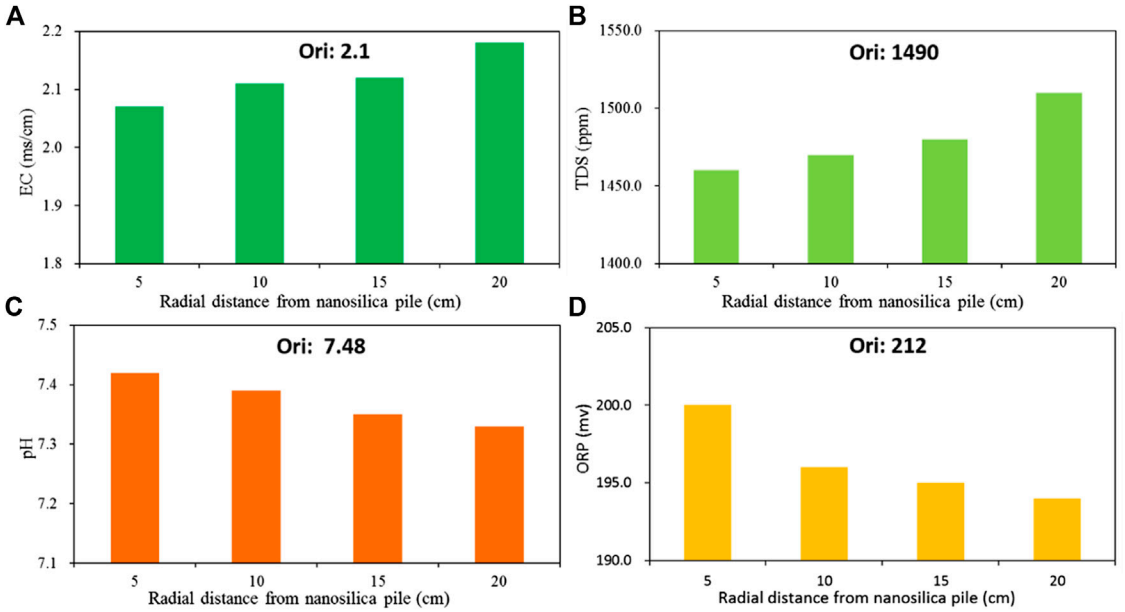

FIGURE 12 | Chemical properties of treated loess at different radial distances from the nano-SiO_2 pile: **(A)** EC; **(B)** TDS; **(C)** pH; **(D)** ORP.

Link Between Microscopic Characteristics and Macroscopic Behaviors

The observation of macroscopic behaviors and microscopic features identified a vital link. Nano-SiO_2 particle migration results in an isotropic aggregate in the treated loess, causing a denser and dryer state (**Figures 4–8**). Based the observation of SEM photograph and necessary state (**Figure 5** and **Figure 8**), an increase in micro-pores occurs at the expense of the macropores, with a significant decrease in the total pore volume of the treated loess. Meanwhile, the agglomerated effect causes the formation of coarser aggregates and the denser packing accompanying the consumption of water (**Figures 4–8**), which generates greater mechanical strength (**Figure 10**) and smaller SSA and CEC in the treated loess (**Figure 11**). The chemical properties indicate slight changes in CE, TDS, pH, and ORP, without significant modification of the treated loess (**Figure 12**). Thus, the nano-SiO_2 has the potential to be used as an eco-friendly additive in soil improvement. On the other hand, no new XRD diffractograms are generated in the treated loess, but SEM observation affords a direct method for changes to the microscopic characteristics.

CONCLUSION

The microscopic characteristics (such as mineralogical and structural properties) and macroscopic behaviors (such as basic state, mechanical, and physicochemical properties) of loess treated with the nano-SiO_2 pile were observed. Based on the test results, the following conclusions can be drawn:

1 The nano-SiO_2 migration induced the changes in microscopic characteristics and macroscopic behaviors of the treated loess, producing an interactional relationship among them. The linked relationships facilitate the understanding of the mechanism of changes in nano-SiO_2 pile-treated loess properties.

2 No obvious changes occurred in the mineralogical composition of XRD diffractograms, but SEM photographs and slake tests show apparent structural modification in the treated loess with the nano-SiO_2 pile. An isotropic process is evident with coarser particles, more filling and denser packing due to crystallinity. As a result, the treated loess with the nano-SiO_2 pile have stronger water stability.

3 The loess treated with nano-SiO_2 pile produces a solidification process, causing a decrease in water content and void ratio as well as an increase in natural density, thereby improving its mechanical strength.

4 The loess treated with nano-SiO_2 pile modifies the physicochemical properties. The SSA and CEC of treated loess are smaller than those of the original loess but include an increasing trend moving farther from the pile, resulting in a slight change in chemical properties.

On the whole, the nano-SiO_2 pile migration induced the relevant changes in the treated loess due to the nanoparticle dispersion. The modification of the physical structure and basic state resulted in the improvement of the performance of the treated loess. Meanwhile, nano-SiO_2 has the potential to be an eco-friendly stabilized additive in loess performace improvement due to its slight changes in chemical properties.

DATA AVAILABILITY STATEMENT

The original contributions presented in the study are included in the article/supplementary material, further inquiries can be directed to the corresponding author.

AUTHOR CONTRIBUTIONS

RK performed the tests and analyzed the data, RK wrote the manuscript text. LG, WZ and BZ revised the manuscript, RK and LG sourced the funds for the study.

FUNDING

This study was partially supported by Gansu University Innovation Fund Project (No. 2021A-255) and Industrial support and guidance project of colleges and universities in Gansu Province in 2019: Research and key technology of coal mine reclamation in Gansu Province (No.:2019C-16).

ACKNOWLEDGMENTS

The authors are also grateful to the two reviewers and editor for their valuable comments to improve the quality of this paper.

REFERENCES

Abiodun, A. A., and Nalbantoglu, Z. (2014). Lime Pile Techniques for the Improvement of clay Soils. *Can. Geotechnical J.* 52, 760–768. doi:10.1139/cgj-2014-0073

Arrua, P., Aiassa, G., and Eberhardt, M. (2010). Loess Soil Stabilized with Cement for Civil Engineering Applications. *Int. J. Earth Sci. Eng.* 5, 10–17.

ASTMD422-63 (2007). *Standard Test Method for Particle-Size Analysis of Soils*. West Conshohocken, PA: ASTM International.

Barker, J. E., Rogers, C. D., and Boardman, D. I. (2006). Physio-chemical Changes in clay Caused by Ion Migration from Lime Piles. *J. Mater. Civ. Eng.* 18, 182–189. doi:10.1061/(asce)0899-1561(2006)18:2(182)

Barker, J. E., Rogers, C. D. F., and Boardman, D. I. (2007). Ion Migration Associated with Lime Piles: a Review. *Proc. Inst. Civil Eng. - Ground Improvement* 11, 87–98. doi:10.1680/grim.2007.11.2.87

Castro, J. (2017). Modeling Stone Columns. *Materials* 10, 782. doi:10.3390/ma10070782

Choo, H., Larrahondo, J., and Burns, S. E. (2015). Coating Effects of Nano-Sized Particles onto Sand Surfaces: Small Strain Stiffness and Contact Mode of Iron Oxide-Coated Sands. *J. Geotech. Geoenviron. Eng.* 141, 04014077. doi:10.1061/(asce)gt.1943-5606.0001188

Choquette, M., Bérubé, M., and Locat, J. (1987). Mineralogical and Microtextural Changes Associated with Lime Stabilization of marine Clays from Eastern Canada. *Appl. Clay Sci.* 2, 215–232. doi:10.1016/0169-1317(87)90032-9

Çokça, E., and Birand, A. A. (1993). Determination of Cation Exchange Capacity of Clayey Soils by the Methylene Blue Test. *Geotechnical Test. J.* 16, 518–524. doi:10.1520/GTJ10291J

Dolgikh, P. D. (1966). Stabilization of Slumping Loess Soils by Injection of a Lime-Slag Suspension. *Soil Mech. Found. Eng.* 3, 272–273. doi:10.1007/bf01703524

Galindo, R., López-Delgado, A., Padilla, I., and Yates, M. (2015). Synthesis and Characterisation of Hydrotalcites Produced by an Aluminium Hazardous Waste: A Comparison between the Use of Ammonia and the Use of Triethanolamine. *Appl. Clay Sci.* 115, 115–123. doi:10.1016/j.clay.2015.07.032

Gallagher, P. M., Pamuk, A., and Abdoun, T. (2007). Stabilization of Liquefiable Soils Using Colloidal Silica Grout. *J. Mater. Civ. Eng.* 19, 33–40. doi:10.1061/(asce)0899-1561(2007)19:1(33)

GB/T50123 (1999). *Standard for Soil Test Method*. Ministry of Construction, P.R. China. (in Chinese).

Haeri, S. M., Akbari Garakani, A., Roohparvar, H. R., Desai, C. S., Seyed Ghafouri, S. M. H., and Salemi Kouchesfahani, K. (2019). Testing and Constitutive Modeling of Lime-Stabilized Collapsible Loess. I: Experimental Investigations. *Int. J. Geomech.* 19, 04019006. doi:10.1061/(asce)gm.1943-5622.0001364

Helle, T. E., Aagaard, P., and Nordal, S. (2017). *In Situ* improvement of Highly Sensitive Clays by Potassium Chloride Migration. *J. Geotech. Geoenviron. Eng.* 143, 04017074. doi:10.1061/(asce)gt.1943-5606.0001774

Hendraningrat, L., and Torsæter, O. (2015). A Stabilizer that Enhances the Oil Recovery Process Using Silica-Based Nanofluids. *Transp. Porous Med.* 108, 679–696. doi:10.1007/s11242-015-0495-8

Kong, R., Yan, B., Xu, J., Shi, Z., Peng, Q., and Lin, X. (2019). Physical Homogenization and Chemical Stability of Nano-SiO_2 Treated Loess. *Soil Mech. Found. Eng.* 56, 336–339. doi:10.1007/s11204-019-09611-9

Kong, R., Zhang, F., Wang, G., and Peng, J. (2018). Stabilization of Loess Using Nano-SiO_2. *Materials* 11, 1014. doi:10.3390/ma11061014

Larsson, S., Stille, H., and Olsson, L. (2005). On Horizontal Variability in Lime-Cement Columns in Deep Mixing. *Géotechnique* 55, 33–44. doi:10.1680/geot.55.1.33.58586

Li, G. (2004). Properties of High-Volume Fly Ash concrete Incorporating Nano-SiO_2. *Cement Concrete Res.* 34, 1043–1049. doi:10.1016/j.cemconres.2003.11.013

Li, H., Xiao, H.-g., and Ou, J.-p. (2004). A Study on Mechanical and Pressure-Sensitive Properties of Cement Mortar with Nanophase Materials. *Cement Concrete Res.* 34, 435–438. doi:10.1016/j.cemconres.2003.08.025

Metelková, Z., Boháč, J., Přikryl, R., and Sedlářová, I. (2012). Maturation of Loess Treated with Variable Lime Admixture: Pore Space Textural Evolution and Related Phase Changes. *Appl. Clay Sci.* 61, 37–43. doi:10.1016/j.clay.2012.03.008

Pei, X., Zhang, F., Wu, W., and Liang, S. (2015). Physicochemical and index Properties of Loess Stabilized with Lime and Fly Ash Piles. *Appl. Clay Sci.* 114, 77–84. doi:10.1016/j.clay.2015.05.007

Quang, N. D., and Chai, J. C. (2015). Permeability of Lime- and Cement-Treated Clayey Soils. *Can. Geotech. J.* 52, 1221–1227. doi:10.1139/cgj-2014-0134

Rajasekaran, G., and Narasimha Rao, S. (2002). Permeability Characteristics of Lime Treated marine clay. *Ocean Eng.* 29, 113–127. doi:10.1016/s0029-8018(01)00017-8

Ren, X., and Hu, K. (2014). Effect of Nanosilica on the Physical and Mechanical Properties of Silty clay. *Nanosci. Nanotechnol. Lett.* 6, 1010–1013. doi:10.1166/nnl.2014.1857

Rogers, C. D. F., and Glendinning, S. (1997). Improvement of clay Soils *In Situ* Using Lime Piles in the UK. *Eng. Geology* 47, 243–257. doi:10.1016/s0013-7952(97)00022-7

Santamarina, J. C., Klein, K. A., Wang, Y. H., and Prencke, E. (2002). Specific Surface: Determination and Relevance. *Can. Geotech. J.* 39, 233–241. doi:10.1139/t01-077

Saoudi, N. K. S. A., Rahil, F., and Abbawi, Z. (2013). Soft Soil Improved by Stone Columns And/or Ballast Layer. *Ground Improvement* 168, 179–186.

Sariosseiri, F., and Muhunthan, B. (2009). Effect of Cement Treatment on Geotechnical Properties of Some Washington State Soils. *Eng. Geology* 104, 119–125. doi:10.1016/j.enggeo.2008.09.003

Selvakumar, S., and Soundara, B. (2019). Swelling Behaviour of Expansive Soils with Recycled Geofoam Granules Column Inclusion. *Geotextiles and Geomembranes* 47, 1–11. doi:10.1016/j.geotexmem.2018.08.007

Souli, H., Fleureau, J.-M., Trabelsi-ayadi, M., and Taibi, S. (2013). A Multi-Scale Study of the Effect of Zinc and lead on the Hydromechanical Behaviour and Fabric of a Montmorillonite. *Géotechnique* 63, 880–884. doi:10.1680/geot.13.p.016

Tabarsa, A., Latifi, N., Meehan, C. L., and Manahiloh, K. N. (2018). Laboratory Investigation and Field Evaluation of Loess Improvement Using Nanoclay - A Sustainable Material for Construction. *Construction Building Mater.* 158, 454–463. doi:10.1016/j.conbuildmat.2017.09.096

Taha, M. R., and Taha, O. M. E. (2012). Influence of Nano-Material on the Expansive and Shrinkage Soil Behavior. *J. Nanoparticle Res.* 14, 1–13. doi:10.1007/s11051-012-1190-0

Tchakalova, B., and Todorov, K. (2008). Plastic Soil-Cement Mixtures for Isolation Barriers. *Geologica Balcanica* 37, 91–96.

Tystovich, N., Abelev, M., and Takhirov, I. (1971). "Compacting Saturated Loess Soils by Means of Lime Piles," in *Processings of Fourth Conference on Soil Mechanics and Foundation Engineering*. Editor A. Kezdi (Budapest: Akademiai Kiado), 837–842.

Wu, Z., Deng, Y., Liu, S., Liu, Q., Chen, Y., and Zha, F. (2016). Strength and Microstructure Evolution of Compacted Soils Modified by Admixtures of Cement and Metakaolin. *Appl. Clay Sci.* 127-128, 44–51. doi:10.1016/j.clay.2016.03.040

Yao, X., Tan, S., Huang, Z., and Jiang, D. (2005). Dispersion of Talc Particles in a Silica Sol. *Mater. Lett.* 59, 100–104. doi:10.1016/j.matlet.2004.09.025

Zhang, C.-l., Jiang, G.-l., Su, L.-j., and Zhou, G.-d. (2017). Effect of Cement on the Stabilization of Loess. *J. Mt. Sci.* 14, 2325–2336. doi:10.1007/s11629-017-4365-4

Zhang, F., Kong, R., and Peng, J. (2018b). Effects of Heating on Compositional, Structural, and Physicochemical Properties of Loess under Laboratory Conditions. *Appl. Clay Sci.* 152, 259–266. doi:10.1016/j.clay.2017.11.022

Zhang, F., Pei, X., and Yan, X. (2018a). Physicochemical and Mechanical Properties of Lime-Treated Loess. *Geotech. Geol. Eng.* 36, 685–696. doi:10.1007/s10706-017-0341-6

Zhang, F., and Wang, G. (2018). Effect of Irrigation-Induced Densification on the post-failure Behavior of Loess Flowslides Occurring on the Heifangtai Area, Gansu, China. *Eng. Geology* 236, 111–118. doi:10.1016/j.enggeo.2017.07.010

Zhang, F., Wang, G., Kamai, T., Chen, W., Zhang, D., and Yang, J. (2013). Undrained Shear Behavior of Loess Saturated with Different Concentrations of Sodium Chloride Solution. *Eng. Geology* 155, 69–79. doi:10.1016/j.enggeo.2012.12.018

Zia, N., and Fox, P. J. (2000). Engineering Properties of Loess-Fly Ash Mixtures for Roadbase Construction. *Transportation Res. Rec.* 1714, 49–56. doi:10.3141/1714-07

Conflict of Interest: The authors declare that the research was conducted in the absence of any commercial or financial relationships that could be construed as a potential conflict of interest.

Publisher's Note: All claims expressed in this article are solely those of the authors and do not necessarily represent those of their affiliated organizations, or those of the publisher, the editors and the reviewers. Any product that may be evaluated in this article, or claim that may be made by its manufacturer, is not guaranteed or endorsed by the publisher.

frontiers in Earth Science

ORIGINAL RESEARCH
published: 24 November 2021
doi: 10.3389/feart.2021.777551

Seismic Response of a Water Transmission Pipeline Across a Fault Zone Adopting a Large-Scale Vibration Table Test

Longsheng Deng[1,2]*, *Wenzhong Zhang*[3,4], *Yan Dai*[1], *Wen Fan*[1,2]*, *Yubo Li*[3,4], *Sen Ren*[1] and *Pei Li*[1]

[1]School of Geological Engineering and Geomatics, Chang'An University, Xi'an, China, [2]Mine Geological Disasters Mechanism and Prevention Key Laboratory, Xi'an, China, [3]China Railway First Survey and Design Institute Group Co., Ltd., Xi'an, China, [4]Shaanxi Railway and Underground Traffic Engineering Key Laboratory (FSDI), Xi'an, China

The seismic response is generally amplified significantly near the fault zone due to the influence of discontinuous interfaces and weak-broken geotechnical structures, which imposes a severe geologic hazard risk on the engineering crossing the fault. The Hanjiang to Weihe River Project (phase II) crosses many high seismic intensity regions and intersects with eight large-scale regional active faults. Seismic fortification of the pipelines across the fault zone is significant for the design and construction of the project. A large-scale vibration table test was adopted to investigate the seismic response and fault influences. The responses of accelerations, dynamic stresses, strains, and water pressures were obtained. The results show that the dynamic responses were amplified significantly by the fault zone and the hanging wall. The influence range of fault on acceleration response is approximately four times the fault width. The acceleration amplification ratio in the fault zone generally exceeds 1.35, even reaching 1.8, and the hanging wall amplification ratio is approximately 1.2. The dynamic soil pressure primarily depends on the acceleration distribution and is apparently influenced by pipeline location and model inhomogeneity. The pipeline is bent slightly along the axial direction, accompanied by expansion and shrinkage in the radial direction. The maximum tensile and compressive strains appear at the lower and upper pipeline boundaries near the middle section, respectively. Massive *y*-direction cracks developed in the soil, accompanied by slight seismic subsidence. The research findings could provide reasonable parameters for the seismic design and construction of the project.

Keywords: vibration table test, seismic response, pipeline across fault zone, loess site, influence of fault

OPEN ACCESS

Edited by:
Yueren Xu,
China Earthquake Administration, China

Reviewed by:
Ming Zhang,
China University of Geosciences Wuhan, China
Luigi Di Sarno,
University of Liverpool, United Kingdom

***Correspondence:**
Longsheng Deng
dlsh@chd.edu.cn
Wen Fan
fanwen@chd.edu.cn

Specialty section:
This article was submitted to Geohazards and Georisks, a section of the journal Frontiers in Earth Science

Received: *15 September 2021*
Accepted: *04 November 2021*
Published: *24 November 2021*

Citation:
Deng L, Zhang W, Dai Y, Fan W, Li Y, Ren S and Li P (2021) Seismic Response of a Water Transmission Pipeline Across a Fault Zone Adopting a Large-Scale Vibration Table Test. Front. Earth Sci. 9:777551. doi: 10.3389/feart.2021.777551

INTRODUCTION

Faults are one of the most important geological settings in the Earth's crust and are developed extensively in western China. Fault activities generally induce various geological disasters, such as ground dislocations, landslides, collapses, and debris flows, posing a significant threat to people's lives, properties and engineering constructions (Dhakal, 2021; Peng et al., 2021). Pipelines constitute one of the critical infrastructure elements of modern societies and are used to transport gases and waters over long distances. As a lifeline project built either on the ground surface or buried in the soil,

the pipeline cannot avoid crossing a fault belt in most conditions. Studying the assessment, mitigation, and treatment of pipelines across faults is significant for the design and construction of projects.

Significant research has been devoted to understanding the behavior of pipelines subjected to a fault. Scientists and engineers generally focus on the following aspects: 1) investigation of seismic damage of pipelines under strong earthquakes; 2) assessment of pipelines crossing the fault adopting analytical methods, numerical simulations, and physical modeling experiments; and 3) mitigation and prevention of pipelines crossing the fault belt.

The stick-slip action of faults generally triggers strong earthquakes, which can cause large displacements to appear at the ground surface, produce strong ground motions in high seismic intensity regions, and pose severe damage to structures. The damage to pipelines in typical strong earthquakes, such as the 1975 Haicheng (Sun and Hou, 1991), 1976 Tangshan (Sun and Shien, 1983), 2002 Alaska (Hall et al., 2003; Honegger et al., 2004), and 2008 Wenchuan earthquakes (Wang et al., 2012), was investigated, which presented the destruction features of structures and primary influencing factors on destructiveness. In the 1978 Miyagiken-Oki earthquake, approximately 350 cases of damage to water and gas pipelines were investigated near the cut-and-fill boundaries of newly developed residential areas (Liang and Sun, 2000). Experiences from strong earthquakes show that underground structures usually suffer minor damage compared with ground structures during a seismic event (Corigliano et al., 2011), and cut-and-cover tunnels are more vulnerable than circular bored tunnels (Hashash et al., 2001). According to statistical analysis, the peak ground velocity, pipeline type, and size are attributed to the seismic damage of buried pipelines (Toprak and Taskin, 2007). The site conditions are more significant than seismic intensity in contributing to pipeline damage. All the investigations provide detailed damage characteristics, models, and mechanisms for the analysis and design of the pipeline.

The behaviors of lifeline engineering structures crossing faults have been investigated by many researchers adopting the methods of theoretical analysis. Newmark and Hall (Newmark and Hall, 1975) developed a simplified analysis method assuming that a pipeline is subjected to direct stress by the dislocation, ignoring nonuniform lateral soil resistance. On this basis, many researchers extended corresponding works (Kennedy et al., 1979; Duan et al., 2011; Uckan et al., 2015). A refined analysis method for the buried pipeline was presented considering some modification of previous assumptions, which is applicable to both strike-slip and reverse strike-slip faults (Wang and Yeh, 1985). Researchers investigated the buried pipeline responses to strike-slip fault movement, where the large deflection pipeline crossing the fault zone is modeled as an elastica, and the remaining portion of the small deflection pipeline is modeled as a semi-infinite beam on an elastic foundation (Chiou et al., 1994). A simplified method was developed to estimate the curvatures of continuous pipelines due to normal fault movement (Shi et al., 2018). All analytical methods provide the basis for the rapid evaluation of structural deformation and damage across fault zones.

Considerable numerical simulations and large-scale physical model tests were adopted to analyze structures that cross faults under special and complex conditions. The influence of pipeline shell thickness, buried depth, fault zone width, fault displacement, intersection angle of pipeline and fault, material nonlinear characteristic, etc., were taken into account systematically during the numerical simulations (Joshi et al., 2011; Karamitros et al., 2011; Chen et al., 2012; Yang et al., 2013; Vazouras and Karamanos, 2017; Demirci et al., 2018; Dezhkam and Nouri, 2018; Sarvanis et al., 2018; Yifei et al., 2018; Fard et al., 2019; Fadaee et al., 2020). Centrifuge model tests were implemented for segmental tunnels subjected to a normal fault and for a high-density polyethylene pipeline crossing a strike-slip fault (Abdoun et al., 2009; Kiani et al., 2016). A few shaking table tests on deep-buried pipelines (Yan et al., 2018), mountain tunnel flexible joints (Shen et al., 2020), and shield tunnel multiscale physical models (Bao et al., 2017) that passed through a fault zone were also implemented. The vulnerability assessment of natural gas pipelines subjected to seismic actions was explored (Tsinidis et al., 2019; Tsinidis et al., 2020a; Tsinidis et al., 2020b). All of these results provided parameters, methods, and schemes for the design and construction of engineering structures across a fault zone and paved the way for subsequent scientific research.

Engineers are usually very concerned about reducing the possibility of damage to the facilities triggered by faulting. To date, the avoidance principle is still the most recommended method in actual projects. For pipelines crossing fault belts, a combination of ground treatment, structure improvement, and seismic monitoring is generally adopted to mitigate the risk (Honegger et al., 2004). One efficient seismic protection is pipeline placement within culverts or the use of flexible joints (Gantes and Melissianos, 2016). However, the seismic design of a buried pipeline across a fault is complex and governed by many factors, such as the ground and structure conditions, fault activities, and damage mechanisms.

The effect of faults on engineering mainly includes the following three aspects: 1) stick-slip action triggering earthquakes, strong ground motions, and seismic disasters; 2) creep-slid deformation causing permanent ground dislocations threatening the engineering crossing the fault; and 3) fault amplification on geologic hazards due to the influence of discontinuous interfaces and weak-broken geotechnical structures. Regardless of any of the above effects, severe engineering damage can be produced near the fault belt and cause significant challenges in design and construction for projects crossing a fault. However, the current research mainly focuses on aspects 1) and 2), and few studies focus on 3). The fault influence range and amplification are significant and need to be explored.

The Hanjiang to Weihe River Diversion Project is intended to alleviate the water shortage and optimize the strategic allocation of water resources in central and northern Shaanxi Province.

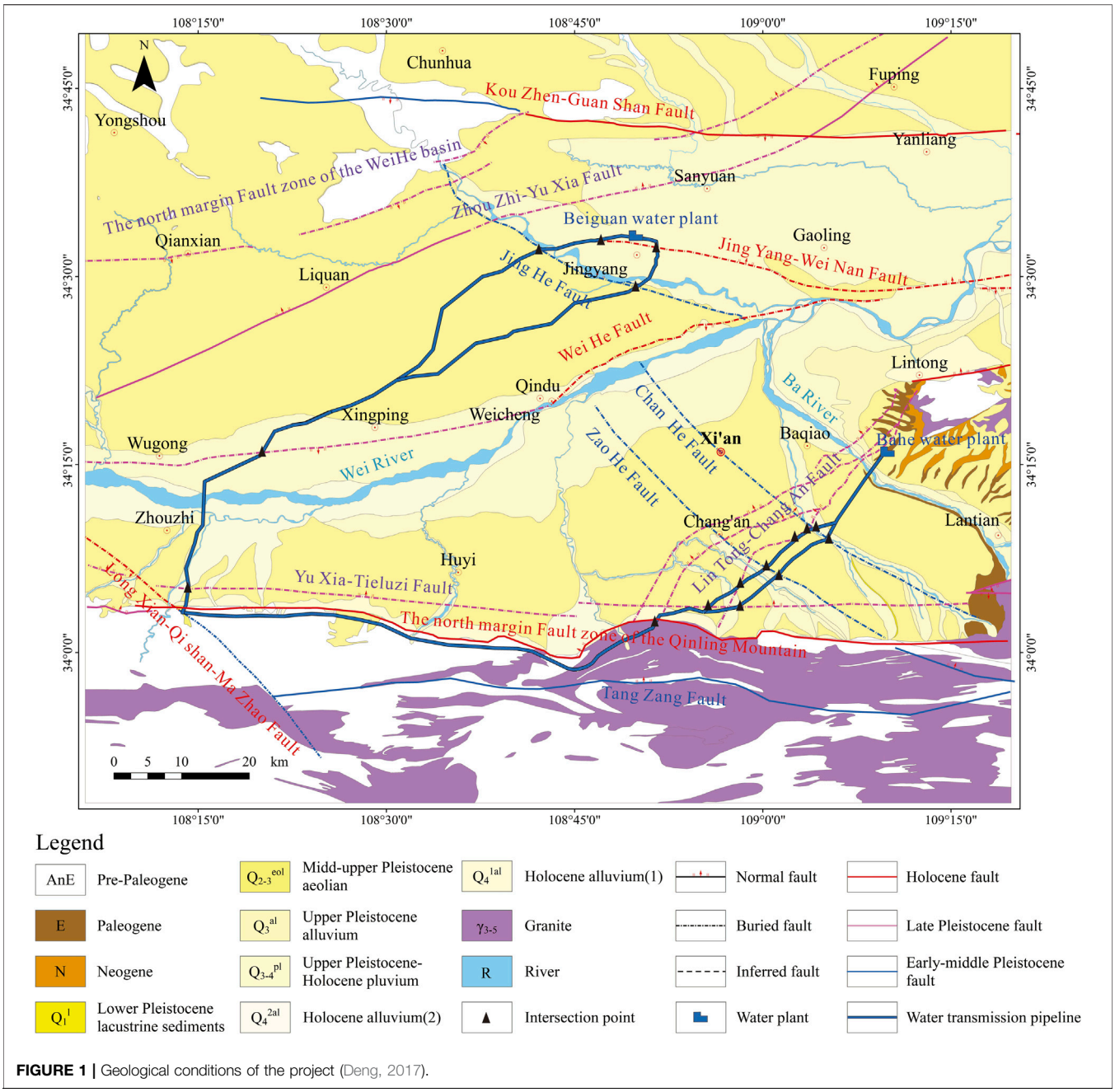

FIGURE 1 | Geological conditions of the project (Deng, 2017).

Phase II of the project is water transmission engineering, including the southern and northern branches. Due to the high seismic intensity and development of active faults in engineering regions, it is essential to accurately implement seismic fortification for the design and construction of pipelines. This paper aims to investigate the seismic response of pipelines across the fault zone. The large-scale vibration table test was adopted to investigate the response of acceleration, dynamic stresses, strains, and water pressures for the surrounding soil and pipeline in detail. The results could provide more reasonable parameters for the seismic design of the project.

TECTONIC BACKGROUND OF THE HANJIANG TO WEIHE RIVER DIVERSION PROJECT

Phase II of the project starts from the Huangchi ditch and is then divided into two branches. The south branch is distributed eastward along northern Qinling Mountain, ending at the Bahe Water Plant with a total route length of 103.5 km. The north branch extends northwards through Zhouzhi and Xingping and terminates at the Jingyang Beiguan Water Plant with a total route length of 88.7 km. The water transmission engineering structure is designed as a circular concrete pipeline with an

TABLE 1 | Intersection conditions of the faults and pipeline.

No	Fault name	Latest activity era	Intersection coordinates of the faults and pipeline	Cross angles of the faults and pipeline
1	North Qinling fault	Q_h	①E = 108.85°, N = 34.03°	64°
2	Weihe fault	Q_P^3-Q_h	①E = 108.34°, N = 34.28°	53°
3	Lintong-Chang'an fault	Q_P^3	①E = 108.97°, N = 34.09°	30°; 50°; 49°; 48°
—	—	—	②E = 108.95°, N = 34.06°	—
—	—	—	③E = 108.87°, N = 34.05°	—
—	—	—	④E = 108.86°, N = 34.04°	—
4	Yuxia-Tieluzi fault	Q_P^{2-3}	①E = 108.24°, N = 34.08°	82°; 38°; 47°
—	—	—	②E = 108.93°, N = 34.06°	—
—	—	—	③E = 108.96°, N = 34.06°	—
5	Jingyang-Weinan fault	Q_h	①E = 108.86°, N = 34.53°	79°; 17°
—	—	—	②E = 108.75°, N = 34.54°	—
6	Jinghe fault	Q_P^2	①E = 108.72°, N = 34.54°	28°; 59°
—	—	—	②E = 108.84°, N = 34.49°	—
7	Chanhe fault	Q_P^{1-2}	①E = 109.07°, N = 34.17°	48°; 60°
—	—	—	②E = 109.09°, N = 34.16°	—
8	Zaohe fault	Q_P^{1-2}	①E = 109.01°, N = 34.11°	52°; 64°
			②E = 106.02°, N = 34.10°	

Annotation: the superscript number (1, 2, and 3) represents the formation sequence, E means east longitude, and N means north latitude.

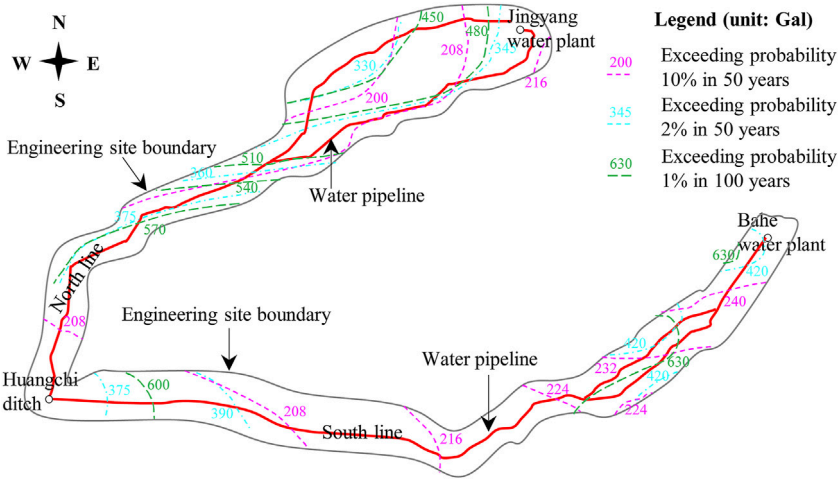

FIGURE 2 | Distribution of peak ground acceleration for typical exceeding probabilities (Deng, 2017).

outer radius of 2.7 m, partly combined with rectangular box culverts. The water supply amount of the project can reach a total of 1.5 billion m^3 per year (Deng, 2017). The distribution and geological conditions of the Hanjiang to Weihe River Project (phase II) are presented in **Figure 1**.

According to the seismic tectonic background, a total of 20 faults developed in the near-field regions, among which seven are Holocene (Q_h) faults and eight are Late Pleistocene (Q_p) faults. The project intersects with eight of the faults (Deng, 2017). The fault names, intersection point coordinates, cross angles, and latest activity eras of the eight faults are shown in **Table 1**.

The soil category of the site is evaluated as medium-hard (category II). The peak seismic acceleration of the ground was calculated by adopting the probability analysis of the seismic risk method. According to the calculation results, the peak ground acceleration for exceeding probabilities of 63, 10, 5, and 2% in 50 years is 76–86 Ga l, 200–240 Ga l, 260–310 Ga l, 330–420 Ga l, respectively, and the peak ground acceleration for exceeding probabilities of 5, 2, and 1% in 100 years is 312–384 Ga l, 347–485 Ga l, and 450–630 Ga l, respectively (Deng, 2017). The distribution of peak ground seismic acceleration for typical exceeding probabilities is presented in **Figure 2**. The seismic precautionary intensity for the project is VIII degrees.

Consequently, the geological tectonic activities are intense in the engineering regions. High seismic intensity regions are distributed widely. Eight large-scale regional faults are intersected, and the investigation of faults' effect on water pipe construction is critical. To date, the influence of fault creep-

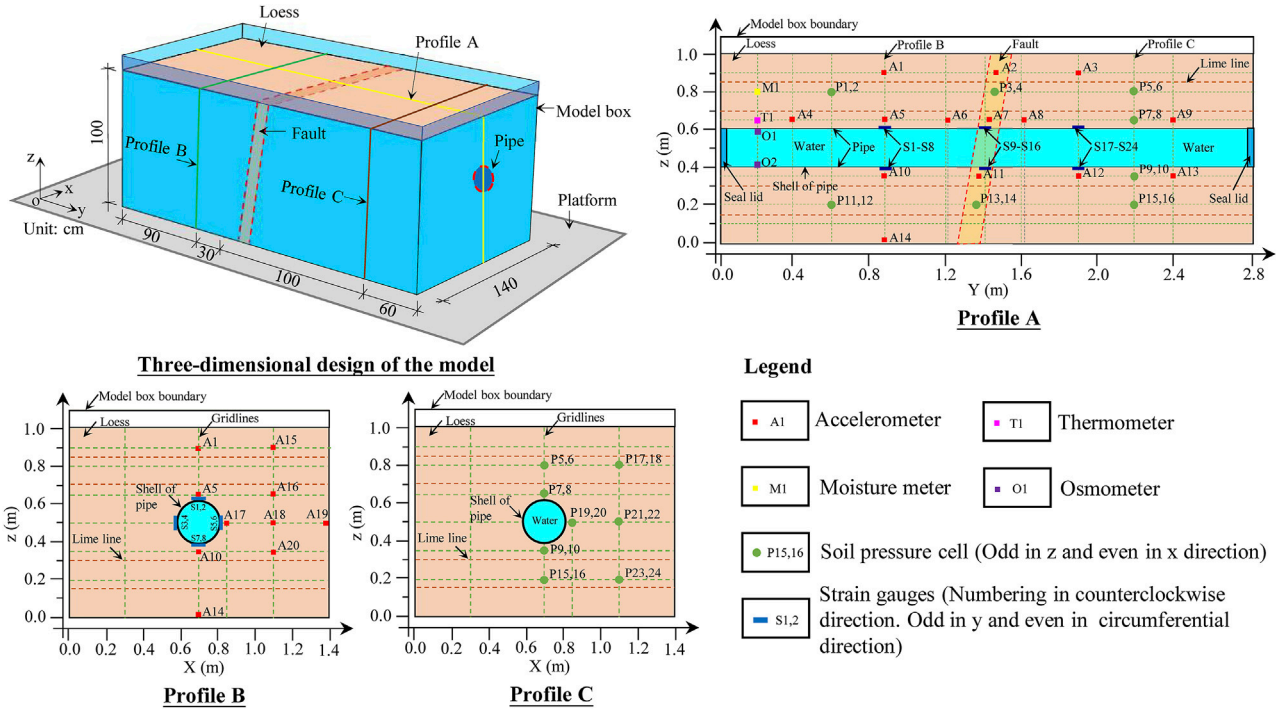

FIGURE 3 | Design and profiles of the vibration table experiment.

sliding activities and stick-slip movements on engineering has been extensively considered, and many significant results have been obtained to provide a reference for engineering construction. However, due to the influence of discontinuous interfaces and broken geotechnical structures, the seismic response is generally amplified significantly near the fault belts, which was generally ignored in actual projects, possibly inducing a severe geologic hazard risk on the engineering structures. The dynamic response characteristics and mechanism of the water pipeline crossing the fault zone are significant for the seismic fortification of the project. Consequently, the vibration table test was adopted to study a water pipeline's seismic response crossing the fault zone, with which the response characteristics of acceleration and stresses in the surrounding soil, dynamical strain on the pipe shell, seismic amplification coefficient and influence scope of fault belt, etc., were elucidated.

DESIGN OF THE VIBRATION TABLE TEST

Model Design, Monitoring Scheme, and Material Parameters

According to the project data, the pipeline is made of concrete, and the cross-section is generally circular with an outer diameter of 5.0 m and pipe wall thickness of 0.2 m. The depth of the pipeline in loess is mainly 1.0–2.0 m and can reach 7.0–8.0 m near some steep slope. An enormous depth at the intersection of the north Qinling fault is approximately 80.0 m, which is the geomorphic boundary of Qinling and pluvial fans. The involving eight faults of the project are all positive faults which dip angle are basically 70–80.

An appropriate model size is essential to obtain a reliable result for the vibration table test. Due to the limitations of the width, length, and power of the vibration table, it is challenging to implement physical model tests of a large size. Comprehensively analyzing the similarity ratio, embedment depth and capacity of the vibration table, the geometric similarity ratio was finally designed to be 1:20, with which the outer diameter of the model pipe is 25.0 cm and the water pipe depth was finally determined at 40.0 cm. The outer dimensions of the model box were considered to be 2.8 m × 1.1 m × 1.4 m.

The frame of the physical model box was welded using profile steel. The sides of the box are four pieces of Plexiglas, and the bottom is a sheet of steel plate. A steel hoop and eight vertical reinforcement bars were installed around the box to maintain the stiffness of the model box during the experiment. Four pieces of foam boards with a thickness of 8.0 cm were installed around the box's inner sides to reduce the boundary's influence on the dynamical response. The dip angle and width of the fault were designed at 80° and 20.0 cm for the experiment, respectively. A steeper dip angle was adopted considering the actual occurrence of involved faults, size limitation and boundary influences of the vibration table test. The dimensions, distribution of sensors, and details of the critical profiles of the vibration table experiment are presented in **Figure 3**.

A total of 21 accelerometers, 24 soil pressure cells, 24 strain gauges, 2 osmometers, 1 thermometer, and one moisture meter

TABLE 2 | Physical and mechanical properties of loess from the test.

Loess	Unit of mass (g/cm^3)	Bulk modulus (MPa)	Shear modulus (MPa)	Adhesion (kPa)	Inner friction angle (°)
	1.4	22.22	15	20	20
PVC pipeline	Unit of mass (g/cm^3)	Bulk modulus (MPa)	Poisson's ratio	tensile strength (MPa)	—
	1.6	3,000	0.31	53	—
Soil in the fault	Unit of mass (g/cm^3)	Bulk modulus (MPa)	Poisson's ratio	Adhesion (kPa)	Inner friction angle (°)
	1.2	30	20	12	25

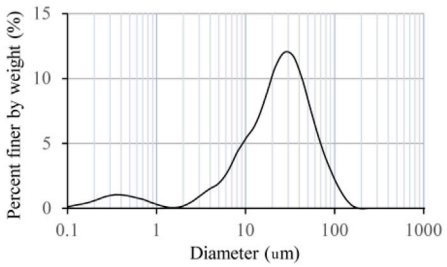

FIGURE 4 | Particle size distribution of the experimental loess.

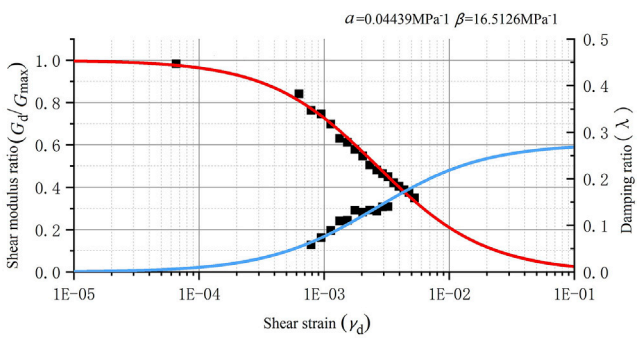

FIGURE 5 | Curves of the dynamic modulus of elasticity and damping ratio.

were installed in the model. The accelerometer is an EY version with a monitoring range of 0.0–2.0 g, a sensitivity coefficient of 451.92 mV/g, and a size of 16 × 15 × 8 mm^3. The soil pressure cell (model: BWM) has a monitoring range of 0.0–0.1 MPa, an accuracy of ±0.3 F.S, a diameter of 28 mm, and a thickness of 6.5 mm. The strain gauge (model: 120–5AA) shows a monitoring range of ±50,000 με, a sensitivity coefficient of 2.0 ± 1%, a length of 8.5 mm, and a width of 3.6 mm. The osmometer(model: BWMK) has a monitoring range, accuracy, diameter, and thickness of 0–100 kPa, ±0.01 kPa, 15.8 mm, and 21 mm, respectively. The model of moisture meter and thermometer are CS655 and Campbell 257, respectively. The monitoring direction is x for acceleration, x and z for soil pressure, and y and circumference for the strain gauge.

The water pipeline's surrounding soil is remolding loess, and the fault zone component is a mixture of sawdust and fine sand. The tube was full of water, and both ends were sealed with a lid. To avoid pipe rupture and water leakage under strong vibration, a Polyvinyl Chloride (abbreviation as PVC) plastic pipe with appropriate plasticity and flexibility is adopted for the experiment. The physical and mechanical parameters of loess, PVC pipe, and fault zone soil are shown in **Table 2**. The distribution of particle size and dynamical parameters are presented in **Figure 4** and **Figure 5**, respectively. The symbols α and β in **Figure 5** are the loess test parameters of Hardin model.

Loading Scheme

The amplitude, excellent frequency, and effective duration of the time history are the critical factors of seismic waves, significantly influencing the results of the dynamical response. For the comparative analysis, three time-histories were chosen as the excitation wave: the EI-Centro wave (EI), Tangyu wave (Ty), and artificial wave (Ar). The EI wave represents the seismic time history characteristics of a long-distance earthquake for the engineering site. The Ty wave, recorded at the Tangyu seismic station in the Wenchuan earthquake (data sources: National Earthquake Data Center of China), represents the influence of a major historical earthquake on the project. The Ar wave is an artificial seismic wave, which was calculated from the intersection site of the Qinling fault adopting the method of probability analysis of seismic risk, with an exceeding probability of 10% in 50 years. The Ar wave represents the characteristics of potential seismic waves and can be used for seismic fortification design and construction of the project. **Figure 6** shows the excitation loading seismic time histories and corresponding Fourier spectrum. **Table 3** presents the loading scheme in detail.

ACCELERATION DYNAMIC RESPONSE

Distribution Characteristics of Acceleration Response

Peak acceleration is one of the most critical parameters for seismic load and ground motions. According to the results of the vibration table test, the acceleration time histories were recorded at the monitoring points, with which the peak accelerations were obtained. Typical longitudinal and transverse profiles A and B were selected to depict the peak acceleration distribution contours adopting the least square method. Because of the similarity of contours under various loadings, only partial results are presented as a description in **Figure 7**.

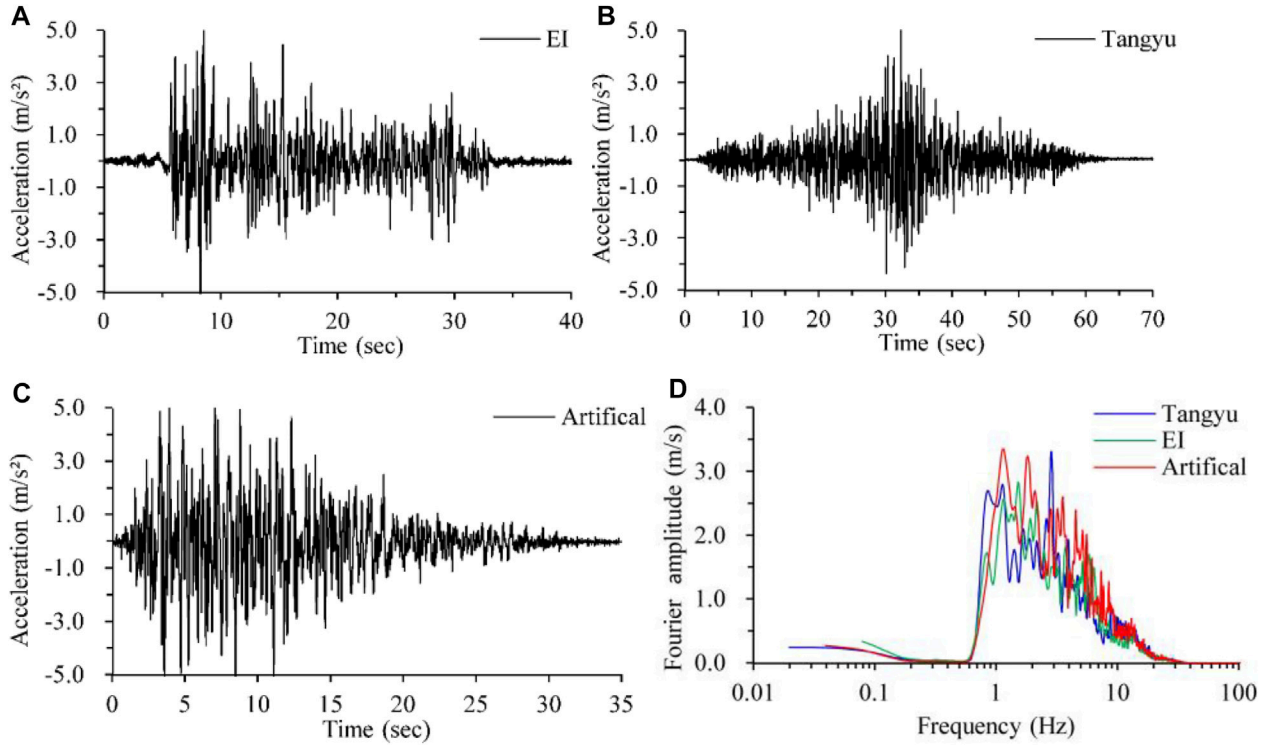

FIGURE 6 | Condition of the excitation waves. **(A)** Time history of El-Centro wave. **(B)** Time history of Tangyu waves from the Wenchuan earthquake (data sources: National Earthquake Data Center of China). **(C)** Time history of the artificial wave. **(D)** Fourier spectrum of the excitation wave.

The contours of profile A show that a more considerable peak acceleration generally appears in the hanging wall, especially near the fault zone. The peak acceleration increases gradually with increasing z value. The maximum value is generally distributed close to the upper edge of the pipe located near the fault zone. For a certain depth, the larger and smaller peak accelerations are generally distributed near the fault zone located in the hanging and footwall, respectively. The range of acceleration variation influenced by the fault is approximately 2b in the hanging wall, 1b in the footwall, and 4b in total, where b is the fault zone width. For profile B, a larger peak acceleration was recorded on both sides of the pipeline and is even approximatively equal to the maximum value obtained near the top surface, which might be induced by the significant difference in stiffness between the pipe and surrounding soil.

The central line of profile B was selected, involving four accelerometers numbered A1, A5, A10, and A14, of which the peak acceleration values under various levels of excitation were then obtained. **Figure 8A** presents the distribution of peak acceleration versus depth, and **Figure 8B** shows the variation in the amplification factor with depth. The responsive peak acceleration generally increases with increasing z value and peak excitation acceleration. The increase rate is more significant in the regions above the pipe relative to the lower part. A more apparent increase appears when the amplitude of excitation acceleration is more remarkable, which should relate to the influence of cracking and soil failure under shock. The amplification factor of the peak acceleration with depth can reach 1.2–1.6 when the location is close to the top surface of the model.

Based on the Fourier transformation, the Fourier spectra of recorded time histories for specific points were obtained. The amplification factor along with depth was denoted by the ratio of A1/A14, A5/A14, and A10/A14. The acceleration response spectrum and corresponding amplification factor along with depth were determined, as shown in **Figure 9**. The comparison of the Fourier spectrum shows that the amplification factors are significant in the frequency range of 3–225 Hz, but only the range of 3–8 Hz possesses an excellent Fourier spectrum amplitude. Consequently, the amplification of the Fourier spectrum amplitude with depth is mainly concentrated in the frequency range of 3–8 Hz. The amplification of the acceleration response spectrum is concentrated mainly in the period of 0.05–0.5 s, especially in the period of 0.05–0.26 s.

Consequently, the peak acceleration amplification is prominent in the range of the fault zone, hanging wall, and nearby the pipe. The fault influence range is approximately four times the fault width. The amplification factor of peak acceleration with depth can reach 1.2–1.6, mainly induced by seismic waves with a frequency range of 3–8 Hz. The amplification of the acceleration response spectrum concentrates primarily in 0.05–0.26 s.

TABLE 3 | Loading scheme of the vibration table experiment.

Loading no	Input wave	Peak acceleration (g)	Loading direction	Annotation
1	Sine wave	0.05	x	Sweep
2	El-Centro wave (El)	0.05	x	El-0.05 g
3	Tangyu wave (Ty)	0.05	x	Ty-0.05 g
4	Artificial wave (Ar)	0.05	x	Ar-0.05 g
5	El-Centro wave (El)	0.1	x	El-0.1 g
6	Tangyu wave (Ty)	0.1	x	Ty-0.1 g
7	Artificial wave (Ar)	0.1	x	Ar-0.1 g
8	El-Centro wave (El)	0.2	x	El-0.2 g
9	Tangyu wave (Ty)	0.2	x	Ty-0.2 g
10	Artificial wave (Ar)	0.2	x	Ar-0.2 g
11	Sine wave	0.1	x	Sweep
12	El-Centro wave (El)	0.3	x	El-0.3 g
13	Tangyu wave (Ty)	0.3	x	Ty-0.3 g
14	Artificial wave (Ar)	0.3	x	Ar-0.3 g
15	Sine wave	0.1	x	Sweep
16	El-Centro wave (El)	0.4	x	El-0.4 g
17	Tangyu wave (Ty)	0.4	x	Ty-0.4 g
18	Artificial wave (Ar)	0.4	x	Ar-0.4 g
19	Sine wave	0.1	x	Sweep
20	El-Centro wave (El)	0.5	x	El-0.5 g
21	Tangyu wave (Ty)	0.5	x	Ty-0.5 g
22	Artificial wave (Ar)	0.5	x	Ar-0.5 g
23	Sine wave	0.1	x	Sweep
24	Artificial wave (Ar)	0.6	x	Ar-0.6 g
25	Sine wave	0.1	x	Sweep
26	Artificial wave (Ar)	0.7	x	Ar-0.7 g
27	Sine wave	0.1	x	Sweep
28	Artificial wave (Ar)	0.8	x	Ar-0.8 g
29	Sine wave	0.1	x	Sweep
30	Artificial wave (Ar)	0.9	x	Ar-0.9 g
31	Sine wave	0.1	x	Sweep
32	Artificial wave (Ar)	1.0	x	Ar-1.0 g
33	Sine wave	0.1	x	Sweep
34	Artificial wave (Ar)	1.1	x	Ar-1.1 g
35	Sine wave	0.1	x	Sweep
36	Artificial wave (Ar)	1.2	x	Ar-1.2 g

Influence of Fault on Acceleration Response

For quantifying the effect of faults on peak acceleration distributions, the amplification ratio was defined and calculated. Based on the contours, the maximal, minimal, and general values of peak accelerations at a depth of z = 0.65 m were extracted, with which the amplification ratios of maximum to minimum and the hanging wall mean to footwall mean were calculated, respectively. The result is presented in **Figure 10**. The ratio of maximum to minimum decreases gradually with increasing excitation acceleration. The maximum ratio tends to 1.8 when the input peak acceleration approaches zero, the minimum ratio tends to 1.35 when the excitation reaches 1.2, and the amplification ratio approximates 1.5 when the excitation adopts an exceeding probability of 10% in 50 years of the engineering site. The ratio of the hanging wall to the footwall increases gradually with increasing excitation peak acceleration, and the increase rate is maintained at a relatively small level of approximately 1.2.

The fault zone affects not only the responsive peak acceleration but also the frequency of the time history. The acceleration Fourier spectra and response spectra recorded at specific points are presented in **Figure 11** and **Figure 12**, respectively. According to the Fourier spectra, the excellent frequencies are mainly in the range of 1–10 Hz. The Fourier amplitude ratios of A5, A6, A7, and A8 to A9 were calculated and are presented in **Figure 11C**. The amplification ratios are

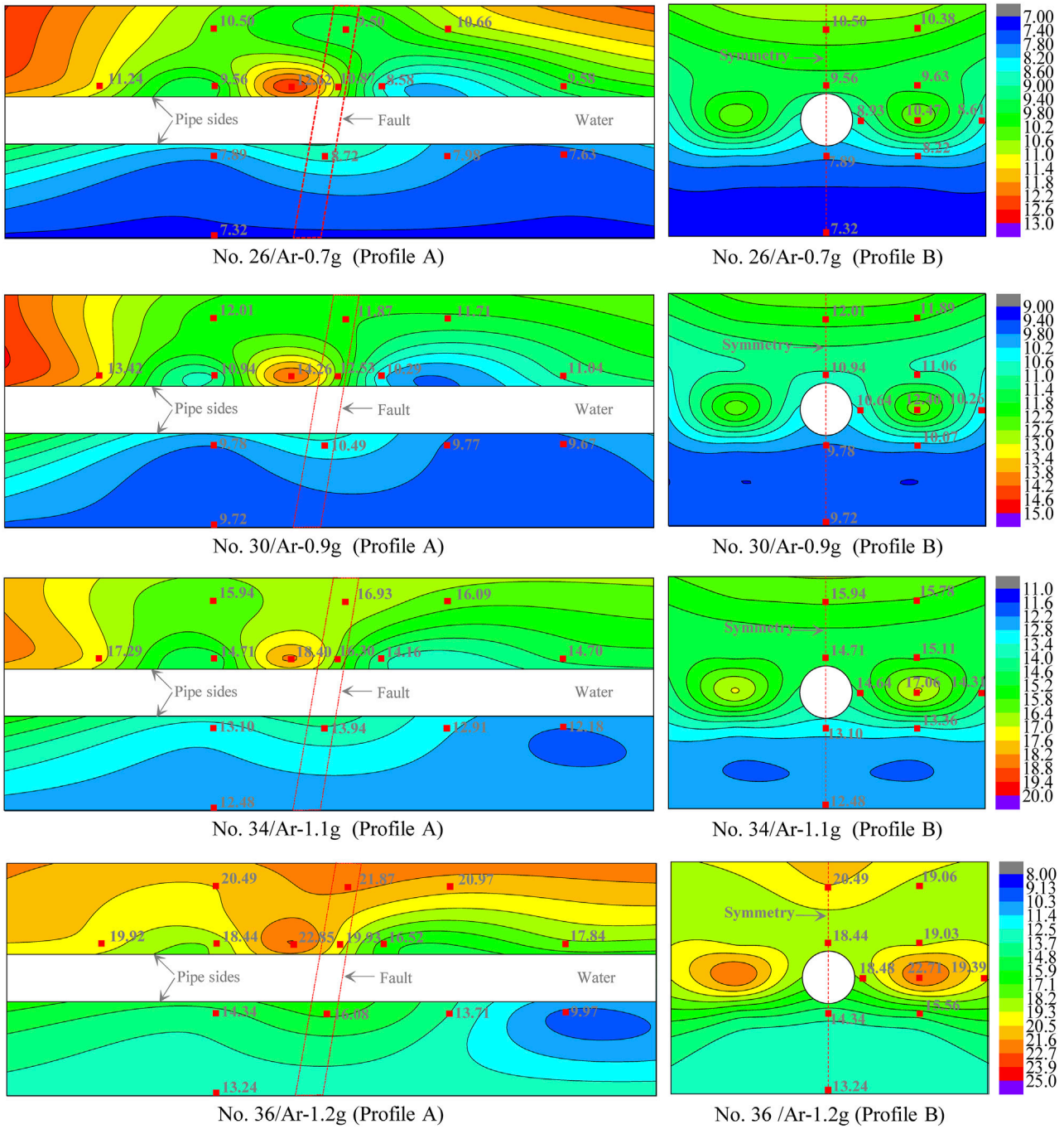

FIGURE 7 | Distribution characteristics of the peak acceleration response on profiles A and B (unit: m/s^2).

approximately constant for a certain monitoring point when the frequency falls into the frequency range of 1–6 Hz, fluctuate slightly when the frequency is equal to 6–10 Hz and fluctuate significantly when the frequency is greater than 10 Hz. In the excellent frequency range of 1–10 Hz, the amplification ratio of the Fourier spectrum is approximately 1.3 at point A6 and 1.1–1.2 at points A5, A7, and A8. In addition, the changes in excitation peak acceleration have a small impact on the amplification ratios of the Fourier spectrum, which is presented in **Figure 11C, D**. The acceleration response spectra are calculated adopting the damping ratio of h = 5% and time histories of specific points, which are shown in **Figure 12A**. The diversity is remarkable in the period of 0.05–2.0 s, especially in the period of 0.1–1.0 s. The response spectrum ratios of A5, A6, A7, and A8 to A9 are

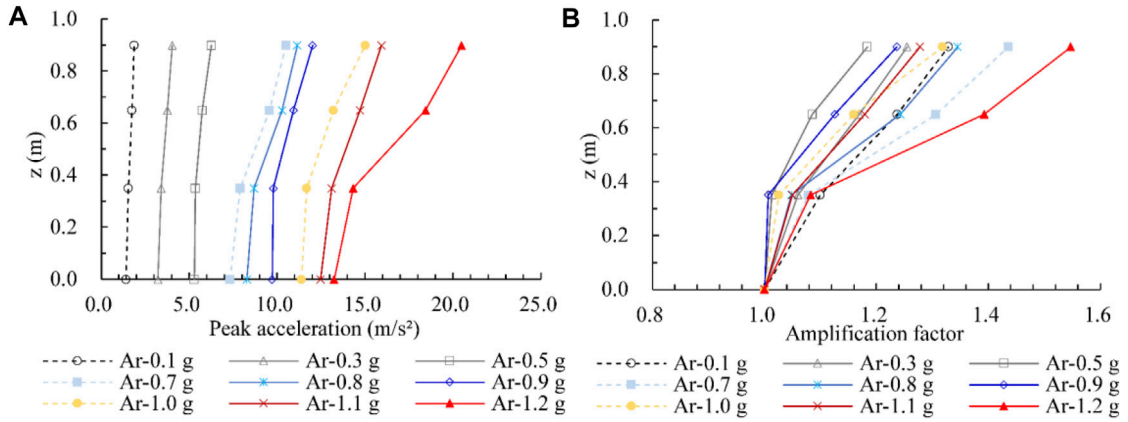

FIGURE 8 | Peak acceleration response curves for various depth. **(A)** Peak acceleration versus depth, **(B)** acceleration amplification factor versus depth.

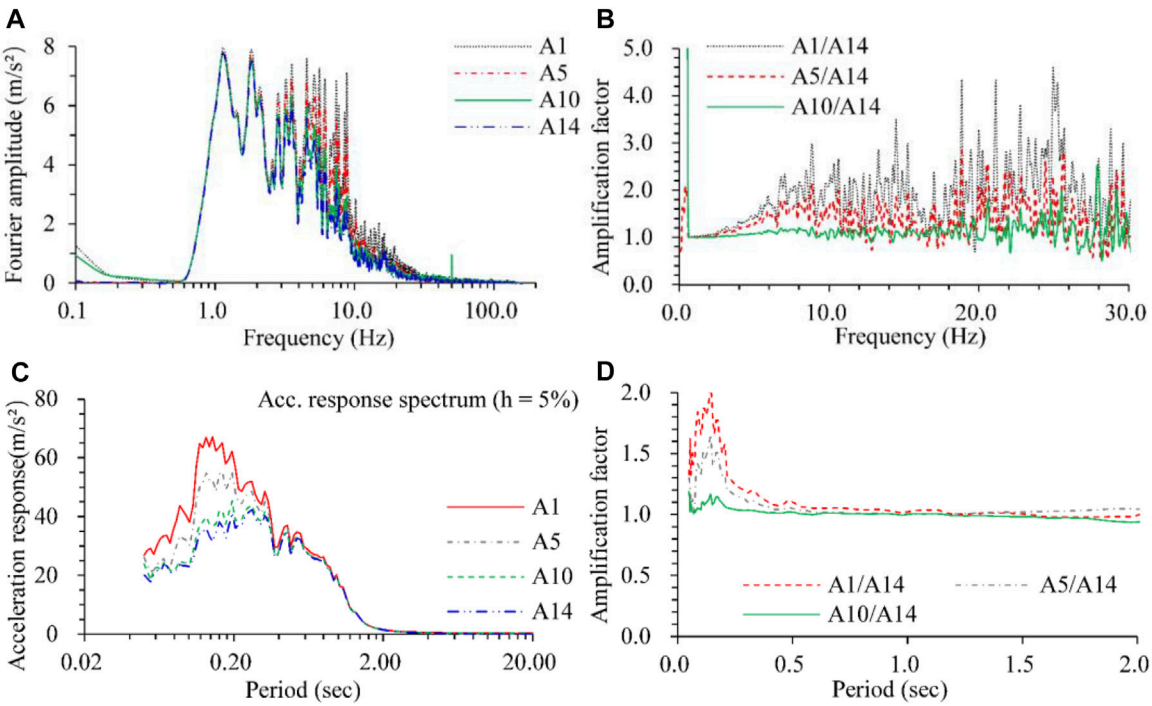

FIGURE 9 | Fourier spectrum and response spectrum at No.36–1.2 g. **(A)** Fourier spectrum of specific points, **(B)** amplification factor of Fourier spectrum, **(C)** acceleration response spectrum of specific points, **(D)** amplification factor of acceleration response spectrum.

calculated and presented in **Figure 12B**. The ratios are approximately constant in the period of 0.1–2.0 s and attenuate rapidly when the period is greater than 2.0 s. The amplification ratio reaches 1.25–1.30 for the A6 point in the platform part.

Consequently, the acceleration amplification ratio in the fault zone generally exceeds 1.35, even up to 1.8, and the hanging wall amplification ratio is approximately 1.2. The magnification ratio of faults on the Fourier spectrum and response spectrum can reach 1.3, mainly in the range of excellent frequency and period.

Influence of Excitation Waves on Acceleration Response

The spectrum characteristics and effective durations of excitation waves will significantly influence the dynamic response. The responsive peak acceleration contours for different excitation waves with the same amplitude are presented in **Figure 13**. **Figure 14** shows the comparison of responsive peak acceleration versus depth. Although the specific data of responsive peak acceleration vary for different excitations, the distribution characteristics and variation laws are always the

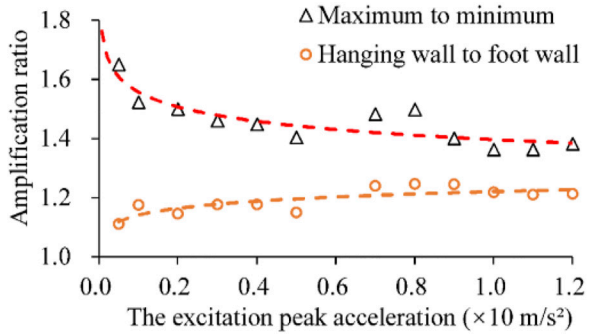

FIGURE 10 | Influence of faults on the responsive peak acceleration distribution.

same. The acceleration responses triggered by the EI wave are generally better than those triggered by the Ar and Ty waves. The acceleration amplification ratio on depth is defined as the ratio of peak acceleration at a certain depth to that of the model's bottom, which varies with the change of excitation waves and amplitude.

The Fourier spectrum of the time histories recorded at A1 is highly similar to that of the corresponding excitation wave, as shown in **Figure 15A** and **Figure 6D**. The Fourier spectrum ratio of A1 to A14 was calculated and is presented in **Figure 15B**, which shows slight amplification when the frequency is in the 15–35 Hz range, significant amplification when the frequency is equal to 50 Hz, and almost identical amplification when the frequency is in the range of excellence. The corresponding response spectrum was calculated adopting a damping ratio of 5%, with which the amplification ratio of A1/A14 was obtained, as shown in **Figure 15C, D**. A great disparity is shown for the response spectrum when the period is in the 0.05–2.0 s range. The amplification ratio of the response spectrum varies considerably when the period is in the 0.05–0.2 s range.

DYNAMIC RESPONSE CHARACTERISTICS OF THE SOIL STRESS

Dynamic pressures or stresses in the soil are critical parameters that significantly affect the site deformation and stability under earthquake. The value, distribution, and variation of dynamic soil stresses are generally influenced by the peak acceleration of excitation, stratum lithology, soil density, burial depth, and features of the embedded structures, etc. The monitoring of dynamic soil stresses is critical for the evaluation, prevention, and mitigation of seismic disasters for foundation engineering. Soil pressure cells with various locations and orientations were designed and embedded in the vibration table test. The distribution of soil pressure cells is presented in **Figure 3**. The time history curves of dynamical soil stresses for typical points are shown in **Figure 16**. The peak soil stresses versus excitation accelerations are presented in **Figure 17**.

According to the recorded results, the stresses in soil respond to the excitation sensitively, nonlinearly, and nonuniformly in

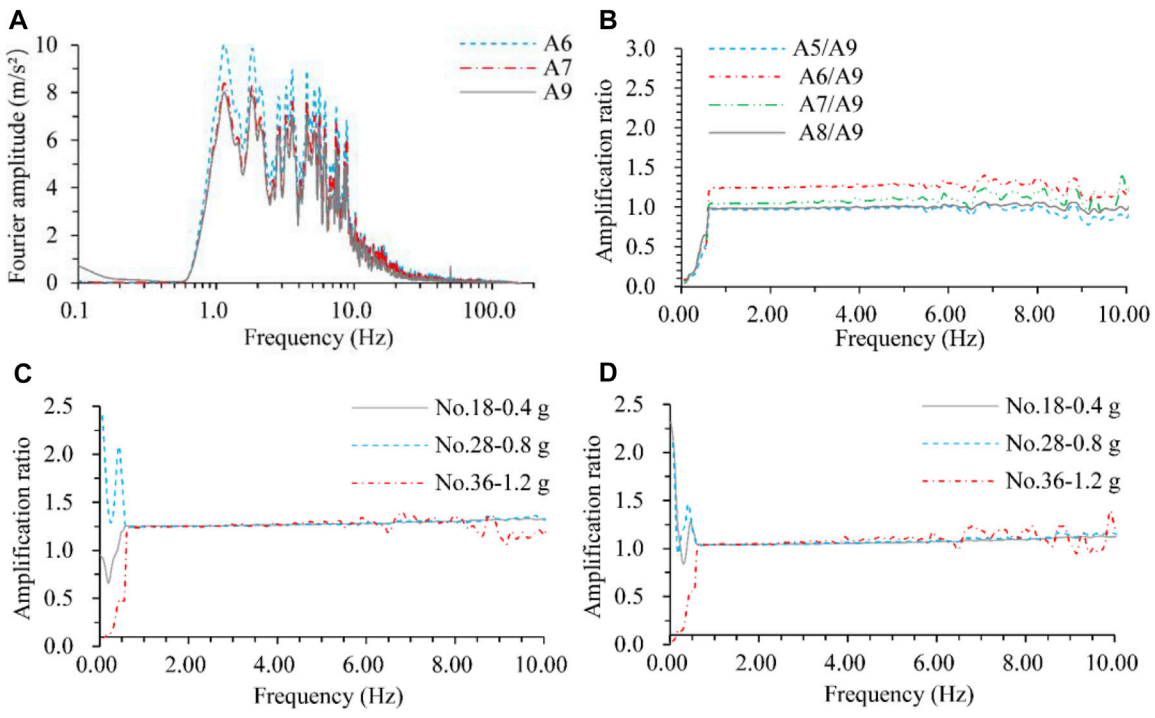

FIGURE 11 | Fourier spectrum and fault amplification ratio. **(A)** Fourier spectrum of specific points at loading No.36–1.2 g, **(B)** Amplification ratio of Fourier spectrum at loading No.36–1.2 g, **(C)** Amplification ratio of Fourier spectrum at point A6, **(D)** Amplification ratio of Fourier spectrum at point A7.

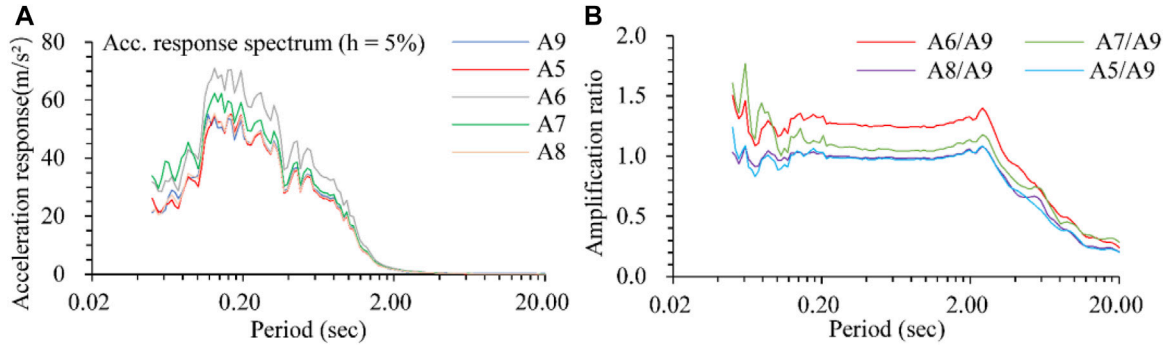

FIGURE 12 | Acceleration response spectrum and amplification ratio of fault at loading No. 36–1.2 g. **(A)** Acceleration response spectrum for specific points, **(B)** Amplification ratio of acceleration response spectra.

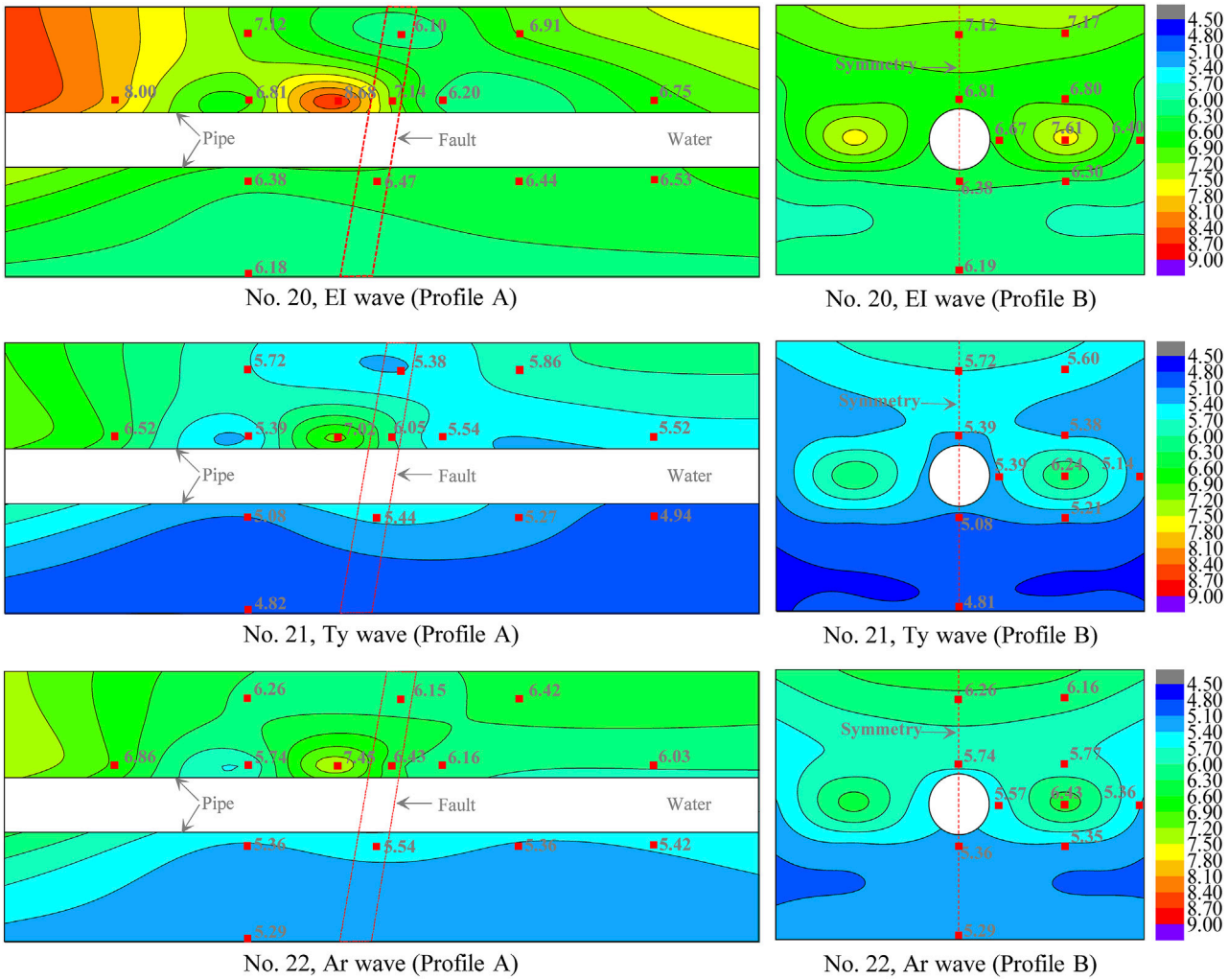

FIGURE 13 | Responsive peak acceleration contours for different excitation waves (unit: m/s^2).

both directions x and z. During a specific loading, the amplitude of responsive stress increases remarkably when the peak of excitation acceleration arrives. The envelope lines of the responsive stress time-history curves approximatively synchronize with that of the excitation acceleration for most monitoring points. The responsive stress amplitude generally

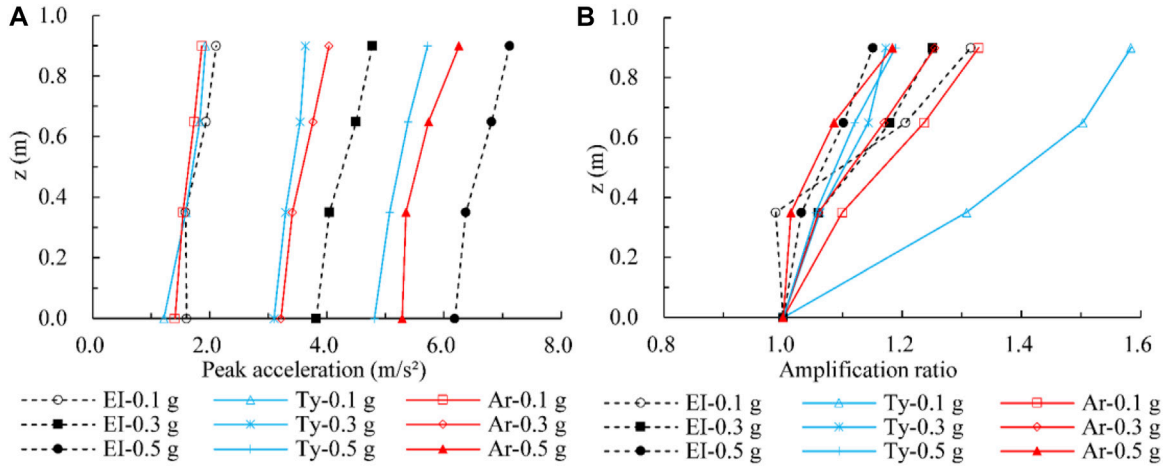

FIGURE 14 | Comparison of peak acceleration response for different excitation waves, **(A)** peak acceleration versus depth, and **(B)** acceleration amplification ratio versus depth.

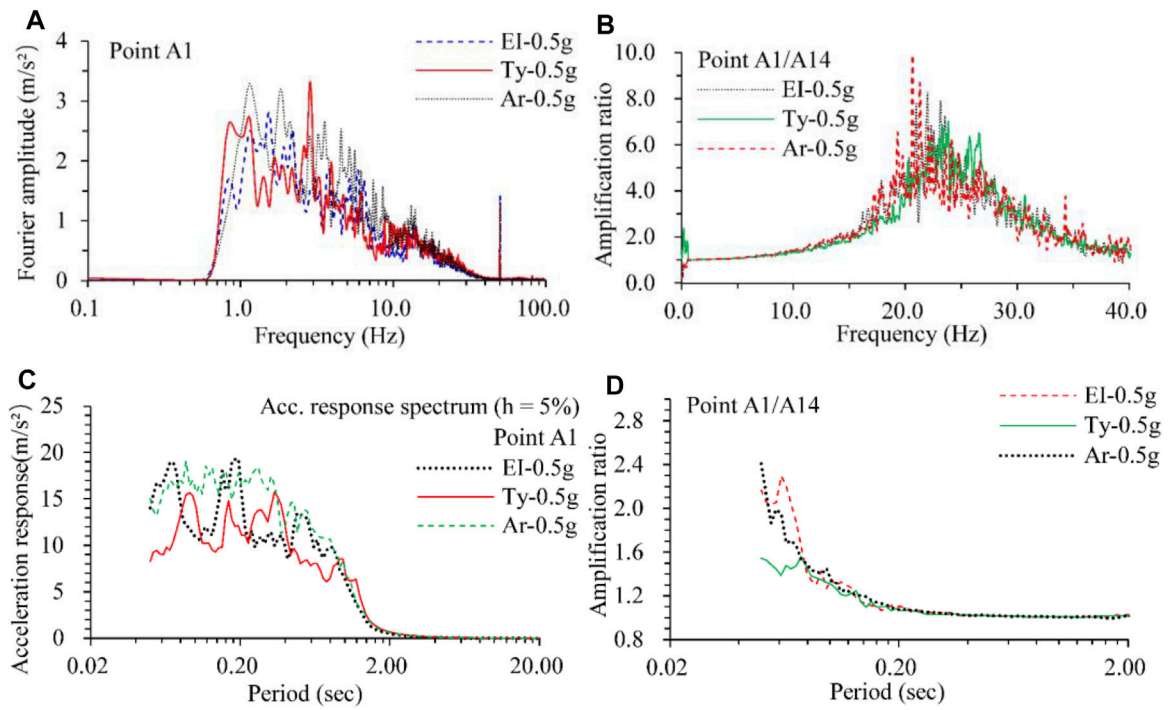

FIGURE 15 | Comparison of Fourier spectrum and response spectrum, **(A)** Fourier spectrum of time history recorded at point A1, **(B)** the Fourier spectrum ratio of A1 to A14, **(C)** response spectrum of the time history recorded at A1, **(D)** the response spectrum ratio of A1 to A14.

increases with increasing excitation, and the increase rate is more significant when the input peak acceleration is greater, especially for the regions near the pipeline and close to the model bottom. Regardless, the distribution of responsive dynamic stress in the surrounding soil is complicated and mainly affected by the excitation acceleration and specific structural characteristics in the model. Due to the influence of nonuniform deformations, the structure and soil contact zone will raise considerable dynamic stresses.

DYNAMIC STRAIN RESPONSE OF THE PIPE

The pipeline strain response under earthquake could reflect the dynamic micro-deformation characteristics, potential damage location, range, model of the pipeline, etc., to a great extent. Dynamic strain monitoring could provide important information and data conducive to the stress analysis and seismic-resistant design of pipeline axial and crossing sections.

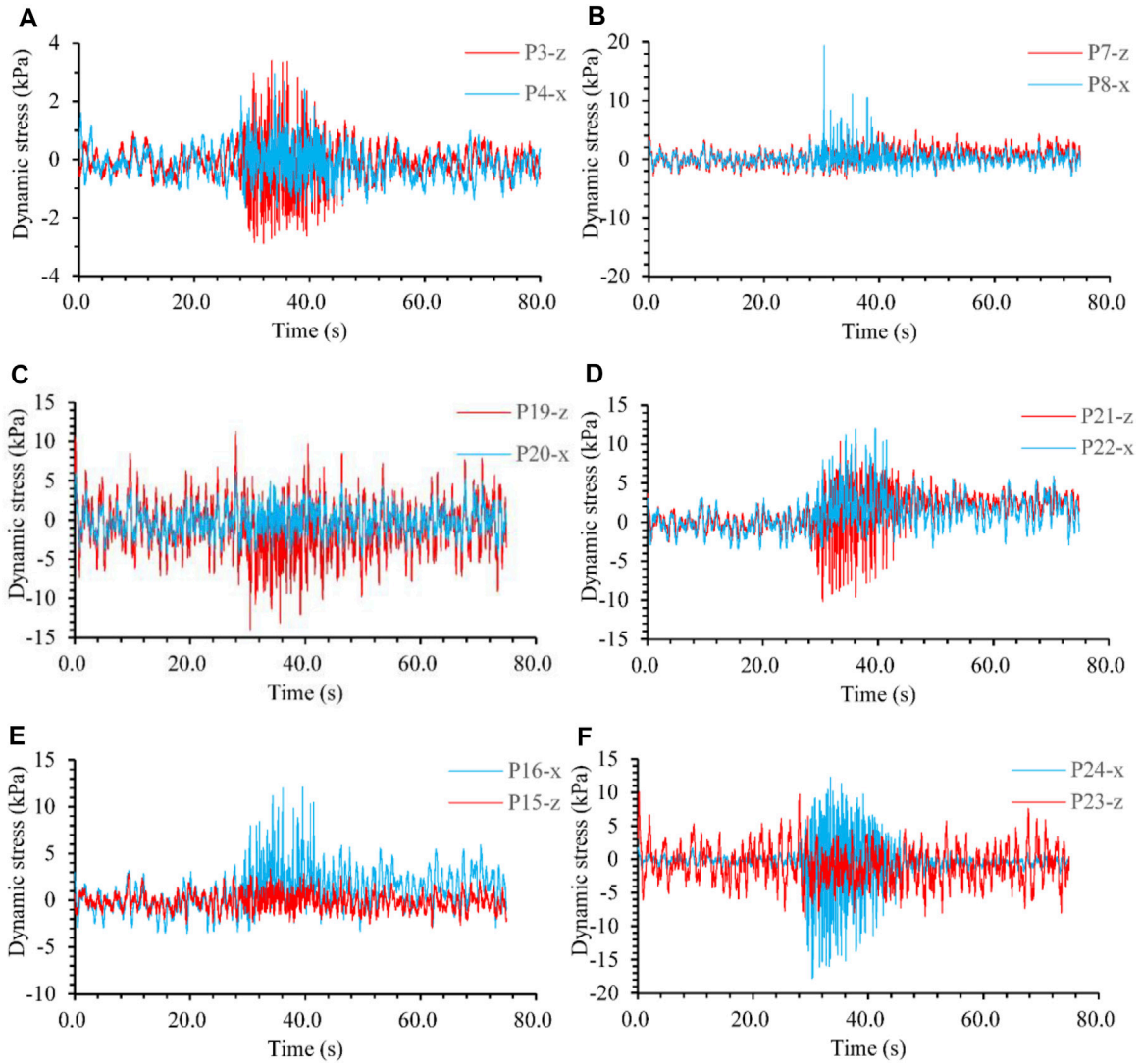

FIGURE 16 | Time history curves of dynamic stress in soil (loading No. 34, 1.1 g of the excitation peak acceleration). **(A)** stress at P3 and P4, **(B)** stress at P7 and P8, **(C)** stress at P19 and P20, **(D)** stress at P21 and P22, **(E)** stress at P15 and P16, and **(F)** stress at P23 and P24.

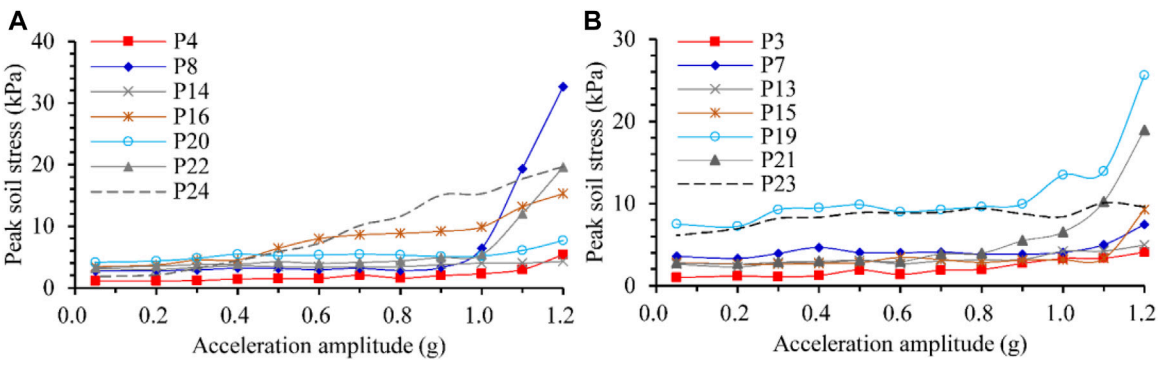

FIGURE 17 | The peak stresses in soil versus the excitation acceleration. **(A)** Stresses in the *x* direction and **(B)** stresses in the *z* direction.

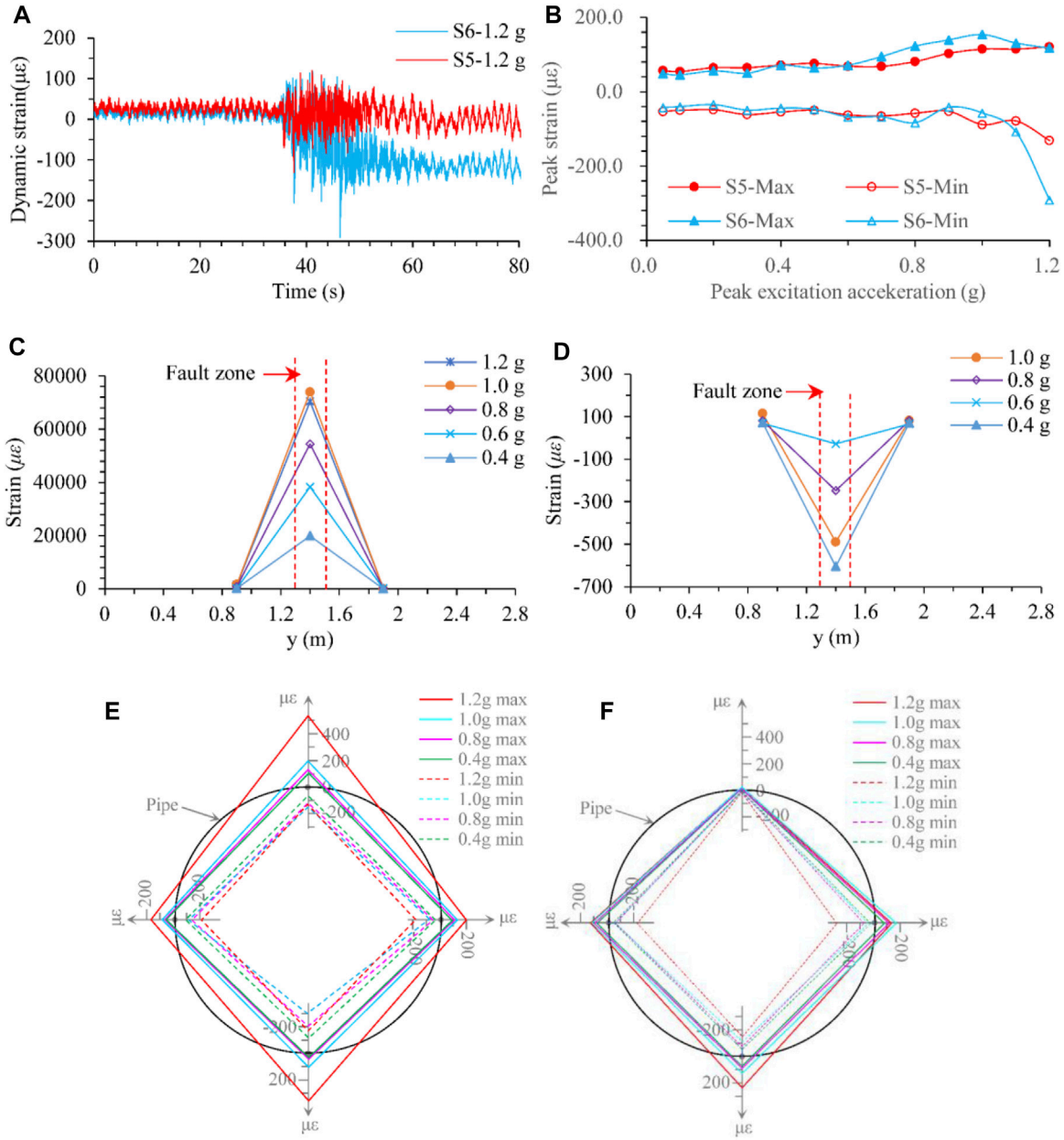

FIGURE 18 | Responsive dynamic strain of the pipe. **(A)** Strain time-history curves of typical monitoring points, **(B)** peak of responsive strain versus excitation acceleration, **(C)** peak axial strain variation along the pipe bottom, **(D)** peak axial strain variation along the pipe side, **(E)** peak circumferential strain along the cross-section of y = 1.4 m, **(F)** peak circumferential strain along the cross-section of y = 0.9 m.

In this experiment, a total of 24 strain gauges were affixed in three cross-sections of the pipeline with horizontal ordinates of y = 0.9 m, 1.4 m, and 1.9 m. The strain gauges numbered S1-S8 are for **Section I** (y = 0.9 m), among which S1 and S2 lie at the pipeline top, S7 and S8 are located at the pipeline bottom, and S3-S6 are on both sides of the pipeline. All the strain gauges appear in pairs, where the odd numbers are for axial (y) direction, and even numbers are for circumferential direction. S9-S16 and S17-S24 belong to **sections II** (y = 1.4 m) and III (y = 1.9 m), respectively, and the numbering sequence and rules are consistent with those of **Section I**. The distribution of strain gauges is shown in **Figure 3**.

Although the specific data and strain time-history curves generally vary from points to points and are greatly dependent on the monitoring locations, loading conditions, etc., the overall characteristics are always the same. Consequently, only typical monitoring results are selected as an illustration. **Figure 18A** presents the responsive dynamic strain time-history curves of S5 and S6 with an excitation peak acceleration of 1.2 g. Although the seismic load acting on the bottom of the model is just in the

TABLE 4 | Crack characteristics of the model top surface.

No	Peak of excitation acceleration (g)	Crack distribution on the top surface	Crack development characteristics
1	0.5	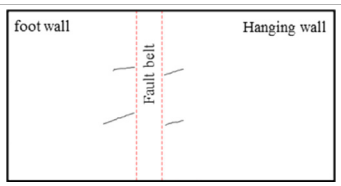	Small cracks first appear from both sides of the fault with a length of about 5–8 cm and approximately along the *y*-direction
2	0.6	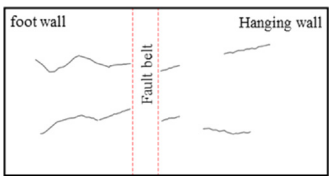	The cracks extend gradually, accompanied by the appearance of new intermittent cracks in the extension direction. The crack length reaches 12–28 cm
3	0.7	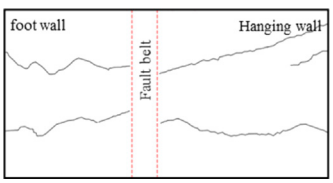	The cracks develop reaching y-boundary of the model and a new small crack appears near the right border line. The crack is always closed
4	0.8	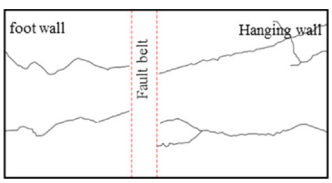	The *x*-direction cracks begin to appear near the boundary, and many small branches arise from the main cracks
5	0.9	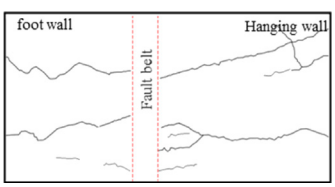	Surface seismic subsidence of about 0.5 cm occurs. The cracks extend mainly along y accompanying many branches in *x* direction
6	1.0	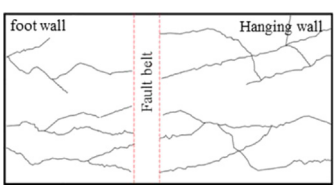	The model surface is full of cracks and the crack width increases quickly. The seismic subsidence reaches 0.8 cm
7	1.1	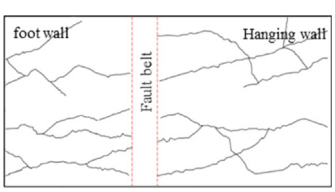	The model surface is damaged completely, and the crack width deepens but no appearance of a new crack. The cracks are generally y-oriented. The seismic subsidence reaches 1.5 cm

x-direction, the dynamic strain of the pipeline responds obviously in both the axial (*y*-direction) and circumferential directions. During a specific level of loading, the strain response increases greatly when t = 35–60 s. The mean lines of the strain time-history curves tend to a small negative value for S5 and an apparent negative value for S6, which indicates that this point is in a compressive state, with a bending deformation tendency along the axial and circumference directions. The peak

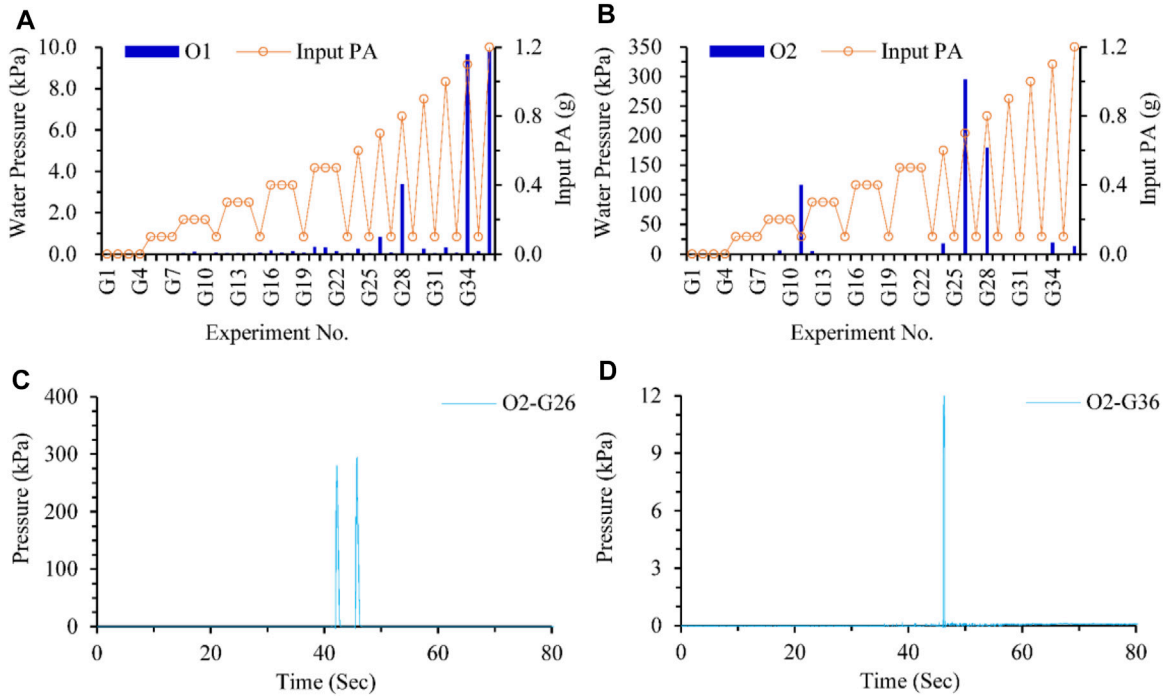

FIGURE 19 | Dynamic water pressure response inside the pipeline. **(A)** Water pressure response of O1 under various loadings. **(B)** Water pressure response of O2 under various loadings. **(C)** Water pressure response of O2 under G26. **(D)** Water pressure response of O2 under G36.

acceleration of excitation versus the maximum (positive value represents the tensile state) and minimum (negative value refers to the compressive state) responsive strain of typical points is shown in **Figure 18B**. The peak strain generally increases gradually with increasing excitation. The variation rate increases quickly for S6 when the acceleration is more significant than 1.0 g, which indicates that a large bending deformation is produced along the circumference. **Figure 18C, D** show the variation in strain along the axial direction of the pipe bottom and a pipe side, respectively. The maximum strain generally appears in the fault zone, and the peak value significantly decreases from the midpoint to both ends of the pipeline. According to the distribution characteristics of axial strain, bending deformation occurs along the pipeline in both the vertical and horizontal directions. **Figure 18E, F** show the variation of circumferential strain along the cross-section of y = 1.4 m and y = 0.9 m. The pipeline mainly undergoes expansion and shrinkage deformation in the radial direction. In the cross-section of y = 1.4 m, the pipeline shows an approximate symmetrical deformation. The maximum tensile and compressive strain occurs at the top and bottom of the pipeline, respectively. In the cross-section of y = 0.9 m, the deformation is asymmetric with a more significant value at the pipe bottom.

Consequently, under the action of an earthquake, the water-filled pipeline crossing a fault zone primarily undergoes bending deformation along the axial direction, accompanied by expansion and shrinkage in the radial direction. The maximum tensile and compressive strain occur at the central section of the pipe in the fault zone.

CRACK CHARACTERISTICS OF THE SOIL

Understanding the failure process and mechanism of the engineering site under excitation is one of the most significant and applicable results from the vibration table test. It was possible to discern the vulnerable regions by analyzing the crack characteristics, and the methods of mitigation damage for the engineering could be obtained.

The crack characteristics of the model top surface are presented in **Table 4**. Small cracks first appeared from both sides of the fault when the excitation peak acceleration reached 0.5 g. The quantity, length, width, and depth of the cracks increased gradually with increasing excitation acceleration amplitude. The cracks originated from both sides of the fault asymmetrically, which should relate to the distribution characteristics of responsive acceleration and fault amplification. Meanwhile, the cracks all develop along the *y*-direction, which may be affected by the model's inconsistent stiffness between the rigid boundary, structure, and soil. Slight seismic collapses occur in the unsaturated loess site when the excitation peak acceleration is excellent, reaching 1.0 g.

DISCUSSION

Strata in the fault zone sites related to this project vary and generally involve interbedded layers of loess and paleosol. However, the consideration of strata variation would cause an

obvious complexity in the test design because a large number of sensors have to be arranged near the discontinuous interface to monitor the dynamic response. Too many sensors and wires would be embedded, which would influence the model structural uniformity and increase the costs significantly. More importantly, this study mainly focuses on the dynamic response characteristics of the water pipeline crossing a fault, and ignoring strata variation might result in a more apparent influence law for the fault. Consequently, the stratum was designed as uniform loess in the vibration table test.

We also monitored the dynamic response of the water pressure inside the pipeline. The distribution histograms and curves are presented in **Figure 19**. The dynamic response of water pressure is generally close to zero with a few occasional impulses. The impulse amplitude reaches 10 kPa for sensor O1 and 300 kPa for O2. The dynamic water pressure of O2 is significantly greater than that of O1. Although the shear waves cannot propagate in the water inside the pipe, tremendous dynamic water pressure still occurred due to the influence of the impulses.

CONCLUSION

A large-scale vibration table test was adopted to investigate the seismic response of the water transmission pipeline crossing the fault. The responses of accelerations, dynamic stresses, strains, and water pressures for the pipeline and surrounding loess were obtained. The results are presented as follows.

1) The dynamic response is significantly amplified in the fault zone and hanging wall. The fault influence range is approximately four times the fault width. The maximum acceleration amplification ratio in the fault zone generally exceeds 1.35, reaches up to 1.8, and approximates 1.5 when excitation is adopted with an exceeding probability of 10% in 50 years. The ratio of the hanging wall to the footwall is maintained at a relatively slightly small level of approximately 1.2. The spectrum characteristics and effective durations of excitation waves also significantly influence the dynamic response.
2) The distribution of responsive dynamic stresses in the surrounding soil is complicated and mainly affected by the excitation acceleration properties and specific structural characteristics in the model. Due to the influence of nonuniform deformations, the structure and soil contact zone will raise considerable dynamic stresses.
3) The pipeline mainly undergoes bending deformation along the axial direction, accompanied by expansion and shrinkage in the radial direction. The maximum tensile and compressive strain occur at the central section of the pipe in the fault zone. Massive cracks developed along the *y*-direction, accompanied by slight seismic subsidence.

The research findings could provide reasonable parameters for the seismic design and construction of the project.

DATA AVAILABILITY STATEMENT

The original contributions presented in the study are included in the article/Supplementary Material, further inquiries can be directed to the corresponding authors.

AUTHOR CONTRIBUTIONS

WF proposed and participated in designing the study; YD participated in implement the test; SR participated in implement the test; PL participated in dealing with the data; All authors approved the final version of the manuscript.

FUNDING

This study was sponsored by the National Natural Science Foundation of China (grant numbers 41877245 and 41630634), Open Foundation of China Railway First Survey and Design Institute Group Co., Ltd (SPS-D-04), and Natural Science Foundation of Shaanxi Province (grant numbers 2021JQ-243).

REFERENCES

Abdoun, T. H., Ha, D., O'Rourke, M. J., Symans, M. D., O'Rourke, T. D., Palmer, M. C., et al. (2009). Factors Influencing the Behavior of Buried Pipelines Subjected to Earthquake Faulting. *Soil Dyn. Earthquake Eng.* 29, 415–427. doi:10.1016/j.soildyn.2008.04.006

Bao, Z., Yuan, Y., and Yu, H. (2017). Multi-scale Physical Model of Shield Tunnels Applied in Shaking Table Test. *Soil Dyn. Earthquake Eng.* 100, 465–479. doi:10.1016/j.soildyn.2017.06.021

Chen, J., Jiang, L., Li, J., and Shi, X. (2012). Numerical Simulation of Shaking Table Test on Utility Tunnel under Non-uniform Earthquake Excitation. *Tunnelling Underground Space Technol.* 30, 205–216. doi:10.1016/j.tust.2012.02.023

Chiou, Y.-J., Chi, S.-Y., and Chang, H.-Y. (1994). A Study on Buried Pipeline Response to Fault Movement. *J. Press. Vessel Technol* 116, 36–41. doi:10.1115/1.2929556

Corigliano, M., Scandella, L., Lai, C. G., and Paolucci, R. (2011). Seismic Analysis of Deep Tunnels in Near Fault Conditions: a Case Study in Southern Italy. *Bull. Earthquake Eng.* 9, 975–995. doi:10.1007/s10518-011-9249-3

Demirci, H. E., Bhattacharya, S., Karamitros, D., and Alexander, N. (2018). Experimental and Numerical Modelling of Buried Pipelines Crossing Reverse Faults. *Soil Dyn. Earthquake Eng.* 114, 198–214. doi:10.1016/j.soildyn.2018.06.013

Deng, L. S. (2017). *Earthquake Safety Evaluation Report of the Hanjiang-To-Weihe River Diversion Project (Phase II).* Xi'an, China: Chang'An university.

Dezhkam, B., and Nouri, A. Z. (2018). Dynamic Response of Nanoparticle-Water Pipes Buried in the Soil Subjected to Far-Fault Earthquake Using Numerical Method. *Soil Dyn. Earthquake Eng.* 113, 174–179. doi:10.1016/j.soildyn.2018.06.002

Dhakal, Y. P. (2021). Strong-motions from Damaging Moderate Magnitude (5.9 ≥ Mw) Earthquakes in Japan Recorded by K-NET and KiK-Net. *Front. Earth Sci.* 9, 618400. doi:10.3389/feart.2021.618400

Duan, M.-l., Mao, D.-f., Yue, Z.-y., Estefen, S., and Li, Z.-g. (2011). A Seismic Design Method for Subsea Pipelines against Earthquake Fault Movement. *China Ocean Eng.* 25, 179–188. doi:10.1007/s13344-011-0016-7

Fadaee, M., Farzaneganpour, F., and Anastasopoulos, I. (2020). Response of Buried Pipeline Subjected to Reverse Faulting. *Soil Dyn. Earthquake Eng.* 132, 106090. doi:10.1016/j.soildyn.2020.106090

Fard, S. S., Nekooei, M., Oskouei, A. V., and Aziminejad, A. (2019). Experimental and Numerical Modeling of Horizontally-Bent Buried Pipelines Crossing Fault Slip. *Lat. Am. J. Solids Struct.* 16, e175. doi:10.1590/1679-78255463

Gantes, C. J., and Melissianos, V. E. (2016). Evaluation of Seismic protection Methods for Buried Fuel Pipelines Subjected to Fault Rupture. *Front. Built Environ.* 2, 34. doi:10.3389/fbuil.2016.00034

Hall, W. J., Nyman, D. J., Johnson, E. R., and Norton, J. D. (2003). "Performance of the Trans-Alaska Pipeline in the November 3, 2002 Denali Fault Earthquake," in *Advancing Mitigation Technologies and Disaster Response for Lifeline Systems*, 522–534. doi:10.1061/40687(2003)54

Hashash, Y. M. A., Hook, J. J., Schmidt, B., I-Chiang Yao, J., and Yao, C. (2001). Seismic Design and Analysis of Underground Structures. *Tunnelling underground Space Technol.* 16, 247–293. doi:10.1016/s0886-7798(01)00051-7

Honegger, D. G., Nyman, D. J., Johnson, E. R., Cluff, L. S., and Sorensen, S. P. (2004). Trans-Alaska Pipeline System Performance in the 2002 Denali Fault, Alaska, Earthquake. *Earthquake spectra* 20, 707–738. doi:10.1193/1.1779239

Joshi, S., Prashant, A., Deb, A., and Jain, S. K. (2011). Analysis of Buried Pipelines Subjected to Reverse Fault Motion. *Soil Dyn. Earthquake Eng.* 31, 930–940. doi:10.1016/j.soildyn.2011.02.003

Karamitros, D. K., Bouckovalas, G. D., Kouretzis, G. P., and Gkesouli, V. (2011). An Analytical Method for Strength Verification of Buried Steel Pipelines at normal Fault Crossings. *Soil Dyn. Earthquake Eng.* 31, 1452–1464. doi:10.1016/j.soildyn.2011.05.012

Kennedy, R. P., Short, S. A., and Darrow, A. C. (1979). Seismic Design of Oil Pipeline Systems. *J. Tech. Counc. ASCE* 105, 119–134. doi:10.1061/jtcad9.0000022

Kiani, M., Akhlaghi, T., and Ghalandarzadeh, A. (2016). Experimental Modeling of Segmental Shallow Tunnels in Alluvial Affected by normal Faults. *Tunnelling Underground Space Technol.* 51, 108–119. doi:10.1016/j.tust.2015.10.005

Liang, J., and Sun, S. (2000). Site Effects on Seismic Behavior of Pipelines: a Review. *J. Press. Vessel Technol* 122, 469–475. doi:10.1115/1.1285974

Newmark, N. M., and Hall, W. J. (1975). "Pipeline Design to Resist Large Fault Displacement," in Proceedings of US national conference on earthquake engineering, 416–425.

Peng, D., Yueren, X., Qinjian, T., and Wenqiao, L. (2021). Using Google Earth Images to Extract Dense Landslides Induced by Historical Earthquakes at the Southwest of Ordos, China. *Front. Earth Sci.* 8, 633342. doi:10.3389/feart.2020.633342

Sarvanis, G. C., Karamanos, S. A., Vazouras, P., Mecozzi, E., Lucci, A., and Dakoulas, P. (2018). Permanent Earthquake-Induced Actions in Buried Pipelines: Numerical Modeling and Experimental Verification. *Earthquake Engng Struct. Dyn.* 47, 966–987. doi:10.1002/eqe.3001

Shen, Y. S., Wang, Z. Z., Yu, J., Zhang, X., and Gao, B. (2020). Shaking Table Test on Flexible Joints of Mountain Tunnels Passing through normal Fault. *Tunnelling Underground Space Technol.* 98, 103299. doi:10.1016/j.tust.2020.103299

Shi, J., Wang, Y., and Chen, Y. (2018). A Simplified Method to Estimate Curvatures of Continuous Pipelines Induced by normal Fault Movement. *Can. Geotech. J.* 55, 343–352. doi:10.1139/cgj-2017-0044

Sun, S. (1991). in *Earthquake Damages of Pipelines in China, Earthquake Resistance of Buried Pipelines*. Editor Z. Hou (Beijing: Academic Press), 1–9.

Sun, S., and Shien, S. (1983). "Analysis of Seismic Damage to Buried Pipelines in Tangshan Earthquake," in *Earthquake Behavior and Safety of Oil and Gas Storage Facilities, Buried Pipelines and Equipment, PVP-77* (New York: American Society of Mechanical Engineers (ASME)), 365–367.

Toprak, S., and Taskin, F. (2007). Estimation of Earthquake Damage to Buried Pipelines Caused by Ground Shaking. *Nat. Hazards* 40, 1–24. doi:10.1007/s11069-006-0002-1

Tsinidis, G., Di Sarno, L., Sextos, A., and Furtner, P. (2019). A Critical Review on the Vulnerability Assessment of Natural Gas Pipelines Subjected to Seismic Wave Propagation. Part 2: Pipe Analysis Aspects. *Tunnelling Underground Space Technol.* 92, 103056. doi:10.1016/j.tust.2019.103056

Tsinidis, G., Di Sarno, L., Sextos, A., and Furtner, P. (2020). Optimal Intensity Measures for the Structural Assessment of Buried Steel Natural Gas Pipelines Due to Seismically-Induced Axial Compression at Geotechnical Discontinuities. *Soil Dyn. Earthquake Eng.* 131, 106030. doi:10.1016/j.soildyn.2019.106030

Tsinidis, G., Di Sarno, L., Sextos, A., and Furtner, P. (2020). Seismic Fragility of Buried Steel Natural Gas Pipelines Due to Axial Compression at Geotechnical Discontinuities. *Bull. Earthquake Eng.* 18 (2020), 837–906. doi:10.1007/s10518-019-00736-8

Uckan, E., Akbas, B., Shen, J., Rou, W., Paolacci, F., and O'Rourke, M. (2015). A Simplified Analysis Model for Determining the Seismic Response of Buried Steel Pipes at Strike-Slip Fault Crossings. *Soil Dyn. Earthquake Eng.* 75, 55–65. doi:10.1016/j.soildyn.2015.03.001

Vazouras, P., and Karamanos, S. A. (2017). Structural Behavior of Buried Pipe Bends and Their Effect on Pipeline Response in Fault Crossing Areas. *Bull. Earthquake Eng.* 15, 4999–5024. doi:10.1007/s10518-017-0148-0

Wang, L. R.-L., and Yeh, Y.-H. (1985). A Refined Seismic Analysis and Design of Buried Pipeline for Fault Movement. *Earthquake Engng. Struct. Dyn.* 13, 75–96. doi:10.1002/eqe.4290130109

Wang, X., Guo, E., and Zhang, M. (2012). Analysis and Countermeasures on Seismic Damage to Gas Pipeline in Wenchuan Earthquake. *World Earthquake Eng.* 28, 44–50.

Yan, K., Zhang, J., Wang, Z., Liao, W., and Wu, Z. (2018). Seismic Responses of Deep Buried Pipeline under Non-uniform Excitations from Large Scale Shaking Table Test. *Soil Dyn. Earthquake Eng.* 113, 180–192. doi:10.1016/j.soildyn.2018.05.036

Yang, Z., Lan, H., Zhang, Y., Gao, X., and Li, L. (2013). Nonlinear Dynamic Failure Process of Tunnel-Fault System in Response to strong Seismic Event. *J. Asian Earth Sci.* 64, 125–135. doi:10.1016/j.jseaes.2012.12.006

Yifei, Y., Bing, S., Jianjun, W., and Xiangzhen, Y. (2018). A Study on Stress of Buried Oil and Gas Pipeline Crossing a Fault Based on Thin Shell FEM Model. *Tunnelling Underground Space Technol.* 81, 472–479. doi:10.1016/j.tust.2018.08.031

Conflict of Interest: The authors declare that the research was conducted in the absence of any commercial or financial relationships that could be construed as a potential conflict of interest.

Author WZ and YL are employed by China Railway First Survey and Design Institute Group Co., Ltd. All authors declare no other competing interests.

Publisher's Note: All claims expressed in this article are solely those of the authors and do not necessarily represent those of their affiliated organizations, or those of the publisher, the editors and the reviewers. Any product that may be evaluated in this article, or claim that may be made by its manufacturer, is not guaranteed or endorsed by the publisher.

frontiers in Earth Science

ORIGINAL RESEARCH
published: 03 December 2021
doi: 10.3389/feart.2021.806921

Interaction Between Animal Burrowing and Loess Cave Formation in the Chinese Loess Plateau

Haopeng Geng, Ru Liu, Weishan Zheng, Yunbo Zhang, Rong Xie, Yu Guo and Baotian Pan*

Key Laboratory of Western China's Environmental Systems (Ministry of Education), College of Earth and Environmental Sciences, Lanzhou University, Lanzhou, China

Although the interactions between biotic and geomorphic processes usually occur on small spatial and short temporal scales, many of the mechanisms remain to be investigated. This study provides the first direct evidence of the interaction between biotic burrowing and loess cave formation in the Chinese Loess Plateau (CLP). The study area is the Qingshui Valley in the western CLP, near Lanzhou. We surveyed the target site (with an area of ~13,367 m^2) four times from Jul 2019 to Dec 2020, using an unmanned aerial vehicle (UAV). High resolution UAV images enabled us to determine the temporal and spatial dynamics of biotic burrowing and loess caves. The results show that loess caves tended to develop down valley below collapses, while animal burrows were preferentially located upslope away from collapses. Despite the distinct "topographic niches" for both biotic and abiotic processes, we observed an interaction between the two processes in space when tracking their temporal dynamics. Three out of seven new loess caves were in the process of formation at typical "topographic niches" of animal burrows and there was a significantly high animal burrow density around these three caves before their initiation. These results indicate that the three caves were directly initiated from animal burrows and/or developed under the influence of biotic activities. Therefore, biotic burrowing promotes the spatial heterogeneity of loess cave distribution. We also found significant decreases in animal burrow density surrounding the newly-formed loess caves after their initiation. This may reflect a risk avoidance strategy of animal burrowing, which causes animals to avoid areas of recent mass movement (i.e., collapses and new caves). The formation and expansion of loess caves can dictate the distribution of active areas of biotic disturbance. Our results demonstrate a clear interaction between biotic burrowing and loess cave formation, and they emphasize the role of biological agents as a mechanism for the formation of loess caves, which enrich the understanding of searching fingerprints of life during landscape evolution.

Keywords: loess cave, biotic burrowing, Chinese Loess Plateau, biotic disturbance, forming mechanism, landscape evolution

OPEN ACCESS

Edited by:
Mark Allen,
Durham University, United Kingdom

Reviewed by:
Sheng Hu,
Northwest University, China
Xiaodong Gao,
Northwest A and F University, China

****Correspondence:***
Haopeng Geng
hpgeng@lzu.edu.cn

Specialty section:
This article was submitted to Geohazards and Georisks, a section of the journal Frontiers in Earth Science

Received: *01 November 2021*
Accepted: *12 November 2021*
Published: *03 December 2021*

Citation:
Geng H, Liu R, Zheng W, Zhang Y, Xie R, Guo Y and Pan B (2021) Interaction Between Animal Burrowing and Loess Cave Formation in the Chinese Loess Plateau. Front. Earth Sci. 9:806921. doi: 10.3389/feart.2021.806921

INTRODUCTION

The Chinese Loess Plateau (CLP) experiences some of the most serious soil erosion on Earth (Shi and Shao, 2000; Zhao et al., 2013; Chen et al., 2018). The loess structure is characterized by well-developed macropores and vertical joints (Feng et al., 2021), making it prone to underground processes such as seepage and piping erosion (Verachtert et al., 2013; Li et al., 2020). Consequently, loess caves, as a unique underground landform, are widely distributed in the CLP (Peng et al., 2018; Li et al., 2020). The frequent rainstorm events in the region significantly accelerate the development of loess caves (Hu et al., 2020) and also increase soil erosion (Shi and Shao, 2000; Wu et al., 2018). Previous studies have often emphasized the contribution of loess caves to the total soil erosion rate of the CLP (Zhu, 1997, 2003; Zhu et al., 2002; Li et al., 2020). For example, loess caves were shown to deliver at least 43% of the annual catchment outflow discharge and 57% of the annual basin sediment yield during 15 storm events in the upper Yangdaogou catchment (Zhu, 1997; Zhu et al., 2002). By inference, the net erosion by loess caves may contribute at least 25–30% of basin sediment yields (Zhu, 2003).

Biotic burrowing is a universal underground process, which can disturb soil and influence landscape evolution (Darwin, 1881; Gilbert, 1909; Gabet, 2000; Ballová et al., 2019). Many areas in the CLP have a large population of subterranean rodents (Su et al., 2013; Sui et al., 2014; Zhang et al., 2021), because of the habitable grassland environment (Yu et al., 2017) and unlimited burrowing potential of loess (Krasnov et al., 1997). This burrowing activity has both direct and indirect impacts on geomorphic processes (Hall et al., 1999; Hall and Lamont, 2003; Escapa et al., 2007; Germain et al., 2021; Sanders et al., 2021). The burrowing process may directly cause soil displacement (Black and Montgomery, 1991) and alter the slope micromorphology (Zhao et al., 2021) as well as soil compactness (Rogasik et al., 2014). These indirect impacts were previously emphasized in terms of changing the soil water holding capacity (Zhang et al., 2003), increasing erosion by overland flow (Li T. et al., 2019), and increasing slope instability (Harvey et al., 2019). As a result, animal burrowing can induce an equivalent soil erosion of ~1 mm yr^{-1} (Winchell et al., 2016) and transport sediment at rates ranging from 0.01 t ha^{-1} y^{-1} to 2.40 t ha^{-1} y^{-1} (Voiculescu et al., 2019). Given their role in landscape evolution, animals such as subterranean rodents are known as "ecosystem engineers" (Huntly and Inouye, 1988; Jones et al., 1994; Reichman and Seabloom, 2002; Zhang et al., 2003; Davidson et al., 2008; Su et al., 2020).

Although many previous studies have proposed a potential relationship between loess cave development and animal burrowing (Pierson, 1983; Botschek et al., 2002; Verachtert et al., 2010; Bernatek-Jakiel et al., 2016; Wang et al., 2019), this biotic mechanism has not been demonstrated by direct observation. Since animal burrows and loess caves are difficult to detect, the most likely possibility is that both processes produce maze-like tunnel systems with a complex underground space (Vleck, 1981; Zhu, 1997; Voigt, 2014; Got et al., 2020). The tunnel systems excavated by subterranean animals can create preferential paths for subsurface water flow (Botschek et al., 2002), which will in turn enlarge the tunnel space (Wilson et al., 2015), increase soil erosion (Chen et al., 2021), and eventually promote loess cave formation (Verachtert et al., 2013). Regardless of the validity of this biotic mechanism, the reliability of the potential relationship between the two underground processes remains to be investigated. Therefore, a systematic examination of whether biotic burrowing could promote loess cave development may improve our understanding of the formation mechanism of loess caves.

Another issue raised by the foregoing is whether there is an interaction between biotic and geomorphic processes (Hall and Lamont, 2003; Bendix and Cowell, 2010; Corenblit et al., 2011; Zaitlin and Hayashi, 2012; Cienciala et al., 2020). For example, salmon migration upstream has a significant impact on the longitudinal profile of the stream bed and thus on the evolution of entire watersheds; and as a feedback, additional habitats may be created that promote the evolution of species including salmon (Fremier et al., 2018). Although ecologists focus on population dynamics, while geomorphologists are more concerned with the energy and stress effects of geomorphic processes (Yoo et al., 2005; Winchell et al., 2016), both biology and geomorphology may interact on a large spatial and long temporal scale (Butler, 1995; Winchell et al., 2016). However, the interactions between biotic and geomorphic processes usually occur at small spatial and short temporal scales, many mechanisms of which are uninvestigated (Dietrich and Perron, 2006). Therefore, an interesting question is how geomorphic processes influence the spatial distribution of burrowing activity and the temporal dynamics of biotic behaviors. Recent biological studies in the CLP have provided several clues. It has been found that subterranean rodents (such as zokors) have adapted to excavating tunnels in thick, loose soil with high air permeability, in order to provide a living space (Zhou and Dou, 1990; Zhou et al., 2010; Song et al., 2017). These subterranean rodents always prefer flat, open areas for excavation (Li and Wang, 2015), which could subsequently be affected or altered by geomorphic processes. These initial findings encouraged us to explore the potential interaction between biotic burrowing and the formation of loess caves in the Chinese Loess Plateau.

The specific objectives of the present study were: (1) to map the spatial distribution and track the temporal dynamics of both animal burrows and loess caves; (2) to examine the associated topographic conditions and soil properties; and (3) to compare the temporal dynamics of the two processes and to explore their potential connection. To this end, we used an unmanned aerial vehicle (UAV) to survey the study site (the Qingshui Valley in the western CLP) four times from Jul 2019 to Dec 2020. We located the animal burrows and loess caves each time and collected 12 soil samples from the study areas. Based on these data, we present the first direct evidence of the interaction between biotic burrowing and loess cave formation in the CLP.

STUDY AREA

The Chinese Loess Plateau is located in the middle and upper reaches of the Yellow River and covers an area of ~430,000 km^2 (Liu, 1985) (**Figure 1**). The region has a continental climate and

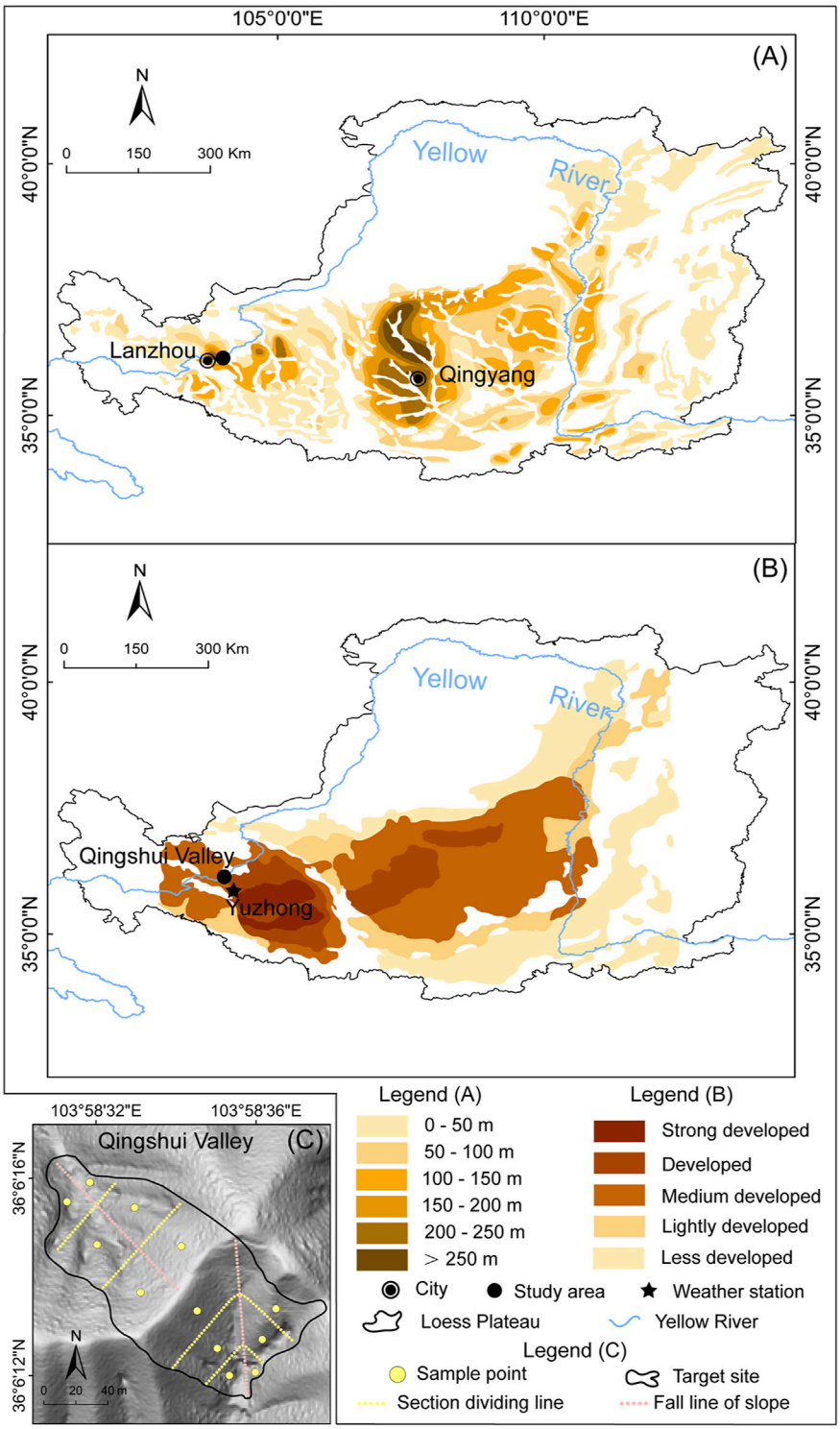

FIGURE 1 | (A) The spatial distribution of loess thickness across the CLP (modified from Wang et al., 2010) **(B)** Development intensity map of loess caves in the CLP (modified from Peng et al., 2018) and **(C)** Shaded relief map of the target site in the Qingshui Valley showing the locations of the 12 sample points (yellow solid points). The two hillslopes were divided into three equal parts: slope top, slope middle, and slope toe (yellow dashed lines), according to their slope lengths in the direction of fall line (pink dashed lines).

annual precipitation increases from northwest to southeast with the range of 200–800 mm (Feng et al., 2016). The vegetation cover also increases in the same direction, showing a gradual transition from grassland to forest (Chen et al., 2008). The loess particles have been transported from the northwestern desert by wind and have accumulated in the CLP since the beginning of the Quaternary (Zhang et al., 2016). The loess particle size becomes finer from northwest to southeast, with increasing distance from the desert sources, and over 50% of loess particles are silt (Liu and Zhang, 1962). The spatial distribution of loess thickness shows two depocenters, near Lanzhou and Qingyang, and the depth in the west is generally thicker than that in the east (**Figure 1A**). Previous qualitative research suggested that the density of loess caves has a striped distribution pattern, with the density decreasing from southwest to northeast (**Figure 1B**).

The typical subterranean rodent species, the zokors (Chinese zokor *Myospalax fontanierii* and Gansu zokor *Myospalax cansus*) are widely distributed in the CLP (Lin et al., 2008; Sui et al., 2014). The population of Chinese zokors is ~320–400 million across the entire CLP (Sui et al., 2014). The Chinese zokor density of Gansu province in the western CLP is ~8 ha^{-1} (Chen et al., 2021). The Gansu zokor is a endemic rodent species in the CLP (Lin et al., 2021). The density of the Gansu zokor in Gansu province is ~16–57 ha^{-1} (Cao and Wang, 1994).

The study area is located in Lanzhou City in Gansu Province in the western CLP. The mean annual precipitation is ~310 mm and the mean annual temperature is ~10°C; the natural vegetation is grassland (Feng and Wang, 2012; Zhang et al., 2016). The loess deposits in Lanzhou provide one of the most complete and continuous continental sediment archives, with maximum depths up to 400 m (Zhang et al., 2016; Guo et al., 2020). Loess caves in the study area are developed to an intermediate degree (Peng et al., 2018). The target site (**Figure 1C**) consists of two hillslopes with a total area of 13,367 m^2, located in the Qingshui Valley (103.57°E–103.59°E, 36.05°N–36.07°N). The altitudinal range of the area is 1,549–2,010 m, and the average slope is 36.5°. Field investigations show a high degree of animal burrowing activity and negligible human influence.

MATERIALS AND METHODS

Field Survey and UAV Mapping

We surveyed the animal burrows and loess caves in the target site a total of four times from Jul 2019 to Dec 2020 (Jul 2019, Nov 2019, Jul 2020 and Dec 2020). Animal burrows were identified in the field by their tunnel systems, including surface mounds and underground burrows (Miller, 1948). According to the characteristics of the mounds and burrows, we divided the burrows into active burrows and inactive burrows. The mounds of active burrows were clearly visible with fresh excavation traces (consisting of a mixture of loose material and grass, **Figure 2A**), or were partially visible with debris at the entrance (**Figure 2B**). If the mound debris was completely removed by geomorphic processes (**Figure 2C**), we checked for excavation traces on the tunnel sidewalls, which are usually smooth because the soil is compacted by the rodents. However, the inactive burrows had no evidence of current excavation, and grasses had regrown at the entrance (**Figure 2D**); also, the sidewall of the tunnel had partially collapsed and was no longer smooth. Here, we only focus on the active burrows. According to Peng et al. (2018), loess caves can be divided into vertical caves and parallel hidden caves, based on shape. The radius of the caves ranges from several centimeters to several meters. The depth of the caves varies from several tens of centimeters to tens of meters. Given that the diameter of the zokor burrow entrance is ~8–12 cm (Chen et al., 2021), we only considered vertical loess caves with a diameter exceeding 12 cm and a depth of several tens of centimeters to tens of meters. In this study, we only considered caves with the above dimensions and which were usually exposed and clearly visible in the field (**Figure 2E**).

In the field, we used red flags (20 × 30 cm) to mark the animal burrows and blue flags (40 × 60 cm) to mark the loess caves. We then used an unmanned aerial vehicle (UAV, DJI Phantom 4 V2.0) to carry out photogrammetry. We reconstructed the 3D terrain in Pix4Dmapper and generated a DOM (digital orthophoto map) with a resolution of 8.1 cm/pixel and a DSM (digital surface model) with a resolution of 6.5 cm/pixel. We then mapped the spatial distribution of the animal burrows and loess caves based on the DOMs according to the colored flags.

The study area contains of two hillslopes with distinct aspects: a north-facing slope (N-slope) and a south-facing slope (S-slope). According to their slope lengths in the direction of fall line (116 m for the S-slope and 102 m for the N-slope; the pink dashed line in **Figure 1C**), we divided them into three equal sections (slope top, slope middle and slope toe; the yellow dashed lines in **Figure 1C**). We calculated the distribution density of the animal burrows and loess caves for the six sections for the four time periods, and the density changes in different sections were analyzed and listed in **Table 1**. Given the significant number and dynamics of animal burrows, we estimated the density distribution of animal burrows using the kernel density tool in ArcGIS 10.2, with a search radius of 20 m.

Topographic Analysis

In order to reduce micro-scale noise in the topographic data, we resampled the UAV-derived DSMs to a spatial resolution of 3 m, which is an optimal resolution to capture geomorphic processes (Heimsath et al., 1999). Topographic variables of animal burrows and loess caves were calculated using ArcGIS 10.2, including slope angle, plan curvature, profile curvature, and upslope contributing area. We combined the data for the four periods to cover the maximum animal burrow set and calculated the distribution of burrows for all topographic variables. We calculated the loess cave distribution for topographic variables for the final period (Dec 2020) since it comprises the largest dataset. The plan curvature describes the hillslope planform, which influences the convergence and divergence of flow (i.e., >0 is divergent; < 0 is convergent). The profile curvature affects the acceleration or deceleration of flow and indicates the downslope morphology (i.e., >0 is concave; < 0 is convex; ≈0 indicates a straight slope). The upslope contributing area here

FIGURE 2 | Photographs of typical active animal burrows **(A, B and C)**, an inactive animal burrow **(D)**, and a loess cave **(E)**. The red arrows in panels **(A, B, C and D)** point to the entrance of the burrow. The white dashed line in panel **(A)** indicates the intact fresh mound of an active burrow. The white dashed line in panel **(B)** indicates a partially visible mound with debris at the entrance of an active burrow. The white dashed line in panel **(C)** indicates excavation traces on the tunnel sidewall of an active burrow. The white dashed line in panel **(D)** indicates the typical entrance of an inactive burrow with obvious grass regrowth and no evidence of current excavation. The white dashed line in panel **(E)** indicates a typical loess cave.

enumerates all of the upslope grids that could potentially produce runoff to the location. We extracted the topographic variables corresponding to the locations of marked animal burrows and loess caves. We then calculated the frequency of animal burrows and loess caves under different topographic variables to obtain their topographic preference.

Soil Properties and Precipitation Records

Soil properties have been proposed to impact the development of loess caves (Peng et al., 2018) and the activity of burrowing animals (Vleck, 1981). To study the influence of soil properties on the distribution of animal burrows and loess caves, we collected 12 samples from the 6 sections across the study area (the yellow solid points in **Figure 1C**). Measured soil properties included soil bulk density, saturated hydraulic conductivity and soil porosity, all of which may physically affect geomorphic processes. Bulk density and soil porosity are important soil physical properties that influence soil water retention capacity and infiltration rate, while the saturated hydraulic conductivity is a critical soil hydraulic property that affects water flow (i.e., infiltration and evaporation) and soil water redistribution. We used metal cylinders (100 cm^3 volume) to collect soil samples in the field. In the laboratory, the cylinders were wetted with water to saturation before measuring the saturated hydraulic conductivity using the constant head permeability test (Hu et al., 2012). The soil columns were then oven-dried at 105°C for 24 h to calculate the bulk density from the sample volume and mass. Soil porosity was estimated from the bulk density and soil

TABLE 1 | Distribution density of loess caves and animal burrows over the four mapping periods.

Position		Period I (Jul 2019)		Period II (Nov 2019)		Period III (Jul 2020)		Period IV (Dec 2020)	
Slope aspect	Slope section part	Burrow density (ha^{-1})	Loess cave density (ha^{-1})	Burrow density (ha^{-1})	Loess cave density (ha^{-1})	Burrow density (ha^{-1})	Loess cave density (ha^{-1})	Burrow density (ha^{-1})	Loess cave density (ha^{-1})
S	Top	134	3	221	3	188	3	101	3
	Middle	83	0	186	0	124	5	21	15
	Toe	0	43	230	43	29	43	0	58
	Total	102	7	210	7	149	8	63	13
N	Top	156	6	263	9	162	9	196	12
	Middle	0	18	7	18	25	18	42	18
	Toe	0	32	87	32	134	32	173	39
	Total	69	15	134	16	104	16	133	19
Total		84	11	168	12	124	13	102	16

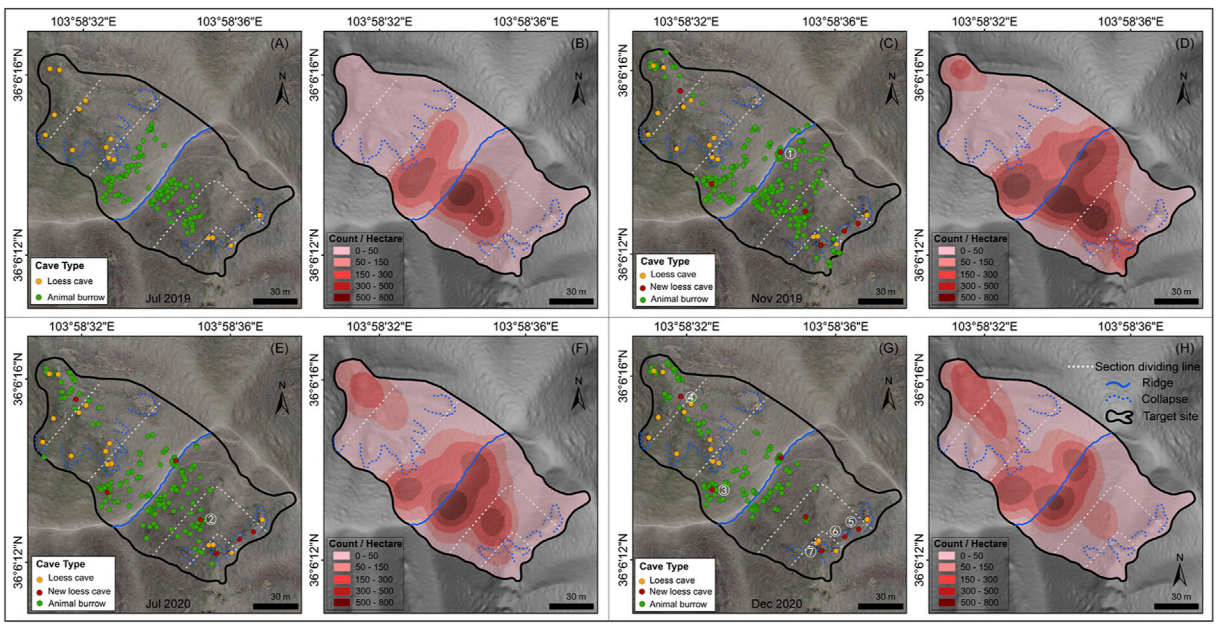

FIGURE 3 | Spatial distribution and temporal dynamics of loess caves and animal burrows. Panels **(A, C, E and G)** show the distribution of loess caves (orange and red points) and animal burrows (green points) overlying the orthophotos of the target site for the four survey periods. The seven new loess caves are marked by red points and numbered in white (1–7). Panels **(B, D, F and H)** show the density (count·ha^{-1}) of animal burrows. The blue dashed line indicates the collapse and the blue solid line is the ridge dividing the two slope aspects. The white lines are the boundary of the three equal sections (slope top, slope middle and slope toe) of each slope.

particle density. Soil particle density is generally assumed to be 2.65 g cm^{-3} (Blanco-Canqui et al., 2006). Soil bulk density and the saturated hydraulic conductivity were measured in the Key Laboratory of Western China's Environmental Systems (Ministry of Education), Lanzhou University.

We also selected precipitation from nearby weather station, Yuzhong station (35.87°N, 104.15°E, in **Figure 1B**), of which the records are available to cover our investigation period (downloaded from NOAA's National Centers for Environmental Information (NCEI), https://www.ncei.noaa.gov). We prepared the records in monthly precipitation and showed the results in **Figure 4** below.

RESULTS

Spatial Distribution and Temporal Dynamics of Loess Caves and Animal Burrows

The spatial distribution of loess caves and animal burrows over the four mapping periods are presented in **Figure 3**. The density and numbers of caves and burrows for the six sections are listed in **Table 1** and illustrated in **Figure 3**. The total density of loess caves on the N-slope is higher than on the S-slope and the density at the slope toes is higher than in the other sections (**Table 1**). The number of loess caves was relatively stable through time

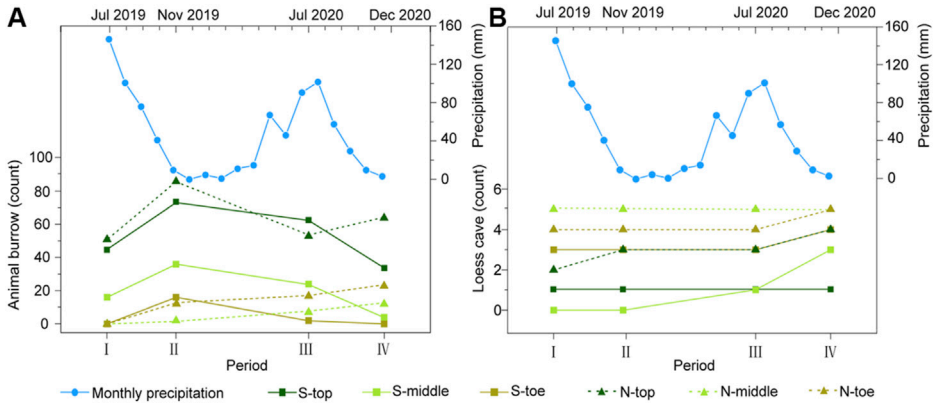

FIGURE 4 | Counts of animal burrows **(A)** and loess caves **(B)** for the six slope sections over the four periods. The blue lines with dots are the monthly precipitation records during our investigation period.

(**Figure 3**) and they were located mainly beneath the collapses (blue dashed lines in **Figure 3**). During the survey period, seven new caves started to develop; four were located below the collapse near the slope toe, while the other three were located above the collapse near the slope top. These three caves were respectively developed: 1) at the slope top near the ridge in Nov 2019 (**Figure 3C**); 2) in the middle of the S-slope in Jul 2020 (**Figure 3E**); and 3) at the slope top on the N-slope in Dec 2020 (**Figure 3G**).

For the animal burrows, the total distribution density for the S-slope was always greater than that for the N-slope, except for Dec 2020 (period IV, in **Table 1**). In addition, with the exception of Nov 2019 (period II), the density at the slope top was always larger than that at the middle and toe, irrespective of slope aspect (**Table 1**). These results indicate that animal burrows have a significant topographic preference, like loess caves. However, unlike loess caves, the animal burrows show clear temporal dynamics (i.e., the counts of animal burrows at slope top increase from period I to period II then suddenly decrease from period II to period III) (**Figure 4**), which is further illustrated by the kernel density maps (**Figures 3B,D,F,H**). Furthermore, animal burrows at the slope top have a high density (101–263 ha^{-1}) and 75–100% burrows are located above the collapses with a density of 122–170 ha^{-1} (**Figure 3**).

In general, the loess caves and animal burrows show an opposite tendency in both time and space. The number of loess caves shows a uniform rate of increase, but the numbers of animal burrows fluctuate substantially over time (**Figure 4**). The loess caves tend to develop downslope below collapses, while animal burrows tend to be located upslope away from collapses. However, we did not find any unusual rainfall event during our investigation period (blue lines with dots in **Figure 4**). We then suggest that the opposite tendency of two processes in both time and space represents their dynamic status in nature. Therefore, it is noteworthy that the density of animal burrows surrounding new caves (30 m radius) decreases substantially (~21–63%). This phenomenon suggests that the animal burrowing activities are influenced by geomorphic processes like loess cave formation.

Topographic Preferences of Loess Caves and Animal Burrows

The distribution of the loess caves and animal burrows reveals different topographic preferences, such as slope angle, upslope contributing area, plan curvature, and profile curvature (**Figure 5**). The results show that 86% of the animal burrows are located on slope angles from 10° to 40°, with a median of 36°; while 67% of the loess caves are located on slope angles from 40° to 60°, with a median of 44°. This means that animal burrows tend to be excavated on gentler slopes than loess caves (**Figure 5A**). The upslope contributing areas of loess caves are significantly larger than those of animal burrows (**Figure 5B**). Most of the animal burrows (92%) distributed in upslope contributing areas of <50 m^2, but 71% of loess caves require an upslope contributing area >50 m^2. The differences in topographic preference are also featured in the plan curvature and profile curvature (**Figures 5C,D**). The loess caves tend to develop in convergent landforms and concave topography, while the animal burrows have a strong dependency on convex topography, although there is no preference of plan curvature. Different from the four new caves below collapses near the slope toe, the three new caves located above the collapse near the slope top are all located in topographic contexts similar to animal burrows. These three loess caves have slope angles <40° and have upslope contributing areas <50 m^2. In addition, they are all located in convex topographies and divergent landforms, which are unsuited to loess cave formation.

Influence of Soil Properties on Loess Cave Density and Burrowing Activity

Having examined the topographic preferences of loess caves and animal burrows, we now consider the potential influence of soil properties on their spatial distribution. The six sections of the study area differ only slightly in bulk density and porosity but show significant differences in saturated hydraulic conductivity (**Table 2**). The results show that the average porosity and

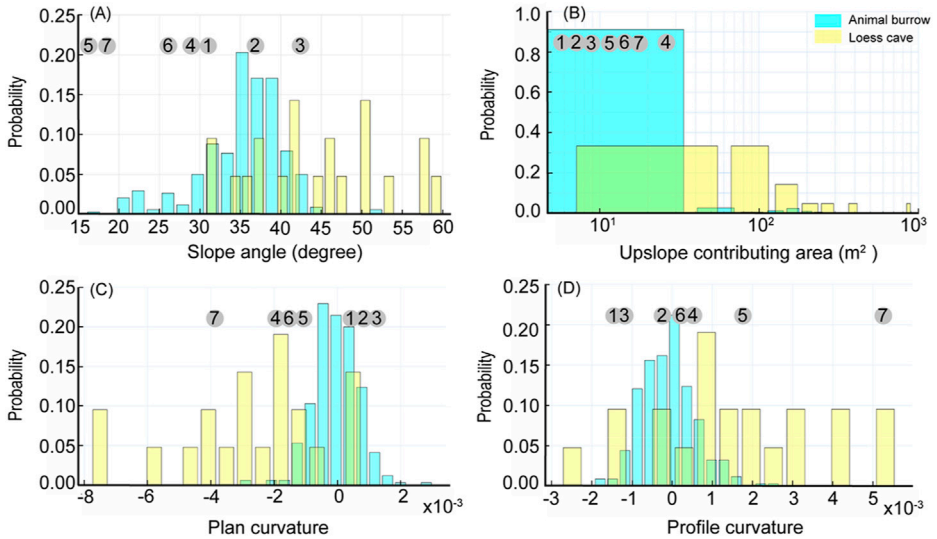

FIGURE 5 | Probability histograms comparing the distribution of topographic conditions **(A)**: Slope angle, **(B)**: Upslope contributing area, **(C)**: Plan curvature and **(D)**: Profile curvature) for loess caves (yellow) and animal burrows (blue). The numbers in gray circles (1–7) correspond to the topographic conditions of the seven new loess caves.

TABLE 2 | Soil properties of the six slope sections.

Hillslope part		Bulk density (g·cm^{-3})	Porosity (%)	Saturated hydraulic conductivity (10^{-2} cm min^{-1})
S	Slope top	1.17 (1.19, 1.15)[a]	55.91 (55.13, 56.68)	2.72 (2.49, 2.95)
	Slope middle	1.14 (1.12, 1.16)	57.02 (57.85, 56.19)	4.87 (6.35, 3.40)
	Slope toe	1.16 (1.16, 1.16)	56.32 (56.42, 56.23)	4.45 (5.03, 3.87)
	Mean	1.16	56.42	4.02
N	Slope top	1.09 (1.13, 1.06)	58.72 (57.47, 59.96)	3.16 (3.13, 3.18)
	Slope middle	1.00 (1.01, 0.99)	62.25 (61.85, 62.64)	4.27 (5.21, 3.33)
	Slope toe	1.10 (1.19, 1.15)	58.34 (61.02, 55.66)	6.63 (9.24, 4.02)
	Mean	1.07	59.77	4.68

[a]*Note that two samples were collected from each section and their values are shown within parentheses. The other value is the mean.*

saturated hydraulic conductivity on the S-slope are both lower than on the N-slope. The porosity and saturated hydraulic conductivity at the slope tops are both generally lower than in the remaining parts. Although the bulk density on the S-slope is systematically higher than that on the N-slope, there is no significant difference within the two slope aspects. We therefore correlated the density of loess caves and animal burrows with porosity and saturated hydraulic conductivity. The results indicate that there is no correlation between loess cave density and porosity (**Figure 6A**), while there is a slight positive correlation between loess cave density and saturated hydraulic conductivity (**Figure 6B**). The density of animal burrows has no correlation with either porosity and saturated hydraulic conductivity (**Figures 6C,D**). These results suggest that the variation of soil properties at the slope scale has little influence on loess cave development and animal burrowing activity. Therefore, we conclude that soil properties are not responsible for the temporal dynamics of loess caves and animal burrows.

DISCUSSION

Topographic Controls on Loess Cave Development and Burrowing Activity

The distribution of loess caves in the Qingshui Valley shows topographic preferences in terms of slope angle and upslope contributing area. More importantly, loess caves tend to develop in convergent landforms and areas of concave topography (**Figure 5**), from which we infer that the loess cave formation processes depend on surface runoff. This mechanism may explain the higher loess cave density at the slope toe compared to the other slope sections (**Table 1**). Runoff-induced loess cave development might be expected given the sparse vegetation and storm-dominated rainfall in the area, where land cover has a limited influence on overland flow processes (Hessel and Van Asch, 2003; Geng et al., 2015). Therefore, the preferred topographic areas of loess caves are conducive to forming concentrated flow (Garland and Humphrey, 1992; Faulkner,

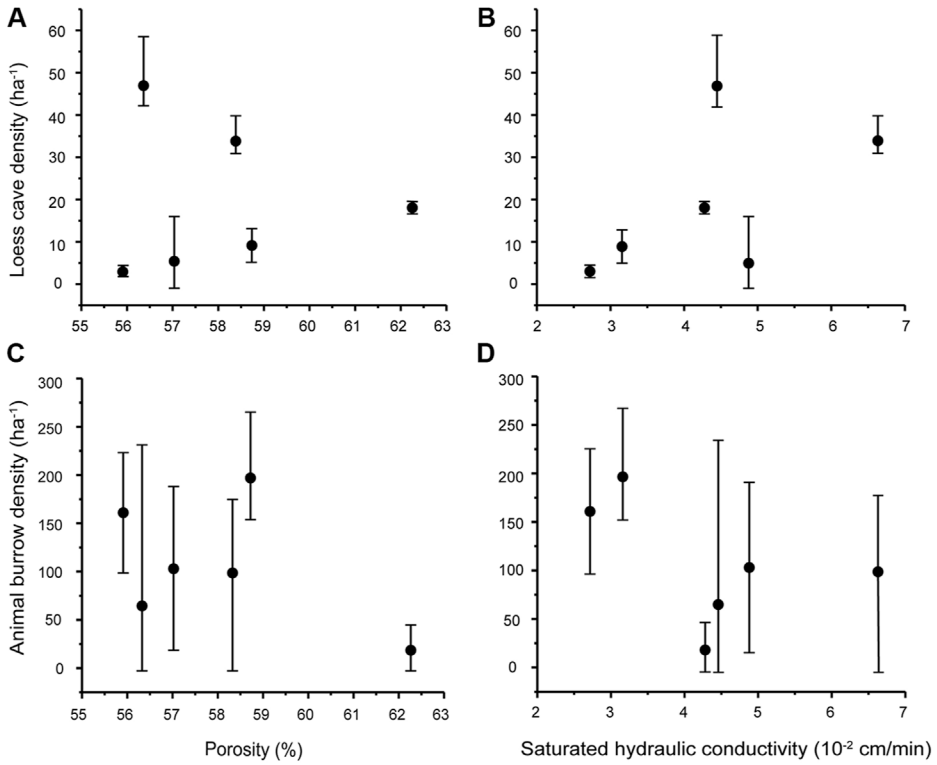

FIGURE 6 | Scatter plots of loess cave density and animal burrow density versus porosity **(A and C)** and saturated hydraulic conductivity **(B and D)**. The black dots are the average values of loess cave density/animal burrow density for the six slope sections, and the error bars represent the corresponding minimum and maximum.

2006). The flow could easily erode the well-developed vertical joints (Xu, 1999) and then cause the expansion and disaggregation of the surrounding loess particles (Li X.-A. et al., 2019b), by inference, forming loess caves (Hu et al., 2020). This is probably why previous studies found that loess cave formation tended to occur at gully heads or on hillslopes with furrows and depressions (Zhu, 2006). Thus, the observed topographic preferences of loess caves in the study area are consistent with previous research.

Animal burrows also have a topographic preference, tending to occur on gentle slopes (**Figure 5A**), with a small upslope contributing area (**Figure 5B**) and convex topography (**Figure 5D**). We consider it likely that the preferred burrowing locations of rodents are closely related to their living habits. The most important aspect of selecting a habitable environment is a spatial unit that provides the necessary conditions for survival (Morris et al., 2008). Besides avoiding predators and seeking an adequate food supply (Forsman and Martin, 2009), topographic conditions are crucial in determining a habitable environment on the slope scale (Bailey, 2005). The preferred burrowing topography is a location that minimizes the formation of concentrated flow. A gentle slope angle could facilitate infiltration and decrease the amount of overland flow (Fox et al., 1997). In addition, a convex topography is concentrated at the slope top where the upslope contributing area is small and there is a limited opportunity to form concentrated flow. Biotic behavior is another reason guiding the selection of a gentle slope. For example, Seabloom et al. (2000) found that a steep slope angle will lead to the falling back of excavated material, which may be the reason why the excavation angle to the horizontal plane was smaller than the angle of repose of the loose mound of excavated soil; therefore, a gentle slope will reduce the cost of excavation (Vleck, 1981). Accordingly, the topographic preference of animal burrows reflects the survival needs and minimum excavation cost for the typical subterranean rodent species in the study area.

We found that both loess cave development and animal burrowing activity demonstrate significant topographic controls, although they have different topographic preferences. However, the variation of soil properties at the slope scale has little influence on preferred locations. Loess caves are dominantly developed in the valley below the collapse, while animal burrows are dominantly located upslope away from collapses. The varied topographic preferences lead to distinct "topographic niches" for both biotic and abiotic processes, with little probability for overlapping in space.

Interaction Between Loess Cave Development and Animal Burrowing Activity

We observed the initiation of seven new loess caves during the survey period. Four caves are still located below the collapse near the slope toe, which is consistent with the concept of "topographic niches" and with the observations of a previous

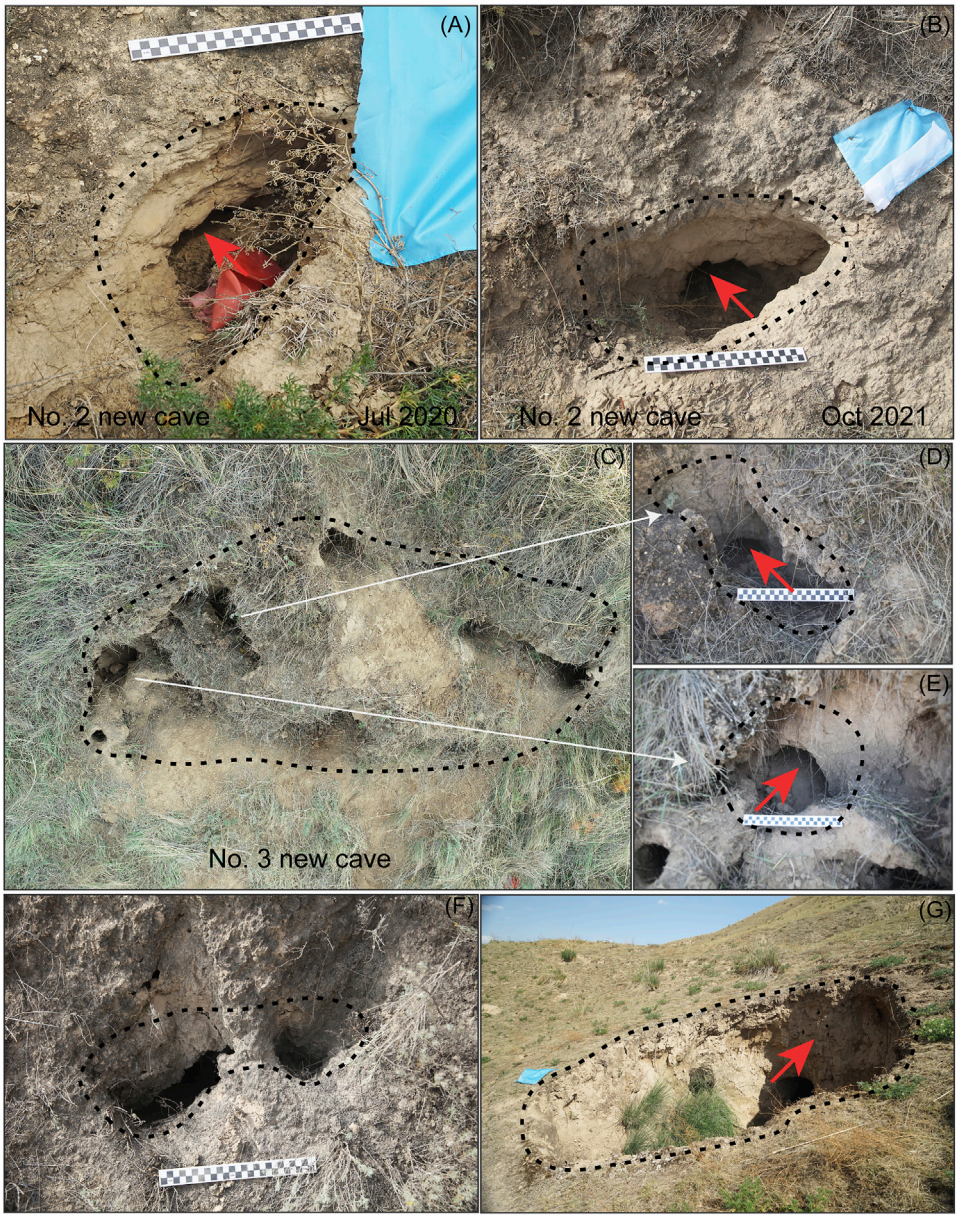

FIGURE 7 | Evidence that loess caves can "inherit" animal burrows **(A, B, D, E and F)** and develop under the influence of biotic activities **(C and G)**. Both panel **(A and B)** are the No.2 new cave, which were photographed in Jul 2020 and Oct 2021 respectively. Panel **(C)** is the No.3 new cave, which consists of eight sub-caves [such as sub-cave in panel **(D)** and sub-cave in panel **(E)**]. The new cave in panel **(F)** and the mature cave in panel **(G)** are observed near our study area. The black dashed lines indicate the entrances of loess caves. The red arrows in panels **(A, B, D, E, F, and G)** indicate the remaining animal burrows in loess caves.

study (Zhu, 2012). However, the remaining three caves (No. 1–3 in **Figure 3**) are all located above the collapse near the slope top, which is an unexpected location for loess cave formation based on our statistics. It is surprising that these three new caves are forming in the typical "topographic niches" of animal burrows, and we suggest the possibility that these caves were directly initiated (or "inherited") from animal burrows and/or developed under the influence of biotic activities.

Our observations suggest that loess caves can inherit animal burrows, and one example is new cave No. 2, in a mid-slope location and with an average diameter of ~28 cm and depth of ~20 cm, that was initiated in Jul 2020 (**Figure 7A**). In this case there were visible animal tunnel remnants near the bottom of the cave (red arrow in **Figure 7A**). Interestingly, the average diameter of the entrance of new cave No. 2 (**Figure 7B**) was enlarged to 35 cm and the depth deepened to 40 cm by the time of our final survey (Oct 2021), which provides direct evidence

for the role of animal burrowing in initiating loess cave formation.

Other new caves may also have developed under the influence of biotic activity. New cave No. 3 (**Figure 7C**) at the slope top on the N-slope consists of eight sub-caves; one sub-cave had an average diameter of 30 cm and depth of 20 cm (**Figure 7D**) and another sub-cave had an average diameter of 35 cm and depth of 30 cm (**Figure 7E**). There are also remnant animal burrows near the base of these sub-caves (indicated by the red arrows in 7D and 7E). There were many signs of collapse in new cave No. 3, which were in the process of expansion. Field observation indicates that animal burrowing can enhance water infiltration, either by altering the microtopography and then extending the runoff path, or by supplying loose material to the surface which promotes water penetration (Chen et al., 2021). Given the abundant joints and macropores in the loess (Zhang et al., 2018), the enhanced infiltration will cause the rapid expansion and collapse of the loess during rainfall (Zhuang and Peng, 2014), thus accelerating the development of new loess caves.

Our results also show a high level of animal burrow density around the three new caves before their initiation. For example, the density for cave No. 1 is 184 ha^{-1} (30 m radius); that for cave No. 2 is 279 ha^{-1}; and that for cave No. 3 is 149 ha^{-1}. Thus, there is both direct and indirect evidence supporting our speculation that biotic activities can induce and accelerate the development of loess caves. This phenomenon is actually very common in the CLP. For example, of two loess caves observed near our study area, one is a new cave (**Figure 7F**) with an average diameter of 28 cm and depth of 50 cm, consisting of two animal burrow entrances; while the inner part of the cave has collapsed and expanded to form an integrated cave, suggesting inheritance from animal burrows. Moreover, there were numerous signs of animal burrowing on the wall of a mature cave (**Figure 7G**), which further verifies the role of animal burrowing in accelerating the development of loess caves. Overall, our findings underline the potential role of biological activity in initiating and developing underground geomorphic phenomena (e.g., piping). In loess areas in northern Mississippi, Wilson et al. (2015) suggested that old roots or other biological channels are highly susceptible to the formation of soil pipes due to strong internal erosion. In addition, the burrows of moles and mice enable immediate water infiltration and direct vertical and lateral water movement; and earthworms were found to provide a high transport capacity for soil water via creating abundant macropores in a loess-rich soil in Germany (Botschek et al., 2002). Pipe formation resulting from biological activity can modify soil properties and soil texture, making the soil prone to erosion by runoff or groundwater (Verachtert et al., 2013). The existence of animal burrows as a condition for pipe development has also been reported in areas without loess (Czeppe, 1960; Bernatek-Jakiel et al., 2016).

Animal burrowing is a dynamic phenomenon on the annual scale and is influenced by geomorphic processes such as loess cave formation. For example, we observed an abrupt decrease in animal burrow density on the S-slope in Dec 2020, after the initiation of cave No. 2. We speculate that the formation and expansion of loess caves may dictate the location of active areas of biotic disturbance. This is indicated by the significant decrease in animal burrow density surrounding the newly formed loess caves after their initiation, which reflects a risk avoidance strategy for animals in the long-term natural selection process, which requires that organisms inherit behaviors in order to avoid risks and enhance survival rates (Lima et al., 1985; Blanchard et al., 2001; Nemati et al., 2013). Migration to a safe location is a type of inherited activity, developed via a long process of random mutation and natural selection (Kirschvink, 2000). Rodents such as burrowing animals may have a greater capacity for risk prediction than animals above ground, because their hearing is extremely acute (Heffner and Masterton, 1980). We therefore infer that the excavation activities of animals are indeed restricted by recent mass movement processes (i.e., cave formation and collapses), thus promoting their migration.

The proposed interaction between biotic burrowing and loess cave formation in the Chinese Loess Plateau has significant implications for landscape evolution. First, the biotically-induced loess cave formation mechanism is an important supplement to runoff-induced cave formation. This biotic mechanism could promote the spatial heterogeneity of the distribution of loess caves. In this study, we found that three out of seven new loess caves were developing via a biotic mechanism. We also found that 14% of loess caves were located in areas with a convex topography and divergent landforms (**Figure 5**), which are typical "topographic niches" for animal burrows. We propose tentatively that these caves were all induced by animal burrowing. Second, the formation of loess caves promotes the migration of animals, which in turn will extend the area of burrowing activity and increase the rate of soil loss via frequent underground excavation. Although biotic disturbance has been proposed as an important agent of surface erosion (Reichman and Seabloom, 2002; Gabet et al., 2003; Stallins, 2006; Winchell et al., 2016). It also could introduce bias to the sediment flux calculated by geomorphic transport laws and promote the spatial heterogeneity of hillslope processes (Roering et al., 1999; Dietrich et al., 2003). However, this process has not been comprehensively investigated in the CLP. Further quantitative studies are needed to determine the geomorphic contribution of different animals to soil erosion across the Chinese Loess Plateau.

CONCLUSION

We have investigated the spatial distribution of animal burrows and loess caves based on field investigations including UAV mapping of a site in the Qingshui Valley. We surveyed the site four times, from Jul 2019 to Dec 2020, in order to track the temporal dynamics of both processes. We

found that both loess cave development and animal burrowing activity show a significant topographic control, although they have different topographic preferences in term of slope angle, plan curvature, profile curvature, and upslope contributing area. The preferred topographic areas of loess caves are conducive to forming concentrated flow, supporting a runoff-induced mechanism of loess cave development. Animals prefer topographic contexts that are unlikely to form concentrated flows. These topographic preferences lead to distinct "topographic niches" for both biotic and abiotic processes with little chance for overlapping in space.

Seven new loess caves started to develop during the survey period. Four of the caves were consistent with their "topographic niches", but the other three new caves were developing in the typical "topographic niches" of animal burrows. We also observed a significantly high animal burrow density around three new caves before their initiation. Thus, we conclude that these three caves were directly initiated from animal burrows and/or develop under the influence of biotic activities. Animal burrowing activity is seemingly arbitrary but with a clear risk avoidance strategy, which leads them to avoid areas of recent mass movement (e.g., caves and collapses), concentrated flow paths, and newly formed loess caves. The formation and expansion of loess caves can dictate the active areas of biotic disturbance, while biotic burrowing in turn promotes the spatial heterogeneity of the loess cave distribution. Our study emphasizes the role of biological agents in formation of loess caves and provides the first direct evidence of the interaction between biotic burrowing and loess cave formation in the CLP.

DATA AVAILABILITY STATEMENT

The original contributions presented in the study are included in the article/supplementary material, further inquiries can be directed to the corresponding author.

AUTHOR CONTRIBUTIONS

This manuscript was written by HG and RL. This manuscript was designed by HG and BP, HG, RL, and WZ analyzed the topographic data. RL and YZ measured the soil properties. RL, WZ, YZ, RX, YG, attended the field work.

FUNDING

This work was co-supported by the National Natural Science Foundation of China (42041006, 41971001 and 41501002), and the Fundamental Research Funds for the Central Universities (lzujbky-2020-70).

ACKNOWLEDGMENTS

We thank Pro. Lixun Zhang for his guidance on the identification of the animal burrows. Thanks to Wenqian Yang and Ke Yan for their assistance with field work, and Dr. Jan Bloemendal for revising the language.

REFERENCES

Bailey, D. W. (2005). Identification and Creation of Optimum Habitat Conditions for Livestock. *Rangel. Ecol. Manag.* 58, 109–118. doi:10.2111/03-147.1

Ballová, Z., Pekárik, L., Píš, V., and Šibík, J. (2019). How Much Do Ecosystem Engineers Contribute to Landscape Evolution? A Case Study on Tatra Marmots. *Catena* 182, 104121. doi:10.1016/j.catena.2019.104121

Bendix, J., and Cowell, C. M. (2010). Fire, Floods and Woody Debris: Interactions between Biotic and Geomorphic Processes. *Geomorphology* 116, 297–304. doi:10.1016/j.geomorph.2009.09.043

Bernatek-Jakiel, A., Kacprzak, A., and Stolarczyk, M. (2016). Impact of Soil Characteristics on Piping Activity in a Mountainous Area under a Temperate Climate (Bieszczady Mts., Eastern Carpathians). *Catena* 141, 117–129. doi:10.1016/j.catena.2016.03.001

Black, T. A., and Montgomery, D. R. (1991). Sediment Transport by Burrowing Mammals, Marin County, California. *Earth Surf. Process. Landf.* 16, 163–172. doi:10.1002/esp.3290160207

Blanchard, R. J., Yudko, E., Dulloog, L., and Blanchard, D. C. (2001). Defense Changes in Stress Nonresponsive Subordinate Males in a Visible Burrow System. *Physiol. Behav.* 72, 635–642. doi:10.1016/S0031-9384(00)00449-2

Blanco-Canqui, H., Lal, R., Post, W. M., Izaurralde, R. C., and Shipitalo, M. J. (2006). Organic Carbon Influences on Soil Particle Density and Rheological Properties. *Soil Sci. Soc. Am. J.* 70, 1407–1414. doi:10.2136/sssaj2005.0355

Botschek, J., Krause, S., Abel, T., and Skowronek, A. (2002). Hydrological Parameterization of Piping in Loess-Rich Soils in the Bergisches Land, Nordrhein-Westfalen, Germany. *J. Plant Nutr. Soil Sci.* 165, 506–510. doi:10.1002/1522-2624(200208)165:4<506:aid-jpln506>3.0.co;2-7

Butler, D. R. (1995). *Zoogeomorphology: Animals as Geomorphic Agents*. Cambridge, UK: Cambridge University Press, 231.

Cao, Z., and Wang, M. (1994). Study on the Biological Characteristics of Gansu Zokor (In Chinese). *Gansu Agricl Sci.Tech.* 5, 32–33.

Chen, H., Shao, M., and Li, Y. (2008). Soil Desiccation in the Loess Plateau of China. *Geoderma* 143, 91–100. doi:10.1016/j.geoderma.2007.10.013

Chen, H., Zhang, X., Abla, M., Lü, D., Yan, R., Ren, Q., et al. (2018). Effects of Vegetation and Rainfall Types on Surface Runoff and Soil Erosion on Steep Slopes on the Loess Plateau, China. *Catena* 170, 141–149. doi:10.1016/j.catena.2018.06.006

Chen, M., Ma, L., Shao, M., Wei, X., Jia, Y., Sun, S., et al. (2021). Chinese Zokor (Myospalax Fontanierii) Excavating Activities Lessen Runoff but Facilitate Soil Erosion - A Simulation experiment. *Catena* 202, 105248. doi:10.1016/j.catena.2021.105248

Cienciala, P., Nelson, A. D., Haas, A. D., and Xu, Z. (2020). Lateral Geomorphic Connectivity in a Fluvial Landscape System: Unraveling the Role of Confinement, Biogeomorphic Interactions, and Glacial Legacies. *Geomorphology* 354, 107036. doi:10.1016/j.geomorph.2020.107036

Corenblit, D., Baas, A. C. W., Bornette, G., Darrozes, J., Delmotte, S., Francis, R. A., et al. (2011). Feedbacks between Geomorphology and Biota Controlling Earth Surface Processes and Landforms: A Review of Foundation Concepts and Current Understandings. *Earth-Sci. Rev.* 106, 307–331. doi:10.1016/j.earscirev.2011.03.002

Czeppe, Z. (1960). Suffosional Phenomena in Slope Loams of the Upper Sau Drainage basin. *Inst. Geol. Biuletin (Warsaw)* 9, 232–297.

Darwin, C. (1881). *The Formation of Vegetable Mould: Through the Action of Worms, with Observations on Their Habits*: London John Murray Press.

Davidson, A. D., Lightfoot, D. C., and McIntyre, J. L. (2008). Engineering Rodents Create Key Habitat for Lizards. *J. Arid Environ.* 72, 2142–2149. doi:10.1016/j.jaridenv.2008.07.006

Dietrich, W. E., and Perron, J. T. (2006). The Search for a Topographic Signature of Life. *Nature* 439, 411–418. doi:10.1038/nature04452

Dietrich, W. E., Bellugi, D. G., Sklar, L. S., Stock, J. D., Heimsath, A. M., and Roering, J. J. (2003). Geomorphic Transport Laws for Predicting Landscape Form and Dynamics. *Geophys. Monogr. Geophys. Union.* 135, 103–132. doi:10.1029/135GM09

Escapa, M., Minkoff, D. R., Perillo, G. M. E., and Iribarne, O. (2007). Direct and Indirect Effects of Burrowing Crab Chasmagnathus Granulatus Activities on Erosion of Southwest Atlantic Sarcocornia -dominated Marshes. *Limnol. Oceanogr.* 52, 2340–2349. doi:10.4319/lo.2007.52.6.2340

Faulkner, H. (2006). "Piping hazard on collapsible and dispersive soils in Europe," in *Soil Erosion in Europe*. Editors J. Boardman and J. Poesen (Hoboken: John Wiley and Sons, Ltd Press), 537–562.

Feng, X., and Wang, S. (2012). Influence of Different Weather Events on Concentrations of Particulate Matter with Different Sizes in Lanzhou, China. *J. Environ. Sci.* 24, 665–674. doi:10.1016/S1001-0742(11)60807-3

Feng, X., Fu, B., Piao, S., Wang, S., Ciais, P., Zeng, Z., et al. (2016). Revegetation in China's Loess Plateau Is Approaching Sustainable Water Resource Limits. *Nat. Clim Change.* 6, 1019–1022. doi:10.1038/nclimate3092

Feng, L., Zhang, M., Jin, Z., Zhang, S., Sun, P., Gu, T., et al. (2021). The Genesis, Development, and Evolution of Original Vertical Joints in Loess. *Earth-Sci. Rev.* 214, 103526. doi:10.1016/j.earscirev.2021.103526

Forsman, J. T., and Martin, T. E. (2009). Habitat Selection for Parasite-free Space by Hosts of Parasitic Cowbirds. *Oikos* 118, 464–470. doi:10.1111/j.1600-0706.2008.17000.x

Fox, D. M., Bryan, R. B., and Price, A. G. (1997). The Influence of Slope Angle on Final Infiltration Rate for Interrill Conditions. *Geoderma* 80, 181–194. doi:10.1016/S0016-7061(97)00075-X

Fremier, A. K., Yanites, B. J., and Yager, E. M. (2018). Sex that Moves Mountains: The Influence of Spawning Fish on River Profiles over Geologic Timescales. *Geomorphology* 305, 163–172. doi:10.1016/j.geomorph.2017.09.033

Gabet, E. J., Reichman, O. J., and Seabloom, E. W. (2003). The Effects of Bioturbation on Soil Processes and Sediment Transport. *Annu. Rev. Earth Planet. Sci.* 31, 249–273. doi:10.1146/annurev.earth.31.100901.141314

Gabet, E. J. (2000). Gopher Bioturbation: Field Evidence for Non-linear Hillslope Diffusion. *Earth Surf. Process. Landforms* 25, 1419–1428. doi:10.1002/1096-9837(200012)25:13<1419:aid-esp148>3.0.co;2-1

Garland, G., and Humphrey, B. (1992). Field Measurements of Discharge and Sediment Yield from a Soil Pipe in the Natal Drakensberg, South Africa. *zfg* 36, 15–23. doi:10.1127/zfg/36/1992/15

Geng, H., Pan, B., Milledge, D. G., Huang, B., and Zhang, G. (2015). Quantifying Sheet Wash Erosion Rates in a Mountainous Semi-arid basin Using Environmental Radionuclides and a Stream Power Model. *Earth Surf. Process. Landforms* 40, 1814–1826. doi:10.1002/esp.3761

Germain, D., Ianăș, A.-N., and Voiculescu, M. (2021). Sediment Transport by the Burrowing Activity of Snow Vole (Chionomys Nivalis) in Subalpine Prairies of the Parâng Mountains (Romania): Quantitative Modelling and Methodological Perspectives. *Geomorphology* 374, 107519. doi:10.1016/j.geomorph.2020.107519

Gilbert, G. K. (1909). The Convexity of Hilltops. *J. Geol.* 17, 344–350. doi:10.1086/621620

Got, J. B., Bielders, C. L., and Lambot, S. (2020). Characterizing Soil Piping Networks in Loess-derived Soils Using Ground-penetrating Radar. *Vadose Zone J.* 19, e20006. doi:10.1002/vzj2.20006

Guo, B., Peng, T., Yu, H., Hui, Z., Ma, Z., Li, X., et al. (2020). Magnetostratigraphy and Palaeoclimatic Significance of the Late Pliocene Red Clay-Quaternary Loess Sequence in the Lanzhou Basin, Western Chinese Loess Plateau. *Geophys. Res. Lett.* 47, 1–10. doi:10.1029/2019GL086556

Hall, K., and Lamont, N. (2003). Zoogeomorphology in the Alpine: Some Observations on Abiotic-Biotic Interactions. *Geomorphology* 55, 219–234. doi:10.1016/S0169-555X(03)00141-7

Hall, K., Boelhouwers, J., and Driscoll, K. (1999). Animals as Erosion Agents in the alpine Zone: Some Data and Observations from Canada, Lesotho, and Tibet. *Arctic, Antarctic, Alp. Res.* 31, 436–446. doi:10.1080/15230430.1999.12003328

Harvey, G. L., Henshaw, A. J., Brasington, J., and England, J. (2019). Burrowing Invasive Species: An Unquantified Erosion Risk at the Aquatic-Terrestrial Interface. *Rev. Geophys.* 57, 1018–1036. doi:10.1029/2018RG000635

Heffner, H., and Masterton, B. (1980). Hearing in Glires: Domestic Rabbit, Cotton Rat, Feral House Mouse, and Kangaroo Rat. *The J. Acoust. Soc. Am.* 68, 1584–1599. doi:10.1121/1.385213

Heimsath, A. M., E. Dietrich, W. W., Nishiizumi, K., and Finkel, R. C. (1999). Cosmogenic Nuclides, Topography, and the Spatial Variation of Soil Depth. *Geomorphology* 27, 151–172. doi:10.1016/S0169-555X(98)00095-6

Hessel, R., and Van Asch, T. (2003). Modelling Gully Erosion for a Small Catchment on the Chinese Loess Plateau. *Catena* 54, 131–146. doi:10.1016/S0341-8162(03)00061-4

Hu, W., Shao, M. A., and Si, B. C. (2012). Seasonal Changes in Surface Bulk Density and Saturated Hydraulic Conductivity of Natural Landscapes. *Eur. J. Soil Sci.* 63, 820–830. doi:10.1111/j.1365-2389.2012.01479.x

Hu, S., Qiu, H., Wang, N., Cui, Y., Wang, J., Wang, X., et al. (2020). The Influence of Loess Cave Development upon Landslides and Geomorphologic Evolution: A Case Study from the Northwest Loess Plateau, China. *Geomorphology* 359, 107167. doi:10.1016/j.geomorph.2020.107167

Huntly, N., and Inouye, R. (1988). Pocket Gophers in Ecosystems: Patterns and Mechanisms. *BioScience* 38, 786–793. doi:10.2307/1310788

Jones, C. G., Lawton, J. H., and Shachak, M. (1994). "Organisms as Ecosystem Engineers," in *Ecosystem Management* (New York, NY: Springer), 130–147. doi:10.1007/978-1-4612-4018-1_14

Kirschvink, J. L. (2000). Earthquake Prediction by Animals: Evolution and Sensory Perception. *Bull. Seismol. Soc. Am.* 90, 312–323. doi:10.1785/0119980114

Krasnov, B. R., Shenbrot, G. I., Medvedev, S. G., Vatschenok, V. S., and Khokhlova, I. S. (1997). Host-habitat Relations as an Important Determinant of Spatial Distribution of Flea Assemblages (Siphonaptera) on Rodents in the Negev Desert. *Parasitology* 114, 159–173. doi:10.1017/S0031182096008347

Li, Q., and Wang, X. (2015). Into Tibet: An Early Pliocene Dispersal of Fossil Zokor (Rodentia: Spalacidae) from Mongolian Plateau to the Hinterland of Tibetan Plateau. *Plos One* 10, e0144993–18. doi:10.1371/journal.pone.0144993

Li, T., Jia, Y., Shao, M. a., and Shen, N. (2019a). Camponotus Japonicus Burrowing Activities Exacerbate Soil Erosion on Bare Slopes. *Geoderma* 348, 158–167. doi:10.1016/j.geoderma.2019.04.035

Li, X. A., Wang, L., Yan, Y., Hong, B., and Li, L. (2019b). Experimental Study on the Disintegration of Loess in the Loess Plateau of China. *Bull. Eng. Geol. Environ.* 78, 4907–4918. doi:10.1007/s10064-018-01434-6

Li, X. A., Wang, L., Hong, B., Li, L. C., Liu, J., and Lei, H. n. (2020). Erosion Characteristics of Loess Tunnels on the Loess Plateau: A Field Investigation and Experimental Study. *Earth Surf. Process. Landforms.* 45, 1945–1958. doi:10.1002/esp.4857

Lima, S. L., Valone, T. J., and Caraco, T. (1985). Foraging-efficiency-predation-risk Trade-Off in the Grey Squirrel. *Anim. Behav.* 33, 155–165. doi:10.1016/S0003-3472(85)80129-9

Lin, G. H., Cai, Z. Y., Zhang, T. Z., Su, J. P., and Thirgood, S. J. (2008). Genetic Diversity of the Subterranean Gansu Zokor in a Semi-natural Landscape. *J. Zoolog.* 275, 153–159. doi:10.1111/j.1469-7998.2008.00423.x

Lin, J., Fan, L., Han, Y., Guo, J., Hao, Z., Cao, L., et al. (2021). The mTORC1/eIF4E/HIF-1α Pathway Mediates Glycolysis to Support Brain Hypoxia Resistance in the Gansu Zokor, Eospalax Cansus. *Front. Physiol.* 12, 626240. doi:10.3389/fphys.2021.626240

Liu, T., and Zhang, Z. (1962). Loess in China (In Chinese). *Acta Geol. Sin.* 42 (1), 1–14.

Liu, T. (1985). *Loess and Environment*. Beijing: China Ocean Press, 1–481.

Miller, M. A. (1948). Seasonal Trends in Burrowing of Pocket Gophers (Thomomys). *J. Mammal.* 29, 38–44. doi:10.2307/1375279

Morris, D. W., Clark, R. G., and Boyce, M. S. (2008). Habitat and Habitat Selection: Theory, Tests, and Implications. *Isr. J. Ecol. Evol.* 54, 287–294. doi:10.1560/IJEE.54.310.1560/ijee.54.3-4.287

Nemati, F., Kolb, B., and Metz, G. A. (2013). Stress and Risk Avoidance by Exploring Rats: Implications for Stress Management in Fear-Related Behaviours. *Behav. Process.* 94, 89–98. doi:10.1016/j.beproc.2012.12.005

Peng, J., Sun, P., Igwe, O., and Li, X. A. (2018). Loess Caves, a Special Kind of Geo-hazard on Loess Plateau, Northwestern China. *Eng. Geol.* 236, 79–88. doi:10.1016/j.enggeo.2017.08.012

Pierson, T. C. (1983). Soil Pipes and Slope Stability. *Q. J. Eng. Geol. Hydrogeol.* 16, 1–11. doi:10.1144/gsl.qjeg.1983.016.01.01

Reichman, O. J., and Seabloom, E. W. (2002). The Role of Pocket Gophers as Subterranean Ecosystem Engineers. *Trends Ecol. Evol.* 17, 44–49. doi:10.1016/S0169-5347(01)02329-1

Roering, J. J., Kirchner, J. W., and Dietrich, W. E. (1999). Evidence for Nonlinear, Diffusive Sediment Transport on Hillslopes and Implications for Landscape Morphology. *Water Resour. Res.* 35, 853–870. doi:10.1029/1998WR900090

Rogasik, H., Schrader, S., Onasch, I., Kiesel, J., and Gerke, H. H. (2014). Micro-scale Dry Bulk Density Variation Around Earthworm (Lumbricus Terrestris L.) Burrows Based on X-ray Computed Tomography. *Geoderma* 213, 471–477. doi:10.1016/j.geoderma.2013.08.034

Sanders, H., Rice, S. P., and Wood, P. J. (2021). Signal Crayfish Burrowing, Bank Retreat and Sediment Supply to Rivers: A Biophysical Sediment Budget. *Earth Surf. Process. Landforms.* 46, 837–852. doi:10.1002/esp.5070

Seabloom, E. W., Reichman, O. J., and Gabet, E. J. (2000). The Effect of Hillslope Angle on Pocket Gopher (*Thomomys bottae*) Burrow Geometry. *Oecologia* 125, 26–34. doi:10.1007/PL00008888

Shi, H., and Shao, M. (2000). Soil and Water Loss from the Loess Plateau in China. *J. Arid Environ.* 45, 9–20. doi:10.1006/jare.1999.0618

Song, Y. C., Liu, Y., Lin, Y. Y., Liang, T., and Shi, L. (2017). Burrow Characteristics and Microhabitat Use of the Turpan Wonder Gecko Teratoscincus Roborowskii (Squamata, Gekkonidae). *Asian Herpetol. Res.* 8, 61–69. doi:10.16373/j.cnki.ahr.160028

Stallins, J. A. (2006). Geomorphology and Ecology: Unifying Themes for Complex Systems in Biogeomorphology. *Geomorphology* 77, 207–216. doi:10.1016/j.geomorph.2006.01.005

Su, J., Wang, J., Hua, L., Gleeson, D., and Ji, W. (2013). Complete Mitochondrial Genome of the Gansu zokor,Eospalax cansus(Rodentia, Spalacidae). *Mitochondrial DNA* 24, 651–653. doi:10.3109/19401736.2013.772166

Su, J., Ji, W., Li, H., Yao, T., Wang, J., and Nan, Z. (2020). Zokor Disturbances Indicated Positive Soil Microbial Responses with Carbon Cycle and mineral Encrustation in alpine Grassland. *Ecol. Eng.* 144, 105702. doi:10.1016/j.ecoleng.2019.105702

Sui, D.-D., Wu, J.-L., Zhang, H., Li, H., Zhou, Z.-M., Zhang, D.-H., et al. (2014). Molecular Cloning, Structural Analysis, and Expression of Zona Pellucida Glycoprotein ZP3 Gene from Chinese Zokor, Myospalax Fontanierii. *Mol. Biol.* 48, 646–654. doi:10.1134/S0026893314050148

Verachtert, E., Van Den Eeckhaut, M., Poesen, J., and Deckers, J. (2010). Factors Controlling the Spatial Distribution of Soil Piping Erosion on Loess-Derived Soils: A Case Study from central Belgium. *Geomorphology* 118, 339–348. doi:10.1016/j.geomorph.2010.02.001

Verachtert, E., Van Den Eeckhaut, M., Poesen, J., and Deckers, J. (2013). Spatial Interaction between Collapsed Pipes and Landslides in Hilly Regions with Loess-Derived Soils. *Earth Surf. Process. Landforms.* 38, 826–835. doi:10.1002/esp.3325

Vleck, D. (1981). Burrow Structure and Foraging Costs in the Fossorial Rodent, *Thomomys bottae*. *Oecologia* 49, 391–396. doi:10.1007/BF00347605

Voiculescu, M., Ianăş, A.-N., and Germain, D. (2019). Exploring the Impact of Snow Vole (Chionomys Nivalis) Burrowing Activity in the Făgăraş Mountains, Southern Carpathians (Romania): Geomorphic Characteristics and Sediment Budget. *Catena* 181, 104070. doi:10.1016/j.catena.2019.05.016

Voigt, C. (2014). An Example of Burrow System Architecture of Dispersing Damaraland Mole-Rats. *Afr. Zoolog.* 49, 148–152. doi:10.1080/15627020.2014.11407627

Wang, T., Wu, J., Kou, X., Oliver, C., Mou, P., and Ge, J. (2010). Ecologically Asynchronous Agricultural Practice Erodes Sustainability of the Loess Plateau of China. *Ecol. Appl.* 20, 1126–1135. doi:10.1890/09-0229.1

Wang, L., Li, X.-A., Li, L.-C., Hong, B., and Liu, J. (2019). Experimental Study on the Physical Modeling of Loess Tunnel-Erosion Rate. *Bull. Eng. Geol. Environ.* 78, 5827–5840. doi:10.1007/s10064-019-01495-1

Wilson, G. V., Rigby, J. R., and Dabney, S. M. (2015). Soil Pipe Collapses in a Loess Pasture of Goodwin Creek Watershed, Mississippi: Role of Soil Properties and Past Land Use. *Earth Surf. Process. Landforms* 40, 1448–1463. doi:10.1002/esp.3727

Winchell, E. W., Anderson, R. S., Lombardi, E. M., and Doak, D. F. (2016). Gophers as Geomorphic Agents in the Colorado Front Range Subalpine Zone. *Geomorphology* 264, 41–51. doi:10.1016/j.geomorph.2016.04.003

Wu, L., Jiang, J., Li, G.-x., and Ma, X.-y. (2018). Characteristics of Pulsed Runoff-Erosion Events under Typical Rainstorms in a Small Watershed on the Loess Plateau of China. *Sci. Rep.* 8, 1–12. doi:10.1038/s41598-018-22045-x

Xu, J. (1999). Erosion Caused by Hyperconcentrated Flow on the Loess Plateau of China. *Catena* 36, 1–19. doi:10.1016/S0341-8162(99)00009-0

Yoo, K., Amundson, R., Heimsath, A. M., and Dietrich, W. E. (2005). Process-Based Model Linking Pocket Gopher (*Thomomys bottae*) Activity to Sediment Transport and Soil Thickness. *Geology* 33, 917–920. doi:10.1130/G21831.1

Yu, C., Zhang, J., Pang, X. P., Wang, Q., Zhou, Y. P., and Guo, Z. G. (2017). Soil Disturbance and Disturbance Intensity: Response of Soil Nutrient Concentrations of alpine Meadow to Plateau Pika Bioturbation in the Qinghai-Tibetan Plateau, China. *Geoderma* 307, 98–106. doi:10.1016/j.geoderma.2017.07.041

Zaitlin, B., and Hayashi, M. (2012). Interactions between Soil Biota and the Effects on Geomorphological Features. *Geomorphology* 157-158, 142–152. doi:10.1016/j.geomorph.2011.07.029

Zhang, Y., Zhang, Z., and Liu, J. (2003). Burrowing Rodents as Ecosystem Engineers: The Ecology and Management of Plateau Zokors Myospalax Fontanierii in alpine Meadow Ecosystems on the Tibetan Plateau. *Mammal Rev.* 33, 284–294. doi:10.1046/j.1365-2907.2003.00020.x

Zhang, J., Li, J., Guo, B., Ma, Z., Li, X., Ye, X., et al. (2016). Magnetostratigraphic Age and Monsoonal Evolution Recorded by the Thickest Quaternary Loess deposit of the Lanzhou Region, Western Chinese Loess Plateau. *Quat. Sci. Rev.* 139, 17–29. doi:10.1016/j.quascirev.2016.02.025

Zhang, Y., Hu, Z., Li, L., and Xue, Z. (2018). Improving the Structure and Mechanical Properties of Loess by Acid Solutions - an Experimental Study. *Eng. Geol.* 244, 132–145. doi:10.1016/j.enggeo.2018.07.023

Zhang, X., Zou, Y., Nan, X., and Han, C. (2021). DNA Metabarcoding Uncover the Diet of Subterranean Rodents in China. *bioRxiv [Preprint]*. Available at: https://www.biorxiv.org/content/10.1101/2021.09.20.461124v1.full.(Accessed September 20, 2021).

Zhao, G., Mu, X., Wen, Z., Wang, F., and Gao, P. (2013). Soil Erosion, Conservation, and Eco-Environment Changes in the Loess Plateau of China. *Land Degrad. Develop.* 24, 499–510. doi:10.1002/ldr.2246

Zhao, J., Tian, L., Wei, H., Zhang, T., Bai, Y., Li, R., et al. (2021). Impact of Plateau Pika (Ochotona Curzoniae) Burrowing-Induced Microtopography on Ecosystem Respiration of the alpine Meadow and Steppe on the Tibetan Plateau. *Plant Soil* 458, 217–230. doi:10.1007/s11104-019-04122-w

Zhou, W. Y., and Dou, F. M. (1990). Studies on Activity and home Range of Plateau Zokor. *Aacta Theriol. Sin.* 10, 31–39. doi:10.16829/j.slxb.1990.01.00610.1016/0956-053x(90)90069-w

Zhou, X. R., Guo, Z. G., and Guo, X. H. (2010). The Role of Plateau Pika and Plateal Zokor in alpine Meadow. *Pratacultural ence* 27, 38–44. doi:10.3724/SP.J.1011.2010.01351

Zhu, T. X., Luk, S. H., and Cai, Q. G. (2002). Tunnel Erosion and Sediment Production in the Hilly Loess Region, North China. *J. Hydrol.* 257, 78–90. doi:10.1016/S0022-1694(01)00544-3

Zhu, T. X. (1997). Deep-seated., Complex Tunnel Systems - a Hydrological Study in a Semi-arid Catchment, Loess Plateau, China. *Geomorphology* 20, 255–267. doi:10.1016/s0169-555x(97)00027-5

Zhu, T. X. (2003). Tunnel Development over a 12 Year Period in a Semi-arid Catchment of the Loess Plateau, China. *Earth Surf. Process. Landforms.* 28, 507–525. doi:10.1002/esp.455

Zhu, T. X. (2006). Initiation and Development Processes of Tunnel Systems in the Hilly Loess Region of Northern China. *Int. J. Sediment. Res.* 21, 171–179. doi:10.3724/SP.J.1011.2010.01351

Zhu, T. X. (2012). Gully and Tunnel Erosion in the Hilly Loess Plateau Region, China. *Geomorphology* 153-154, 144–155. doi:10.1016/j.geomorph.2012.02.019

Zhuang, J.-q., and Peng, J.-b. (2014). A Coupled Slope Cutting-A Prolonged Rainfall-Induced Loess Landslide: a 17 October 2011 Case Study. *Bull. Eng. Geol. Environ.* 73, 997–1011. doi:10.1007/s10064-014-0645-1

Conflict of Interest: The authors declare that the research was conducted in the absence of any commercial or financial relationships that could be construed as a potential conflict of interest.

Publisher's Note: All claims expressed in this article are solely those of the authors and do not necessarily represent those of their affiliated organizations, or those of the publisher, the editors and the reviewers. Any product that may be evaluated in this article, or claim that may be made by its manufacturer, is not guaranteed or endorsed by the publisher.

frontiers in Earth Science

ORIGINAL RESEARCH
published: 24 December 2021
doi: 10.3389/feart.2021.801293

Precision Evaluation and Fusion of Topographic Data Based on UAVs and TLS Surveys of a Loess Landslide

Zhonglei Mao[1,2], *Sheng Hu*[1,2,3]*, *Ninglian Wang*[1,2,3]* *and Yongqing Long*[1,2]

[1]Shaanxi Key Laboratory of Earth Surface System and Environmental Carrying Capacity, Northwest University, Xi'an, China, [2]College of Urban and Environmental Sciences, Northwest University, Xi'an, China, [3]Institute of Earth Surface System and Hazards, Northwest University, Xi'an, China

In recent years, low-cost unmanned aerial vehicles (UAVs) photogrammetry and terrestrial laser scanner (TLS) techniques have become very important non-contact measurement methods for obtaining topographic data about landslides. However, owing to the differences in the types of UAVs and whether the ground control points (GCPs) are set in the measurement, the obtained topographic data for landslides often have large precision differences. In this study, two types of UAVs (DJI Mavic Pro and DJI Phantom 4 RTK) with and without GCPs were used to survey a loess landslide. UAVs point clouds and digital surface model (DSM) data for the landslide were obtained. Based on this, we used the Geomorphic Change Detection software (GCD 7.0) and the Multiscale Model-To-Model Cloud Comparison (M3C2) algorithm in the Cloud Compare software for comparative analysis and accuracy evaluation of the different point clouds and DSM data obtained using the same and different UAVs. The experimental results show that the DJI Phantom 4 RTK obtained the highest accuracy landslide terrain data when the GCPs were set. In addition, we also used the Maptek I-Site 8,820 terrestrial laser scanner to obtain higher precision topographic point cloud data for the Beiguo landslide. However, owing to the terrain limitations, some of the point cloud data were missing in the blind area of the TLS measurement. To make up for the scanning defect of the TLS, we used the iterative closest point (ICP) algorithm in the Cloud Compare software to conduct data fusion between the point clouds obtained using the DJI Phantom 4 RTK with GCPs and the point clouds obtained using TLS. The results demonstrate that after the data fusion, the point clouds not only retained the high-precision characteristics of the original point clouds of the TLS, but also filled in the blind area of the TLS data. This study introduces a novel perspective and technical scheme for the precision evaluation of UAVs surveys and the fusion of point clouds data based on different sensors in geological hazard surveys.

Keywords: UAVs photogrammetry, TLS survey, precision evaluation, point clouds fusion, loess landslide

OPEN ACCESS

Edited by:
Fanyu Zhang,
Lanzhou University, China

Reviewed by:
Weile Li,
Chengdu University of Technology, China
Qingkai Meng,
Qinghai University, China

***Correspondence:**
Sheng Hu
shenghu@nwu.edu.cn
Ninglian Wang
nlwang@nwu.edu.cn

Specialty section:
This article was submitted to Geohazards and Georisks, a section of the journal Frontiers in Earth Science

Received: *25 October 2021*
Accepted: *30 November 2021*
Published: *24 December 2021*

Citation:
Mao Z, Hu S, Wang N and Long Y (2021) Precision Evaluation and Fusion of Topographic Data Based on UAVs and TLS Surveys of a Loess Landslide. Front. Earth Sci. 9:801293. doi: 10.3389/feart.2021.801293

1 INTRODUCTION

Landslides are an extensively studied natural phenomenon, and they can sometimes cause serious economic losses and casualties (Lindner et al., 2015; Peppa et al., 2017; Hu et al., 2018; Godone et al., 2020; Zhang et al., 2021). With the rapid development of measurement techniques, the use of non-contact measurement methods (e.g., unmanned aerial vehicles (UAVs), interferometric synthetic

aperture radar (InSAR), and terrestrial laser scanner (TLS) to obtain high spatial resolution landslide terrain data has become a common task in many research and engineering applications (Kowalski, 2018; Carey et al., 2019; Ji and Luo, 2019; Li et al., 2019). In practical applications, the data are often required to have a spatial density and measurement accuracy of millimeters or centimeters (Zang et al., 2019; Samodra et al., 2020; Yan et al., 2021). The two most commonly used remote sensing methods used for this fine three-dimensional (3D) mapping are the TLS and UAVs methods (Mancini et al., 2013; Neugirg et al., 2016; Chatzistamatis et al., 2018; Guisado-Pintado et al., 2019). The former uses active laser emission to record the 3D coordinates and reflectivity of the scanned object, with a sub-centimeter level accuracy (Neugirg et al., 2016; Brede et al., 2019; Sasak et al., 2019; Wijesingha et al., 2019). The latter is a digital photogrammetry technique based on the Structure-to-Motion (SfM) algorithm; a UAVs is usually used as the sensor platform, and it has a centimeter level accuracy (Yu et al., 2017; Galvan Rangel et al., 2018; Lee and Min, 2018; Jaud et al., 2020; Yang et al., 2021). The TLS and UAVs methods are widely used in landslide monitoring and disaster assessment and play an important role in natural disaster research (Ma et al., 2018; Hu et al., 2019; Hu et al., 2020; Stringer et al., 2021). For example, Carey et al. (2019) used a global positioning system (GPS)-supported drone to obtain aerial images of the upper Scenic Drive landslide over 2 days and used the images to generate a digital elevation model (DEM) with a high spatial resolution (3–10 cm/pixel). Godone et al. (2020) resumed monitoring of farmland, houses, and infrastructure through UAVs flights and assessed the remaining risks caused by large-scale landslides. Hendrickx et al. (2020) used the UAVs and TLS methods to survey a talus slope on the Col du Sanetsch (Swiss Alps) for three consecutive summers and successfully detected debris flows, snow push, and rill erosion.

Although multisource surveying and mapping techniques provide a wealth of surveying and mapping data, there may also be problems such as missing data and a low spatial resolution (Martinez-Carricondo et al., 2018; Medjkane et al., 2018; Bakirman et al., 2020). For example, the quality of the images produced by different types of UAVs will vary greatly due to differences in their performances, their flight modes, the weather conditions, and the layout of their ground control points (GCPs) (Zhang et al., 2018; Lee et al., 2019; Aguera-Vega et al., 2020). The TLS has a fixed scanning angle, and there may be mutual occlusion phenomena in the research area, so the finally obtained point clouds data contain data shadows (Pellicani et al., 2019; Kamnik et al., 2020; Tsunetaka et al., 2020). Owing to the different types of data, data obtained using multiple measurement techniques results in data fusion problems (Saponaro et al., 2019; Feng et al., 2020; Rechberger et al., 2021). Several studies have used separate UAVs and TLS methods for topographic mapping (Rossi et al., 2018; Ouyang et al., 2019; Carrera-Hernandez et al., 2020; Ferrer-Gonzalez et al., 2020; Qu et al., 2021), to evaluate the accuracy of the point clouds generated by TLS and UAVs (Zhou et al., 2020; Senkal et al., 2021), and to evaluate the accuracy of digital surface models (DSMs) and digital elevation models (DEMs) generated using point clouds (Rogers et al., 2020; Xu et al., 2020; Liu et al., 2021). In terms of landslide terrain, few researchers have considered the integration of UAVs-SfM and TLS point clouds, and the accuracy of the fusion of the point clouds has not been evaluated.

In this study, the Beiguo landslide in Heyang County, Loess Plateau, China was taken as an example, and the UVA and TLS methods were used to map the landslide topography. The landslide topography data were obtained by designing different UAVs mapping schemes, i.e., using different UAVs models in the photogrammetry operations using or not using GCPs during modeling. Geomorphic Change Detection Software (GCD 7.0) and Cloud Compare Software were used to evaluate the point clouds and the DSM accuracy of the different schemes. Finally, we used the iterative closest point (ICP) algorithm to fuse the TLS point clouds with the UAVs point clouds. The goals of this research are as follows: 1) We quantify the differences in the DSMs produced using different UAVs with or without GCPs, and evaluate the accuracy of the point clouds and the DSM data acquired using different sensor and mapping schemes 2) Owing to the influence of the elevation differences, shadow, and other factors, the point clouds obtained using UAVs photogrammetry sometimes have a large error. The point clouds obtained using TLS have a very high accuracy, but there are blind areas in the field of vision. We fuse their point clouds data to overcome their shortcomings and to improve the accuracy of the point clouds. 3) We hope the results of this study can provide a reference for other researchers conducting UAVs and TLS surveys and data processing.

2 STUDY AREA

China has the most extensive loess distribution in the world. A continuous loess layer covers the middle reaches of the Yellow River, forming the ravine Loess Plateau (Hu et al., 2018; Hu et al., 2020; Li et al., 2021). The landslide investigated in this study is located on the west bank of the Yellow River in Beiguo Village, Heyang County, Shaanxi Province, China, on the southeastern part of the tableland (**Figure 1**). The study area has an arid and semiarid continental monsoon climate and is located in the warm temperate zone, with an average annual precipitation of 556.7 mm, which is concentrated between July and September. According to field surveys, the Beiguo landslide is a resurrected loess landslide caused by continuous rainfall. It has a continuous sedimentary loess layer and has been affected by the Quaternary Neotectonic Movement. The vertical uplift and subsidence are very obvious. According to historical satellite images, before 2017, several small-scale landslides and collapse events occurred in and around the landslide of interest, and the landslide was in an unstable state. The largest landslide occurred in the winter of 2017. This new landslide had a maximum width of 365 m and a maximum length of 267 m, covering an area of 72,000 m^2, with a total accumulation of 326,923 (±9,862) m^3. Readers can scan the QR code in **Figure 1B** or click on the link below (https://720yun.com/t/03vkObqh72q#scene_id=58455158) to view a 3D panorama of the Beiguo landslide.

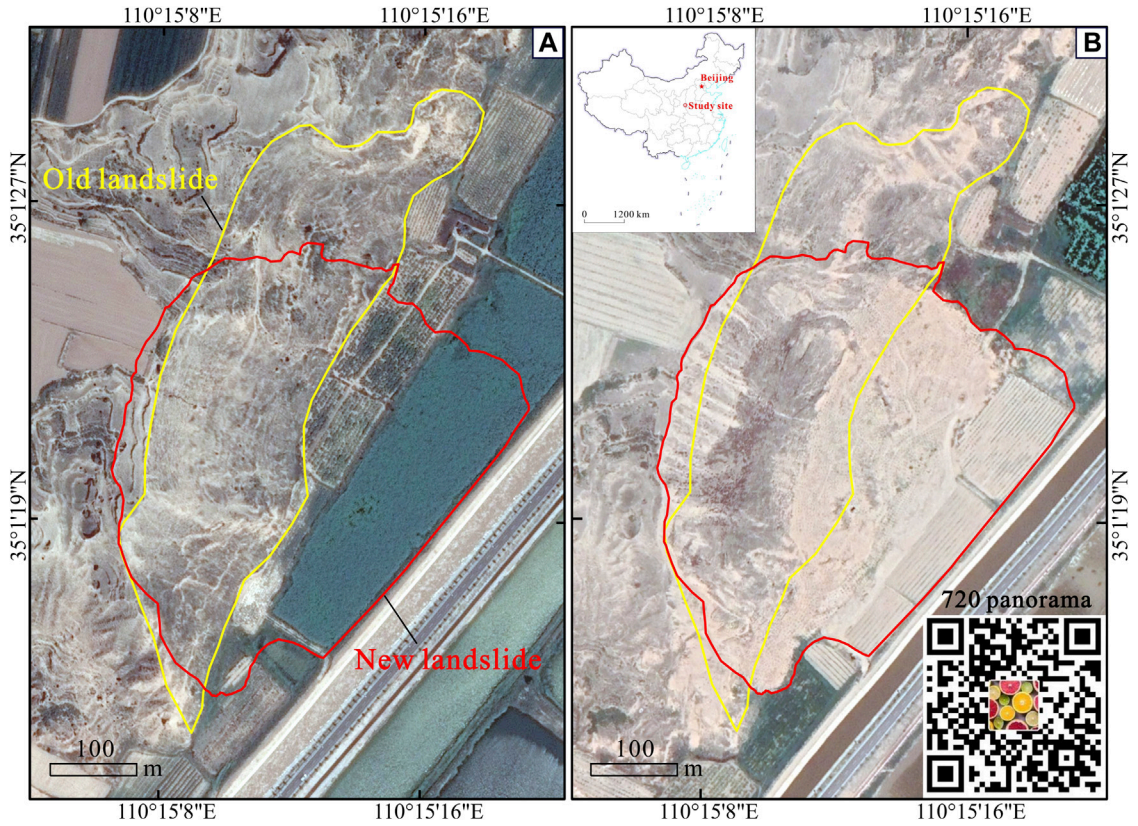

FIGURE 1 | Overview of the study area: **(A)** Image before sliding, **(B)** Image after sliding.

TABLE 1 | UAVs specification.

Parameters	Mavic pro UAVs	Phantom 4 RTK UAVs
Overview		
Dimension (cm)	19.8 × 8.3 × 8.3	25.0 × 25.0 × 24.0
Weight (g)	734	1,391
Max flight time (min)	27	30
Sensor (CMOS)	1/2.3″	1″
Effective pixels (MP)	12.35	20
Equivalent focus (mm)	23	35
GNSS	GPS + GLONASS	GPS + GLONASS + Galileo
GNSS vertical accuracy (m)	±0.5	±0.1
GNSS horizontal accuracy (m)	±1.5	±0.1
Cost ($)	~1,200	~4,000

3 DATA SOURCES AND METHODOLOGY

3.1 Measurement Equipment

In this study, two consumer-grade UAVs (**Table 1**), a DJI Mavic Pro and a DJI Phantom 4 RTK, were used for low-altitude observations to obtain multitemporal images and terrain data after the landslides occurred (http://developer.dji.com/products/). The detailed specifications of the UAVs are described in **Table 1**. This type of drone was chosen because of its flexibility, real-time monitoring, and low cost. First, the two drones were equipped with small digital cameras to obtain images of the landslide and surface information. Then, based on the principles of computer vision and

TABLE 2 | TLS specification.

Parameters	Maptek I-Site 8,820
Overview	
Dimension (cm)	44.5 × 24.6 × 37.8
Weight (kg)	12
Max measuring range (m)	>2000
Min measuring range (m)	2.5
Range accuracy (mm)	6 mm at 100 m
Laser divergence angle (m rad)	0.25
Acquisition frequency (kHz)	80, 40
Angle measurement range (°)	360° horizontal, 80° vertical
Wavelength	Near infrared

low-altitude auxiliary flight control data, three-dimensional modeling of the landslide terrain was conducted using the image topology relationship (Hu et al., 2018; Ma et al., 2018; Lamsters et al., 2020; Ma et al., 2021). By generating three-dimensional point clouds data containing color information, the spatial distribution characteristics and local detailed structure of the landslide were visually expressed, and a landslide DSM was established (Lindner et al., 2015; Kowalski, 2018; Cheng et al., 2021).

A Maptek I-Site 8820 TLS (**Table 2**) was used to scan the ground point clouds. This instrument is a rear-view oriented remote laser scanner, with a maximum measurement distance of 2000 m and a measurement accuracy of 6 mm. This type of 3D laser scanner was chosen because it has the advantages of fast data collection, non-contact, high precision, and direct collection of 3D landslide surface data (Medjkane et al., 2018; Brede et al., 2019; Zang et al., 2019; Senkal et al., 2021). The system mainly uses a grid method to scan the data, which is characterized by a high precision, high density, high speed, and no prism (Zang et al., 2019; Kamnik et al., 2020; Rechberger et al., 2021).

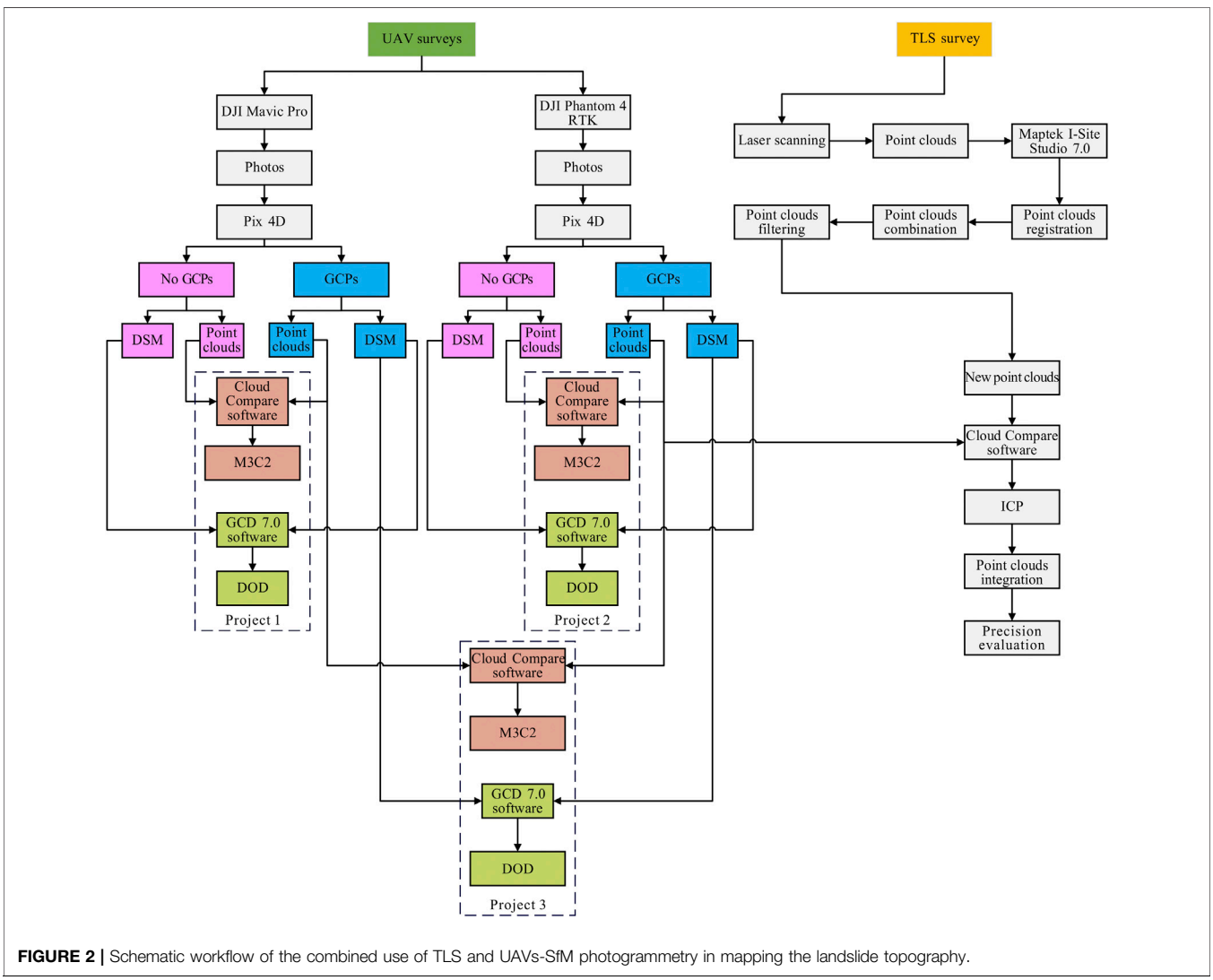

FIGURE 2 | Schematic workflow of the combined use of TLS and UAVs-SfM photogrammetry in mapping the landslide topography.

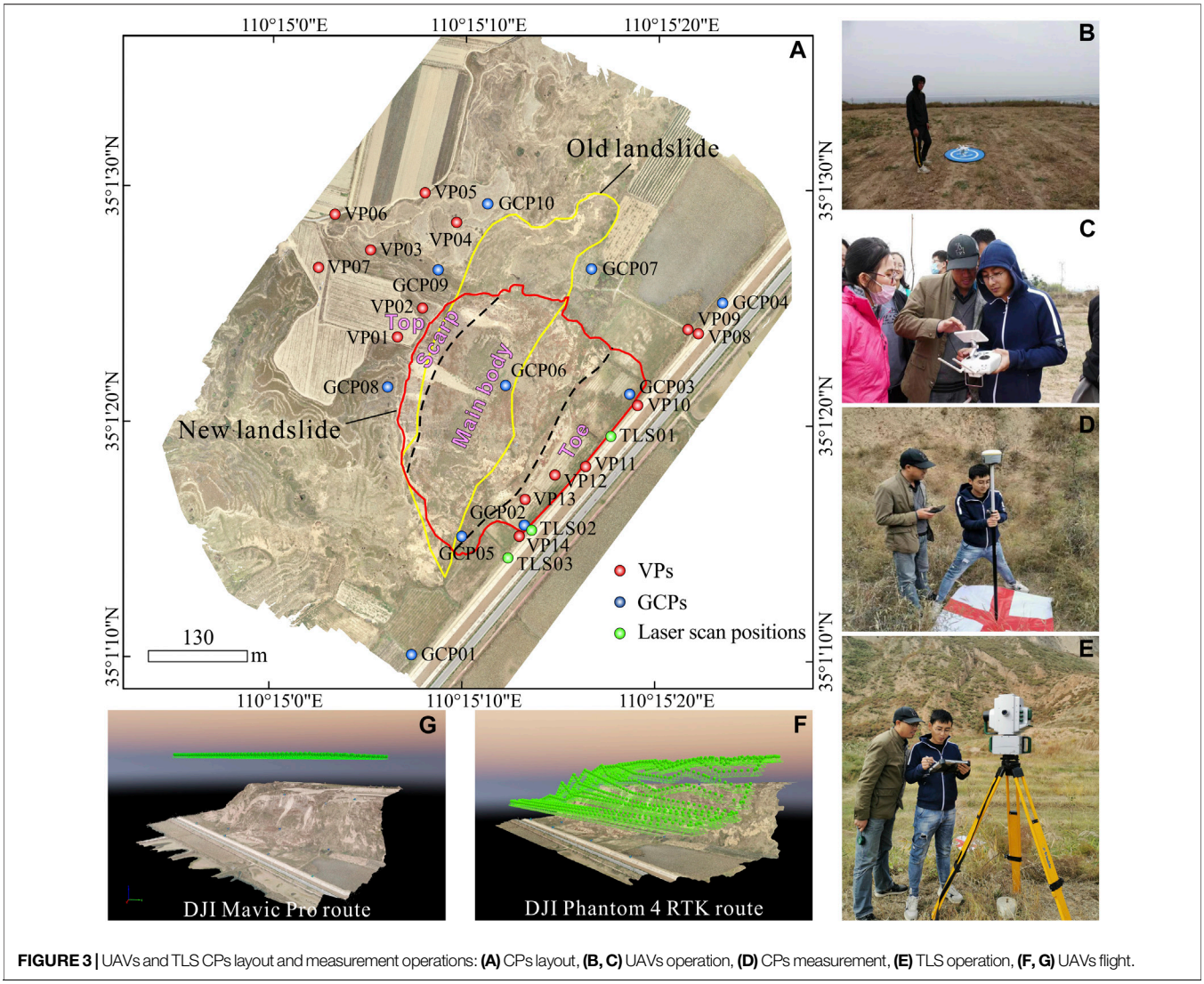

FIGURE 3 | UAVs and TLS CPs layout and measurement operations: **(A)** CPs layout, **(B, C)** UAVs operation, **(D)** CPs measurement, **(E)** TLS operation, **(F, G)** UAVs flight.

3.2 Workflow

Owing to the important role of GCPs in UAVs surveys and TLS surveys (Mancini et al., 2013; Galvan Rangel et al., 2018; Lee and Min, 2018; Zang et al., 2019), first we conducted field surveys around the study area and evenly arranged 24 control points (CPs). Subsequently, the two DJI consumer drones were used to conduct flight operations in the research area, and the accuracy was evaluated with and without GCPs. In terms of the TLS, a series of preprocessing steps, including filtering and splicing of the obtained point clouds data, were conducted, and the processed point clouds were fused with the DJI Phantom 4 RTK (with GCPs) point clouds data. Finally, the accuracies of the point clouds before and after the fusion were evaluated using the Cloud Compare software. The complete workflow is shown in **Figure 2**.

3.3 Field Work

3.3.1 UAVs Survey

GCPs and verification points (VPs) are necessary for high-precision topographic mapping because GCPs play a fundamental role in the workflow (Martinez-Carricondo et al., 2018; Aguera-Vega et al., 2020; Carrera-Hernandez et al., 2020). Therefore, we used real-time kinematic (RTK) positioning technology to accurately measure the coordinates of the 24 deployed CPs when operating the drone in the research area. According to the actual terrain, first we sat up a total of 10 GCPs (GCP 01–GCP 10) and 14 VPs (VP 01–VP 14) on the landslide and its surrounding areas. We created a Qianxun positioning service account, set the base station parameters, and finally measured the coordinates (**Figure 3D**). It should be noted that the horizontal error of the Qianxun's position is 2 cm, and the vertical error is 5 cm.

The UAVs was flown at 15:00 (Beijing time) on October 24, 2020, when the weather conditions were good and were suitable for UAVs operations. The DJI GS Pro professional software was used to create flight missions for the UAVs, and a total of 12 routes were designed. In all of the automated grid tasks, the drone's flight routes were straight lines. The course overlap rate was set to 90%, and the side overlap rate was set to 70%. The camera shooting mode selected was time-lapse shooting, the flying altitude was set to 150 m, the fixed altitude flight mode was selected for the DJI Mavic Pro UAVs, and the ground-like flight mode was selected for the DJI Phantom 4 RTK. The flight routes

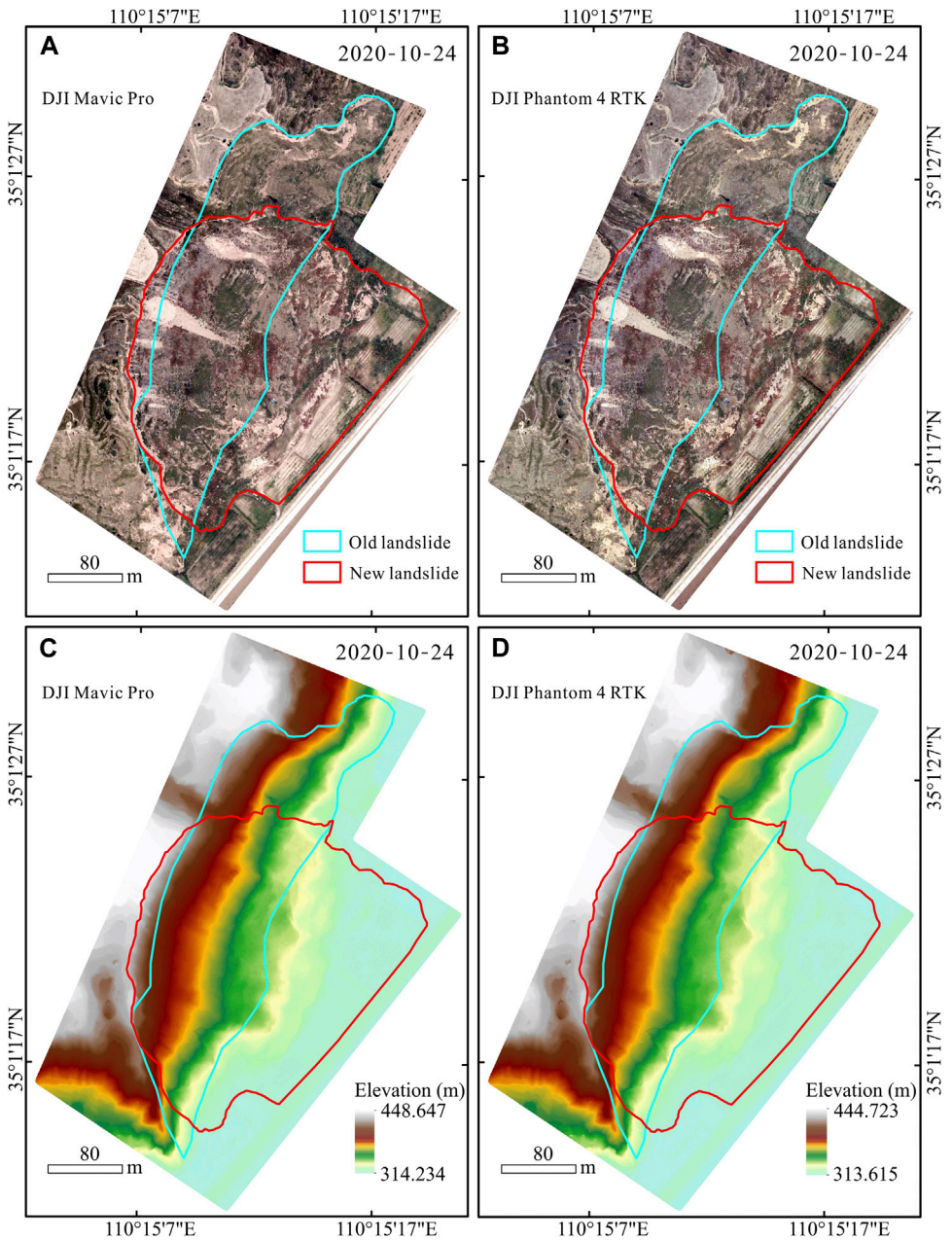

FIGURE 4 | DOM and DSM of DJI Mavic Pro UAVs and DJI Phantom 4 RTK UAVs: **(A, C)** are the DOM and DSM generated by DJI Mavic Pro UAVs, **(B, D)** are the DOM and DSM generated by DJI Phantom 4 RTK UAVs respectively.

of the DJI Mavic Pro UAVs and DJI Phantom 4 RTK UAVs are shown in **Figure 3G**. It should be noted that the ground-like flight mode can maintain a constant distance between the UAVs and the target object, adapt to different terrain, automatically generate a higher route according to the terrain of the survey area, and keep the ground resolution consistent to obtain better data effects.

3.3.2 TLS Survey

In TLS measurements, it is important to establish an optimal scanner position distribution to completely cover the three-dimensional space or object to be scanned (Neugirg et al., 2016; Kowalski, 2018; Medjkane et al., 2018; Rechberger et al., 2021). The ruggedness and accessibility of the terrain were considered when selecting the continuous position of the scanner to eliminate possible data shadows and ensure that the point clouds of two adjacent positions had enough space to overlap. The scanning position was set on the lower part of the landslide, close to the flat area of the road, to ensure that some of the GCPs could be seen by the TLS at each scanning position (**Figure 3A**). We installed a Maptek I-Site 8820 TLS on a tripod and then placed the leveled instruments at TLS01,

TLS02, and TLS03 to collect the point clouds data. The scanning time for each measuring station was about 7–8 min. The entire survey took about 40 min.

3.4 Data Processing and Accuracy Assessment

3.4.1 UAVs Data Preprocessing

The DJI Mavic Pro UAVs and DJI Phantom 4 RTK UAVs were used to obtain 735 and 813 images of the study area, respectively. We processed the images using the Pix4D mapper professional software, and used the SfM to complete the construction of the three-dimensional landslide model with and without GCPs. The main processing step of the Pix4D mapper includes preliminary processing, air triple encryption, and the generation of a DSM and digital orthophoto map (DOM). The specific process is as follows: 1) add photos; 2) determine the internal orientation elements and calibrate the camera; 3) search and match points with the same name using the scale-invariant feature transform (SIFT) algorithm; 4) use the same name points and the location information of the image for regional network leveling and calculate the difference to restore the position and posture of the image; 5) use the CPs or matching points for the air triple encryption to generate image point clouds; and 6) generate a DSM and DOM from the image point clouds. **Figure 4** shows the DOM and DSM generated using the two UAVs when the GCPs were added. The left side of **Figure 4** is the product generated using the DJI Mavic Pro UAVs, and the right side is the product generated using the DJI Phantom 4 RTK UAVs.

3.4.2 TLS Point Clouds Data Preprocessing

The raw laser point clouds data were processed using the Maptek I-Site Studio 7.0 software. First, the single point clouds obtained at each scanning position were assigned red-green-blue (RGB) values that represent natural colors. Then, we performed the preprocessing operations on the laser point clouds, including adding geo-references, registering the individual point clouds at different scanning positions; filtering the vegetation, terrain, and isolated points; and diluting the point clouds. Finally, we exported the processed point clouds data for use in the next step of the point clouds data fusion.

3.4.3 UAVs and TLS Point Cloud Data Fusion Method

The point clouds registration step mainly included two steps: rough registration and precise registration. Since different point clouds are relative to their respective coordinate systems, spatial offsets may occur. Therefore, integrating the point clouds into the correct position in the required coordinate system is referred to as rough registration. This step is also convenient for rough registration. The same point of spatial overlap in subsequent operations is quickly identified. The precise registration involves using the ICP algorithm to minimize the 3D distance between the polydata points by translating and/or rotating the entire point clouds along the X, Y, and *Z* axes until it reaches as far as possible between the polydata points (Xu et al., 2014; Du et al., 2015; Sasak et al., 2019). Finally, fusion of the point clouds data is achieved by setting the number of iterations, root mean square error, and overlap of the ICP algorithm.

The ICP algorithm checks the distance between all of the points in the point clouds and aligns the clouds with each other by extracting the features in the overlapping area of each cloud to obtain the smallest error (Sasak et al., 2019; Tsunetaka et al., 2020). It should be noted that owing to the heterogeneity of the UAVs and TLS point clouds data, the point clouds data need to be standardized before fusion, that is, the format is synonymously converted to the. las format.

3.4.4 Accuracy Assessment Method

ArcGIS 10.5, GCD 7.0, and Cloud Compare v2.11.2 were used to evaluate the accuracy of the mapping of the landslide topography. It should be noted that since the acquired data came from different data sources, spatial calibration, projection transformation, and elevation datum registration needed to be performed on the data. To accurately quantify the erosion phenomenon, we used the most popular GCD 7.0 to distinguish the noise information in the DSM, and we performed DSM uncertainty analysis on the real geomorphological changes. Therefore, the detection results are reliable.

In addition, to calculate the difference between the reference point clouds and the comparison point clouds relative to the local surface normal direction, we used the multiscale model-to-model clouds comparison (M3C2) algorithm in the Cloud Compare v2.11.2 software. This algorithm uses a set of core points to calculate the distance between and confidence interval of the points (Martinez-Carricondo et al., 2018; Ferrer-Gonzalez et al., 2020). The software operation steps are as follows. First, evaluate the density of each point clouds using the density tool in the "Calculate Geometric Features" drop-down menu to verify whether the two clouds can guarantee a uniform and similar distribution of the information. Then, set an appropriate clouds search radius and search height to ensure that the distance between the two point clouds is correctly evaluated. Finally, use different colors to express the positive and negative differences. In this process, the M3C2 algorithm provides a scalar field in which the distribution of these distances is expressed, which is the index of the M3C2 algorithm. It is an effective method for calculating the distance of a 3D point clouds. Currently, this algorithm is rarely used (Martinez-Carricondo et al., 2018; Ferrer-Gonzalez et al., 2020).

The GCD 7.0 software can be downloaded at http://gcd.riverscapes.xyz/. Cloud Compare v2.11.2 is a free open source software, which can be downloaded at http://cloudcompare.org/.

4 RESULTS

4.1 Accuracy Assessment of UAVs Terrain Data

To evaluate the impact of the GCPs on the different types of UAVs, we sat up three testing schemes—Project 1: Mavic Pro UAVs (with GCPs)-Mavic Pro UAVs (without GCPs) (**Figure 5**); Project 2: Phantom 4 RTK UAVs (with GCPs)- Phantom 4 RTK UAVs (without GCPs) (**Figure 6**); and Project 3: Phantom 4 RTK UAVs (with GCPs)- Mavic Pro UAVs (with GCPs) (**Figure 7**)—and used

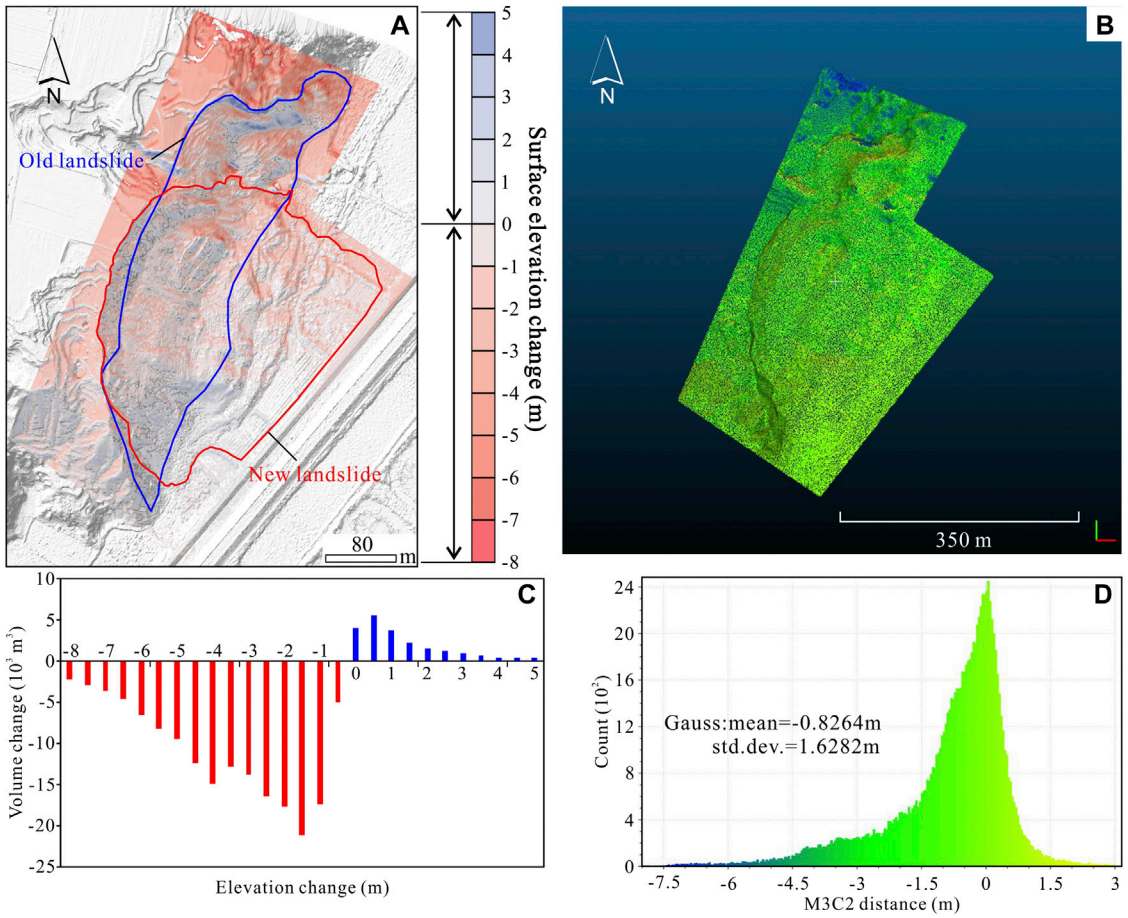

FIGURE 5 | Accuracy evaluation results of Project 1 (DSM based on DJI Mavic Pro UAVs with GCPs subtract DSM based on DJI Mavic Pro UAVs without GCPs): **(A)** 0.5 m threshold DOD map, **(B)** M3C2 distance space expression map, **(C)** Distribution statistics of volume elevation changes, **(D)** M3C2 distance distribution statistics.

GCD 7.0 and Cloud Compare v2.11.2 to evaluate the accuracy of the landslide terrain data. The results of the topography detection changes and the spatial distribution of the M3C2 of the first two schemes were obtained with and without GCPs. The results of the third scheme were obtained using the DJI Phantom 4 RTK UAVs minus the DJI Mavic Pro UAVs. It should be noted that the M3C2 distance calculated using the three schemes is the three-dimensional straight-line distance between two points, while the DSM of the difference (DOD) results show the elevation changes during the two periods of the DEM, which may cause differences between the M3C2 distance statistics table and the landform detection change results. In addition, owing to the existence of steep ridges and sinkholes in the study area, there were anomalous elevation change values in the DOD results, which were manually eliminated. The accuracy evaluation results of each program are described below.

4.1.1 Project 1 Accuracy Assessment

Figure 5A shows the results of the landform detection changes for Project 1, and **Figure 5B** shows the spatial distribution of the reference and comparison clouds calculated using M3C2. **Figure 5C** presents a statistical table of the landslide volume changes, and **Figure 5D** presents a statistical table of the M3C2 distances. We assimilated the M3C2 distance statistics table into a Gauss distribution, with a mean value of −0.8264 m and a standard deviation of 1.6282 m. **Figure 5A** illustrates the overestimation of the elevation of the landslide without GCPs using the DJI Mavic Pro UAVs (the resulting image is generally red), and the surface elevation deviation is within the range of −8 to 5 m. Most of the M3C2 distances are within a range of −2 to 1 m. According to the analysis of the above results, the accuracies of the terrain data acquired using the DJI Mavic Pro UAVs with and without GCPs are quite different. Although the DJI Mavic Pro UAVs can perform terrain mapping without GCPs, if GCPs are used, its accuracy will be greatly improved.

4.1.2 Project 2 Accuracy Assessment

Figure 6A shows the results of the landform detection change in Project 2, and **Figure 6B** shows the spatial distribution of the reference point clouds and comparison point clouds calculated using M3C2. **Figure 6C** presents a statistical table of the landslide volume change, and **Figure 6D** presents a statistical table of the

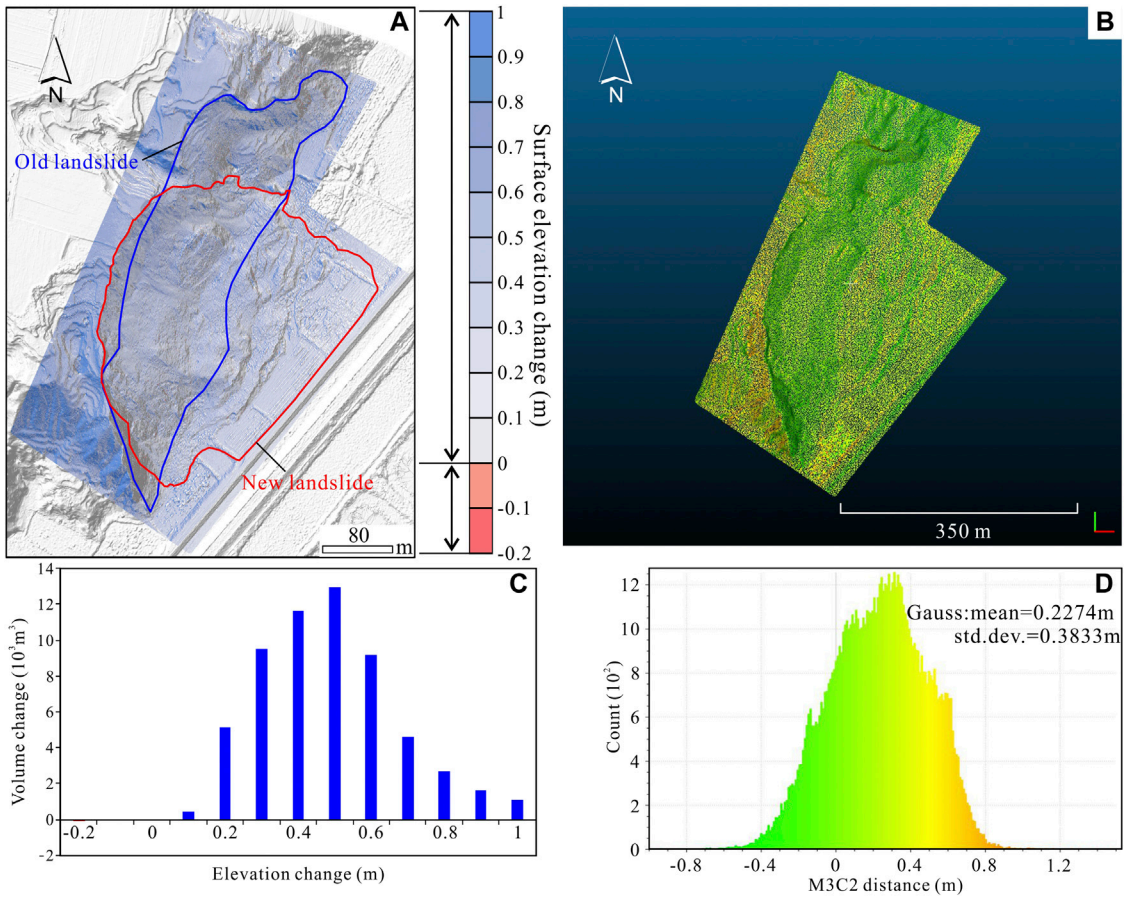

FIGURE 6 | Accuracy evaluation results of Project 2 (DSM based on DJI Phantom 4 RTK UAVs with GCPs subtract DSM based on DJI Phantom 4 RTK UAVs without GCPs): **(A)** 0.5 m threshold DOD map, **(B)** M3C2 distance space expression map, **(C)** Distribution statistics of volume elevation changes, **(D)** M3C2 distance distribution statistics.

M3C2 distances. The M3C2 distances were assimilated into a Gauss distribution, with a mean value of 0.2274 m and a standard deviation of 0.3833 m. By comparing Project 2 with Project 1, it was found that DJI Phantom 4 RTK UAVs has a higher average and standard deviation in terms of the accuracy and precision, and its overall accuracy is much higher than that of the DJI Mavic Pro UAVs. Although the surface elevation deviation is −0.2 to 1 m, which may be caused by the rapid undulation of the surface in a short distance, the overall analysis result is light blue (**Figure 6A**), and the M3C2 distance is mostly between −0.4 and 0.8 m. This shows that this UAVs can control the error within a very small range without GCPs.

4.1.3 Project 3 Accuracy Assessment

Figure 7A shows the results of the landform detection changes in Project 3, and **Figure 7B** shows the spatial distribution of the reference point clouds and comparison point clouds calculated using M3C2. **Figure 7C** presents the statistical table of the landslide volume changes, and **Figure 7D** presents the statistical table of the M3C2 distances. The M3C2 distances were assimilated into a Gauss distribution, with a mean value of −0.4857 m and a standard deviation of 0.7026 m. Under the same conditions and with GCPs, the terrain data obtained using DJI Mavic Pro UAVs are generally too large, and most of the difference results are negative. The DJI Phantom 4 RTK UAVs has a higher surveying accuracy, which is higher than that of the RTK positioning system. This is related to the resolution of the sensor.

Through analysis of the three sets of projects, it was concluded that the setting of GCPs is very important for the DJI Mavic Pro UAVs, and whether they are set or not significantly affects the obtained terrain data. Therefore, when conducting landslide terrain mapping, a UAVs with an RTK function should be selected, and a certain number of GCPs should also be set to ensure the accuracy of the terrain data.

4.2 *UAVs and TLS Point Clouds Data Fusion Results*

First, rough registration was performed based on the feature points recognized by four people so that the UAVs-SfM and TLS point clouds were closer in 3D space. Subsequently, owing to the large range of the UAVs data acquisition, the point clouds obtained using the UAVs were cropped according to the TLS area. Finally, the two point clouds were merged together using the

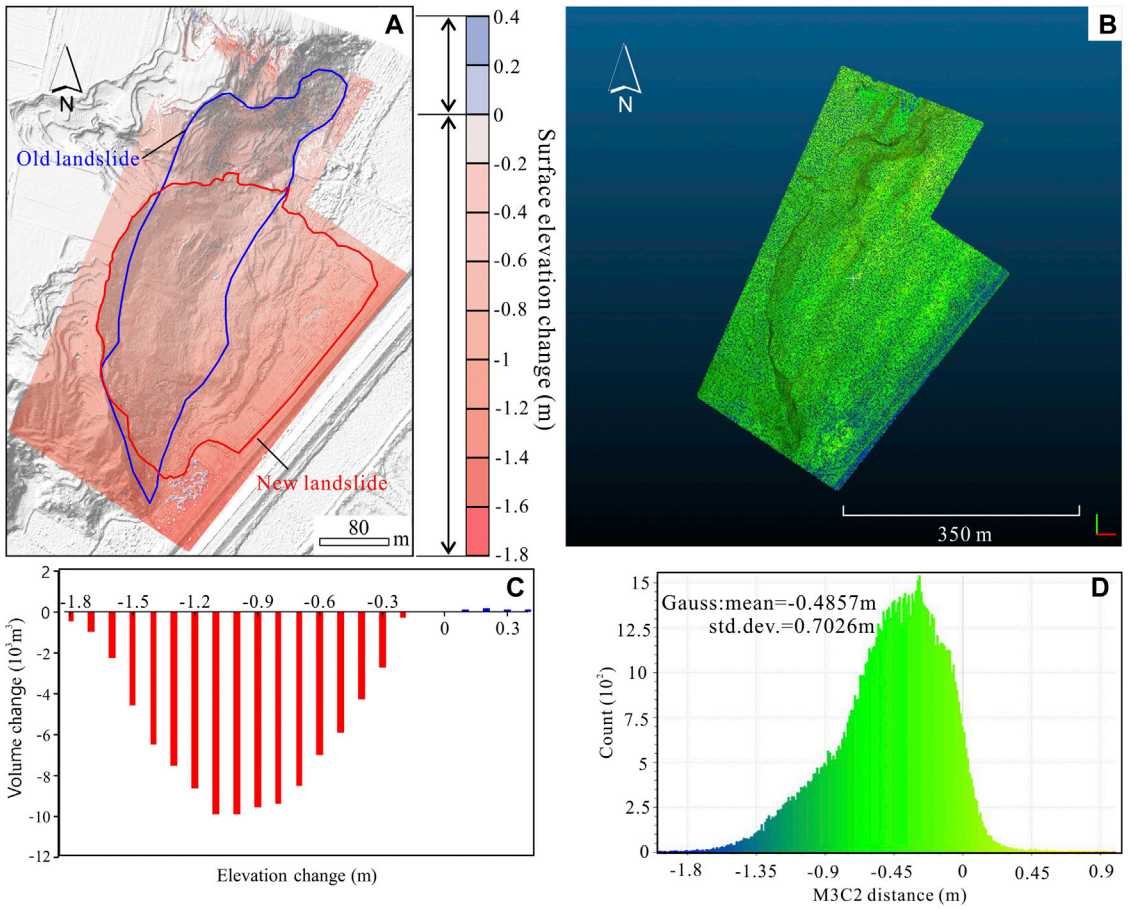

FIGURE 7 | Accuracy evaluation results of the Project 3 (DSM based on DJI Phantom RTK with GCPs subtract DSM based on DJI Mavic Pro UAVs with GCPs): **(A)** 0.5 m threshold DOD map, **(B)** M3C2 distance space expression map, **(C)** Distribution statistics of volume elevation changes, **(D)** M3C2 distance distribution statistics.

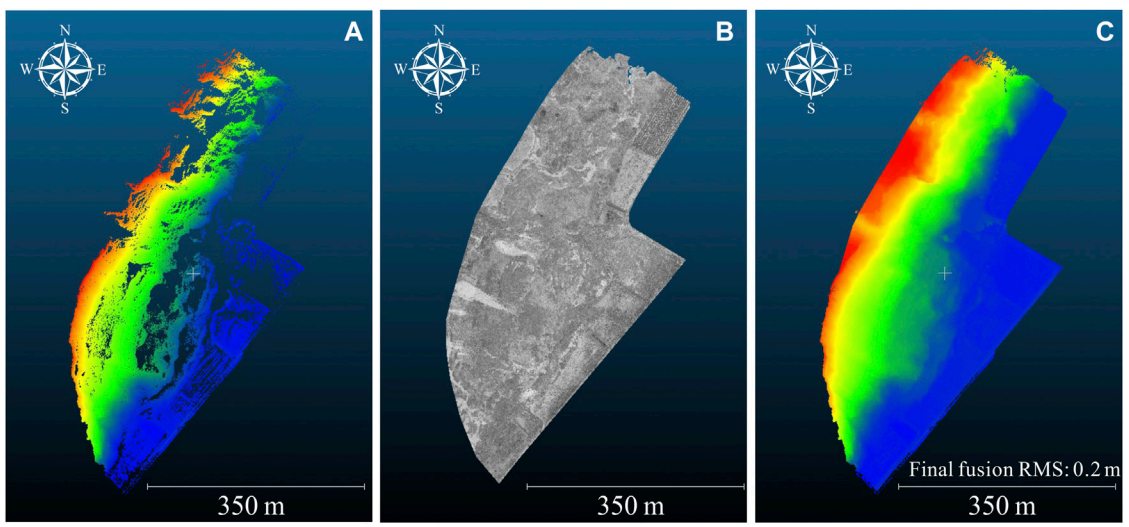

FIGURE 8 | TLS-UAVs data fusion: **(A)** TLS scanning point clouds, **(B)** UAVs point clouds, **(C)** Fusion point clouds.

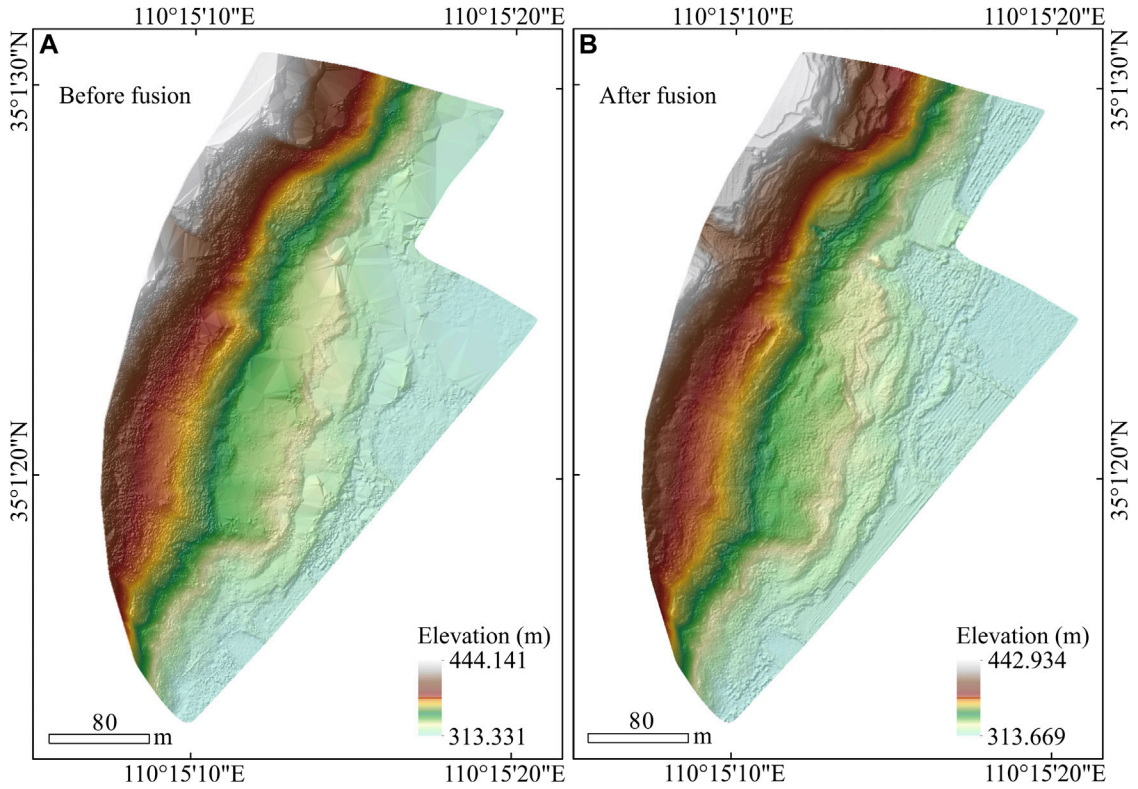

FIGURE 9 | DSMs before and after fusion: **(A)** DSM generated by TLS point clouds, **(B)** DSM generated by fusion point clouds.

TABLE 3 | Elevation accuracy test of terrain data obtained by different equipment with GCPs.

Points	Measured value by RTK			Extracted Z value from DSMs							
	X	Y	Z	Z1 (Mavic pro)	△Z1	Z2 (phantom 4 RTK)	△Z2	Z3 (TLS)	△Z3	Z4 (UAVs-TLS)	△Z4
VP01	431,720.426	3877426.748	442.467	442.905	0.438	442.467	0.000	—	—	—	—
VP02	431,753.452	3877464.442	440.858	441.207	0.349	440.861	0.003	—	—	439.887	−0.971
VP03	431,685.098	3877540.511	430.508	430.722	0.214	430.489	−0.019	—	—	—	—
VP04	431,798.044	3877576.670	439.289	439.329	0.040	439.273	−0.016	—	—	439.281	−0.008
VP05	431,756.819	3877615.454	445.473	445.464	−0.009	445.476	0.003	—	—	—	—
VP06	431,638.531	3877587.314	445.142	445.000	−0.142	445.043	−0.099	—	—	—	—
VP07	431,616.566	3877517.533	443.438	443.500	0.062	443.390	−0.048	—	—	—	—
VP08	432,115.914	3877430.911	318.714	319.876	1.162	318.729	0.015	319.040	0.326	318.725	0.011
VP09	432,102.152	3877436.401	315.078	315.938	0.860	315.080	0.002	315.871	0.793	315.110	0.032
VP10	432,035.867	3877337.063	318.670	319.994	1.324	318.622	−0.048	319.694	1.024	318.614	−0.056
VP11	431,967.678	3877257.137	318.755	319.995	1.240	318.714	−0.041	317.052	−1.703	318.784	0.029
VP12	431,927.400	3877246.039	317.124	318.131	1.007	317.114	−0.010	317.683	0.559	317.135	0.011
VP13	431,888.090	3877214.075	316.470	317.626	1.156	316.483	0.013	316.952	0.482	316.481	0.011
VP14	431,880.584	3877166.044	317.308	318.708	1.400	317.321	0.013	317.341	0.033	317.962	0.654
ME (m)	—	—	—	—	0.650	—	−0.017	—	0.216	—	−0.032
MAE (m)	—	—	—	—	0.672	—	0.024	—	0.703	—	0.182
RMSE (m)	—	—	—	—	0.848	—	0.035	—	0.864	—	0.391

ICP point clouds registration algorithm. In this process, the registration error was reduced by changing the number of iterations and removing the elevation anomaly point clouds. Finally, the TLS point clouds (**Figure 8A**) were used as the reference benchmark, and the UAVs point clouds (**Figure 8B**) were used to supplement the fusion point clouds of the shadow (hole) area in the TLS data (**Figure 8C**). The final fusion root mean square error (RMSE) of the two point clouds was 0.2 m, and the theoretical overlap was 100%. The fused point clouds were imported into ArcGIS 10.5 to generate the DSM of the Beiguo

landslide (**Figure 9B**). Compared with the DSM generated using the TLS point clouds (**Figure 9A**), the accuracy of the DSM generated using the fused point clouds is significantly improved, and it can be seen from the DSM that the fusion result is more detailed and has more prominent texture.

4.3 *VPs Accuracy Analysis*

Before the flying missions, the UAVs used the RTK positioning technology to obtain the precise coordinates of the VPs, which were used to evaluate the accuracy of the UAVs and TLS in terms of mapping the landslide topography. **Table 3** lists the three-dimensional coordinates of the VPs and the elevation values output by multiple DSMs (DSM resampled to 0.5 m resolution). Based on these results, it was found that the accuracy of the VP coordinates obtained using the DJI Phantom 4 RTK UAVs is much higher than that obtained using the DJI Mavic Pro UAVs. In addition, after fusing the UAVs point clouds data with the TLS point clouds data, the accuracy of the obtained coordinates was also significantly improved. It should be noted that because the TLS scanning area was smaller than the drone flight area, the coordinates of some of the VPs were missing.

For better precision exploration, we selected three indicators for verification: mean error (ME), mean absolute error (MAE), and RMSE. The equations used to calculate these values are as follows:

$$M_{\text{mean}} = \frac{\sum_{i=1}^{n} (X_i - Y_i)}{n}, \tag{1}$$

$$\text{MAE}(X, h) = \frac{1}{n} \sum_{i=1}^{n} \left| h(x_i) - y_i \right|, \tag{2}$$

$$\text{RMSE} = \sqrt{\frac{\sum_{i=1}^{n} (X_i - Y_i)^2}{n}}. \tag{3}$$

In **Eqs 1–3**, n is the number of measurements, X_i is the measured value, and Y_i is the true value.

The calculation shows that the overall performance of the DJI Phantom 4 RTK UAVs was better than that of the DJI Mavic Pro UAVs for the landslide terrain, with ME values of 0.650 and −0.017 m, MAE values of 0.672 and 0.024 m, and RMSE values of 0.848 and 0.035 m, respectively. These results are because the DJI Phantom 4 RTK UAVs is a professional drone developed for surveying and mapping. It contains a brand-new RTK module and has stronger anti-magnetic interference and precise positioning capabilities. In addition, it provides real-time centimeter-level positioning data, which significantly improves the absolute accuracy of the image metadata. However, it is much expensive than the DJI Mavic Pro UAVs. Based on the above calculations, we found that the DJI Phantom 4 RTK UAVs can still guarantee quite high data accuracy without GCPs, which is also beneficial for engineering surveys conducted in high-risk areas. Of course, it is recommended that GCPs be arranged evenly throughout the study area to meet higher surveying and mapping requirements.

The difference between the accuracies before and after the TLS-UAVs fusion is large, with ME values of 0.216 and −0.032 m, MAE values of 0.703 and 0.182 m, and RMSE values of 0.864 and 0.391 m, respectively. The above results verify the feasibility of using the point clouds fusion method in mapping landslide topography. We know that UAVs surveying and mapping can achieve data collection over a large area in a short time of time. However, in some low visibility and/or rugged and steep mountain areas, the number of GCPs that can be deployed is small and/or the weather affects the results, resulting in UAVs tilt photogrammetry. The accuracy is reduced, and the data fusion between the UAVs and TLS will improve the overall accuracy to a certain extent.

5 DISCUSSION

At present, the most commonly used remote sensing methods for fine 3D mapping are the TLS and UAVs-SfM methods (Saponaro et al., 2019; Sasak et al., 2019; Kamnik et al., 2020; Tsunetaka et al., 2020; Rechberger et al., 2021). Among them, the UAVs method is more widely used because of its portability, mobility, and low cost (Mancini et al., 2013; Lindner et al., 2015; Ma et al., 2018; Guisado-Pintado et al., 2019; Lu et al., 2020). In landslide terrain, a large part of the area is not reachable by land methods. Using UAVs photogrammetry in this type of terrain is advantageous in terms of time and cost (Lindner et al., 2015; Peppa et al., 2017; Pellicani et al., 2019). However, this method is strongly affected by weather conditions. For example, in strong winds, heavy rains, and areas with low visibility, the accuracy of UAVs products cannot be guaranteed (Ji and Luo, 2019; Aguera-Vega et al., 2020). In addition, in rugged and steep mountain areas, it is impossible to evenly deploy GCPs to improve the overall accuracy of the results. When the GCPs are unevenly distributed or the number of deployments is small, the UAVs image data are prone to distortion (Lee et al., 2019; Rogers et al., 2020). Under these conditions, the TLS method can still obtain high-precision point clouds data, and it uses less GCPs for geo-referencing (Chatzistamatis et al., 2018; Guisado-Pintado et al., 2019; Ji and Luo, 2019). However, owing to factors such as the terrain, slope, and scanner location, the point clouds products finally obtained using the TLS may contain data holes (Sasak et al., 2019; Tsunetaka et al., 2020). Preliminary studies have shown that for areas with low undulations, low texture, or high vegetation coverage, the accuracy of topographic mapping using TLS is lower (Ji and Luo, 2019; Hendrickx et al., 2020). The data fusion of TLS and UAVs photogrammetry combines the advantages of the two techniques to obtain detailed models of complex objects and produces better results (Chatzistamatis et al., 2018; Tsunetaka et al., 2020). The ICP algorithm has become a popular method for the mutual positioning of two spatially overlapping point clouds (point clouds registration) (Balsa-Barreiro and Fritsch, 2017). Combining the 3D point clouds of the UAVs-SfM and TLS with the ICP can greatly reduce data shadows (voids) and obtain realistic images.

We used two consumer UAVs, the DJI Mavic Pro UAVs and DJI Phantom 4 RTK UAVs, to photograph the study area, and we explored the impact of using GCPs on the different types of UAVs produced by DJI. We also used a Maptek I-Site 8820 TLS to scan the Beiguo landslide, and then we merged the resulting point

clouds with the UAVs point clouds using the ICP algorithm. To verify the feasibility of fusing these point clouds, we used the M3C2 distance indicator in the Cloud Compare software to compare the distance between the clouds. In summary, when compared with using only a UAVs or TLS, the method of fusing the point clouds of both effectively solves the problem of missing data caused by special terrain, and it also improves the accuracy of the landslide terrain data.

It should be noted that in the accuracy verification process, because the horizontal accuracy error of the CPs measured by the RTK in this study is 2 cm and the vertical accuracy error is 5 cm, the CP coordinates measured in the field may appear within the accuracy range. The internal error will affect the data accuracy evaluation of the above described two UAVs and TLS methods to a certain extent. In the future, when measuring CPs, we will choose a static global navigation satellite system (GNSS) measurement method to reduce this error. Since our study area is mostly bare loess, tall vegetation is rare and the vegetation cover is largely sparse grassland. Therefore, we did not consider the problem of filtering vegetation in the point clouds data processing and fusion. The influences of the GCP distribution, local topography, and surface vegetation clearance on the DSM data will be the focus of our future research.

In addition, the two UAVs used in this study were equipped with optical lenses that cannot penetrate vegetation, and the TLS used had a fixed angular measurement range (360° horizontally, 80° vertical) and needed to be placed in a relatively stable area. Thus, the area blocked by the hillside cannot be well scanned by the laser. In the future, we will also try to choose a UAVs equipped with Lidar so that the point clouds data obtained will have a higher accuracy and precision. The fusion of airborne Lidar and TLS point clouds data will greatly reduce the impact of the vegetation and other features on the acquisition of the terrain information. The fusion effect that can be achieved needs to be explored further.

6 CONCLUSION

In the elevation accuracy evaluation of the terrain data obtained using the DJI Phantom 4 RTK UAVs and DJI Mavic Pro UAVs, we found that the DJI Phantom 4 RTK UAVs has a high mapping accuracy with and without GCPs. Although the DJI Mavic Pro UAVs is capable of topographic surveying and mapping without GCPs, its accuracy is greatly improved if GCPs are used. The expensive DJI Phantom 4 RTK UAVs is equipped with an RTK module and can receive network RTK signals (one prerequisite is in an area with a mobile network signal), so it is very suitable for high-precision terrain mapping. When limited by the terrain and other factors, the accuracy of the DJI Phantom 4 RTK UAVs in the No GCP operation mode is also acceptable. The DJI Phantom 4 RTK UAVs is better than the DJI Mavic Pro UAVs in terms of performance due to its integrated RTK module, but it is also more expensive. Owing to the constraints of scientific research costs and the fact that different projects have different mapping accuracy requirements, researchers can choose appropriate UAVs models and mapping schemes according to the actual situation.

Owing to the influence of elevation differences, weather, hill shade, and other factors, the accuracy of UAVs photogrammetry has a great uncertainty. In particular, when the underlying surface is very similar or the ground feature points are not easy to identify, the terrain point clouds or DSM generated by the UAVs will have even larger errors in some places. Because the UAVs takes orthophotos, there are basically no blind spots in the field of vision. Compared with UAVs, the TLS can actively transmit and receive laser signals, so it can obtain more 3D, more real, and more accurate topographic point clouds data. However, because the TLS is operated by setting up scanning stations, it is inevitable that there will be blind areas in TLS scanning due to the constraints of the terrain conditions. To integrate the advantages of the two sets of point clouds data, the TLS point clouds data were used as the reference data. Based on the ICP algorithm, the point clouds obtained using the DJI Phantom 4 RTK UAVs was integrated with the TLS point clouds data, which successfully solved the problem of missing data in the TLS blind areas. The ICP algorithm evaluation report shows that the RMSE of the final fusion of the two point clouds is 0.2 m and the theoretical overlap is 100%, indicating that the point clouds after fusion have a very high degree of matching and precision, and the new fusion point clouds have the advantages of the UAVs photogrammetry and TLS scanning methods. This study provides a solution for data fusion of point clouds obtained using optical lens UAVs and point clouds obtained using a TLS.

DATA AVAILABILITY STATEMENT

The raw data supporting the conclusion of this article will be made available by the authors, without undue reservation.

ETHICS STATEMENT

Written informed consent was obtained from the relevant individual(s) for the publication of any potentially identifiable images or data included in this article.

AUTHOR CONTRIBUTIONS

This paper represents a result of collaborative teamwork. ZM: Field investigation, data management, article writing. SH: Theoretical guidance, supervision, article revision, funding. NW: Resources, supervision. YL: Field projects design, measurement.

FUNDING

This research was funded by the National Natural Science Foundation of China (Grant No. 42001006), and the China Postdoctoral Science Foundation (Grant No. 2019M663792).

REFERENCES

Agüera-Vega, F., Agüera-Puntas, M., Martínez-Carricondo, P., Mancini, F., and Carvajal, F. (2020). Effects of point Cloud Density, Interpolation Method and Grid Size on Derived Digital Terrain Model Accuracy at Micro Topography Level. *Int. J. Remote Sensing* 41, 8281–8299. doi:10.1080/01431161.2020.1771788

Bakirman, T., Bayram, B., Akpinar, B., Karabulut, M. F., Bayrak, O. C., Yigitoglu, A., et al. (2020). Implementation of Ultra-light UAV Systems for Cultural Heritage Documentation. *J. Cult. Heritage* 44, 174–184. doi:10.1016/j.culher.2020.01.006

Balsa-Barreiro, J., and Fritsch, D. (2018). Generation of Visually Aesthetic and Detailed 3D Models of Historical Cities by Using Laser Scanning and Digital Photogrammetry. *digital Appl. archaeology Cult. heritage* 8, 57–64. doi:10.1016/J.DAACH.2017.12.001

Brede, B., Calders, K., Lau, A., Raumonen, P., Bartholomeus, H. M., Herold, M., et al. (2019). Non-destructive Tree Volume Estimation through Quantitative Structure Modelling: Comparing UAV Laser Scanning with Terrestrial LIDAR. *Remote Sensing Environ.* 233, 111355. doi:10.1016/j.rse.2019.111355

Carey, J. A., Pinter, N., Pickering, A. J., Prentice, C. S., and DeLong, S. B. (2019). Analysis of Landslide Kinematics Using Multi-Temporal Unmanned Aerial Vehicle Imagery, La Honda, California. *Environ. Eng. Geosci.* 25, 301–317. doi:10.2113/eeg-2228

Carrera-Hernández, J. J., Levresse, G., and Lacan, P. (2020). Is UAV-SfM Surveying Ready to Replace Traditional Surveying Techniques? *Int. J. Remote Sensing* 41, 4820–4837. doi:10.1080/01431161.2020.1727049

Chatzistamatis, S., Kalaitzis, P., Chaidas, K., Chatzitheodorou, C., and Soulakellis, N. (2018). Fusion of Tls and Uav Photogrammetry Data for post-earthquake 3d Modeling of a Cultural Heritage Church. *Geoinformation Disaster Manage.* XLII-3/W4, 143–150. doi:10.5194/isprs-archives-xlii-3-w4-143-2018

Cheng, Z., Gong, W., Tang, H., Juang, C. H., Deng, Q., Chen, J., et al. (2021). UAV Photogrammetry-Based Remote Sensing and Preliminary Assessment of the Behavior of a Landslide in Guizhou, China. *Eng. Geology.* 289, 106172. doi:10.1016/j.enggeo.2021.106172

Du, S., Liu, J., Zhang, C., Zhu, J., and Li, K. (2015). Probability Iterative Closest point Algorithm for M-D point Set Registration with Noise. *Neurocomputing* 157, 187–198. doi:10.1016/j.neucom.2015.01.019

Feng, M., Yang, M., Xia, Y., and Bai, H. (2020). 3D Laser Scanning and Oblique Photogrammetry for 3D Modeling of High Scarps. *Sci. Surv. Mapp.* 45, 99–122. doi:10.16251/j.cnki.1009-2307.2020.01.015

Ferrer-González, E., Agüera-Vega, F., Carvajal-Ramírez, F., and Martínez-Carricondo, P. (2020). UAV Photogrammetry Accuracy Assessment for Corridor Mapping Based on the Number and Distribution of Ground Control Points. *Remote Sensing* 12, 2447. doi:10.3390/rs12152447

Godone, D., Allasia, P., Borrelli, L., and Gullà, G. (2020). UAV and Structure from Motion Approach to Monitor the Maierato Landslide Evolution. *Remote Sensing* 12, 1039. doi:10.3390/rs12061039

Guisado-Pintado, E., Jackson, D. W. T., and Rogers, D. (2019). 3D Mapping Efficacy of a Drone and Terrestrial Laser Scanner over a Temperate beach-dune Zone. *Geomorphology* 328, 157–172. doi:10.1016/j.geomorph.2018.12.013

Hendrickx, H., De Sloover, L., Stal, C., Delaloye, R., Nyssen, J., and Frankl, A. (2020). Talus Slope Geomorphology Investigated at Multiple Time Scales from High-resolution Topographic Surveys and Historical Aerial Photographs (Sanetsch Pass, Switzerland). *Earth Surf. Process. Landforms* 45, 3653–3669. doi:10.1002/esp.4989

Hu, S., Qiu, H., Pei, Y., Cui, Y., Xie, W., Wang, X., et al. (2019). Digital Terrain Analysis of a Landslide on the Loess Tableland Using High-Resolution Topography Data. *Landslides* 16, 617–632. doi:10.1007/s10346-018-1103-0

Hu, S., Qiu, H., Wang, N., Cui, Y., Wang, J., Wang, X., et al. (2020). The Influence of Loess Cave Development upon Landslides and Geomorphologic Evolution: A Case Study from the Northwest Loess Plateau, China. *Geomorphology* 359, 107167. doi:10.1016/j.geomorph.2020.107167

Hu, S., Qiu, H., Wang, X., Gao, Y., Wang, N., Wu, J., et al. (2018). Acquiring High-Resolution Topography and Performing Spatial Analysis of Loess Landslides by Using Low-Cost UAVs. *Landslides* 15, 593–612. doi:10.1007/s10346-017-0922-8

Jaud, M., Bertin, S., Beauverger, M., Augereau, E., and Delacourt, C. (2020). RTK GNSS-Assisted Terrestrial SfM Photogrammetry without GCP: Application to Coastal Morphodynamics Monitoring. *Remote Sensing* 12, 1889. doi:10.3390/rs12111889

Ji, H., and Luo, X. (2019). 3D Scene Reconstruction of Landslide Topography Based on Data Fusion between Laser point Cloud and UAV Image. *Environ. Earth Sci.* 78, 534. doi:10.1007/s12665-019-8516-5

Kamnik, R., Nekrep Perc, M., and Topolšek, D. (2020). Using the Scanners and Drone for Comparison of point Cloud Accuracy at Traffic Accident Analysis. *Accid. Anal. Prev.* 135, 105391. doi:10.1016/j.aap.2019.105391

Kowalski, A. (2018). Monitoring of Anthropogenic Landslide Activity with Combined UAV and Lidar-Derived DEMS a Case Study of the Czerwony Wawoz Landslide (SW Poland. Western Sudetes). *Acta Geodynamica et Geomaterialia* 15, 117–129. doi:10.13168/agg.2018.0008

Lamsters, K., Karušs, J., Krievāns, M., and Ješkins, J. (2020). High-resolution Orthophoto Map and Digital Surface Models of the Largest Argentine Islands (The Antarctic) from Unmanned Aerial Vehicle Photogrammetry. *J. Maps* 16, 335–347. doi:10.1080/17445647.2020.1748130

Lee, J., Kang, J., and Lee, S. (2019). A Study on the Improvement of UAV Based 3D Point Cloud Spatial Object Location Accuracy Using Road Information. *Korean J. Remote Sensing* 35, 705–714. doi:10.7780/kjrs.2019.35.5.1.7

Lee, J., and Min, S. S. (2018). Assessment of Positioning Accuracy of UAV Photogrammetry Based on RTK-GPS. *J. Korea Academia-Industrial cooperation Soc.* 19, 63–68. doi:10.5762/kais.2018.19.4.63

Li, H.-b., Yang, X.-g., Sun, H.-l., Qi, S.-c., and Zhou, J.-w. (2019). Monitoring of Displacement Evolution during the Pre-failure Stage of a Rock Block Using Ground-Based Radar Interferometry. *Landslides* 16, 1721–1730. doi:10.1007/s10346-019-01228-1

Li, Z., Wang, J., and Zhang, D. (2021). Creep Behavior of Intact Loess Followed Unloading Paths. *Front. Earth Sci.* 9, 744864. doi:10.3389/feart.2021.744864

Lindner, G., Schraml, K., Mansberger, R., and Hübl, J. (2015). UAV Monitoring and Documentation of a Large Landslide. *Appl. Geomat* 8, 1–11. doi:10.1007/s12518-015-0165-0

Liu, Z., Qiu, H., Ma, S., Yang, D., Pei, Y., Du, C., et al. (2021). Surface Displacement and Topographic Change Analysis of the Changhe Landslide on September 14, 2019, China. *Landslides* 18, 1471–1483. doi:10.1007/s10346-021-01626-4

Lu, H., Ma, L., Fu, X., Liu, C., Wang, Z., Tang, M., et al. (2020). Landslides Information Extraction Using Object-Oriented Image Analysis Paradigm Based on Deep Learning and Transfer Learning. *Remote Sensing* 12, 752. doi:10.3390/rs12050752

Ma, S., Qiu, H., Hu, S., Yang, D., and Liu, Z. (2021). Characteristics and Geomorphology Change Detection Analysis of the Jiangdingya Landslide on July 12, 2018, China. *Landslides* 18, 383–396. doi:10.1007/s10346-020-01530-3

Ma, S., Xu, C., Shao, X., Zhang, P., Liang, X., and Tian, Y. (2018). Geometric and Kinematic Features of a Landslide in Mabian Sichuan, China, Derived from UAV Photography. *Landslides* 16, 373–381. doi:10.1007/s10346-018-1104-z

Mancini, F., Dubbini, M., Gattelli, M., Stecchi, F., Fabbri, S., and Gabbianelli, G. (2013). Using Unmanned Aerial Vehicles (UAV) for High-Resolution Reconstruction of Topography: The Structure from Motion Approach on Coastal Environments. *Remote Sensing* 5, 6880–6898. doi:10.3390/rs5126880

Martínez-Carricondo, P., Agüera-Vega, F., Carvajal-Ramírez, F., Mesas-Carrascosa, F.-J., García-Ferrer, A., and Pérez-Porras, F.-J. (2018). Assessment of UAV-Photogrammetric Mapping Accuracy Based on Variation of Ground Control Points. *Int. J. Appl. Earth Observation Geoinformation* 72, 1–10. doi:10.1016/j.jag.2018.05.015

Medjkane, M., Maquaire, O., Costa, S., Roulland, T., Letortu, P., Fauchard, C., et al. (2018). High-resolution Monitoring of Complex Coastal Morphology Changes: Cross-Efficiency of SfM and TLS-Based Survey (Vaches-Noires Cliffs, Normandy, France). *Landslides* 15, 1097–1108. doi:10.1007/s10346-017-0942-4

Neugirg, F., Stark, M., Kaiser, A., Vlacilova, M., Della Seta, M., Vergari, F., et al. (2016). Erosion Processes in Calanchi in the Upper Orcia Valley, Southern Tuscany, Italy Based on Multitemporal High-Resolution Terrestrial LiDAR and UAV Surveys. *Geomorphology* 269, 8–22. doi:10.1016/j.geomorph.2016.06.027

Ouyang, C., An, H., Zhou, S., Wang, Z., Su, P., Wang, D., et al. (2019). Insights from the Failure and Dynamic Characteristics of Two Sequential Landslides at Baige Village along the Jinsha River, China. *Landslides* 16, 1397–1414. doi:10.1007/s10346-019-01177-9

Pellicani, R., Argentiero, I., Manzari, P., Spilotro, G., Marzo, C., Ermini, R., et al. (2019). UAV and Airborne LiDAR Data for Interpreting Kinematic Evolution of Landslide Movements: The Case Study of the Montescaglioso Landslide (Southern Italy). *Geosciences* 9, 248. doi:10.3390/geosciences9060248

Peppa, M. V., Mills, J. P., Moore, P., Miller, P. E., and Chambers, J. E. (2017). Brief Communication: Landslide Motion from Cross Correlation of UAV-Derived Morphological Attributes. *Nat. Hazards Earth Syst. Sci.* 17, 2143–2150. doi:10.5194/nhess-17-2143-2017

Qu, F., Qiu, H., Sun, H., and Tang, M. (2021). Post-failure Landslide Change Detection and Analysis Using Optical Satellite Sentinel-2 Images. *Landslides* 18, 447–455. doi:10.1007/s10346-020-01498-0

Rangel, J. M. G., Gonçalves, G. R., and Pérez, J. A. (2018). The Impact of Number and Spatial Distribution of GCPs on the Positional Accuracy of Geospatial Products Derived from Low-Cost UASs. *Int. J. Remote Sensing* 39, 7154–7171. doi:10.1080/01431161.2018.1515508

Rechberger, C., Fey, C., and Zangerl, C. (2021). Structural Characterisation, Internal Deformation, and Kinematics of an Active Deep-Seated Rock Slide in a valley Glacier Retreat Area. *Eng. Geology.* 286, 106048. doi:10.1016/j.enggeo.2021.106048

Rogers, S. R., Manning, I., and Livingstone, W. (2020). Comparing the Spatial Accuracy of Digital Surface Models from Four Unoccupied Aerial Systems: Photogrammetry versus LiDAR. *Remote Sensing* 12, 2806. doi:10.3390/rs12172806

Rossi, G., Tanteri, L., Tofani, V., Vannocci, P., Moretti, S., and Casagli, N. (2018). Multitemporal UAV Surveys for Landslide Mapping and Characterization. *Landslides* 15, 1045–1052. doi:10.1007/s10346-018-0978-0

Samodra, G., Ramadhan, M. F., Sartohadi, J., Setiawan, M. A., Christanto, N., and Sukmawijaya, A. (2020). Characterization of Displacement and Internal Structure of Landslides from Multitemporal UAV and ERT Imaging. *Landslides* 17, 2455–2468. doi:10.1007/s10346-020-01428-0

Saponaro, M., Pratola, L., Saponieri, A., Tarantino, E., and Fratino, U. (2019). "Cloud-To-Cloud Comparison and Integration of Tls and Uav Surveys for the Maintenance of Coastal protection Systems," in Paper presented at the International Short Course/Conference on Applied Coastal Research Engineering, Geology, Ecology & Management (SCACR2019), Bari, Italy, September 11, 2019.

Šašak, J., Gallay, M., Kaňuk, J., Hofierka, J., and Minár, J. (2019). Combined Use of Terrestrial Laser Scanner and UAV Photogrammetry in Mapping Alpine Terrain. *Remote Sensing* 11, 2154. doi:10.3390/rs11182154

Senkal, E., Kaplan, G., and Avdan, U. (2021). Accuracy Assessment of Digital Surface Models from Unmanned Aerial Vehicles' Imagery on Archaeological Sites. *Int. J. Eng. Geosciences* 6, 81–89. doi:10.26833/ijeg.696001

Stringer, J., Brook, M. S., and Justice, R. (2021). Post-earthquake Monitoring of Landslides along the Southern Kaikōura Transport Corridor, New Zealand. *Landslides* 18, 409–423. doi:10.1007/s10346-020-01543-y

Tsunetaka, H., Hotta, N., Hayakawa, Y. S., and Imaizumi, F. (2020). Spatial Accuracy Assessment of Unmanned Aerial Vehicle-Based Structures from Motion Multi-View Stereo Photogrammetry for Geomorphic Observations in Initiation Zones of Debris Flows, Ohya Landslide, Japan. *Prog. Earth Planet. Sci.* 7, 24. doi:10.1186/s40645-020-00336-0

Wijesingha, J., Moeckel, T., Hensgen, F., and Wachendorf, M. (2019). Evaluation of 3D point Cloud-Based Models for the Prediction of Grassland Biomass. *Int. J. Appl. Earth Observation Geoinformation* 78, 352–359. doi:10.1016/j.jag.2018.10.006

Xu, Q., Li, W.-l., Ju, Y.-z., Dong, X.-j., and Peng, D.-l. (2020). Multitemporal UAV-Based Photogrammetry for Landslide Detection and Monitoring in a Large Area: a Case Study in the Heifangtai Terrace in the Loess Plateau of China. *J. Mt. Sci.* 17, 1826–1839. doi:10.1007/s11629-020-6064-9

Xu, Z., Wu, L., Shen, Y., Li, F., Wang, Q., and Wang, R. (2014). Tridimensional Reconstruction Applied to Cultural Heritage with the Use of Camera-Equipped UAV and Terrestrial Laser Scanner. *Remote Sensing* 6, 10413–10434. doi:10.3390/rs61110413

Yan, Y., Ma, S., Yin, S., Hu, S., Long, Y., Xie, C., et al. (2021). Detection and Numerical Simulation of Potential Hazard in Oil Pipeline Areas Based on UAV Surveys. *Front. Earth Sci.* 9, 665478. doi:10.3389/feart.2021.665478

Yang, D., Qiu, H., Hu, S., Pei, Y., Wang, X., Du, C., et al. (2021). Influence of Successive Landslides on Topographic Changes Revealed by Multitemporal High-Resolution UAS-Based DEM. *Catena* 202, 105229. doi:10.1016/j.catena.2021.105229

Yu, M., Huang, Y., Zhou, J., and Mao, L. (2017). Modeling of Landslide Topography Based on Micro-unmanned Aerial Vehicle Photography and Structure-From-Motion. *Environ. Earth Sci.* 76, 520. doi:10.1007/s12665-017-6860-x

Zang, Y., Yang, B., Li, J., and Guan, H. (2019). An Accurate TLS and UAV Image Point Clouds Registration Method for Deformation Detection of Chaotic Hillside Areas. *Remote Sensing* 11, 647. doi:10.3390/rs11060647

Zhang, C., Yang, S., Zhao, C., Lou, H., Zhang, Y., Bai, j., et al. (2018). Topographic Data Accuracy Verification of Small Consumer UAV. *J. Remote Sensing* 22, 185–195. doi:10.11834/jrs.20186483

Zhang, F., Peng, J., Wu, X., Pan, F., Jiang, Y., Kang, C., et al. (2021). A Catastrophic Flowslide that Overrides a Liquefied Substrate: the 1983 Saleshan Landslide in China. *Earth Surf. Process. Landforms* 46, 2060–2078. doi:10.1002/esp.5144

Zhou, T., Hasheminasab, S. M., Ravi, R., and Habib, A. (2020). LiDAR-Aided Interior Orientation Parameters Refinement Strategy for Consumer-Grade Cameras Onboard UAV Remote Sensing Systems. *Remote Sensing* 12, 2268. doi:10.3390/rs12142268

Conflict of Interest: The authors declare that the research was conducted in the absence of any commercial or financial relationships that could be construed as a potential conflict of interest.

Publisher's Note: All claims expressed in this article are solely those of the authors and do not necessarily represent those of their affiliated organizations, or those of the publisher, the editors, and the reviewers. Any product that may be evaluated in this article, or claim that may be made by its manufacturer, is not guaranteed or endorsed by the publisher.

frontiers in Earth Science

ORIGINAL RESEARCH
published: 07 January 2022
doi: 10.3389/feart.2021.806832

An Empirical Shear Model of Interface Between the Loess and Hipparion Red Clay in a Loess Landslide

Yanbo Zhu[1]*, *Shuaisheng Miao*[1], *Hongfei Li*[1], *Yutao Han*[1] and *Hengxing Lan*[1,2]*

[1]College of Geological Engineering and Geomatics, Chang'an University, Xi'an, China, [2]Institute of Geographic Sciences and Natural Resources Research, CAS, Beijing, China

Quaternary loess is widely distributed over the tertiary Hipparion red clay on the Loess Plateau of China. Large-scale loess landslides often occur along the weak contact interface between these two sediment materials. To investigate the failure mode and shear strength characteristics of the loess–Hipparion red clay contact interface, a series of shearing experiments were performed on interface specimens using purpose-built shear equipment. In this article, the relationship between shear strength and interface morphology is discussed, and an empirical shear model of the interface is proposed based on the experimental results and theoretical work. The results indicate that discontinuities between the loess and the Hipparion red clay reduce the shear strength of specimens significantly. The contribution of the contact interface to shear performance including failure mode, shear deformation, and shear strength varies with the interface morphology and the applied normal stress. With low interface roughness or normal stress, sliding failure is likely to occur. With increasing interface roughness and normal stress, the peak strength increases rapidly. With further increase in the interface roughness and normal stress, the increment of peak strength decreases gradually as the failure mode transitions from sliding mode to cutoff mode. A staged shear model that takes the failure mode into consideration is developed to express the non-linear change in the interface shear strength. The shear model's capability is validated by comparing model estimates with experimental data. This work improves our understanding of shear mechanisms and the importance of considering the effects of interfacial properties in the mechanical behavior of contact interfaces.

Keywords: loess, Hipparion red clay, contact interface, shear strength, shear model

OPEN ACCESS

Edited by:
Fanyu Zhang,
Lanzhou University, China

Reviewed by:
Zelin Zhang,
China Agricultural University, China
Xin Peng,
Chinese Academy of Geologi-cal Sciences (CAGS), China

***Correspondence:**
Yanbo Zhu
zhuyanbo@chd.edu.cn
Hengxing Lan
lanhx@igsnrr.ac.cn

Specialty section:
This article was submitted to Geohazards and Georisks, a section of the journal Frontiers in Earth Science

Received: *01 November 2021*
Accepted: *16 December 2021*
Published: *07 January 2022*

Citation:
Zhu Y, Miao S, Li H, Han Y and Lan H (2022) An Empirical Shear Model of Interface Between the Loess and Hipparion Red Clay in a Loess Landslide. Front. Earth Sci. 9:806832. doi: 10.3389/feart.2021.806832

INTRODUCTION

On China's Loess Plateau, loess was deposited on the Hipparion red clay, forming a discontinuous weak interface. Approximately 55% of the large loess landslides occur mainly along this loess–Hipparion red clay interface related to the groundwater activity (Wen et al., 2005; Wang et al., 2019a; Peng et al., 2019). Recent research studies on this type of landslides have shown that the Hipparion red clay is an important factor controlling and affecting the formation of landslides (Qu et al., 1999; Li et al., 2012a). For example, the Hipparion red clay has low permeability and is easy to be weathered (Lei and Qu, 1991); when under the action of water, the red clay is prone to generate creep deformation, and this long-term deformation results in the formation of a sliding surface (Song

et al., 1994; Jiang, 2009; Wang et al., 2012; Xin et al., 2014). Meanwhile, a better understanding of the shear strength of the weak interface between loess and Hipparion red clay is necessary for elucidating the mechanism of loess landslides (Lawrence et al., 2011; Li et al., 2012b; Wu et al., 2014; Peng et al., 2019). However, most recent research on the slip zone of this type of landslides mainly focused on the shear mechanics of pure loess or pure Hipparion red clay (Xu et al., 2008; Jia et al., 2014; Wu et al., 2014; Wang et al., 2018; Wang et al., 2019b; Liu et al., 2020; Zhu et al., 2021a). The shear strength of the interface between loess and the Hipparion red clay in a loess landslide is not clear.

Past research studies have focused on the shear behavior on the interface between soil and different structures, such as the interface between sand and concrete (Skempton, 1985; Uesugi et al., 1990; Hebeler et al., 2016), clay and concrete (Feligha et al., 2016), soil and steel plate (Mortara et al., 2010), soil and geomembrane (Sayeed et al., 2014; Prashanth et al., 2016; Ammar et al., 2019), and soil and bedrock interface (Jahanian and Sadaghiani, 2015). The shear behavior (shear mechanical characteristics, shear failure modes, and strength-influencing factors) of these interfaces has been investigated using experimental shear tests (Fleming et al., 2006; Mortara et al., 2010; Chai and Saito, 2016). It was found that the interfaces have obvious lower shear strength than pure soils and structures (Zhang et al., 2005) and that their shear behavior is influenced by interface roughness, normal stress, and shear rate (Tiwari et al., 2010). For example, the interfacial shear strength was found to increase gradually with increasing interface roughness (Huck et al., 1974; Canakci et al., 2016), and failure modes, such as sliding along the interface, shear-off through the interface, and simultaneous sliding and shear-off, were found to vary with interface roughness (Feligha et al., 2016; Zhou et al., 2019).

Based on these shear tests, researchers have informed attempts to establish theoretical and empirical shear strength criteria for the interface between geotechnical materials and structures (Gómez et al., 2003; Kosoglu et al., 2010; Kang and Liao, 2019; Kang et al., 2021). These include shear strength models for the interface between different rock types (Patton, 1966; Barton, 1973; Grasselli and Egger, 2003; Cottrell, 2009; Wu et al., 2018), rock and concrete (Andjelkovic et al., 2015; Krounis et al., 2016), soil and concrete (Gómez et al., 2003; Yazdani et al., 2019), and soil and geotextile (Esterhuizen et al., 2001; Iryo and Rowe, 2005; Tolooiyan et al., 2009; Portelinha and

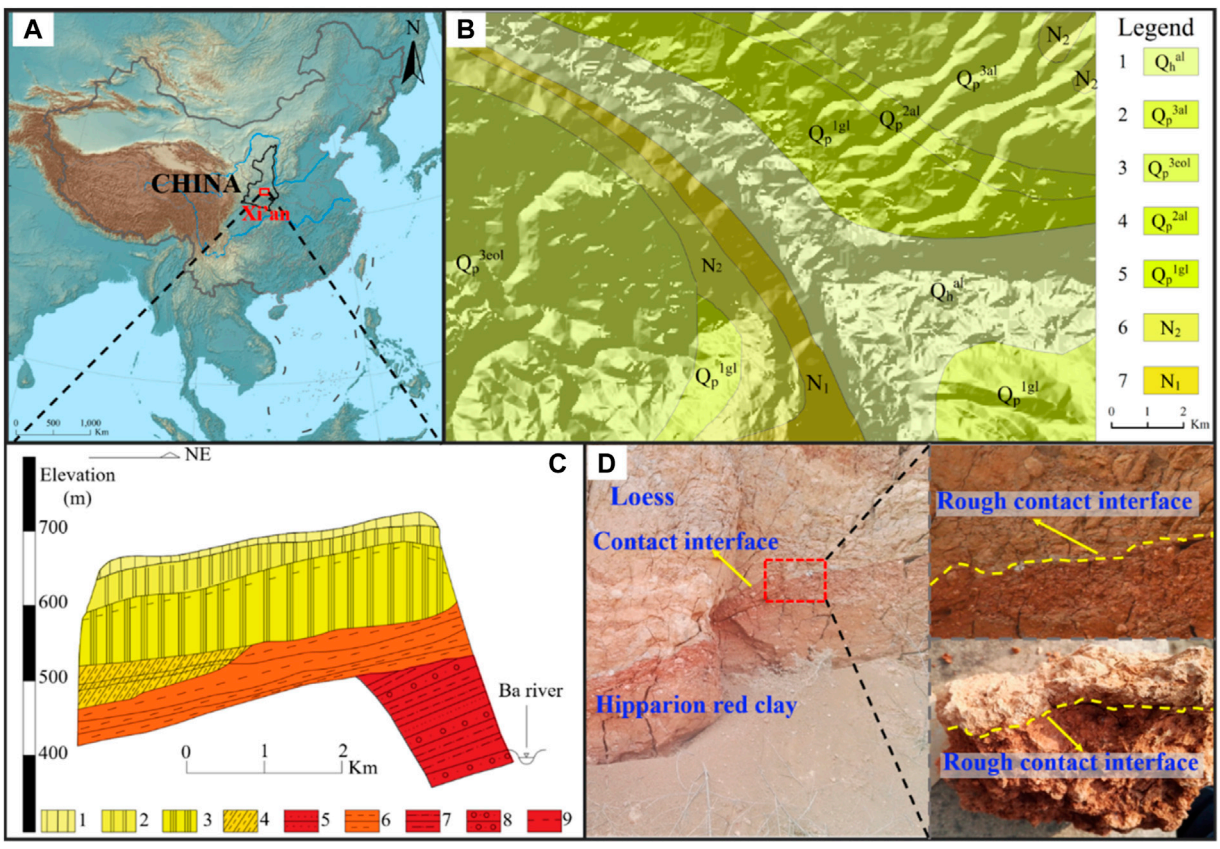

FIGURE 1 | Location of research area and sampling site. **(A)** Research location and **(B)** geological map of research area: 1 the Holocene alluvial sediment, 2 the Upper Pleistocene alluvial loess, 3 the Upper Pleistocene aeolian loess, 4 the Middle Pleistocene alluvial loess, 5 the Lower Pleistocene glacial loess, 6 the Middle Neogene Stratum, 7 the Lower Neogene stratum, and **(C)** engineering geological profile of the study area (modified form the survey report of the second hydrological team of Shaanxi Bureau of Geology and mineral resources, 1979): 1 Malan loess, 2 Wucheng loess, 3 Lishi loess, 4 mild clay, 5 sand soil, 6 mudstone, 7 sandy mudstone, 8 conglomerate, 9 ground water table, and **(D)** rough loess—Hipparion red clay interface.

Zornberg, 2017). Due to the non-linear change in interfacial shear strength, new guidelines for shear model development consider the effect of the interface morphology on shear strength. For regular rough contact samples, Patton (1966) and Serrano et al. (2014) established some bilinear interfacial strength criteria based on two mechanisms of interface shear failure: slippage between asperities, and asperity failure. Other shear models were developed for regular contact interfaces by considering a continuum of three shear modes: sliding, separation, and cutoff of asperities (Ladanyi and Archambault, 1970; Huang et al., 2002; Johansson and Stille, 2014; Zhou et al., 2019). For irregular rough contact samples, models were proposed to take into account the interface roughness and contact intimacy to predict the variation of interface strength (Maerz et al., 1990; Shen et al., 2019).

In summary, although the shear characteristics of the interface between soils/sediments and various structures have received extensive attention, only a few studies have investigated the shear behavior of discontinuities between different soil/sediment types (Indraratna and Jayanathan, 2005; Jahanian and Sadaghiani, 2015), especially for loess with extensive interface contact types. Several investigations of the shear behavior of the loess–sand interface, loess–concrete interface, and loess–mudstone interface have found that the shear strength of these interfaces is much lower than that of pure materials, and some new strength criteria for anisotropy of interface are obtained (Qiao et al., 2016; Liu et al., 2018; Hong et al., 2019; Yang et al., 2020). However, the shear strength of interfaces between loess/Hipparion red clay remains poorly understood. This is especially the case for the interface between loess and Hipparion red clay, the slip zone of many large loess landslides in the Loess Plateau.

To address this lacuna, in this study, we investigate the shear characteristics of the loess–Hipparion red clay interface, the effect of the interface contact angle on failure mode, the shear deformation characteristics, and strength properties. Our study involves experimental work and modeling. Interface specimens with different contact angles were prepared with a specimen preparation device, and a series of direct shear tests were performed on these specimens under different normal stress conditions using purpose-built direct shear equipment. Based on these experimental results, we discuss the failure mode and the effect of the interface angle and normal stress on the shear behavior of the interface. We also developed an empirical shear model that takes into consideration the failure mode to estimate the peak shear strength of the interface. The accuracy of the proposed model is tested by comparing the experimental results with the model-derived values.

MATERIALS AND METHODS

Soil Materials

The research area is in Xi'an that is located south of Loess Plateau in China (**Figure 1A**). In the area, there are five layers including Malan loess (Q_3), Lishi loess (Q_2), Wucheng loess (Q_1), Hipparion red clay (N_2^2), and sandy mudstone and sandstone (N_2^1) (**Figures 1B,C**). The Wucheng loess overlies the Hipparion red clay, and it forms a rough contact interface with different angles (Lawrence et al., 2011) (**Figure 1D**). The loess–Hipparion red clay interface is directly related to the slip zone of some loess landslides, such as the Chenjiapo landslide in Bailu Platform (Wang et al., 2012). Thus, it is necessary to investigate the shear strength of the loess–Hipparion red clay interface by the direct shear test. Remodeled samples are adopted because of the inhomogeneity (http://dict.youdao.com/w/inhomogeneity/javascript:void(0)) of intact samples. The remodeled samples with a rough contact surface are made from the Wucheng loess and tertiary Hipparion red clay around the slip zone that is fine-grained (**Figure 2**), high-density deposit. For preparing the remodeled samples, the initial dry density and initial water content are set to 1.85 g/cm^3 and 15%, respectively.

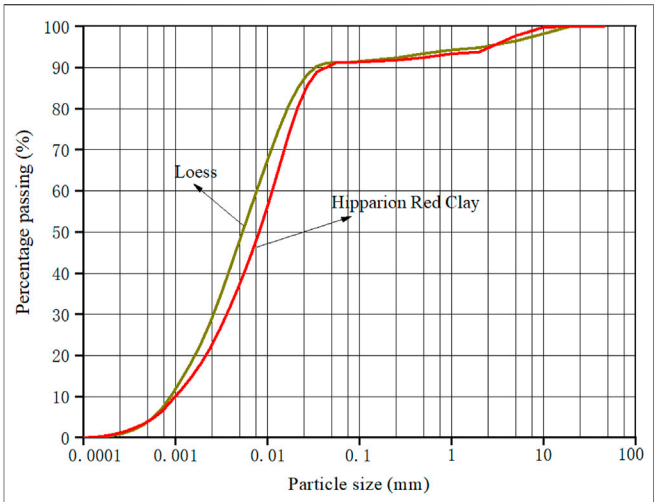

FIGURE 2 | Grain size distribution of the soil materials.

Specimen Preparation

Two types of contact interfaces in the remodeled samples should be set in the remodeled samples, to investigate the shear strength of the loess–red clay interface that is rough in the original layers at Chenjiapo landslide. The rough interface and smooth interface are set in the remodeled samples. The rough interface is set using a special device that comprises a bracket, a jack, and a specimen compaction cylinder consisting of a top cap, a cylinder, a base, and interface molds (Zhu et al., 2021b). The angle of the rough interface includes 0°,15°, 30°, 45°, and 60° made in a set of regular sawtooth metal molds that have the same length of 7.7 mm, and different heights of 0, 1.03, 2.22, 3.85, and 6.66 mm.

The remodeled samples with a rough interface are made in three steps. In the first step, the sawtooth mold was placed in the compaction cylinder, and the loess material is set in the specimen compaction cylinder and compacted. Then the sawtooth mold and the specimen were extracted from the compaction cylinder and detached, and the sawtooth joint was cloned on the loess specimen. The prepared loess specimen was then placed in the compaction cylinder as a mold, with the rough interface facing upward, and some Hipparion red clay material was inserted in the

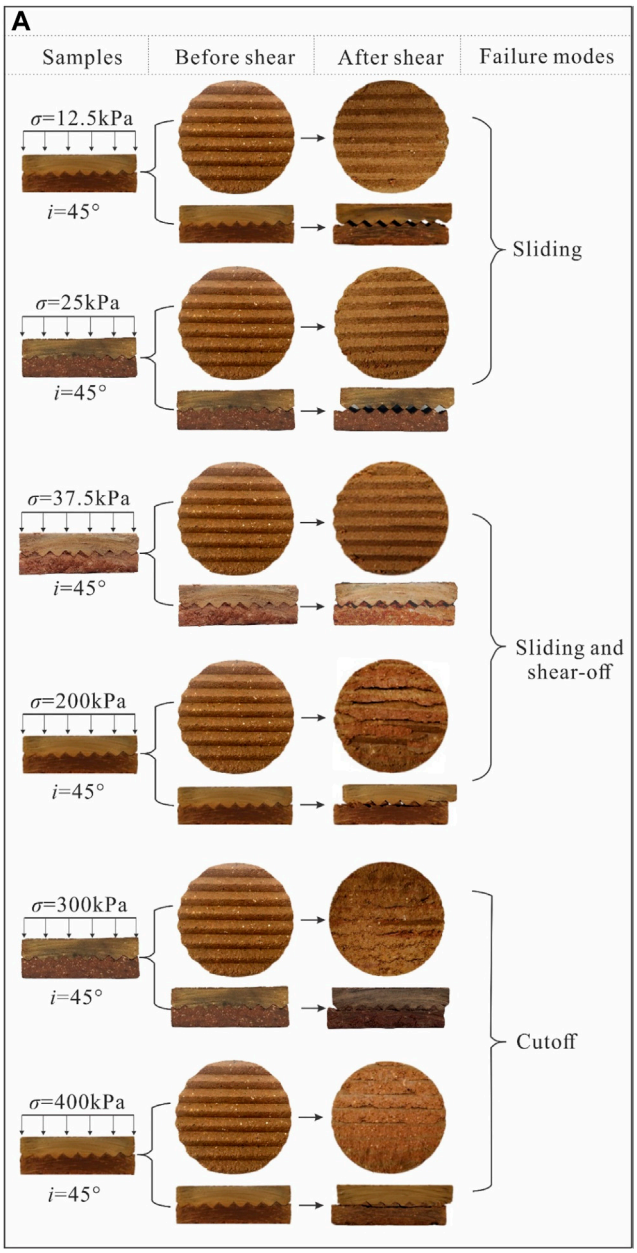

FIGURE 3 | Failure modes of interface specimens. **(A)** Failure modes of specimens with the sawtooth angle *i* of 45° under various normal stresses, and **(B)** failure modes of specimens with various interface angles under normal stress of 200 kPa.

compaction cylinder, above the loess mold. After that, the cylinder fill was compacted again, so that the base of the Hipparion red clay material fitted the rough surface of the loess specimen exactly. Finally, the compressed specimen is extracted from the compaction cylinder using a jack. After the aforementioned steps, the specimen with the size of 61.8 mm in diameter and 20 mm in height was prepared (Zhu et al., 2021b).

Test Equipment and Procedure

The direct shear test on the specimens with loess–Hipparion red clay interface is conducted using computer-controlled direct shear equipment developed by Chang'an University and Zhongzhi Geotechnical Technology Co., Ltd, Nanjing (Zhu et al., 2021b). The equipment consists of a normal loading unit, a shear loading unit, a shear box, a data acquisition and controlling unit, and a measurement unit. The normal loading unit uses an air pressure cylinder to apply normal load in the range of 0–500 kPa, with an accuracy of ±1%. Pressure is provided by an air compressor. The shear loading unit uses a servomotor (type: RS57, with strain control from 0.025 to 6.35 mm/min and accuracy of ±5%, Nanjing, China) to apply the shear load in a strain-controlled manner. The shear box is made into two shapes and sizes suitable for different test standards:

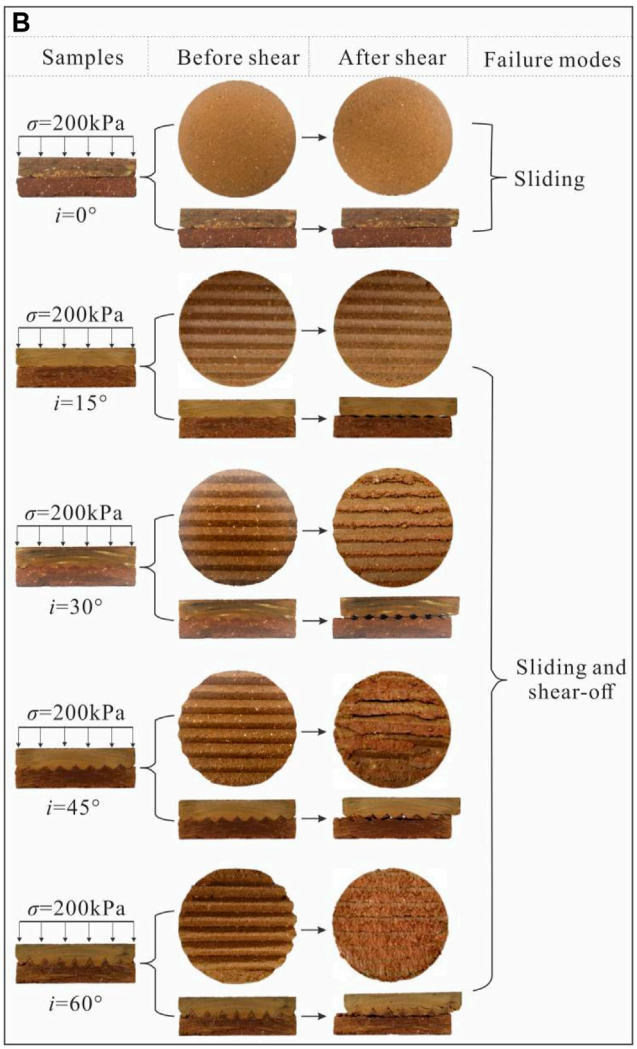

FIGURE 3 | (Continued).

square (61.8 mm in side length; 20 mm in height) and circular (61.8 mm in diameter; 20 mm in height). The measurement unit consists of horizontal linear variable differential transformers (LVDTs; type: Fxg-81N; range: 0–10 mm; accuracy: 0.2%; Fuxin, China), vertical LVDTs (type: Fxg-80N; range: 0–5 mm; accuracy: 0.1%; Fuxin, China), and stress sensors (type: CSF-A; range: 0–2 kN; accuracy: 0.2%; Bengbu, China). The measurement unit allows automatic recording of the displacement and shear stress of the tested specimens by a controlling computer. The data acquisition and controlling unit consists of the controlling computer and the data acquisition and controlling instrument, which can be used to servo-control the normal and shear loading and to collect and transfer the data acquired by the measurement unit in real time.

Using computer-controlled direct shear equipment, five groups of specimens with sawtooth angles i of 0°, 15°, 30°, 45°, and 60° were tested. Samples in each group were tested under eight normal stress levels: 12.5, 25, 37.5, 50, 100, 200, 300, and 400 kPa. The direct shear test was carried out after fixing the interface specimen between the upper and lower shear boxes according to the method ASTM D5321/D5321M-14 (2014). Each specimen was settled in the shear box, and the normal load was applied at a rate of 1 kPa/s until a certain value. The normal load was kept constant during the following shearing process. Then the shear load was applied at a shear displacement rate of 0.8 mm/min until the shear displacement reached 4 mm that corresponds to the post-peak stage. During the direct shear test, the normal load, vertical displacement, shear load, and shear displacement were recorded automatically using a computer in real time.

FAILURE MODES

Exploring the failure modes is important for understanding the shear behavior of an interface. The final failure modes of interface specimens after shear testing are shown in **Figure 3**. It was found that the shear plane was generated along the contact interface of

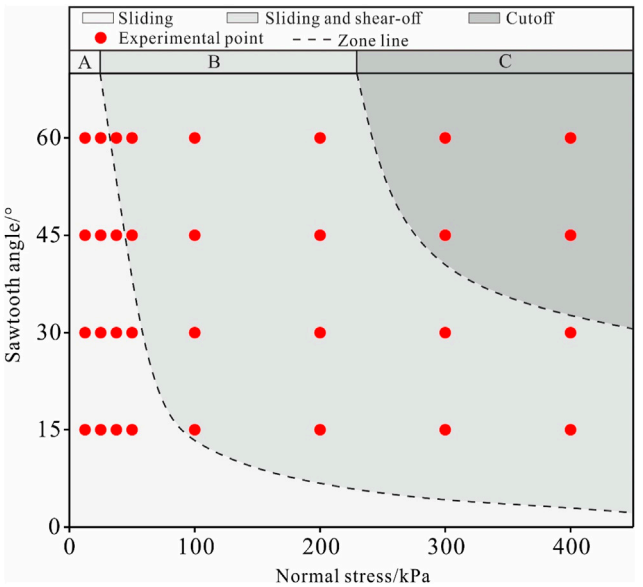

FIGURE 4 | Dependency of failure modes on the sawtooth angles and normal stresses.

loess–Hipparion red clay. However, the failure modes are different due to different normal stress conditions and sawtooth angles. Based on the two types of shear behaviors—sliding along the sawtooth surface and failure through the sawtooth, the failure mode can thus be divided into three types: sliding, sliding, and shear-off, and cutoff (see **Figure 3**).

Figure 3 indicates that the failure mode depends on both the sawtooth angle and the normal stress, that is, the failure mode varies with the normal stress if the same sawtooth angle is the same, such as the specimen with a sawtooth angle i of 45° (**Figure 3A**). Under low normal stress ($\sigma \leq 25$ kPa), the failure mode is sliding. Under medium normal stress (37.5 kPa $\leq \sigma \leq$ 200 kPa), the shear failure mode is sliding and shear-off. Under high normal stress ($\sigma \geq 300$ kPa), the shear failure mode is cutoff. Overall, as the normal stress increases, the failure mode transitions gradually from sliding to cutoff. Besides, the failure mode varies with the sawtooth angle if the normal stress is the same, such as the specimens under a normal stress of 200 kPa (**Figure 3B**). The failure mode transitions from sliding to shear-off with an increasing sawtooth angle. For the sliding mode, the interface specimens mainly slid along the sawtooth contact surface during the entire shear process. For sliding and shear-off modes, sliding along the sawtooth surface occurred first, and then the interfaces specimen was sheared off above the root of the sawtooth. For cutoff mode, the interface specimen was cutoff along the root of the sawtooth. These indicate that the shear process is pure sliding, or pure cutoff, or coupling of sliding and shear-off.

Furthermore, the dependency of the failure modes on the sawtooth angles and normal stresses is discussed in the normal stress–sawtooth angel plane, as shown in **Figure 4**. In the article,

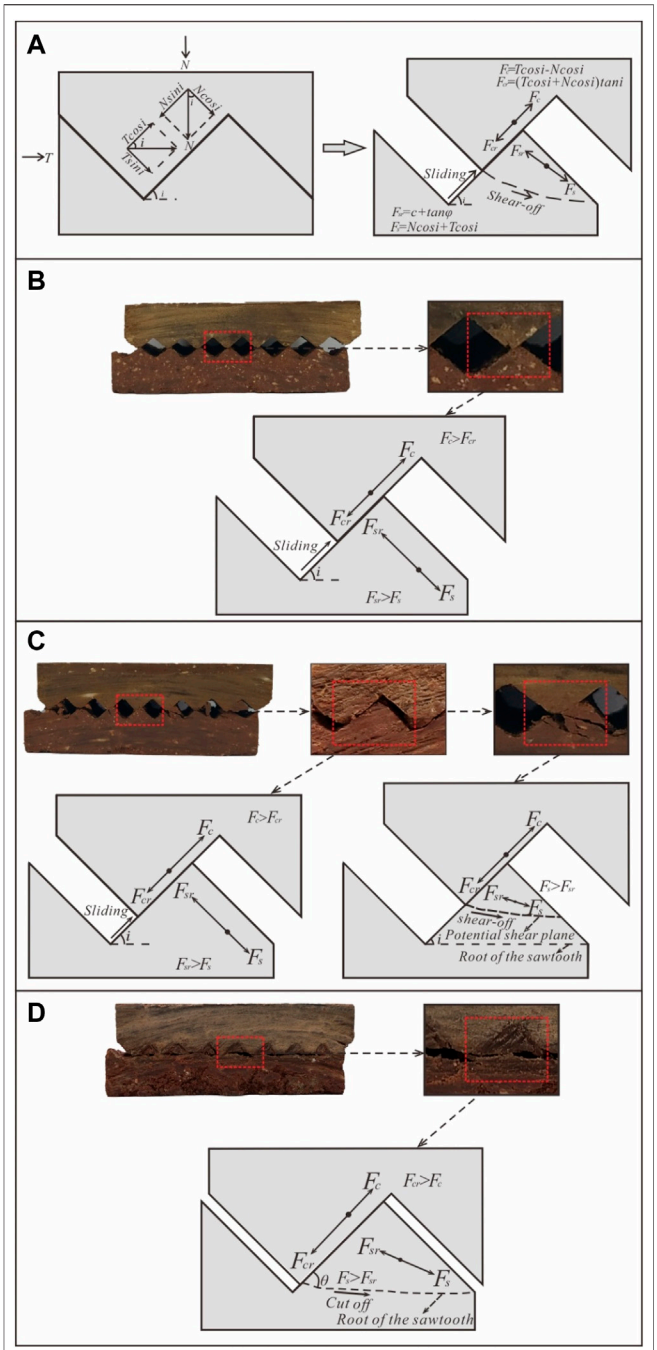

FIGURE 5 | Force diagram for the sawtooth of specimen in different failure modes. **(A)** Force state of sawtooth before and after shear, **(B)** specimens in sliding mode, **(C)** specimens in sliding and shear-off mode, and **(D)** specimens in cutoff mode.

the normal stress and sawtooth angle for the transition of different failure modes are called the threshold values. The range of threshold values was divided according to the failure mode of samples as shown in the zone line (A-B line and B-C line) in **Figure 4**. It is obvious that the threshold values that distinguish different failure modes are not constant, which is related to

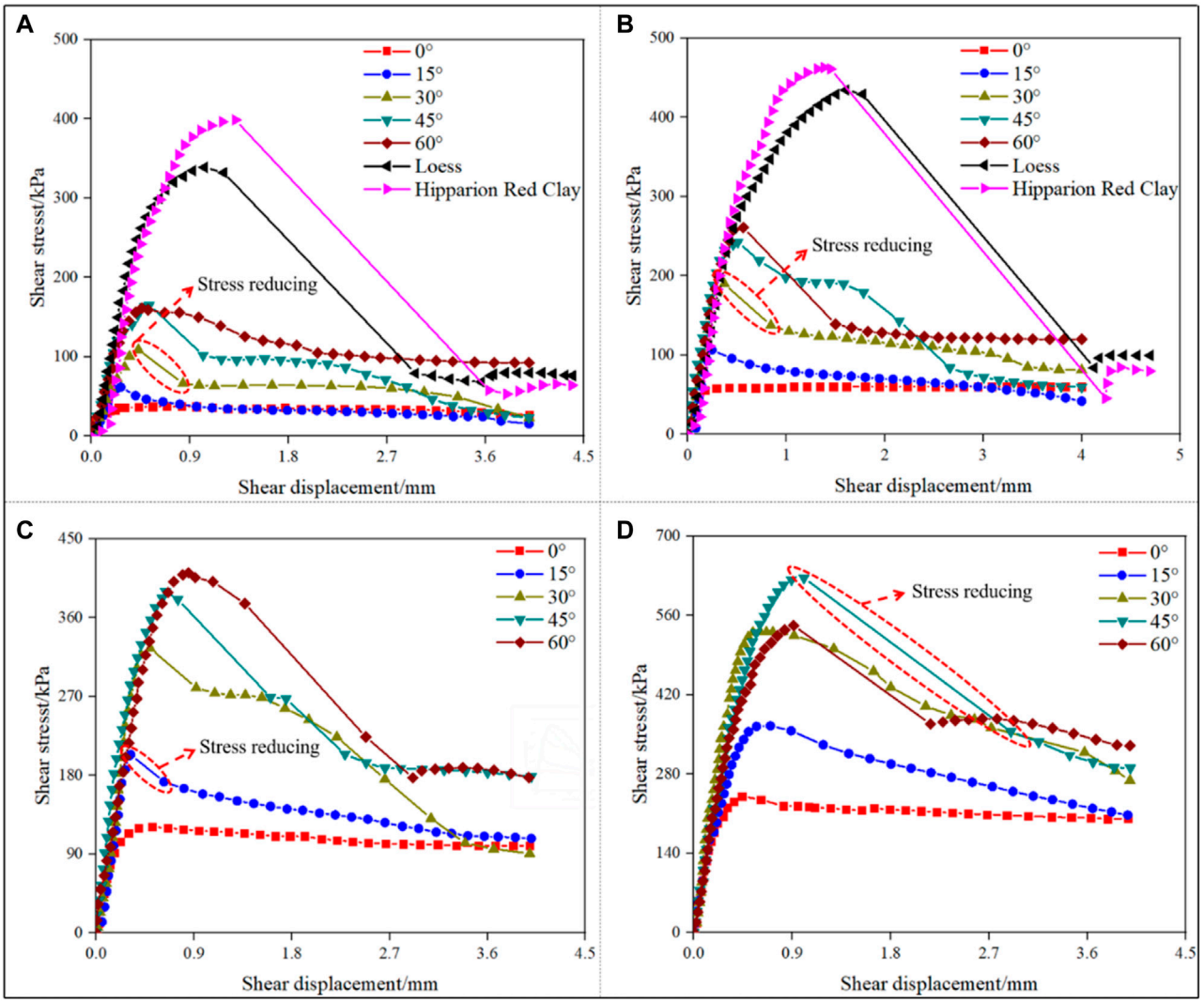

FIGURE 6 | Shear stress–shear displacement curves for interface specimens with different sawtooth angles. **(A)** Normal stress with 50 kPa, **(B)** normal stress with 100 kPa, **(C)** normal stress with 200 kPa, and **(D)** normal stress with 400 kPa.

normal stress and sawtooth angle. It should be noted that the cutoff mode is more likely to occur with a higher sawtooth angle and normal stress, whereas the sliding mode tends to occur with a lower sawtooth angle and normal stress.

To further explore the aforementioned failure modes, it is necessary to investigate the stress state of the sawtooth. Although the shear failure of discontinuity surfaces have been studied (Lee et al., 2001; Asadi et al., 2013; Serrano et al., 2014; Hong et al., 2016), few studies have focused on the stress state of a single asperity at a certain inclination angle (Zhang et al., 2019). In order to analyze the stress state of the sawtooth during shearing, we, respectively, define the sliding thrust F_c as the power force that makes the specimen slide upward along the sawtooth surface, the sliding resistance F_{cr} as the resistance that prevents the specimen from sliding upward along the sawtooth surface, the shear thrust F_s as the power force that makes the specimen to be sheared off through the sawtooth, and the shear resistance F_{sr} as the resistance that prevents the specimen from being sheared off through the sawtooth, as shown in **Figure 5A**.

The normal and shear load generate the sliding thrust F_c, parallel to the contact interface, and generate the shear thrust F_s, perpendicular to the contact interface, as shown in **Figure 5A**. The calculation formulas of F_c and F_s are as follows:

$$F_c = T\cos i - N\sin i \text{ and} \quad (1)$$

$$F_s = N\cos i + T\sin i, \quad (2)$$

where N is the normal load /kPa, T is the shear load /kPa, and i is the sawtooth angle/°.

The sliding resistance F_{cr} is composed of the friction strength between the sawtooth surfaces, and its value is rated to normal load and sawtooth angle (**Figure 5A**). The shear resistance F_{sr} is composed of the shear strength of sawtooth, and its value is rated

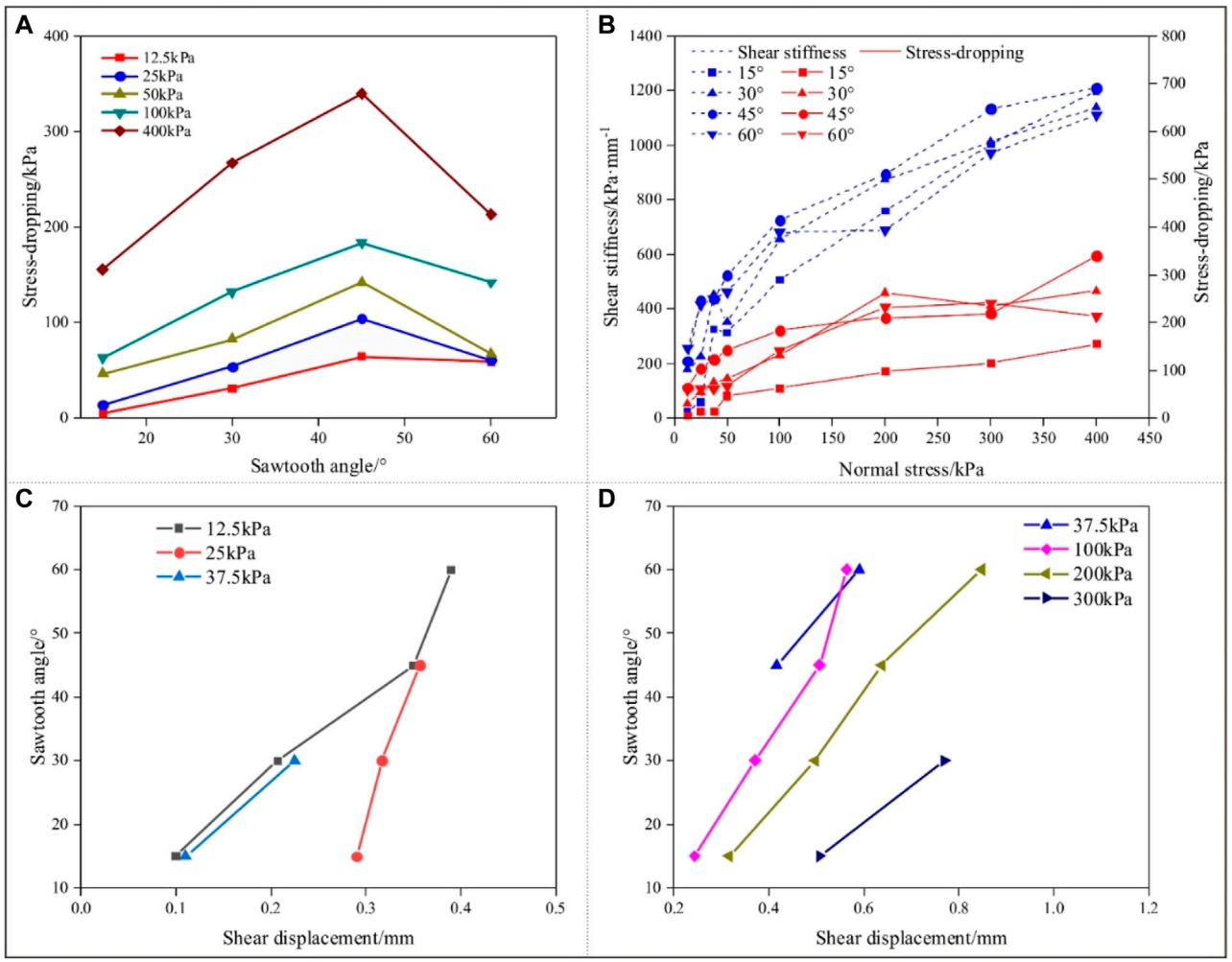

FIGURE 7 | Variation of shear stiffness, post-peak stress and shear displacement of interface specimens. **(A)** Post-peak stress-dropping, **(B)** shear stiffness, and post-peak stress-dropping, **(C)** shear displacement corresponding to peak stress of specimens in sliding mode, and **(D)** shear displacement corresponding to peak stress of specimens in sliding and shear-off mode.

to shear plane position of the sawtooth (**Figure 5A**). The calculation formulas of F_{cr} and F_{sr} are as follows:

$$F_{cr} = (N\cos i + T\sin i)\tan i \quad (3)$$

$$F_{sr} = c + \sigma\tan\varphi \quad (4)$$

where λ is the friction coefficient of the sawtooth surface, c is the cohesion of sawtooth materials /kPa, φ is the friction angle of sawtooth materials/°.

According to **Figure 5A**, it is clear that the failure mode of the interface depends on the relationship between the sliding thrust acting on the sawtooth and the sliding resistance between the sawtooth surface, F_c and F_{cr}, and, also, on the relationship between the shear thrust acting on the sawtooth and the shear resistance of the sawtooth, F_s and F_{sr}. **Figure 5** shows the force diagram for the sawtooth of the specimen in different failure modes. At low normal stress and sawtooth angle, the sliding resistance F_{cr} between the sawtooth surface is also low, and the sliding thrust F_c can easily overcome it. In this situation, sliding occurs along the sawtooth surface (**Figure 5B**). With increasing normal stress and sawtooth angle, at the initial stage of shearing, the shear thrust F_s is smaller than the shear resistance F_{sr}, but the sliding thrust F_c can overcome the sliding resistance F_{cr}. In this condition, sliding along the sawtooth surface occurs first. Then the potential shear plane position on the sawtooth surface continues to move up with sliding until the shear thrust F_s can overcome the shear resistance F_{sr} of the potential cut part of the sawtooth. At this moment, the specimen is sheared off through the sawtooth, and the shear-off plane is located above the root of the sawtooth (**Figure 5C**). With even higher normal stress and sawtooth angles, the sliding resistance F_{cr} increases continually, and the sliding thrust F_c is insufficient to overcome the increasing sliding resistance F_{cr}. However, shear thrust F_s can overcome the shear resistance F_{sr}, and then the specimen is cutoff directly through the root of the sawtooth (**Figure 5D**).

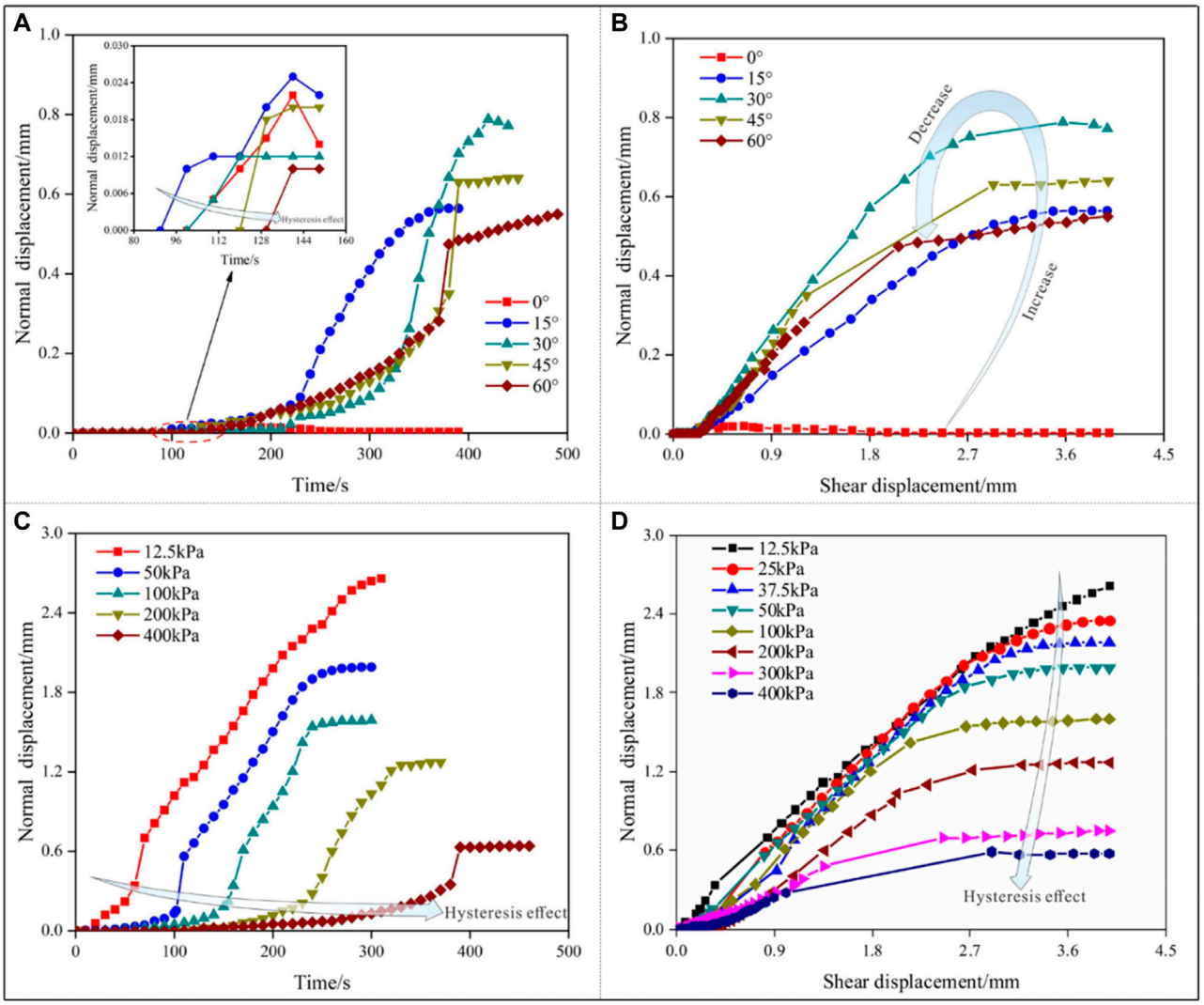

FIGURE 8 | Normal displacement curves of interface specimens. **(A)** Normal displacement–time curves of specimens subjected to the normal stress of 400 kPa, **(B)** normal displacement–shear displacement curves of specimens subjected to the normal stress of 400 kPa, **(C)** normal displacement–time curves of specimens with sawtooth angle of 45°, and **(D)** normal displacement–shear displacement curves of specimens with sawtooth angle of 45°.

SHEAR DEFORMATION CHARACTERISTICS

Shear Stress Versus Shear Displacement

Figure 6 shows the typical shear curves for specimens with different sawtooth angles subjected to different normal stresses. It is obvious that the shear strength of the interface specimen is lower than that of pure loess or pure Hipparion red clay specimens. Most of the shear curves are non-linear with stress reducing sharply after peak stress as the shear displacement increases. The stress reducing sharply means the interface specimen is cutoff along the potential shear plane in the sawtooth. Then the shear stress gradually comes to a stable state corresponding to the residual shear strength. The evolution characteristics of shear curves are related to the normal stress and sawtooth angles. First, the sawtooth angle has a great effect on the shear curves of the interface, especially the peak strength and the post-peak stress-dropping behavior, that is, the peak strength of the interface increases with increasing sawtooth angle; however, the post-peak stress-dropping first increases and then decreases as the sawtooth angle increases (**Figure 7A**). Second, the normal stress also greatly affects the shear behavior of the interface, especially the pre-peak curves, peak strength, and the post-peak curves (**Figure 6**), that is, both shear stiffness and peak strength of the interface increase gradually with increasing normal stress, and the post-peak stress drop is more pronounced with increasing normal stress, suggesting that the difference between the peak shear stress and the residual shear becomes larger (**Figure 7B**).

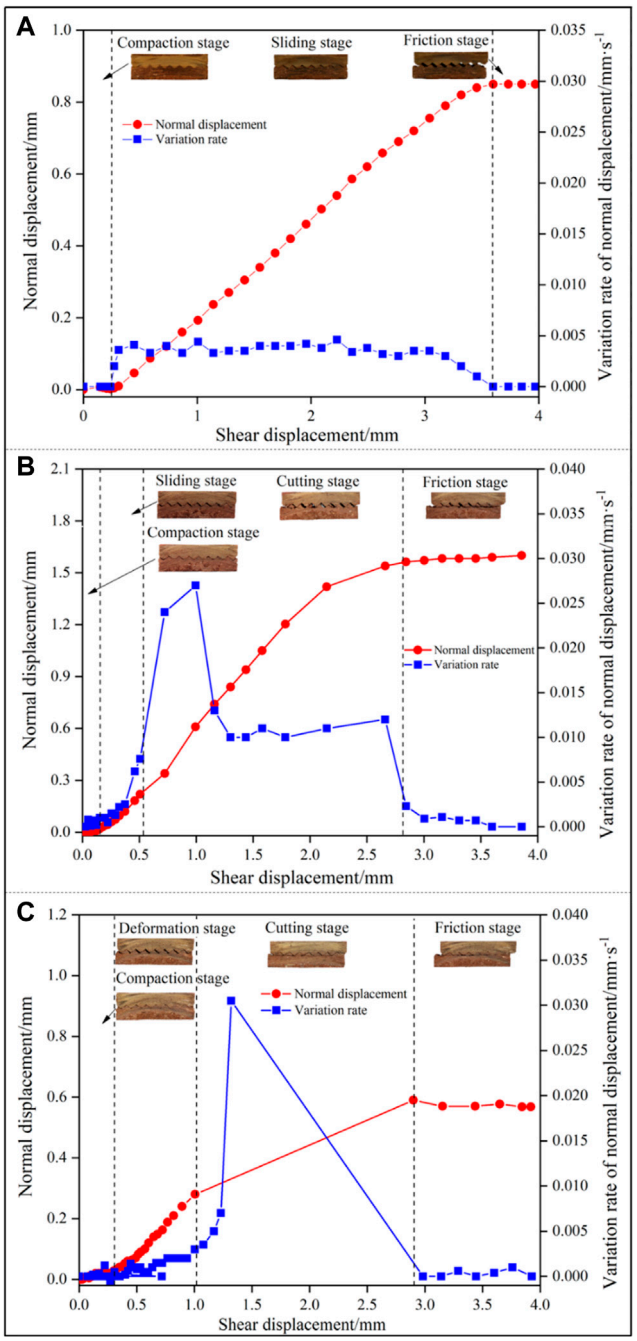

FIGURE 9 | Stage division of normal displacement of interface specimens with different failure modes. **(A)** Sliding: specimen with sawtooth angle of 15° under normal stress of 25 kPa, **(B)** sliding and shear-off: specimen with sawtooth angle of 45° under normal stress of 100 kPa, and **(C)** cutting off: specimen with sawtooth angle of 45° under normal stress of 400 kPa.

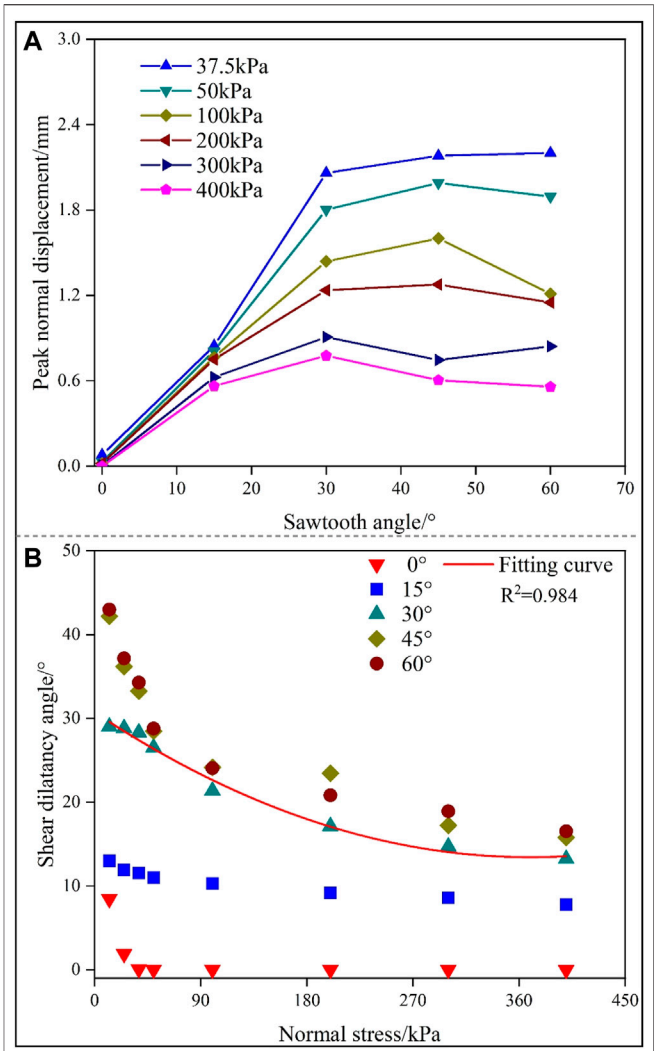

FIGURE 10 | Variation of peak normal displacement and shear dilatancy angle of interface specimens. **(A)** Peak normal displacement of specimens with different sawtooth angles and **(B)** peak shear dilatancy angle of specimens with different normal stresses.

The aforementioned change in the shear curves reflects different failure modes that are related to normal stress and sawtooth angle. When normal stress or sawtooth angle is small, the sliding mode takes place along the contact interface after peak stress (**Figure 5B**). The shear displacement corresponding to peak stress reflects the occurrence of the sliding failure, and the sliding failure occurs earlier if shear displacement corresponding to peak stress is small (**Figure 7C**). Furthermore, the shear displacement corresponding to peak stress increases with the increasing sawtooth angle, indicating the larger sliding displacement at failure (**Figure 7C**).The sliding failure will transform from the sliding mode to the shear-off mode as normal stress and sawtooth angle increase (**Figure 7D**). This can be verified by the sharper shear stress dropping after peak stress (**Figure 7A**), which corresponds to the cutoff failure of the sawtooth. Furthermore, the shear-off failure occurs earlier if the shear displacement corresponding to peak stress is smaller. Smaller shear displacement corresponding to peak stress indicates that the plastic deformation of the interface specimen at failure is smaller, and this usually occurs for the interface specimen with relatively small sawtooth angles (**Figure 7D**).

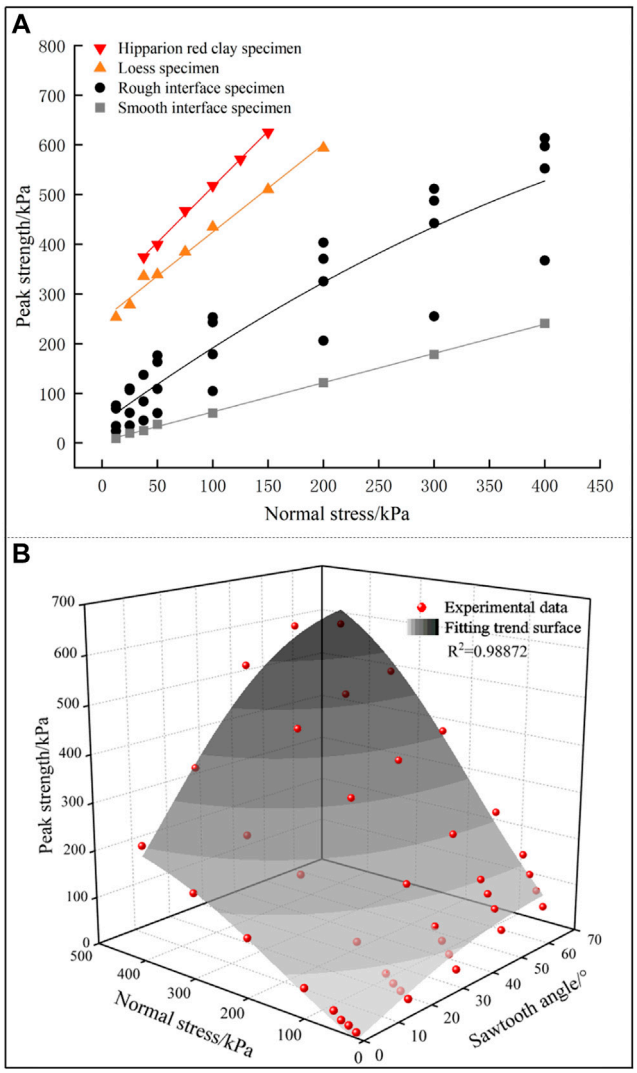

FIGURE 11 | Variation of peak strength of interface samples. **(A)** Peak strength–normal stress curves and **(B)** relationship of peak strength versus normal stresses and sawtooth angles.

Shear Dilatancy Characteristics

Normal Displacement

The normal deformation is caused by the sliding along the interface, which is influenced by normal stress and sawtooth angle, as shown in **Figure 8**. Such as the typical normal displacement curves of interface specimens with different sawtooth angles subjected to the normal stress of 400 kPa (**Figures 8A,B**), the normal displacement first increases and then stabilizes as shear displacement and shearing time increase. However, with an increasing sawtooth angle, there is an obvious hysteresis effect in the occurrence time of normal displacement (**Figure 8A**); after its onset, the normal displacement first increases and then decreases with the increasing sawtooth angle (**Figure 8B**). This influence of the sawtooth angle on normal displacement is mainly related to the failure model. With a low sawtooth angle, the sliding mode is more likely to occur, so the normal deformation increases with an increasing sawtooth angle at first. As the sawtooth angle continues to increase, the shear failure gradually transitions from the sliding mode to the shear-off mode (**Figure 3B**).In this case, the sliding of the interface decreases during shearing, which results in attenuation of normal displacement with an increasing sawtooth angle (**Figures 8A,B**).

The evolution of normal displacement is also significantly affected by normal stress. **Figures 8C,D** present typical normal displacement curves of interface specimens with a sawtooth angle of 45° subjected to different normal stress. With increasing normal stress, there is also an obvious hysteresis effect in the occurrence time of normal displacement (**Figure 8C**); after its emergence, the normal displacement decreases gradually with increasing normal stress (**Figure 8D**). This influence in normal stress on normal displacement is mainly related to the failure mode. With low normal stress, sliding along the sawtooth surface results in a rapid increase in the normal displacement with increasing shearing time (**Figure 8C**). As the normal stress continues to increase, the shear failure gradually transitions to the cutoff mode (**Figure 3A**), and thus, the decreased sliding results in the reduction of the normal displacement during shearing, as shown in **Figure 8D**.

The normal displacement develops in stages according to the increment rate of the normal displacement. **Figure 9** shows the typical stage division of normal displacement curves of interface specimens with different failure modes, which indicates the stage division of these curves is different from failure modes. **Figure 9A** presents the stage division for interface specimens with sliding mode. The normal displacement curve can be divided into three stages: compaction of the sawtooth interface in the compaction stage, sliding along the sawtooth surface in the sliding stage, and the friction on the shear plane in the friction stage. For interface specimens with sliding and shear-off modes, the normal displacement curve can be divided into four stages: compaction of the sawtooth interface in the compaction stage, sliding along the sawtooth surface in the sliding stage, cutting through the sawtooth in the cutting stage, and friction on the shear plane in friction stage (**Figure 9B**). For interface specimens with a cutoff mode, the normal displacement curve can be divided into four stages: compaction of the sawtooth interface in the compaction stage, plastic deformation of the sawtooth in the deformation stage, cutting through the sawtooth in the cutting stage, and friction on the shear plane in friction stage (**Figure 9C**).

The variation in normal displacement at the different stages above is different. In the compaction stage, although the shear displacement increases, the normal displacement is almost absent (**Figures 9A–C**). This is because the sawtooth is continuously compacted under the action of horizontal shear in this stage with no sliding. In the sliding stage, the normal displacement rapidly increases with the shear displacement, indicating that the sawtooth slides upward along the sawtooth interface quickly in this stage (**Figures 9A,B**). In the cutting stage, the increase rate of shear normal displacement increases abruptly at first and then

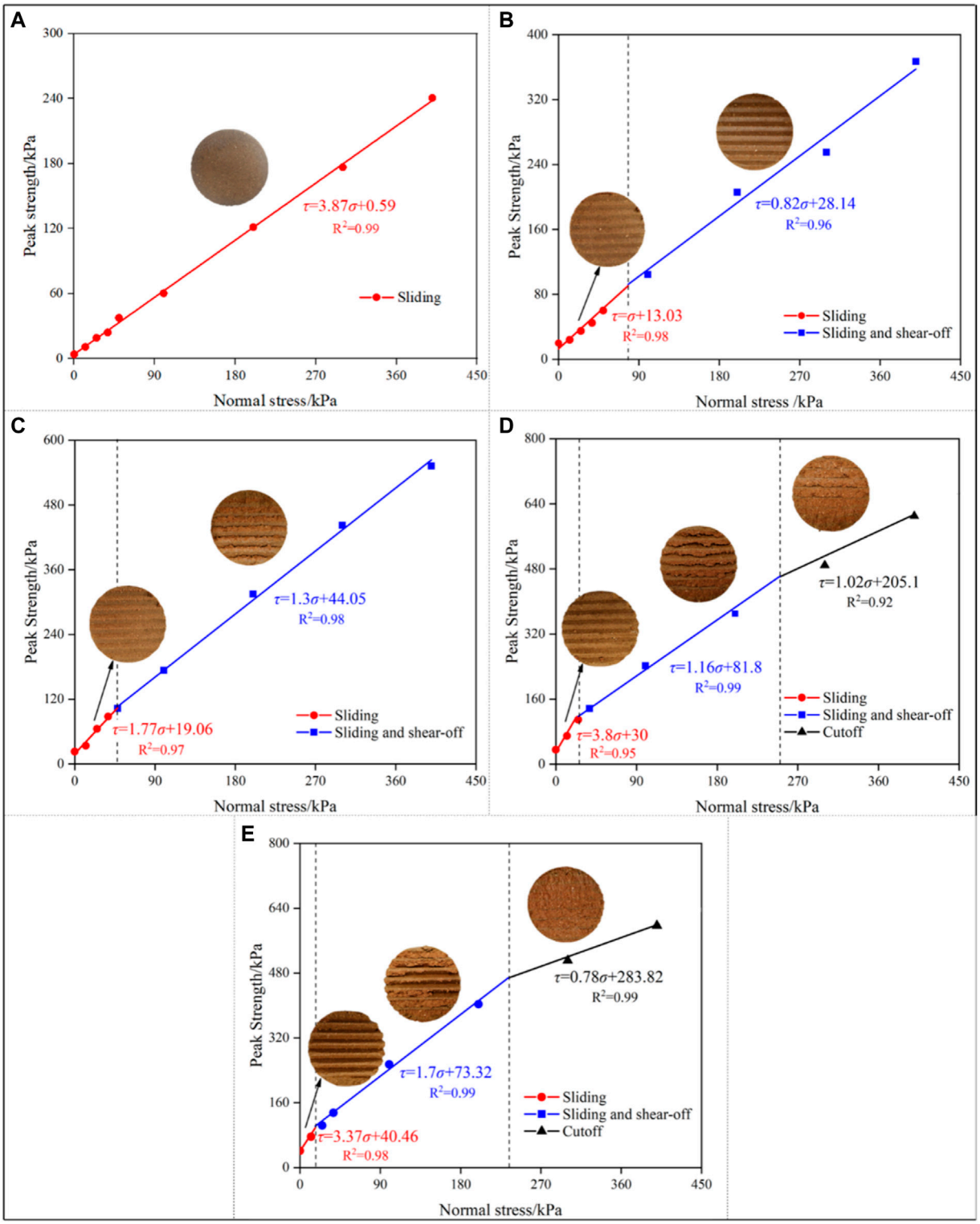

FIGURE 12 | Shear strength envelope of interface specimens. **(A)** Sawtooth angle with 0°, **(B)** sawtooth angle with 15°, **(C)** Sawtooth angle with 30°, **(D)** sawtooth angle with 45°, and **(E)** sawtooth angle with 60°.

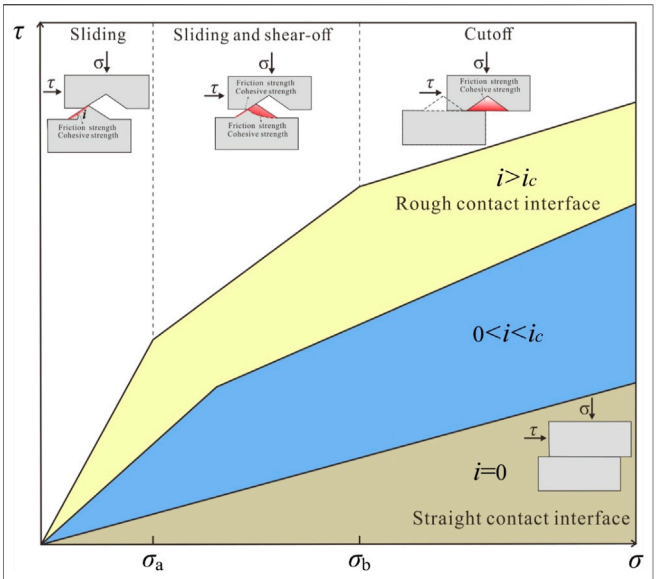

FIGURE 13 | Shear strength envelope of the interface expressed in stages based on the proposed shear model.

decreases gradually (**Figure 9B**). The normal displacement thus increases by leaps to a peak value, indicating that the specimen is instantaneously sheared off through the sawtooth in this stage (**Figure 9B**). During the friction stage, the normal displacement remains steady, indicating that only frictional behavior along the shear plane occurs in this stage (**Figures 9A–C**).

Peak Shear Dilatancy Angle

The peak normal displacement is the maximum dilatation of the interface specimen after failure. The ratio of the peak normal displacement to the horizontal displacement is defined as the peak shear dilatancy angle in this article. It was found that all specimens exhibit shear dilatation, as shown in **Figure 10**. **Figure 10A** shows that the peak normal displacement is influenced by the sawtooth angle and normal stress. That is, the peak normal displacement decreases with increasing normal stress and increases first and then decreases with the increasing sawtooth angle. As shown in **Figure 10B**, the peak shear dilatancy angle also changes significantly with the sawtooth angle and normal stress. Specifically, the peak shear dilatancy angle decreases with increasing normal stress, and this indicates that the volumetric deformation of the interface gradually decreases after shear failure. In addition, the peak shear dilatation angle increases with the increasing sawtooth angle, and its increment drops with increasing normal stress. This indicates that the increment of volumetric deformation of the specimen gradually decreases after shear failure. It should be mentioned that the changing of the peak normal displacement and peak dilatancy angle are all related to the failure mode of the interface including sliding mode, sliding and shear-off mode, and cutoff mode (see **Figure 3** and **Figure 10**), that is, shear dilatation is more obvious when the sliding mode occurs, while the shear dilatation is small when sliding and shear-off mode occurs.

SHEAR STRENGTH CHARACTERISTICS

Interfacial Shear Strength

Figure 11 shows the influence of the sawtooth angle and normal stress on the peak strength in a three-dimensional space coordinate system. It is obvious that the peak strength of the interfacial specimen is lower than that of the pure loess specimen or pure Hipparion red clay specimen, indicating that discontinuities between the loess and the Hipparion red clay reduce the shear strength of specimens significantly (**Figure 11A**). The peak strength increases linearly with increasing normal stress if the interface is smooth (with a sawtooth angle of zero). While the peak strength increases non-linearly with increasing normal stress if the interface is rough (with a sawtooth angle larger than zero), and the increment of peak strength decreases gradually (**Figure 11B**). This influence is related to the failure mode including sliding mode, sliding and shear-off mode, and cutoff mode. The sliding mode occurs if normal stress and the sawtooth angle are small (see **Figure 4**), and the peak strength is related to the friction strength between the interface that increases with increasing normal stress and the sawtooth angle, as shown in **Figure 5**. Therefore, the peak strength increases rapidly with increasing normal stress and sawtooth angle (**Figure 11**). However, the cutoff mode occurs with continuous increase in normal stress and the sawtooth angle (**Figure 4**), and the peak strength is related to the shear strength of the sawtooth, as shown in **Figure 5**. The shear strength of the sawtooth increases with the increasing normal stress and sawtooth angle, but its increment is lower than that of friction strength between the interface with the increasing normal stress and sawtooth angle. Therefore, the increment of peak strength with the increasing normal stress and sawtooth angle drops gradually.

The shear strength curves of the interface specimens were divided into stages according to the failure mode. **Figure 12** presents the staged shear strength curves of interface specimens under normal stress in the 0–400 kPa range. As this figure shows, there are three types of curves. When the contact interface angle is zero, the shear strength curve is linear (**Figure 12A**). When the sawtooth angle is 15° or 30°, the shear strength curve is divided into two stages (**Figures 12B,C**). When the sawtooth angle is 45° and 60°, the shear strength curve is divided into three stages (**Figures 12D,E**). Evidently, the staged expression of the shear strength envelope can accurately reflect the evolution of the interfacial shear strength, and the shear strength in each stage conforms to the Coulomb strength criterion. The dividing points σ_a and σ_b that demarcate each stage are defined as the normal stress thresholds. When $\sigma \leq \sigma_a$, the shear failure is the sliding mode; when $\sigma_a < \sigma \leq \sigma_b$, the shear failure is the sliding and shear-off mode; and when $\sigma > \sigma_b$, the shear failure is the cutoff mode. The normal stress thresholds σ_a and σ_b can be obtained as follows: based on the experimentally observed failure mode of the

TABLE 1 | Values of the shear model parameters.

Sawtooth angle/°	Failure mode	Model parameters					
		ϕ_s/°	ϕ_r/°	C_i/ kPa	C_r/ kPa	*a*	b
15	Sliding	30.14	—	13.03	—	—	—
	Sliding and shear-off	30.14	31.942	13.03	130.4	0.0003	0.017
	Cutoff	—	31.942	—	—	—	—
30	Sliding	30.14	—	19.06	—	—	—
	Sliding and shear-off	30.14	41.669	19.06	170.5	0.0087	0.0051
	Cutoff	—	—	—	—	—	—
45	Sliding	30.14	—	29.99	—	—	—
	Sliding and shear-off	30.14	35.82	29.99	205.1	0.1218	0.0025
	Cutoff	—	27.64	—	205.1	—	—
60	Sliding	30.14°	—	40.46	—	—	—
	Sliding and shear-off	30.14	33.156	40.46	283.8	0.0759	0.0082
	Cutoff	—	26.12	—	283.8	—	—

TABLE 2 | Experimental and model values of the shear strength of interfaces.

Sawtooth angle/°	Strength values/kPa	Normal stress/kPa							
		12.5	25	37.5	50	100	200	300	400
15	Experimental value	24.05	35.12	35.12	60.18	104.47	205.71	255.09	366.92
	Model-derived values	24.69	35.45	46.24	56.49	104.05	188.67	260.69	362.93
	Error/%	–2.66	–0.94	–31.66	6.13	0.40	8.28	–2.20	1.09
30	Experimental value	33.95	60.65	83.62	108.78	178.5	325	442.33	552.43
	Model-derived values	39.89	60.4	79.83	108.79	180.6	325.27	439.62	553.24
	Error/%	–5.94	0.25	3.79	–0.01	–2.1	–0.27	2.71	–0.81
45	Experimental value	69.44	109.60	137.11	163.26	242.79	370.63	487.34	613.23
	Model-derived values	68.86	91.31	144.7	152.29	220	378.47	493.53	582.35
	Error/%	0.84	16.68	–5.54	6.72	9.39	–2.12	–1.27	5.04
60	Experimental value	75.61	106.21	137.11	176.24	253.05	403.3	511.6	597.14
	Model-derived values	81.35	129.79	151.78	159.33	233.3	407.33	557.9	621.11
	Error/%	–7.59	–22.20	–10.70	9.59	7.80	–1.00	–9.05	–4.01

interface under different normal stress (**Figure 4**), the measured shear strength of specimens with the same failure mode is fitted with linear Coulomb strength criterion. The intersection point of each linear strength line corresponds to the normal stress threshold. Note that the normal stress threshold used to divide the shear strength curve is not a constant, and it varies with sawtooth angle.

An Empirical Shear Model of Interface

The experimental results indicate that the shear strength of the interface changes in a non-linear manner; therefore, the non-linear change in shear strength of the interface cannot be evaluated by the linear Coulomb criterion. Thus, it is necessary to formulate an empirical shear model to describe the non-linear shear strength change of interface inspired by other non-linear strength models of geotechnical materials with structural planes (Patton, 1966; Ladanyi and Archambault, 1970; Maerz et al., 1990; Serrano et al., 2014; Barton, 1973; Huang et al., 2002; Andjelkovic et al., 2015; Zhou et al., 2019). Based on the stage division of the shear strength of the interface (**Figure 12**), a staged interfacial shear model is formulated as follows:

$$\tau = \sigma \tan\phi + C, \tag{5}$$

where σ is the normal stress; ϕ is the total friction angle containing the friction angle between the sawtooth contact interface and the friction angle of the sawtooth, and C is the total cohesion containing the cohesion between the sawtooth contact interface and the cohesion of the sawtooth.

The staged interfacial shear model is established according to the failure mode as follows:

Sliding Mode

When the shear failure of the interface specimen is the sliding mode, the shear strength consists of the friction strength and the cohesive strength between the sawtooth contact interface (see **Figure 13**), and the friction strength is related to the sawtooth contact angle and normal stress. In many shear strength formulas of structural interfaces on geotechnical materials (Patton, 1966; Ladanyi and Archambault, 1970; Barton, 1973), the relationship between shear strength and dilatancy angle was established. Especially for rock samples with regular sawtooth interfaces, as the dilatancy angle is equal to the sawtooth contact angle, the relationship between shear strength and dilatancy angle can be

established directly. Inspired by this, the functional relationship between shear strength and dilatancy angle can be established as follows:

$$\tau = \sigma\tan\left(\phi_s + \beta_p\right) + C_i, \qquad (\sigma < \sigma_a), \tag{6}$$

where ϕ_s is the static friction angle between the sawtooth contact interface (which is equal to the friction angle between the sawtooth contact interface when the sawtooth angle is zero); β_p is the dilatancy angle corresponding to the peak strength of the interface; and C_i is the cohesion between the sawtooth contact interface.

Sliding and Shear-off Mode

When the shear failure is the sliding and shear-off mode, the shear strength consists of the friction and cohesive strength between the sawtooth contact interface (corresponding to the sliding process), and the friction and cohesive strength of the sawtooth (corresponding to the shear-off process), as shown in **Figure 13**. Therefore, we need to establish a strength formula that can reflect the whole process of sliding and shear-off.

The friction strength between the sawtooth contact interface, related to the sawtooth angle and normal stress, can be established as a function of the peak dilatancy angle. The friction strength of the sawtooth can be established as a function of the basic friction angle of the sawtooth determined by the residual strength. Taboada et al. (2006) studied the interfacial shear strength of cohesive granular materials and reported that the dilatancy angle at the peak state can be expressed as a function of the difference between the peak and the residual friction angles. Inspired by this work, the peak friction angle of the interface, ϕ_p, is established as the sum of two terms of different origins: the basic friction angle, ϕ_r, and the peak dilatancy angle, β_p, as follows:

$$\phi_p = \phi_r + \beta_p, \tag{7}$$

where ϕ_p is the peak friction angle, determined by the peak strength; ϕ_r represents the contribution of pure friction to the shear strength, determined by the residual strength; and β_p represents the contribution of dilatancy to the shear strength.

The cohesive strength of the interface is composed of the cohesive strength between the sawtooth contact interface, C_i, and the cohesive strength of the sawtooth, C_s. The cohesive strength C_s, related to the shearing position of the sawtooth (**Figure 13**), can be expressed as follows:

$$C_s = kC_r, \tag{8}$$

where C_r is the cohesive strength of the sawtooth when the specimen is sheared off through the root of the sawtooth (see **Figure 10**) and k is a correction coefficient related to the normal stress and the position of shear plane. k is calculated as follows:

$$k = ae^{b\sigma}, \tag{9}$$

where a and b are test parameters. Note that that k is a coefficient smaller than 1.

Therefore, the shear model of an interface with sliding and shear-off mode can be expressed as follows:

$$\tau = \sigma\tan\left(\phi_r + \beta_p\right) + C_i + kC_r \qquad (\sigma_a < \sigma < \sigma_b). \tag{10}$$

Cutoff Mode

When the shear failure is the cutoff mode, the shear strength is mainly composed of the cohesive strength and the friction strength of the sawtooth (**Figure 13**). The friction strength of the interface can be regarded as the combination of dilatancy and friction. Therefore, the shear model of an interface with the cutoff mode is expressed as follows:

$$\tau = \sigma\tan\left(\phi_r + \beta_p\right) + C_r \qquad (\sigma > \sigma_b), \tag{11}$$

According to the aforementioned analysis, an empirical shear model of an interface is obtained as follows:

$$\begin{aligned} \tau &= \sigma\tan\left(\phi_s + \beta_p\right) + C_i && (\sigma < \sigma_a), \\ \tau &= \sigma\tan\left(\phi_r + \beta_p\right) + C_i + kC_r && (\sigma_a < \sigma < \sigma_b), \text{ and} \\ \tau &= \sigma\tan\left(\phi_r + \beta_p\right) + C_r && (\sigma > \sigma_b), \end{aligned} \tag{12}$$

The shear model parameters ϕ_s, ϕ_r, β_p, C_i, and C_r were obtained from the test-derived values of peak strength, residual strength, dilatancy displacement, and shear displacement of the interface specimens. The shear model parameters a and b were calculated from the fitted line of shear strength expressed in stages (**Figure 12**). The values of the shear model parameters are listed in **Table 1**.

Model Validation

In order to verify the accuracy of the proposed shear model, firstm the theoretical values of the shear strength of the interface under different normal stress were calculated by using **Eq. 12**. Then the model-derived values of shear strength of interfaces were compared with the experimental values, as shown in **Table 2**. It is obvious that the proposed interface shear model shows a satisfying prediction accuracy with prediction errors were between −31.66% and +16.68%. This indicates that the proposed interfacial shear model can be used to estimate the shear strength of the loess–Hipparion red clay interface with relative accuracy.

Based on the proposed shear model, the shear strength envelope of the interface can be expressed in stages, as shown in **Figure 13**. If the contact interface of the specimen is smooth, that is, when the sawtooth surface angle is 0, the shear strength of the interface specimens conforms to the linear Coulomb strength criterion. If the contact interface of the specimen is rough, the shear strength curve is a non-linear, composed of three stages related to the failure mode: sliding mode for $\sigma \le \sigma_a$, sliding and shear-off mode for $\sigma_a < \sigma \le \sigma_b$, and cutoff mode for $\sigma > \sigma_b$. The normal stress thresholds σ_a and σ_b are not constant and decrease with increasing sawtooth angle (see **Figure 4** and **Figure 12**).

Furthermore, **Figures 12**, **13** also show that the shear strength curves can be divided into two or three stages under the range of normal stress used in this test (0–400 kPa). This indicates that

there is also a sawtooth angle threshold, i_c (**Figure 13**), that is, when the sawtooth angle $i < i_c$, the shear strength curve is two-staged because the cutoff mode does not occur under normal stress in the range of 0–400 kPa; when $i > i_c$, the shear strength curve is three-staged, indicating that all three modes of shear failure including sliding, sliding and shear-off, and cutoff occur. Based on the stage division of the shear strength curves (**Figure 4** and **Figure 12**), the sawtooth angle threshold i_c is estimated between 30° and 45°.

Based on the shear strength characteristics of interface specimens, it is noted that the discontinuous loess–Hipparion red clay interface has significantly lower shear strength, and the contribution of the interface to shear performance (failure mode, shear deformation, and shear strength) varies with the interface roughness and applied normal stress. For the loess–Hipparion red clay interface, if the contact interface is approximately flat, the interfacial shear strength is lower. However, if the contact surface is rough, the interfacial strength is higher than that of the flat interface, and increases with increasing roughness. Therefore, for the genetic mechanism analysis of loess landslides, the weak shear strength of sedimentary unconformity interface between loess and Hipparion red clay should be fully considered. Nevertheless, the influence of the contact interface roughness on the formation of loess slopes requires further research.

CONCLUSION

A list of shearing tests on the loess–Hipparion red clay interface was conducted to better explore the interface's shear performance and influencing factors. In the shearing tests, rough interface specimens with different contact angles were prepared and subjected to different normal stress. The test results indicate that contact interface roughness and normal stress greatly influence the shear performance including failure mode, shear deformation, and shear strength. The detailed conclusions are shown as follows:

1) The shear failure mode of the loess–Hipparion red clay interface can be divided into three types. The shear failure modes are related to the interface roughness and normal stress, and different failure modes can be identified according to the shear dilatancy in the shear process. The loess–Hipparion red clay interface undergoes the sliding mode if interface roughness is low and large shear dilatation of specimens due to sliding can be observed. With higher interface roughness, the cutoff mode is more likely to occur, and the shear dilatation of specimens is small with this failure mode.
2) Discontinuities between loess and the Hipparion red clay reduce the shear strength of the soil/sediment significantly. The roughness of the contact interface greatly affects the shear strength. The peak shear strength is found to increase non-linearly with increasing interface roughness. Meanwhile, the increment of shear strength decreases for high-angle contact interfaces. It should be noted that the trend of interfacial shear strength is related to the shear failure mode. The sliding mode is likely to occur if the interface roughness or normal stress is small, and the peak strength increases rapidly with increasing friction resistance on the interface. The increment of peak strength decreases gradually as the mode of interface failure transitions from the sliding mode to cutoff mode if the interface roughness and normal stress further increase.
3) An empirical shear model considering the shear failure mode was developed to describe the non-linear variation of shear strength of interfaces with interface angle and normal stress. The model was further validated by comparing the model prediction and experimental results. The results indicate that the empirical shear model can capture the peak shear strength of the interface with relative accuracy (estimation errors −18.17–10.35%). The aforementioned results not only provide a reference for understanding the interfacial shear but also explore both the importance of interfacial properties and normal stress in the mechanical behavior of contact interfaces, especially the shear behavior of interfaces between different soils and sediments.

DATA AVAILABILITY STATEMENT

The original contributions presented in the study are included in the article/supplementary material; further inquiries can be directed to the corresponding authors.

AUTHOR CONTRIBUTIONS

SM and HL conducted model test. YZ and SM wrote the paper. YH made figures. HL provided article revision.

FUNDING

This study was financially supported by the National Natural Science Foundation of China (41877247, 41790443, and 41927806).

REFERENCES

Ammar, A., Najjar, S., and Sadek, S. (2019). Mechanics of the Interface Interaction between Hemp Fibers and Compacted clay. *Int. J. Geomechanics* 19 (4), 1–15. doi:10.1061/(asce)gm.1943-5622.0001368

Andjelkovic, V., Pavlovic, N., Lazarevic, Z., and Nedovic, V. (2015). Modelling of Shear Characteristics at the concrete-rock Mass Interface. *Int. J. Rock Mech. Mining Sci.* 76, 222–236. doi:10.1016/j.ijrmms.2015.03.024

Asadi, M. S., Rasouli, V., and Barla, G. (2013). A Laboratory Shear Cell Used for Simulation of Shear Strength and Asperity Degradation of Rough Rock Fractures. *Rock Mech. Rock Eng.* 46 (4), 683–699. doi:10.1007/s00603-012-0322-2

ASTM Standard (2014). *D5321/D5321M-14 Standard Test Method for Determining the Strength of Soil-Geosynthetic and Geosynthetic-Geosynthetic Interfaces by Direct Shear*. West Conshohocken: ASTM International.

Barton, N. (1973). Review of a New Shear-Strength Criterion for Rock Joints. *Eng. Geology.* 7 (4), 287–332. doi:10.1016/0013-7952(73)90013-6

Canakci, H., Hamed, M., Celik, F., Sidik, W., and Eviz, F. (2016). Friction Characteristics of Organic Soil with Construction Materials. *Soils and Foundations* 56 (6), 965–972. doi:10.1016/j.sandf.2016.11.002

Chai, J. C., and Saito, A. (2016). Interface Shear Strengths between Geosynthetics and Clayey Soils. *Int. J. Geosynthetics Ground Eng.* 2 (3), 19. doi:10.1007/s40891-016-0060-8

Cottrell, B. (2009). *Updates to the GG-Shear Strength Criterion*. Dissertation: University of Toronto.

Esterhuizen, J. J. B., Filz, G. M., and Duncan, J. M. (2001). Constitutive Behavior of Geosynthetic Interfaces. *J. Geotechnical Geoenvironmental Eng.* 127 (10), 834–840. doi:10.1061/(asce)1090-0241(2001)127:10(834)

Feligha, M., Hammoud, F., Belachia, M., and Nouaouria, M. S. (2016). Experimental Investigation of Frictional Behavior between Cohesive Soils and Solid Materials Using Direct Shear Apparatus. *Geotech Geol. Eng.* 34 (2), 567–578. doi:10.1007/s10706-015-9966-5

Fleming, I. R., Sharma, J. S., and Jogi, M. B. (2006). Shear Strength of Geomembrane-Soil Interface under Unsaturated Conditions. *Geotextiles and Geomembranes* 24 (5), 274–284. doi:10.1016/j.geotexmem.2006.03.009

Gómez, J. E., Filz, G. M., and Ebeling, R. M. (2003). Extended Hyperbolic Model for Sand-To-concrete Interfaces. *J. Geotechnical Geoenvironmental Eng.* 129 (11), 993–1000. doi:10.1061/(asce)1090-0241(2003)129:11(993)

Grasselli, G., and Egger, P. (2003). Constitutive Law for the Shear Strength of Rock Joints Based on Three-Dimensional Surface Parameters. *Int. J. Rock Mech. Mining Sci.* 40 (1), 25–40. doi:10.1016/s1365-1609(02)00101-6

He, X. (2014). *Research on the Formation Mechanism of Landslide on the Left Bank of Bahe River in Xi'An –case Study on Chendongpo Landslide*. Beijing: China University of Geosciences.

Hebeler, G. L., Martinez, A., and Frost, J. D. (2016). Shear Zone Evolution of Granular Soils in Contact with Conventional and Textured CPT Friction Sleeves. *KSCE J. Civ Eng.* 20 (4), 1267–1282. doi:10.1007/s12205-015-0767-6

Hong, E.-S., Kwon, T.-H., Song, K.-I., and Cho, G.-C. (2016). Observation of the Degradation Characteristics and Scale of Unevenness on Three-Dimensional Artificial Rock Joint Surfaces Subjected to Shear. *Rock Mech. Rock Eng.* 49 (1), 3–17. doi:10.1007/s00603-015-0725-y

Hong, Y., Zhou, R., Zheng, X. Y., and Ling, X. C. (2019). Shear Mechanical Properties of Sand-Loess under Different Drainage Conditions. *J. Jilin Univ. (Earth Sci. Edition)* 49 (4), 1073–1081. doi:10.13278/j.cnki.jjuese.20170320

Huang, T. H., Chang, C. S., and Chao, C. Y. (2002). Experimental and Mathematical Modeling for Fracture of Rock Joint with Regular Asperities. *Eng. Fracture Mech.* 69 (17), 1977–1996. doi:10.1016/s0013-7944(02)00072-3

Huck, P. J., Liber, T., and Chiapetta, R. L. (1974). Dynamic Response of Soil/concrete Interface at High Pressure. *Int. J. Rock Mech. Mining Sci.* 13 (11), 132.

Indraratna, B., and Jayanathan, M. (2005). Measurement of Pore Water Pressure of Clay-Infilled Rock Joints During Triaxial Shearing. *Geotechnique* 55 (10), 759–764. doi:10.1680/geot.2005.55.10.759

Iryo, T., and Rowe, R. K. (2005). Infiltration into an Embankment Reinforced by Nonwoven Geotextiles. *Can. Geotech. J.* 42 (4), 1145–1159. doi:10.1139/t05-035

Jahanian, H., and Sadaghiani, M. H. (2015). Experimental Study on the Shear Strength of sandy clay Infilled Regular Rough Rock Joints. *Rock Mech. Rock Eng.* 48 (3), 907–922. doi:10.1007/s00603-014-0643-4

Jia, L., Zhu, Y. P., and Zhu, J. C. (2014). Influencing Factors for Shear Strength of Malan and Lishi Compacted Loess in Lanzhou. *Chin. J. Geotech. Eng.* 36 (2), 120–124. doi:10.11779/CJGE2014S2020

Jiang, M. (2009). *Research on the Mechanism and Stability of Loess-Redbed Landslide in Baoji*. Beijing: China University of Geosciences.

Johansson, F., and Stille, H. (2014). A Conceptual Model for the Peak Shear Strength of Fresh and Unweathered Rock Joints. *Int. J. Rock Mech. Mining Sci.* 69, 31–38. doi:10.1016/j.ijrmms.2014.03.005

Kang, X., and Liao, H. (2019). Bounding Surface Plasticity Model for Jointed Soft Rocks Considering Overconsolidation and Structural Decay. *Comput. Geotechnics* 108, 295–307. doi:10.1016/j.compgeo.2018.12.029

Kang, X., Liao, H., Huang, Q., and Dai, Q. (2021). Enhanced Anisotropic Bounding Surface Plasticity Model Considering Modified Spacing Ratio of Anisotropically Consolidated clay. *Acta Geotech* [Epub ahead of print]. doi:10.1007/s11440-021-01314-6

Kosoglu, L. M., Bickmore, B. R., Filz, G. M., and Madden, A. S. (2010). Atomic Force Microscopy Method for Measuring Smectite Coefficients of Friction. *Clays Clay Miner.* 58 (6), 813–820. doi:10.1346/ccmn.2010.0580609

Krounis, A., Johansson, F., and Larsson, S. (2016). Shear Strength of Partially Bonded concrete-rock Interfaces for Application in Dam Stability Analyses. *Rock Mech. Rock Eng.* 49 (7), 2711–2722. doi:10.1007/s00603-016-0962-8

Ladanyi, B., and Archambault, G. (1970). "Simulation of Shear Behavior of a Jointed Rock Mass," in Proc.11th Symp. on Rock Mechanics: Theory and Practice, New York, USA (AIME), 105–125.

Lawrence, J. F., Deng, T., Wang, Y., Xie, G. P., Hou, S. K., Pang, L. B., et al. (2011). Observations on the Hipparion Red Clays of the Loess Plateau. *Vertebrata Palasiatica* 49 (3), 275–284. doi:10.1631/jzus.B1000197

Lee, H. S., Park, Y. J., Cho, T. F., and You, K. H. (2001). Influence of Asperity Degradation on the Mechanical Behavior of Rough Rock Joints under Cyclic Shear Loading. *Int. J. Rock Mech. Mining Sci.* 38 (7), 967–980. doi:10.1016/s1365-1609(01)00060-0

Lei, X. Y., and Qu, H. J. (1991). The Stability of Loess Landslides on the Edges of the Bailu tableland,Xi`an and Their Relationship with Human Activities. *Geol. Rev.* 37 (3), 258–264.

Li, B., Wu, S. R., and Shi, J. S. (2012b). Analysis on the Cause of Formation of Large-Scale Loess Landslide in Weibei Loess Plateau. *Res. Soil Water Conservation* 19 (1), 206–211.

Li, B., Wu, S. R., and Si, J. S. (2012a). Research and Analysis on Large-Scale Loess Landslides in Loess Tableland Area of Weibei. *Reaearch of Soil and water Conservation* 12, 1918–1924.

Liu, J. W., Fan, H. H., Song, X. Y., and Yang, X. J. (2020). Characteristics of Shear Strength and Deformation of Compacted Q3 Loess. *Soil Mech. Found. Eng.* 57, 65–72. doi:10.1007/s11204-020-09672-1

Liu, W., Chen, W., Lin, G., Wang, J., Sun, G., and Zhong, X. (2018). "Shear Strength of Slip Surface in Loess-Mudstone Interface Landslide," in Proceedings of GeoShanghai 2018 International Conference: Fundamentals of Soil Behaviours. GSIC 2018, Singapore, May 27-30, 2018. Editors A. Zhou, J. Tao, X. Gu, and L. Hu (Springer), 531–539. doi:10.1007/978-981-13-0125-4_59

Maerz, N. H., Franklin, J. A., and Bennett, C. P. (1990). Joint Roughness Measurement Using Shadow Profilometry. *Int. J. Rock Mech. Mining Sci. Geomechanics Abstr.* 27 (5), 329–343. doi:10.1016/0148-9062(90)92708-m

Mortara, G., Ferrara, D., and Fotia, G. (2010). Simple Model for the Cyclic Behavior of Smooth Sand-Steel Interfaces. *J. Geotech. Geoenviron. Eng.* 136 (7), 1004–1009. doi:10.1061/(asce)gt.1943-5606.0000315

Patton, F. D. (1966). Multiple Modes of Shear Failure in Rock. Proc. 1st Congress ISRM.

Peng, J., Wang, S., Wang, Q., Zhuang, J., Huang, W., Zhu, X., et al. (2019). Distribution and Genetic Types of Loess Landslides in China. *J. Asian Earth Sci.* 170, 329–350. doi:10.1016/j.jseaes.2018.11.015

Portelinha, F. H. M., and Zornberg, J. G. (2017). Effect of Infiltration on the Performance of an Unsaturated Geotextile-Reinforced Soil Wallffect of Infiltration on the Performance of an Unsaturated Geotextile-Reinforced Soil wall. *Geotextiles and Geomembranes* 45 (3), 211–226. doi:10.1016/j.geotexmem.2017.02.002

Prashanth, V., Murali Krishna, A., and Dash, S. K. (2016). Pullout Tests Using Modified Direct Shear Test Setup for Measuring Soil-Geosynthetic Interaction Parameters. *Int. J. Geosynth. Ground Eng.* 2 (2), 10. doi:10.1007/s40891-016-0050-x

Qiao, L. J., Zhou, G. Q., Shang, X. Y., Lv, X. L., and Zhao, G. S. (2016). Study on the Influence of Water Content on Mechanical Behavior of Loess-Sand Mortar Interface and its Application. *Chin. J. Underground Space Eng.* 6 (2), 1660–1664.

Qu, Y. X., Zhang, Y. S., and Tan, Z. M. (1999). Hipparion Laterite and Landslide Hazards on Loess Plateau of Northwestern China. *J. Eng. Geology.* 7 (3), 257–265.

Sayeed, M. M. A., Ramaiah, B. J., and Rawal, A. (2014). Interface Shear Characteristics of Jute/polypropylene Hybrid Nonwoven Geotextiles and Sand Using Large Size Direct Shear Test. *Geotextiles and Geomembranes* 42 (1), 63–68. doi:10.1016/j.geotexmem.2013.12.001

Serrano, A., Olalla, C., and Galindo, R. A. (2014). Micromechanical Basis for Shear Strength of Rock Discontinuities. *Int. J. Rock Mech. Mining Sci.* 70 (70), 33–46. doi:10.1016/j.ijrmms.2014.02.021

Shen, Y., Wang, Y., Yang, Y., Sun, Q., Luo, T., and Zhang, H. (2019). Influence of Surface Roughness and Hydrophilicity on Bonding Strength of concrete-rock Interface. *Construction Building Mater.* 213, 156–166. doi:10.1016/j.conbuildmat.2019.04.078

Skempton, A. W. (1985). Residual Strength of Clays in Landslides, Folded Strata and the Laboratory. *Géotechnique* 35 (1), 3–18. doi:10.1680/geot.1985.35.1.3

Song, K. Q., Cui, Z. X., Yuan, J. G., and Li, B. (1994). Creep Characteristics Analysis and Prediction of GuliuSlide. *Chin. J. Geotechnical Eng.* 16 (4), 54–64.

Taboada, A., Estrada, N., and Radjaï, F. (2006). Additive Decomposition of Shear Strength in Cohesive Granular Media from Grain-Scale Interactions. *Phys. Rev. Lett.* 97 (9), 098302. doi:10.1103/PhysRevLett.97.098302

Tiwari, B., Ajmera, B., and Kaya, G. (2010). Shear Strength Reduction at Soil Structure Interface. *Proc. GeoFlorida*, 1747–1756. doi:10.1061/41095(365)177

Tolooiyan, A., Abustan, I., Selamat, M. R., and Ghaffari, S. H. (2009). A Comprehensive Method for Analyzing the Effect of Geotextile Layers on Embankment Stability. *Geotext. Geomembr.* 27 (5), 399–405. doi:10.1016/j.geotexmem.2008.11.013

Uesugi, M., Kishida, H., and Uchikawa, Y. (1990). Friction between Dry Sand and concrete under Monotonic and Repeated Loading. *Jpn. Geotechnical Soc.* 27 (6), 115–128. doi:10.3208/sandf1972.30.115

Wang, G. L., Zhang, M. S., Wu, F. Q., Zeng, Q. M., and Zhang, X. S. (2012). Review on Study of Mechanism of Loess Landslides Controlled by Hipparion Red clay. *J. Eng. Geology.* 20, 170–175.

Wang, J., Xu, Y., Ma, Y., Qiao, S., and Feng, K. (2018). Study on the Deformation and Failure Modes of Filling Slope in Loess Filling Engineering: a Case Study at a Loess Mountain Airport. *Landslides* 15 (12), 2423–2435. doi:10.1007/s10346-018-1046-5

Wang, J., Zhang, D., Wang, N., and Gu, T. (2019b). Mechanisms of Wetting-Induced Loess Slope Failures. *Landslides* 16, 937–953. doi:10.1007/s10346-019-01144-4

Wang, S. K., Peng, J. B., Zhuang, J. Q., Kang, C. Y., and Jia, Z. J. (2019a). Underlying Mechanisms of the Geohazards of Macro Loess Discontinuities on the Chinese Loess Plateau. *Eng. Geology.* 263, 1–13. doi:10.1016/j.enggeo.2019.105357

Wen, B. P., Wang, S. J., Wang, E. Z., Zhang, J. M., Wu, Y. G., and Wang, X. L. (2005). Deformation Characteristics of Loess Landslide along the Contact between Loess and Neocene Red Mudstone. *Acta Geologica Sinica* 79 (1), 139–150. doi:10.1111/j.1755-6724.2005.tb00930.x

Wu, Q., Xu, Y., Tang, H., Fang, K., Jiang, Y., Liu, C., et al. (2018). Investigation on the Shear Properties of Discontinuities at the Interface between Different Rock Types in the Badong Formation, China. *Eng. Geology.* 245, 280–291. doi:10.1016/j.enggeo.2018.09.002

Wu, W. J., Su, X., Liu, W., Wei, W. H., Feng, L. T., and Yang, T. (2014). Characteristics and Genesis of Landslide at Loess-Mudstone Interface. *J. Glaciology Geocryology* 36 (5), 1167–1175. doi:10.7522/j.issn.1000-0240.2014.0139

Xin, P., Wu, S. R., Shi, J. S., Wang, T., and Shi, L. (2014). Research on Kinematics and Dynamic Mechanism of Large-Scale Deep-Seated Landslide on the north Bank of Baoji Stream Segment of Weihe River in Loess Plateau. *Acta Geologica Sinica* 88 (7), 1341–1352.

Xu, L., Dai, F. C., Kuang, G. L., and Min, H. (2008). Types and Characteristics of Loess Landslides at Heifangtai Loess Plateau, China. *J. Mountain Sci.* 26 (3), 364–371. doi:10.16089/j.cnki.1008-2786.2008.03.011

Yang, X., Wang, Y., and Sun, Z. (2020). The Shearing Anisotropy Characteristics on the Interface of Loess with Bedrock. *Bull. Eng. Geol. Environ.* 79, 5205–5212. doi:10.1007/s10064-020-01887-8

Yazdani, S., Helwany, S., and Olgun, G. (2019). Influence of Temperature on Soil-Pile Interface Shear Strength. *Geomechanics Energ. Environ.* 18, 69–78. doi:10.1016/j.gete.2018.08.001

Zhang, X. B., Jiang, Q. H., Kulatilake, P. H. S. W., Feng, X., Yao, C., and Tang, Z. C. (2019). Influence of Asperity Morphology on Failure Characteristics and Shear Strength Properties of Rock Joints under Direct Shear Tests. *Int. J. Geomechanics* 19 (2), 1–13. doi:10.1061/(asce)gm.1943-5622.0001347

Zhang, X. S., Liao, H. J., and Xing, X. K. (2005). Laboratory Test Study on Mechanical Properties of Pile-Soil Interaction. *Geotechnical Invest. Surv.* (6), 1–4.

Zhou, H., Cheng, G. T., Zhu, Y., Chen, J., Lu, J. J., and Cui, G. J. (2019). Experimental Study of Shear Deformation Characteristics of marble Dentate Joints. *Rock Soil Mech.* 40 (3), 1–9. doi:10.16285/j.rsm.2017.0964

Zhu, Y. B., Han, Y. T., Miao, S. S., Li, H. F., Li, W. J., Lan, H. X., et al. (2021b). Influencing Factors on the Shear Strength of Sliding Zone of Loess-Hipparion Red clay Landslide. *J. Earth Sci. Environmen.* 43 (4), 744–759. doi:10.19814/j.jese.2021.05024

Zhu, Y. B., Liu, Z. Q., Miao, S. S., Li, H. F., and Lan, H. X. (2021a). Experimental Investigation of Influencing Factors on Long- Term Strength of Sliding Zone of the Loess-Hipparion Red Clay Landslide. *Hydrogeology Eng. Geology.* 1-11, 12–14. doi:10.16030/j.cnki.issn.1000-3665.202104012

Conflict of Interest: The authors declare that the research was conducted in the absence of any commercial or financial relationships that could be construed as a potential conflict of interest.

Publisher's Note: All claims expressed in this article are solely those of the authors and do not necessarily represent those of their affiliated organizations, or those of the publisher, the editors, and the reviewers. Any product that may be evaluated in this article, or claim that may be made by its manufacturer, is not guaranteed or endorsed by the publisher.

frontiers in Earth Science

ORIGINAL RESEARCH
published: 13 January 2022
doi: 10.3389/feart.2021.777467

Microscopic Mechanism Angle of Repose in Friable Loess and Its Relationship With Slope Angle

Haoyu Dong, Jiading Wang, Dengfei Zhang*, Yuanjun Xu and Zhenxiao Li*

State Key Laboratory of Continental Dynamics, Department of Geology, Northwest University, Xi'an, China

The angle of repose in soil particles plays a key role in slope stability. There was a need for the investigation on the association between the angle of repose in loess particles and the angle of slopes. The fixed funnel methods with different particle sizes were carried out. The pressure of particle gravity weight was obtained based on the vibration stacking test. Four contact structures in loess particles were put forward including the triangular pyramid contact structure (TS), rectangular pyramid contact structure (RS), pentagonal pyramid contact structure (PS), and hexagon contact structure (HS). The particles transformed successively in four kinds of contact structures. The transformation of entropy value of the particles in different accumulation areas was discussed during the process of accumulation. The relationship between the natural angle of repose and the evolution of the contact structures was established. Combined with the existing experimental conclusion that loess particles transform in four stable states, in turn, the reason that the friction angle of uniform sand particles proposed by Shields in 1936 is 33° was explained. The formation theory of the loess angle of repose was well extended to speculate the formation process of the loess slope system. It is verified that loess slopes were mainly distributed under 30°.

Keywords: loess slope, granular particles, microscopic contact structure, angle of repose, angle of slope

OPEN ACCESS

Edited by:
Fanyu Zhang,
Lanzhou University, China

Reviewed by:
Siyuan Ma,
China Earthquake Administration, China
Yulong Cui,
Anhui University of Science and Technology, China

****Correspondence:***
Jiading Wang
wangjd@nwu.edu.cn
Dengfei Zhang
dfzhang87@nwu.edu.cn

Specialty section:
This article was submitted to Geohazards and Georisks, a section of the journal Frontiers in Earth Science

Received: *15 September 2021*
Accepted: *20 December 2021*
Published: *13 January 2022*

Citation:
Dong H, Wang J, Zhang D, Xu Y and Li Z (2022) Microscopic Mechanism Angle of Repose in Friable Loess and Its Relationship With Slope Angle. Front. Earth Sci. 9:777467. doi: 10.3389/feart.2021.777467

INTRODUCTION

Loess, as a special sedimentary product of the Quaternary, has a very wide distribution. As shown in **Figure 1**. In the northern and northwestern regions of China, the loess deposits cover an area of 6.24 × 10^5 km^2 (Xu et al., 2017). According to the survey, about 100 million people live on the loess land. However, the loess has the characteristics of vertical joint development, porous and strong water collapsibility. Those features lead to the instability and failure of loess slopes easily. As a result, the loess slopes which exist nearby the human living areas threaten people's life and property safety momentarily. So the stability problem of loess slopes has always been an urgent research problem for national geologists. For example, Wang et al. (2018) took a loess mountain airport as the research object and conducted a large number of research studies on the failure mechanism of slope deformation. Huntley et al. (2019) took the slow-moving landslide which is near Ashcroft, British Columbia, Canada, as the research object. The failure mechanism of the slow-moving landslide was investigated by using the multidimensional electrical dispersion tomography datasets.

In general, the inducing factors of loess landslide can be summarized as vibration (Xu et al., 2020a; Xu et al., 2000b; Zhang et al., 2021), rainfall (Ma et al., 2019; Wang et al., 2019a), and the coupling effect of vibration and rainfall (Wang et al., 2021). Just like engineering problems in **Figure 2**. It is

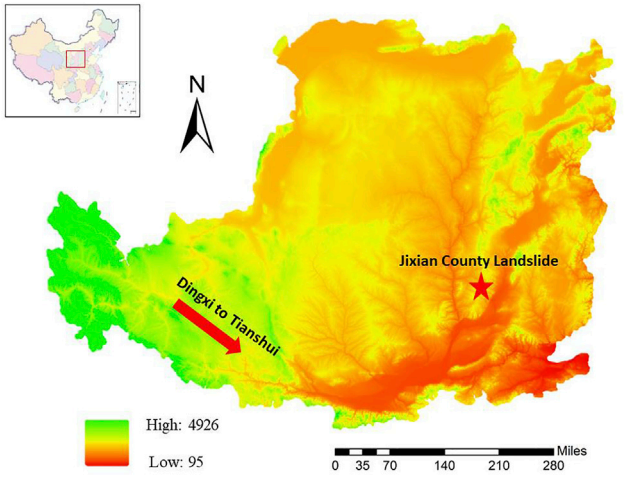

FIGURE 1 | Local loess distribution of China and cases sites.

worth noting that inducible factors such as external factors still act on the internal particles ultimately. The movement direction of the internal particles is the real reason that controls the deformation mode of macroscopic objects (Duran, 2001). According to the hypothesis of the eolian origin for loess, the birth of loess landform is still based on deposition and accumulation. As a large accumulation body, the stability of the loess slope is closely related to the accumulation stability of granular particles, that is, the controlling factors that maintain the stability of the loess slope are similar to those that maintain the stability of granular particles (Evesque and Rajchenbach, 1989; Pahtz et al., 2021).

After years of research, it has been found that the accumulation stability of granular particles is related to the accumulation threshold angle. Once the accumulation angle exceeds this threshold angle, granular particles will show their characteristic of flow. Therefore, only below this threshold angle, the accumulation body will show its characteristic of stability. But this angle is not a fixed value. Just as the example, the stable stacking angle of large particles is smaller than those minimal particles (Holsappl. 2013; Li et al., 2020). This average threshold angle under unconstrained conditions at the time of stacking without collapsing is called the angle of repose (Muller et al., 2021).

As for the angle of repose, there are related studies in different disciplines. In the field of agronomy, Karimi et al. (2009) studied the effects of moisture content of wheat grain and bottom roughness of valley mound on the angle of repose. In the field of biology, Bacherikov et al. (2021) took *Pinus sylvestris* L. seeds as the research object and used different measurement methods to determine the angle of repose in order to solve the problem of reasonable discrete feeding of seeds. In the field of geotechnical engineering, Lajeunesse et al. (2004) used the fixed funnel method to research the effects of particle size, substrate roughness, substrate stiffness, and granular particle mass on the angle of repose. Atwood–Stone and McEwen (2013) studied the variation of granular particles' angle of repose under low-gravity conditions. Chou et al. (2013) used image processing technology and particle tracking technology to explore the relationship between fluid viscosity, particle density, and the angle of repose. Soltanbeigi (2021) proposed several methods to represent the shape of the accumulation body through the angle of repose and direct shear tests. In addition, the angle of repose has been used in many fields such as hydrodynamics, sedimentology, particle technology, and material science.

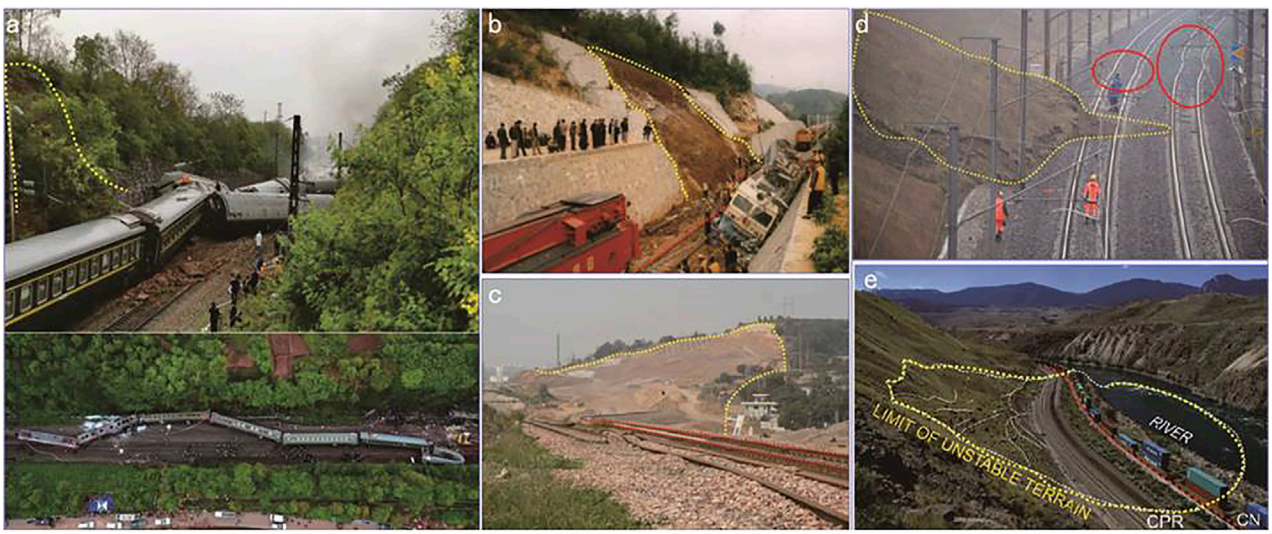

FIGURE 2 | New geological hazards induced by vibration, rainfall, or the coupling effect. **(A)** Landslide in the Yonghua section of the Beijing–Guangzhou Railway. **(B)** Typical landslides along a heavy-load railway in Shanxi. **(C)** Landslide along the Yang-Da Railway (Wang et al., 2021). **(D)** Landslides along the section close to Strasbourg at the France and Germany border as TGV (Train À Grande Vitesse) is approaching (https://www.sohu.com/a/377989394_100016456). **(E)** Landslides along the railway near Ashcroft, Canada (Huntley et al., 2019).

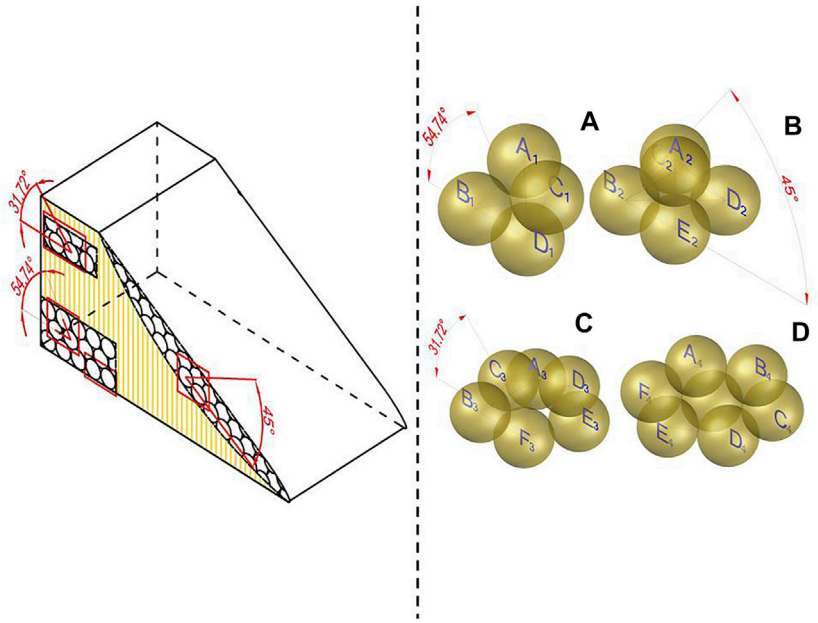

FIGURE 3 | Four different contact models. **(A)** Triangular pyramid contact structure; **(B)** rectangular pyramid contact structure; **(C)** pentagonal pyramid contact structure; **(D)** hexagon contact structure.

However, few scholars have associated the angle of repose with the stability of the loess slope. In fact, as the threshold angle for the accumulation body to maintain its stability, the angle of repose also has a controlling effect on the loess slope which is considered as large deposition. In order to explore the relationship between the angle of repose and the stability of the loess slope, four different contact models are proposed in this article. The fixed funnel method and vibration stacking test are used to prove the rationality of the contact models directly and describe the contact transformation of granular particles during the accumulation process. Furthermore, the formation mechanism of accumulation body's angle of repose is explained from the perspective of particles. And it is extended to the loess slope. Based on the principle that controlling the maximum accumulation angle of granular particles is the angle of repose, the allowable variation range of loess slope angle under the condition of maintaining its stability is deduced. Then the theoretical relationship between the angle of repose and slope stability is established.

STRUCTURES AND METHODS

Contact Structures

The accumulation body is not the superposition of multiple particles simply but the chimera of particles and accumulation body. In most cases, the sedimentary particles will be embedded into the accumulation body and form a new contact structure together with it. For the loess accumulation body, this chimeric structure is the structure of the soil accumulation body. Therefore, it is the foundation for the study of the soil structure to explore the contact structure of particles. That is also the problem of how particles embed with each other and form the basic contact models. The contact structure of loess is very complex. However, the first step to studying any complex problem is to discuss and understand the characteristics of the most important relevant properties of this problem under ideal conditions. In order to facilitate the study and discussion of the contact structure between loess particles, the contact models established in this article are all proposed under some special assumptions. That is to say, the deposited loess particles are spherical, rigid, and equal in size and have complete homogeneity. The loess accumulation body only contains the pores caused by the contact models themselves. The pores caused by other factors will not be discussed temporarily. Therefore, the deformation of particles, sedimentation rotation caused by occlusion, and the dominant subsidence channels generated by particles in the process of sedimentation compression are not considered in the test. The test time of this experiment is transitory. The spatial position and temperature fluctuation of the test are also very small. Therefore, the air humidity will also not have a great fluctuation, and the air humidity will not affect the microscopic effect between particles.

According to the conditions of assumptions, the deposited loess particles are spherical, rigid, and equal in size and have complete homogeneity. One of the spherical particles is taken as the object of observation, and other particles are inserted around the spherical particles. The center points of spherical particles contacting each other are connected to determine the shape of the contact model and name it accordingly. The structure of the accumulation body is a three-dimensional spatial concept, so the contact model reflecting its structure must be a three-dimensional

structural model. A single or even three spherical particles cannot satisfy the basic concept which is a three-dimensional structural model. The three-dimensional structure is not constructed successfully until the fourth spherical particle is considered. That is, the other three spherical particles at the bottom around the spherical particle at the top together form a triangular pyramid structure, called the triangular pyramid contact structure (TS). As the top particle moves down, the space at the bottom gradually expands until the fourth spherical particle at the bottom can be embedded. Four spherical particles at the bottom around the top spherical particle together form a rectangular pyramid structure. It is known as the rectangular pyramid contact structure (RS). In the same way, it can be known that there is a pentagonal pyramid contact structure (PS) and hexagon contact structure (HS). As shown in **Figure 3**. Strictly speaking, HS is a two-dimensional structural model. It is contrary to the basic concept which is the three-dimensional structural model. In addition, when there are particles embedded in the upper layer of HS stably, the HS and TS express the same contact form. But the HS is a special contact form of TS. It can more clearly express the particles' contact form at continuous but distinct interfaces. For example, when particles are stacked on a flat interface, the contact structure of the particles is a typical HS. Moreover, the process from the TS to HS is a continuous transformation. It is of great significance in understanding and studying the transformative process of particles' contact structure in the stacking process. Therefore, the HS can be and needs to be listed separately to form a special contact model.

Fixed Funnel Method Test

According to relevant studies, when the particle size is less than 50 μm, cohesion plays a major role in the connection between particles (Lumay et al., 2012). However, the main content of this study is to explore the influence of the particle structure on the stability of the accumulation body. Hence, the uniform particle size of the accumulated particles is required to be greater than 50 μm. As shown in **Figure 4**. In order to prove the influence of the structure of loess particles on the stability of the accumulation body more directly, three kinds of particles with different particle sizes are screened through the screening method in this fixed funnel method test: a) angular gravel whose particle size exceeds 2.000 mm and particle content accounts for the size is more than 50% of the total mass; b) coarse sand whose particle size exceeds 0.500 mm and particle content accounts for the size is more than 50% of the total mass; and c) sand loess whose particle size exceeds 0.075 mm and particle content accounts for the size is more than 50% of the total mass. These three kinds of particle sizes are used for experiments.

The main purpose of this test is to simulate the transformation of particles' contact structure under the conditions of deposition and accumulation and to measure the angle of repose of the accumulation body. In order to simulate the real situation of particles with certain kinetic energy during deposition and accumulation accurately, the fixed funnel method is used in the stacking test. According to the provisions of 2.582 in the FEM standard, the ratio between the diameter and the particle size of the accumulation body should be more than 20. However, on the basis of the study of Rackl et al. (2017), the ratio between the diameter and the particle size should be more than 40. Judging by the requirements of particle size in this fixed funnel method test, the maximum particle size is 0.500 mm. Therefore, the diameter of the accumulation body in this accumulation test is required to exceed 200 mm uniformly.

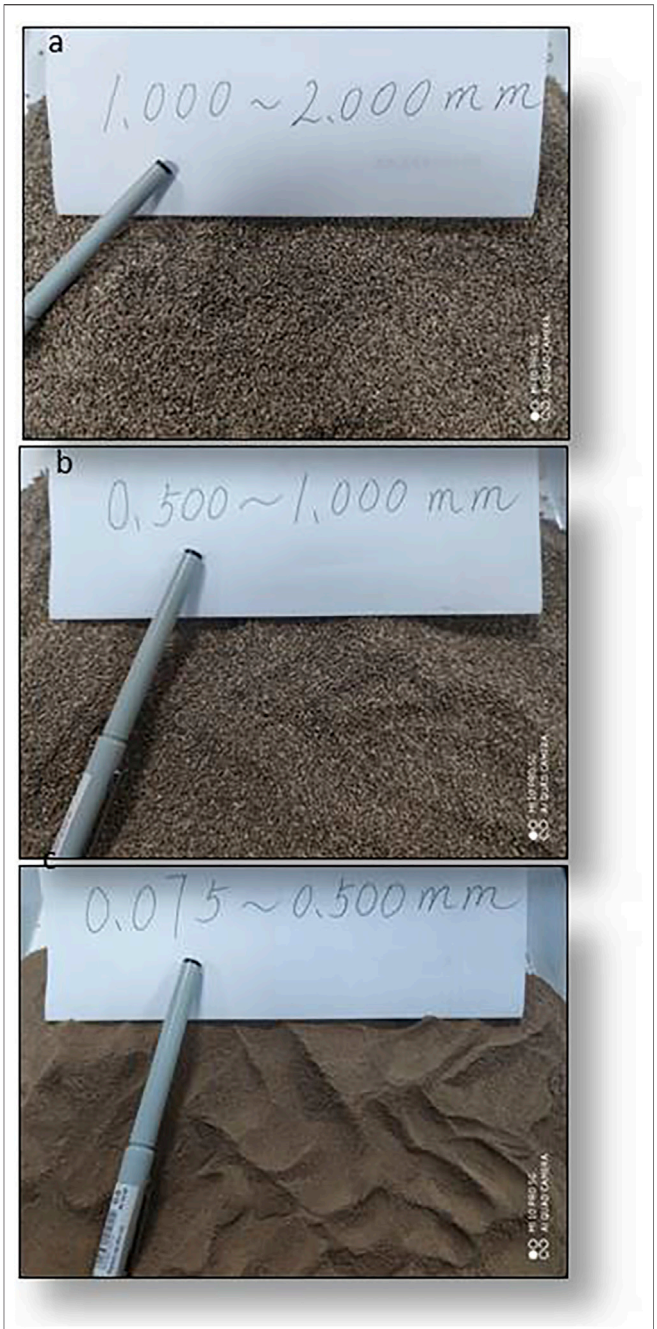

FIGURE 4 | Screening results of particles with three sizes. **(A)** Angular gravel with a diameter of 1.000–2.000 mm. **(B)** Coarse sand with a diameter of 0.500–1.000 mm. **(C)** Sand loess with a diameter of 0.075–0.500 mm.

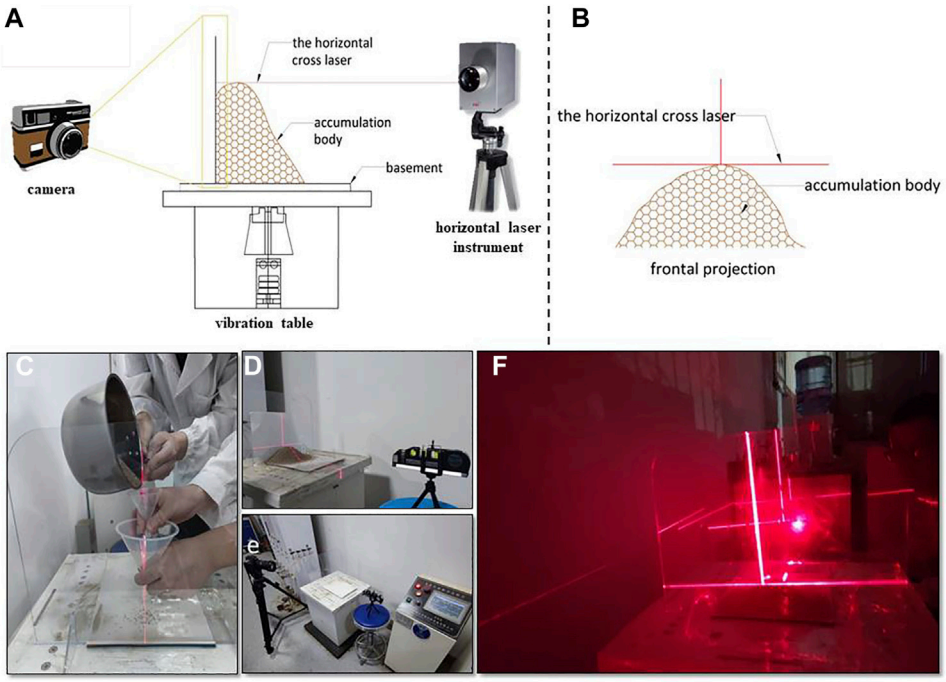

FIGURE 5 | (A) Fixed funnel method principle. **(B)** Frontal projection of laser measurement. **(C)** Fixed funnel method. **(D)** Measure the angle with laser. **(E)** Vibration table **(F)** Cross laser penetrating the accumulation body.

Based on the research results of Liu (2011), the funnel lifting speed can be divided into two ways: low speed (2~3 cm/s) and high speed (7~8 cm/s). The process of loess particle deposition and accumulation simulated in this research is a natural process. The huge disturbance caused by humans or unpredictable earthquakes is not taken into account. Therefore, the fixed funnel method test should not be lifted up too fast. The test adopts the way of low-speed lifting. The angle of repose of the accumulation body is also affected by the roughness of the basement. The rougher the basement is, the larger the particles' angle of repose will be. Therefore, the emery paper with stronger roughness is uniformly used in this accumulation test to control the diffusion range of the first layer of particles. When the diffusion range of the first layer of particles can be controlled, most of the particles will accumulate and have contact. Then, the contact structure in the accumulation body will be observed more easily because only the contact structure on the surface of the accumulation body can be observed through the fixed funnel method. The method cannot reflect the transformation of particle contact structure inside the accumulation body well. So the test is improved according to the fixed funnel method. A transparent separator is erected beside the sand outlet at the bottom of the funnel. Relative to the accumulation body, the transparent separator can be considered as the boundless side limit in this direction. But for the other directions, the transparent separator has no influence. After the completion of the fixed funnel method test, the experimenter can observe the transformation of particle contact structure inside the accumulation body through the transparent separator. Since the transparent separator only restricts the orientation of the partition and has no effect on the other directions, when the accumulation body is in a critical state that can be accumulated without collapsing, the angle of accumulation body observed through the transparent separator is the angle of repose that needs to be measured. As shown in **Figure 5**.

So far, the measurement of the angle of repose in the fixed funnel method test is mainly divided into two kinds. The first one is measured by the protractor directly. But this approach has an obvious flaw that the measurement accuracy is not enough. The other way is to adopt the overlapping multi-sphere clump method in the discrete element method (DEM) to simulate accumulation body effectively. Then, the size of the angle of repose is calculated (Zheng and Hryciw. 2016; Zhou et al., 2018; Hua and Shultis. 2021). But this simulating method cannot completely simulate the irregularity and diversity of angular particles, and the calculation of the angle of repose is not accurate enough. To solve this problem, the test also made some improvements in data measurement. The horizontal cross laser is fired by using the horizontal laser instrument. Because the cross laser cannot penetrate the accumulation body, the cross focus cannot be found on the ruler of the transparent partition board. At the time, the cross focus can be found on the ruler of the transparent partition board; it means that the cross laser just passes the top of the accumulation body. At this time, the height of the cross laser's focus on the ruler H is the height of accumulation body. Similarly, the points on both sides of the bottom of the accumulation body can be found, and the diameter L of the accumulation body can be measured.

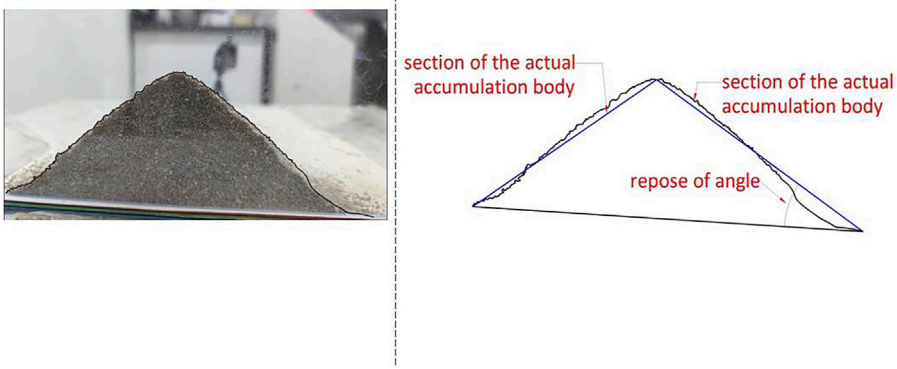

FIGURE 6 | Accumulation body and measured surface.

According to **formula 1**, the angle of repose of α can be calculated as follows:

$$\alpha = \tan^{-1}\frac{2H}{L}, \tag{1}$$

The angle of repose based on this calculative method is the base angle of an idealized cone which is formed by connecting the top and bottom accumulation points of the accumulation body. As shown in **Figure 6**. The generatrix of the idealized cone is a straight line which is against the fact. The fact is that the generatrix of the accumulation body is irregular. After multiple fixed funnel method tests, it is found that the accumulation body presents a convex shape locally. Just like the slope of Zaoling landslide in Shanxi Province, the pre-slide slope, on the upper part, is steep with 53°and the pre-slide slope on the lower part is 37° (Cui et al., 2020). Therefore, the method used by Penkavova et al. (2021) is adopted by determining the angle of repose. A Canon SD126601 camera is used to photograph the frontal projection of the accumulation body. And then CAD is used to depict and measure the angle of repose θ of the accumulation body directly. Several groups of repose angles are obtained by multiple measurements. The average value of laser repose angle $\bar{\alpha}_1$, as in **formula 2**, can be calculated for the first fixed funnel method test.

$$\bar{\alpha}_1 = \frac{\frac{\sum_1^n \alpha_n}{n} + \theta}{2}, \tag{2}$$

After many fixed funnel method tests, the final mean value of laser measured angle of repose $\bar{\alpha}$ was calculated as **formula 3**.

$$\bar{\alpha} = \frac{\sum_1^n \bar{\alpha}_n}{n}, \tag{3}$$

Vibration Stacking Test

A stacking test can show contact structures of particles intuitively. But for a small laboratory test, the gravity pressure of friable deposits is not enough to make particles move and even not enough to promote the contact models to transform from each other. Even if the giant particles deposit with enough gravity pressure, it really needs a long time to consolidate due to its gravity pressure. Decades of years may appear very tiny changes. To strengthen the particle rolling effect under gravity pressure and to promote the transformation of each contact model, the vertical vibration load is added on the basis of the stacking test. As shown in **Figure 7**. The downward momentum of particles keeps converting into gravitational potential energy by adopting the vertical vibration whose frequency is 20 Hz and strength is 15%. This way can promote the transformation of contact models under the gravity pressure. The vibration frequency and strength can be controlled by using a VT 700 vibration table.

RESULTS AND DISCUSSION

Microscopic Mechanism of Angle of Repose

As for the accumulation body, during the process of deposition and accumulation, particles on both sides will continue to roll down, while the interior of the accumulation body will gradually compact and the overall height will decrease. Individual particles will first roll down from the dominant channel before compaction. Therefore, it should be mentioned that the change in the contact structure between particles is carried out after compaction. The results of the accumulation test are shown in **Figures 8**, **9**. The main distribution ranges of the angle of repose of the three particle sizes are slightly different. The main distribution range of the angle of repose of the angular gravel deposit is 32°–34°. The main distribution range of the coarse sand deposit is 34°–36°. And the main distribution range of the angle of repose of the sandy loess deposit is 36°–38°. Even in the vibration stacking test, the main distribution range of the angle of repose of angular gravel deposit body is less than 20°. The main distribution range of the angle of repose of coarse sand deposit body is 21°–24°,

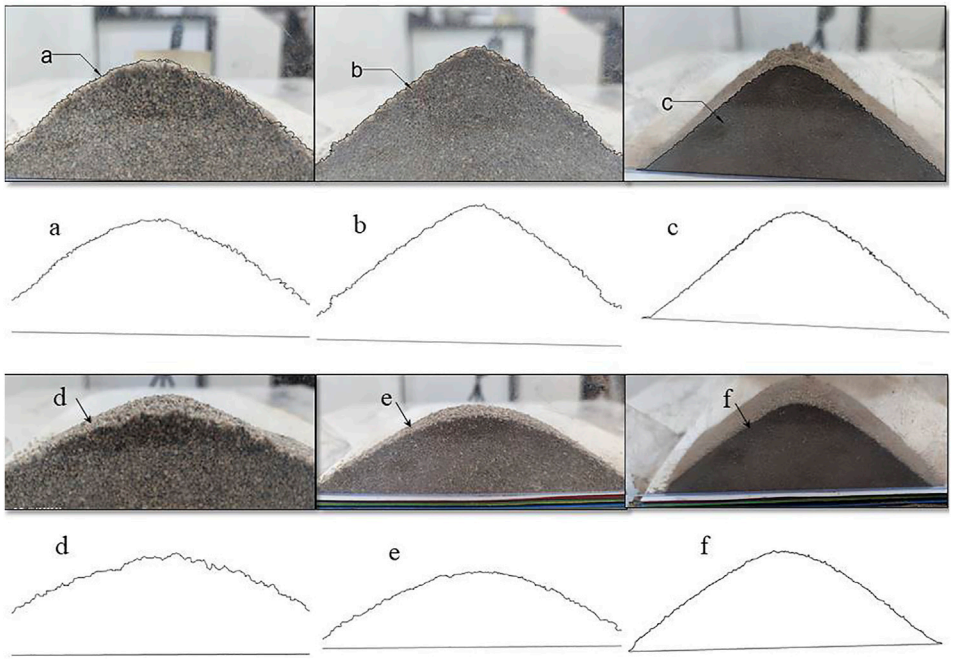

FIGURE 7 | Surface of stacking test results with different particle sizes [**(A–C)** is before vibration. **(D–F)** is after vibration. A and D is the angular gravel. **(B, E)** is coarse sand. **(C, F)** is sand loess from left to right successively].

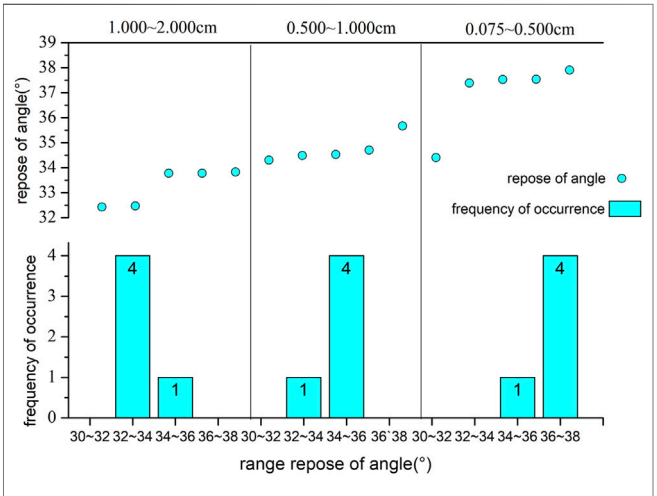

FIGURE 8 | Stacking test results and angle of repose distribution without vibration.

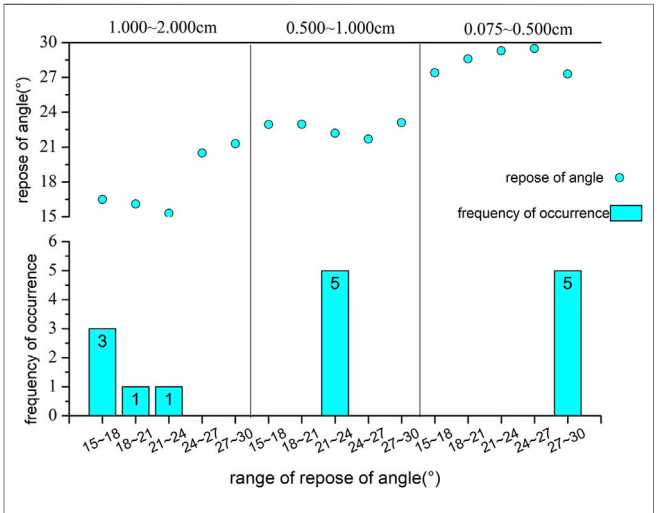

FIGURE 9 | Stacking test results and angle of repose distribution under vibration.

and the main distribution range of the angle of repose of sandy loess deposit body is 27°–30°. The accumulation body before and after vibration has the same change trend. Based on all those data, the angle of repose of the accumulation body is inversely proportional to the particle size. And the reason is closely related to the accumulation process. In the process of accumulation which is under the vibration load test, for example, the particles of gravity stress are enough to change the contact structure. The first layer of particles flats out in the basement initially and spreads around constantly. Because the basement has certain roughness, the kinetic energy of particles has been dissipated as the accumulation of particles spreads. As a result, the accumulation body cannot spread indefinitely. If the particles have a smaller diffusion range, the higher the height at which the accumulation can be maintained without collapsing under the same accumulation mass and the greater the angle of repose will be. It also suggests that the roughness of the basement for particles has a certain control effect. If the basement is rougher, the dissipation of the kinetic energy will be faster.

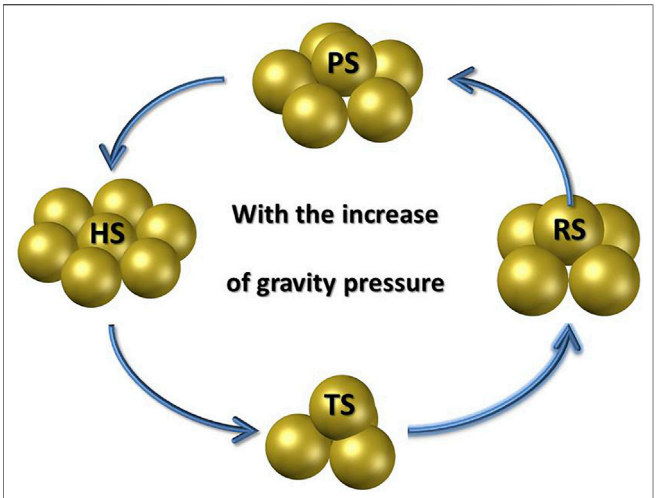

FIGURE 10 | Model transformation process under gravity weight pressure.

And the smaller the particle diffusion range is, the greater the angle of repose will be. When the diffusion range of particles is defined, the tiled particles of the first layer gradually contacted each other with the increase in the accumulated particles. The HS is formed. The form of HS also means that the bottom layer of TS has been formed. Since the particles in the upper accumulation body are tiny and the gravity weight of the particles is small, the stability of the contact structure can be maintained when the top particles are rolled into the middle of the three particles at the bottom. At this point, the TS is formed. The deposit weight of upper particles is larger and larger along with the increase in the accumulated particle number. The particles at the top of TS are subjected to the gradually increasing gravity weight pressure at the upside. And then the particles at the bottom are constantly pressed down. According to Metcalf (1966), the motion of particles is basically in the form of rolling. And only under certain special circumstances can sliding occur between particles. The upper part of the particles' gravity weight pressure is not distributed uniformly in the process of accumulation. So it is supposed that the particles at the top side, in the process of accumulation, are in a state of rolling down in this study. The excess kinetic energy is transferred to the bottom, causing the bottom particles to spread around. And the diffusion range of the bottom particles of the accumulation body becomes larger and redefined. Until the bottom particles of TS are expanded enough for the insertion of the fourth particle, and RS is formed. Similarly, when the space required by the fifth particle is squeezed out due to the increasing gravity weight pressure, PS is formed immediately. And the HS is formed again until the top of PS is squeezed to the bottom. As the particle size is inversely proportional to the kinetic energy dissipation rate (Li et al., 2017), the smaller the particle size dissipation rate is, the more excess kinetic energy is dissipated by the base, and the larger the range of the bottom particles to be redefined, the smaller the angle of repose will be. Therefore, the angle of repose of the accumulation body is inversely proportional to the particle size.

As shown in **Figure 10**. The transformation process of the contact models, just like samsara, is very interesting. It seems to show that the samsara itself is the most essential change law in nature. In fact, in the whole process of transformation, the closer you get to a certain stable state during the transition of the contact models, the more difficult it is to achieve. Although the tensile strength of soil is far less than the compressive strength and shear strength of soil (Wang et al., 2019b), the soil is rarely subjected to the action of tension. In most cases, the load form of soil is compressive load. And the shear strength of soil is also relatively smaller than the compressive strength of soil. So when the contact structure between the particles is suitable for resistance to shearing action, the soil will show more stability. In particle contact models, the transformation process from TS to PS is the compaction process of soil under compressive stress. When the top particle moves horizontally relative to the entire contact model causing the contact model to be damaged, it is the process of shear damage of the soil. The process of diffusion decomposition of the contact model is the process of destruction caused by tension, as shown in **Figure 11**. If particles at the bottom act the same force on the top particles in the whole process of contact models transformation, the shear strength φ which resists granular horizontal sliding force will gradually be strengthened as the angle of its connection between the contact points of the spherical particles and the center of the contact model decreases. And the relative forces f between the particles decreases. This means that at the later stage of the transformation of the contact models, the top particles need more force to make the bottom particles move. It also indicates that the transformation process of the contact models from TS to PS is a gradual stabilization process.

According to existing studies, the angle of repose of the accumulation body is related to the angle of internal friction linearly. And the size of the angle of repose is basically close to the size of the angle of internal friction. Even under ideal conditions, the tangent of the angle of repose of the accumulation body is the static friction coefficient of particles (Metcalf. 1966; Ghazavi et al., 2008; Liu, 2011; Al-Hashemi and Al-Amoudi, 2018). Although the contact model can be viewed as the smallest accumulation body, the angle of connection between the bottom particles and the top particles in different contact models is different. Those different connections cause that the shear strength φ required to break through for particle movement is different. Furthermore, the internal friction angle of the accumulation body is different from the angle of repose of the accumulation body. The stability of the contact models reflects the stability of the deposit essentially. Under ideal conditions, that is, the particle size is exactly the same, and the bottom of the contact model is parallel to the basement of the accumulation body, the contact model's angle that the connection between the top particle and the bottom particle center of the model with the horizontal plane is equal to its angle of repose. Combined with the stacking test, the angle of sandy soil under various particle sizes distribute in the range of 32°–38°. That may prove that the vast majority of particles, at the beginning of the accumulation, are in the transition of the RS to PS contact structure in the complex particle contact

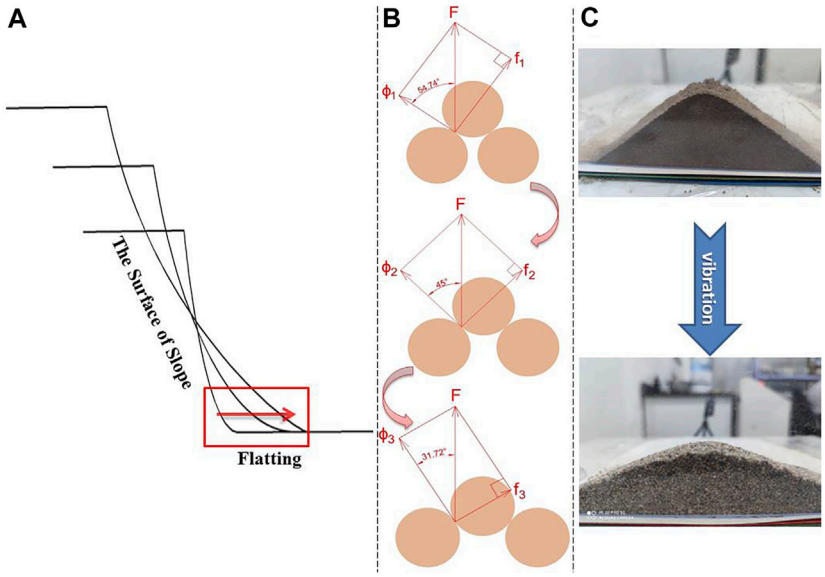

FIGURE 11 | (A) Slope changes caused by vibration. **(B)** Vibration induced contact model changes in slopes. **(C)** The change of accumulation body caused by vibration.

structures. It is enough to make the particle contact structure stay in a stable state temporarily under the static state. But in the later accumulation which is during the period of consolidation, the particles in the transition contact state from RS to PS will transform to PS under the gravity weight pressure until most of the particles are in PS in order to maintain absolute stability. The angle which is the connection between the spherical center of the top particles and the bottom particles with the horizontal plane is 31.72°. It is close to the 32° measured in the fixed funnel method test. It also conforms to the conclusion that the friction angle of uniform sand particles is 33°proposed by Shields in 1936.

In order to explain the evolution process of the angle of repose during the accumulation process better, the concept of entropy in the second law of thermodynamics is introduced to explain the cause of the angle of repose from the indicator of order and chaos. Entropy was first proposed by Rudolf Julius Emanuel Clausius, a German mathematician, to solve thermodynamic problems. Later, it was gradually extended to the field of physics. Since then, the concept of entropy gradually became clear. That is, the essence of entropy is to reflect the level of chaos inside a system. The stack arrangement of TS which is also the HS is very simple. And even multiple TS can be completely repeated and extremely ordered, so its entropy value is pretty low. In the transformation process from TS to PS, the arrangement of multiple contact models gradually becomes complicated and disordered, so its entropy value is relatively higher. According to the law of entropy increase, if there is no addition of external energy, the isolated system will always develop toward the direction of entropy increase and become a chaotic and disordered stable body. Therefore, TS will gradually transform to PS even without the addition of energy. That also can be considered as the consolidation process of soil. New particles are constantly added to the surface of the accumulation body in the process of accumulation of friable particles. The upper part of the deposit gravity pressure is very small, so the particles form TS initially. For this reason, the surface of the accumulation body tends to be a relatively regular and orderly unstable state first. That state also means the entropy caused by external energy. Under the action of gravity pressure, particles on the surface of the deposit slip. It transforms from an unstable structure to a relatively stable structure gradually. While the bottom particle gradually becomes stable due to the gravity weight pressure of the upper particle and gradually transitions from TS to PS. It is the process of entropy increase. As the top particles are undergoing the same transformation process of the bottom particles, the accumulation body system contains both entropy increase and entropy decrease. But on the whole, the accumulation body is in a state of entropy decrease and reaches some disordered structure finally. This structure is in a stable state.

The Relationship With Slope Angle

The German geographer F. Richthofen put forward the hypothesis of the eolian origin for loess in 1877. He believed that loess originated from the desert and Gobi. The particles from the desert or Gobi become the atmospheric dust through the wind transport and gradually deposited and accumulated with the weakening of wind. Therefore, the loess landform itself is a huge accumulation body. The loess slopes are not an exception. The accumulative body produced by using the indoor stacking test is equivalent to a miniature version of the loess slope. The angle of repose as a threshold angle shows that particles are stacking without collapsing is the slope angle relative to the loess slope. The natural loess slope is in a state of stability or in a critical state, so the natural deposit slope angle is less than or equal to the angle of repose. Once its size exceeds the angle of

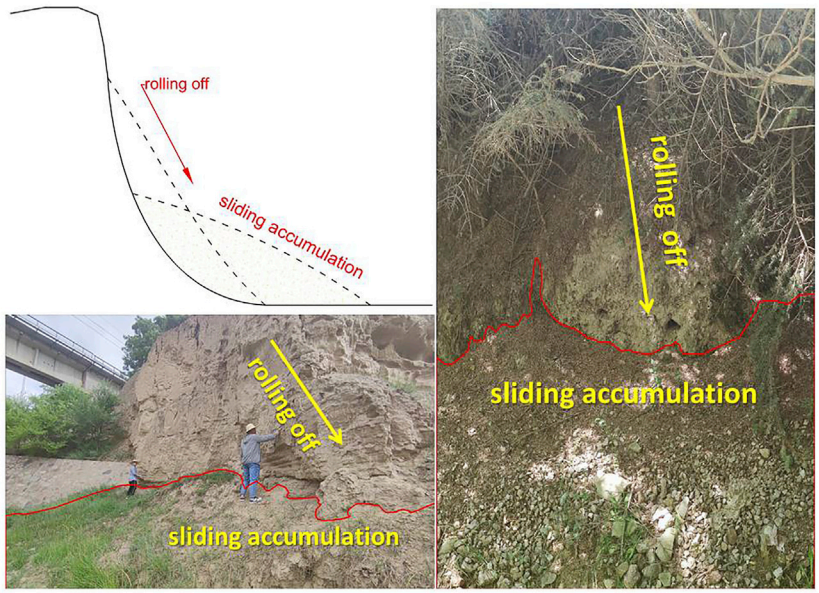

FIGURE 12 | Areas of particle rolling down and slide accumulation in the slope.

repose, the surface of the slope will produce the phenomenon of particles rolling off. Just like the surface of the accumulation body in a stacking test, so as to maintain the stability of the whole slope. Therefore, the slope angle also has a controlling effect on the slope stability. Since the gravity weight of particles has a great influence on the angle of repose of the accumulation body (Kleinhans et al., 2011), the gravity weight pressure of particles should also be taken into account for the slope. So the stacking test under vibration will be more in line with the actual situation of the loess slope. According to the results of the vibration stacking test, the main distribution range of the angle of repose of the angular gravel deposit body is less than 20°. The main distribution range of the angle of repose of the coarse sand deposit body is 21°–24°, and the main distribution range of angle of repose of sandy loess deposit body is 27°–30°. Therefore, it is speculated that under long-term gravity weight pressure, the critical slope angle of loess slope is no more than 30°. And not all slopes are in a critical state. Because of the external factors of non-gravity pressure, the slope angle concentration range of most slopes is usually less than 30°. In order to verify this conclusion, this article uses the research results of scholar (Hu et al., 2018) to verify the measurement results of 2,443 slopes selected from 6,627 slopes randomly. Among the 2,443 slopes, only 39 slope angles are greater than 30°, and 2404 slope angles are all less than 30°. And the concentration range of slope angles is 10°–20°, which is less than 30° under the critical condition. The actual investigation results are in full agreement with the speculative conclusion.

In fact, a large number of phenomena can prove this hypothesis indirectly. In the process of natural deposition, slope surface particles rolled off and adjusted the slope angle which promoted the slope body to maintain its overall stability. As shown in **Figure 12**, there are a large number of accumulation bodies at the foot of the slope along the line from Dingxi to Tianshui in Gansu Province. This kind of accumulation body can even stretch several kilometers, but its height is greatly different from the overall slope. The accumulation volume is small, and the slope is significantly reduced. There is no obvious disturbance around the slope because the slope is accumulated in the process of natural sedimentation regulation. And the reality is that the loess has cohesive force. The instantaneous change will cause severe geological disasters. In Jixian Jichang town of Shanxi Province, there was a large area of loess slope with the collapse of natural geological disasters. Twenty-two people were buried. There were no rains, vibrations, or other factors before the natural disasters. Experts called it a typical loess slope collapse. This shows that the slope angle is too large due to long-term sedimentation. And in order to adjust its stability, the slope can produce landslides and other major geological disasters.

CONCLUSION

In this article, a principle about the accumulation of friable deposits until the generation of their angle of repose is proposed from the perspective of particles. The principle is extended to the loess slope, and the relationship between the stability of microscopic particle structure and the stability of macroscopic slope is established from a new point of view. This method can help readers understand the formation process of the accumulation body from the perspective of particles. And it can also connect the accumulation body with the slope which is two objects with large variability of their scales. It will help readers to understand that the slope is only a large accumulation body and the stability of slope is controlled by the

base angle just like the small accumulation body. The conclusions of this article are as follows:

1) According to the gravity pressure of static particles in different positions is different, four kinds of contact models which are triangular pyramid contact structure (TS), rectangular pyramid contact structure (RS), pentagonal pyramid contact structure (PS), and hexagon contact structure (HS) are set up and the transformation principle of those four contact models is put forward. The stability of four contact models is compared with the view of mechanics. It is proved that the process from TS to HS is a gradually stable process.
2) The modified fixed funnel method is conducted to test the particles with different sizes. It reveals that four contact structures exist between particles in the process of accumulation and proves the universality of the contact models under different particle sizes conditions directly. According to the test results, the distribution range of sand repose angle is 32°–38°. It explains Shields' conclusion that the friction angle of uniform sand particles is 33°.
3) It is more corresponding to the real situation that vertical vibration load is applied to the stacking test to strengthen the effect of particle gravity pressure for the slope. Thus, the relationship between the repose angle of accumulation body and slope angle is established. Therefore, it is speculated that the distribution range of the slope angle is less than 30°. Combined with field investigation data, the rationality of this relationship is proved. The reliability of the hypothesis is verified by two engineering cases which are the line from Dingxi to Tianshui in Gansu Province and the slope in Jixian Jichang town of Shanxi Province.

The contact models will be improved later. In order to get closer to the real characteristics of loess particles and the contact models can be extended to all other loess particles, it is not only considered the friction between particles but also put the cohesive force between particles, the shape, and the size of particles into the calculation scope of contact models. In addition, the real loess slope is subject to many disturbance factors, such as precipitation, vibration, and other single factors as well as various coupling effects. Therefore, these are also one of the problems to be solved urgently in the future.

DATA AVAILABILITY STATEMENT

The raw data supporting the conclusion of this article will be made available by the authors, without undue reservation.

AUTHOR CONTRIBUTIONS

The main content of this article is written by HD. The theme of the article is guided by JW and the details of the experiment are guided by DZ. The pictures are modified by YX. Finally, the content language is modified by ZL.

FUNDING

This research was supported by the National Science Foundation of China (Grant Nos. 42027806 and 41630639) and National Key Research and Development Program (Grant No. 2018YFC1504703).

REFERENCES

Al-Hashemi, F. M. B., and Al-Amoudi, O. S. B. (2018). A Review on the Angle of Repose of Granular Materials, *Powder Tech.*, 330, 397–417. doi:10.1016/j.powtec.2018.02.003

Atwood-Stone, C., and McEwen, A. S. (2013). "Measuring Dynamic Angle of Repose in Low Gravity Enviornments Using Martian Sand Dunes", in 44th Lunar and Planetary Science Conference, March 18–22, 2013, Woodlands, Texas, 3, 1175–1177.

Bacherikov, I., Novikov, A., and Petrishchev, E. (2021). Discrete Seed Feeder Designing for Mobile Apparatus: Early Results for Pinus Sylvestris L. Species. *Inventions* 6 (1), 14–21. doi:10.3390/inventions6010014

Chou, H. T., Chou, S. H., and Hsiau, S. S. (2014). The Effects of Particle Density and Interstitial Fluid Viscosity on the Dynamic Properties of Granular Slurries in a Rotating Drum. *Powder Tech.* 252, 42–50. doi:10.1016/j.powtec.2013.10.034

Cui, Y., Xu, C., Xu, S., Chai, S., Fu, G., and Bao, P. (2020). Small-scale Catastrophic Landslides in Loess Areas of China: An Example of the March 15, 2019, Zaoling Landslide in Shanxi Province. *Landslides* 17 (3), 669–676. doi:10.1007/s10346-019-01322-4

Duran, J. (2001). Sand, Powders and Grains; An Introduction to the Physics of Granular Materials, Spring-Verlag. *Butsuri* 56 (1), 52–53. doi:10.11316/butsuri1946.56.1.52_2

Evesque, P., and Rajchenbach, J. (1989). Instability in a Sand Heap. *Phys. Rev. Lett.* 62 (1), 44–46. doi:10.1103/PhysRevLett.62.44

Ghazavi, M., Hosseini, M., and Mollanouri, M. (2008). "A Comparison between Angle of Repose and Friction Angle of Sand," in The 12th International Conference of International Association for Computer Methods and Advances in Geomechanics (IACMAG), Goa, India, 1272–1275.

Holsapple, K. A. (2013). Modeling Granular Material Flows: The Angle of Repose, Fluidization and the Cliff Collapse Problem. *Planet. Space Sci.* 82-83, 11–26. doi:10.1016/j.pss.2013.03.001

Hu, S., Qiu, H., Wang, X., Gao, Y., Wang, N., Wu, J., et al. (2018). Acquiring High-Resolution Topography and Performing Spatial Analysis of Loess Landslides by Using Low-Cost UAVs. *Landslides* 15 (3), 593–612. doi:10.1007/s10346-017-0922-8

Hua, X., and Shultis, K. (2021). Kinematics of Cohesive and Elongated Particulate Materials in a Vertical axis Mixer. *Powder Tech.* 386 (prepublish), 540–546. doi:10.1016/j.powtec.2021.03.030

Huntley, D., Bobrowsky, P., Hendry, M., Macciotta, R., Elwood, D., Sattler, K., et al. (2019). Application of Multi-Dimensional Electrical Resistivity Tomography Datasets to Investigate a Very Slow-Moving Landslide Near Ashcroft, British Columbia, Canada. *Landslides* 16, 1033–1042. doi:10.1007/s10346-019-01147-1

Karimi, M., Kheiralipo, K., Tabatabaee, A., Khoubakht, G. M., Naderi, M., and Heidarbeig, K. (2008). The Effect of Moisture Content on Physical Properties of Wheat. *Pakistan J. Nutr.* 8 (1), 90–95. doi:10.3923/pjn.2009.90.95

Kleinhans, M. G., Markies, H., de Vet, S. J., in 't Veld, A. C., and Postema, F. N. (2011). Static and Dynamic Angles of Repose in Loose Granular Materials under Reduced Gravity. *J. Geophys. Res.* 116 (E11), 1–13. doi:10.1029/2011JE003865

Lajeunesse, E., Mangeney-Castelnau, A., and Vilotte, J. P. (2004). Spreading of a Granular Mass on a Horizontal Plane. *Phys. Fluids* 16 (7), 2371–2381. doi:10.1063/1.1736611

Li, C., Honeyands, T., O'Dea, D., and Moreno-Atanasio, R., (2017). The Angle of Repose and Size Segregation of Iron Ore Granules: DEM Analysis and Experimental Investigation. *Powder Tech.* 320, 257–272. doi:10.1016/j.powtec.2017.07.045

Li, W., Yue, D., Colombera, L., Mountney, N. P., and Wu, S. (2020). A Novel Method for Estimating Sandbody Compaction in Fluvial Successions. *Sediment. Geology.* 404, 105675. doi:10.1016/j.sedgeo.2020.105675

Liu, Z. C. (2011). Measuring the Angle of Repose of Granular Systems Using Hollow Cylinders. Available at: http://d-scholarship.pitt.edu/6401/(Acessed 11 22, 2011).

Lumay, G., Boschini, F., Traina, K., Bontempi, S., Remy, J.-C., Cloots, R., et al. (2012). Measuring the Flowing Properties of Powders and Grains. *Powder Tech.* 224, 19–27. doi:10.1016/j.powtec.2012.02.015

Ma, P. H., Peng, J. B., Wang, Q. Y., Zhuang, J. Q., and Zhang, F. Y. (2019). The Mechanisms of a Loess Landslide Triggered by Diversion-Based Irrigation: A Case Study of the South Jingyang Platform, China. *Bull. Eng. Geol. Environ.* 78 (7), 4945–4963. doi:10.1007/s10064-019-01467-5

Metcalf, J. R. (1966). Angle of Repose and Internal Friction. *Int. J. Rock Mech. Mining Sci. Geomech. Abstr.* 3 (2), 155–161. doi:10.1016/0148-9062(66)90005-2

Müller, D., Fimbinger, E., and Brand, C. (2021). Algorithm for the Determination of the Angle of Repose in Bulk Material Analysis. *Powder Tech.* 383, 598–605. doi:10.1016/j.powtec.2021.01.010

Pähtz, T., Liu, Y., Xia, Y., Hu, P., He, Z., and Tholen, K. (2021). Unified Model of Sediment Transport Threshold and Rate Across Weak and Intense Subaqueous Bedload, Windblown Sand, and Windblown Snow. *J. Geophys. Res. Earth Surf.* 126 (4), 1–36. doi:10.1029/2020JF005859

Penkavova, V., Kulaviak, L., Ruzicka, M. C., and Puncochar, M. (2021). Anisometric Granular Materials: Compression and Shear Properties. *Granular Matter* 23 (2), 29–46. doi:10.1007/s10035-020-01082-2

Rackl, M., Grötsch, F. E., Rusch, M., and Fottner, J. (2017). Qualitative and Quantitative Assessment of 3D-Scanned Bulk Solid Heap Data. *Powder Tech.* 321, 105–118. doi:10.1016/j.powtec.2017.08.009

Soltanbeigi, B., Podlozhnyuk, A., Kloss, C., Pirker, S., Ooi, J. Y., and Papanicolopulos, S.-A. (2021). Influence of Various DEM Shape Representation Methods on Packing and Shearing of Granular Assemblies. *Granular Matter* 23 (2), 25–41. doi:10.1007/s10035-020-01078-y

Wang, J., Xu, Y., Ma, Y., Qiao, S., and Feng, K. (2018a). Study on the Deformation and Failure Modes of Filling Slope in Loess Filling Engineering: A Case Study at a Loess Mountain Airport. *Landslides* 15 (12), 2423–2435. doi:10.1007/s10346-018-1046-5

Wang, J., Zhang, D., Wang, N., and Gu, T. (2019a). Mechanisms of Wetting-Induced Loess Slope Failures. *Landslides* 16 (5), 937–953. doi:10.1007/s10346-019-01144-4

Wang, J., Li, P., Gu, Q., Xu, Y., and Gu, T. (2019b). Changes in Tensile Strength and Microstructure of Loess Due to Vibration. *J. Asian Earth Sci.* 169, 298–307. doi:10.1016/j.jseaes.2018.10.011

Wang, J., Xu, Y., Zhang, D., and Gu, T. (2021). Vibration-induced Acceleration of Infiltration in Loess. *Sci. China Earth Sci.* 64 (04), 611–630. doi:10.1007/s11430-020-9741-x

Xu, X.-Z., Guo, W.-Z., Liu, Y.-K., Ma, J.-Z., Wang, W.-L., Zhang, H.-W., et al. (2017). Landslides on the Loess Plateau of china: A Latest Statistics Together with a Close Look. *Nat. Hazards* 86 (3), 1393–1403. doi:10.1007/s11069-016-2738-6

Xu, Y., Allen, M. B., Zhang, W., Li, W., and He, H. (2020a). Landslide Characteristics in the Loess Plateau, Northern China. *Geomorphology* 359, 107150. doi:10.1016/j.geomorph.2020.107150

Xu, Y., Liu-Zeng, J., Allen, M. B., Allen, M. B., Zhang, W., and Du, P. (2020b). Landslides of the 1920 Haiyuan Earthquake, Northern China. *Landslides* 18 (3), 935–953. doi:10.1007/s10346-020-01512-5

Zhang, F. Y., Peng, J. B., Huang, X. W., and Lan, H. X. (2021). Hazard Assessment and Mitigation of Non-seismically Fatal Landslides in China. *Nat. Hazards* 106 (prepublish), 785–804. doi:10.1007/s11069-020-04491-x

Zheng, J., and Hryciw, R. D. (2016). A Corner Preserving Algorithm for Realistic DEM Soil Particle Generation. *Granular Matter* 18 (4), 83–101. doi:10.1007/s10035-016-0679-0

Zhou, Y., Wang, H. B., Zhou, B., and Li, J. M. (2018). DEM-aided Direct Shear Testing of Granular Sands Incorporating Realistic Particle Shape. *Granular Matter* 20 (3), 54–66. doi:10.1007/s10035-018-0828-8

Conflict of Interest: The authors declare that the research was conducted in the absence of any commercial or financial relationships that could be construed as a potential conflict of interest.

Publisher's Note: All claims expressed in this article are solely those of the authors and do not necessarily represent those of their affiliated organizations, or those of the publisher, the editors, and the reviewers. Any product that may be evaluated in this article, or claim that may be made by its manufacturer, is not guaranteed or endorsed by the publisher.

frontiers in Earth Science

ORIGINAL RESEARCH
published: 21 January 2022
doi: 10.3389/feart.2021.762508

Mesoscopic Characteristics and Performance Evaluation of Loess Treated by Different Anti-Seismic Subsidence Technologies

Ping Wang[1,2]*, *Shuya Xu*[3], *Shengjun Shao*[1]*, *Huijuan Wang*[2], *Xudong Li*[2] *and Ziling Qian*[2]

[1]Institute of Geotechnical Engineering, Xi'an University of Technology, Xi'an, China, [2]Key Laboratory of Loess Earthquake Engineering, China Earthquake Administration, Lanzhou, China, [3]Geophysical Exploration Center, China Earthquake Administration, Zhengzhou, China

The meso-structure of the soil has an important restriction on its engineering properties. Based on dynamic triaxial tests and SEM meso-structure test experiments, this study investigated the meso-scale structural deformation characteristics of Q_3 loess samples treated by physical, chemical, and compound improvement methods, before and after strong earthquakes of typical seismic subsidence loess. On this basis, the seismic subsidence performance of the improved method is given under the conditions of frequent earthquakes, fortifying earthquakes, and rare earthquakes. The results show that 1) the physical improvement method has the most obvious effect on the elimination of macropores and overhead pore structures; 2) the chemical method can generate unique glass beads or flocculated fine structures, which can greatly enhance the strength of the soil and play the role of filling, cementing, or buffering, respectively, in the event of a strong earthquake; 3) for several improved treatment methods, the amount of seismic subsidence increases non-linearly with the increase in peak acceleration; and 4) in the event of frequent earthquakes, the earthquake subsidence can be eliminated by the method of adding fly ash, and when the fortification earthquake comes, the dynamic composite method can completely eliminate the seismic subsidence of the site. The related results can give reasonable suggestions for the treatment of seismic subsidence of different foundations in the "resilient urban and rural" and key engineering construction and seismic design of China's loess area.

Keywords: seismic subsidence loess, modification treatment, mesoscopic features, strong earthquake, seismic performance

OPEN ACCESS

Edited by:
Yueren Xu,
China Earthquake Administration, China

Reviewed by:
Panpan Guo,
Zhejiang University, China
Tao Wang,
Chinese Academy of Geological Sciences (CAGS), China

***Correspondence:**
Ping Wang
lanzhouwang_p@126.com
Shengjun Shao
sjshao@xaut.edu.cn

Specialty section:
This article was submitted to Geohazards and Georisks, a section of the journal Frontiers in Earth Science

Received: *22 August 2021*
Accepted: *17 November 2021*
Published: *21 January 2022*

Citation:
Wang P, Xu S, Shao S, Wang H, Li X and Qian Z (2022) Mesoscopic Characteristics and Performance Evaluation of Loess Treated by Different Anti-Seismic Subsidence Technologies. Front. Earth Sci. 9:762508. doi: 10.3389/feart.2021.762508

INTRODUCTION

China's Loess Plateau and adjacent areas have recorded 395 earthquakes with a magnitude MS ≥ 5 (Xu et al., 2018). The areas with seismic intensity above VII in the loess area account for 54.21% of the total areas, and the risk of strong earthquakes is extremely high (Wang, 2017; Gao et al., 2015). The systematic study of loess engineering properties in China began in the early days of founding of our country. From the early 1950s to the mid-1960s, Chinese researchers began to carry out a large number of indoor and field experimental research on the engineering properties of collapsible loess on the Loess Plateau such as Lanzhou, Xi'an, Taiyuan, and Luoyang (Huang, 1963). From 1966 to

1978, researchers found that the newly accumulated loess has similar characteristic indexes to Q3 loess, but it has high compressibility and low bearing capacity (Shaanxi Comprehensive Survey Institute, 1973). Since 1978, a breakthrough has been made in the microstructure, pore structure, and its influence on the engineering properties of loess (Gao, 1980; Wang and Lin, 1990; Xu and Guo, 2020; Xu et al., 2020). Unfortunately, none of these methods take into account the dynamic stress like earthquake. The unique macroporous and weakly cemented overhead structure of loess makes the area extremely sensitive to earthquakes (Wang, 2003). Seismic investigations have shown that the earthquake subsidence caused by strong earthquakes, disasters such as ground cracks, and landslides have caused serious damage to housing constructions and road and railway subgrades (Zhang, 2016; Wang, 2018). Therefore, for major construction projects in areas that have been judged as seismic subsidence, site selection not only needs to meet the seismic fortification standards but also should fully consider what kind of foundation anti-seismic treatment method is most effective under fortified earthquakes and rare earthquakes. This is the actual problem of the transformation of infrastructure construction to prevention oriented in the new concept of earthquake prevention and disaster reduction. It is also an urgent problem in scientific research.

A large number of loess seismic subsidence studies have produced fruitful results in three aspects: microstructure and mechanism, determination of seismic subsidence, and estimation of seismic subsidence (Garratt-Reed and Bell, 2005; Shi and Qiu, 2011; Ng et al., 2017; Shao et al., 2018; Dal et al., 2012; Romero and Simms, 2008; Lin et al., 2019; Bruchon et al., 2013; Wen and Yan, 2014; Zhu et al., 2019; Jiang et al., 2014; Wang et al., 2019; Wang and Zhang, 1993). The anti-seismic subsidence treatment technology of the relevant loess foundation is based on fully grasping the characteristics of the loess seismic subsidence and the disaster-causing mechanism. Foundation modification (improvement) methods can be broadly classified into physical modification treatment and chemical modification treatment. These methods have been relatively mature and widely used in dealing with general site and collapsible loess foundation seismic subsidence (Teng et al., 2012; Li et al., 2012). However, there are still few research studies on the improvement methods for the seismic settlement of the loess site under the action of earthquakes of different intensities; furthermore, they still lack systematic and quantitative research and evaluation about the effectiveness of different foundation treatment methods for the same loess engineering site (Deng et al., 2012; Wang et al., 2013; Wang et al., 2016).

The view that the seismic subsidence of the loess foundation is mainly controlled by its microscopic structure has been recognized by many scholars. Shi Yucheng et al. and Deng Jin et al. discussed the influence of medium and large pores and particle skewness on loess seismic subsidence and affirmed the feasibility of studying loess structural changes with microstructure (Shi and Li, 2003; Deng et al., 2007); Wang Lanmin et al. and Li Lan et al. obtained quantitative data on the area of overhead pores through electron microscope photos and established the relationship between loess seismic subsidence characteristics and soil constitutive models (Wang et al., 2007; Li et al., 2005). With the development of microstructure analysis theory, such as the introduction of fractal theory, the improvement of CT technology, and image processing technology, a new feasible method for studying loess earthquake disasters from a microscopic perspective has been provided (Gu et al., 2011; Zhu and Chen, 2009; Wei, 2019).

This study uses indoor dynamic triaxial tests, scanning electron microscopy, image processing technology, and numerical simulation to improve the commonly used loess foundation physical improvement method and dynamic compaction method, which can effectively solve the general building foundation deformation and settlement problems. The cement modification method and fly ash modification method are applied to the seismic settlement loess site (fly ash modification method, which can recycle industrial waste, is an environmental protection technology) to reveal the meso-structure characteristics of the foundation treatment methods under strong earthquake loads, get results of statistical analysis of the particle size and pore size distribution of the sample before and after the test with different seismic subsidence treatment techniques, get the correlation with the macroscopic failure characteristics of the sample, and then discuss the effect of seismic subsidence treatment. On this basis, the most scientific and economical treatment method for seismic subsidence loess engineering site is proposed.

RESEARCH METHOD

Sample Preparation

The undisturbed area along the Yuzhong County of Lanzhou City on the Baolan Passenger Dedicated Line with strong seismic subsidence is selected. This area is a typical area with thick loess coverage. The thickness of Q_3 loess reaches 28m, which can be used as ideal loess seismic settlement study place. The undisturbed samples were obtained through the excavation of artificial exploration wells, and the sampling depth was 4 m. All the soil samples were undisturbed Q_3 loess, and their physical properties are shown in **Table 1**.

The original sample (YZ-1) is cut into a cylinder of 50 mm × 100 mm (diameter × height). In order to ensure the consistency of its physical parameters, the essential effects of different anti-seismic subsidence improvement methods are analyzed; a sufficient amount of loose soil samples is taken around the same depth of the exploratory shaft wall. There have been previous studies on the optimal addition amount of fly ash and cement (refer to the references). Related experiments will not be repeated here, and the relevant data will be quoted directly. The fly ash content in the fly ash improvement method is 18% (Wang et al., 2013). In the cement–soil improvement method, #425 Portland cement was selected, and the optimal cement content was selected at 5% for the ratio, according to the previous research results (Wang, 2018). Various samples and their physical properties are shown in **Table 2**. When using chemical methods, prepare a set of fly ash (FMH-1) and

TABLE 1 | Soil physical property parameter table.

Type	Soil	Density/(g/cm^3)	Void ratio	Moisture content/%	Soil composition (%)		
					Sand	Powder	Cosmid
Undisturbed	Silty Loess	1.39	1.08	9.31	13.0	76.5	10.5

TABLE 2 | Physical property parameters of original and modified samples.

Type number	Improvement measures	Additives	Additive content/%	Density/(g/cm^3)	Moisture content/%
YZ-1	No measures	Nothing	0	1.39	9.3
QH-1	Physical	Nothing	0	1.75	9.1
FMH-1	Chemistry	Fly ash	18	1.41	9.0
SN-1	Chemistry	Cement	5	1.40	9.2
FH-1	Composite (dynamic compaction + fly ash)	Fly ash	18	1.75	9.0
FH-2	Composite (dynamic compaction + cement)	Cement	5	1.75	9.1

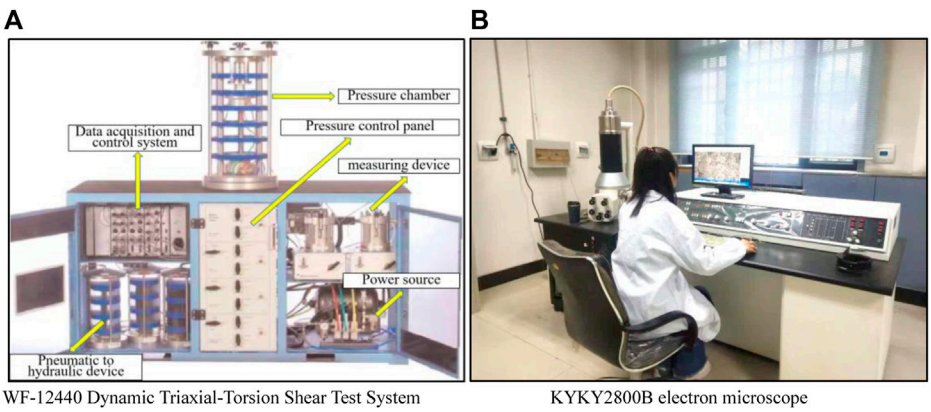

FIGURE 1 | Test system. **(A)** WF-12440 dynamic triaxial-torsion shear test system and **(B)** KYKY2800B electron microscope.

cement–soil (SN-1) samples with a density consistent with the natural density of the site soil of 1.39 g/cm^3; when using physical improvement methods, according to the compaction requirements of loess foundation in the actual project, a set of dynamic compaction samples (QH-1) are made with a density of 1.75 g/cm^3; the compound improvement methods means to prepare one set of dynamic compaction–fly ash (FH-1) and dynamic compaction–cement–soil (FH-2) samples; and the additive content and sample density are consistent with physical and chemical improvement methods, respectively. All the above methods are adopted.

The sample of the visual structure test is the soil sample before and after the abovementioned indoor dynamic triaxial test. First, the undisturbed loess, dynamic compaction, fly ash, and cement-modified samples before and after the dynamic triaxial test are 12 groups. After natural drying, they are completely air-dried. The air-dried samples are separated, and the cross sections are obtained and selected. The small soil block that is leveled and has the original fresh surface is used as the observation sample, prepared into a thin slice of 10 mm × 10 mm × 2 mm (length × width × height), and the bottom is leveled.

Test Equipment

The test instrument is the WF-12440 dynamic triaxial-torsion shear test system of the Key Laboratory of Loess Earthquake Engineering of China Earthquake Administration (as shown in **Figure 1A**). The test adopts the consolidated undrained test (CU). The axial stress during consolidation is 200kPa, and the consolidation ratio Kc is 1.69 (Sheng et al., 1999). The microstructure image of the soil sample was acquired using the KYKY2800B electron microscope of the Key Laboratory of Loess Earthquake Engineering, China Earthquake Administration, as shown in **Figure 1B**. After scanning the soil sample, select images of the same magnification and secondary images with clear particles and pores were used for quantitative analysis, and we used image processing software for normalization and binarization of the secondary images for analysis to get the required parameters (Xu et al., 2017).

Seismic Subsidence Test and Selection of Seismic Load in the Test

After the consolidation and deformation are stabilized, dynamic stresses of different amplitudes are applied to 7–10 specimens in the

TABLE 3 | Classification of loess pore microstructure.

Pore classification	Pore area/μm^2	Pore diameter/μm	Pore properties
I	4.5	r ≤ 2	Micro porosity
II	28.3	2 < r ≤ 6	Small pores
III	113.5	6 < r ≤ 12	Intergranular pores
IV	708.9	12 < r ≤ 30	Overhead pores
V	2,835.7	30 < r ≤ 60	Secondary macropores, intergranular pores

same group, and the relationship curves between dynamic stress σ_d and residual strain ε_p under different vibration times are obtained, that is, the seismic subsidence curve. At the same time, according to Mansing's irregular loading and unloading criteria and the researchers' tests and calculations on the applicability of loess, the failure strain standard of loess is set to 3% strain. According to the above principles, the residual strain time history of each sample in each group is recorded at its corresponding amplitude, and the residual strain of the same group of samples is plotted and connected according to the amplitude from small to large. We obtained the seismic depression curve (Zhang and Duan, 1986). In the test, in order to simulate the relationship between the stress and strain, strength, and deformation of the soil under the earthquake load, the equivalent amplitude method of the earthquake load proposed by Seed was adopted, and the equivalent amplitude ratio was selected as 0.65; the relationship between the seismic intensity and the number of equivalent cycles is as follows: when the seismic intensity is VII degree, VIII degree, and IX degree, the corresponding number of equivalent cycles is 20 times, 30 times, and 40 times, respectively (Zhang and Ling, 2016). A sine constant amplitude reciprocating load with a frequency of 1 Hz was applied to the dynamic triaxial test system, and the cyclic vibration times was used to equate the strength of the ground motion.

Data Extraction Principles and Classification Methods

This research focuses on the quantitative analysis of loess grain and pore changes, number, size, shape, cementation form, and fractal characteristics of loess particles before and after the earthquake in different method. The classification refers to 12 types of microstructures that have been widely recognized (Shi and Li, 2003). The skeletal morphology of loess particles seen in the electron microscope can be roughly divided into three types: single-grain, aggregated, and agglomerated. Single particles include clay particles (less than 5 μm), powder particles (5–50 μm), and sand particles (greater than 50 μm). In addition to a small amount of these three particles accumulated in a separate form to form scattered point contacts and mosaic contacts, they are mainly aggregated or the clot shape appears. Aggregate (50–100 μm) is a unit with low strength, which has collapsed and disintegrated. In addition to elastic deformation, it also produces partial plastic deformation. After unloading, the rebound of the clot is constrained by the aggregate to form a residual strain. The clot (30–70 μm) is a unit with higher strength and only undergoes elastic deformation. The pore size is undoubtedly one of the important factors affecting the occurrence of seismic subsidence. Generally, a pore diameter is used as the standard for classification (Gao, 1980; Deng et al., 2007). The classification standard is shown in **Table 3**.

The processing of microstructure images mainly includes image binarization, repair of fractures, removal of noise, automatic/manual identification of particles and pores, and statistics of their quantity and geometric information.

ANALYSIS OF THE MICROSCOPIC CHARACTERISTICS OF THE SAMPLES BEFORE AND AFTER THE SEISMIC SUBSIDENCE TEST

The microstructure images of 12 samples before and after the seismic subsidence test under 400 times magnification were obtained which include undisturbed loess and modified loess sample, and the grain characteristics and pore characteristics of the samples were analyzed.

Image of the Microstructure of the Original Sample

For general loess samples, except for a small amount of clay, powder, and sand in the form of single particles, soil particles are mainly presented in the form of aggregates. Under 400 times magnification, it can be clearly seen that the microstructure is characterized by a large aggregate particle size, a large number of coarse mineral particles, and point contact between the particles, and an overhead structure is formed between multiple particles, as shown in **Figure 2A**. After the test, the overhead pore structure of the undisturbed sample is significantly reduced and the average particle size of the aggregates is reduced, but the particle numbers has risen. This is consistent with the collapse of the overhead pore structure obtained earlier, which is an important cause of seismic subsidence. At the same time, it can be seen that the sample in this area is relatively loose so that the microstructure of the sample is still in point contact and there are many large and medium pores in the case of seismic subsidence.

Microstructure Image of Dynamic Compaction Sample

The microstructure of the sample before and after the seismic subsidence test after the dynamic compaction is shown in

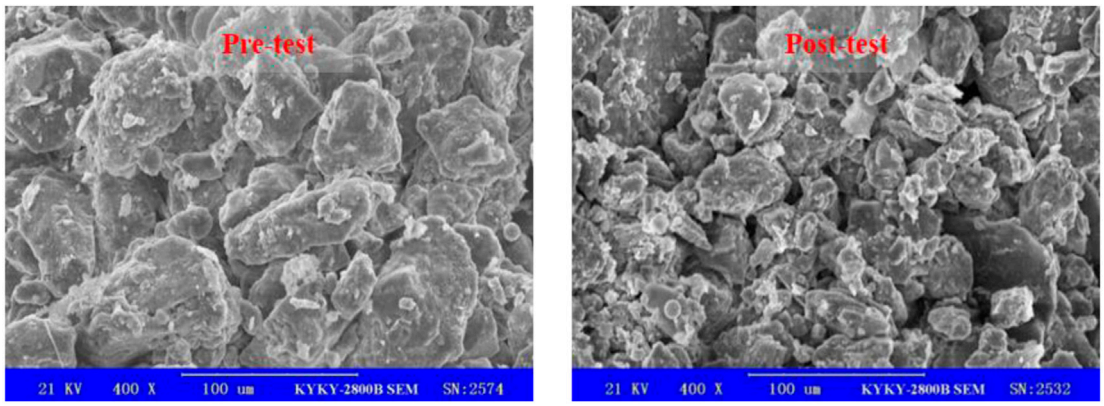

（a）Microstructure image of the undisturbed specimen before and after the seismic subsidence test

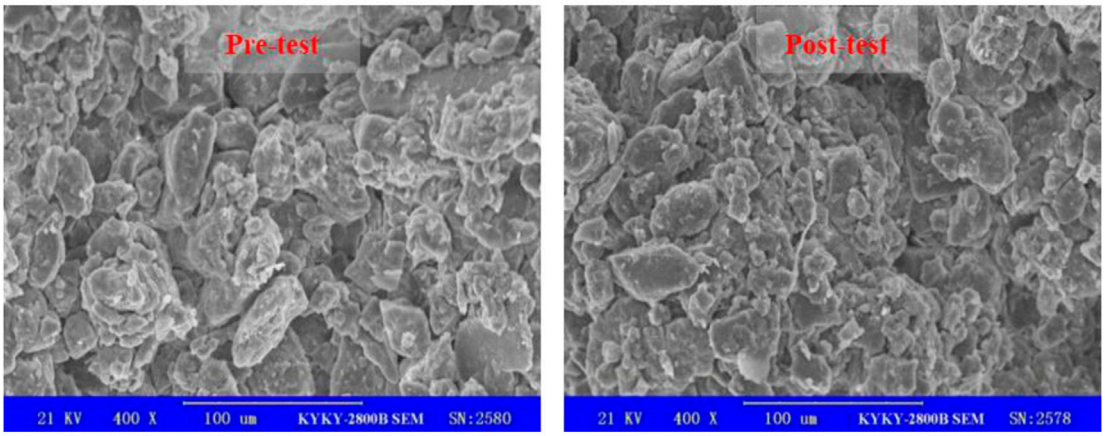

（b） Microstructure images of the dynamic compaction sample before and after the seismic subsidence test

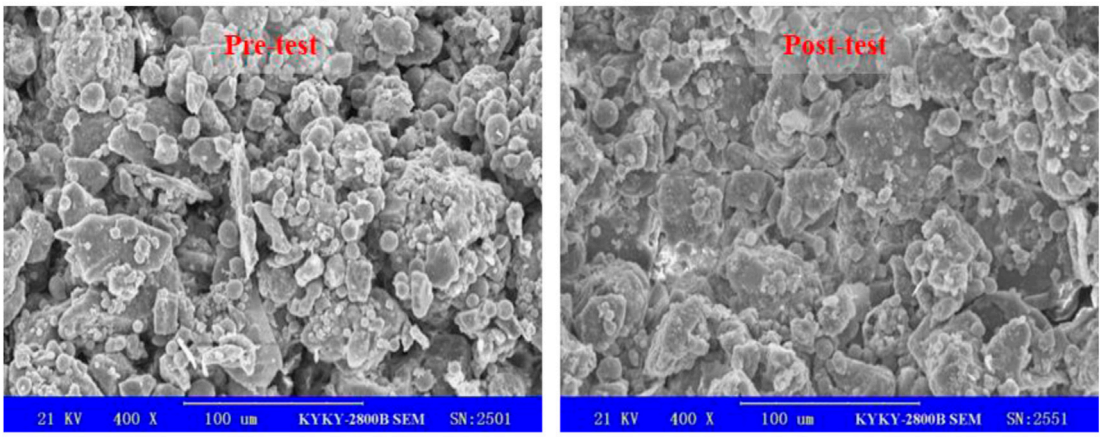

(c) Microstructure images of fly ash samples before and after the seismic subsidence test

FIGURE 2 | (Continued)

Figure 2B. Before the test, the loess shows obvious flocculent structure. The large aggregates collapsed due to compaction and further broke into small aggregates; the particles were arranged more densely, and they are in the area of contact. After the test, the vibrating effect of the strong earthquake makes the granular mosaic structure of the dynamic compaction sample after the test more obvious than that before the test, that is, the small and medium particles are filled in the middle of the pores, and the contact between the particles is no longer point-like. The contact area is larger but not completely embedded, and the boundary between particles is still relatively obvious, which is convenient for dividing it in statistical analysis.

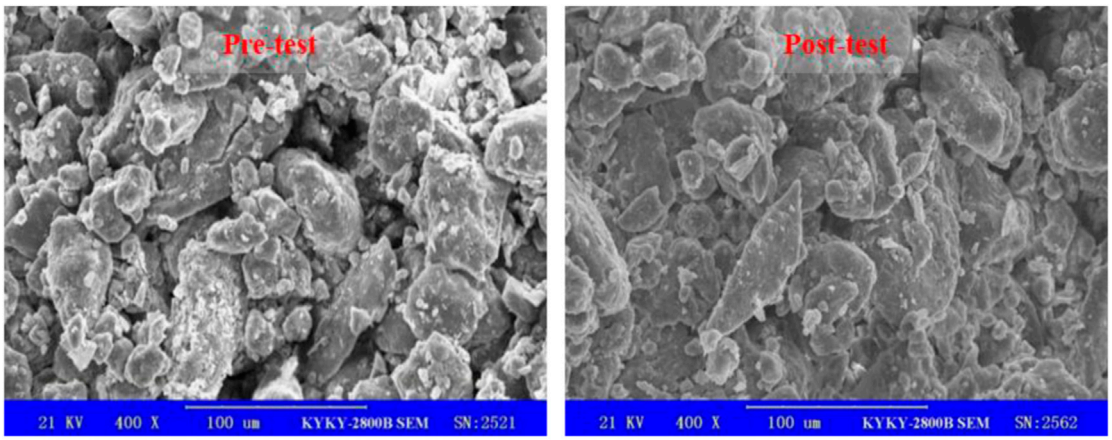

(d)Microstructure images of cement samples before and after the seismic subsidence test

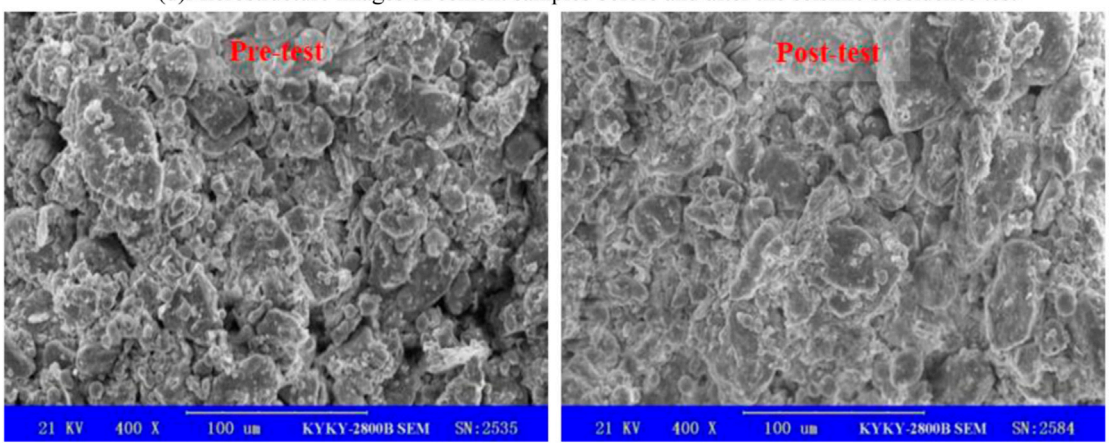

(e) Microstructure image of composite modified (dynamic compaction-fly ash) sample before seismic subsidence test

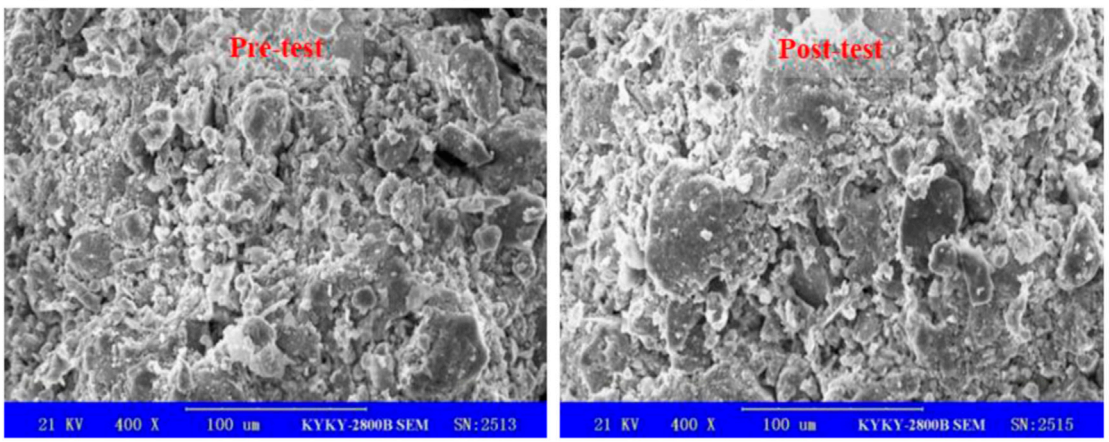

(f) Microstructure images of composite modified (dynamic compaction-cement) samples before and after the seismic subsidence test

FIGURE 2 | Microstructure image of samples before and after the seismic subsidence test. **(A)** Microstructure image of the undisturbed specimen before and after the seismic subsidence test. **(B)** Microstructure images of the dynamic compaction sample before and after the seismic subsidence test. **(C)** Microstructure images of fly ash samples before and after the seismic subsidence test. **(D)** Microstructure images of cement samples before and after the seismic subsidence test. **(E)** Microstructure image of composite modified (dynamic compaction–fly ash) sample before seismic subsidence test. **(F)** Microstructure images of composite modified (dynamic compaction–cement) samples before and after the seismic subsidence test.

Microstructure Image of fly Ash Sample

The microstructure of the modified fly ash sample before and after the test is shown in **Figure 2C**. Before the test, the sample structure showed that the surface of the soil particles is covered with unique spherical particles, that is, glass beads with a content of more than 70% in the fly ash. These microbeads

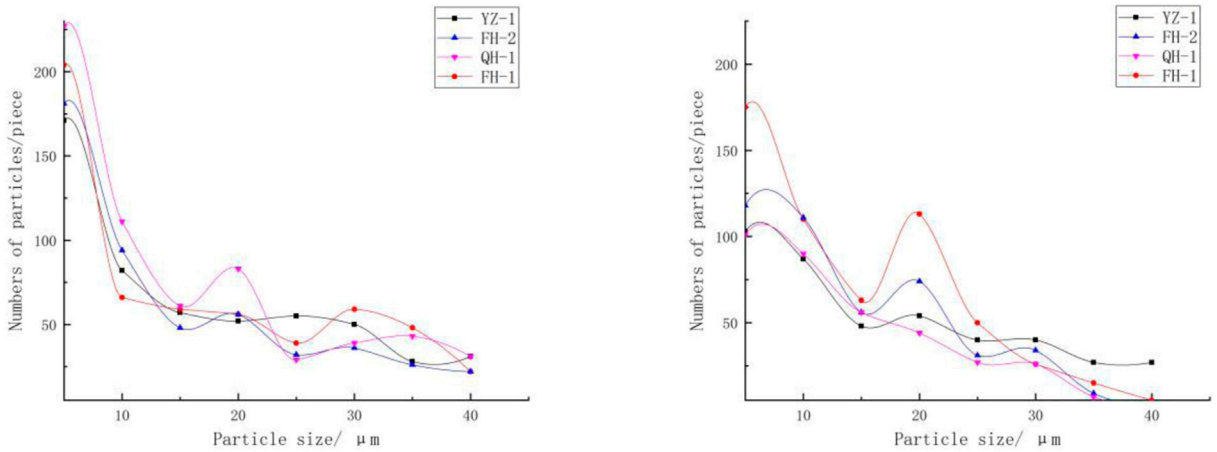

FIGURE 3 | Particle size–quantity distribution statistics of various samples. All samples follow the distribution law that the larger the particle size is, the fewer the number of particles is, and more than 60% of the particles are concentrated within 15 um.

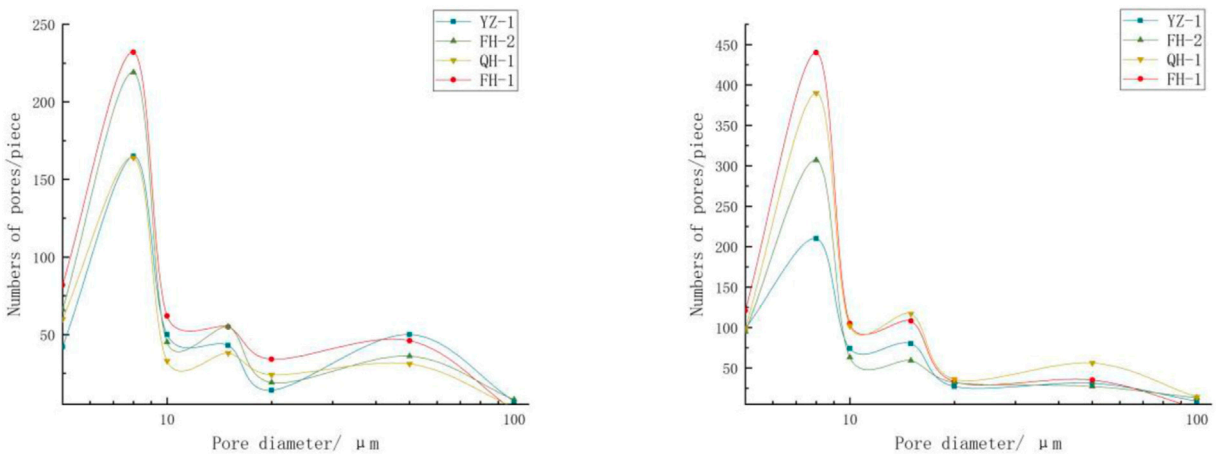

FIGURE 4 | Statistical graph of the pore size–quantity distribution of various samples. After the seismic subsidence test, the large and medium pores are almost completely eliminated due to the application of the modified method and the effect of cyclic load.

are mostly on the surface of loess particles or filled in the medium and large pores, which undoubtedly have a compact and homogeneous effect on the soil; on the other hand, the soluble oxides (SiO_2 and Al_2O_3, etc.) in fly ash forms hydrated salts with water and soil hydrates, which increase the strength of intergranular cementation. The glass microbeads formed by fly ash not only increase the small and medium particles but also fill and eliminate some of the overhead and large and medium pores; more importantly, the unique spherical microbeads close to the standard form play a role in adjusting the particle arrangement. As a result, the sample does not undergo shear failure after the triaxial test but manifested itself as swelling in the middle of the sample and microscopically as the peak of the curve caused by the formed particles or glass beads between 20 and 30 um; the reduction of small particle size particles is more obvious.

Microstructure Image of Cement Sample

The microstructure of the sample before and after the test after adding cement is shown in **Figure 2D**. Before the test, the particle size of the sample does not change much, but the cement obviously changes the form of cementation between the soil particles; the particles are superimposed, and even the cementation becomes for large clots; and the arrangement of particles has also changed to an obvious mosaic structure, and the boundaries between the clots are obvious. For the cement modification method, after the test, as mentioned in the chemical principle, although the strength of the soil is

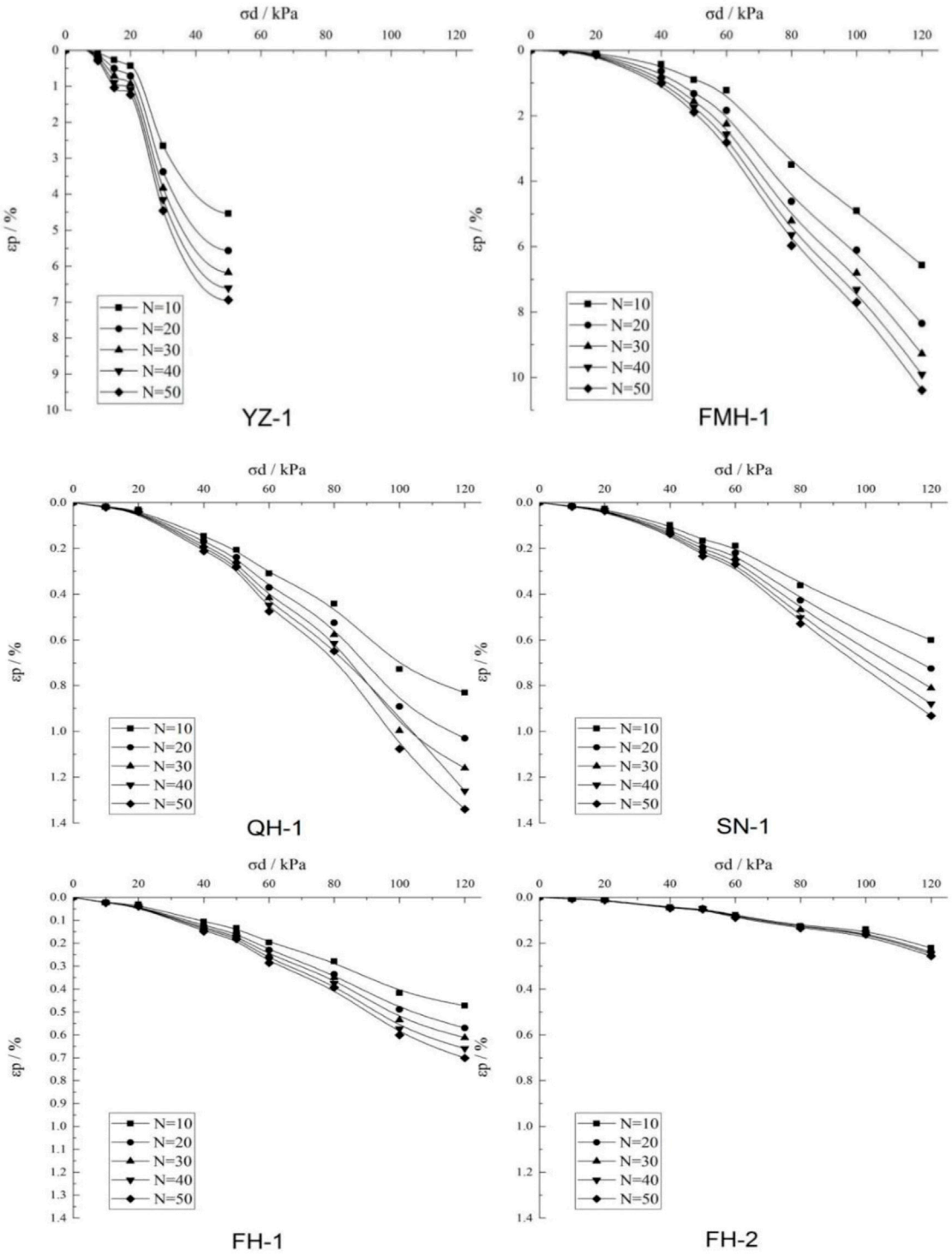

FIGURE 5 | Seismic subsidence coefficients of original and improved loess samples under different vibration times.

enhanced after the reaction, the brittleness of the soil is also greatly enhanced. The significance of this in actual engineering is that under the condition of the same amount of earthquake subsidence, the foundation with fly ash shows gradual and uniform settlement, while the cement-compacted foundation shows sudden failure. Shear deformation and fracture occur, and this is confirmed by the macroscopic phenomenon of the triaxial test, as shown

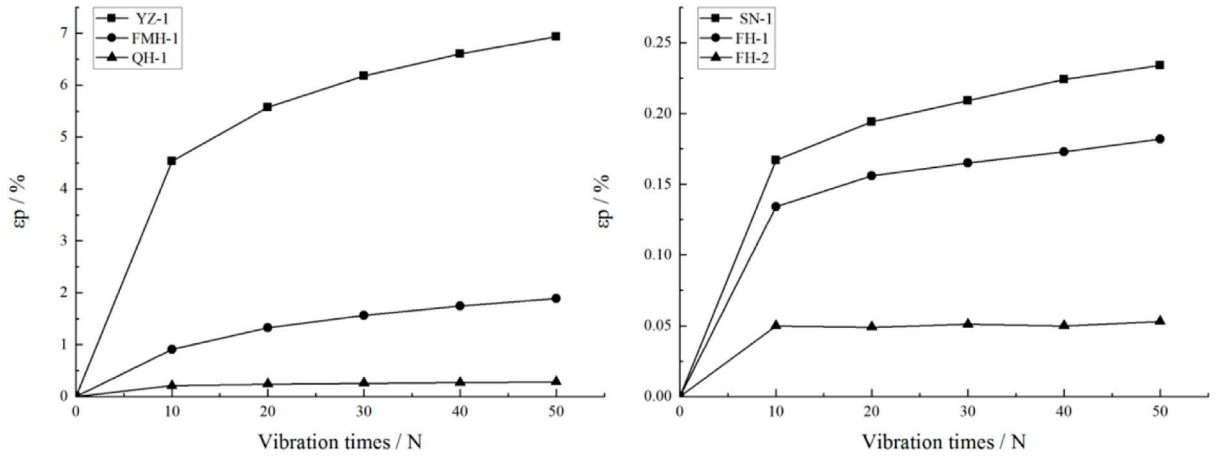

FIGURE 6 | Vibration frequency and residual strain curves of original and improved soil samples.

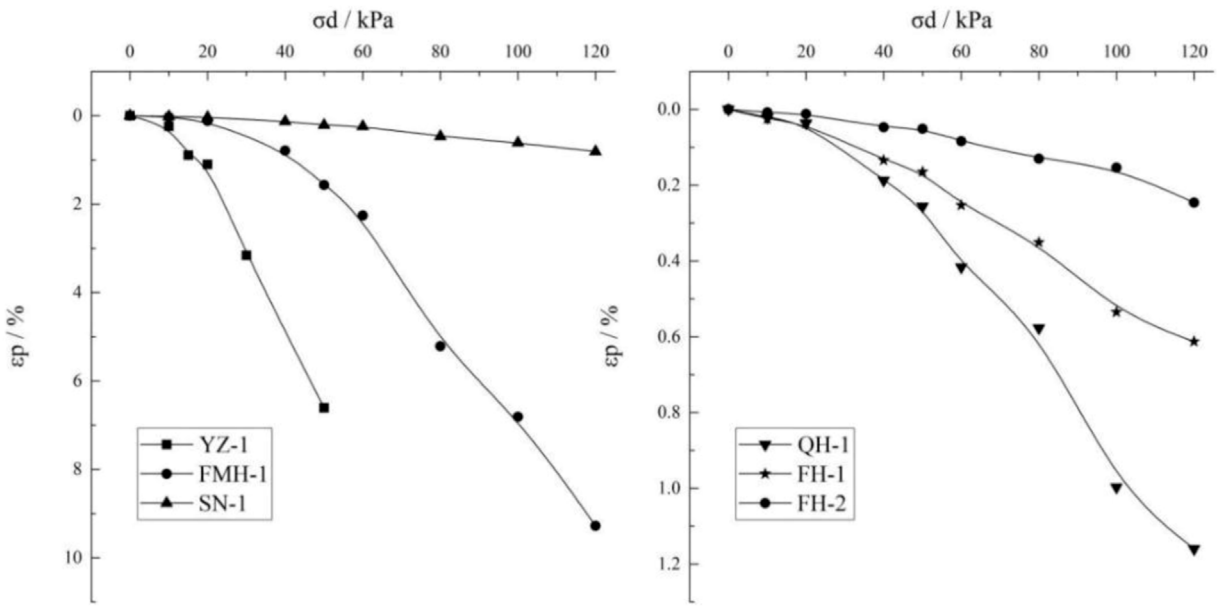

FIGURE 7 | Original and improved loess seismic subsidence curve (*N* = 30).

in **Figure 9C**; then uneven settlement occurs, which has a great impact on the buildings on it.

Dynamic Compaction-Microstructure Image of Fly Ash Sample

The microstructure of the sample before and after the dynamic compaction–fly ash composite improvement test is shown in **Figure 2E**. In addition to the unique presence of a large number of spherical glass beads, the particle morphology is completely clotted compared with the method of adding fly ash only. The form of intergranular connection is mainly cementation, the arrangement of clots is very dense, and there is no obvious directionality, and the pores are denser after the test.

Dynamic Compaction-Microstructure Image of Cement Sample

The microstructure of the sample before and after the dynamic compaction–cement composite improvement test is shown in **Figure 2F**. Compared with the sample of adding cement only, the particles are more obvious as flocculent substances. The small clots are also completely removed, no obvious clot boundaries can be seen; the particles are completely cemented; the medium and small pores are also eliminated, almost becoming a large

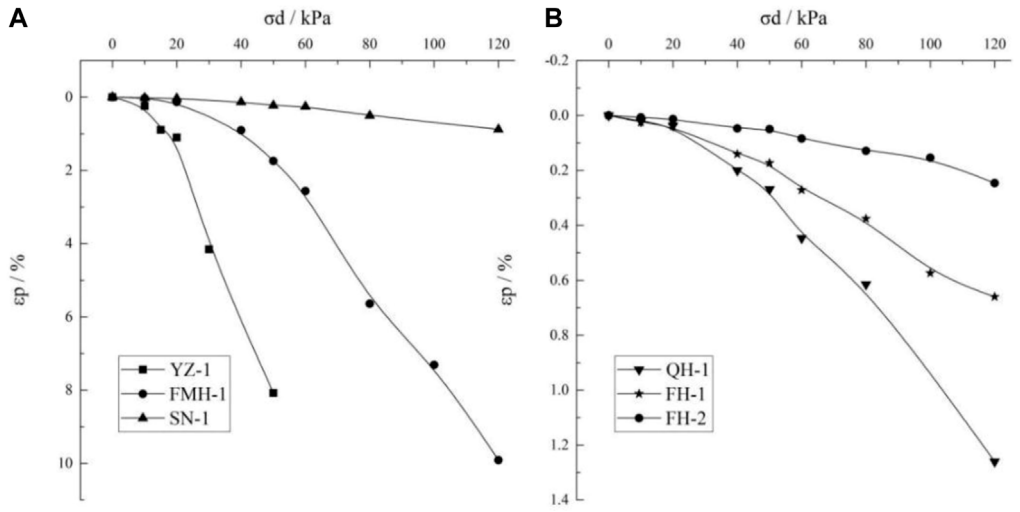

FIGURE 8 | Seismic depression curve of original and improved loess (*N* = 40). **(A)** The original state, fly ash and cement samples. **(B)** The dynamic compaction and two composite treatment samples.

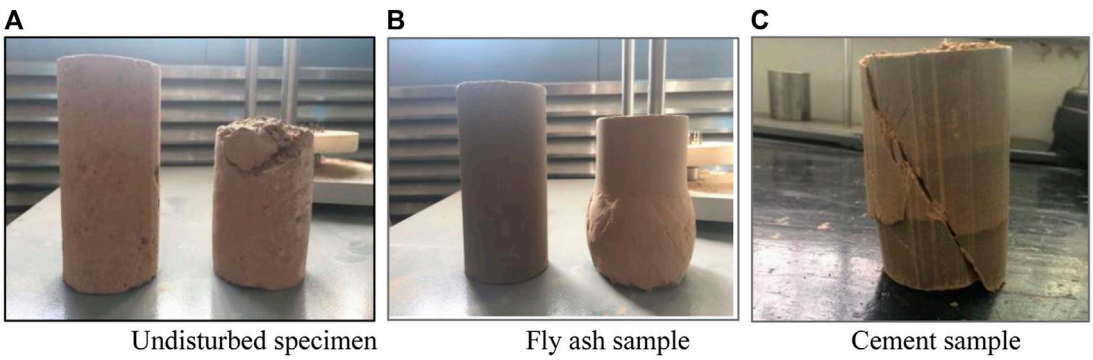

FIGURE 9 | Macroscopic failure of the original, fly ash, and cement samples after the test. **(A)** Undisturbed specimen, **(B)** fly ash sample, and **(C)** cement sample.

aggregate; and there is no obvious change in the microstructure before and after the test.

In general, after the seismic subsidence test, the application of the modification method combined with the cyclic load effect almost eliminated the large and medium pores. At the same time, the decomposing of the aggregate was caused by compaction and vibration in the new medium and small pores in the soil sample. During this dynamic change process, the pores had the largest rate of change in the area with smaller particle size. Therefore, it can be seen that in the modified side, the micropores are greatly increased, the overhead pores are completely eliminated, and the large pores are greatly reduced. It is worth noting that in the dynamic compaction samples, the number of micro- and small pores has increased significantly, but the overall pore area has been greatly reduced. This shows that although the number of medium and large pores is small, their elimination is very important. The growth of micropores does not affect the seismic subsidence of loess. For the two types of chemical modification methods, similarly, the micro- and small pores have increased significantly. Although the number of pores has changed greatly, the total pore area has not changed much compared to before the earthquake subsidence, and its anti-seismic subsidence effect is far better than that of macropores. The tamping method further proves that for the loess samples added with chemical materials, the improvement effect is mainly reflected in the contact and cementation of the particles, rather than the improvement of the pores.

Distribution of Particle Size and Pore Size Before and After the Test

Through the quantitative statistics of the particle morphology parameters in the image of a large number of original loess samples and different improved methods at 400 times, the particle size and pore size distribution before the test results are shown in **Figures 3**, **4**. For the composite modified sample dynamic compaction-fly ash method and dynamic compaction–cement method, the particles and aggregates are

TABLE 4 | Prediction results of seismic subsidence of loess field with different foundation treatment measures.

Foundation type	Calculation depth (m)	Maximum seismic subsidence under each earthquake intensity (cm)			Corresponding seismic subsidence level		
		VII (127.4gal)	VIII (274.4gal)	IX (548.8gal)	VII	VIII	IX
Undisturbed loess	20	44.10	183.30	-	III	IV	IV
Fly ash	20	9.20	54.10	-	II	III	IV
Cement–soil	20	3.00	6.20	19.40	I	I	II
Dynamic compaction	20	3.30	12.10	38.60	I	II	III
Fly ash (tamped)	20	2.30	6.90	19.30	I	I	II
Cement–soil (tamped)	20	0.70	2.20	6.80	I	I	I

arranged too densely, and the edges cannot be identified. It is considered that the particles are almost completely cemented, and the pores between the particles and the clots are completely eliminated. Therefore, no statistics are made.

According to the quantitative statistics of the particle size of the sample, no matter what kind of improvement method is used, it has the same rule as the original loess that the larger the particle size, the fewer the number of particles, and more than 60% of the particles are concentrated within 15 um. At the same time, the difference of the improvement methods also shows some differences: the dynamic compaction can identify and count the largest number of soil particles under the same area and, mainly, crush the medium and large particles above 30 um into 5–20 um. Particles: the number of particles is followed by the fly ash–modified sample. At the same time, it is noted that the curve has a small peak around 30 um. This phenomenon is not unrelated to the glass beads formed by fly ash at 30 um and the cement improvement method; although the number of small and medium particles has been increased to a certain extent and the number of particles with larger diameters has been reduced, the effect is slightly weaker than that of the other two methods.

Similarly, the quantitative statistics of the pore size of the sample show that the pore size–quantity distribution of dynamic compaction and fly ash and cement improvement methods have a relatively consistent trend with that of undisturbed loess, this is related to the particle size–quantity performance. The statistics also shows that the fly ash method significantly increased the number of pores within 10um, followed by the cement modification method. This is mainly due to the chemical method that generates fine particulate and increases the number of small and medium pores. At the same time, these chemicals are all over; filling the original particle pores has played a role in dividing the large pores, that is, the small number of large pores is divided into a large number of small and medium pores; the dynamic compaction method does not change the number of micro and small pores within 10 um significantly, but for 10 um the dynamic compaction method reduces the number of pores the most. In other words, the dynamic compaction method eliminates the medium and large pores more obviously, while the two chemical improvement methods mainly reduce the large pores or overhead pores above 50 um. There is even an increasing trend in the statistics of small and mesopores in range of 10–50 um.

PERFORMANCE EVALUATION OF DIFFERENT ANTI-SEISMIC SUBSIDENCE TREATMENT TECHNOLOGIES

Seismic Subsidence Curve

Figure 5 shows the seismic subsidence coefficients of six types of loess samples when the vibration times N is gradually increased. Under the same dynamic stress, with the increase in vibration times, the residual strain of each type of specimen shows a gradual increase trend. The difference is that the seismic subsidence coefficient of undisturbed loess is the most sensitive to the increase in vibration times, followed by fly ash samples. The other four treatment methods greatly reduce the sensitivity of the seismic subsidence coefficient to the vibration times, and the seismic subsidence curves are very close, especially the dynamic compaction–cement method in the compound improvement method, which is not sensitive to the vibration times. Take the dynamic stress as 50 kPa and use the vibration times as the abscissa to draw the residual strain curve of the original and improved loess, as shown in **Figure 6**. It can be seen that regardless of the applied dynamic stress, the original sample shows strong sensitivity to the vibration times N, and the first 10 vibrations have accumulated more than 80% of the total residual deformation. This law is also consistent with the previous ones (Wang, 2003). Although different improvement methods have reduced its seismic subsidence to varying degrees, its residual deformation growth with the number of vibrations still has a similar law to that of the undisturbed soil, that is, the main deformation occurs in the first 10 vibrations, almost linearly increasing, and then the increase in the amount of earthquake subsidence gradually slowed down.

The dynamic stress and residual strain curve of the sample is further analyzed after processing the dynamic stress and residual strain curve of the sample with 30 (fortification earthquake) and 40 (rare earthquake) times, respectively, under the action of strong earthquakes, as shown in **Figure 7**. Due to the large difference in the magnitude of the seismic subsidence caused by the effects of several improvements, in order to better show the difference between the curves, the original state, fly ash, and cement samples are used as a group to describe the seismic subsidence curve (**Figure 8A**). The dynamic compaction and two composite treatment samples are analyzed and described as a set (**Figure 8B**). The undisturbed loess sample exhibits strong shock sensitivity, and the shear deformation curve of the sample

shows a sharp upward trend with the increase in dynamic stress. When the dynamic stress is loaded to 20–30 kPa, the strain reaches 3%, and when it is loaded to 50 kPa, the residual strain reaches 6%. Then the macroporous structure in the sample is destroyed (The microstructure is shown in **Figure 2A**), and the sample is macroscopically collapsed, so the residual strain value reaches to 6% after the test stops, and the value no longer rises.. The seismic subsidence curves of the two chemical improvement methods (fly ash and cement) mainly show three stages: 1) at the 0–20 kPa stage, the effect of the two improvement methods is almost the same, and the seismic subsidence of loess can be completely eliminated. 2) At the 20 kPa–60 kPa stage, both methods can increase the seismic performance of loess by more than 5 times, but the fly ash method begins to show the difference from the cement-soil method. The growth of the dynamic stress begins to accelerate, but the maximum residual deformation produced does not exceed 3% of the failure strain standard, which still has a good effect of improvement. 3) When the dynamic stress exceeds 60kPa, the residual deformation of the fly ash modification method produces a rapid growth stage with the application of dynamic stress. It is worth noting that the residual strain far exceeds the 3% strain standard, but it is different from the original test. In contrast, the sample body hardly produces fracture damage, can be supported until the dynamic stress is loaded above 120 kPa, and its deformation reaches 7% and above; the seismic subsidence curve of the cement-soil improvement method basically no longer increases with the continuous increase in the dynamic stress. When the dynamic stress reaches 120 kPa, the residual strain is still less than 1%. **Figures 7**, **8** on the right show the dynamic compaction, fly ash, fly ash when the dynamic load vibration times N are 30 (fortification earthquakes) and 40 (rare earthquakes) times, and the density is increased to 1.75 g/cm^3. First of all, the residual strain of these three types of improvement methods is far superior to the first three types of specimens in magnitude, and their residual deformations do not exceed 1.5% under strong seismic loads. This result fully confirms that the increase in density has the improvement of seismic subsidence performance is of vital importance. In the treatment effect of the composite method, the cement-soil method after compaction is obviously the best and the fly ash method is the second. Especially for fly ash samples, the anti-seismic sinking effect is greatly enhanced after compaction treatment. When the dynamic stress reaches 100 kPa ($N = 30$), the residual deformation is only 0.54%, which is 6.28% lower than before compaction, which is almost eliminated seismic. Therefore, the test proves that the chemical modification method can effectively improve the seismic subsidence performance of the foundation, and the effect of tamping is the best.

Specimen Macroscopic Deformation Characteristics

The research results show that the undisturbed loess samples have strong dynamic fragility. When the dynamic stress reaches about 50kPa, the residual strain reaches the peak value and the sample collapses, as shown in **Figure 9A**. **Figure 9** shows the macroscopic phenomena of original and improved samples before and after the test. In the original sample, as shown in **Figure 9A**, it randomly contains calcareous nodules all over the sample; therefore, there are micro-cracks between the nodules and the surrounding soil. When stress is applied, the tips of the larger micro-cracks in the nodules are more likely to have stress concentration and rapidly expand, leading to the fracture of sample, and the position of the fractured surface often present an irregular form; the soil at the fracture site is loose and broken and dense micro-cracks are generated in other parts of the column. In the sample with fly ash, although the dynamic load caused considerable residual deformation of the sample, the sample did not appear to be broken or cracked but was manifested as the expansion of the column caused by the axial stress extrusion, as shown in **Figure 9B**. This also fully supports the role played by the "fly ash effect" in foundation treatment, that is, more than 70% of the glass beads contained therein play a role in compactness and homogenization and at the same time play a good lubricating effect. Therefore, although there will be residual deformation, it is shown as intermittent and gradual deformation so that sudden brittle failure will not occur. For the sample with cement, there is no visible change during the dynamic stress loading process. When the dynamic stress is loaded to the critical dynamic stress, the sample will undergo instantaneous segmental failure, as shown in **Figure 9C**. It shows that the column has X-shape through cracks, with obvious shear planes, and the whole process is abrupt. Due to the high strength of the two types of composite modified samples, there is no significant macroscopic deformation when loaded to 120 kPa, and the specimens have no significant height reduction phenomenon.

CONCLUSION AND SUGGESTION

In summary, it can be seen from the residual strain curve that the anti-seismic subsidence improvement methods for this seismic subsidence loess area are effective. Especially, it gives the qualitative evaluation of different improvements for Q_3 loess under the conditions of fortified earthquake and rare earthquake. In microscopic view, physical improvement methods have the most obvious effect on eliminating large pores and overhead pore structures; chemical modification methods can generate unique glass beads or flocculated fine structures, which greatly increase the strength of the soil and play a role in filling, cementing, or buffering in strong earthquakes. From a dynamic point of view, under the conditions of frequent earthquakes, fortified earthquakes, and rare earthquakes, the amount of subsidence shows a non-linear growth trend with the increase in peak acceleration; therefore, for the actual engineering site, it is necessary to do a quantitative prediction of the amount of seismic subsidence under a specific earthquake intensity, and then take corresponding improvement measures according to suggestion in this study. In order to quantify the demand and better apply it to engineering practice, taking the sample collection area as an example, the amount of seismic subsidence under specific earthquake intensity is calculated: the total seismic

subsidence of the site soil was obtained by the layered sum method based on the results of the indoor test, the seismic subsidence was predicted, and the effect evaluation of the modification treatment method was carried out. The ground motion parameters take the upper limit of the maximum horizontal ground acceleration a_{max} under the 50-year probability of exceeding 63.2, 10, and 2%. The corresponding seismic intensity is VII degree, VIII degree, and IX degree, respectively, and the value range of peak ground acceleration (PGA) is 0.055–0.130 g, 0.170–0.280 g, and 0.314–0.560 g, respectively. To calculate the dynamic shear stress τ_d suffered by the soil layer (Zhang et al., 1999).

For the layered sum method, the amount of seismic subsidence is not only determined by the seismic subsidence coefficient but also inseparable from the soil thickness of the site. According to the seismic design standard, the calculated depth of foundation treatment was extended to 20 m. For sites with a thickness of less than 20m, the actual thickness is calculated. The calculation results and evaluation results of the seismic subsidence are shown in **Table 4** (Department of Disaster Prevention, China Earthquake Administration, 1993).

Combining the calculation results of the earthquake subsidence with **Table 4** for analysis, for the undisturbed loess site, there is no doubt that it has extremely strong "seismic sensitivity," which can cause severe earthquake subsidence in the foundation under frequent earthquakes. When the maximum horizontal ground acceleration a_{max} is 127gal, that is, when frequent earthquakes occur, in addition to the method of adding fly ash, the use of the other four methods reduces the seismic subsidence of the field to below 4.00 cm. For general engineering sites, it can be considered that the earthquake subsidence has been eliminated. When a_{max} is 274gal, that is, when the earthquake is fortified, the cement method in chemical modification and the two compound improvement methods, dynamic compaction–fly ash method and dynamic compaction–cement–soil method, will still maintain the amount of seismic subsidence below 7.00 cm; the anti-seismic subsidence effect of the physical improvement dynamic compaction method has begun to show its shortcomings. When a rare earthquake occurs, that is, when a_{max} is 548gal, the seismic subsidence of the dynamic compaction–cement–soil method is still less than 7.00 cm, which means the method has completely eliminated the seismic subsidence of the site, and the use of cement-soil method and dynamic compaction–fly ash method to keep the earthquake damage at medium damage has also shown good results. For a project site with local intensity level, when selecting the improvement method, the amount of seismic subsidence should be less than corresponding grade and economic efficiency shall be taken into account.

DISCUSSION

Loess in this site has extremely low water content. It is well known that loess has special structure, which makes it particularly sensitive to water. Therefore, the increase in loess moisture content caused by natural factors and human activities will increase the seismic subsidence and reduce the seismic subsidence performance. Therefore, the possible increase or decrease in water content of foundation soil and the drainage state of anti-seismic settlement measures should also be considered in the anti-seismic settlement treatment, which needs to be further studied.

DATA AVAILABILITY STATEMENT

The raw data supporting the conclusions of this article will be made available by the authors, without undue reservation.

AUTHOR CONTRIBUTIONS

PW is responsible for the overall implementation and writing manuscripts; SX is responsible for different earthquake in processing dynamic triaxial test, scanning electron microscopy (SEM) test, the implementation of the specific test, and data analysis; SS has carried on the theory of technical guidance to the whole manuscript. Graduate student, XL and ZQ as the main persons, participate in the test and manuscript finishing work.

FUNDING

This study was supported by the Central Public-Interest Scientific Institution Basic Research Fund (2020IESLZ07), the Joint funds for Earthquake Science (U1939209), the Key R&D Program in Gansu Province of China (18YF1FA101), and the Key Tasks of Emergency Youth of CEA(CEA_EDEM-2021).

ACKNOWLEDGMENTS

The authors are grateful to the members in the group, Shaofeng Chai, Shiyang Xu, Jinlian Ma, and Gaofeng Che, for their help in field tests and thankful to Wang for reviewing the manuscript.

REFERENCES

Bruchon, J.-F., Pereira, J.-M., Vandamme, M., Lenoir, N., Delage, P., and Bornert, M. (2013). Full 3D Investigation and Characterisation of Capillary Collapse of a Loose Unsaturated Sand Using X-ray CT. *Granular Matter* 15 (06), 783–800. doi:10.1007/s10035-013-0452-6

Dal Ferro, N., Delmas, P., Duwig, C., Simonetti, G., and Morari, F. (2012). Coupling X-ray Microtomography and Mercury Intrusion Porosimetry to Quantify Aggregate Structures of a Cambisol under Different Fertilisation Treatments. *Soil Tillage Res.* 119, 13–21. doi:10.1016/j.still.2011.12.001

Deng, J., Wang, L., and Wu, Z. (2012). Acid Modification Method and Microstructure Analysis of Seismic Substance Deformation of Loess. *Rock Soil Mech.* 33 (12), 3624–3631. cnki: sun: ytlx.0.2012-12-017(In Chinese with English abstract).

Deng, J., Wang, L., and Zhang, Z. (2007). Microstructure Characteristics and Seismic Collapsibility of Loess. *Chin. J. Geotechnical Eng.* 29 (4), 542~548, 2007 . (In Chinese with English abstract). doi:10.3321/j.issn:1000-4548.2007.04.012

Department of Disaster Prevention, China Earthquake Administration (1993). *Seismic Disaster Prediction and Evaluation Manual*. Beijing: Seismological Press. (In Chinese).

Gao, G. (1980). Microstructure Analysis of Loess and its Application in Engineering Investigation. *Eng. Invest. Surv.* (06), 2583–2884. cnki:sun: gckc.0.1980-06-008 (In Chinese with English abstract).

Gao, G. (1980). Microstructure Classification and Collapsibility of Loess. *Chin. Sci.* 23 (12), 1203–1208. cnki:sun:jaxk.0.1980-12-008(In Chinese with English abstract).

Gao, M., Chen, G., Xie, F., Xu, X., Li, X., Yu, Y., et al. (2015). *Zoning Map of Ground Motion Parameters in China*. Beijing: Standards Press. (In Chinese).

Garratt-Reed, A., and Bell, D. (2005). *Energy-dispersive X-ray Analysis in the Electron Microscope*. Oxfordshire: BIOS Scientific Publishers Ltd.

Gu, T., Wang, J., Guo, L., Wu, D., and Li, K. (2011). Study on Microstructure Changes of Q3 Loess Based on Image Processing. *Chin. J. Rock Mech. Eng.* 30 (S1), 3185–3192. (In Chinese with English abstract).

Huang, Q. (1963). Discussion on Evaluation of Collapsible Loess Foundation. *J. Civil Eng.* 9 (2), 25–31. (In Chinese with English abstract).

Jiang, M., Zhang, F., Hu, H., Cui, Y., and Peng, J. (2014). Structural Characterization of Natural Loess and Remolded Loess under Triaxial Tests. *Eng. Geology.* 181, 249–260. doi:10.1016/j.enggeo.2014.07.021

Li, H., Tu, J., Wang, L., Mo, Y., Ma, L., Huo, H., et al. (2012). *Local Standard of Gansu Province-Code for Seismic Design of Buildings*. (In Chinese).

Li, L., Wang, L., and Wang, J. (2005). Quantitative Study of Microstructural Porosity of Loess in the Seismic Area of the Yongdeng M5.8 Earthquake. *Chin. J. Seismological Res.* 28 (3), 282–287. (In Chinese with English abstract). doi:10.3969/j.issn.1000-0666.2005.03.016

Lin, R.-S., Wang, X.-Y., Lee, H.-S., and Cho, H.-K. (2019). Hydration and Microstructure of Cement Pastes with Calcined Hwangtoh clay. *Materials* 12 (03), 458. doi:10.3390/ma12030458

Ng, C. W. W., Mu, Q. Y., and Zhou, C. (2017). Effects of Soil Structure on the Shear Behaviour of an Unsaturated Loess at Different Suctions and Temperatures. *Can. Geotech. J.* 54 (02), 270–279. doi:10.1139/cgj-2016-0272

Romero, E., and Simms, P. H. (2008). Microstructure Investigation in Unsaturated Soils: A Review with Special Attention to Contribution of Mercury Intrusion Porosimetry and Environmental Scanning Electron Microscopy. *Geotech Geol. Eng.* 26 (06), 705–727. doi:10.1007/s10706-008-9204-5

Shaanxi Comprehensive Survey Institute (1973). Characteristics of Loess and Loess like Soil in China and Evaluation Methods for Their Collapsibility and Bearing Capacity. *Surv. Tech. Data* 3 (3), 1–20. (In Chinese).

Shao, X., Zhang, H., and Tan, Y. (2018). Collapse Behavior and Microstructural Alteration of Remolded Loess under Graded Wetting Tests. *Eng. Geology.* 233, 11–22. doi:10.1016/j.enggeo.2017.11.025

Sheng, S., Dou, Y., Tao, X., Zhu, S., Xu, B., Li, Q., et al. (1999). *Code for Geotechnical Testing*. Beijing: China water resources and Hydropower Press. (In Chinese).

Shi, Y., and Li, L. (2003). Micro-analysis of Seismic Subsidence Characteristics of Loess. *J. Rock Mech. Eng.* 24 (2), 129–134. (In Chinese with English abstract). doi:10.3321/j.issn:1000-6915.2003.z2.061

Shi, Y., and Qiu, G. (2011). Constitutive Relationship of Seismic Subsidence of Loess Based on Microstructure. *Chin. J. Geotechnical Eng.* 33 (S1), 7–12. cnki: sun:ytgc.0.2011-S1-002 (In Chinese with English abstract).

Teng, Y., Zhang, Y., Yan, M., Zhang, F., Zhang, D., Yuan, N., et al. (2012). *Technical Code for Foundation Treatment of Buildings*. Beijing: China Construction Industry Press. (In Chinese).

Wang, J.-D., Li, P., Ma, Y., Vanapalli, S. K., and K, S. (2019). Evolution of Pore-Size Distribution of Intact Loess and Remolded Loess Due to Consolidation. *J. Soils Sediments* 19 (3), 1226–1238. doi:10.1007/s11368-018-2136-7

Wang, J., Wang, Q., Wang, P., Zhong, X., and Chai, S. (2013). Effect of Adding Amount of Fly Ash on Dynamic Constitutive Relationship of Modified Loess. *Chin. J. Geotechnical Eng.* 35 (S1), 156–160. cnki:sun: ytgc.0.2013-S1-025 (In Chinese with English abstract).

Wang, L., Deng, J., and Huang, Y. (2007). Microscopic Quantitative Analysis of Seismic Collapsibility of Loess. *Chin. J. Rock Mech. Eng.* 26 (Suppl. 1), 3025–3031. (In Chinese with English abstract). doi:10.3321/j.issn:1000-6915.2007.z1.066

Wang, L. (2003). *Loess Dynamics*. Beijing: Seismological Press. (In Chinese).

Wang, L., and Zhang, Z. (1993). Estimation Method of Seismic Subsidence of Loess during Earthquake. *J. Nat. Disasters* 2 (3), 85–94. (In Chinese with English abstract).

Wang, Q., Liu, H., Ma, H., Wang, J., and Li, N. (2016). Anti-liquefaction Behavior and Mechanism of Cement-Stabilized Loess. *Chin. J. Geotechnical Eng.* 38 (11), 2128–2134. (In Chinese with English abstract). doi:10.11779/cjge201611025

Wang, Q. (2018). *Study on the Earthquake Subsidence Characteristic of Loess and the Analysis and Evaluation Methods of Earthquake Subsidence in Loess Site*. Xi'an: Xi'an University of Technology. (In Chinese with English abstract).

Wang, Y., and Lin, Z. (1990). *Structural Characteristics and Physical and Mechanical Properties of Loess in China*. Beijing: Science Press, 105–172. (In Chinese).

Wang, Z. (2017). Loess Plateau Region. *J. Glob. Change Data* 1 (01), 113+236.

Wei, Y. (2019). *Three-dimensional Microstructure Evolution and Collapsibility Mechanism of Loess under Water Action*. Xi'an, China: Doctorates Discourse of ChangAn University. (In Chinese with English abstract).

Wen, B.-P., and Yan, Y.-J. (2014). Influence of Structure on Shear Characteristics of the Unsaturated Loess in Lanzhou, China. *Eng. Geology.* 168, 46–58. doi:10.1016/j.enggeo.2013.10.023

Xu, C., Wu, X., and Xu, X. (2018). Seismic Landslides in the Loess Plateau and its Adjacent Areas. *J. Eng. Geology.* 26 (Suppl. l), 260–273. (In Chinese with English abstract). doi:10.13544/j.cnki.jeg.2018208

Xu, S., Wu, Z., Zhao, W., and Zhao, T. (2017). Study of the Microscopic Pores of Structured Loess Based on MATLAB and IPP. *China Earthquake Eng. J.* 39 (1), 8094, 2017 . (In Chinese with English abstract). doi:10.3969/j.issn.1000-0844.2017.01.0080

Xu, Y., and Guo, P. (2020). Disturbance Evolution Behavior of Loess Soil under Triaxial Compression. *Adv. Civil Eng.* 2020, 1–14. doi:10.1155/2020/4160898

Xu, Y., Guo, P., Wang, Y., Zhu, C.-W., Cheng, K., Lei, G., et al. (2021). Modelling the Triaxial Compression Behavior of Loess Using the Disturbed State Concept. *Adv. Civil Eng.* 2021, 1–17. doi:10.1155/2021/6638715

Xu, Y., Guo, P., Zhu, C., Lei, G., and Cheng, K. (2021). Experimental Investigation into Compressive Behaviour and Preconsolidation Pressure of Structured Loess at Different Moisture Contents. *Geofluids* 2021, 1–9. doi:10.1155/2021/5585392

Zhang, Z., Duan, R., Sun, C., Wang, L., Wang, J., Shi, Y., et al. (1999). *Prediction of Loess Earthquake Disaster*. Beijing: China Seismological Press. (In Chinese).

Zhang, K., and Ling, X. (2016). *Geotechnical Seismic Engineering and Engineering Vibration*. Beijing: Science Press. (In Chinese).

Zhang, Z., and Duan, R. (1986). "Discussion on Seismic Subsidence of Loess Sites in the north West of China during Earthquakes," in *Proceedings of the International Symposium on Engineering Geology Problems in Seismic Areas* (Bari, Italy: Geologia Applicata ed Idrogeologia), 65–76.

Zhang, Z. (2016). *Research on the Initiation Mechanism and Disaster Mode of Typical Seismic Loess Landslide*. Wuhan: Doctoral Dissertation of China University of Geosciences. (In Chinese with English abstract).

Zhu, H., Ju, Y., Huang, C., Han, K., Qi, Y., Shi, M., et al. (2019). Pore Structure Variations across Structural Deformation of Silurian Longmaxi Shale: An Example from the Chuandong Thrust-fold Belt. *Fuel* 241, 914–932. doi:10.1016/j.fuel.2018.12.108

Zhu, Y., and Chen, Z. (2009). Experimental Study on Dynamic Evolution of Meso-Structure of Intact Q3 Loess during Loading and Collapse Using CT and Triaxial Apparatus. *Chin. J. Geotechnical Eng.* 31 (08), 1219–1228. (In Chinese with English abstract). doi:10.1086/670653

Conflict of Interest: The authors declare that the research was conducted in the absence of any commercial or financial relationships that could be construed as a potential conflict of interest.

frontiers in Earth Science

BRIEF RESEARCH REPORT
published: 25 January 2022
doi: 10.3389/feart.2022.815275

Experimental Study on Creep Characteristics of Saturated Q_2 Loess

Xiaowei Liu[1,2]*, *Xudong Zhang*[2], *Xiaogang Fu*[2], *Tianxiang Yang*[2] and *Zisong Su*[2]

[1]Key Laboratory of Mechanics on Disaster and Environment in Western China, The Ministry of Education of China, Lanzhou University, Lanzhou, China, [2]College of Civil Engineering and Mechanics, Lanzhou University, Lanzhou, China

Catastrophic failures often occur to engineered infrastructure in areas underlain by saturated loess due to its high moisture content (degree of saturation >85%), low shear strength, and large deformation. Time effect (rheological property) and water are the most important factors affecting the mechanical properties of saturated loess. The rheological mechanism and characteristics of saturated loess are vital to understanding the interaction between infrastructure and foundation and the trigger of failures. Based on step-load testing, this study obtains the displacement-time relationship of saturated Q_2 loess to analyze its creep behavior. Experimental results show that the creep strength of saturated Q_2 loess is 75–80% of its unconfined compression strength, and the creep behavior can be simulated by the Burgers model. Additionally, the rheological parameters under different load conditions are obtained using the improved Marquardt iterative method. All these parameters can be used for numerical analysis of the rheological behavior of saturated Q_2 loess.

Keywords: saturated loess, creep, step load, burgers model, flow failure

OPEN ACCESS

Edited by:
Yueren Xu,
China Earthquake Administration, China

Reviewed by:
Chao Kang,
University of Northern British Columbia Canada, Canada
R. M. Yuan,
China Earthquake Administration, China

***Correspondence:**
Xiaowei Liu
liuxw@lzu.edu.cn

Specialty section:
This article was submitted to Geohazards and Georisks, a section of the journal Frontiers in Earth Science

Received: *15 November 2021*
Accepted: *03 January 2022*
Published: *25 January 2022*

Citation:
Liu X, Zhang X, Fu X, Yang T and Su Z (2022) Experimental Study on Creep Characteristics of Saturated Q_2 Loess. Front. Earth Sci. 10:815275. doi: 10.3389/feart.2022.815275

INTRODUCTION

Loess occurs widely across China. The regions covered by loess account for 6.31×10^5 km^2 (Dijkstra et al., 1994), where it serves as the primary building material, building environment, or the foundation for the infrastructure. Due to the unique genesis of loess (Liu et al., 1985; Zhang et al., 1989; An et al., 1998; Sun, 2005; Chen et al., 2019; Fu et al., 2021), it possesses particular characteristics in deformation, strength, and stability (Wang, 1982; Feng and Zheng, 1982; Zheng, 1982; Lei, 1987), and abundant studies have been carried out on loess in the world. Loess below the groundwater table has high water content and a degree of saturation greater than 85%. Compared with unsaturated loess, saturated loess has lower strength, larger deformation, higher compressibility, and is more sensitive (Qiao and Li, 1990). These characteristics lead to geotechnical problems such as slope flow failure (Wen and Jiang, 2017; Xu et al., 2018; Xie et al., 2018), tunnel collapse, and piping in saturated loess areas (Peng et al., 2015).

The Loess Plateau is the core area of the Belt and Road Program and the primary site of Western Development. Many major projects, including Lanzhou-Chongqing railway, Zhengzhou-Xi'an high-speed railway, Xi'an-Lanzhou high-speed railway, Lanzhou-Xinjiang high-speed railway, and the Tao River Diversion Project, have traversed through saturated Q_2 loess areas to a certain extent. Along with these projects, increasingly more problems have emerged due to the seepage failure of saturated Q_2 loess. For example, six tunnels out of 15 in phase I of the Tao River Diversion Project passed through saturated

Abbreviations: E, Elastic modulus; η, Viscosity coefficient; σ, Step load. ε, Total strain at time t (s).

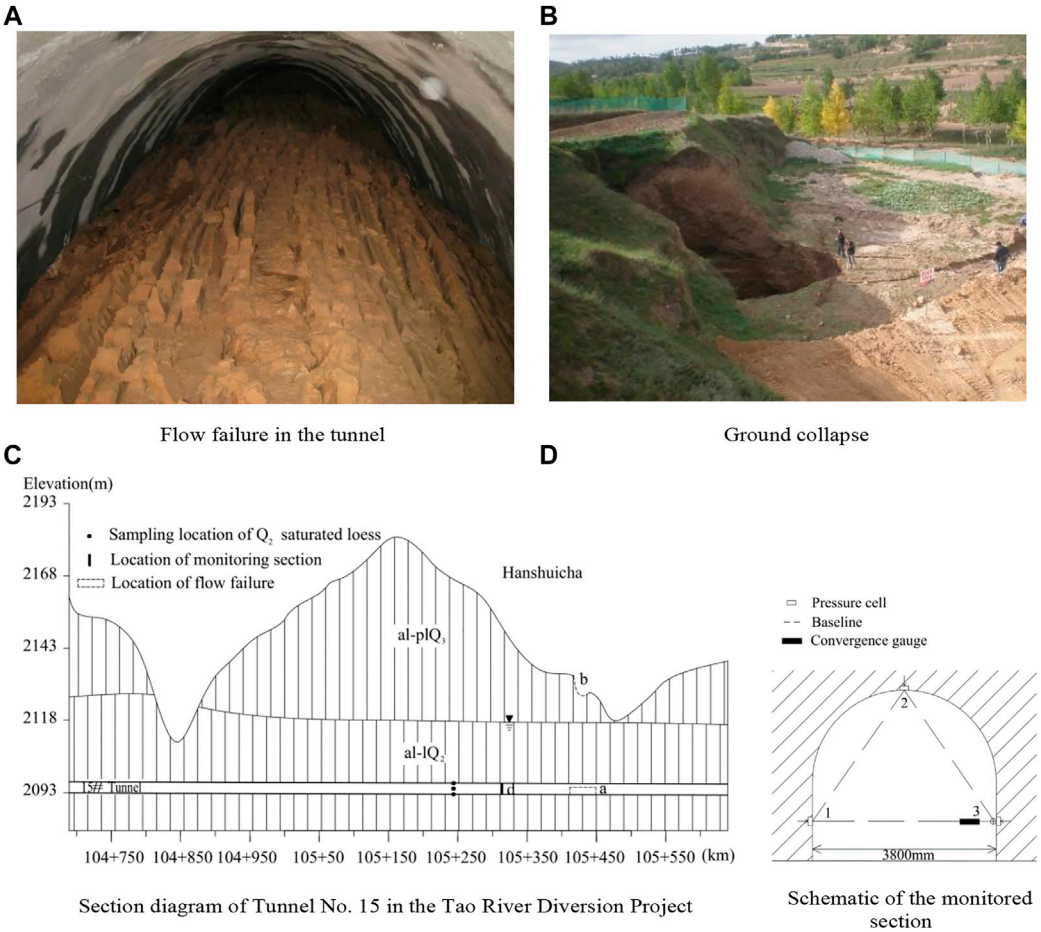

FIGURE 1 | Flow failure of saturated Q2 loess in Tunnel No. 15 of the Tao River Diversion Project. **(A)** Flow failure in the tunnel. **(B)** Ground collapse. **(C)** Section diagram of Tunnel No. 15 in the Tao River Diversion Project. **(D)** Schematic of the monitored section.

loess. During the construction of Tunnel No. 15, flow failure (**Figure 1A**) occurred in a segment of about 30 m long, leading to roof collapse (**Figure 1B**) and construction delay of nearly 1 year. Another example is the Dayingliang tunnel through saturated Q_2 loess along the second track of Baoji-Lanzhou Railway, which is less than 2 km away from Tunnel No. 15 of the Tao River Diversion Project. It was seriously damaged due to seepage during the construction by traditional methods. A much more expensive construction method, i.e., the ground freezing by liquid nitrogen, was adopted to finish some tunnel sections.

The study of rock and soil creep is extensive. For example, Wang et al. (2020) used step-loading triaxial creep tests under different moisture content to reveal the relationships between the steady-state creep rate and the initial strain and shear modulus. Lin et al. (2020) introducd the nonlinear viscoplastic element into the classic Burgers model and verified the rationality of the model by the shear creep test results of rock discontinuity, the results show that the modified Burgers model can reflect the mechanical properties of rock in three creep stages. Xia et al. (2021) proposed an improved simulation method based on the classical Burgers model and the Parallel Bonded model in the Particle Flow Code (PFC) and applied it to simulate the full-stage creep process in soft rock. Tang et al. (2019) studied the creep behavior of loess under different moisture content and confining pressure conditions, they revealed that the creep behavior of loess is prominent at high moisture content and minor time-dependent deformation occurs at high confining pressures. Zhu et al. (2013) investigated the creep characteristics of red-bed sliding soil under different vertical loads and water content through direct shear creep tests. Other significant studies on the creep behavior of different geotechnical materials include Fabre and Pellet. (2006), Wang et al. (2014), and Ye et al. (2015). However, the studies on the creep characteristics of saturated Q_2 loess are rare.

Engineering incidents quickly increase along with major projects in loess areas (Palmer, 2017; Wang et al., 2018). The key to curbing these incidents and mitigating the risks related to saturated Q_2 loess is to understand its rheological mechanism and characteristics. This paper conducts creep tests of saturated Q_2 loess obtained from a tunnel construction site by step loading. Testing results, including the displacement-time relationship and creep strength, are presented. In addition, the Burgers model was used to simulate the creep behavior, and the rheological

TABLE 1 | Grain size distribution of the Q_2 loess.

Sample number	Granulometric composition (%)			Uniformity coefficient	Curvature coefficient
	Sand particles	Silt particle	Clay particle		
	>75 μm	75~5 μm	<5 μm	C_u	C_c
1	5.2	66.3	28.5	26.8	1.61
2	8.0	63.3	28.7	25.3	1.72
3	7.0	61.2	31.8	28.6	1.44
4	7.3	62.2	30.5	27.3	1.53

TABLE 2 | Uniaxial compressive strength of saturated Q_2 loess.

Sample number	Water content (%)	σ_c (MPa)	Sample number	Water content (%)	σ_c (MPa)
1	22.61	0.57	3	23.21	0.52
2	23.89	0.50	4	21.37	0.60

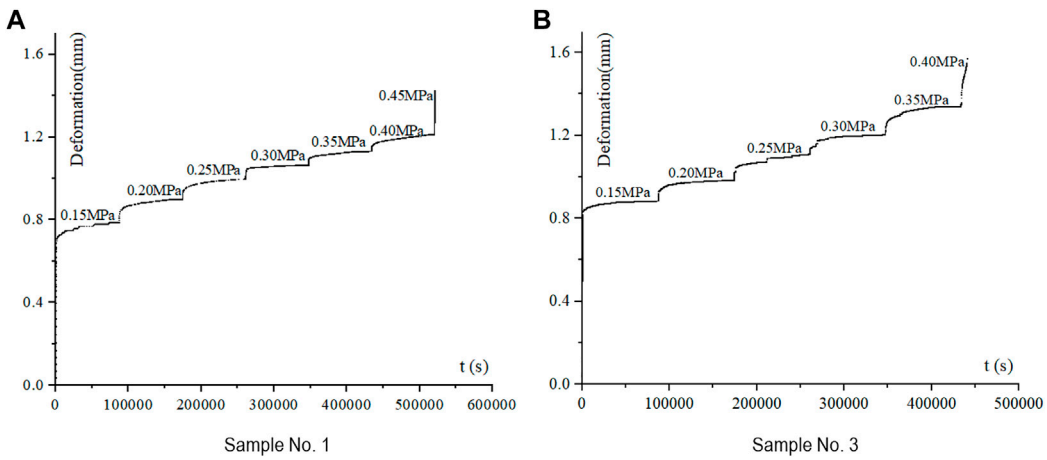

FIGURE 2 | Displacement vs. time from the creep tests of saturated Q_2 loess. **(A)** Sample No. 1. **(B)** Sample No. 3.

parameters under different load conditions are obtained using the improved Marquardt iterative method. At the same time, deformation prediction by using laboratory experimental results agrees favorably with field observations.

Experiments and Results

Undisturbed saturated loess samples were obtained at section km105 + 240 (**Figure 1C**), the pressure and deformation were monitored by pressure boxes and convergence meter at 100 m away from the flow failure location in km 105 + 410, as shown in (**Figure 1D**). This section describes its grain size distribution, uniaxial compressive strength, and creep test scheme.

Grain Size Distribution

The particle size distribution of Q_2 loess was obtained by a laser particle size analyzer, and the results are listed in **Table 1**. The Q_2 loess samples have relatively uniform particle sizes, consisting of 5.2–8.0% of sand content, 28.5–31.8% of clay content, and more than 60% of silt content. The clay content of the Q_2 loess is high and can be classified as silty clay.

Uniaxial Compressive Strength

The compressive strength is one of the essential mechanical properties of geomaterials, including the Q_2 loess. Additionally, it serves as a crucial reference for determining the step loads at various stages of the creep test. This study conducted uniaxial compression tests to obtain the unconfined compressive strength, σ_c, of saturated Q_2 loess samples, as presented in **Table 2**. The results show that the values of σ_c range between 0.5 and 0.6 MPa, and the strength decreases sharply with increasing water content.

Creep Test and Results

Loess is a complex porous geomaterial with a unique sensibility to water. The influence of pore water on its mechanical properties, such as deformation, strength, and constitutive behavior, has

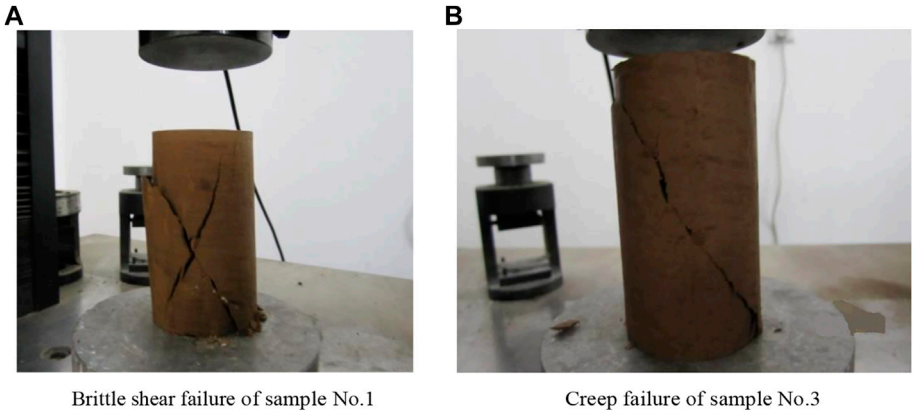

FIGURE 3 | Failure patterns of saturated Q_2 loess during creep. **(A)** Brittle shear failure of sample No.1. **(B)** Creep failure of sample No.3.

TABLE 3 | Failure stress of creep.

Specimen number	Water content/%	σ_c/MPa	Failure stress value/MPa	Percentage of σ_c/%
1	22.61	0.57	0.45	78.9
3	23.21	0.52	0.40	76.9

always been at the center of the study (Xie and Qi, 1999). Both the stress and deformation of loess are closely related to time (Huang, 1983; Qian and Yin, 1996). Time effect (rheological property) and water are the two most important factors affecting the mechanical properties of loess. In China, previous efforts mainly focused on the rheological behavior of loess. For instance, Chen et al. (1989) uncovered the quadratic time effect and proposed a rheological constitutive equation and the sheet structure theory for clay. Zhao et al. (2011) proposed a rheological model considering instantaneous plastic deformation based on results obtained through triaxial creep testing of undisturbed loess samples from Xi'an, China. Wang and Luo. (2009) analyzed the effects of deviatoric stress level, moisture content, and dry density on the creep characteristics of loess through the triaxial creep test. Pang. (2017) studied the rheological constitutive model of compacted loess under different levels of dynamic compaction based on the creep test. Shan et al. (2021) proposed the loading and unloading stress history has a cumulative effect on the creep deformation of loess.

Engineering practice has demonstrated that the results of the uniaxial creep test can meet the requirements of design and construction (Zhou, 1990). Therefore, this study adopted the uniaxial creep test to analyze the creep properties of saturated Q_2 loess. Specifically, a CSS-44100 electronic universal testing machine with a closed-circuit control system was used. It is capable of applying a load ranging from 400 N to 100 kN with an error of less than 0.1%. Six to seven testing specimens of 5 cm in diameter and 10 cm in height were prepared for each of the two groups of undisturbed saturated Q_2 loess samples.

The step loading protocol was adopted for the creep test. Specifically, six to seven gradually increasing loading steps were applied on the same specimen, with the maximum load controlled at 75% σ_c (Refer to **Table 2**). Uniform loading was adopted to reach the first load level in 600 s. Each loading step was terminated when the displacement increment (or the maximum value when the loading time reaches 24 h) was less than 0.001 mm/h. The stress and strain data was obtained every 30 s and 200 s in the loading stage and stable stage after loading. **Figure 2** depicts representative deformation vs. time data from the creep tests of saturated Q_2 loess samples.

The following observations can be made for saturated Q_2 loess from **Figure 2**:

a) A large instantaneous deformation occurs when the saturated Q_2 loess specimen is subjected to a step load, accounting for more than 50% of the total deformation of each loading stage. However, with the increase in load, the proportion of the instantaneous deformation out of the total gradually decreases. The deformation accumulates with time at decreasing rates until it plateaus. This pattern can be classified as the attenuated or damped rheological stage or initial rheological stage.
b) Following the initial rheological stage, there is a segment where the deformation accumulates at a constant rate for all stages of loading except for the last one. The rate at which the deformation occurs, or the creep rate, in this segment is almost constant under the same level of load, is very close even under different levels of load. This pattern can be categorized into the constant rheological stage or the steady rheological stage.
c) When the stress level is high (e.g., the last load step), if the deformation increases sharply, the specimen usually undergoes quick failure, i.e., entering into accelerated creep stage without the constant rheological stage. It often takes a

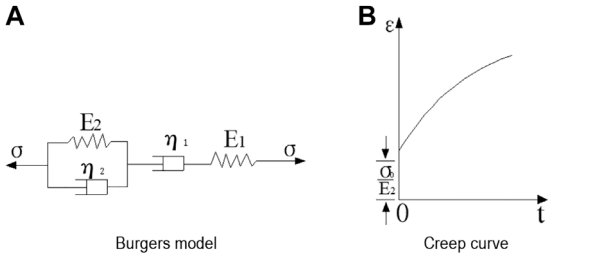

FIGURE 4 | Burgers model. **(A)** Burgers model. **(B)** Creep curve.

very short time from accelerated deformation to specimen collapse. As illustrated in **Figure 3**, one can see that cracks appear outside the specimen and rapidly expand throughout the entire specimen, forming an inclined slip surface. Therefore, the creep failure under uniaxial compression load is essentially a shear failure accompanied by noticeable lateral bulging. For sample No.1, the accelerated creep trend appeared at load step six, but failure did not occur within the loading time of this stage. It is presumed that creep failure would occur if the loading time is sufficient. When the load exceeds 0.45 MPa, brittle shear failure occurred instantly on sample No. 1 (**Figure 3A**). For sample No.3, the accelerated creep occurred at the load step six (i.e., 0.40 MPa), and creep failure occurred 2 hours after the loading was applied.

d) Theoretically, the stress corresponding to the asymptotic line at t = ∞ is its long-term strength. According to the deformation vs. time curves in **Figure 2**, the long-term strength values of specimens No. 1 and No. 3 are 0.45 MPa and 0.40 MPa, respectively. It can be seen from that the failure stress of saturated Q_2 loess is generally about 75%–80% of its uniaxial compressive strength. In engineering application, it is suggested to take 75% of the uniaxial compressive strength as the long-term strength of saturated Q_2 loess.

DISCUSSION

Rheological constitutive models and appropriate parameters based on experimental data are essential for gaining an in-depth understanding of the creep behavior of geomaterials. Representative rheological models include those consisting of a combination of elements such as springs and dashpots, empirical models, integral models, damage-based models, and models based on classic elastic-viscoplastic potential theory (Xia and Sun, 1996; Zheng et al., 1997; Wang et al., 2004). Among these models, the element model is simple to construct, has clear physical meanings, and can comprehensively reflect various rheological properties of geomaterials such as creep and stress relaxation, and is selected for modeling the creep behavior of saturated Q_2 loess. Typical element models include the Burgers model, the Maxwell model, the Generalized Maxwell model, the Kelvin model, the Kelvin-Voigt model, the Bingham model, the Poynting-Thomson model, the Nishihara model, etc. **Table 3**.

The creep test data in **Figure 2** demonstrate that saturated Q_2 loess exhibits obvious three-stage creep characteristics. Based on the observed deformation vs. time behavior and the features of various element models, it is found that the Burgers model can better describe the creep characteristics of saturated Q_2 loess (**Figure 4**).

The creep equation of the Burgers model is:

$$\varepsilon = \frac{\sigma_0}{E_1} + \frac{\sigma_0 t}{\eta_1} + \frac{\sigma_0}{E_2}\left[1 - \exp\left(-\frac{E_2}{\eta_2}t\right)\right] \quad (1)$$

Where E_1, E_2 are elastic modulus; η_1, η_2 are viscosity coefficients; σ_0 is the step load.

TABLE 4 | Creep parameters of saturated Q_2 loess sample No. 1

Load step	Stress/MPa	$E_1/10^7$Pa	$E_2/10^8$Pa	$\eta_1/10^{13}$ Pa·s	$\eta_2/10^{10}$ Pa·s
1	0.15	5.73	0.33	1.78	1.29
2	0.20	1.97	2.90	3.31	6.99
3	0.25	1.78	3.38	3.35	7.66
4	0.30	1.48	3.51	9.29	41.39
5	0.35	1.40	3.68	5.45	41.80
6	0.40	1.32	4.04	4.23	46.01
7	0.45	0.92	4.52	0.005	60.56

TABLE 5 | Creep parameters of saturated Q_2 loess sample No. 3

Load step	Stress/MPa	$E_1/10^7$Pa	$E_2/10^8$Pa	$\eta_1/10^{13}$ Pa·s	$\eta_2/10^{10}$ Pa·s
1	0.15	5.08	0.27	2.37	0.66
2	0.20	1.69	2.16	3.12	9.11
3	0.25	1.53	2.17	3.87	9.67
4	0.30	1.34	2.40	4.31	12.53
5	0.35	1.24	2.83	2.76	18.77
6	0.40	1.12	3.36	0.11	65.68

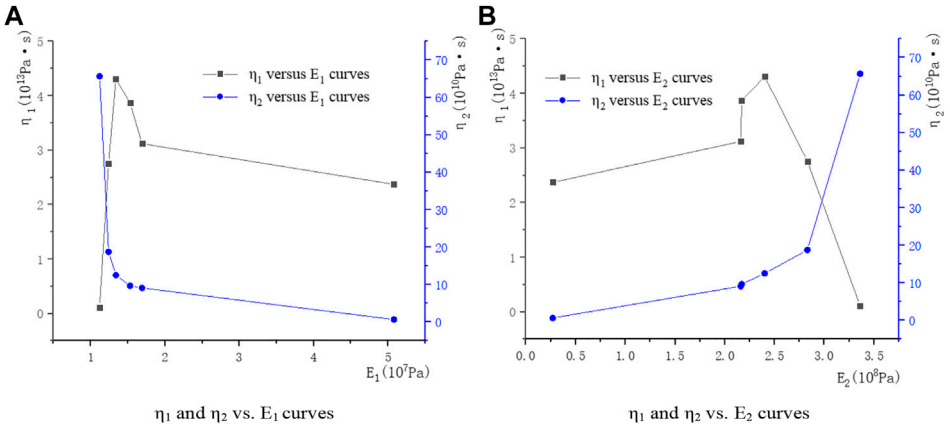

FIGURE 5 | η_1 and η_2 versus E_1 and E_2 curves. **(A)** η_1 and η_2 vs. E_1 curves. **(B)** η_1 and η_2 vs. E_2 curves.

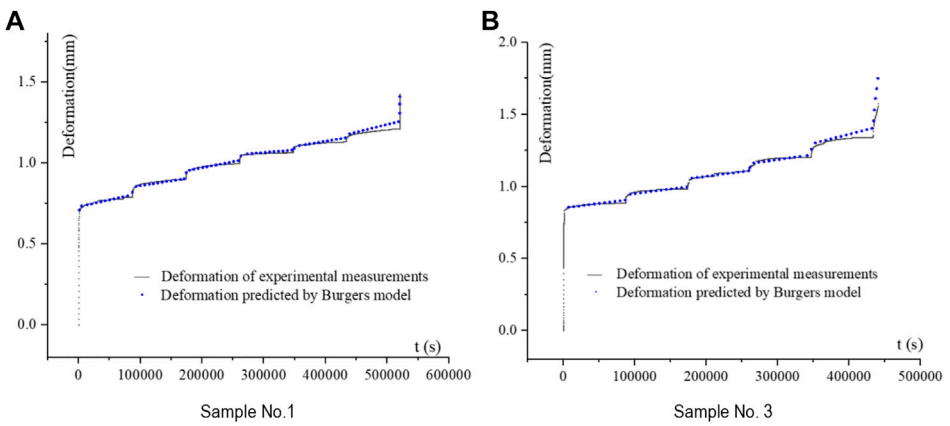

FIGURE 6 | Simulated deformation vs. time relationship using the Burgers Model. **(A)** Sample No. 1. **(B)** Sample No. 3.

Because of the complex constitutive equation of the creep model, it is difficult to obtain the model parameters directly according to the test results. Yang et al. (2004) provided a method to obtain creep model parameters based on the axial strain, instantaneous elastic strain, and other parameters. Since the instantaneous elastic strain is often not available in practical applications, the least square fitting method is generally used to determine the parameters in the element model. However, the least square method usually requires the selection of initial parameter values, and improper initial parameter values can easily lead to divergence during iteration. Marquardt damped least-squares method is an extremely powerful tool for the iterative solution of nonlinear problems. In this study, the modified Marquardt method was used to determine the rheological parameters based on the experimental data, and the results are listed in **Tables 4**, **5**.

The results in **Tables 4**, **5** show that the values of elastic modulus and viscosity coefficient range in 10–70 MPa and 1.0×10^9–9.0×10^{13} Pa·s, respectively. The two main indexes reflecting the creep characteristics are far lower than those of hard rock, i.e., 50–100 GPa and 1.0×10^{16}–1.0×10^{17} Pa·s, indicating that saturated Q_2 loess has a more prominent creep tendency. It can be seen from **Tables 4**, **5** that, as the loading stress rises, E_1 decreases but E_2 increases. Meanwhile, η_1 grows first, reaches a maximum, then falls as the stress level increases. However, η_2 consistently increases with the rise in the stress level and surges when creep failure occurs. The viscosity coefficients reflect the increase in the viscosity of saturated loess specimen as the stress rises. The results indicate that the creep property of saturated Q_2 loess becomes more and more evident with the increase in load, and saturated Q_2 loess is a nonlinear viscoelastic material.

Taking **Table 4** as an example, draw the curves of η_1 and η_2 vs E_1 and E_2. It can be seen from **Figure 5** that the relationship curves of η_1 and η_2 vs. E_1 and E_2 are almost symmetrical. η_1 first increases and then decreases with the increase in E_1 and E_2; η_2 decreases with the rise in E_1 and increases with the increase in E_2.

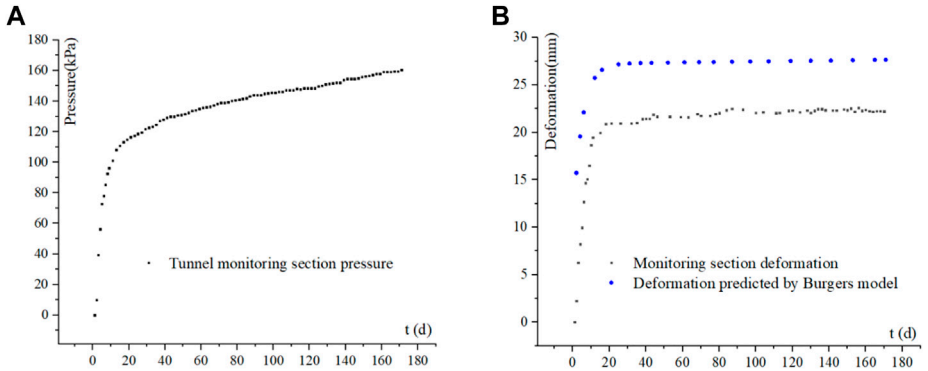

FIGURE 7 | Monitored pressure and strain vs. time. **(A)** Monitored Pressure results vs. time. **(B)** Monitored strain results and simulated strain results by the Burgers model.

Comparison of Model-Simulated and Experimental Creep Curves of Saturated Q_2 Loess

To verify the applicability of the Burgers model of saturated Q_2 loess, the creep parameters of saturated loess (obtained from **Table 4** and **Table 5**) were substituted into the Burgers model to calculate and obtain the simulated creep curve. Comparing the simulated curve with the experimental one in **Figure 6**, it is found that the Burgers model can be used to simulate the experimental data. The model-simulated and the experimental curves almost coincide under the first four loadings. When the load continues to increase, the model-simulated curve is slightly higher than the experimental one, indicating that the trend of the model-simulated accelerated stage is more obvious at the last two loading levels.

It can be seen from the comparison between the theoretical simulation curve and the experimental curve that the four-parameter Burgers model can well simulate the rheological curve of saturated Q_2 loess, and the model parameters can be used for the elastic-viscoplastic analysis of saturated Q_2 loess.

Application of Burgers Model to project(Case Study)

Tunnel No. 15 of the Tao River Diversion Project adopts two-way excavation. The tunnel is surrounded by saturated soft and plastic Q_2 loess with an average water content of more than 28%. When one side of the tunnel was excavated to km105 + 410, the palm surface moved outward, and the arch frame sank and collapsed. On the 10th day, flow failure suddenly occurred. Saturated loess slid nearly 30 m from the palm surface within a few minutes, resembling toothpaste being squeezed out from a tube. After about 3 hours, the flow failure in the tunnel was stable. And 4 hours later, the tunnel roof at about 30 m above the tunnel base collapsed.

On the other side of the tunnel, the pressure and deformation at 100 m away from the flow failure location in km 105 + 410 section were monitored by pressure boxes and convergence meter, as shown in **Figure 1D**. The pressure boxes and the convergence meter are synchronously arranged, and the monitoring time of both is 170 d. From the pressure monitoring curve (**Figure 7A**), it can be seen that an inflection point appeared on the surrounding rock pressure of the tunnel at 110 kPa after about 10 days and then the pressure rose slowly, reaching the maximum of 160 kPa during the monitoring period. Meanwhile, an inflection point also occurred on the deformation of baselines 1-3 of the monitoring section as shown in **Figure 7B** at 18.649 mm on the 10th day, with the maximum reaching 22.6 mm during the monitoring period.

According to the results of pressure and deformation monitoring, combined with the creep test load gradient, select Burgers model creep parameters at 150 kpa as the simulation parameters of the monitoring section. The indoor creep test accelerated the stress loading process, and the completion time of samples No.1 and No.3 under the first stage load was 600 s. Using the equivalent time method, the actual observed stress inflection point time (10 d) is equivalent to the first stage loading completion time (600 s) in the laboratory, and the residual stress monitoring 160 d is equivalent to the stable loading time after the first stage loading. Under the equivalent time, according to Burgers model and combined with the tunnel diameter, the surrounding rock deformation of the tunnel is simulated. Also, the trend of the simulation deformation results are in good agreement with that of the monitored, with the simulated deformation being about 5 mm larger. The discrepancy can be attributed to the following reasons: 1) the selected Burgers model creep parameters are the creep parameters obtained at 150 kPa, but the *in-situ* pressure is 110–160 kPa; and 2) the tunnel surrounding rock is supported after excavation, hence reducing the actual deformation.

CONCLUSION

The uniaxial compressive strength of saturated Q_2 loess is about 0.5–0.6 MPa, and decreases sharply with the increase in moisture

content. Creep testing results of saturated Q_2 loess show that the proportion of instantaneous deformation at each loading stage decreases with the increase in loading level, and its rheological curve consists of three typical phases, including the initial, steady, and accelerated creep stages.

The creep failure of saturated Q_2 loess belongs to shear failure. Specimen failure is often accompanied by obvious lateral bulging. The failure stress of saturated Q_2 loess is generally about 75–80% of uniaxial compressive strength. In engineering applications, it is suggested to take 75% of uniaxial compressive strength as the long-term strength of saturated Q_2 loess.

The elastic modulus and viscosity coefficient of saturated Q_2 loess are far lower than those of hard rock, revealing its more prominent creep tendency obvious. The parameters obtained for the Burgers model can be used for rheological numerical analysis of saturated Q_2 loess.

It can be seen from the case study and comparison between the theoretical simulation curve and the experimental curve that the four-parameter Burgers model is suitable for saturated Q_2 loess, which can well simulate the rheological curve of saturated Q_2 loess, and the model parameters can be used for the elastic-viscoplastic analysis of saturated Q_2 loess.

The experimental results shed light on the creep characteristics of saturated Q_2 loess. However, in practice, rheological failures often occur several years or even decades after constructing the projects. In addition, uniaxial creep tests were conducted with relatively short durations due to test equipment limitations. Therefore, the creep parameters obtained need further experimental and numerical verification.

DATA AVAILABILITY STATEMENT

The original contributions presented in the study are included in the article/Supplementary Material, further inquiries can be directed to the corresponding author.

AUTHOR CONTRIBUTIONS

XL drafted the manuscript. XZ finished the comparison of model-simulated and experimental creep curves of saturated Q_2 loess. XF prepared the data analysis. TY and ZS prepared the data collection. All authors have read and approved the final manuscript.

FUNDING

The Fundamental Research Funds for the Central Universities of Lanzhou University: Experimental Study on flow sliding failure mechanism of saturated loess (Number: lzujbky-2014-3).

ACKNOWLEDGMENTS

The first author would like to express warm gratitude to the Fundamental Research Funds for the Central Universities of Lanzhou University. We thank Professor Wenwu Chen for his helpful suggestions and Dr. Pengbo Yuan for his experimental help. The authors would also like to thank the reviewers for reviewing the draft version of the manuscript.

REFERENCES

An, Z., Wang, S., Wu, X., Chen, M., Sun, D., and Liu, X. (1998). Aeolian Evidence on the Loess Plateau of China: the Beginning of the Great Ice Age in the Northern Hemisphere in the Late Cenozoic and the Uplift Drive of the Tibetan Plateau. *Sci. China (D)* 28 (6), 481–489.

Chen, H., Jiang, Y., Niu, C., Leng, G., and Tian, G. (2019). Dynamic Characteristics of Saturated Loess under Different Confining Pressures: a Microscopic Analysis. *Bull. Eng. Geol. Environ.* 78 (2), 931–944. doi:10.1007/s10064-017-1101-9

Chen, Z., Shi, Z., Yu, Z., Wu, X., and Jin, J. (1989). Measurement of Expansion, Creep and Relaxation of Brittle Rocks by 8000KN Multifunctional Triaxial Apparatus. *J. Rock Mech. Eng.* 8 (2), 97–118.

Dijkstra, T. A., Rogers, C. D. F., Smalley, I. J., Derbyshire, E., Li, Y. J., and Meng, X. M. (1994). The Loess of north-central China: Geotechnical Properties and Their Relation to Slope Stability. *Eng. Geology.* 36, 153–171. doi:10.1016/0013-7952(94)90001-9

Fabre, G., and Pellet, F. (2006). Creep and Time-dependent Damage in Argillaceous Rocks. *Int. J. Rock Mech. Mining Sci.* 43 (6), 950–960. doi:10.1016/j.ijrmms.2006.02.004

Feng, L., and Zheng, Y. (1982). *Collapsible Loess in China*. Beijing: China Railway Publishing House.

Fu, Y., Gao, Z., Hong, Y., Li, T., and Garg, A. (2021). Destructuration of Saturated Natural Loess: From Experiments to Constitutive Modeling. *Int. J. Damage Mech.* 30 (4), 575–594. doi:10.1177/1056789520939300

Huang, W. (1983). *Engineering Properties of Soil*. Beijing: Water Resources and Electric Power Press.

Lei, X. (1987). Pore Types and Collapsibility of Loess in China. *Sci. China (B)* (12), 1309–1316.

Lin, H., Zhang, X., Cao, R., and Wen, Z. (2020). Improved Nonlinear Burgers Shear Creep Model Based on the Time-dependent Shear Strength for Rock. *Environ. Earth Sci.* 79, 149. doi:10.1007/s12665-020-8896-6

Liu, D. (1985). *Loess and Environment*. Beijing: Science Press.

Palmer, J. (2017). Creeping Earth Could Hold Secret to Deadly Landslides. *Nature* 548, 384–386. doi:10.1038/548384a

Pang, X. (2017). Rheological Constitutive Model of Compacted Loess Based on Creep Test. *J. Railway Sci. Eng.* 14 (06), 1206–1216. doi:10.19713/j.cnki.43-1423/u.2017.06.013

Peng, J., Fan, Z., Wu, D., Zhuang, J., Dai, F., Chen, W., et al. (2015). Heavy Rainfall Triggered Loess-Mudstone Landslide and Subsequent Debris Flow in Tianshui, China. *Eng. Geology.* 186, 79–90. doi:10.1016/j.enggeo.2014.08.015

Qian, J., and Yin, Z. (1996). *Geotechnical Principle and Calculation*. Beijing: China Water and Power Press.

Qiao, P., and Li, Z. (1990). *Engineering Geology in Loess Area*. Beijing: Water Resources and Electric Power Press.

Shan, S., Xie, W., Zhu, R., and Yang, H. (2021). Creep Characteristics of Compacted Loess in Yan'an New District under Loading and Unloading Conditions. *J. Arid Land Resour. Environ.* 35 (07), 144–155. doi:10.13448/j.cnki.jalre.2021.198

Sun, J. (2005). *Loess Ology (First Part)*. Hong Kong: Hong Kong Archaeology Society Press.

Tang, H., Duan, Z., Wang, D., and Dang, Q. (2019). Experimental Investigation of Creep Behavior of Loess under Different Moisture Contents. *Bull. Eng. Geol. Environ.* 79, 411–422. doi:10.1007/s10064-019-01545-8

Wang, G., Zhang, L., Zhang, Y., and Ding, G. (2014). Experimental Investigations of the Creep-Damage-Rupture Behaviour of Rock Salt. *Int. J. Rock Mech. Mining Sci.* 66 (1), 181–187. doi:10.1016/j.ijrmms.2013.12.013

Wang, S., and Luo, Y. (2009). Research on Creep Characteristics of Loess under Complex Stress. *Rock Soil Mech.* 30 (Suppl. 2), 43–47. doi:10.16285/j.rsm.2009.s2.098

Wang, S., Yang, Z., and Fu, B. (2004). *Century Achievements and New Historical mission of Rock Mechanics and Engineering in China*. Nanjing: Hohai University Press.

Wang, X., Wang, J., Zhan, H., Li, P., Qiu, H., and Hu, S. (2020). Moisture Content Effect on the Creep Behavior of Loess for the Catastrophic Baqiao Landslide. *Catena* 187, 104371. doi:10.1016/j.catena.2019.104371

Wang, X., Yin, Y., Wang, J., Lian, B., Qiu, H., and Gu, T. (2018). A Nonstationary Parameter Model for the sandstone Creep Tests. *Landslides* 15, 1377–1389. doi:10.1007/s10346-018-0961-9

Wang, Y. (1982). *Microstructure of Loess and its Changes in Geological Age and Region — Study under Scanning Electron Microscope Loess and Quaternary Geology*. Shaanxi People's Publishing House.

Wen, B.-P., and Jiang, X.-Z. (2017). Effect of Gravel Content on Creep Behavior of Clayey Soil at Residual State: Implication for its Role in Slow-Moving Landslides. *Landslides* 14, 559–576. doi:10.1007/s10346-016-0709-3

Xia, C., and Sun, J. (1996). Distinction of Rheological Model and Determination of Parameters on Creep Tests. *J. Tongji Univ.* 24 (5), 498–503.

Xia, C., Liu, Z., and Zhou, C. (2021). Burger's Bonded Model for Distinct Element Simulation of the Multi-Factor Full Creep Process of Soft Rock. *J. Mar. Sci. Eng.* 9, 945. doi:10.3390/jmse90909457

Xie, D., and Qi, J. (1999). Soil Structure Characteristics and New Approach in Research on its Quantitative Parameter. *Chin. J. Geotechnical Eng.* 21 (6), 651–656.

Xie, X., Qi, S., Zhao, F., and Wang, D. (2018). Creep Behavior and the Microstructural Evolution of Loess-like Soil from Xi'an Area, China. *Eng. Geology*. 236, 43–59. doi:10.1016/j.enggeo.2017.11.003

Xu, L., Coop, M. R., Zhang, M., and Wang, G. (2018). The Mechanics of a Saturated Silty Loess and Implications for Landslides. *Eng. Geology*. 236, 29–42. doi:10.1016/j.enggeo.2017.02.021

Yang, S., Zhang, J., and Huang, Q. (2004). Analysis of Creep Model of Jointed Rock. *Rock Soil Mech.* 25 (8), 1225–1228. doi:10.16285/j.rsm.2004.08.010

Ye, G.-l., Nishimura, T., and Zhang, F. (2015). Experimental Study on Shear and Creep Behaviour of green Tuff at High Temperatures. *Int. J. Rock Mech. Mining Sci.* 79, 19–28. doi:10.1016/j.ijrmms.2015.08.005

Zhang, Z., Zhang, Z., and Wang, Y. (1989). *Chinese Loess*. Beijing: Geological Publishing House.

Zhao, L., Ge, K., and Liu, E. (2011). *Study on the Rheological Properties of Loess Building Science* 21 (3), 69–73. doi:10.13614/j.cnki.11-1962/tu.2011.03.004

Zheng, Y. (1982). *Collapsibility of Loess in China*. Beijing: Geological Publishing House.

Zheng, Y., Zhou, C., and Xia, S. (1997). Discussion on Viscoelastic Continuous Damage Constitutive Model of Geotechnical Materials. *J. Hohai Univ.* 25 (2), 114–116.

Zhou, W. (1990). *Advanced Rock Mechanics*. Beijing: Water Resources and Electric Power Press.

Zhu, F., Duan, Z. Y., Wu, Z. Y., Wu, Y. Q., Li, T. L., and Cai, Y. D. (2013). Experimental Study on Direct Shear Creep Characteristics and Long-Term Strength of Red Layer Sliding Zone Soil in Southern Hunan. *Amr* 842, 782–787. doi:10.4028/www.scientific.net/amr.842.782

Conflict of Interest: The authors declare that the research was conducted in the absence of any commercial or financial relationships that could be construed as a potential conflict of interest.

Publisher's Note: All claims expressed in this article are solely those of the authors and do not necessarily represent those of their affiliated organizations, or those of the publisher, the editors and the reviewers. Any product that may be evaluated in this article, or claim that may be made by its manufacturer, is not guaranteed or endorsed by the publisher.

frontiers in Earth Science

ORIGINAL RESEARCH
published: 27 January 2022
doi: 10.3389/feart.2022.818508

Experimental Investigation on Failure Modes and Progressive Failure Process of Earthen Check Dam Triggered by Upstream Flow

Yanbo Zhu[1]*, *Futong Li*[1], *Fanfan Yang*[1], *Yuxuan Zhang*[1], *Wanghui Tian*[1] and *Hengxing Lan*[1,2]*

[1]College of Geological Engineering and Geomatics, Chang'an University, Xi'an, China, [2]Institute of Geographic Sciences and Natural Resources Research, CAS, Beijing, China

The progressive failure of earthen check dams triggered by upstream flow is common in loess gullies on the Loess Plateau of China. However, studies on the formation mechanism of progressive failure are still unclear. To investigate the failure modes and progressive failure process of earthen check dams, a physical model test on an earthen dam influenced by upstream flow was conducted by monitoring and analyzing hydrologic and mechanical parameters, including water content, pore water pressure, soil stress, and displacement. The test results indicate that the progressive failure process of earthen dams is induced by seepage water discharged on the downstream slope, including slope slide and overtopping. Continuous seepage results in the occurrence of creep at the toe, gradually driving the deformation and sliding of the dam slope. The progressive failure begins in the downstream slopes, and this study focuses on analyzing the initiation mechanism of slope slide. The slope failure presents retrogressive sliding, including four repeated slip failures, and each sliding presents a long-time progressive process. This physical model test reproduces the entire life cycle of earthen check dams and reveals the traction sliding mechanism of dams, which is consistent with field observation. The aforementioned results provide an important reference for understanding the failure mechanism of earthen check dams triggered by upstream flow.

Keywords: earthen check dam, loess, gully, seepage, sliding, overtopping, creep

OPEN ACCESS

Edited by:
Fanyu Zhang,
Lanzhou University, China

Reviewed by:
Wei Shen,
University of Bologna, Italy
Rafael Moran,
Polytechnic University of Madrid, Spain

***Correspondence:**
Yanbo Zhu
zhuyanbo@chd.edu.cn
Hengxing Lan
Lanhx@igsnrr.ac.cn

Specialty section:
This article was submitted to Geohazards and Georisks, a section of the journal Frontiers in Earth Science

Received: *19 November 2021*
Accepted: *05 January 2022*
Published: *27 January 2022*

Citation:
Zhu Y, Li F, Yang F, Zhang Y, Tian W and Lan H (2022) Experimental Investigation on Failure Modes and Progressive Failure Process of Earthen Check Dam Triggered by Upstream Flow. Front. Earth Sci. 10:818508. doi: 10.3389/feart.2022.818508

1 INTRODUCTION

The Chinese Loess Plateau is the most severely eroded area in the world (Hessel, 2006; Fu et al., 2017), and check dams are important and effective measures for erosion control in plateau catchments that experience torrents (Romero et al., 2012; Conesa and Lenzi, 2013; Zhao et al., 2017). Up to 2020, nearly 163,000 check dams have been built, mainly on tributary channels under the project "Gully Land Consolidation" (GLC) (Jin et al., 2019). However, because of low design standards, most check dams built without flood discharge facilities or spillways had relatively short lives as they rapidly filled with sediment or were breached by extreme flood events (Zhao et al., 2017; Fang et al., 2019). For example, 516 check dams in Yan'An city, China, were damaged by the "7.26" extreme rainstorm on July 26, 2017 (Yang et al., 2020). Therefore, understanding check dam failure is crucial for risk assessment and decision-making.

The failure modes of dams generally include overtopping, piping, and slope failure (Okeke and Wang, 2016; Rifai et al., 2017; Zhu et al., 2020; Kouzehgar et al., 2021). These modes are affected by many factors such as construction materials, geometry of the dam, upstream flow, and channel bed conditions (Gregoretti et al., 2010; Chen et al., 2015; Jiang et al., 2020a). Check dams on the Loess Plateau are most likely to be destroyed by inflow corresponding to extreme rainstorms (Yang et al., 2020). Approximately 53% of check dam accidents there are caused by permeability damage due to upstream inflow (Foster et al., 2000; Xu et al., 2019). Therefore, it is necessary to study the seepage failure modes of check dams.

The dam failure process is a complex interaction between water and sediment, involving hydraulics, soil mechanics, and sediment movement mechanics (Li et al., 2020). Most dams experienced a suite of quantitative and qualitative changes prior to failure (Wang et al., 2018). Seepage is usually observed during impounding (Jiang et al., 2020b), and seepage flow could cause a progressive variation of the internal structure of the dam, leading to dam failure (Dunning et al., 2006; Richard and Reddy, 2007; Wang et al., 2018). Many model tests (Gregoretti et al., 2010; Chen et al., 2015; Zhu et al., 2019), along with field observation (Xu et al., 2019; Zhang et al., 2019) and numerical simulation (Calamak et al., 2020; Marti et al., 2020), have been used to study the seepage failure progress and mechanism of dam-breaks worldwide. However, research studies on the progressive failure of check dams in the Loess Plateau are limited.

The progressive failure process of check dams caused by seepage failure on the plateau is complex due to the particularity of loess, the special structure of check dams, extreme rainfall, and unqualified construction and management (2014; Xu et al., 2019; Yang et al., 2020). Unfortunately, because most of the check dam controlled areas on the Loess Plateau contain no hydrometeorological stations (Li et al., 2016), the research on the failure of check dams is mainly through field investigation and remote sensing before and after the dam failure (Xu et al., 2019; Zhang et al., 2019). Furthermore, real-life dam failure events in the plateau have been poorly documented because there were few eyewitnesses or lack of field monitoring, so the details of progressive failure are unclear, for example, the hydraulic evolution and the erosion characteristics in progressive failure mode are still unknown (Wu et al., 2011). The aforementioned research on check dam failure, whether by field investigation or numerical simulation, must be verified by physical experiments to better understand the spectrum of failure processes and mechanisms (Zhang et al., 2019). The progressive failure mechanism of natural dams is mainly seepage and overtopping erosion (Cao et al., 2011), but the seepage and the induced instability of the downstream slope were less mentioned (Jiang et al., 2019), especially for the progressive slope failure mode of natural dams (Jiang et al., 2020a).

Therefore, in this study, we conducted a physical model test to study the failure process of earthen check dams triggered by upstream flow based on a scaled prototype. To achieve this objective, variations in water content, pore water pressure, soil stress, and displacement of the model dam were monitored during the experiment. Based on these data, we explored and analyzed the characteristics of the progressive failure process and the failure mechanism of earthen check dams. The results of this study provide valuable insights into the failure process of earthen check dams and thus are useful for preventing future failures.

2 MATERIALS AND METHODS

2.1 Dam Break Event

The study area is located in a small watershed called Xingshuyaozi in Yan'An city, Shaanxi Province. Earthen check dam #19 that failed due to seepage in this watershed, as shown in **Figure 1**, was chosen as the experimental prototype in the present model test. The natural dam crest width and the height of check dam #19 are 3.8 and 6.0 m, respectively. The length of the dam was about 37 m, with upstream and downstream slopes of 50° and 45°, respectively. A small reservoir with a depth of 5 m formed at the back of the dam from upstream runoff because the check dam had no spillway or other drainage capabilities. This natural dam was built in the winter of 2017 under the "Gully Land Consolidation" project, and it broke on April 30, 2018, due to seepage. Notably, the failure of the downstream slope is a progressive process accompanied by four sliding events, which were observed by cameras (**Figure 2**). The continuous seepage resulted in the first sliding of the dam on April 30, 2018 (**Figure 2A**). With continuous creep of the dam, the second, third, and fourth failures of the dam occurred on June 30, July 29, and August 13, 2018, respectively (**Figures 2B–D**). Finally, the overtopping occurred due to the four successive slides (**Figure 2E**). Each dam breach event is a slow creep process.

2.2 Model Design and Model Materials

To study the mechanism of progressive failure of natural check dams, we designed a physical model test based on a prototype dam. According to earthen check dam design data, the size of the chamber, and topographic features of the dam site, the geometric proportion of this experiment was determined to be 1:10. Based on geometrical similarity, the height and crest width of the earthen check dam model were set at 0.6 and 0.38 m, respectively. The upstream and downstream slopes of the model dam were set at 50° and 45°, respectively, the same as the prototype dam. In order to simulate the hydrologic conditions of the prototype dam as much as possible in the model test, we set the height of water storage behind the model dam at 0.5 m, referring to the ratio of water storage height on-site to the prototype dam height. The model material is consistent with the natural dam material, which is homogeneous compacted loess. The grain size distribution curve of the dam material is shown in **Figure 3**, indicating that the dam material consists of clay (particle diameter less than 0.005 mm), silt (particle diameter between 0.005 and 0.075 mm), and sand (particle diameter greater than 0.075 mm), with contents of 29.62, 69.01, and 1.37%, respectively. According to the particle size distribution test, the median diameters d_{50}, the coefficient of non-uniformity, and the coefficient of curvature of the soil material are 0.025 mm, 12.71, and 1.83, respectively. The physical parameters of the

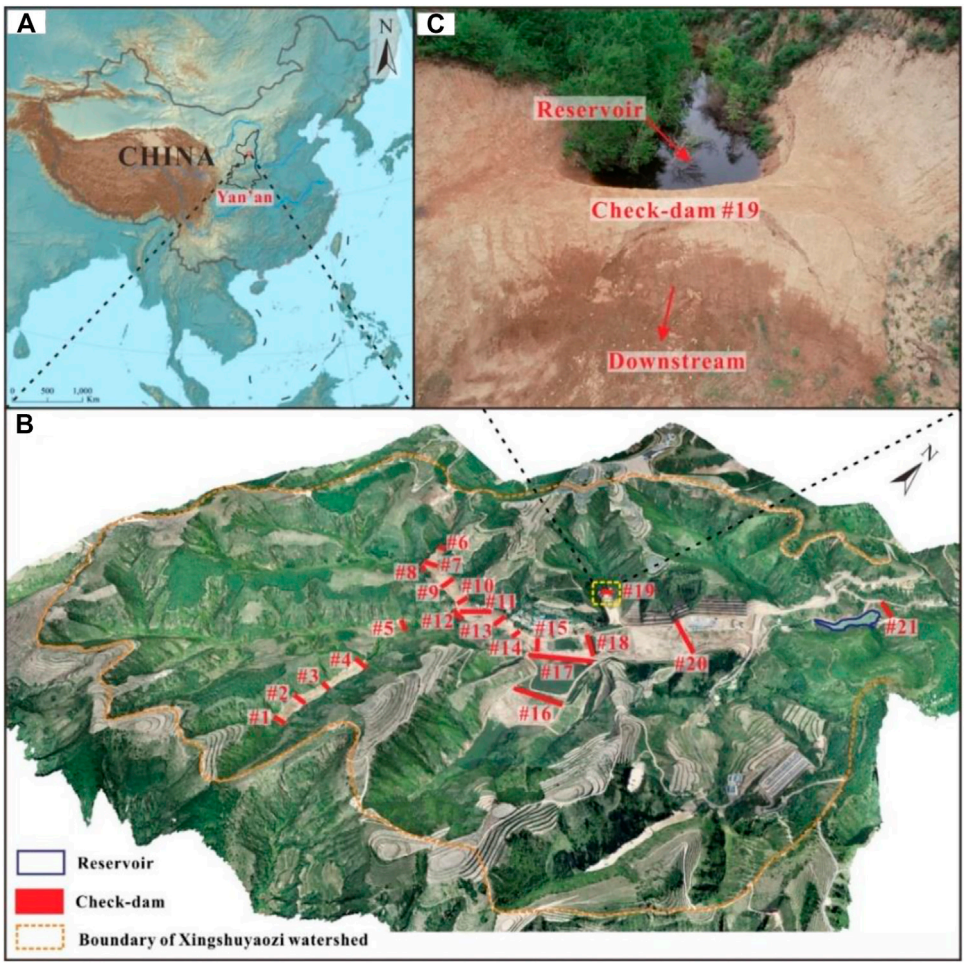

FIGURE 1 | Location of research area and studying check dam. **(A)** Research location, **(B)** remote sensing image of research watershed based on UAV, and **(C)** research check dam.

material are obtained at 29.29% of the liquid limit and 16.46% of the plastic limit. The compaction density of the test model is consistent with the dry density of the natural check dam body, which is 1.51 g/cm^3. The initial moisture content of the compacted model material is configured at 15%. Under this moisture content, the strength parameters of the model material such as cohesion and friction angle are 22.52 kPa and 24.03°, respectively; and the permeability coefficient is 1.46 × 10^{-4} cm/s.

2.3 Experimental Apparatus and Procedures

The physical model test was carried out by a specially designed chamber in the Geological Hazard Simulation Laboratory at Chang'an University (**Figure 4A**). The chamber was 3.6 m in length, 1.2 m in width, and 1.35 m in height. The gradient of the bottom of the model chamber made of welded steel was zero. On clear reinforced glass installed on both sides of the model chamber, 5 × 5-cm grids were drawn to assist in the observation of the phreatic line and dam deformation. The back and bottom of the model chamber were sealed with a steel disc, while the top and front sides remained open. Therefore, the bottom, left, and right sides of the model container formed impermeable boundaries. We located a storage tank with a length of 0.6 m, a width of 1.2 m, and a depth of 1.35 m at the head of the chamber. Water can be poured into it, and we can read the level of water from a liquid level indicator installed on the side of the tank. The collection pool, with a length of 1.4 m, a width of 1.2 m, and a depth of 1.0 m, was positioned at the toe of the model chamber to store water and mud exiting from upstream.

First, we drew an outline of the model dam on the glass of the chamber according to its proposed shape and size. Then, we applied a density-controlled method to build the model dam. To ensure structural homogeneity, six layers of soil, each with a thickness of 10 cm, were compacted into the model container. Prior to packing, the soil samples were successively tedded, crushed, broken, and sieved through 2-mm sieves. The sieved soil samples were subsequently spread evenly in the model

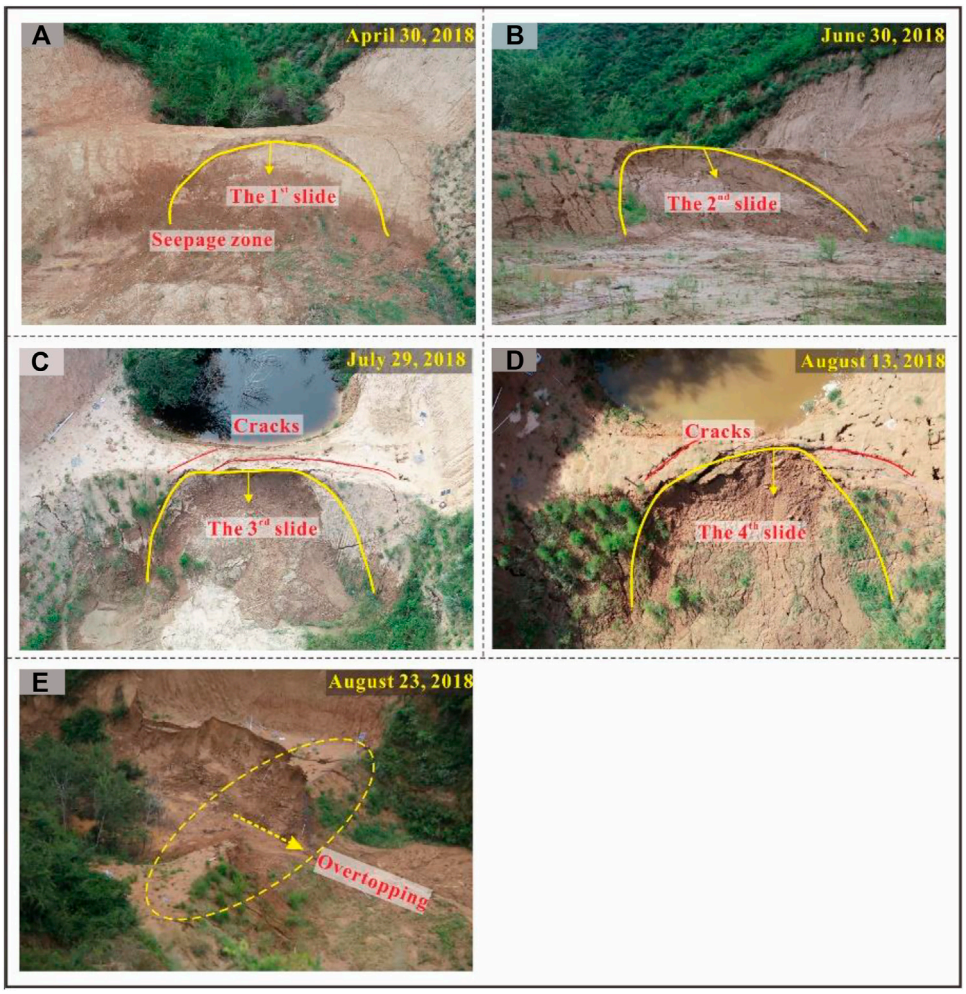

FIGURE 2 | Progressive failure process of prototype dam. **(A)** First slide, **(B)** second slide, **(C)** third slide, **(D)** fourth slide, and **(E)** overtopping.

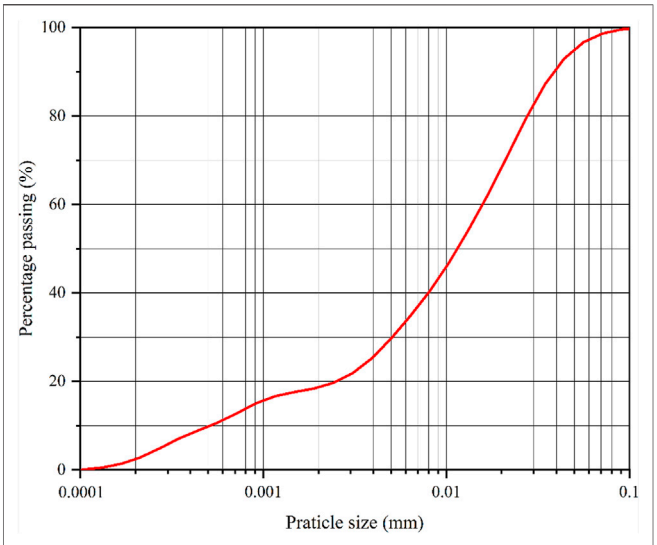

FIGURE 3 | Particle size distribution of dam material.

container and compacted with a dry density of 1.50 g/cm^3 and a water content of 15%. After finishing each layer, the interfaces between each layer were roughed to minimize the boundary influence on the experimental results. It should be noted that a 10-cm-thick cushion with a water content of 15% and a density of 2.0 g/cm^3 was laid at the bottom of the model container to avoid the generation of concentrated seepage at the contact between the metal plate and the model dam. After construction, the dam model (**Figure 4A**) was allowed to stand for 72 h. During the experiment, water can be discharged quickly from the water tank to simulate the upstream flow, and a small reservoir forms at the rear of the model dam. In addition, the valve behind the storage tank can be adjusted to keep the water level at the rear of the dam constant during testing.

2.4 Measurements

We monitored various hydrologic and mechanical parameters, including water content, pore water pressure, soil stress, and displacement of the model dam. Ten monitoring points were

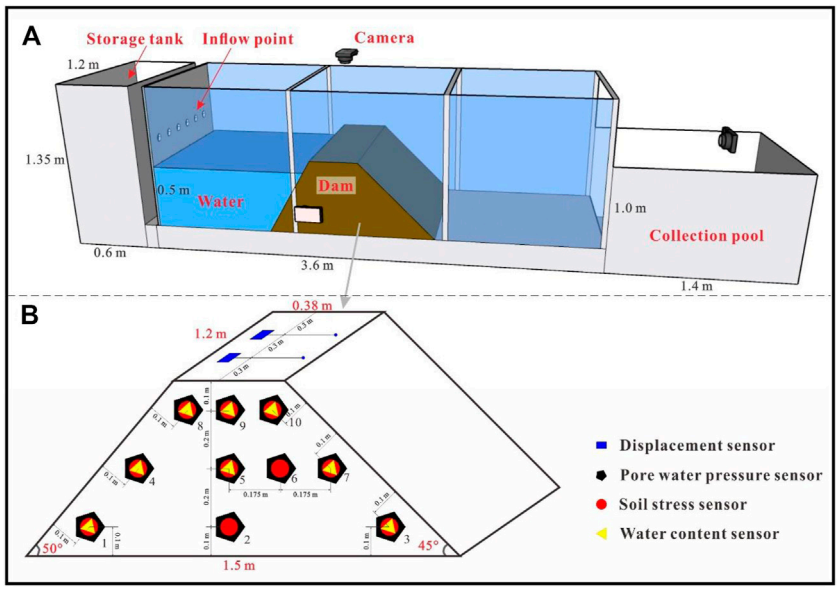

FIGURE 4 | Schematic diagram of the experimental setup. **(A)** Developed model test chamber and **(B)** sensors layout in the test model.

arranged fully inside the model dam, and all but two displacement sensors were located on the central axis of the dam; the locations of the sensors are shown in **Figure 4B**. Each monitoring point contained one pore water pressure sensor (ATJ-6007, with a measurement range of 0–20 kPa, accuracy = ±0.5%), one soil stress sensor (ATJ-7002, with a measurement range of 0–200 kPa, accuracy = ±0.5%), and one water content sensor (EC-5, with a measurement range of 0–100%, accuracy = ±0.25%). Besides, there were two displacement sensors (MPS-S-2000MM-V1, with a measurement range of 0–2000 mm, accuracy = ±0.1%) at the crest of the model dam, which monitored the generation and evolution of crevices at the dam crest. All sensors have factory calibrations that give us the needed conversion formulas. Sensors automatically send pore water pressure, soil stress, water content, and displacement through an iDAQ-1800 dynamic data acquisition instrument. The data acquisition rate was five per second. All of the sensors connected to the corresponding data acquisition instruments were calibrated before the test. To capture the deformation evolution of the check dam, three digital video cameras collected side, front, and vertical views, as shown in **Figure 4A**. Based on the images of the dam morphology change, the deformation strain field of the model dam can be analyzed by the image processing technique DIC (He et al., 2020).

3 RESULTS

3.1 General Features

The failure progress of the test model lasted 258.2 h from seepage to dam breach. Three significant features of the progressive failure were observed: seepage on the downstream slope, sliding of the downstream slope, and overtopping (**Figure 5**). The seepage stage lasted 24 h. The slope sliding stage began at the 24 h mark and lasted 232 h until the final overtopping at 256 h. **Figure 5A** shows that in the seepage stage, water was driven by hydrodynamic force under the upstream slope, causing the soil there to reach the saturation point. At this point, the toe of the downstream slope begins to creep, generating tension cracks in the middle part of the downstream slope extending to both sides (**Figure 5B**). Crack formation announces the arrival of the sliding stage, also a complex progressive process. **Figure 5B** depicts views of four different sliding events, which lasted 21, 35, 70, and 106 h, respectively. Note that the volume of each slide gradually increases and shows an obvious retrogressive tendency, that is, the slope progressively fails from toe to crest. After the multiple sliding of the downstream slope, the height of the dam decreases, and water behind quickly overflows the crest, forming a breach and rapidly destroying the dam (**Figure 5C**).

3.2 Characteristics of Progressive Failure

The progressive failure process of the model dam is comprehensively reflected by the morphological changes of the dam slope and the variations monitored by the sensors in the dam body. The detailed progressive characteristics of each stage are analyzed in the following section.

3.2.1 Characteristics of Seepage Flow

Figure 6A plots the evolution line of capillary flows inside the dam at different moments obtained by the camera. The capillary flow line started upstream and gradually moved downstream in a vertical shape. The basic water level, along with the trapezoidal dam shape and significant capillarity of compacted loess, induced the aforementioned features of the capillary flow evolution. Note that the capillary flow line in the dam crest is distributed above the static water level because of the strong capillarity of

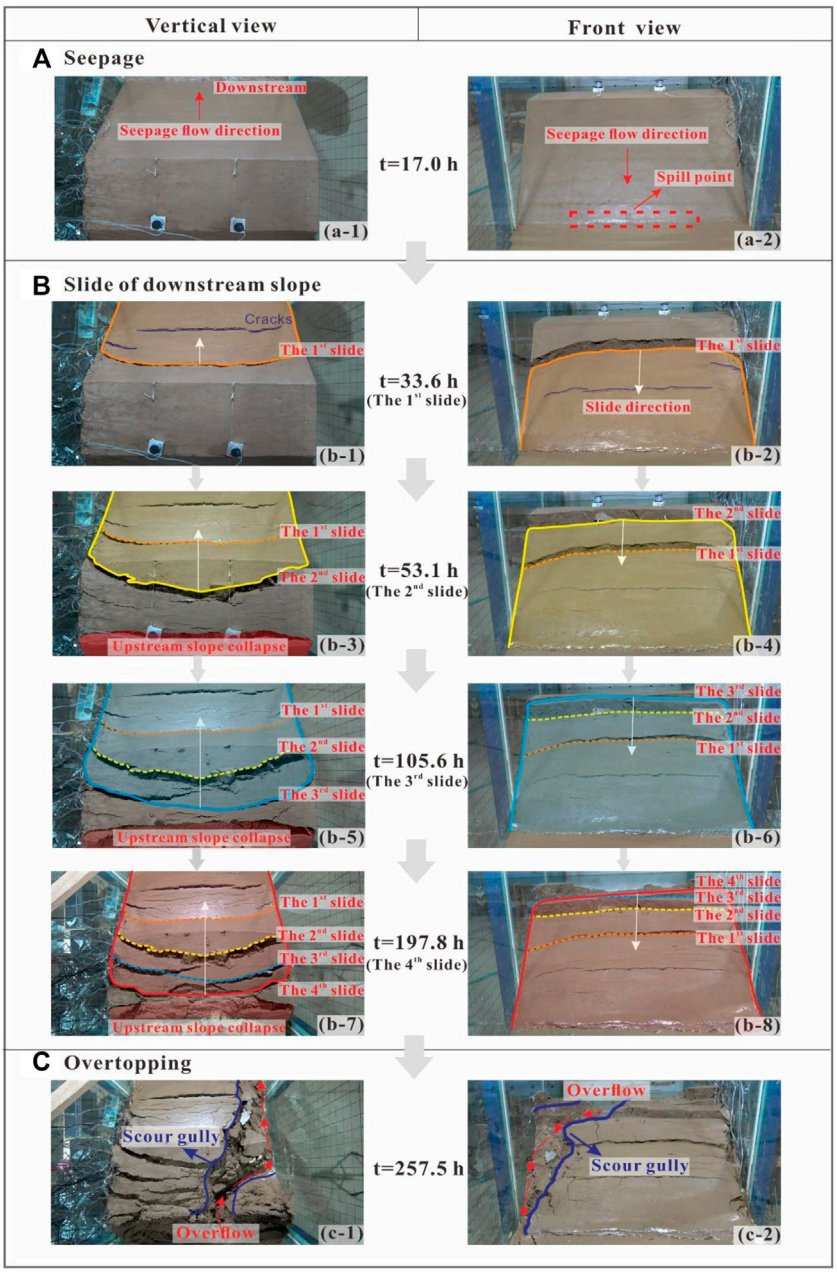

FIGURE 5 | Progressive failure process of model dam by vertical view and front view. **(A)** Seepage, **(B)** slide of downstream slope, and **(C)** overtopping.

compacted loess (see area affected by capillarity in **Figure 6A**). With the development of the phreatic line, the spill point of the seepage gradually moved upward toward the dam crest, causing the soil below the spill point to become saturated and softened, resulting in the reduction of its strength. Then, the seepage flow leads to the creep deformation of the downstream slope. The strain field during seepage processed by DIC is shown in **Figure 6B**, which indicates that the displacement, which is reflected by the concentrated strain at the toe, gradually moved upstream. This continuous creep at the toe of the dam contributed to the instability of the downstream slope.

The responses of water content, pore water pressure, and soil stress can better reveal the seepage process described earlier (**Figure 7**). **Figure 7A** shows the variation of water content response to seepage with a range of 15–45%. Notably, three variations of water content behavior are evident: 1) The water content increases to the maximum value in a short period of time after the capillary line reaches the monitoring sensors and then remains constant (e.g., W-1 and W-4); 2) the water content gradually increases to the maximum value and then remains constant (e.g., W-9 and W-10); and 3) the variation of the water content shows a hysteresis reflection with different sensors. This

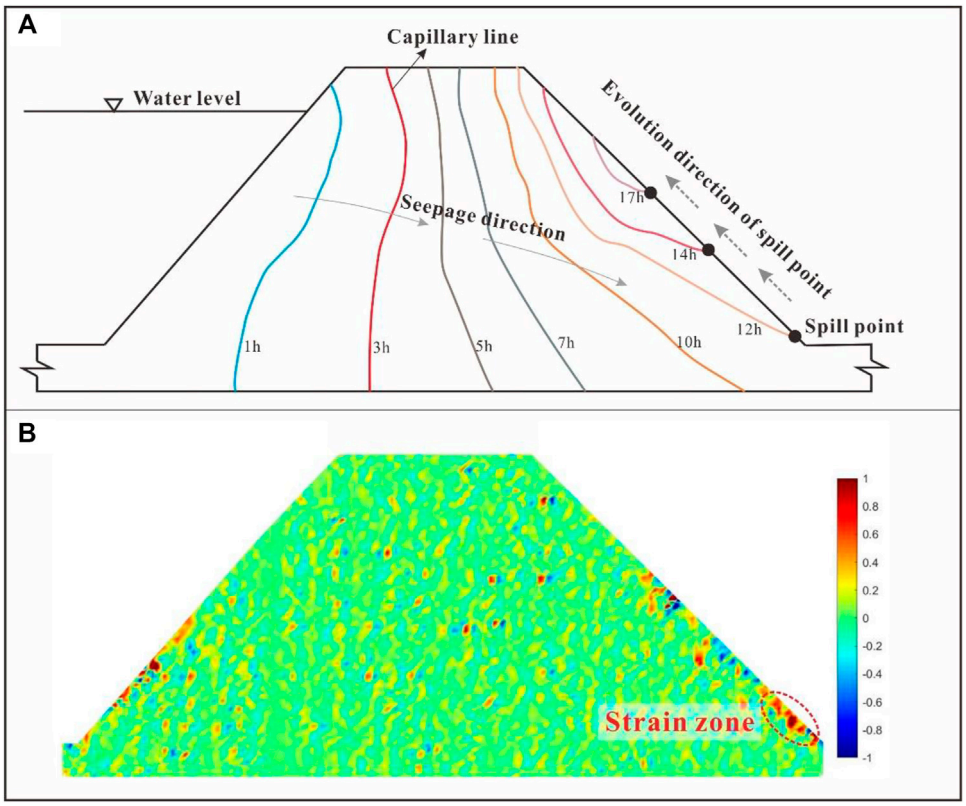

FIGURE 6 | Evolution of the capillary line inside the dam. **(A)** Positions of the capillary line at different times during seepage process and **(B)** strain field of model dam during seepage from side view by DIC.

hysteresis reflection of water content relates to the distance between the moisture sensor and the water storage behind the dam. It is precisely because of the different sensor positions that a lag in content water evolution was observed. According to **Figure 7A**, the water content response sequence was, in turn, upstream sensors (W-1, W-4, and W-8), then middle (W-5 and W-9), and downstream sensors (W-3, W-7, and W-10). This hysteresis reflection of water content corresponds to the evolution process of the seepage flow (see **Figure 6A** and **Figure 7A**).

Figure 7B illustrates the variation of pore water pressure with time during seepage. Obviously, the pore water pressure is a time-dependent value with a range of 0.1–4.9 kPa. Once the seepage reaches the sensor position, the pore water pressure increases rapidly. For example, the pore water pressure at P-1 has the largest value of 4.9 kPa because the P-1 sensor is closest to the reservoir and at the lowest position. Notably, as the seepage channel completely formed at the bottom of the dam, the pore water pressure dissipated. For example, the pore water pressure at position P-3 dropped to 0.40 kPa. The pore water pressure is also a position-dependent value. Compared to sensors inside the upstream dam, the pore water pressure of sensors inside the downstream dam showed a hysteresis reflection due to the long seepage distance (see **Figure 7B**). For example, the pore water pressure of the sensors P-1 and P-4 responded first, with a sharp increase at 0.13 and 2.60 h, respectively. The sensors located at the downstream toe of the slope responded in turn at the time of 21.40 h.

The soil stress of some sensors has an obvious response to seepage flow (**Figure 7C**), such as the fluctuation change of soil stress at the sensors S-2, S-4, and S-5 that corresponds to the changes in the moisture content and pore water pressure. For example, the soil stress of the sensors S-4 and S-5 drops sharply at 1.0 and 5.1 h, respectively, and then decreases continuously with time. The decrease in soil stress corresponds to the rise in water content because when the seepage flow reaches these positions, the increase in the water content reduces the cohesion of the soil, resulting in a sharp drop in the lateral pressure. The soil stress of the sensor S-2 located at the bottom of the dam recorded fluctuating, increasing, and decreasing trends. This is because the continuous seepage leads to a reduction in soil strength, and thus, the lateral pressure between the dam and soil changes constantly.

In general, during the seepage stage, the capillary line continues to spread downstream and the water content of the dam soil rises gradually, resulting in an increase in pore water pressure and a drop in soil stress. Continuous seepage leads to creep deformation of the downstream slope, which in turn leads to eventual slope sliding.

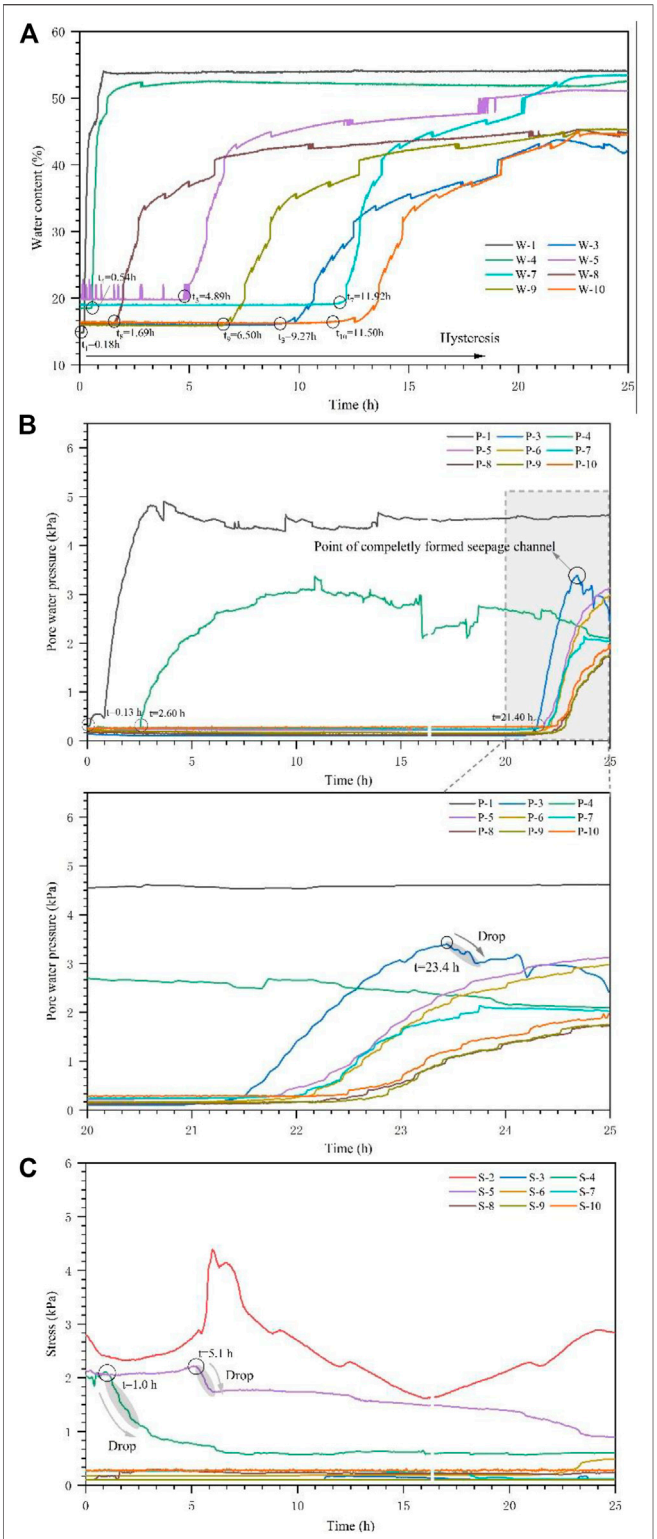

FIGURE 7 | Variation of water content, pore water pressure and soil stress during seepage process. **(A)** Water content, **(B)** pore water pressure, and **(C)** soil stress.

3.2.2 Development of Slope Failure

3.2.2.1 Variation of Dam Morphology

The progressive slope failure process of the model dam lasted about 232 h, during which four sliding events occurred, namely, the first slide, second slide, third slide, and fourth slide. Every slide event was progressive and long-lasting, with a gradually increasing volume, which can be seen from the position of the edge of the sliding body. **Figure 8** shows the progressive development of the first slide from front and vertical views. The first slide was a progressive failure process that lasted for 21 h, including the creep of the slope toe, crack initiation and penetration in the dam, and slope sliding. Ongoing seepage softened the dam soil at the slope toe (**Figures 8A–1**), and the slope there showed obvious creep behavior. This creep behavior generated displacement of the slope toe, which can be identified by the strain zones representing extrusion deformation processed by DIC (**Figures 8A–2**). With continuous creep deformation, the deformation zone at the slope toe expanded (**Figures 8B–1**), and some tensile cracks formed on the downstream slope surface due to the stress concentration (**Figures 8B–2**). Then the tensile cracks penetrated into the dam with a maximum width of 1.5 cm (**Figures 8C–1**). The increased strain zones extending on the entire downstream slope surface warns the emergence of the large sliding deformation of the slope (**Figures 8C–2**). Finally, with further creep, the sliding zone formed, causing the first slide (**Figures 8D–1** and **Figures 8D–2**). After sliding, the maximum tension crack width at the rear edge is about 9 cm (**Figures 8D–1**).

Figure 9 shows the progressive development of the second slide from the vertical view. The second slide is also a creep-controlled process that lasted for 35 h, including crack initiation, crack propagation, crack penetration in the dam, and slope sliding. After the first slide, continuous seepage caused the dam body to continue to deform downstream (**Figures 9A–1**), shown as the red strain area in **Figures 9A–2**. The continuous creep of the dam body initiated tensile cracks in the back wall of the first sliding body. With further creep, the crack on the dam crest continued to expand (**Figures 9B–1A) and a** large strain concentration appeared on the crest of the dam (**Figures 9B–2**). Then, with the tension cracks on the top of the dam body penetrating (**Figures 9C–1**), the multiple cracks gradually developed internally, forming an arc-shaped sliding surface (**Figures 9D–1**). Finally, the second slide occurred at 53.1 h. The red strain zone on the dam body represents the sliding body, and the red strain band on the dam crest top represents the edge of the second slide (**Figures 9C–2** and **Figures 9D–2**). The third slide and fourth slide also show a creep-controlled sliding process, including crack initiation, crack propagation, crack penetration, and slope sliding following in a similar fashion as the first slide and second slide. Each sliding evolution process can not only be observed from the above macroscopic morphological changes but also from the quantitative data, such as pore water pressure, soil stress, and displacement, obtained from the monitoring sensors.

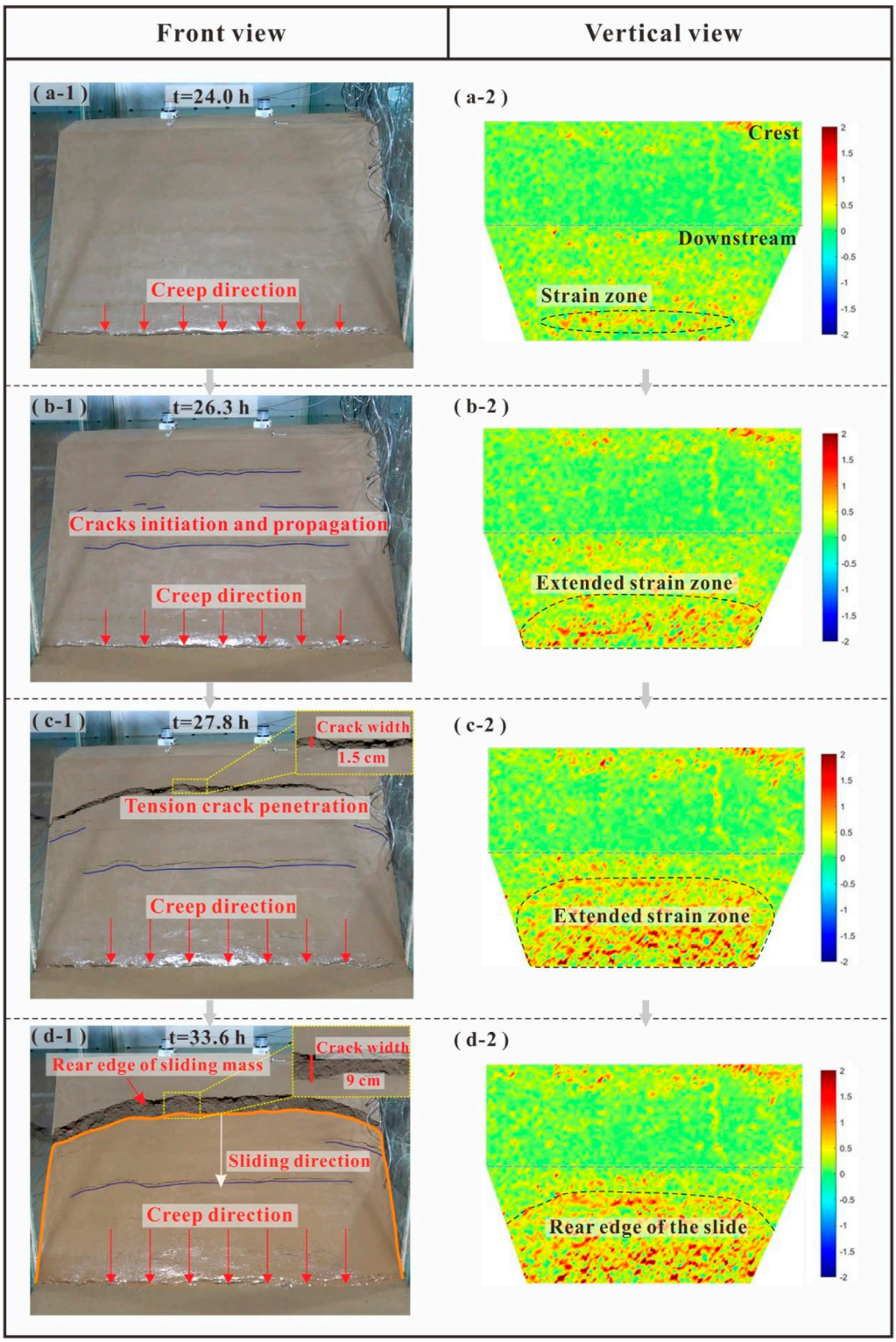

FIGURE 8 | Progressive process of the first slide from front view and vertical view. **(A)** Creep at the dam toe, **(B)** crack initiation and propagation, **(C)** crack penetration, and **(D)** sliding.

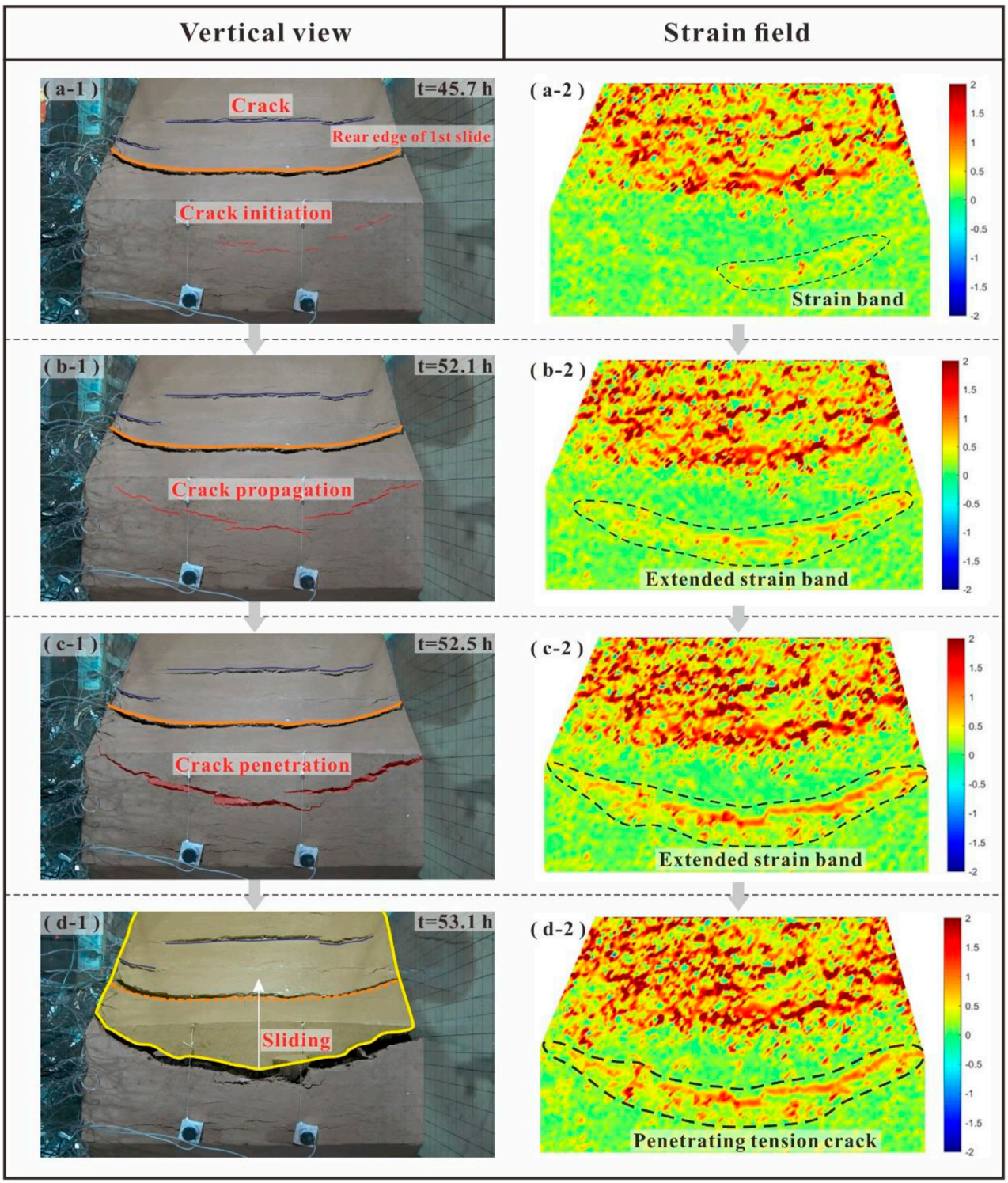

FIGURE 9 | Progressive process of the second slide from the vertical view. **(A)** Crack initiation, **(B)** crack propagation, **(C)** crack penetration, and **(D)** sliding.

3.2.2.2 Variation of Pore Water Pressure

We select the sensors P-3, P-6, and P-9 located inside the sliding body and the sensor P-5 located outside the sliding body as examples to analyze pore water pressure and soil stress during sliding, as shown in **Figure 10A**. It is obvious that the changes in pore water pressure are different before and after sliding due to

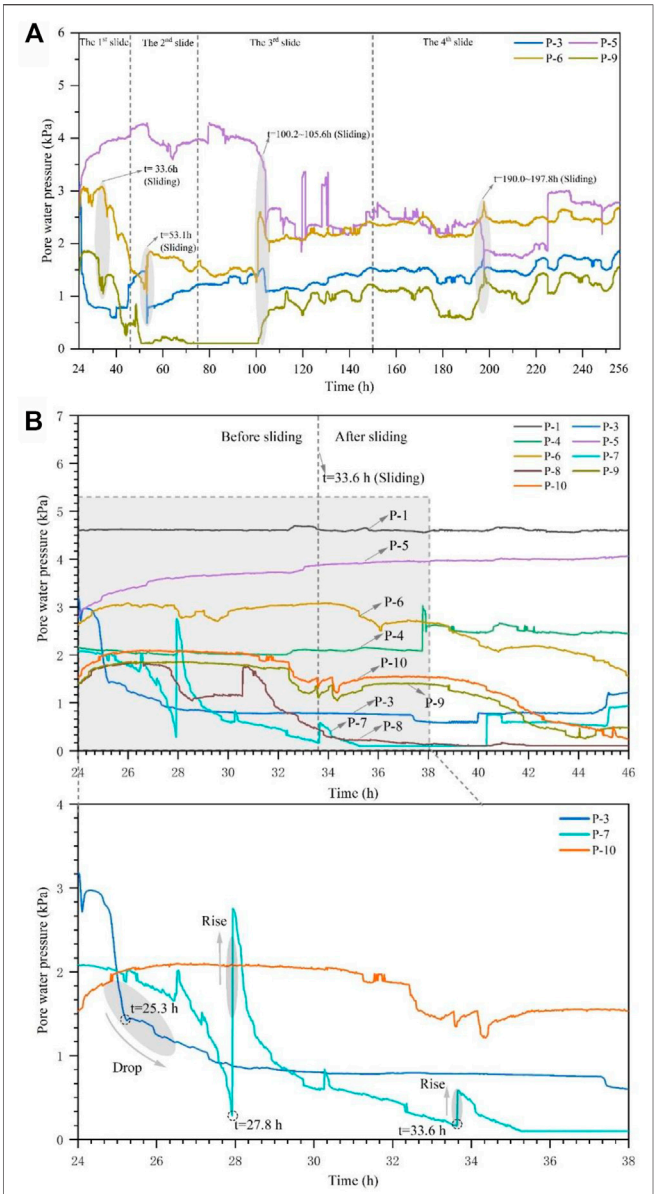

FIGURE 10 | Variation of pore water pressure during slope failure. **(A)** Pore water pressure during the whole sliding, **(B)** pore water pressures during the 1st slide, **(C)** pore water pressure during the 2nd slide, **(D)** pore water pressure during the 3rd slide, and **(E)** pore water pressure during the 4th slide.

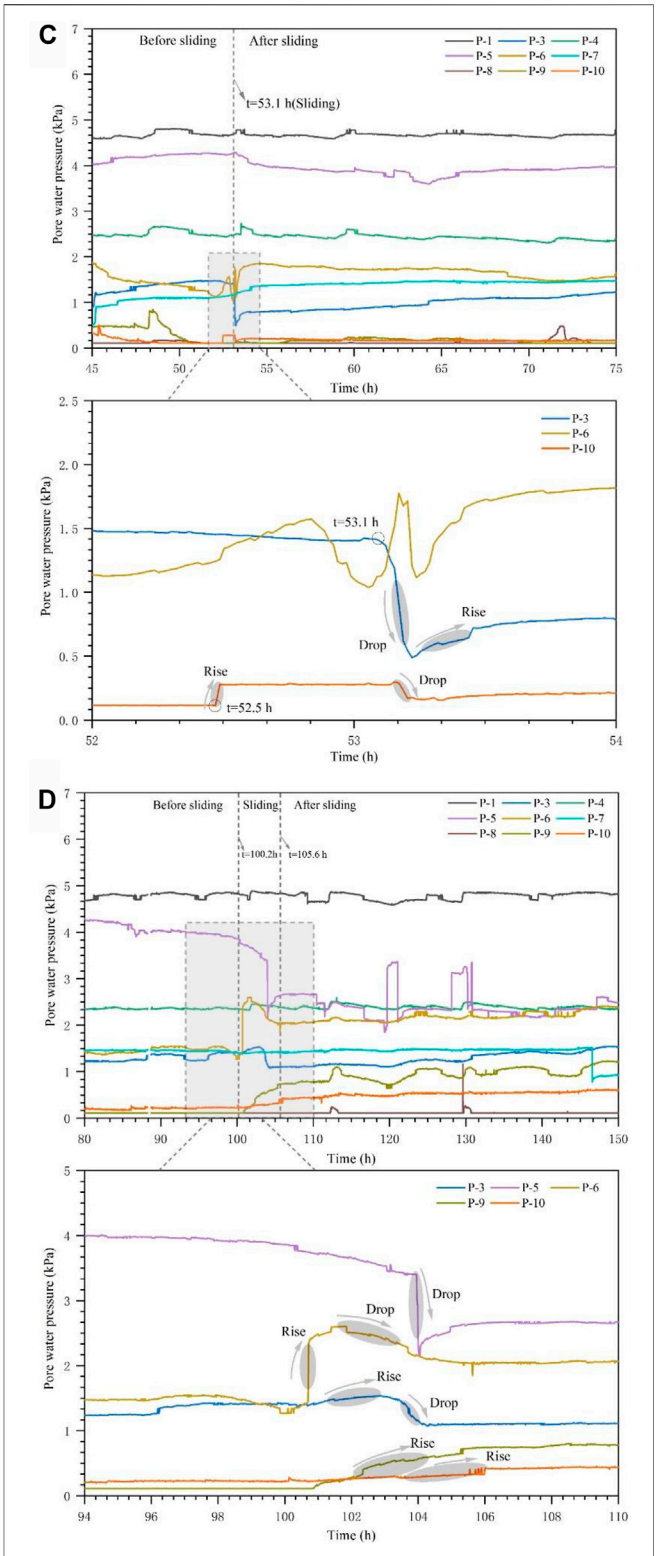

FIGURE 10 | (Continued).

their different positions. The pore water pressure of the sensors P-3, P-6, and P-9 showed four fluctuations corresponding to the four slides (see the gray ellipse in **Figure 10A**), that is, the pore water pressure increased sharply before sliding and decreased sharply after sliding. This actually reflects the accumulation and release of the pore water pressure inside the dam body, which is related to the opening and closing of the dominant seepage channel formed during sliding. The reduction of the pore water pressure during the first slide is the largest. This is mainly related to the release of pore water pressure caused by the reduction in the seepage path length of the rear dam during sliding. In the second slide stage, the pore water pressure is maintained at a low level until it surges to a higher level after the

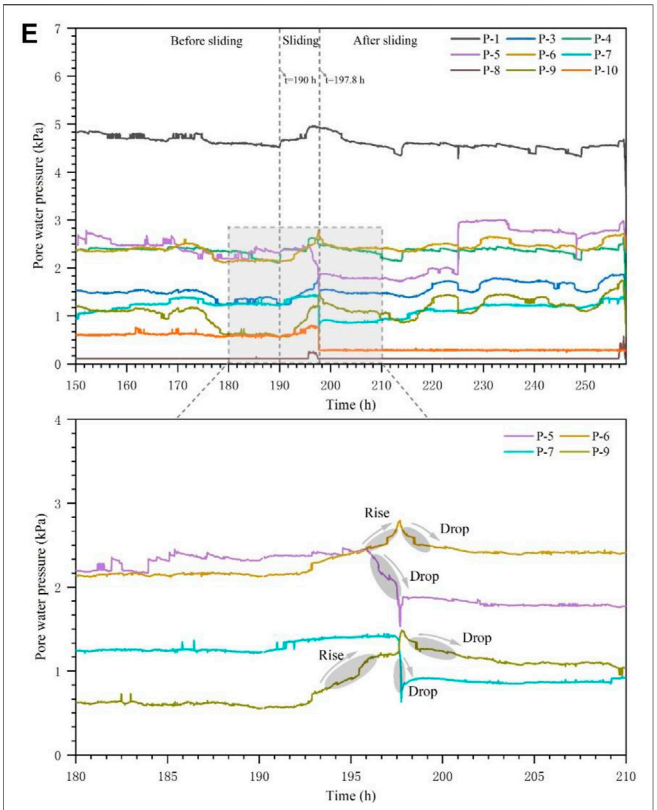

FIGURE 10 | (Continued).

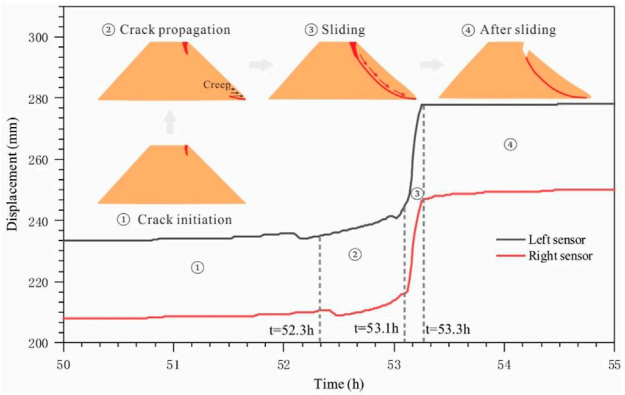

FIGURE 11 | Variation of displacement on the dam crest during the second slide.

third and fourth slides. This is because the accumulation of the seepage flow in the preferential seepage channel formed during sliding results in an increase in the pore water pressure. However, the pore water pressure of the sensor of P-5 has obvious response only in the third and fourth slide stages, that is, the pore water pressure drops sharply after sliding. This is because the sensor of P-5 is located at the rear side of the sliding surface, and the later slides release the seepage pressure in the part of the dam behind the sliding body.

From the previous discussion, it can be seen that various sensors respond to each sliding, so we can analyze each progressive sliding in combination with more sensors in detail. During the first slide, the pore water pressures at the sensors P-3, P-6, P-7, P-8, P-9, and P-10 changed greatly (**Figure 10B**) because these sensors are located near the dam slope surface and thus are sensitive to the slope sliding. **Figure 10B** plots the response of the pore water pressure of the sensors P-3, P-7, and P-10. As evident from the data, the pore water pressures vary due to their different locations. With the seepage channel forming at the bottom of the dam, the pore water pressure of the sensor P-3 decreased sharply between 24 and 25.3 h. Meanwhile, the pore water pressure of the sensor P-7 also declined, indicating the formation of some new seepage channels in the middle part of the dam body. At 27.8 h, the pore water pressure at P-7 increased sharply at first and then decreased gradually. This is because the seepage flow poured into the tensile crack formed at the rear edge of the sliding body (**Figures 8C–1**), resulting in the increasing pore water pressure first, and then with continuous seepage, the pore water pressure dissipated finally. With the gradual formation of the sliding surface (at 33.6 h), a preferential seepage channel is formed. Thus, the pore water pressure at P-7 increased first and then decreased due to the generation and dissipation of the pore water pressure in the aforementioned preferential seepage channel during sliding. After sliding, the leading edge of the sliding body squeezed and blocked the original seepage channel, resulting in a slight increase in the pore water pressure of the sensors of P-3 and P-7 at 40.3 and 45.1 h, respectively. **Figure 10B** shows that the response of the pore water pressure of the sensor P-10 decreased after sliding, that is, the pore water pressure at P-10 dropped sharply before sliding (at 33.6 h). This is because this sensor is located above the sliding body, and the continuous penetration of cracks in the slope provides the seepage channels the opportunity for the release of pore water pressure. After sliding, the pore water pressure of P-10 decreased slowly to less than 1 kPa. A change in the seepage path at the dam crest is caused by the first slide, resulting in these pressure reductions. **Figure 10C** displays the variation of the pore water pressure during the second slide. The sensors P-3, P-6, and P-10 located near the slip surface responded strongly; especially at a sliding time of 53.1 h, the pore pressures at P-3, P-6, and P-10 fluctuated sharply. The pore water pressure at P-3, located at the front part of the sliding body, dropped sharply after sliding. This is because the seepage flowed out from the sliding surface, reducing the pore water pressure in the sliding body. Then, the pore water rose slightly due to the continuous re-entry of the seepage into the sliding dam body. For the sensor at P-6, located at the back part of the sliding body, the pore water pressure decreased first before the sliding and then increased during the sliding. This is because the development of cracks inside the dam before sliding provided some preferential seepage channels for the seepage flow, resulting in the reduction in the pore water pressure; during sliding, the seepage channel was blocked

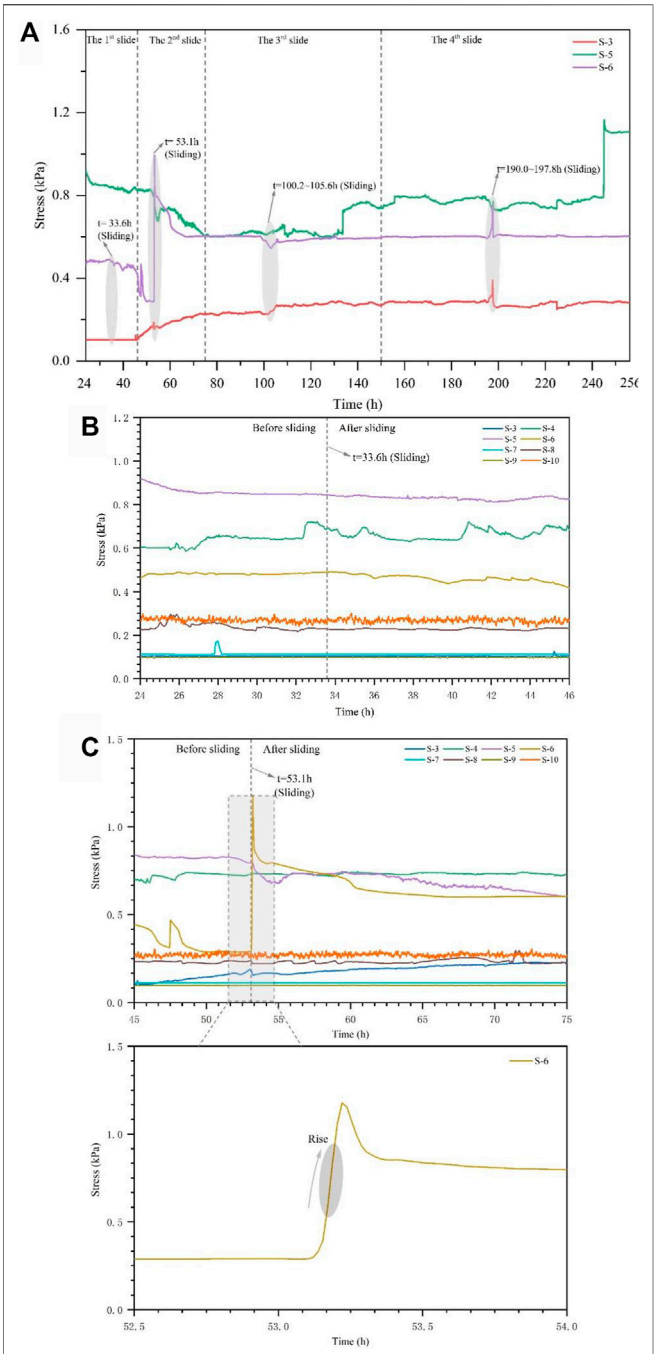

FIGURE 12 | Variation of soil stress during slope failure. **(A)** Soil stress during the whole sliding, **(B)** soil stress during 1st slide, **(C)** soil stress during the 2nd slide, **(D)** soil stress during the 3rd slide, and **(E)** soil stress during the 4th slide.

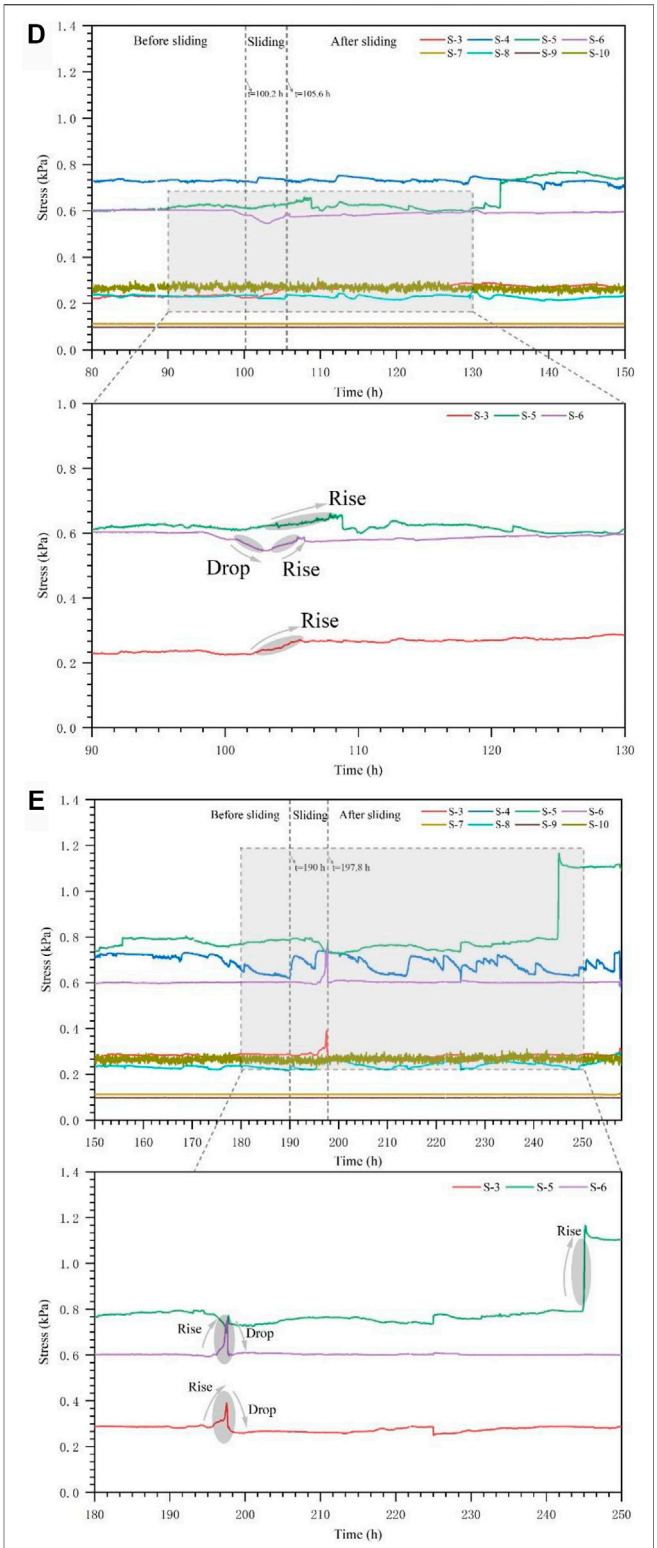

FIGURE 12 | (Continued).

due to the squeezing of the sliding body, resulting in an increase in the pore water pressure. The pore water pressure of the sensor P-10, located at the rear edge of the sliding body, rose sharply before sliding (at 52.5 h) and dropped after sliding (at 53.5 h) (**Figures 9B–2** and **Figure 10C**). In this case, the tensile cracks on the dam crest concentrated the seepage flow before sliding, thus the pore water pressure increased first. After sliding, seepage water in the cracks dissipated, resulting in a reduction in the pore water pressure.

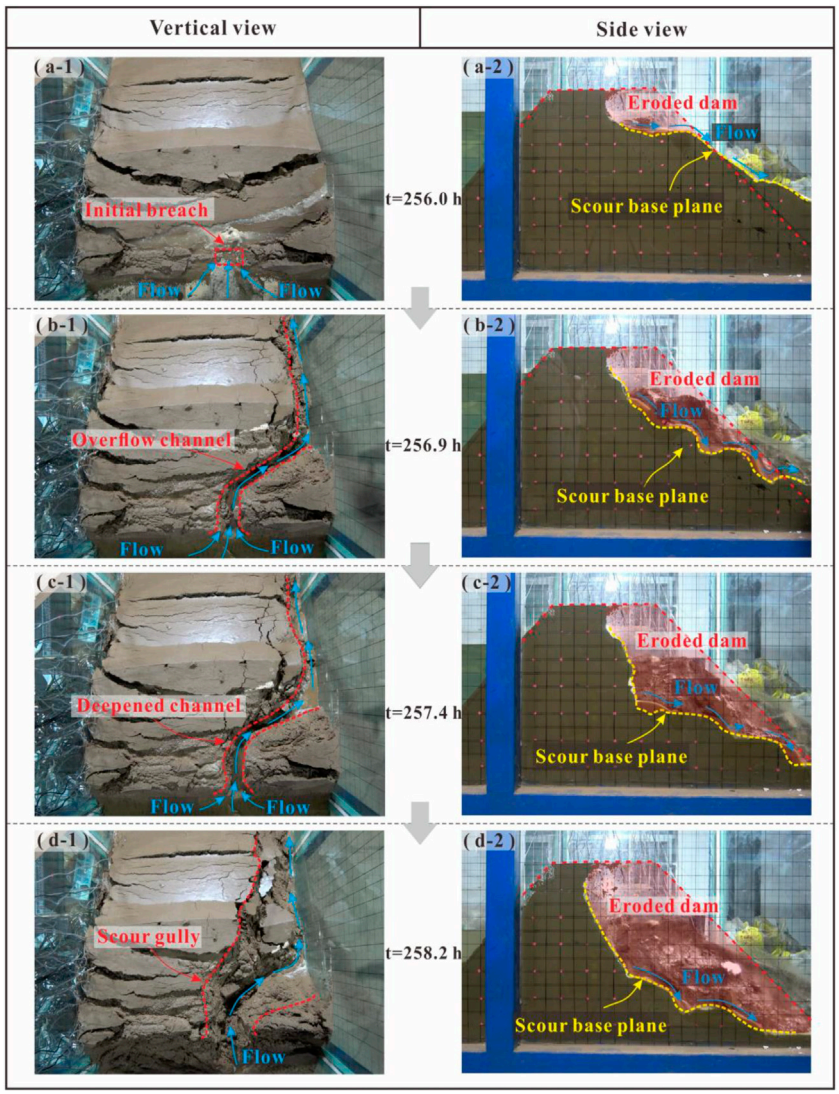

FIGURE 13 | Progressive process of overtopping from vertical view and side view.

In the third and fourth slides, the pore water stress sensor responds to each sliding noticeably, such as the sharp increase and decrease in the pore water pressure before and after the sliding, in a similar fashion as with the previous two sliding (**Figures 10D,E**). However, the difference is that the progressive failure process of the third slide and fourth slide lasts longer, and the sliding volume body gets larger. Accordingly, the sensor also presents some different characteristics from those in the previous two slides. All sensors respond during the last two slidings, and the monitored data fluctuates greatly, indicating that the sliding volume is larger. In addition, the fluctuation of the monitored data lasts longer, indicating that the sliding process is longer. For example, in the third slide and fourth slide stages, the sliding process lasts for about 5–8 h, during which the pore water pressure and soil pressure continuously rise and drop (**Figures 10D,E**).

3.2.2.3 Variation of Displacement

The sensors that monitor the displacement of the dam crest respond only during the second slide, as shown in **Figure 11**. The sliding process is divided into four stages, including crack initiation, propagation in the dam, sliding, and stable stage. At the initiation stage (before 52.3 h), the cracks on the dam crest nucleated at low speed, and there was no obvious displacement on the dam crest. At the crack propagation stage (52.3–53.1 h), the cracks at the dam crest expanded gradually, resulting in an increasing displacement with a slow rate of increase. Then, the displacement of the dam crest increased sharply, with a maximum growth range of 33.8 mm in only 0.2 h, marking the occurrence of the sliding. After sliding (after 53.1 h), the changes in the two displacement sensors tend to be stable, with a maximum displacement of 46.5 mm, indicating the end of the sliding.

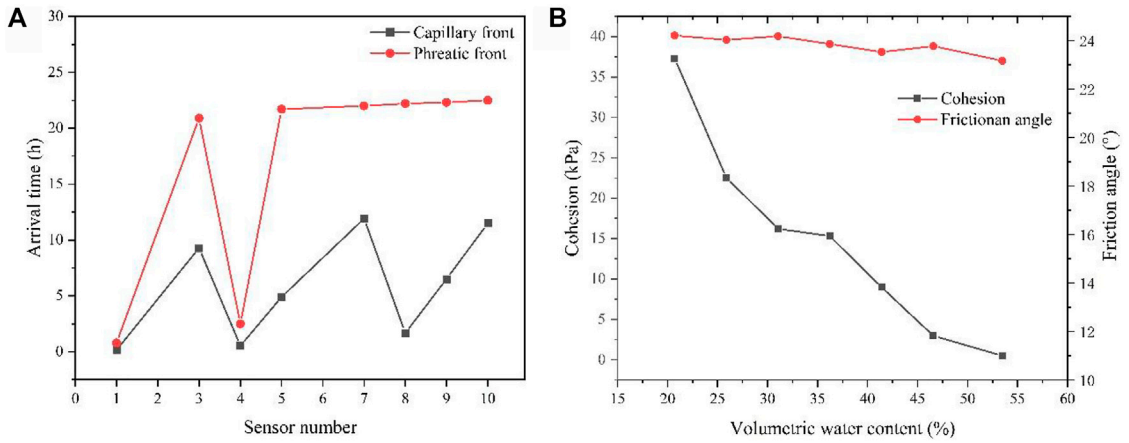

FIGURE 14 | Variation of capillary front, phreatic front, and shear strength parameters of dam material during seepage. **(A)** Arrival time of capillary front and phreatic front at the positions of water content sensors. **(B)** Shear strength parameters of dam material with different water content.

3.2.2.4 Variation of Soil Stress

Figure 12A shows the response of the sensors S-3, S-5, and S-6 representing the soil stress in the sliding body, at the sliding surface, and at the back of the sliding body, respectively. The soil stress of the sensors S-3 and S-6 shows fluctuating changes in response to each sliding, especially during the second slide. The soil stress of sensor S-5 shows a decreasing trend in the first two slides and increases in the third slide and fourth slide stages. This is because the lateral stress in the dam soil decreases due to the first two slides, resulting in a reduction in soil stress. After the third and fourth slides, the massive sliding caused a loss of support at the rear of the dam, resulting in an increase in the lateral soil stress inside the dam. Therefore, the soil stress pressure of the dam shows an increasing trend. **Figure 12B** shows the variation of soil stress during the first slide. Because the sliding volume is small, the soil stress changes little. The soil was soaked at the back of the dam for a long time, so the soil stress values at S-4 and S-8 fluctuate only slightly. During the second slide, the soil stress at S-6 rises sharply at 53.1 h with the occurrence of sliding (**Figure 12C**). This is because the sliding made the rear of the dam lose its front support, resulting in an increase in the lateral soil stress. During the third and fourth slides, the sliding process lasts for about 5–8 h, during which the pore water pressure and soil pressure continuously rise and drop (**Figures 12D,E**).

3.2.3 Erosion Characteristics of Overtopping

The multi-sliding of the downstream slope caused sufficient structural damage to the dam and overtopping occurred at 256 h. **Figure 13** shows the overtopping process from vertical and side views. The sliding of the downstream slope reduced the height of the dam crest, and overflowing water gradually eroded the dam crest (**Figures 13A–1**). As the soil material on the dam crest constantly eroded away (**Figures 13A–2**), some slender overflow channels appeared there, and the slope beside the overflow channel collapsed under the action of erosion (**Figures 13B–1**). The scour base plane continued to develop downward, and different flow velocities in gullies led to the stepped multi-level scarps, as shown in **Figures 13B–2**. Continuous erosion deepened and widened the initial crest breach as well as the overflow channel (**Figures 13C–1**). When the water flowed through the scarp, a waterfall torrent was formed, which quickly cut down and eroded the upstream, forming a still larger scarp (**Figures 13C–2**). Then, the gully deepened continually, and the dam soil on the sides collapsed and was washed away by the water flow (**Figures 13D–1**). The erosion flows exacerbated the undercutting of the upstream, making the scour base plane develop rapidly to the bottom of the model container. With the decline of the reservoir water level, the overtopping process stopped gradually. **Figures 13D–2** show the final shape of the broken dam.

4 DISCUSSION

This model test revealed the whole life cycle of the check dam satisfactorily and showed that the complex failure process of an earthen dam consists of seepage on the downstream slope, sliding of the downstream slope, and overtopping, which are consistent with the aforementioned field observations, especially for the progressive multi-stage slope sliding. A dam is prone to slope failure due to seepage when it has steep upstream and downstream faces and suffers high pour water pressure (Costa and Shuster, 1988; Jiang et al., 2018). Distinct from the progressive process of non-cohesive natural dams (Gregoretti et al., 2010) that suffer collapse due to gradual soil particle migration (Jiang et al., 2020b), our model failure included four progressive sliding events. This is caused by the strong seepage in the homogeneous, fine-grained dam material.

Due to the upstream flow, the seepage flow gradually shifted from upstream to downstream. The seepage movement in the dam can be observed through the “capillary line” and “phreatic line.” The arrival of the capillary front marks the beginning of the

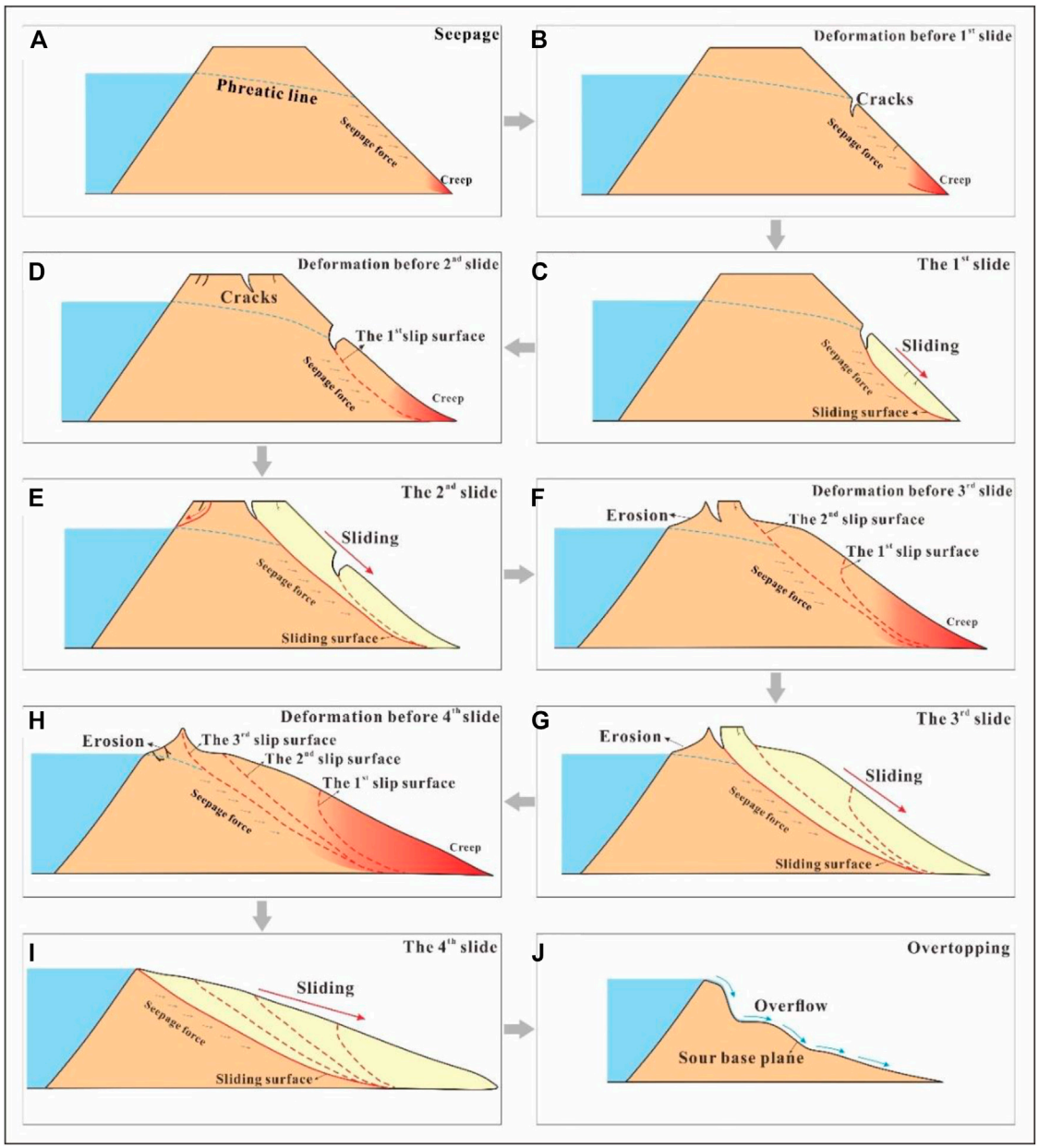

FIGURE 15 | Formation mechanism of the progressive failure of model dam. **(A)** Seepage, **(B)** deformation before the 1st slide, **(C)** 1st slide; **(D)** deformation before the 2nd slide, **(E)** 2nd slide, **(F)** deformation before the 3rd slide, **(G)** 3rd slide, **(H)** deformation before the 4th slide, **(I)** 4th slide, and **(J)** overtopping.

transition from dry to wet soil, and the movement of the capillary front can be captured by cameras (**Figure 6A**) and moisture sensors (**Figure 7A**) in the model test. As the capillary front reached the position of the moisture content sensor, the moisture content of the soil immediately increased. The arrival of the phreatic front marks the saturation of the soil, and the movement of the phreatic front is reflected by the pore water sensors (**Figure 7B**). As the phreatic front reaches the position of the moisture content sensor, the soil moisture content reaches its maximum value and the pore water pressure of the soil immediately increases. The area between the capillary front and the phreatic front is called the capillary zone. The area behind the phreatic front is called the saturated zone. **Figure 14A** shows the arrival time of the capillary front and phreatic front at different positions of the water content sensor, corresponding to the moisture content sensor positions in the dam. Obviously, the capillary front arrives earlier than the phreatic front, and the closer the location of the water content sensor is to the upstream water level (such as the monitoring sensors of W-1, W-4, and W-8), the earlier the capillary front arrives. **Figure 6A** shows that the capillary flow moves mostly perpendicular to the bottom of the dam in the early seepage stage

and parallel to the downstream slope in the later seepage stage. Notably, the capillary flow line is higher than the upstream flow water level, indicating that the capillary phenomenon in the dam material is inevitable due to its loose structure. The arrival time of the phreatic front is at about 20–25 h, which shows that the high permeability of the dam material leads to the rapid evolution of seepage. It should be noted that the arrival time of the phreatic front is greater than that of the capillary front, indicating that the strong capillary phenomenon of the dam material is due to its loose structure.

With seepage, increasing the water content of the dam material reduces its shear strength. **Figure 14B** shows the reduction of the shear strength index of the dam material with increasing water content. It can be seen that the cohesion of the dam material is reduced by 98.7%, and the cohesion of the dam material in the saturated state is only 0.49 kPa. Combined with the seepage force, the soil at the slope toe of the dam begins to deform by creep (**Figure 15A**). The creep region expands further due to the seepage force and softening of the strength of the saturated soil (**Figure 15B**). The creep at the toe of the slope drives the deformation of the whole slope, and some tensile cracks appear on the dam slope. Deformation is the most significant external manifestation of the change in slope stability and slope failure (Xu et al., 2016). As the tensile cracks penetrate, they cause the first slide (**Figure 15C**). Once one part of the slope fails, it becomes increasingly difficult for the remaining parts of the slope to hold together. Thus, after the first slide, the dam body loses the anti-sliding support from the front part of the dam (**Figure 15D**), which furthers reduces dam stability. Meanwhile, the cracks generated by the sliding form new preferential seepage channels, and water flows into the cracks, leading to increased seepage force. Influenced by the double action of the seepage force and the softening of the strength of the saturated soil, cracks at the dam crest extend more deeply and widely, causing the second slide (**Figure 15E**), then the third and fourth slides follow in a similar fashion (**Figures 15F–I**). Finally, overtopping occurs after the fourth slide (**Figure 15J**). It should be noted that each sliding is a long-time creep process, and the creep at the foot of the dam slope drives each slope sliding. The slope slide of the dam presents a retrogressive sliding mechanism, and each slope sliding drives the next sliding, especially the first sliding, which plays an important role in the entire process of slope sliding. The discussion above indicates that the loose dam material, high permeability of dam material, the large width of the dam, and high seepage force caused by the water storage upstream are the controlling factors behind the complex progressive failure of the model dam.

Overall, our model test reveals the progressive failure process of check dams, which has great significance in understanding the failure mechanism of check dams with the slope failure mode. It should be noted that there are some shortcomings in this model that need to be improved. For example, due to the establishment of the scale model in this study, the capillary phenomenon of the compacted dam material is more obvious, making the whole dam soaked, which is slightly different from the prototype check dam. Furthermore, the overtopping does not occurs in the middle of the model dam but along the boundary between the reinforced glass and the model dam. Thus, the boundary effect between the dam and reinforced glass should be noted.

5 CONCLUSION

By using the physical mode test, the failure mode and failure process of the check dam triggered by steady upstream flow were investigated. Then the mechanism causing the progressive failure of the check dam was analyzed based on the variation of dam hydrologic and mechanical conditions. Finally, the physical model test results were compared with field observation to verify the reliability of this study. The main conclusions are as follows:

1) Progressive failure is a major failure mode for natural check dams subjected to seepage, which was recreated in laboratory tests. In this experiment, the failure mode of a model dam triggered by upstream flow is investigated, which involves multi-stage slope slides and overtopping. The progressive failure process of a check dam presents three specific features: seepage on the downstream slope, slide of the downstream slope, and overtopping.
2) During seepage, the capillary line starts from upstream and gradually moves downstream with a vertical shape due to the high permeability of the model materials. With continuous seepage, the seepage overflow at the dam slope toe occurs, which softens the dam material and reduces its strength. Combined with the seepage force of the seepage flow, the soil at the slope toe of the dam begins to deform by creep.
3) Continuous creep deformation of the downstream slope leads to eventual slope sliding. The slope failure of the check dam presents a progressive sliding process that lasts for about 232 h, during which four sliding events occur on the downstream slope. Every slide event is progressive, long lasting, with a gradually increasing volume. Notably, the slope sliding of the entire dam body presents a retrogressive sliding mechanism; the seepage flow is the main factor that triggers the progressive slope failure.
4) The physical model test reproduces the failure process of the check dam throughout its life cycle, which is consistent with the field observations, especially the failure modes and the progressive failure process. The progress failure is the consequence of factors, such as the well-graded dam material, high permeability of dam material, large width of dam, and high water storage upstream."

DATA AVAILABILITY STATEMENT

The original contributions presented in the study are included in the article/Supplementary Material, further inquiries can be directed to the corresponding authors.

AUTHOR CONTRIBUTIONS

FY,WT and YuZ conducted model tests. YaZ and FL wrote the paper. YaZ and FL made figures. HL provided article revision.

FUNDING

This study was financially supported by the National Natural Science Foundation of China (Grant Nos. 41877247, 41790443, and 42041006).

REFERENCES

Calamak, M., Larocque, L. A., and Chaudhry, M. H. (2020). Numerical Modelling of Seepage through Earthen Dams with Animal Burrows: a Case Study. *J. Hydraulic Res.* 59 (3), 488–499. doi:10.1080/00221686.2020.1780502

Cao, Z., Yue, Z., and Pender, G. (2011). Landslide Dam Failure and Flood Hydraulics. Part I: Experimental Investigation. *Nat. Hazards* 59 (2), 1003–1019. doi:10.1007/s11069-011-9814-8

Chen, S.-C., Lin, T.-W., and Chen, C.-Y. (2015). Modeling of Natural Dam Failure Modes and Downstream Riverbed Morphological Changes with Different Dam Materials in a Flume Test. *Eng. Geology.* 188, 148–158. doi:10.1016/j.enggeo.2015.01.016

C. C. Conesa and M. A. Lenzi (Editors) (2013). *Check Dams, Morphological Adjustments and Erosion Control in Torrential Streams*. New York, NY: Nova Science.

Costa, J. E., and Schuster, R. L. (1988). The Formation and Failure of Natural Dams. *Geol. Soc. Am. Bull.*, 100, 1054–1068. doi:10.3133/ofr87392

Dunning, S. A., Rosser, N. J., Petley, D. N., and Massey, C. R. (2006). Formation and Failure of the Tsatichhu Landslide Dam, Bhutan. *Landslides* 3 (2), 107–113. doi:10.1007/s10346-005-0032-x

Fang, N. F., Zeng, Y., Ni, L. S., and Shi, Z. H. (2019). Estimation of Sediment Trapping behind Check Dams Using High-Density Electrical Resistivity Tomography. *J. Hydrol.* 568, 1007–1016. doi:10.1016/j.jhydrol.2018.11.062

Foster, M., Fell, R., and Spannagle, M. (2000). The Statistics of Embankment Dam Failures and Accidents. *Can. Geotech. J.*, 37. , 1000–1024. doi:10.1139/t00-030

Fu, B., Wang, S., Liu, Y., Liu, J., Liang, W., and Miao, C. (2017). "Hydrogeomorphic Ecosystem Responses to Natural and Anthropogenic Changes in the Loess Plateau of China," *Annu. Rev. Earth Planet. Sci.* Editors R. Jeanloz and K. H. Freeman, 45, 223–243. doi:10.1146/annurev-earth-063016-020552

Garcia, C., and Mario, M. (2010). Check Dams, Morphological Adjustments and Erosion Control in Torrential Streams. *Scitech Book News* 34 (4).

Gregoretti, C., Maltauro, A., and Lanzoni, S. (2010). Laboratory Experiments on the Failure of Coarse Homogeneous Sediment Natural Dams on a Sloping Bed. *J. Hydraul. Eng.* 136 (11), 868–879. doi:10.1061/(asce)hy.1943-7900.0000259

He, L. P., Yu, J. Y., Hu, Q. J., Cai, Q. J., Qu, M. F., and He, T. J. (2020). Study on Crack Propagation and Shear Behavior of Weak Muddy Intercalations Submitted to Wetting-Drying Cycles. *Bull. Eng. Geol. Environ.* 79 (9), 4873–4889. doi:10.1007/s10064-020-01842-7

Hessel, R. (2006). Consequences of Hyperconcentrated Flow for Process-Based Soil Erosion Modelling on the Chinese Loess Plateau. *Earth Surf. Process. Landforms* 31 (9), 1100–1114. doi:10.1002/esp.1307

Jiang, X., Wei, Y., Wu, L., Hu, K., Zhu, Z., Zou, Z., et al. (2019). Laboratory Experiments on Failure Characteristics of Non-cohesive Sediment Natural Dam in Progressive Failure Mode. *Environ. Earth Sci.* 78 (17), 538. doi:10.1007/s12665-019-8544-1

Jiang, X., Wei, Y., Wu, L., and Lei, Y. (2018). Experimental Investigation of Failure Modes and Breaching Characteristics of Natural Dams. *Geomatics, Nat. Hazards Risk* 9 (1), 33–48. doi:10.1080/19475705.2017.1407367

Jiang, X., Wörman, A., Chen, P., Huang, Q., and Chen, H. (2020a). Mechanism of the Progressive Failure of Non-cohesive Natural Dam Slopes. *Geomorphology* 363, 107198. doi:10.1016/j.geomorph.2020.107198

Jiang, X., Zhanyuan, Z., Chen, H., Deng, M., Niu, Z., Deng, H., et al. (2020b). Natural Dam Failure in Slope Failure Mode Triggered by Seepage. *Geomatics, Nat. Hazards Risk* 11 (1), 698–723. doi:10.1080/19475705.2020.1746697

Jin, Z., Guo, L., Wang, Y., Yu, Y., Lin, H., Chen, Y., et al. (2019). Valley Reshaping and Damming Induce Water Table Rise and Soil Salinization on the Chinese Loess Plateau. *Geoderma* 339, 115–125. doi:10.1016/j.geoderma.2018.12.048

Kouzehgar, K., Hassanzadeh, Y., Eslamian, S., Yousefzadeh Fard, M., and Babaeian Amini, A. (2021). Physical Modeling into Outflow Hydrographs and Breach Characteristics of Homogeneous Earthfill Dams Failure Due to Overtopping. *J. Mt. Sci.* 18 (2), 462–481. doi:10.1007/s11629-020-6177-1

Li, X., Wei, X., and Wei, N. (2016). Correlating Check Dam Sedimentation and Rainstorm Characteristics on the Loess Plateau, China. *Geomorphology* 265, 84–97. doi:10.1016/j.geomorph.2016.04.017

Li, Y., Chen, A., Wen, L., Bu, P., and Li, K. (2020). Numerical Simulation of Non-cohesive Homogeneous Dam Breaching Due to Overtopping Considering the Seepage Effect. *Eur. J. Environ. Civil Eng.* 25, 1–15. doi:10.1080/19648189.2020.1744481

Martí, J., Riera, F., and Martínez, F. (2020). Interpretation of the Failure of the Aznalcóllar (Spain) Tailings Dam. *Mine Water Environ.*, 40, 189–208. doi:10.1007/s10230-020-00712-8

Okeke, A. C.-U., and Wang, F. (2016). Hydromechanical Constraints on Piping Failure of Landslide Dams: an Experimental Investigation. *Geoenviron Disasters* 3 (1), 4. doi:10.1186/s40677-016-0038-9

Richards, K. S., and Reddy, K. R. (2007). Critical Appraisal of Piping Phenomena in Earth Dams. *Bull. Eng. Geol. Environ.* 66 (4), 381–402. doi:10.1007/s10064-007-0095-0

Rifai, I., Erpicum, S., Archambeau, P., Violeau, D., Pirotton, M., El Kadi Abderrezzak, K., et al. (2017). Overtopping Induced Failure of Noncohesive, Homogeneous Fluvial Dikes. *Water Resour. Res.* 53 (4), 3373–3386. doi:10.1002/2016wr020053

Romero-Díaz, A., Marín-Sanleandro, P., and Ortiz-Silla, R. (2012). Loss of Soil Fertility Estimated from Sediment Trapped in Check Dams. South-Eastern Spain. *Catena* 99, 42–53. doi:10.1016/j.catena.2012.07.006

Wang, F., Okeke, A. C.-U., Kogure, T., Sakai, T., and Hayashi, H. (2018). Assessing the Internal Structure of Landslide Dams Subject to Possible Piping Erosion by Means of Microtremor Chain Array and Self-Potential Surveys. *Eng. Geology.* 234, 11–26. doi:10.1016/j.enggeo.2017.12.023

Wu, W. M., Altinakar, M. S., Al-Riffai, M., Bergman, N., Bradford, S. F., Cao, Z. X., et al. (2011). Earthen Embankment Breaching. *J. Hydraulic Eng.* 137 (12), 1549–1564. doi:10.1061/(ASCE)HY.1943-7900.0000498

Xu, J., Wei, W., Bao, H., Zhang, K., Lan, H., Yan, C., et al. (2019). Failure Models of a Loess Stacked Dam: a Case Study in the Ansai Area (China). *Bull. Eng. Geol. Environ.* 79 (2), 1009–1021. doi:10.1007/s10064-019-01605-z

Xu, Q., Liu, H., Ran, J., Li, W., and Sun, X. (2016). Field Monitoring of Groundwater Responses to Heavy Rainfalls and the Early Warning of the Kualiangzi Landslide in Sichuan Basin, Southwestern China. *Landslides* 13 (6), 1555–1570. doi:10.1007/s10346-016-0717-3

Yang, Y., Fu, S., Liu, B., Sun, B., Liu, C., Wang, Z., et al. (2020). Damage of Check Dams by Extreme Rainstorms on the Chinese Loess Plateau: A Case Study in the Chabagou Watershed. *J. Soil Water Conservation* 75 (6), 746–754. doi:10.2489/jswc.2020.00138

Zhang, F., Yan, B., Feng, X., Lan, H., Kang, C., Lin, X., et al. (2019). A Rapid Loess Mudflow Triggered by the Check Dam Failure in a Bulldoze Mountain Area, Lanzhou, China. *Landslides* 16 (10), 1981–1992. doi:10.1007/s10346-019-01219-2

Zhao, T.-y., Yang, M.-y., Walling, D. E., Zhang, F.-b., and Zhang, J.-q. (2017). Using Check Dam Deposits to Investigate Recent Changes in Sediment Yield in

the Loess Plateau, China. *Glob. Planet. Change* 152, 88–98. doi:10.1016/j.gloplacha.2017.03.003

Zhu, X., Peng, J., Jiang, C., and Guo, W. (2019). A Preliminary Study of the Failure Modes and Process of Landslide Dams Due to Upstream Flow. *Water* 11 (6), 1115. doi:10.3390/w11061115

Zhu, X., Peng, J., Liu, B., Jiang, C., and Guo, J. (2020). Influence of Textural Properties on the Failure Mode and Process of Landslide Dams. *Eng. Geology.* 271, 105613. doi:10.1016/j.enggeo.2020.105613

Conflict of Interest: The authors declare that the research was conducted in the absence of any commercial or financial relationships that could be construed as a potential conflict of interest.

Publisher's Note: All claims expressed in this article are solely those of the authors and do not necessarily represent those of their affiliated organizations, or those of the publisher, the editors, and the reviewers. Any product that may be evaluated in this article, or claim that may be made by its manufacturer, is not guaranteed or endorsed by the publisher.

frontiers in Earth Science

ORIGINAL RESEARCH
published: 02 February 2022
doi: 10.3389/feart.2021.810440

Study on the Structural Plane Characteristics and Disaster-Induced Mechanism of the Yellow River Jingtai Stone Forest, Northwestern Loess Plateau, China

Yan Lyu[1,2], *Gang Gu*[1], *Zuopeng Wang*[1,2]*, *Yanqiu Leng*[1,2], *Penghui Ma*[1,2] and *Jianbing Peng*[1,2]

[1]College of Geological Engineering and Geomatics, Chang'an University, Xi'an, China, [2]Key Laboratory of Western China Mineral Resources and Geological Engineering, Xi'an, China

OPEN ACCESS

Edited by:
Yueren Xu,
China Earthquake Administration, China

Reviewed by:
Huafeng Deng,
China Three Gorges University, China
Shouyun Liang,
Lanzhou University, China

***Correspondence:**
Zuopeng Wang
zpwang@chd.edu.cn

Specialty section:
This article was submitted to Geohazards and Georisks, a section of the journal Frontiers in Earth Science

Received: 07 November 2021
Accepted: 30 December 2021
Published: 02 February 2022

Citation:
Lyu Y, Gu G, Wang Z, Leng Y, Ma P and Peng J (2022) Study on the Structural Plane Characteristics and Disaster-Induced Mechanism of the Yellow River Jingtai Stone Forest, Northwestern Loess Plateau, China. Front. Earth Sci. 9:810440. doi: 10.3389/feart.2021.810440

The Yellow River Jingtai Stone Forest (YJSF) is situated in the northwestern margin of the Chinese Loess Plateau, and it is not only one of the most precious and rare types of natural landforms in the Loess Plateau but also a protected area of valuable geological relics and landscapes in northwest China. Massive rock structural planes are present in the stone forest. However, few studies have been conducted on the rock mass structural planes for the slope's stability. Based on the detailed field investigation, structural planes and their combination types are classified based on the rock mass. On this basis, combined with physical, mechanical, and hydraulic tests, the disaster-induced mechanism of the rock mass structural planes is classified and discussed. Results show that the structural planes of the YJSF can be divided into three types, namely, the primary structural plane, tectonic structural plane, and secondary plane. They not only combine with each other to cut the rock mass into different shape blocks but also jointly control the stability of the rock mass slope. The physical and mechanical tests and water sensitivity characteristics show that the conglomerates and muddy sandstones which are the main components of the YJSF have strong tensile and shear strengths under natural situations, while their strengths are reduced under immersion infiltration; in particular, the muddy sandstones are more sensitive to water and have a lower strength than that of the conglomerates. Finally, the disaster-induced mechanism of the YJSF is mainly related to the combination of various structural planes, which can be divided into four failure patterns, namely, creeping slide-tension failure, gradual failure, slipping failure, and dumping failure; coupling action of endogenic and exogenic geodynamic processes was responsible for their formation. The studied results will provide critical, theoretical, and technical support for the slope stability analysis, scenic geological heritage protection, and disaster warning in this area.

Keywords: structural plane, rock slope, disaster-induced mechanism, Yellow River Jingtai Stone Forest, Chinese Loess Plateau

INTRODUCTION

Chinese Loess Plateau is located in an arid–semiarid region, which is the largest loess accumulation region in the world (An, 2000; Nie et al., 2015; Peng et al., 2019). The YJSF, situated in the northwestern margin of the Loess Plateau, is characterized by different scale peak forest plains and peak cluster depressions. It is not only one of the most precious and rare types of natural landforms in the Loess Plateau but also a protected area of valuable geological relics and landscapes in northwest China, thus attracting thousands of tourists every year.

Due to the extensive development of valleys and complex topography in the YJSF area, geological hazards such as collapses, landslides, and debris flows occur usually, especially in spring and summer. These hazards, on the one hand, lead to a huge threat to the safety of tourists and tourist facilities, and on the other hand, they also pose new challenges to the protection of geological relics and landscape resources. The reason is that the formation of these disasters is not only related to the nature of rock masses and natural conditions in the area but also closely associated with a series of structural planes developed in the rock masses, which control the evolution of the stone forest valleys and the stability of the slope rock masses. However, massive research works on the YJSF have been conducted, but mainly focused on the description of aesthetics and landscape evolution processes (Xu and Fan, 2008; Fan, 2014). Fan (2006) and Zhang (2010) concluded that the formation of the stone forest was related to lithologies, tectonic movements, geomorphology, and weak layers in the rock masses; based on the flowing water, joints, and seasonal winds in this area, Zhang (2014) and Xu and Fan (2008) divided the YJSF landscapes into three major geological relics, consisting of geological structures, geomorphic, and geo-hazard types. These achievements have played an important role in further research of the stone forest. However, it is worth noting that few studies have been conducted on the rock mass structural planes of the stone forest, lacking profound analysis for the slope stability.

A series of observations and research studies have been conducted worldwide on the influences of rock mass structure planes for the slope stability (Lv et al., 2014; Stead and Wolter, 2015). Müller et al. (1970) realized the importance of structure planes to the mechanical characteristics and stability of rock masses; Gu and Wang (1979) put forward the control theory of rock mass structures, clarifying that the existence of rock mass structural planes has an important control effect on the deformation and failure of rock masses. Moreover, the occurrence, scale, density, shape, and combination types of structural planes are the main criteria for analyzing and evaluating the slope stability (Vick et al., 2020).

Hence, based on the detailed field investigation we conducted, this article classifies structural planes and their combination types contained in rock masses of the YJSF, northwestern Loess Plateau, China, in detail. On this basis, combined with physical, mechanical, and hydraulic properties of the rock masses, disaster-induced patterns and mechanisms of the rock mass structural planes are classified and discussed, to shed light on the importance of the structure planes for the slope stability in the YJSF area. The studied results will provide the critical, theoretical, and technical support for the slope stability analysis, scenic geological heritage protection, and disaster warning in this area.

BACKGROUND OF THE STONE FOREST

Geological Characteristics

The Tibetan Plateau and the Loess Plateau are one of the most important landform units in China, attracting a lot of researchers worldwide (Ding et al., 2014; Peng et al., 2019). The YJSF is located in the transition zone between the Loess Plateau and the Tibetan Plateau (**Figure 1A**). Due to the extensive uplifting of the Tibetan Plateau during the Cenozoic period, the transition zone and its surrounding areas are characterized by a series of active faults (Yao et al., 2019), especially the Haiyuan active fault which induced massive earthquakes (Tian et al., 2002; Li et al., 2019; Shi et al., 2020; Xu et al., 2021). The studied area is situated at the Laolongwan Depression on the western part of the Haiyuan fault zone (**Figure 1B**). Research confirmed that the Laolongwan Depression is a small Quaternary rift basin controlled by three groups of faults in the NWW, NEE, and NNE directions (Fan, 2014), with the basin's subsidence range exceeding 200 m. Uplifting fault blocks around the depression periphery were developed, including the Mijia-Hasi Mountain to the north, Songjia Mountain to the south, Hongxiantai to the west, and Liupan Mountain to the east.

The strata in the Laolongwan Depression are mainly composed of Cenozoic sedimentary rocks (Fan, 2006; Fan, 2014), which are dominated by Quaternary fluvial and lacustrine facies with a thickness of up to hundreds of meters (**Figure 2**). According to the degree of rock consolidation, these sedimentary rocks can be divided into upper and lower parts. Among them, the lower part is the Early Pleistocene Wuquanshan Formation with a good degree of consolidation. This formation consists of upper and lower sections, of which the lower rocks are composed of gray–yellow conglomerates with high argillaceous contents and muddy sandstones, while the upper rocks resemble the former, but have lower argillaceous contents. The upper part mainly consists of floodplain facies sandstones and conglomerates, as well as a small amount of aeolian loess. The modern Yellow River flows through the depression basin from west to east, dividing the Cenozoic sedimentary formation into east and west blocks, and the YJSF is developed at the turn of the Yellow River in the western block (**Figure 1B**).

Topography and Geomorphology Characteristics

The terrain of the YJSF is generally high in the southwest and northeast, with low terrain in the middle. The highest elevation is 3,010 m, and the lowest is 1,390 m with an average of 2000 m. According to the classification characteristics of geomorphology, the stone forest displays the typical features of peak-forest plains and peak clusters (**Figure 3**). The top of a single peak shows a conical and flat shape, with obvious differences in height between

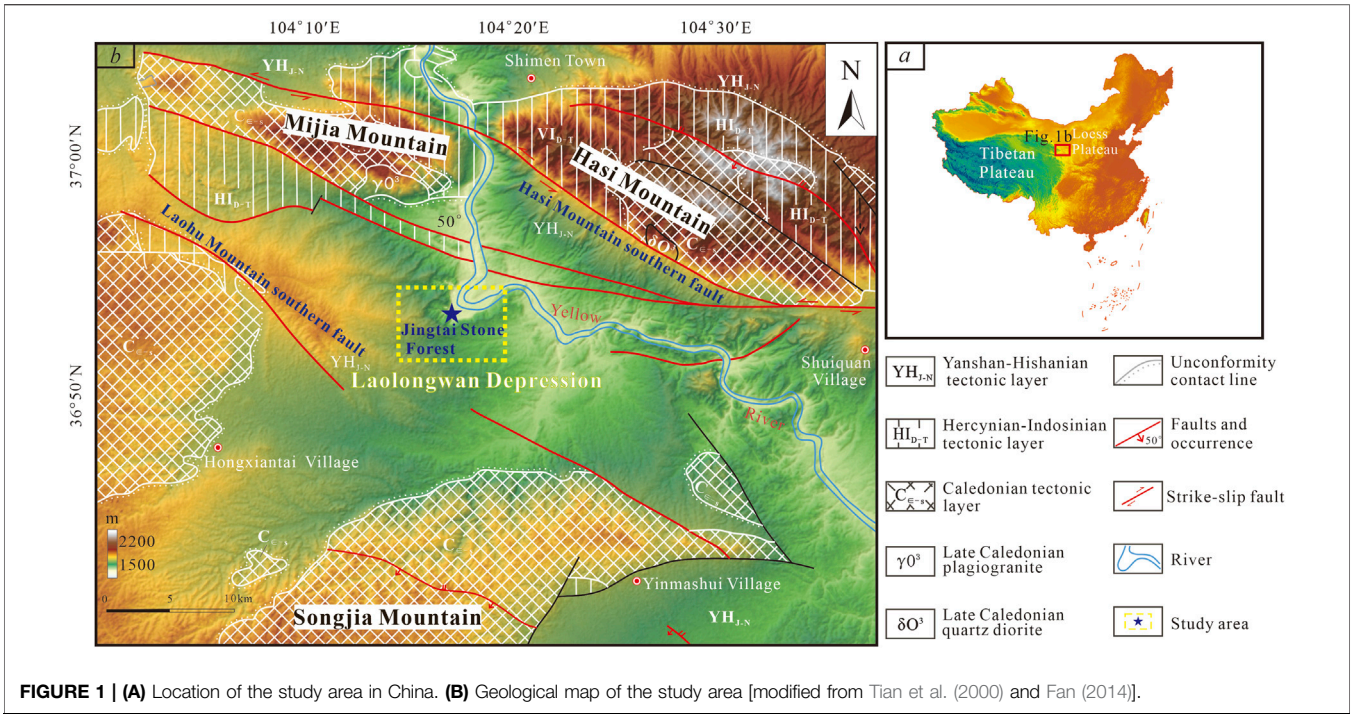

FIGURE 1 | (A) Location of the study area in China. **(B)** Geological map of the study area [modified from Tian et al. (2000) and Fan (2014)].

the peaks. Bases between the peaks were connected to each other, showing two morphologies of "U" and "V" types. Moreover, there are multilevel active fault-related steeps developed in the upper reaches of the valley, and aeolian landforms such as wind-eroded dimples and wind-eroded niches can be seen on both sides of the ditch wall.

Climate and Hydrological Characteristics

The studied area is a typical temperate continental arid climate with scarce precipitation. The precipitation in this area is mainly concentrated in the range of July to September and shows a gradual decrease trend from south to north. Its maximum precipitation in a day can reach 57.1 mm, of which the frequency of heavy rains is 1–2 times/year (Fan, 2014). Additionally, precipitation in a wet year is 2–3 times that of a dry year, showing apparent interannual variation traits. Obviously, drought and low rainfall are the major characteristics of climate and hydrology in this area, which played an important role in the formation and evolution of the YJSF and its slope stability.

Collectively, it can be concluded that the formation of the YJSF was closely related to tectonic activities, rock types, topography, and geomorphology, as well as climate and hydrological conditions.

TYPES AND CHARACTERISTICS OF ROCK-MASS STRUCTURAL PLANES

The types and characteristics of structural planes in rock masses are very important to the slope stability (Gori et al., 2014; Vick et al., 2020). They can result in discontinuity and non-uniformity of the rock masses. The structural planes of the YJSF can be divided into primary, tectonic, and secondary structural planes, according to their geological genesis, and they jointly control the stability of the slope in this area, as described below.

Primary Structural Planes

Primary structural planes in the YJSF are composed of layers and weak interlayers (**Figures 4A–C**). The sedimentary layers are the most widely distributed structural planes in the rock mass of the stone forest, mainly developed during the Quaternary Wuquanshan Formation with extensive outcropping in this area (accounting for 70% in the Laolongwan Depression). The strata tilt toward southwest as a whole, and their dip angles vary between 10° and 30°. Their surfaces are relatively flat and well extended, with the intervals of these layers varying from 0.2 to 1 m. The weak interlayers consist of silty mudstones, claystones, and highly muddy sandstones, with a poor consolidation degree and high clay content, and the thickness ranges from 5 to 10 cm. Compared with the layers, the weak interlayers in rock masses have a significant impact on the stability of the YJSF slope, due to their poorer mechanical properties and easy softening or muddying in contact with water (Peng et al., 2015).

The primary structural planes are a weak structural zone, and thus many cavities such as wind-eroded dens and niches were formed under the action of wind erosion, abrasion, and erosion of rainwater around these planes, which is a common phenomenon in the YJSF area. Moreover, they resulted in the occurrence of a free surface in the rock slope, which is one of the important factors causing the slope instability in the YJSF.

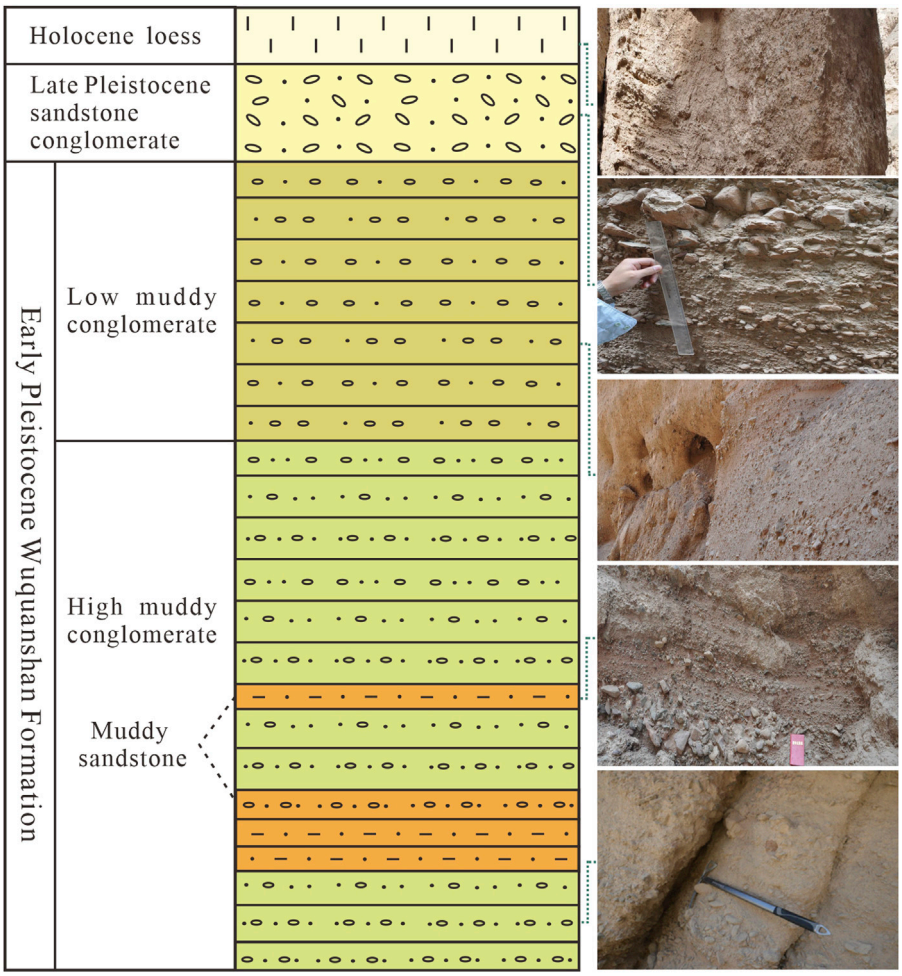

FIGURE 2 | Strata histogram and corresponding lithological photos of the YJSF. The lower part is the Early Pleistocene Wuquanshan Formation consisting of upper and lower sections, with different consolidation degrees. The upper part mainly consists of floodplain facies sandstones and conglomerates, as well as a small amount of aeolian loess.

Tectonic Structural Planes

Tectonic structural planes are a fractured plane in rock and soil caused by tectonic stress, including faults, joints, cleavages, and interlayer dislocation planes (Arai and Chigira, 2019; Shao et al., 2019; Blahüt et al., 2020). The tectonic structural planes of the YJSF mainly consist of faults and joints (**Figures 4D–H**, **5**). These faults are dominated by active faults in the NW and NE directions, extending 2–10 km with a 5- to 30-cm-wide fracture zone developed along the faults. Moreover, the fracture zone is well open and filled with sand and gravel, of which some have been muddied into weak interlayers. A group of X-shaped faults can be seen in the Laolonggou area, the southwestern part of the stone forest, indicating that the direction of regional tectonic principal stress is dominated by the NE–SW directions. These faults controlled the flow direction of the Yellow River and the development of valley's water systems, making the river and its tributaries typical grid-like and comb-like frameworks. Meanwhile, they cut the sedimentary strata into different shape blocks, and the opening degree of the fracture near the slope of the valley is much larger than that of other sections. The development characteristics of these faults provide a prerequisite for the formation of the YJSF.

Except for the faults, joints are also one of the most widely developed structural planes in the studied area, which are mainly distributed in the three regions including the Laolong Valley, Yinma Valley, and Panlong Cave (**Figure 5**). The Laolong Valley is dominated by vertical joints, and their directions are roughly 340°–350°and 65°–70°, with the joint spacing of 3–18 m. Field investigation shows that they were used as the dominant infiltration channel, and some gullies with a width of 50–100 cm have been formed during the erosion of flowing water, where a series of huge sandy gravel blocks were found within the gullies. There are two types of vertical and oblique joints developed in the Yinma Valley. The vertical joint directions display 10° and 345° trends, and the oblique joint dips are NNE and SW, respectively, with a

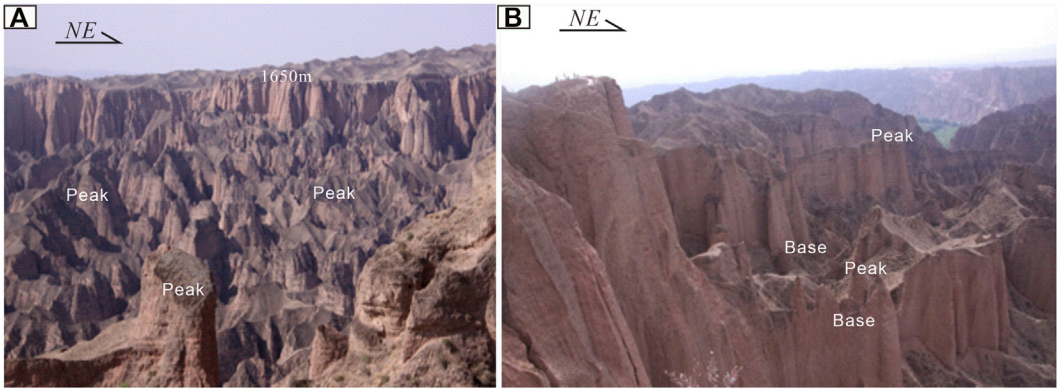

FIGURE 3 | Typical features of peak forest plains and peak clusters in the study area.

dip angle of 20°–30°. The joint spacings range from 2 to 3 m, and their open distances are 5–10 cm. The Panlong Cave joints are relatively simple, and a group of near-vertical tensile joints are developed in the NWW direction. The dip and dip angle are 340° and 80°, respectively, which is nearly parallel to the strike of the Panlong Cave. The average distance between joints is about 9 m. The open gap of joints near the stone forest valley is 50–80 cm, while others are 8–10 cm away from the valley. Massive breccia having weak consolidation is filled with these joint gaps.

Secondary Structural Planes

Secondary structural planes in the YJSF are mainly composed of unloading cracks and secondary intercalated muddy rocks (**Figures 4I, J**), but they are all locally distributed. Unloading cracks were majorly generated at the edge of the slope, characterized by a discontinuous distribution and rough fissure surface. Secondary intercalated muddy rocks were generally filled within the unloading cracks, further leading to the large gaps between fissure surfaces. The formation of secondary structural planes in this area was closely correlated with the gravitational forcing and weathering, coupled with rainfall infiltration.

In summary, the studied primary structural planes were related to the formation of sedimentary rocks, the tectonic structural planes mainly resulted from tectonic activities, and the secondary structural planes were correlated with gravity, water, and wind.

PHYSICAL AND MECHANICAL PROPERTIES AND WATER SENSITIVITY

The YJSF is dominantly composed of conglomerates and muddy sandstones. We sampled 30 representative samples in the Laolong Valley, Yinma Valley, and Panlong Cave areas, to analyze the physical and mechanical properties of these rocks under the conditions of natural situation and immersion infiltration, as well as hydraulic properties. Tensile (splitting method), shear (inclination compression mold), and grain-size analysis tests were designed for the conglomerates and muddy sandstones. In addition, as muddy sandstones have obvious softening and disintegration characteristics after encountering water, a fast shear test for the rock was designed.

Grain-Size Analysis

The grain-size analysis results showed that the conglomerates are characterized by uneven grain-size distribution and continuous particle gradation, and on the contrary, the muddy sandstones have the features of uniform grain-size distribution and discontinuous particle gradation (**Figure 6**). The range diagrams of grain-size content display that both the conglomerates and the muddy sandstones have single-peak curve features; the particles that were cemented into conglomerates are mainly medium-fine gravels, with a small amount of medium-sized sand; and the muddy sandstones are dominated by fine-sized sand and less clay contents, which is one of the critical reasons for the weak cementation of the YJSF.

Tensile and Shear Strength Analyses

The test results showed that the tensile and shear strengths of conglomerates were only 60–70% of those of muddy sandstones under natural situation (**Table 1**), indicating the degree of conglomerate cementation is lower than that of muddy sandstones. However, under the condition of immersion infiltration, the tensile and shear strengths of the conglomerates and muddy sandstones decreased sharply, which is only 5–10% of those of the natural situation, and their shear strengths were much greater than the tensile strength. Meanwhile, under immersion infiltration, the shear strength of conglomerates was greater than that of muddy sandstones.

During the fast shear test, the cohesion and internal friction angle of muddy sandstones under immersion infiltration were 81 kPa and 20.7° (**Table 1**), respectively, which were smaller than the shear strength under the condition of inclination compression mold. Besides, in the direct shear process, when the deformation

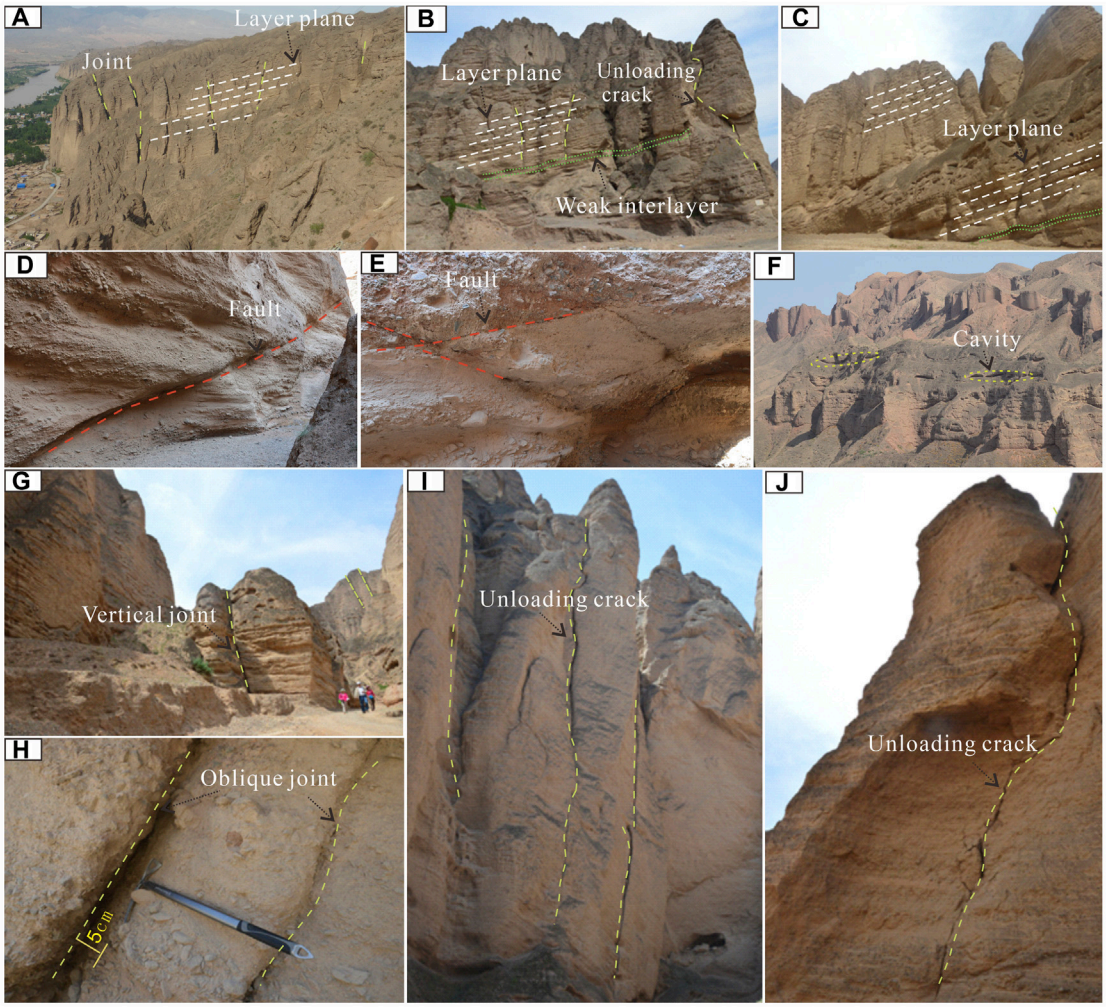

FIGURE 4 | Structural plane types and combination characteristics of typical rock slopes in the study area. **(A)** Layer plane and joint; **(B,C)** layer plane, joint, and weak interlayer; **(D,E)** fault; **(F)** cavity; **(G,H)** vertical and oblique joints; and **(I,J)** unloading fracture.

reached 0.2 mm, the muddy sandstones had a peak strength of 88–192 kPa which increased with increase in the confining pressure (**Figure 7**), and the residual strength differed from it by 5–10%. This result shows that the muddy sandstones in the YJSF are characterized by strain softening.

Thus, under the condition of natural situation, both the conglomerates and muddy sandstones in the YJSF have strong tensile and shear strengths, while under immersion infiltration, the collapsibility of muddy sandstones is more obvious, which usually leads to the lack of rock mass and induces slope instability in this area.

Water Sensitivity Analysis

As aforementioned, the physical property tests show that the conglomerates and muddy sandstones in this area have obvious water sensitivity features. Therefore, in order to explore the causes of water sensitivity, a microscopic identification and composition analysis were carried out on two rocks.

The results showed that the conglomerates and muddy sandstones are composed of debris, interstitials, and storage spaces (**Figure 8**). Among them, the debris that was dominated by quartz and feldspar was the main component of the two rocks accounting for 50–60%; the interstitials were mainly muddy fillings, and obviously appear in muddy sandstones and conglomerates; and the storage spaces were all secondary pores, mainly including water-soluble pores and structural fractures.

It was found that the muddy fillings consist of water-sensitive minerals, such as kaolin, hydromica, and illite. When these minerals meet with water, the particles will swell (Leng et al., 2021), making the rock structure to easily collapse. Moreover, muddy components in the rock masses may be taken away by water, forming water-soluble pores and further enhancing the possibility of structural disintegration. Additionally, the muddy fillings also display colloidal properties after encountering water, and have strong flow plasticity and water holding capacity. After continuous water erosion, clay minerals in the muddy sandstones

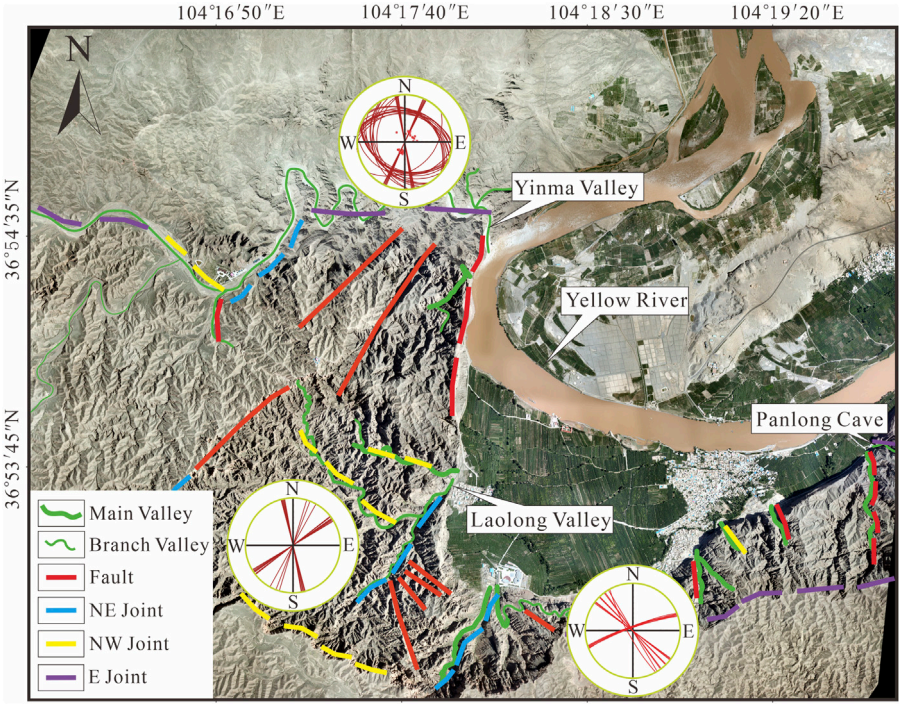

FIGURE 5 | Distribution of faults and joints in the study area. Strikes of faults and joints are dominated by the NWW and NE directions.

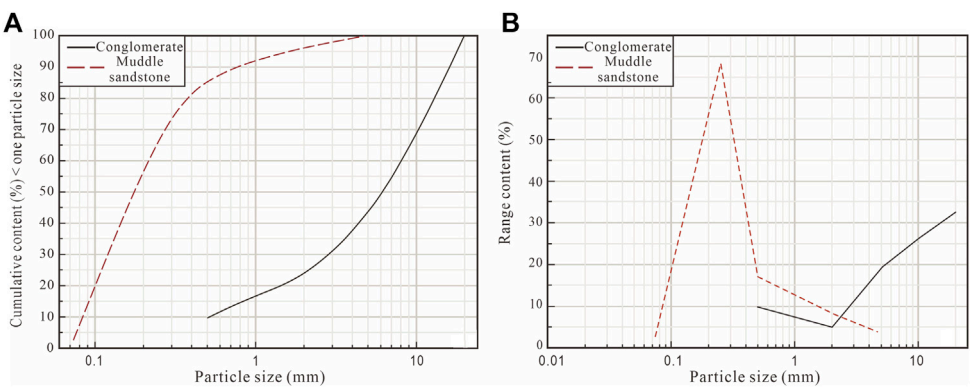

FIGURE 6 | Grain size curves of the conglomerate **(A)** and muddy sandstone **(B)**. The conglomerate is characterized by uneven grain size distribution and continuous particle gradation, and on the contrary, the muddy sandstone has the features of uniform grain size distribution and discontinuous particle gradation.

are lost and their strengths are weakened, resulting in the occurrence of cavities in the rock masses. Therefore, the water sensitivity characteristics of the stone forest have a significant influence on the slope stability.

STRUCTURAL PLANE COMBINATION AND THE FAILURE MECHANISM

According to the aforementioned structural characteristics and their influence on slope stability, this article divides the types of structural planes related to the slope failure of the YJSF into four main types. 1) Combination of vertical joints and weak interlayers (**Figures 4A,B**). The strike of weak layers is consistent with that of the rock slope, and the vertical joints cut rock masses with a certain width to form quadrangular prism–shaped or inverted cone–shaped blocks. 2) Combination of vertical joints and oblique joints (**Figures 4B,D,H**). The dip direction of the oblique joints is consistent with that of the rock slope. They jointly cut the rock mass to form quadrangular prism–shaped or irregular blocks. 3) Combination of vertical joints, oblique joints, and weak interlayers (**Figure 4B**). The dip direction of the oblique

TABLE 1 | Test results on the muddy sandstone and conglomerate in the stone forest.

Type	Tensile strength (MPa)				Shear strength			
Condition	Natural situation		Immersion infiltration		Natural situation		Immersion infiltration	
	Single	Average	Single	Average	C (MPa)	Φ (°)	C (MPa)	Φ (°)
Muddy sandstone	0.724	0.755	0.031	0.039	2.03	40.4	0.141	38.6
	0.728		0.039					
	0.812		0.048					
	-	-	-	-	-	-	0.081 (fast shear)	20.7 (fast shear)
Conglomerate	0.356	0.425	0.030	0.035	1.61	41.3	0.146	39.9

Note: C, cohesion; Φ, internal friction angle.

joints is consistent with that of the weak interlayers. They jointly cut the rock mass to form irregular blocks. 4) Combination of unloading joints and layer planes (**Figures 4I,J**). The dip direction of the unloading joints is consistent with that of the layers, which jointly divide the rock mass into irregular blocks.

This combination of structural planes controls the slope stability of the YJSF, and the corresponding failure patterns and mechanism are as follows:

Creeping Slide-Tension Failure

Studies show that the differences in the degree of softness and hardness of the layered rock masses constituting the slope, as well as the location of the soft and hard layers, have an important impact on the slope stability (Insua-Arévalo et al., 2021; Wang et al., 2021). The stratum formation of the YJSF was characterized by relatively soft layers in the upper section and hard layers in the lower section; the upper part is mainly poorly consolidated floodplain facies and secondary aeolian loess, with low strength, while the lower was the Early Pleistocene Wuquanshan Formation with a long diagenesis time and good degree of consolidation which is hard and not easy to deform. Thus, the contact surface between the two layers was a structurally weak zone, similar to a weak interlayer. Under the long-term action of gravity, this kind of sedimentary construction combination tends to develop creeping deformations and failures of the overlying weak rocks along the structurally weak zone (**Figure 9A**). Additionally, based on the aforementioned physical mechanics and water sensitivity tests, the muddy sandstone strata contained in the conglomerates of the Wuquanshan Formation have relatively weak tensile and shear strengths, and especially under the condition of immersion in water, they are prone to disintegration. Therefore, it can also be found that the interlayers of muddy sandstones generated a non-uniform creep in the overlying stress and the action of water infiltration, causing the overlying relatively hard conglomerate to produce cracking characteristics at its bottom.

Gradual Failure

Investigation results show that there are many cavities in the rock layers of the YJSF area, and their formation was mainly related to the muddy sandstones that were sandwiched between the upper and lower conglomerate layers. The mechanism forming these cavities mainly include two aspects: on the one hand, the local

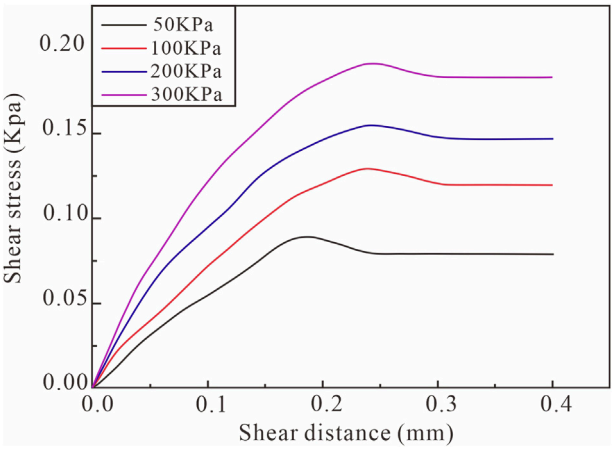

FIGURE 7 | Stress–strain curves of the muddy sandstone under the immersion infiltration (fast shear test).

disintegration and shedding of particles such as quartz and feldspar occur under the action of wind blowing and abrasion; on the other hand, the muddy sandstones contain massive water-sensitive minerals (e.g., kaolin, illite, and montmorillonite), which swells under the action of high rainfall, leading to the destruction of a muddy sandstone structure. Moreover, under the combined action of the two kinds of external dynamic geology, a special phenomenon that underlying soft rocks were absent and upper hard rocks were suspended extensively appears in the rock wall of the YJSF. Specially, when the muddy sandstones were developed at the bottom of the stone forest, due to the continuous later erosion of the Yellow River, massive large cavities were generated in this area resulting in the occurrence of overlying dangerous rock masses that are predominantly composed of conglomerates. These suspended dangerous rock masses will be gradually collapsed and destroyed due to the gravitational forcing, earthquakes, and other actions (**Figure 9B**), of which the point of rupture initiation usually follows the preexisting structural planes within the overlying rock masses.

Slipping Failure

In the YJSF area, especially the Yinma Valley area, the rock masses were jointly cut by multiple sets of vertical joints and a

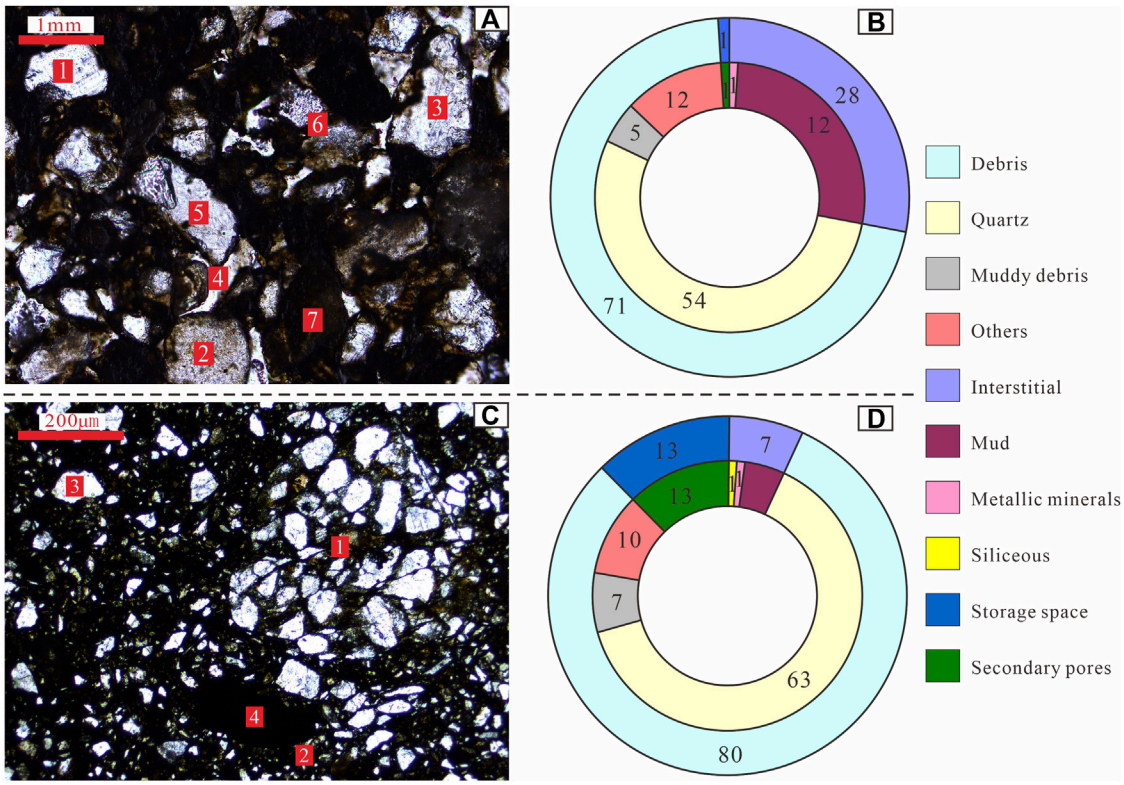

FIGURE 8 | Microscopic characteristics and composition proportion of the conglomerate **(A,B)** and muddy sandstone **(C,D)**. **(A)** 1–6: quart and feldspar debris; 7: muddy fillings; **(C)** 1–3: quart and feldspar debris; and 4: muddy fillings.

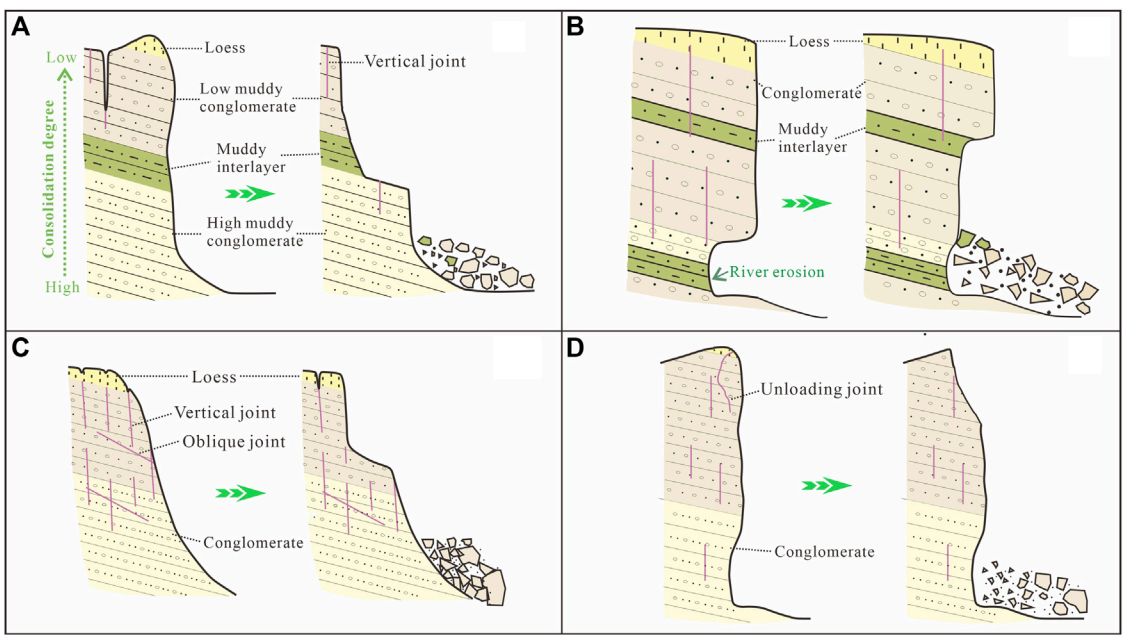

FIGURE 9 | Schematic failure mechanism diagrams of the YJSF. **(A)** Creeping slide-tension failure, **(B)** gradual failure, **(C)** slipping failure, and **(D)** dumping failure.

set of oblique joints, forming different scale rock blocks. The vertical joints are gradually expanded downward under a series of factors, such as self-weight stress of rock mass, regional tectonic uplifting, and rainfall infiltration. When the vertical structural planes are not completely transfixed or supported by other rock masses, the rock masses remain stable. As the vertical joints gradually expand downward into the oblique joint planes, the rock masses could slide out along the inclined direction of the oblique joint in the lower part, thus forming a slipping failure feature (**Figure 9C**).

Dumping Failure

There are a series of unloading cracks developed in the rock slopes of the YJSF, which are curved in shape (**Figures 4I,J**). These cracks were filled with some sands, conglomerates, and loess, and their opening degrees gradually decrease from the top to the bottom. The formation was related to the self-weight stress and weathering unloading. Moreover, the water sensitivity experiments discussed above show that the muddy sandstones and conglomerates contain some argillaceous components, which will swell after encountering water, leading to the destruction of these rock structures and disintegration. During downward expansion of these unloading cracks, the center of gravity of the dangerous rock masses gradually moves outward, and finally, it could result in dumping failure (**Figure 9D**).

DISCUSSION

Structural planes and their combinations have played an important role in the stability of rock-soil mass slopes (Gu and Wang, 1979; Lv et al., 2014). The stability of the YJSF is related to the coupling action of endogenic and exogenic geological processes. The endogenic dynamic geological processes mainly originated from the Cenozoic uplifting, fault activities, and earthquakes of the Tibet Plateau. During the uplifting process, the Cenozoic sediments in the Laolongwan Depression were affected by differential uplifting and compressional tectonics, resulting in the appearance of strata deformation and a series of tectonic structural planes. These processes could lead to the loosening of the rock mass and reduce their strength. In addition, the northeastern margin of the Tibet Plateau is an area of strong earthquakes, such as the 1920 Haiyuan earthquake (Tian et al., 2000; Tian et al., 2002; Yao et al., 2019; Xu et al., 2021). The process of earthquake has the effect of shattering rock mass, leading to the further development of rock mass structural planes in this basin and appearance of different combinations of structural planes as discussed above.

The studied area is located in a temperate continental climate zone (Fan, 2006), and thus the exogenic dynamic geological processes are dominated by rainfalls and winds. Annual rainfall contents in this area are relatively scarce, but heavy rainfall may occur many times (Zhang, 2010; Zhang, 2014). The rainwater infiltrates into the rock masses along the structural planes; on the one hand, it caused the valley erosion and formed a disaster-generating free surface, and on the other hand, the water in the structural planes can generate hydrodynamic and hydrostatic pressures (Peng et al., 2015), which all aggravate the instability of the YJSF slope. Meanwhile, the muddy sandstones in the area are characterized by strong water sensitivity, which is also one of the important factors causing the slope instability. Compared with the effect of rainfalls, the direct effect of winds is not obvious, but it can denude and blow away the surface-weathered materials for a long time, causing the rock masses to unload and rebound, and further aggravating the development of structural planes in the YJSF area.

CONCLUSION

Massive structural planes are developed in rock slopes of the YJSF area, northwestern Loess Plateau, China. This article, based on a detailed field investigation, classifies structural planes and their combination types contained in rock masses of the YJSF. On this basis, combined with physical, mechanical, and hydraulic properties of the rock masses, disaster-induced patterns and mechanisms of the rock mass of structural planes are classified and discussed. The main results gained are as follows:

1) The structural planes of the YJSF can be divided into three types, namely, primary structural plane, tectonic structural plane, and secondary plane. They not only combine with each other to cut the rock masses into different-shape blocks but also jointly control the stability of the rock mass slopes.
2) The physical and mechanical tests and water sensitivity characteristics show that the conglomerates and muddy sandstones which are the main components of the YJSF have greater tensile and shear strengths under natural situation, while their strengths are reduced under immersion infiltration; in particular, the muddy sandstones are more sensitive to water and have a lower strength than that of the conglomerates.
3) The failure mechanism of the YJSF is mainly related to the combination of various structural planes, which can be divided into four failure patterns, namely, creeping slide-tension failure, gradual failure, slipping failure, and dumping failure. This study will have a critical influence on the stability analysis of rock slopes and disaster warning in this area.

DATA AVAILABILITY STATEMENT

The original contributions presented in the study are included in the article/Supplementary Material; further inquiries can be directed to the corresponding author.

AUTHOR CONTRIBUTIONS

YLY performed field investigation, wrote the manuscript, and conducted analysis. GG performed field investigations and experiment. ZW performed field investigations, wrote the

manuscript, and conducted analysis. YL performed field investigation and interpretation of data for the work. PM performed field investigation and conducted analysis. JP designed the work and conducted field investigations and writing.

FUNDING

This research was financially supported by the National Natural Science Foundation of China (Grant No. 41672285) and the Fundamental Research Funds for the Central Universities, CHD (Grant Nos. 300103190742, 300102271403, and 300102261403).

ACKNOWLEDGMENTS

We gratefully appreciate editor YX and two reviewers for their constructive reviews and suggestions, which essentially improved the quality of this article.

REFERENCES

An, Z. (2000). The History and Variability of the East Asian Paleomonsoon Climate. *Quat. Sci. Rev.* 19, 171–187. doi:10.1016/s0277-3791(99)00060-8

Arai, N., and Chigira, M. (2019). Distribution of Gravitational Slope Deformation and Deep-Seated Landslides Controlled by Thrust Faults in the Shimanto Accretionary Complex. *Eng. Geology.* 260, 105236. doi:10.1016/j.enggeo.2019.105236

Blahüt, J., Mitrovic-Woodell, I., Baroň, I., René, M., Rowberry, M., Blard, P. H., et al. (2020). Volcanic Edifice Slip Events Recorded on the Fault Plane of the San Andrés Landslide, El Hierro, Canary Islands. *Tectonophysics* 776, 228317. doi:10.1016/j.tecto.2019.228317

Ding, L., Xu, Q., Yue, Y., Wang, H., Cai, F., and Li, S. (2014). The Andean-type Gangdese Mountains: Paleoelevation Record from the Paleocene-Eocene Linzhou Basin. *Earth Planet. Sci. Lett.* 392, 250–264. doi:10.1016/j.epsl.2014.01.045

Fan, W. J. (2014). Study on the Sustainable Development of the Yellow River Stone Forest Geological Landscape in Gansu Province. Dissertation`s thesis. China, Beijing: China University of Geosciences.

Fan, X. (2006). "Landscape Characteristics and Genesis Mechanism of the Yellow River Stone Forest, Gansu Province," in The 21st Annual Meeting of Tourism Geology and Geoparks Research Branch of Geological Society of China, Xi'an, China, 2006, 363–367. (in Chinese).

Gori, S., Falcucci, E., Dramis, F., Galadini, F., Galli, P., Giaccio, B., et al. (2014). Deep-seated Gravitational Slope Deformation, Large-Scale Rock Failure, and Active normal Faulting along Mt. Morrone (Sulmona basin, Central Italy): Geomorphological and Paleoseismological Analyses. *Geomorphology* 208, 88–101. doi:10.1016/j.geomorph.2013.11.017

Gu, D. Z., and Wang, S. J. (1979). "The Basic Problems of Engineering Geological Mechanics. Engineering Geology Professional Committee, Geological Society of China," in Proceedings Of the 1st Chinese Geological Academic conference, Suzhou (China), 1979, 182–189.

Insua-Arévalo, J. M., Tsige, M., Sánchez-Roldán, J. L., Rodríguez-Escudero, E., and Martínez-Díaz, J. J. (2021). Influence of the Microstructure and Roughness of Weakness Planes on the Strength Anisotropy of a Foliated clay-rich Fault Gouge. *Eng. Geology.* 289, 106186. doi:10.1016/j.enggeo.2021.106186

Leng, Y. Q., Peng, J. B., Wang, S., and Lu, F. (2021). Development of Water Sensitivity index of Loess from its Mechanical Properties. *Eng. Geology.* 280, 105918. doi:10.1016/j.enggeo.2020.105918

Li, B., Chen, X., Zuza, A. v., Hu, D., Ding, W., Huang, P., et al. (2019). Cenozoic Cooling History of the North Qilian Shan, Northern Tibetan Plateau, and the Initiation of the Haiyuan Fault: Constraints from Apatite- and Zircon-Fission Track Thermochronology. *Tectonophysics* 751, 109–124. doi:10.1016/j.tecto.2018.12.005

Lv, Y., Peng, J., and Wang, G. (2014). Characteristics and Genetic Mechanism of the Cuihua Rock Avalanche Triggered by a Paleo-Earthquake in Northwest China. *Eng. Geology.* 182, 88–96. doi:10.1016/j.enggeo.2014.08.017

Müller, L., Malina, H., and Baudendestel, M. (1970). "The Effect of the Geologic Structure on the Stability of an Underground Powerhouse," in 2nd congress Of I. S. R. M, Belgrade, 1970.

Nie, J., Stevens, T., Rittner, M., Stockli, D., Garzanti, E., Limonta, M., et al. (2015). Loess Plateau Storage of Northeastern Tibetan Plateau-Derived Yellow River Sediment. *Nat. Commun.* 6, 8511. doi:10.1038/ncomms9511

Peng, J., Fan, Z., Wu, D., Zhuang, J., Dai, F., Chen, W., et al. (2015). Heavy Rainfall Triggered Loess-Mudstone Landslide and Subsequent Debris Flow in Tianshui, China. *Eng. Geology.* 186, 79–90. doi:10.1016/j.enggeo.2014.08.015

Peng, J., Wang, S., Wang, Q., Zhuang, J., Huang, W., Zhu, X., et al. (2019). Distribution and Genetic Types of Loess Landslides in China. *J. Asian Earth Sci.* 170, 329–350. doi:10.1016/j.jseaes.2018.11.015

Shao, C., Li, Y., Lan, H., Li, P., Zhou, R., Ding, H., et al. (2019). The Role of Active Faults and Sliding Mechanism Analysis of the 2017 Maoxian Postseismic Landslide in Sichuan, China. *Bull. Eng. Geol. Environ.* 78, 5635–5651. doi:10.1007/s10064-019-01480-8

Shi, Y.-t., Gao, Y., Shen, X.-z., and Liu, K. H. (2020). Multiscale Spatial Distribution of Crustal Seismic Anisotropy beneath the Northeastern Margin of the Tibetan Plateau and Tectonic Implications of the Haiyuan Fault. *Tectonophysics* 774, 228274. doi:10.1016/j.tecto.2019.228274

Stead, D., and Wolter, A. (2015). A Critical Review of Rock Slope Failure Mechanisms: The Importance of Structural Geology. *J. Struct. Geology.* 74, 1–23. doi:10.1016/j.jsg.2015.02.002

Tian, Q. J., Ding, G. Y., and Shen, X. H. (2002). Seismic Tectonic Model of the Northeastern Corner of the Tibet Plateau. *Earthquake* 22, 9–16. (in Chinese).

Tian, Q. J., Shen, X. H., Ding, G. Y., Chen, Z. W., and Wei, K. H. (2000). Discovery and Preliminary Study of the Laolongwan Tertiary Pull-Apart basin in the Haiyuan Fault Zone. *Seismology Geology.* 22, 329–336 (in Chinese).

Vick, L. M., Böhme, M., Rouyet, L., Bergh, S. G., Corner, G. D., and Lauknes, T. R. (2020). Structurally Controlled Rock Slope Deformation in Northern Norway. *Landslides* 17, 1745–1776. doi:10.1007/s10346-020-01421-7

Wang, J., Chen, G., Xiao, Y., Li, S., Chen, Y., and Qiao, Z. (2021). Effect of Structural Planes on Rockburst Distribution: Case Study of a Deep Tunnel in Southwest China. *Eng. Geology.* 292, 106250. doi:10.1016/j.enggeo.2021.106250

Xu, K. J., and Fan, X. (2008). Characteristics and Evaluations of Geological Trace Landscapes of Yellow River Hoodoo Nation Geopark. *J. Arid Land Resour. Environ.* 22, 111–115. (in Chinese).

Xu, Y., Liu-Zeng, J., Allen, M. B., Zhang, W., and Du, P. (2021). Landslides of the 1920 Haiyuan Earthquake, Northern China. *Landslides* 18, 935–953. doi:10.1007/s10346-020-01512-5

Yao, W., Liu-Zeng, J., Oskin, M. E., Wang, W., Li, Z., Prush, V., et al. (2019). Reevaluation of the Late Pleistocene Slip Rate of the Haiyuan Fault Near Songshan, Gansu Province, China. *J. Geophys. Res. Solid Earth* 124, 5217–5240. doi:10.1029/2018jb016907

Zhang, T. B. (2014). Evaluation and Utilizing of Yellow River Stone Forest Geoheritage Resource. Master`s thesis. China: Lanzhou University.

Zhang, Y. J. (2010). Genesis Analysis of Geological Relics in Gansu Province. *Gansu Sci. Technol.* 26, 46–49. (in Chinese).

Conflict of Interest: The authors declare that the research was conducted in the absence of any commercial or financial relationships that could be construed as a potential conflict of interest.

Publisher's Note: All claims expressed in this article are solely those of the authors and do not necessarily represent those of their affiliated organizations, or those of the publisher, the editors, and the reviewers. Any product that may be evaluated in this article, or claim that may be made by its manufacturer, is not guaranteed or endorsed by the publisher.

frontiers in Earth Science

ORIGINAL RESEARCH
published: 16 February 2022
doi: 10.3389/feart.2022.818919

The Compression Behavior of Undisturbed and Compacted Loess Under the Controlling of Total Suction and Injected Solutions

Tongwei Zhang[1], Zhengjin Hu[1], Hengxing Lan[2,3]*, Yongfeng Deng[4] and Huyuan Zhang[1]*

[1]College of Civil Engineering and Mechanics, Key Laboratory of Mechanics on Disaster and Environment in Western China MOE, Lanzhou University, Lanzhou, China, [2]School of Geological Engineering and Geomatics, Chang'an University, Xi'an, China, [3]State Key Laboratory of Resources and Environmental Information System, Institute of Geographic Sciences and Natural Resources Research, Chinese Academy of Sciences, Beijing, China, [4]School of Transportation, Institute of Geotechnical Engineering, Southeast University, Nanjing, China

Thousands of square kilometers of habitable land have been created on the Loess Plateau in China. In arid and semi-arid area of Northwest China, the mechanical behavior of structural loess is sensitive to water intrusion and human engineering activities. Meanwhile, the higher water salinity in loess and seasonal variation of ambient humidity are common in this area. Due to different physical and mechanical properties of natural and compacted loess, the impacts of ambient humidity and saline water migration on their deformation are still unclear. This paper developed an oedometer test to investigate the compression behavior of natural and compacted loess under environmental humidity (represented by total suction Ψ) and injection water salinity (represented by osmotic suction Ψ_π) changing. The results showed that the void ratio variation Δe of compacted loess (the dry density is 1.8 g/m^3) under the impact of total suctions (from 14.01 to 146.23 MPa) and salinities of injected solution (0.17 mol/L NaCl, 0.29 mol/L Na_2SO_4 and distilled water) were under 0.01. The variation of void ratio for undisturbed loess increased about 8 times with 10 times decreasing of total suction, which was corresponding to the increase of relative humidity (*RH*). In the stage of solution injection, the deformation of undisturbed loess increased with the Ψ-Ψ_π increasing, and the differences between different samples reached to nearly 20 times. The mechanism was that the salt inside undisturbed loess would deliquescence when the *RH* was higher than DRH (Deliquescence Relative Humidity), and the natural structure collapsed. The compression index C_c of samples generally decreased with Ψ-Ψ_π, and the compressibility of undisturbed loess was higher. The swelling indices C_s of samples slightly decreased with Ψ-Ψ_π, but the variation was not significant. The strain-stress relationships of loess can be well described by Duncan-Chang constitutive model. Interestingly, the difference of initial deformation modulus ΔE_s of two loesses, which represented the structural compression under the coupling of total suction and osmotic suction, linearly related to the Ψ-Ψ_π. The $\Delta\varepsilon_{max}$ between the structural loess and compacted loess exponential increased with Ψ-Ψ_π. In the engineering practice, the humidity and saline water intrusion should be considered in the long-term behavior of loess in shallow layer.

Keywords: compression behavior, undisturbed loess, compacted loess, total suction, injection solutions

OPEN ACCESS

Edited by:
Yueren Xu,
China Earthquake Administration, China

Reviewed by:
Yong He,
Central South University, China
Pengju Qin,
Taiyuan University of Technology, China

****Correspondence:***
Tongwei Zhang
ztw@lzu.edu.cn
Hengxing Lan
Lanhx@igsnrr.ac.cn

Specialty section:
This article was submitted to Environmental Informatics and Remote Sensing, a section of the journal Frontiers in Earth Science

Received: *20 November 2021*
Accepted: *06 January 2022*
Published: *16 February 2022*

Citation:
Zhang T, Hu Z, Lan H, Deng Y and Zhang H (2022) The Compression Behavior of Undisturbed and Compacted Loess Under the Controlling of Total Suction and Injected Solutions. Front. Earth Sci. 10:818919. doi: 10.3389/feart.2022.818919

INTRODUCTION

In recent years, a large number of land reclamation projects in Loess Plateau are in progress, which located in the arid and semi-arid loess area. The loess in Western China is mainly a kind of silty clays, and the groundwater frequently composed of sodium sulfate and sodium chloride. The structural loess is easy to collapse under water intrusion. In the land reclamation area, the different physical properties of compacted and undisturbed loess will lead to uneven settlement near the interface of filling and excavating area. Under the coupling effect of water infiltration (rainfall, irrigation and groundwater migration) and human engineering activities, the mechanical properties of loess deteriorated. Especially, the climate changing leads to environmental humidity change. In the engineering practice, it is doubtful that the humidity and saline water intrusion should be considered in the long-term behavior of loess in shallow layer (Ng and Pang, 2000; Zhang et al., 2013; Daliakopoulos et al., 2016; Chen et al., 2017; Ivushkin et al., 2019).

The water chemistry effects on the compression behavior of soil has been drawn an extensive attention. Lu et al. (2020) (Zuo et al., 2020) indicated that the migration of groundwater will lead to the decrease of ion concentration of pore water, the decrease of bonding strength and the collapse of loess structure. Wen et al. (2014) (Wen and Yan, 2014) considered that the soluble salts existed on the surface of soil particles play a role of skeleton and cementation. Niu et al. (2021) (Niu and Yao, 2021) revealed that the elastic modulus of soil decreased after multiple drying-wetting cycles. Zhang et al. (2019) (Zhang and Wang, 2019) adopted the osmotic suction to characterize the chemical effects of pore water, and investigated its influences on the compression and permeability characteristics of remolded clay. Amir et al. (2018) (Amir Akbari et al., 2018) reported that the saline water infiltration significantly influenced the hydraulic characteristics of unsaturated soil in the subgrade of highway, and resulted in the collapse of soil. The reason was that the matrix suction changed with the environmental humidity.

The particular structure and water sensitivity of loess are the main factors of subgrade settlement. In practice, compaction has been frequently used to improve the strength of soil and bearing capacity of foundation. The water sensitivity of compacted loess is closely related to their mineralogy and microstructure (Ma et al., 2016). During compression, the moisture content of compacted loess increased by 4.4–7.4% (Mu et al., 2020). Then, there are some differences of the structure and water sensitivity between undisturbed and compacted loess. Recently, based on the development of unsaturated soil theory and test methods, there have been many valuable achievements in the study of compression behavior of loesses. Chang et al. (2020) (Chang et al., 2020) conducted consolidation and drainage triaxial shearing tests on undisturbed Q_3 loess and undisturbed Q_2 loess in Yan'an New Area. The results explored that the matrix suction controlled the strength and initial Young's modulus of unsaturated loess. Lan et al. (2021) (Lan et al., 2021) found that the cyclic expansion and contraction of loess slope correlated to the changes of humidity and temperature and established a prediction model. Qin *et al.* (2020) (Qin et al., 2020) indicated that the structural properties of unsaturated and saturated loesses during compression exhibited different trend and the anisotropy of samples tend to be stable as vertical strain increases. Besides of studies on loess, Deng et al. (2018) (Deng et al., 2018) pointed out the mineralogy of saturated remolded soil was the key factor controlling pore water salinity effects on their compression and permeability. Miller et al. (2006) (Debora and Miller, 2006) found that the osmotic suction should be considered in the matrix suction measurement, and the matrix suction was not proper to replace the total suction in unsaturated soil with high salinity. He *et al.* (2020) (He et al., 2020) studied the swelling and shrinkage characteristics of compacted GMZ bentonite by varying the concentration of NaCl solution and total suction. Results showed that the sample saturated with salt solution has a higher degree of saturation than the sample saturated with distilled water for a given total suction.

In summary, many researchers paid attention on the salinity, moisture content and micro-structure effects on mechanical properties of different soils (Loret et al., 2002; Debora and Miller, 2006; Koniorczyk and Gawin, 2008; Zhang et al., 2016; Elkady and Al-Mahbashi, 2017; Jabar and Rasul, 2017; Sato and Hattanji, 2018; He et al., 2020; Wang et al., 2020). While, few studies focus on the response of compression behavior of undisturbed loess and remolded loess to the environmental humidity change and saline water intrusion in the northwest arid and semi-arid areas. This paper aimed to reveal the different performance of engineering properties of remodeling and undisturbed loess under extreme climate and human activities. Then, a modified one-dimensional consolidation test with controlling humidity and intruded water salinity was developed. The compression behavior of undisturbed and remolded loess under the coupling of loading, total suction and osmotic suction were investigated. The results will provide a reference for the evaluation of long-term behavior of land reclamation project in Western China.

MATERIALS

The undisturbed loess was sampled at a depth of 1 m from the excavation area of a land reclamation site in Lanzhou New Area, Gansu Province. The basic physical properties of soil were determined according to Chinese standard GB/T 50,123–2019 for geotechnical tests. As shown in **Table 1**, the initial void ratios of natural loess and compacted loess were 1.14 and 0.53 respectively. The differences of permeability coefficient between these two loesses were 10 times. The particle size distribution of fine particles based on laser analysis is shown in **Figure 1**. The XRD pattern shown in **Figure 2** indicates that the main clay minerals are illite-smectite mixed layer and kaolinite. The KCl, $MgCl_2$, Ki, $ZnSO_4$, K_2CO_3 and Na_2SO_4 were used to prepare saturated salt solution. Meanwhile, sodium chloride (NaCl) and sodium sulfate (Na_2SO_4) solutions with 0.17 mol/L and 0.29 mol/L were prepared respectively. The selected salinities were according to the *in-situ* investigation on loesses in Lanzhou New Area.

TABLE 1 | Physical properties of selected loess.

Types	Natural water content (%)	Specific gravity	Natural density (g/cm^3)	Dry density (g/cm^3)	Void ratio	Liquid limits (%)	Plastic limits (%)	Permeability coefficient (cm/s)
Excavation area	3.7	2.73	1.32	1.2	1.14	26.18	16.83	2.5×10^{-4}
Filling area	12.3	2.73	2.00	1.8	0.53	26.18	16.83	2.1×10^{-5}

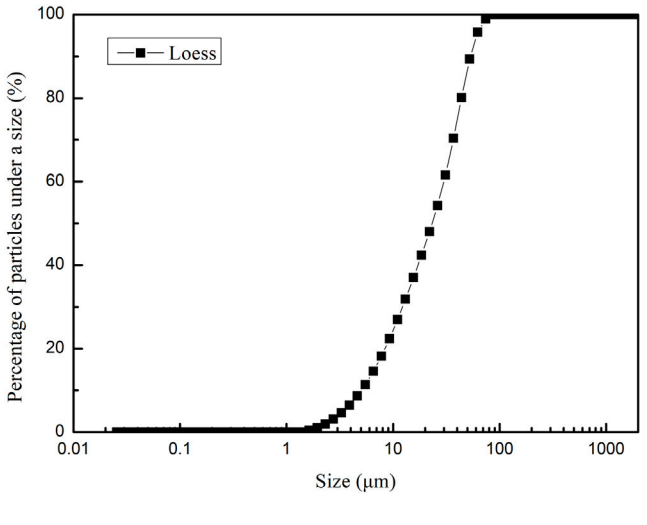

FIGURE 1 | Particle size distribution of selected loess.

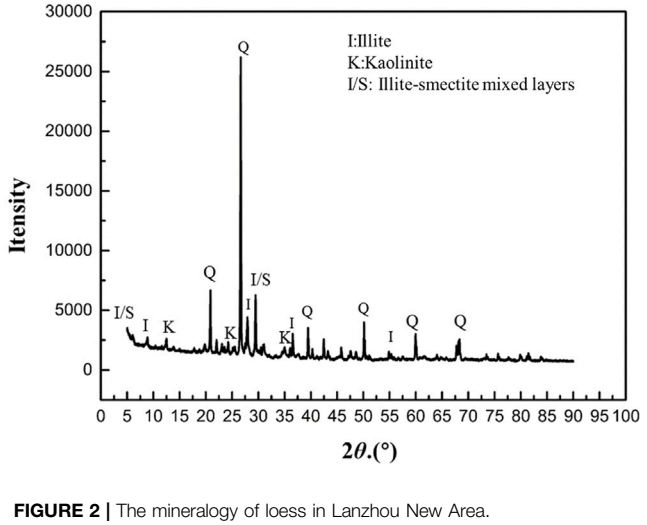

FIGURE 2 | The mineralogy of loess in Lanzhou New Area.

METHODS

Sample Preparing

For the undisturbed loess, the samples with a height 20 mm and diameter 61.8 mm were prepared by cutting the intact soil in field. Then, they were air dried or titrated to a uniform moisture content 3.7%, and sealed for 24 h to reach a homogenous state. For the compacted samples, the remolded loess was statically compressed in the steel ring with a height 20 mm and diameter 61.8 mm according to the physical indexes of compacted loess shown in **Table 1**.

Modified Oedometer Tests

The set-up of modified oedometer tests mainly included a sealed container filling with saturated solution, a peristaltic cycling pump and a loading system. As shown in **Figure 3A**, the vapor of saturated solution was circularly pumped (the speed was 20 rpm) to the top and bottom of installed sample. Besides, the saturated solution was also filled in the container to obtain the homogenization of total suction or humidity in samples. The samples were not allowed to be contaminated with saturated solution in the container. **Figure 3B** presented the scheme of solution injection stage of the compression tests. In this stage, the 0.17 mol/L NaCl and 0.29 mol/L Na_2SO_4 were circularly pumped to soak the bottom of samples.

The osmotic suction and total suction controlled compression tests were performed following these procedures:

1) The loading of 12.5 and 25 kPa were applied to the undisturbed and remolded loess following Chinese standard GB/T 50,123–2019, and each step of loading last for 24 h.
2) Under the load of 25 kpa, the vapor of saturated solution was circularly pumped to samples for reaching the equilibrium of relative humidity as shown in **Figure 3A**. The period of this stage was about 7 days, which was based on the ending of deformation development.

The total suction includes matrix suction and osmotic suction, and normally correlated to the relative humidity in soil. In this test, the saturated solution was used to provide a certain relative humidity in the sealed container. According to thermodynamics, the relationship between the total suction and the relative humidity of the saturated solution was expressed as follows:

$$\psi = \frac{RT\rho_w}{W}\ln\left(\frac{1}{RH}\right) \quad (1)$$

Where Ψ is the total suction in kPa; R is molar gas constant, 8.3145 J/(mol·K); ρ_w is the density of water, kg/m^3; W is the molar mass of water vapor, 18.016 g/mol; T is the absolute temperature in K; RH is relative humidity, %.

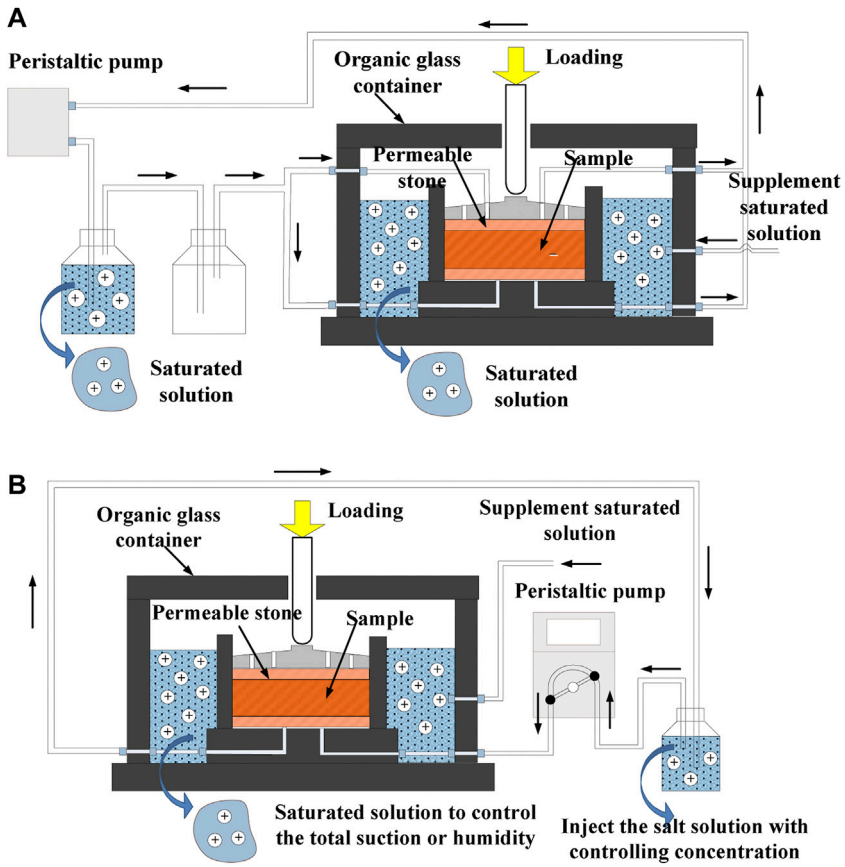

FIGURE 3 | The schematic diagram of modified oedometer tests with controlling total suction and injected solutions: **(A)** The set-up of total suction controlling device; **(B)** The set-up of solution injection device.

TABLE 2 | The total suction and RH of saturated solution (15°C).

Solution	RH (%)	Ψ(MPa)
Saturated $MgCl_2$	33.3	146.23
Saturated KCl	86	20.06
Saturated $ZnSO_4$	90	14.01
Saturated KI	71	45.55
Saturated Na_2SO_4	96	11.09
Saturated K_2CO_3	43.5	110.70

The tests were performed at 15°C, and the relative humidity and calculated total suction corresponding to various saturated salt solutions are shown in **Table 2**.

3) When the vertical deformation was unchanged at stage (2), replace the experimental set-up to control the osmotic suction of inject solution as shown in **Figure 3B**. The samples were soaked with NaCl at a mass content of 1%, Na_2SO_4 at a mass content of 4% and distilled water. Meanwhile, we recorded the vertical deformation of soil under saline water infiltration. The period of solution soaking was maintained to 24 h.

Witteven *et al.* (2013) (Witteveen et al., 2013) experimentally studied the influences of NaCl solution on the suction of illite clay. The results showed that osmotic suction of soil-NaCl mixtures and NaCl solution identified by filter paper method were close, which indicated that the clay minerals almost had negligible influences on the measured osmotic suction. Then, the controlling osmotic suction in soil can be considered as the osmotic suction of injected saline water. Metten 1966) (Wang et al., 2020) proposed that the osmotic suction can be calculated by Van Hoff equation as following:

$$\psi_{\pi} = \upsilon RTc \tag{2}$$

Where Ψ_{π} represents osmotic suction, kPa; υ is the number of ionizable ion, such as NaCl solution $\upsilon = 2$; R is gas constant, $R = 8.3145$ J/mol·K; T is absolute temperature, K; c represents molar concentration of solution (mol/L). The relationship between molar concentration and mass concentration is $c = 1000\omega\rho/M$, where ω represents the mass concentration, ρ is the density of water in g/cm^3, and M is the molar mass of the solute. **Table 3** gives the calculated osmotic suction of 1% sodium chloride (NaCl) solution, 4% sodium sulfate (Na_2SO_4) solution and distilled water based on eq. (Ivushkin et al., 2019).

TABLE 3 | The osmotic suction of selected solution for soaking soil (15°C).

Saline solution	Ion number υ	Molar concentration c (mol/L)	Osmotic suction Ψ_π(MPa)
1% NaCl solution	2	0.17	0.74
4% Na_2SO_4 solution	2	0.29	1.39
Distilled water	0	0	0

4) After the deformation was stable in the soaking stage, the conventional consolidation tests were carried out under the loading from 25 to 1,600 kPa, and then unload to 25 kPa step by step. The loading increment or decrement followed a ratio of 1:2 or 2:1, and the loading or unloading period would last for 24 h. Based on the *e*-lg*p* curves of each sample, the total suction and osmotic suction effects on the compression coefficient, compression index and other mechanical behavior of compacted and undisturbed loess were discussed.

RESULTS AND DISCUSSIONS

The Compression Curves *e*-lg*p*

Figure 4A–C presented the *e*-lg*p* curves of undisturbed loess with vary controlling environmental humidity and salinities. The results showed that the structure of undisturbed loess significantly collapsed under the coupling of total suction and osmotic suction at the 25 kPa, and the compression indices changed after 25 kPa. In **Figure 4A**, the variation of void ratio Δe at 25 kPa reached to about 0.10 under Ψ = 146.23 MPa and Ψ_π = 0.74 MPa for undisturbed loess, while it significantly decreased to about 0.035 under Ψ = 20.06 MPa and Ψ_π = 0.74 MPa. It indicated that the volume of collapse increased with the total suction for a critical osmotic suction. After 25 kPa, the slope of *e*-lg*p* curve under Ψ = 146.23 MPa and Ψ_π = 0.74 MPa was lower than that under Ψ = 20.06 MPa and Ψ_π = 0.74 MPa. In **Figure 4B**, the collapsed volume of samples under Ψ = 45.55 MPa and Ψ_π = 1.39 MPa were larger than that under Ψ = 14.01 MPa and Ψ_π = 1.39 MPa at 25 kPa. While, it is interesting that their slopes in *e*-lg*p* curves were close for the approximately close total suction (the difference was within one order of magnitude). In **Figure 4C**, the Δe of undisturbed samples at 25 kPa under Ψ = 110.7 MPa and Ψ_π = 0 MPa was higher than that under Ψ = 11.09 MPa and Ψ_π = 0 MPa, and the changes of compression indices presented a similar trend which the compression index of samples under Ψ = 11.09 MPa and Ψ_π = 0 MPa was higher.

Figure 5A–C presented the *e*-lg*p* curves of remolded loess, being at a consistent compacted dry density 1.8 g/cm^3 and compressed under vary controlling environmental humidity and salinities. Being different with undisturbed samples, the volume changes Δe at 25 kPa decreased with total suction Ψ increasing for Ψ_π = 1.39 MPa, Ψ_π = 0.74 MPa and Ψ_π = 0 MPa. After 25 kPa, the slopes in *e*-lg*p* curves of compacted loess were not significantly influenced by environmental humidity, and they seemed to be close under an identical Ψ_π. Generally, the final volume changes Δe of samples with lower total suction Ψ at 1,600 kPa was higher than that of samples with larger total suction Ψ for an identical Ψ_π. The differences of final void ratio in two compression curves of each figure were about 0.1. Meanwhile, the impact of total suction and osmotic suction on the collapsed volume of compacted loess significantly decreased comparing to undisturbed loess.

The Volume Change With Elapsed Time at 25 kPa

To compare the deformation of undisturbed loess and compacted loess at different stages, the void ratio e changed with elapsed time T (s) were illustrated in **Figure 6**. The stages included an applied loading of 25 kPa (I), total suction equilibrium (II) and saline water injection (III).

As shown in **Figure 6A**, the primary compression at 25 kPa of undisturbed loess was about 6 times larger than that of compacted loess, which indicated a higher compressibility of structural loess with an initial void ratio larger than 1.0. At the stage of total suction equilibrium, the secondary consolidation settlement Δe of undisturbed and compacted loess were 0.009 and 0.003. When the samples soaked in the solution with osmotic suction equal to 0.74 MPa, the compacted soil collapsed from e = 0.485 to e = 0.47, and the Δe of undisturbed loess was only 0.004. In **Figure 6B**, the volume change of undisturbed loess was about 9 times larger than that of compacted loess at the first stage. Then, the creeping deformation of undisturbed loess was also 5 times than compacted loess at the second stage, but their Δe were both under 0.01. Under the coupling of Ψ = 146.23 MPa and Ψ_π = 0.74 MPa, the volume contraction of undisturbed soil significantly larger than compacted samples, being different with the results shown in **Figure 6A**

In **Figure 6C,D**, the larger primary compression of undisturbed loess under 25 kPa applied was confirmed. The difference of the long-term creeping of two soil was within 10 times under Ψ = 14.01 MPa and Ψ = 45.55 MPa which were less than 100 MPa. At the third stage, the collapsed volume of undisturbed loess were about 2 times higher than that of compacted loess in the case of Ψ_π = 1.39 MPa.

In **Figure 6E,F**, the Δe of undisturbed loess were from 0.03 to 0.06 and that of compacted loess was about 0.01–0.02 at the first stage. Under the higher controlling total suction Ψ = 110.7 MPa, the creeping void ratio decrement of two soils were within 0.01. While the void ratio variations of undisturbed loess and compacted loess were 0.03 and 0.008 in the condition of lower total suction Ψ = 11.09 MPa which corresponding a RH = 96%. When the distilled water induced, the void ratio of undisturbed loess decreased 0.013 and 0.005 in the condition of Ψ = 110.7 MPa and Ψ = 11.09 MPa respectively. At this stage, the volume of

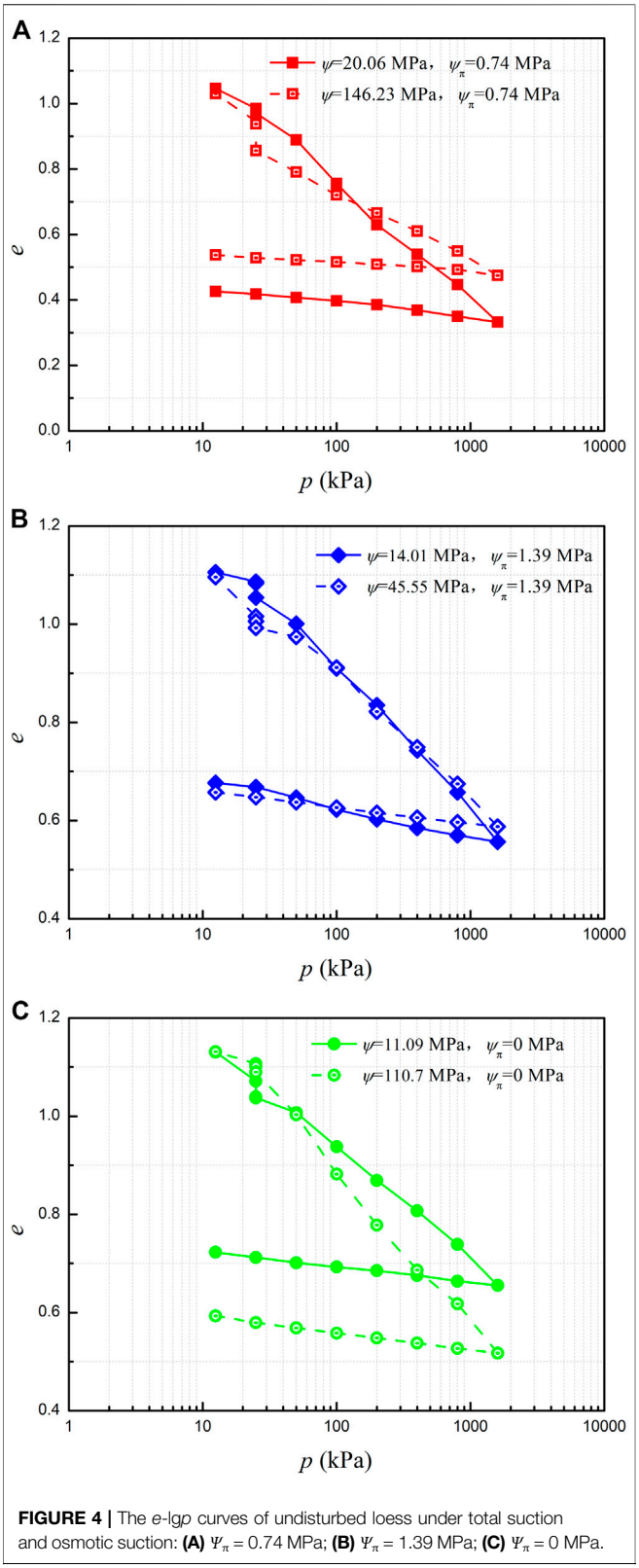

FIGURE 4 | The *e*-lg*p* curves of undisturbed loess under total suction and osmotic suction: **(A)** Ψ_π = 0.74 MPa; **(B)** Ψ_π = 1.39 MPa; **(C)** Ψ_π = 0 MPa.

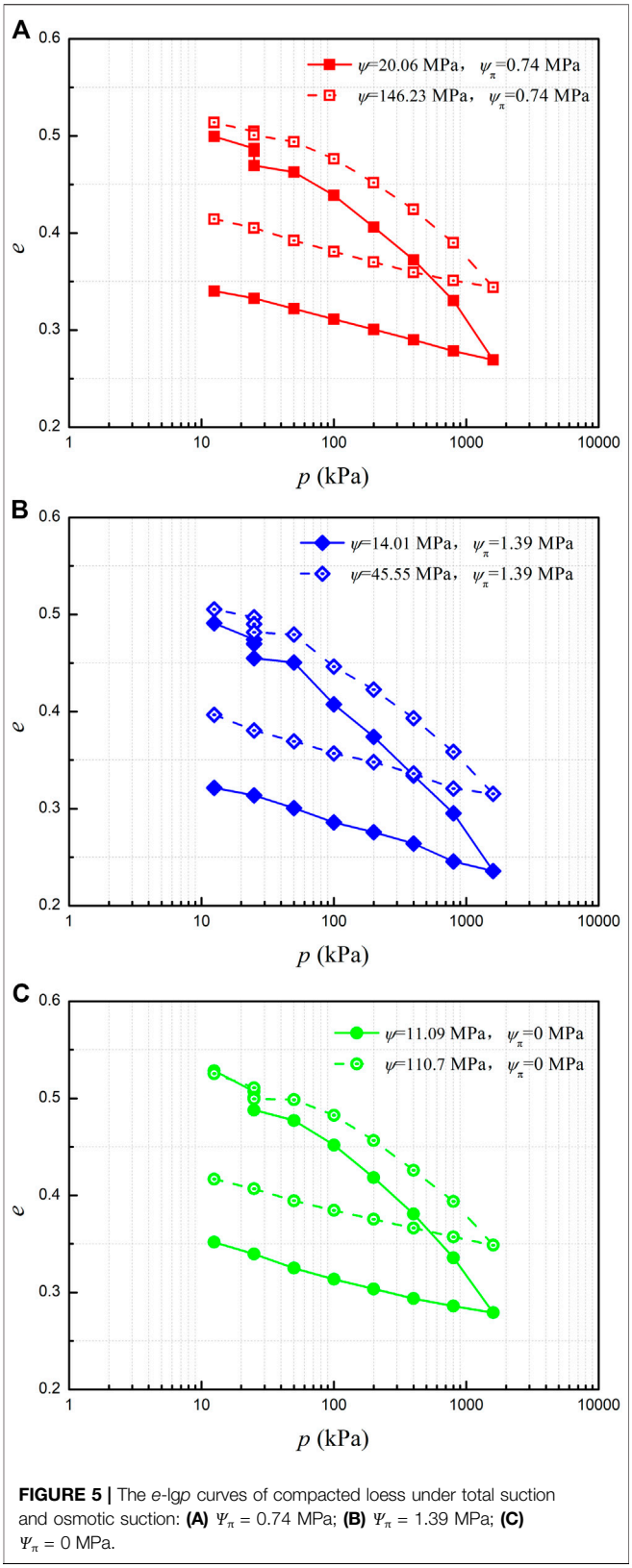

FIGURE 5 | The *e*-lg*p* curves of compacted loess under total suction and osmotic suction: **(A)** Ψ_π = 0.74 MPa; **(B)** Ψ_π = 1.39 MPa; **(C)** Ψ_π = 0 MPa.

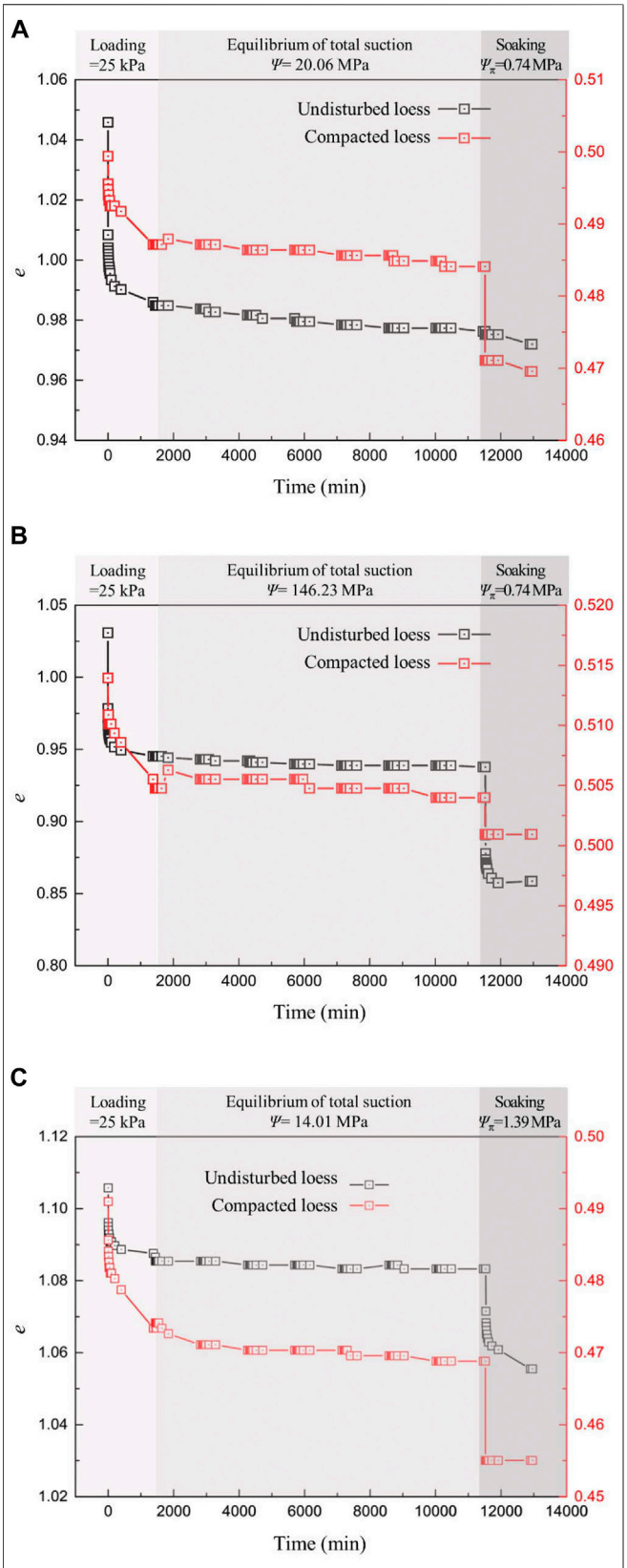

FIGURE 6 | The *e-Time* curves of undisturbed and compacted loess under impact of total suction and osmotic suction: **(A)** Ψ = 20.06 MPa and Ψ_π = 0.74 MPa; **(B)** Ψ = 146.23 MPa and Ψ_π = 0.74 MPa; **(C)** Ψ = 14.01 MPa and Ψ_π = 1.39 MPa; **(D)** Ψ = 45.55 MPa and Ψ_π = 1.39 MPa; **(E)** Ψ = 11.09 MPa and Ψ_π = 0 MPa; **(F)** Ψ = 110.7 MPa and Ψ_π = 0 MPa. (*Continued*)

compacted loess decreased 0.002 and 0.011 for Ψ = 110.7 MPa and Ψ = 11.09 MPa respectively. Generally, the primary compression of samples under a constant loading 25 kPa were controlled by the initial structure and void ratio. Then, the volume changes of primary consolidation of structural loess were higher than that of compacted loess. While, with the *RH* changing and saline water induced, the collapses of loess were significant. **Figure 7A** summarized the void ratio decrement Δe varied with total suction Ψ at the second stage. To characterize the coupling effect of Ψ and Ψ_π on the collapse of loess, the relationships between Δe and Ψ-Ψ_π were presented in **Figure 7B**.

As shown in **Figure 7A**, the results indicated that creeping deformation of undisturbed loess significantly decreased with total suction increasing which corresponding to relative humidity decreasing. When the *RH* < 90%, the Δe at secondary consolidation stage were lower than 0.01. While, the Δe reached to 0.03 when the *RH* = 96%. For the compacted loess, the Δe at secondary consolidation stage were all lower than 0.01 and the media value was 0.005, which seemed to be irrelevant to environmental humidity.

When the solution was induced, the collapse of undisturbed loess increased from 0.005 to 0.08 with the Ψ-Ψ_π increasing as indicated in **Figure 7B**. The highest difference between the samples was nearly 20 times. The higher Ψ-Ψ_π resulted in a higher solution inducing collapse. While, the volume changes of compacted loess decreased with Ψ-Ψ_π increasing, and that of all samples were under 0.015.

Therefore, the creeping in high environmental humidity and the collapse under saline water intrusion being high Ψ-Ψ_π for loess would be considered for the shallow layer, especially the uneven settlements between undisturbed loesses and compacted loesses. For the undisturbed loesses, higher relative humidity resulted in higher creeping without considering water intrusion. Under the groundwater intrusion, the dry loess with higher Ψ-Ψ_π would collapsed dramatically. For the compacted loesses, the creeping seemed to be irrelevant to environmental humidity without considering water intrusion. When saline water induced, a higher collapse of wet loess with lower Ψ-Ψ_π occurred.

The Compression Parameters

The compressibility index of soil based on *e*-lg*p* curves is the fundamental parameters to investigate the soil settlement. The compression index C_c is the slope of the straight section in *e*-lg*p* curve after yielding of soil, and the swelling index C_s the slope of the *e*-lg*p* curve in the unloading stage. Previous studies revealed that the compression index of saturated montmorillonite clay significantly decreased with the increase of osmotic suction and then tend to be constant (Deng et al., 2018; He et al., 2020). In this study, the relationships between the compression index of unsaturated loess and osmotic suction under the changing of ambient humidity represented by total suction were considered.

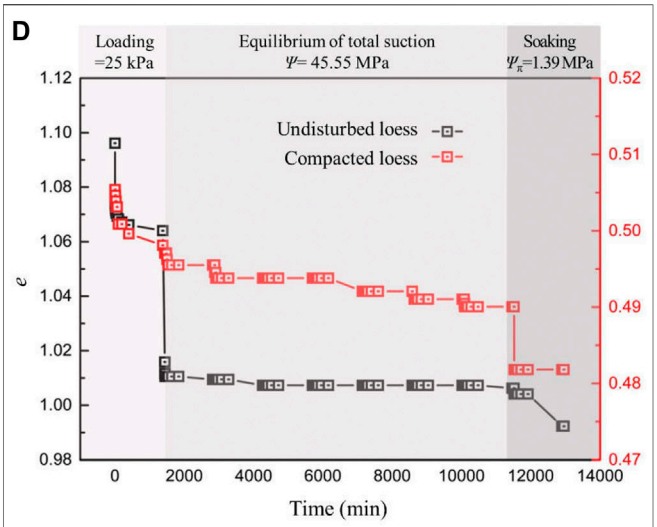

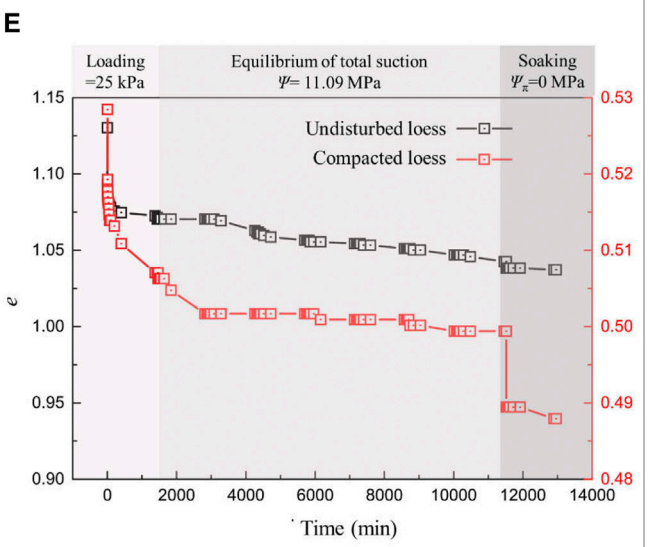

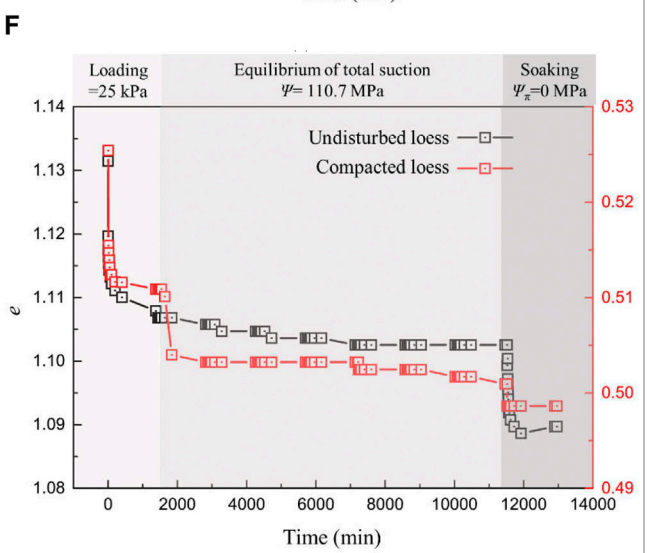

FIGURE 6 | (*continued*).

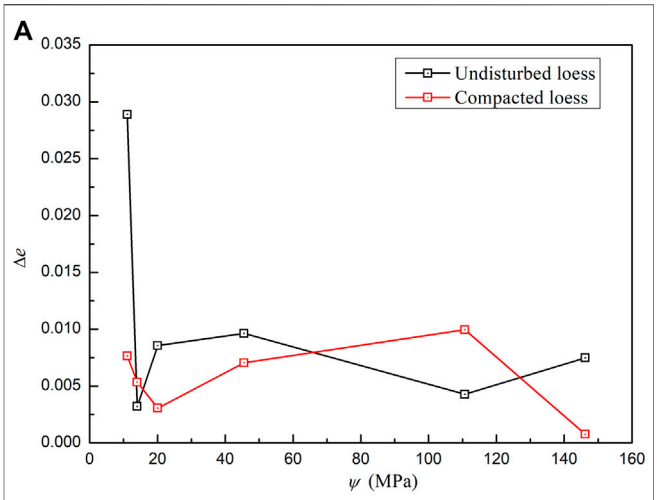

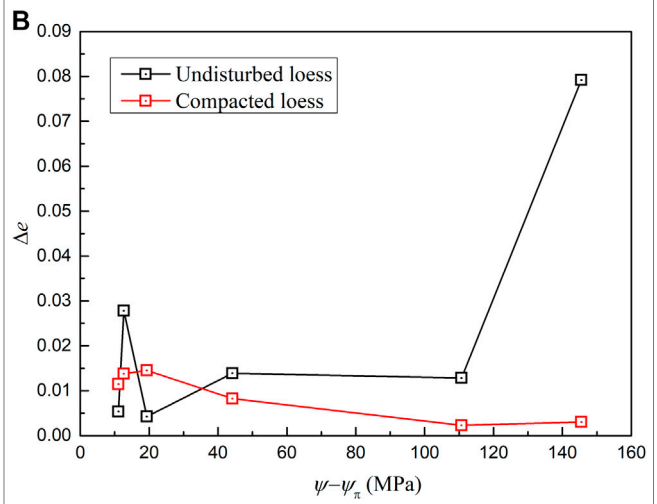

FIGURE 7 | The Δ*e* under impact of total suction and osmotic suction: **(A)** the Δ*e versus* Ψ at the second stage; **(B)** the Δ*e versus* Ψ-Ψ$_\pi$ at the third stage.

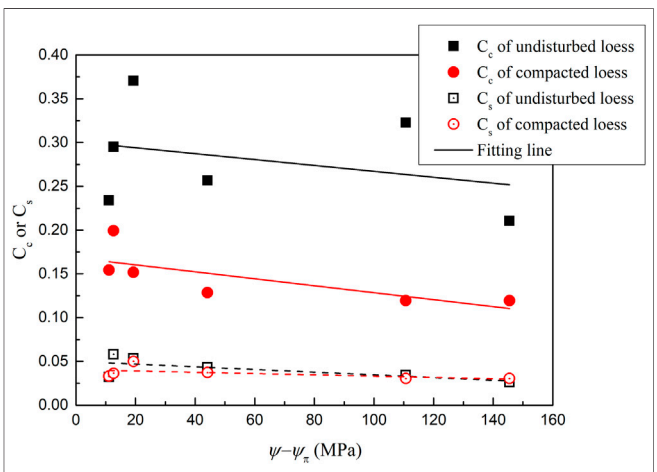

FIGURE 8 | The compression index C_c and swelling index C_s *versus* Ψ-Ψ$_\pi$

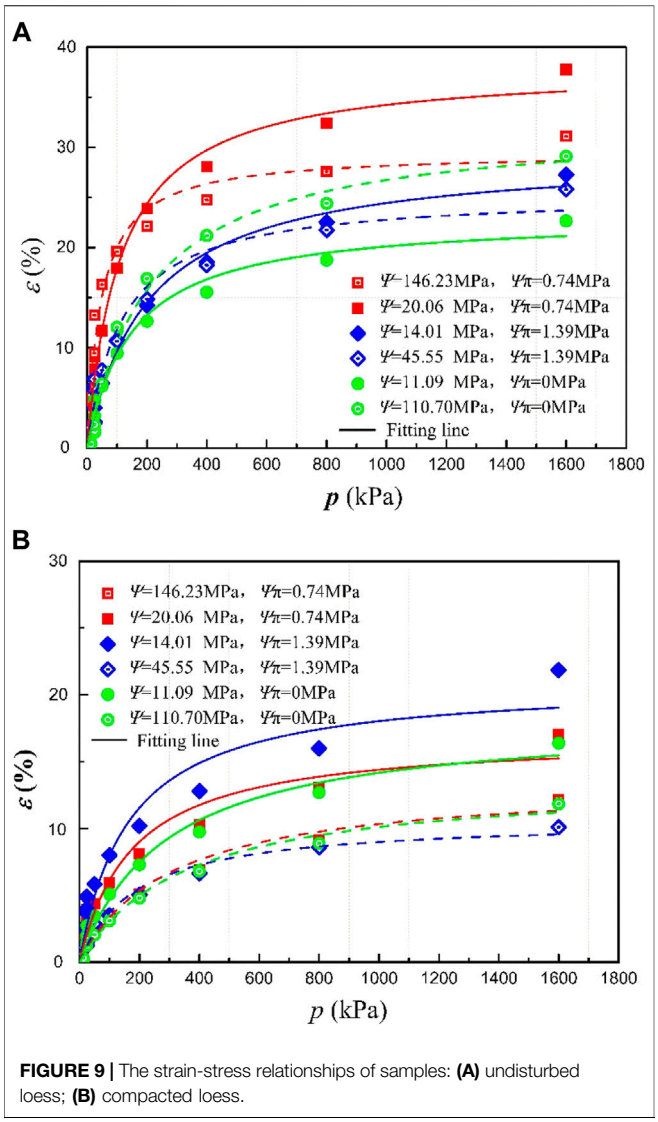

FIGURE 9 | The strain-stress relationships of samples: **(A)** undisturbed loess; **(B)** compacted loess.

As mentioned, the coupling effects of ambient humidity and saline water intrusion on soil settlement were expressed as the relationships between compressibility index and Ψ-Ψ_π. The results plotted in **Figure 8** showed that the compression index C_c of samples generally decreased with Ψ-Ψ_π, and the compressibility of undisturbed loess was higher. The swelling indices C_s of samples also decreased with Ψ-Ψ_π, but the variation was not significant as C_c. The reason is that the swelling of loess is mainly attributed to the elastic deformation of particles. Unlike the montmorillonite soil, water molecule can not go into interlayer of kaolinite or illite and result in soil expansion. Then, the variation of C_s was not significant.

In terms of compression, the responses of undisturbed and remolded loess to environmental humidity and water salinity were different. When the Ψ-Ψ_π reached to 40 MPa, the compression index of remolded loess was almost constant. The Ψ-Ψ_π of undisturbed loess significantly fluctuated after 40 MPa. The maximum C_c and C_s of samples corresponded to the Ψ-Ψ_π being 10–20 MPa. The reason for the higher C_c of undisturbed and remolded loess under higher humidity is that the micro pores in soil absorbed water and moisture content increased. The soil cementation was hydrated resulting in large compressibility of structural loess (Sato and Hattanji, 2018; Wei et al., 2020; Xu et al., 2020). Meanwhile, the sodium sulfate in soil would form hydrated crystals in the process of humidity increasing. It lead to the expansion of soil and the reduction of compressibility (Zhang et al., 2012; Langlet et al., 2013).

The stress-strain relationships of undisturbed and remolded loess were further discussed by elastoplastic model. Among the constitutive models, Duncan Chang model has been widely used in engineering practice. Based on that, the hyperbolic model was also used to describe the one-dimensional stress-strain relationships of soil under confining conditions. The function can be expressed as following:

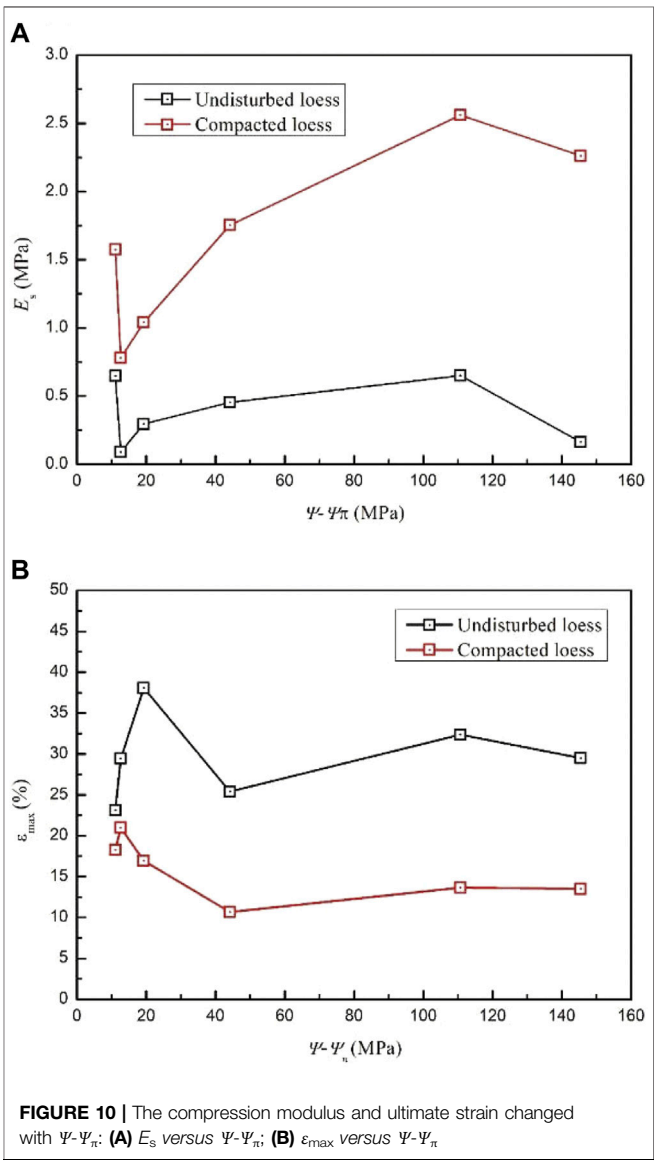

FIGURE 10 | The compression modulus and ultimate strain changed with Ψ-Ψ_π: **(A)** E_s *versus* Ψ-Ψ_π; **(B)** ε_{max} *versus* Ψ-Ψ_π

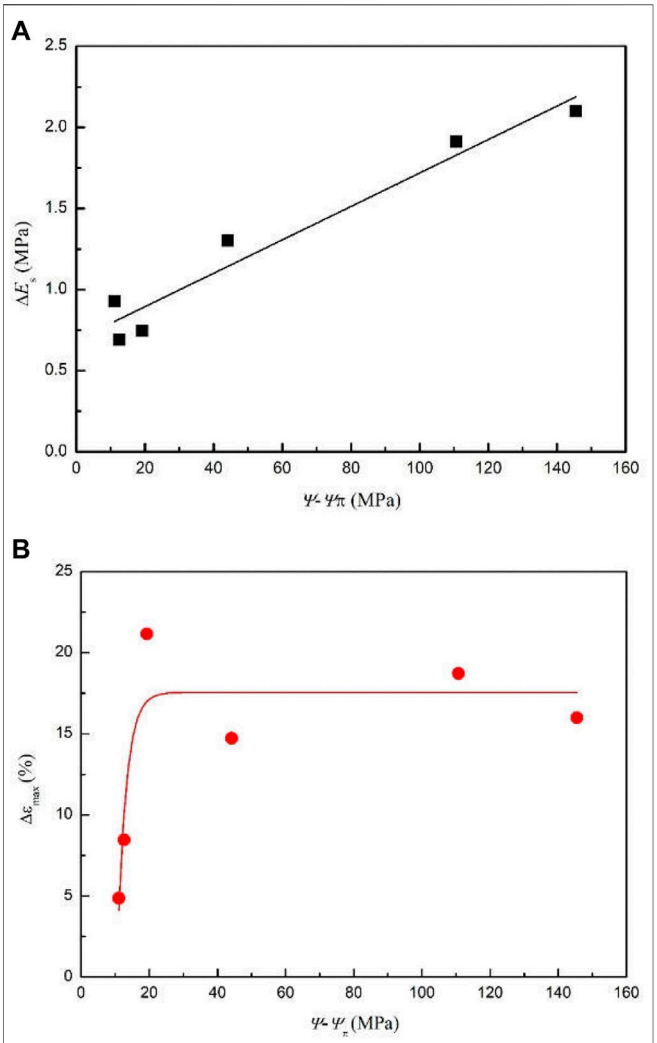

FIGURE 11 | The differences of compression parameters changed with Ψ-Ψ_π: **(A)** ΔE_s *versus* Ψ-Ψ_π; **(B)** $\Delta\varepsilon_{max}$ *versus* Ψ-Ψ_π

$$\varepsilon = \frac{p}{a + bp} \tag{3}$$

Where ε is the vertical strain of the specimen in one-dimensional compression test; p is vertical stress; a and b are the constant. The parameter a is the reciprocal of the slope of the straight section at the initial stage of the curve, which is the compression modulus E_s (MPa) under the lateral confining condition. The parameter b is the reciprocal of the ultimate strain ε_{max} when the stress is infinite. As shown in **Figure 9**, the stress-strain relationships of soil were well described by **Eq. 3**.

The key parameters E_s and ε_{max} in the above formula changed with Ψ-Ψ_π were shown in **Figure 10**. As shown in **Figure 10A**, the trends of the two curves were similar and the initial E_s of compacted loess were higher than that of structural loess. The E_s generally increased with Ψ-Ψ_π, which indicated that the initial compression modulus was higher at lower ambient humidity corresponding to a dry state. While the E_s followed an inverse relationship in the range of 11–14 MPa and 110–146 MPa. It could be attributed to the deliquescence and efflorescence of saline crystals and different pore water chemistry in soil. In the range of 11–14 MPa, the crystals in soil deliquesced at high ambient humidity and the osmotic suction of intrusion liquid increased the applied chemistry loading. The maximum E_s at Ψ-Ψ_π = 110.7 MPa was due to the efflorescence of crystals and increasing of solid phase volume. The results shown in **Figure 10B** indicated that ε_{max} of compacted loess regularly decreased with Ψ-Ψ_π increasing due to the lower moisture content under high total suction. Due to the collapse of structural loess, the ε_{max} of undisturbed loess located above the curve of compacted loess. There existed a peak value at Ψ_π = 0.74 MPa and Ψ = 20.06 MPa, which corresponded to that the NaCl solution induced collapse under high ambient humidity (RH > 85%). It could be impacted by the coupling of initial pore structure and pore water chemistry.

To compare the influences of initial structure of loess, the ΔE_s and $\Delta\varepsilon_{max}$, which were the differences between the E_s or ε_{max} of structural loess and E_s or ε_{max} of compacted soil, were plotted in **Figure 11**. It is interesting that the relationship between ΔE_s and Ψ-Ψ_π subjected to a positive linear function as shown in **Figure 11A**. The results indicated that the elastoplastic modulus was significantly correlated to the Ψ-Ψ_π without considering initial structure of loess under the water intrusion. The scattered data could be attributed to the clay particle flocculation resulted by the ion concentration increasing in pore water. In **Figure 11B**, the $\Delta\varepsilon_{max}$ between the structural loess and compacted loess exponential increased with Ψ-Ψ_π, which indicated that samples with higher total suction would have a larger strain under the liquid intrusion. When the RH decreased, the solution induced volume change became inert with the Ψ-Ψ_π.

Based on the above results, the different physical properties of compacted and undisturbed loess will lead to uneven settlement near the interface of filling and excavating area. In the engineering practice, the humidity and saline water intrusion should be considered in the long-term behavior of loess in shallow layer.

The Mechanism of Total Suction and Osmotic Suction Effects

Normally, the soil was considered as a three-phase material. The saline soil widely distributed in the arid area, and the salt crystals commonly existed between soil particles, composing the inter particle cementation and skeleton. Meanwhile, the dissolved salt in pore water would transform between the liquid phase and crystal in the solid phase under certain conditions. In the condition of relatively dry environment, the excessive salt will change from liquid phase to solid phase. During the upward migration of groundwater, precipitation infiltration or ambient humidity increasing, the salt crystals in the solid phase will change to liquid phase. Thus, the cementation would dissolve and the skeleton would collapse. The NaCl and Na_2SO_4 are two main salts in saline soil, which have a certain degree of deliquescence and moisture absorption capacity. In the process of environmental humidity change, their phase transform played a key role in the structure of loess.

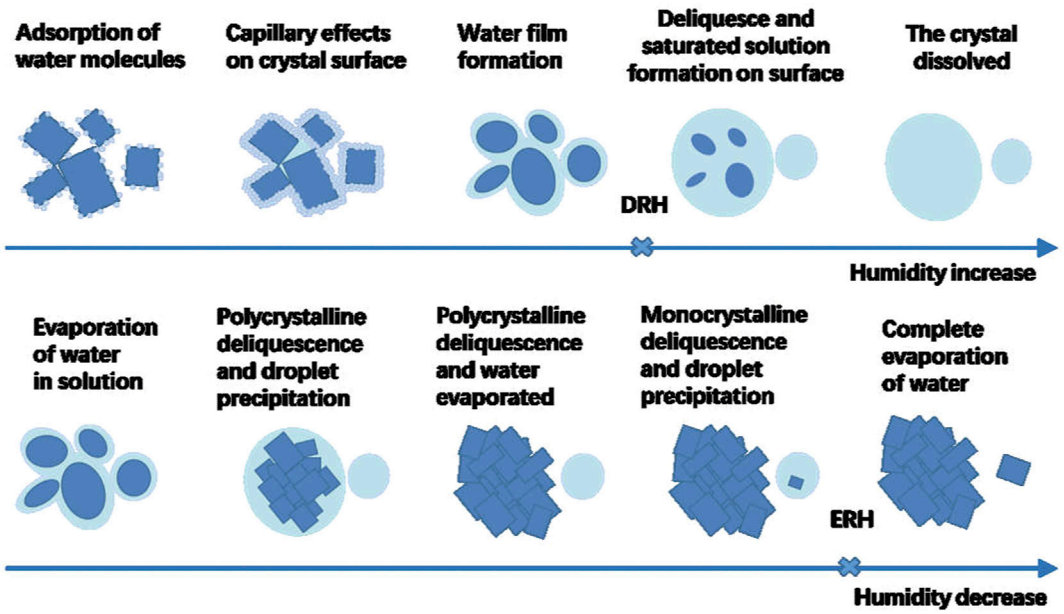

FIGURE 12 | The deliquescence and efflorescence under relative humidity change (Xu et al., 2020).

In recent years, many studies had obtained the variation rule of NaCl crystal deliquescence under environmental humidity changing (Zhang et al., 2012; Langlet et al., 2013). As shown in **Figure 12**, the deliquescence relative humidity (DRH) divided the deliquescence process of NaCl into two stages. When the ambient humidity was less than DRH, the adsorption of water molecules by salt crystals was in term of physical adsorption. With the increase of humidity, water molecules continued to be absorbed and finally formed a water film on the surface of salt crystals. When the ambient humidity was higher than DRH, the salt crystals will deliquesce, and further dissolve with the increase of humidity to form a saturated salt solution. After salt deliquescence, the cementation and skeleton of soil were weakened.

Different from the effects of deliquescence of sodium chloride on the deformation of undisturbed loess, the effects of sodium sulfate on undisturbed deformation were more complex. On one hand, with the increase of humidity, sodium sulfate hydrated with water molecules, resulting in a significant increase in crystal volume. This volume expansion process squeezed the pores, resulting in the loosening and destruction of the microstructure of the soil. On the other hand, a variety of salts in the soil lead to the decrease of DRH of sodium sulfate, and sodium sulfate dissolved to form a saturated solution. The DRH of Na_2SO_4 was about 96%, which show that lower ambient humidity can not make it completely dissolved. When the humidity of the saturated solution of dissolved sodium sulfate decreased, the recrystallization process after efflorescence relative humidity (ERH) occurred. As shown in **Figure 12**, during recrystallization, sodium sulfate crystals resulted in a more dense structure of loess. That is the reason that compression parameters and creeping deformation fluctuated when Na_2SO_4 solution was involved.

CONCLUSION

In this paper, we developed an oedometer test to investigate the compression behavior of natural and compacted loess under environmental humidity (represented by total suction Ψ) and injection water salinity (represented by osmotic suction Ψ_π) changes. Based on the analysis of results, several conclusions were drawn:

1) The creeping of undisturbed and compacted loess under the ambient humidity changing, and the collapse under the coupling of total suction and saline water intrusion were nonnegligible. The volume changes of structural loess, whose initial void ratio was larger than 1.0, were normally higher than that of compacted loess at above two stages. The differences between two loesses were 3–20 times.
2) Under the constant loading of 25 kPa which represented the stresses in shallow layer, the creeping deformation of undisturbed loess significantly decreased with total suction increasing which corresponding to relative humidity decreasing. When the RH < 90%, the Δe at secondary consolidation stage were lower than 0.01. While, the Δe reached to 0.03 as the RH = 96%. For the compacted loess, the Δe at secondary consolidation stage were all lower than 0.01 and seemed to be irrelevant to environmental humidity. When the solution was induced, the collapse of undisturbed loess increased to 0.08 with the Ψ-Ψ_π increasing. The difference under different humidity reached nearly 20 times. The higher Ψ-Ψ_π resulted in a higher solution inducing collapse. While, the volume changes of compacted loess decreased with Ψ-Ψ_π increasing, and that of samples were under 0.015.

3) In the *e*-lg*p* curves, the compression index C_c of samples generally decreased with Ψ-Ψ_π, and the compressibility of undisturbed loess was higher. The swelling indices C_s of samples also decreased with Ψ-Ψ_π, but the variation was not significant. The reason for the higher C_c of undisturbed and remolded loess under higher humidity is that the micro pores in soil absorbed water and moisture content increased. The soil cementation hydrated resulting in larger compressibility of structural loess.
4) In the stress-strain curves, the E_s generally increased with Ψ-Ψ_π, which indicated that the initial compression modulus was higher at lower ambient humidity. The maximum E_s at Ψ-Ψ_π = 110.7 MPa was due to the efflorescence of crystals and increasing of solid phase volume. The ε_{max} of compacted loess regularly decreased with Ψ-Ψ_π increasing due to the lower moisture content under high total suction. Due to the collapse of structural loess, the ε_{max} of undisturbed loess located above the curve of compacted loess. It is interesting that the relationship between ΔE_s (the differences between the structural loess and compacted loess) and Ψ-Ψ_π subjected to a positive linear function. The $\Delta\varepsilon_{max}$ between the structural loess and compacted loess exponential increased with Ψ-Ψ_π.
5) When the ambient humidity was higher than deliquescence relative humidity (DRH), the salt crystals will deliquesce, and further dissolve with the increase of humidity to form a saturated salt solution. After salt deliquescence, the cementation and skeleton of soil were weakened. When the humidity of the saturated solution of dissolved sodium sulfate decreased, the recrystallization process after efflorescence relative humidity (ERH) occurred. During recrystallization, sodium sulfate crystals resulted in a more dense structure of loess.

Based on the above results, the different physical properties of compacted and undisturbed loess will lead to uneven settlement near the interface of filling and excavating area. In the engineering practice, the humidity and saline water intrusion should be considered in the long-term behavior of loess in shallow layer.

DATA AVAILABILITY STATEMENT

The raw data supporting the conclusions of this article will be made available by the authors, without undue reservation.

AUTHOR CONTRIBUTIONS

Plan and paper writing, TZ; Testing and data analysis, ZH; Plan and revision, HL; Discussion and revision, YD; Discussion and revision, HZ.

FUNDING

This study was supported by the National Natural Science Foundation of China (Grant Nos. 42041006, 42090053, 41807225 and 41790443), the National Key Research and Development Program of China (2018YFC1504700), the China Postdoctoral Science Foundation (Grant Nos. 2019M653791), Natural Science Foundation of Gansu Province, China (Grant Nos. 20JR5RA259), Fundamental Research Funds for the Central Universities (Grant Nos. lzujbky-2020-pd08 and lzujbky-2021-ct04).

REFERENCES

Amir Akbari, G., Mohsen, H. S., Ahmadi, G., and Cherati, Y. D. (2018). Effect of Road Salts on the Hydro-Mechanical Behavior of Unsaturated Collapsible Soils. *Transp. Geotech.* 30143. doi:10.1016/j.trgeo.2018.09.005

Chang, Z., Gao, H., Huang, F., Chen, J., Huang, J., and Guo, Z. (2020). Study on the Creep Behaviours and the Improved Burgers Model of a Loess Landslide Considering Matric Suction. *Nat. Hazards* 103, 1479–1497. doi:10.1007/s11069-020-04046-0

Chen, C., Zhang, D., and Zhang, J. (2017). Influence of Stress and Water Content on Air Permeability of Intact Loess. *Can. Geotech J.* 54, 1221–1230. doi:10.1139/cgj-2016-0186

Daliakopoulos, I. N., Tsanis, I. K., Koutroulis, A., Kourgialas, N. N., Varouchakis, A. E., Karatzas, G. P., et al. (2016). The Threat of Soil Salinity: A European Scale Review. *Sci. Total Environ.* 573, 727–739. doi:10.1016/j.scitotenv.2016.08.177

Debora, J., and Miller, J. D. N. (2006). "Osmotic Suction in Unsaturated Soil Mechanics," in 2006 Fourth International Conference on Unsaturated Soils April, Carefree, Arizona, United States.

Deng, Y., Zhang, T., Cui, Y., Chen, Y., Deng, T., and Zhou, X. (2018). Pore Water Salinity Effect on the Intrinsic Compression Behaviour of Artificial Soft Soils. *Appl. Clay Sci.* 166, 299–306. doi:10.1016/j.clay.2018.09.027

Elkady, T. Y., and Al-Mahbashi, A. M. (2017). Effect of Solute Concentration on the Volume Change and Shear Strength of Compacted Natural Expansive clay. *Environ. Earth Sci.* 76. doi:10.1007/s12665-017-6825-0

He, Y., Ye, W. M., Chen, Y. G., Zhang, K. N., and Wu, D. Y. (2020). Effects of NaCl Solution on the Swelling and Shrinkage Behavior of Compacted Bentonite under One-Dimensional Conditions. *B. Eng. Geol. Environ.* 79, 399–410. doi:10.1007/s10064-019-01568-1

Ivushkin, K., Bartholomeus, H., Bregt, A. K., Pulatov, A., Kempen, B., and de Sousa, L. (2019). Global Mapping of Soil Salinity Change. *Remote Sens Environ.* 231, 111260. doi:10.1016/j.rse.2019.111260

Jabar, M., and Rasul, G. S. G. M. (2017). The Effect of Wetting and Drying on the Performance of Stabilized Subgrade Soils. *Transp. Geotech.* 30122-8. doi:10.1016/j.trgeo.2017.09.002

Koniorczyk, M., and Gawin, D. (2008). Heat and Moisture Transport in Porous Building Materials Containing Salt. *J. Build Phys.* 31, 279–300. doi:10.1177/1744259107088003

Lan, H., Zhao, X., Macciotta, R., Peng, J., Li, L., Wu, Y., et al. (2021). The Cyclic Expansion and Contraction Characteristics of a Loess Slope and Implications for Slope Stability. *Sci. Rep.* 11, 2250. doi:10.1038/s41598-021-81821-4

Langlet, M., Benali, M., Pezron, I., Saleh, K., Guigon, P., and Metlas-Komunjer, L. (2013). Caking of Sodium Chloride: Role of Ambient Relative Humidity in Dissolution and Recrystallization Process. *Chem. Eng. Sci.* 86, 78–86. doi:10.1016/j.ces.2012.05.014

Loret, B., Hueckel, T., and Gajo, A. (2002). Chemo-mechanical Coupling in Saturated Porous media: Elastic–Plastic Behaviour of Homoionic Expansive Clays. *Int. J. Sol. Struct.* 39, 2773–2806. doi:10.1016/s0020-7683(02)00151-8

Ma, F., Jing, Y., and Xiao-hong, B. (2016). Water Sensitivity and Microstructure of Compacted Loess. *Transp. Geotech.*, 11, 41–56. doi:10.1016/j.trgeo.2017.03.003

Mu, Q. Y., Zhou, C., and Ng, C. W. W. (2020). Compression and Wetting Induced Volumetric Behavior of Loess: Macro- and Micro-investigations. *Transp. Geotech.* 23, 100345. doi:10.1016/j.trgeo.2020.100345

Ng, C. W., and Pang, Y. W. (2000). Experimental Investigations of the Soil-Water Characteristics of a Volcanic Soil. *Can. Geotech J.* 6, 1252–1264. doi:10.1139/t00-056

Niu, X., and Yao, Y. (2021). Resilient Modulus experiment of Subgrade Soil on Different Wetting–Drying and Salt Washing–Supplying Paths. *Transp. Geotech.* 28, 100512. doi:10.1016/j.trgeo.2021.100512

Qin, P., Liu, Y., Song, Z., Ma, F., and Dong, X. (2020). An Electrical Resistivity Method of Characterizing Hydromechanical and Structural Properties of Compacted Loess during Constant Rate of Strain Compression. *Sensors* 20, 4783. doi:10.3390/s20174783

Sato, M., and Hattanji, T. (2018). A Laboratory experiment on Salt Weathering by Humidity Change: Salt Damage Induced by Deliquescence and Hydration. *Prog. Earth Planet. Sci.* 5, 84. doi:10.1186/s40645-018-0241-2

Wang, P., Ye, Y., Zhang, Q., Liu, J., and Yao, J. (2020). Investigation on the Sulfate Attack-Induced Heave of a Ballastless Track Railway Subgrade. *Transportation Geotechnics.* 23, 100316. doi:10.1016/j.trgeo.2020.100316

Wei, Y., Fan, W., Yu, B., Deng, L., and Wei, T. (2020). Characterization and Evolution of Three-Dimensional Microstructure of Malan Loess. *Catena* 192, 104585. doi:10.1016/j.catena.2020.104585

Wen, B., and Yan, Y. (2014). Influence of Structure on Shear Characteristics of the Unsaturated Loess in Lanzhou, China. *Eng. Geol.* 168, 46–58. doi:10.1016/j.enggeo.2013.10.023

Witteveen, P., Ferrari, A., and Laloui, L. (2013). An Experimental and Constitutive Investigation on the Chemo-Mechanical Behaviour of a clay. *Geotechnique* 63, 244–255. doi:10.1680/geot.sip13.p.027

Xu, J., Li, Y., Ren, C., and Lan, W. (2020). Damage of saline Intact Loess after Dry-Wet and its Interpretation Based on SEM and NMR. *Soils Found.* 60, 911–928. doi:10.1016/j.sandf.2020.06.006

Zhang, F., Wang, G., Kamai, T., Chen, W., Zhang, D., and Yang, J. (2013). Undrained Shear Behavior of Loess Saturated with Different Concentrations of Sodium Chloride Solution. *Eng. Geol.* 155, 69–79. doi:10.1016/j.enggeo.2012.12.018

Zhang, F., Ye, W. M., Chen, Y.-G., Chen, B., and Cui, Y.-J. (2016). Influences of Salt Solution Concentration and Vertical Stress during Saturation on the Volume Change Behavior of Compacted GMZ01 Bentonite. *Eng. Geol.* 207, 48–55. doi:10.1016/j.enggeo.2016.04.010

Zhang, H., Yan, G., and Wang, X. (2012). Laboratory Test on Moisture Adsorption-Desorption of wall Paintings at Mogao Grottoes, China. *J. Zhejiang Univ-sc. A.* 13, 208–218. doi:10.1631/jzus.a1100204

Zhang, T., and Wang, S. (2019). Explanation of the Influence of Sodium Chloride Solution on Volume Deformation and Permeability of Normally Consolidated Clays. *Materials* 12, 1671. doi:10.3390/ma12101671

Zuo, L., Xu, L., Baudet, B. A., Gao, C., and Huang, C. (2020). The Structure Degradation of a Silty Loess Induced by Long-Term Water Seepage. *Eng. Geol.* 272, 105634. doi:10.1016/j.enggeo.2020.105634

Conflict of Interest: The authors declare that the research was conducted in the absence of any commercial or financial relationships that could be construed as a potential conflict of interest.

Publisher's Note: All claims expressed in this article are solely those of the authors and do not necessarily represent those of their affiliated organizations, or those of the publisher, the editors and the reviewers. Any product that may be evaluated in this article, or claim that may be made by its manufacturer, is not guaranteed or endorsed by the publisher.

frontiers in Earth Science

ORIGINAL RESEARCH
published: 21 March 2022
doi: 10.3389/feart.2022.847772

Study on Mechanical Behavior of Slip Zone Soils Under Different Factors—A Case Study

Kai Liu, Xingang Wang, Baoqin Lian, Zhaobo Zhu and Chen Xue*

State Key Laboratory of Continental Dynamics, Department of Geology, Northwest University, Xi'an, China

The mechanical properties of the slip zone soil play an important role in the evolution of the loess landslides. To further understand these characteristics, a series of ring shear tests was conducted on the slip zone soils obtained from Tianshuigou landslide, to investigate the influence of moisture content, dry density, shear rate and shear method on the mechanical characteristics of slip zone soils. The experimental results showed that: an increase in the moisture content of the slip zone loess causes a significant reduction in the residual strength. Specially, both the residual cohesion and residual internal friction angle show a deceasing tendency with moisture content. The change in the residual cohesion is more sensitive to the variation in moisture content. Additionally, a trend that strength increased with the increasing of dry density was observed, and the influence degree of dry density on the increased strength is more pronounced at low moisture contents. Thirdly, shear strength shows a negative relationship with shear rate when the shear rate ranges from 0.01 mm/min and 1 mm/min. When the shear rate increased up to 10 mm/min, a stepped shear band is developed and the strength increased. In addition, the strain-softening phenomenon was observed in the single-stage shear tests, which was not noticed in the multi-stage shear tests and pre-shear tests. The residual strength obtained in pre-shear test and multi-stage shear test is slightly greater than that in the single-stage shear test. The experimental results herein can provide an important basis for analyzing the evolution mechanism and prevention of loess landslides.

Keywords: loess, landslide, slip zone soil, ring shear, mechanical behavior

OPEN ACCESS

Edited by:
Fanyu Zhang,
Lanzhou University, China

Reviewed by:
Yulong Cui,
Anhui University of Science and Technology, China
Sujatha Evangelin Ramani,
SASTRA University, India

****Correspondence:***
Xingang Wang
xgwang@nwu.edu.cn

Specialty section:
This article was submitted to Geohazards and Georisks, a section of the journal Frontiers in Earth Science

Received: *03 January 2022*
Accepted: *04 March 2022*
Published: *21 March 2022*

Citation:
Liu K, Wang X, Lian B, Zhu Z and Xue C (2022) Study on Mechanical Behavior of Slip Zone Soils Under Different Factors—A Case Study. Front. Earth Sci. 10:847772. doi: 10.3389/feart.2022.847772

INTRODUCTION

Loess landslides are widely distributed in northwestern of China. Most loess landslides can trigger catastrophic results (Derbyshire et al., 1994; Wang et al., 2020), even causing serious casualties and road damage (Xu et al., 2012; Pei et al., 2017; Leng et al., 2018). It has been found that the evolution mechanism of a landslide is closely related to the stress state and strength of slip zone soil (Zou et al., 2020). Therefore, understanding the mechanical behavior of slip zone soils is of great significance to study the formation mechanism of landslides and the landslide disaster mitigation (Wen and Aydin, 2003; Chen et al., 2014; Sassa et al., 2014; Zhang et al., 2018).

It is widely known that shear strength parameters can be determined by conducting direct shear test, triaxial compression test and ring shear test (Okada et al., 1998; Nam et al., 2011). Direct shear test and triaxial compression test are efficient ways determining the strength parameters, while the parameters measured cannot completely agree with that determined at site because the shear displacement is small, which cannot simulate the sliding movements of landslides which are

characterized by a long-run out distance. However, ring shear test has been identified as a good method for determining strength parameter due to the fact that the specimen is subjected to a continuous shear deformation without changing the shear area in the ring shear test (Tan et al., 1998; Sadrekarimi and Olson 2009), which is capable of simulating landslides with a great shear deformation (Bishop et al., 1971; Lupini et al., 1981; Tika and Hutchinson 1999; Meehan et al., 2007; Sugimoto et al., 2009). Especially, residual strength of soil is often measured by ring shear apparatus due to its advantages mentioned above (Skempton. 1985; Bishop et al., 1971).

Many scholars have paid great attention to the mechanical behavior of slip zone soils in recent years (Vithana et al., 2012; Zou et al., 2020; Xu et al., 2021). For example, by using the Bromhead-type ring shear apparatus, Dai et al. (1998) concluded that there is an obvious nonlinear relationship between residual strength and effective normal stress. Furthermore, Tika and Hutchinson (1999) conducted ring shear tests on the slip zone soil obtained from Vaiont landslide and pointed out that the soil sample shows a negative rate effect as the shear rate increases. Tiwari and Marui, (2004) carried out ring shear tests with different shear methods, including single-stage shear test, multi-stage ring shear test with increasing load, multi-stage ring shear test with decreasing load. The results revealed that three test methods all showed similar effective residual internal friction angles, while the effective residual shear intercept is different. Lian et al. (2019) conducted ring shear tests on the soil collected from a loess landslide and found that the increase of moisture content causes the color of the scratches on the shear surface to change from the original color yellow to brown, and the thickness of the shear band decreases as well. Zhang et al. (2015) proposed the reactivation mechanism of landslides after carrying out ring shear tests on the soil collected from a giant landslide in southwestern of China. Based on the high-speed ring shear test, Hu et al. (2015) explored the cause of the giant Yigong landslide and reported that the pore water pressure could not be dissipated in time during the high-speed shear process in which the shear surface was liquefied. In general, there are many factors that affect the shear strength of slip zone soil, including normal stress (Dai et al., 1998; Kimura et al., 2015), moisture content (Derbyshire et al., 1994; Wang et al., 2007; Wang et al., 2021), dry density (Liu et al., 2020; Xu et al., 2020), shear rate (Lemos et al., 1985; Duong et al., 2018; Lian et al., 2020), and shear method (Tiwari and Marui, 2004).

The effect of shear rate on residual strength is complicated (Sugimoto et al., 2009). Previous studies have revealed that the residual strength of soil is various at different shear rates. Lemos et al. (1985) found that the residual strength of the soil with high clay content increased with the increase of the shear rate, while the residual strength of the soil with low clay content was the opposite. Bhat et al. (2013) concluded that the residual strength of the mineral slip surface may vary with the shear rate. The residual strength of kaolin decreases as the shear rate increases from 0.073 mm/min to 0.162 mm/min. When the shear rate is increased from 0.233 mm/min to 0.586 mm/min, the change in residual strength is negligible. However, except for a few studies (Wang et al., 2015; Lian et al., 2020), researchers have not widely investigated the residual strength of slip zone loess at different shear rate. In addition, few studies have been conducted on the residual strength of slip zone loess under different shear methods. Therefore, it is necessary to perform ring shear tests on loess at various shear rates. With this background, to have a deeper understanding in the influence of different factors on the shear strength of slip zone soil of loess landslide, slip zone soils obtained from the Tianshuigou loess landslide were used to conduct ring shear tests. A series of ring shear tests were carried out on slip zone soils to explore the effect of factors (moisture content, dry density, shear rate and shear method) on the shear characteristics of loess. In addition, the development and change law of the strength parameter index were analyzed and compared. This study would provide a reference for a deep insight into the mechanical properties of slip zone soils, the occurrence mechanism of landslides and the prevention and mitigation of landslides.

BACKGROUND OF THE STUDY SITE

The Tianshuigou loess landslide is located at Tianshuigou village (37°31′12.31″N, 110°15′20.27″E), Suide county, Shaanxi province, China (**Figure 1**), which occurred in 2010 and 2015, destroying 20 cave dwellings without causing casualties. The landslide, on the north side of a national highway, directly threatened 54 households with 168 people (including 48 households with 137 permanent residents), 118 cave dwellings and 60 rooms in the south of the slope.

The landslide site is characterized by a concave topography. The arc-shaped landslide had a volume of approximately 1.24 × 105 m^3 (71 m long, 350 m wide and 5 m thick), and a travel distance of about 7 m. The elevation at the foot of the landslide is about 835 m asl (above the sea level).

Field investigation revealed that the landslide is located at the loess hilly and gully area (**Figure 2A**). Landslide scarps, with a height of 3–4 m, are visible on the back edge of the landslide (**Figure 2B**). The back wall of the landslide is in the shape of a circle chair. Gullies and sinkholes with varying sizes were observed on the slope (**Figure 2C**). Clearly, the vertical joints are well-developed (**Figure 2D**) and the slope toe on the front edge of the landslide is steep (**Figure 2E**), threatening the safety of the local residents. According to the field investigation, the study region exposes quaternary stratum, the main profile (**Figure 2F**) shows a typical loess layer with different sedimentary history. According to the lithological characteristics, the strata from new to old can be divided into the Holocene slope deposit (Q_4^{del}), the Upper Pleistocene wind-deposited loess (Q_3^{eol}) and the Middle Pleistocene wind-deposited loess (Q_2^{eol}), respectively. Among them, the overall sedimentary thickness of the Middle Pleistocene wind-deposited loess layer is greater compared to that of the Holocene slope deposit loess layer and the Upper Pleistocene wind-deposited loess layer. It is found that the sliding mass belongs to the Holocene slope deposit. Additionally, the slip zone is clearly exposed on the crown scarp and also found in boreholes, with the buried depth of approximately 2–6 m. The slip zone soils consist mainly of light reddish yellow silt soils with

calcareous nodules. The structure of the slip zone soil is clumpy, penetrated by plant roots and humus.

MATERIALS AND METHODS

Sample Material and Preparation

The slip zone samples that have been identified as Middle Pleistocene silt, were collected from the artificial exploration wells (**Figure 3**). The sampling depth is about 6 m below ground surface. The samples were carefully cut to column shape with diameter of 15 cm and height of about 30 cm, and then wrapped carefully with membrane to reduce sample disturbance during transport to the laboratory.

The loess samples retrieved from the field were firstly air-dried at a temperature of 105 °C for more than 24 h (Yuan et al., 2019; Hong et al., 2021). According to the quality of the samples before and after drying, the natural moisture content of the sliding zone soil was calculated to be 12%. The soil samples were then passed through a 2 mm sieve. After that, the physical parameters such as dry density, plastic limit and liquid limit were determined using sieved soil samples according to the Chinese National Standards (CNS) GB/T50123-2019. The physical index of slip zone soils is shown in **Table 1**. Additionally, the particle size distribution of soils was determined by using a laser particle size analyzer with a dispersant and was plotted in **Figure 4**. Laser particle size analysis demonstrated that the slip zone loess is mainly consist of silt particles (between 0.005 and 0.075 mm), with the percentage of about 70.59%, while the sand content (> 0.075 um) accounts for 19.80%. The soil sample of the slip zone is classified as sandy silt according to the Chinese National Standards (CNS) GB 5007-2011. This type of loess has strong water-sensitive properties, and its mechanical strength will be drastically reduced when it encounters water, which often leads to the occurrence of landslides (Leng et al., 2018).

Prior to testing, deionized water was mixed with the sieved soil samples until the target moisture contents was obtained. Next, the soil samples were placed in cling film bags and then were kept in a sealed container for more than 24 h to hydrate (Zhang and Wang, 2018).

Testing Apparatus

The SRS-150 ring shear apparatus manufactured by the American GCTS company was used and shown in **Figure 5**. The apparatus mainly consists of three modules: main ring shear cell, including axial force and torque actuators; PCP-15U panel for implementation of axis-translation technique; and the data acquisition and transmission system, with data software for real-time processing of the stress and the shear displacements. For the shearing cell, it is mainly composed of a lower shear box and an upper shear box. The apparatus is capable of shearing the soil specimen with a large displacement without change the shear area, thus the residual strength of the soil can be determined with a good accuracy (Lian et al., 2019).

The torsional shear test principle is shown in **Figure 6**. Prior to shearing, the axial load is applied by the pneumatic actuator via

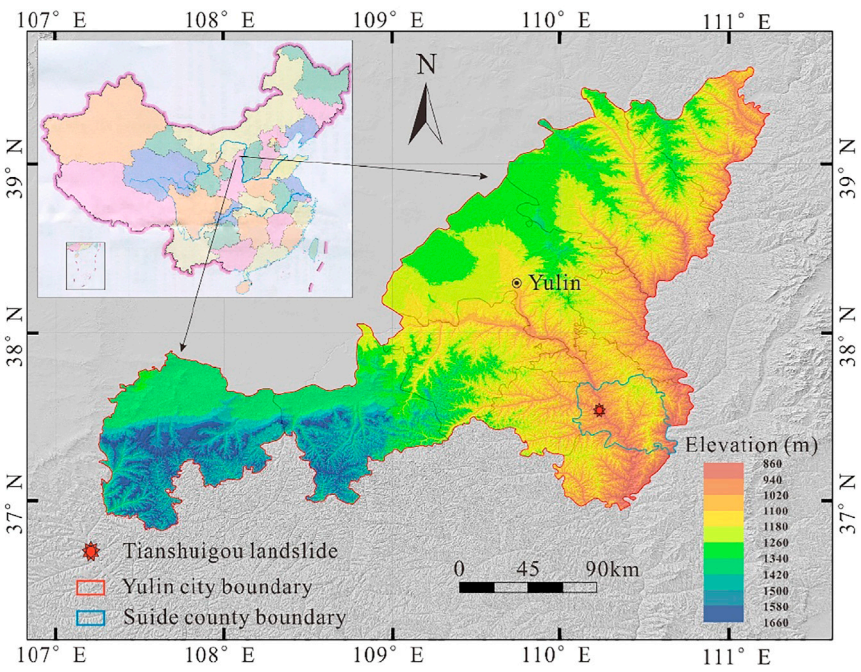

FIGURE 1 | Location of the study area.

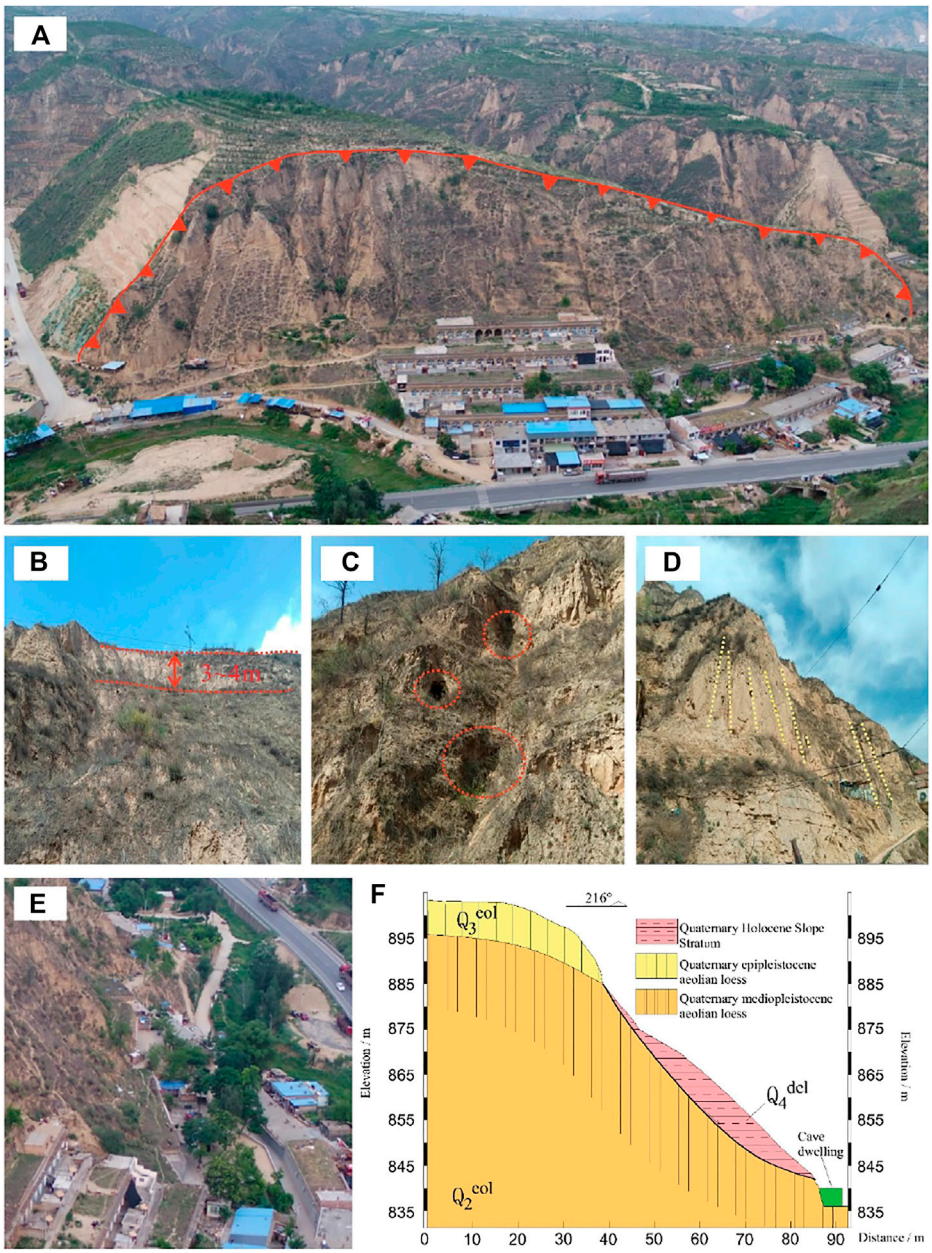

FIGURE 2 | Filed investigation on Tianshuigou landslide. **(A)** Landslide boundary; **(B)** Scarps on the back edge of the landslide; **(C)** Slope gullies and sinkholes; **(D)** Well-developed vertical joints; **(E)** Steep toe at the front of the landslide; **(F)** Main profile of landslide showing stratums.

the upper shear platen, as shown in **Figure 6**. During the shearing process, the upper platen is rotated, while the bottom platen is kept still. The specimen is rotated by applying a torque T via the upper shear disk, after which the specimen would undergo circular shearing upon the application of the torque. During this process, it is assumed that the shear stress is uniformly distributed along the shear plane. The relationship can be expressed as (Trandafir and Sassa, 2004):

$$\overline{\Delta L} = \bar{v} \times t \tag{1}$$

$$\sigma = \frac{F}{\pi\left(R_2^2 - R_1^2\right)} \tag{2}$$

$$\bar{\tau} = \frac{T}{\int_{R_1}^{R_2} 2\pi R^2 dR} = \frac{3T}{2\pi\left(R_2^3 - R_1^3\right)} \tag{3}$$

Where T is the torque; F is the axial load; R_1 is the inner diameter of the ring shear disc; R_2 is the outer diameter of the ring shear disc; t is the shear time; $\bar{\tau}$ is the average shear stress; $\bar{v}$ is the shear rate; $\overline{\Delta L}$ is the average shear displacement.

FIGURE 3 | Sampling photos at the site.

TABLE 1 | Physical parameters of slip-zone loess.

W	ρ	ρ_d	G_S	W_L	W_p	Grain size fractions (%)		
						<0.005 mm	0.005–0.075 mm	>0.075 mm
12	1.51	1.35	2.70	27.1	17.6	9.61	70.59	19.80

Notes: W= *Natural moisture content (%);* ρ = *Natural density (g/cm^3);* ρ_d = *Dry density (g/cm^3);* Gs = *specific gravity of soil particle;* W_L , *Liquid limit (%);* W_p = *Plastic limit (%).*

Experimental Scheme

In this study, four group tests were performed on specimens to investigate the effect of moisture content, dry density, shear rate and shear method on the shear characteristics of slip zone soil (**Table 2**). In this study, 47 sets of ring shear tests were carried out. In addition, the variation law in the strength parameter index with the change in the factor mentioned above was compared and analyzed.

The natural moisture content of the slip zone soil at site is about 12%. According to the physical parameters of the loess (**Table 1**), the saturated water content is calculated to be about 22.4%. Considering the fact that an increase in the moisture content is prevailed due to the rainfall infiltration, the moisture content of the specimens in this study is set as 12%, 14%, 16%, 18%, and 20% respectively. The natural dry density of slip zone soil is 1.35 g/cm^3. The dry density of the deepest slip soil obtained during field sampling (**Figure 3**) is approximately 1.45 g/cm^3. Therefore, the dry density of 1.35 g/cm^3, 1.45 g/cm^3 and 1.55 g/cm^3 was chosen according to the natural dry density *in-situ*. The shear rate of the loess ring shear test conducted by scholars can reach hundreds of millimeters per minute (Hong et al., 2021; Ma et al., 2021). Referring to previous research results, Duong et al. (2018) chose a shear rate of 0.02 mm/min~20 mm/min in the process of studying the effect of shear rate on the residual strength of kaolin-bentonite mixtures. To investigate the shear rate level on the mechanical behavior of loess soil, according to instrument conditions the specimens were sheared at rates of 0.01 mm/min, 0.1 mm/min, 1 mm/min, 10 mm/min, 100 mm/min at the normal stress of 100 kPa, 200 and 300 kPa.

One main advantage of the ring shear apparatus is that the residual strength can be obtained through various shear methods (Tiwari and Marui, 2004; Duong and Hai, 2021). In this work, a total of seven samples were sheared by using three different shear methods, including single-stage shear test, multi-stage shear test and pre-shear test. 1) A series of three single-stage shear tests have been firstly carried out on specimens under different normal stresses, samples 1, 2 and 3 has been sheared at rate of 10 mm/min. The single-stage shear tests mainly consist of consolidation stage and shearing stage. In the consolidation stage, specimens were consolidated for about 12 h in the shear box (Lian et al., 2020). In the shearing stage, the specimens were sheared until the shear stress is basically stable. The basically steady state means that the shear stress remains at a roughly stable minimum shear resistance value within a certain shear displacement range (Lian et al., 2021). 2) Multi-stage shear tests have been performed to investigate the influence of the pre-shear history on the value of the residual strength. In multi-stage shear tests, the tests were

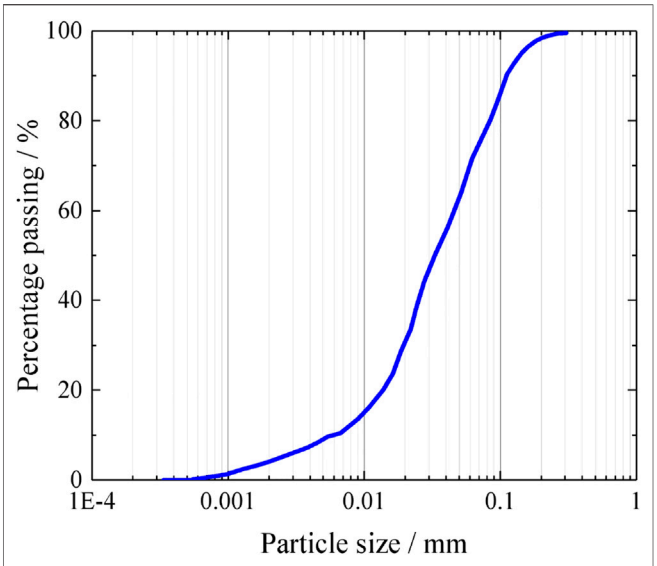

FIGURE 4 | Particle size distribution of slip zone soil.

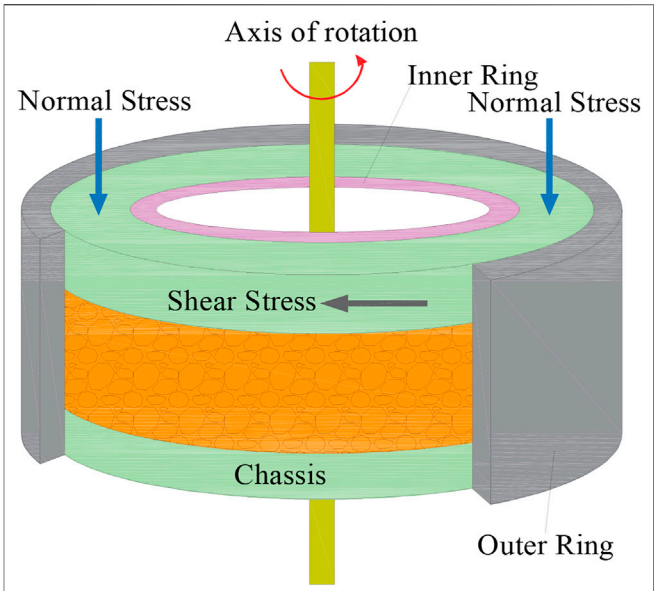

FIGURE 6 | Schematic diagram of ring shear test.

performed by following a multi-stage scheme in which residual strength assessments were made at one or more normal stress value: 50 kPa, 100kPa, 200kPa or 300 kPa. To be more specific, a low normal stress (i.e., 50 kPa) was firstly applied to allow the consolidation of the specimen and then the specimen was sheared until the stable state was achieved. After that, the specimen was subjected to shear until the residual state at this stage was reached under a higher normal stress level (i.e., 100kPa). In this work, the specimen was sheared at four stresses level to obtain the residual strength value of specimens under at four stages. 3) In pre-shear tests, the specimen was firstly sheared at a faster rate until a shear surface was formed. After that, the specimen was subjected to shear at a lower shear rate until the residual state was achieved.

RESULTS

Moisture Content Effect on Residual Strength

The typical stress-shear displacement curves of loess specimens with different moisture contents are shown in **Figure 7**. It can be seen that a sharp increase in shear strength was observed before the peak strength after which shear resistance decrease gradually, and the residual state was achieved at a large shear displacement. The test results revealed that the residual strength of the slip zone soil decreases with the increase of the moisture content. Taking the sample at normal stress of 300 kPa as an example, the residual strength of the specimen fell from 237.8 kPa at the moisture

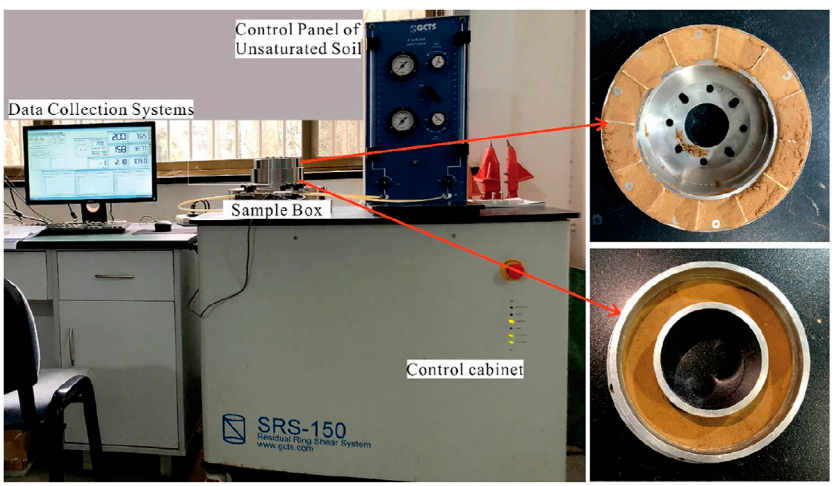

FIGURE 5 | Panoramic view of the entire SRS-150 ring shear apparatus.

TABLE 2 | Ring shear test plan.

Test groups	Moisture content/%	Dry density/g/cm^3	Normal stress/kPa	Shear rate/mm/min	Shear methods
I	12	1.35	100	1	Single-stage shear
	14		150		
	16		200		
	18		250		
	20		300		
II	12	1.35/1.45/1.55	200	1	Single-stage shear
	14				
	16				
III	16	1.35	100/200/300	100	Single-stage shear
				10	
				1	
				0.1	
				0.01	
IV	16	1.35	100	10	Single-stage shear
			200		
			300		
	16	1.35	100	100→10	Pre-shear
			200		
			300		
	16	1.35	50→100→200→300	10	Multi-stage shear

content of 12%–198.9 kPa at the moisture content of 20%, decreasing by roughly 16.4%.

The residual strength parameters including the residual cohesion and residual internal friction angle were determined by using the Mohr-Coulomb shear strength criterion (Labuz and Zang, 2012) according to the changes in residual strength of specimens with different moisture contents (**Figure 8**) and the shear parameters are listed in **Table 3**. Clearly, the residual cohesion decreases greatly as the moisture content increases from 12% to 20%. Specially, the residual cohesion of the specimen decreases from 40.88 kPa with moisture content of 12%–17.94 kPa at the moisture content of 20%, decreasing by about 56.12%. Additionally, a decreasing tendency of the residual internal friction angle with moisture content was observed (**Table 3**). The residual internal friction angle decreases by 7.1% as the moisture content increases from 12% to 20%.

Dry Density Effect on Residual Strength

The shear stress-shear displacement curves of specimens with different dry densities are shown in **Figure 9**. The results showed that a significant increase in the shear strength was observed when the dry density increases. For example, when the moisture content is constant (12%), the residual strength increases from 171.9 kPa at the dry density of 1.35 g/cm^3 to 200.0 kPa at the dry density of 1.55 g/cm^3. Furthermore, the effect of dry density on the shear displacement at which the residual state of loess soil was achieved is obvious.

Take the sample with 12% moisture content as an example (**Figure 9A**), the corresponding shear displacement at residual state is about 22 mm with the dry density of 1.35 g/cm^3, however, the residual strength of the specimens with the dry density of 1.45 g/cm^3 and 1.55 g/cm^3 were achieved at the shear displacement of approximately 25 mm and 31 mm, respectively.

Shear Rate Effect on Residual Strength

Figure 10 presents shear stress against shear displacement at different shear rates. To facilitate a clear view of the variation in the residual strength with shear rate and normal stress, **Figure 11A** shows the residual strength envelope surface in the three-dimensional space of normal stress-residual strength-shear rate. It can be seen that the three-dimensional strength envelope plotted in **Figure 11A** is not continuous and flat, indicating that the turning point of shear rate can be obtained at which the trend of the change in residual strength with shear rate changes. To quantitatively analyze the change trend of residual strength with shear rate and normal stress, **Figure 11B** plots the residual strength against shear rate at the normal stress of 100 kPa, 200kPa, and 300kPa. Obviously, the residual strength decreases as shear rate ranges from 0.01 mm/min to 1 mm/min and from 10 mm/min to 100/min at all normal stress levels, while that increases as shear rate ranges between 1 mm/min and 10 mm/min. The experimental results herein show the decreasing tendency of residual strength with increasing shear rate from 0.01 mm/min to 1 mm/min (speed weakening characteristics (Kimura et al., 2014), i.e., residual strength decreases with increasing shear rate), which is agree well with the conclusion reported by Tika and Hutchinson, (1999) that a negative rate effect on the residual strength was observed when shear rate is within this range.

Shear Methods Effect on Residual Strength

Figure 12 shows shear stress-displacement curves under three different shear methods, respectively. It can be seen from

Figure 12A that strain-softening phenomenon was observed when the specimen is sheared in the single-stage shear tests.

For example, taking the test results at normal stress of 200 kPa as an example, the peak strength is 172.5 kPa and the residual strength is 163.9 kPa, with the peak-residual strength drop of 8.6 kPa. However, no obvious strain-softening phenomenon was observed in the multi-stage shear tests and pre-shear tests (**Figure 12**bc). **Table 4** shows the residual strength of the slip zone soil in different shear tests. It is clear that the residual strength obtained in multi-stage shear tests and pre-shear tests are slightly greater than that obtained in the single-stage shear tests.

DISCUSSION

State of Soil Effect on the Loess Residual Shear Strength Parameters

Moisture Content

The ring shear test results revealed that the shear strength of loess decreases significantly with the increase of moisture content. Other studies have reported the similar conclusion (Derbyshire et al., 1994; Tian et al., 2021). These research results indicated that when water penetrates into the loess, the residual strength of the slip zone soil would be decreased, which contribute to the slope movements and the slope unstability.

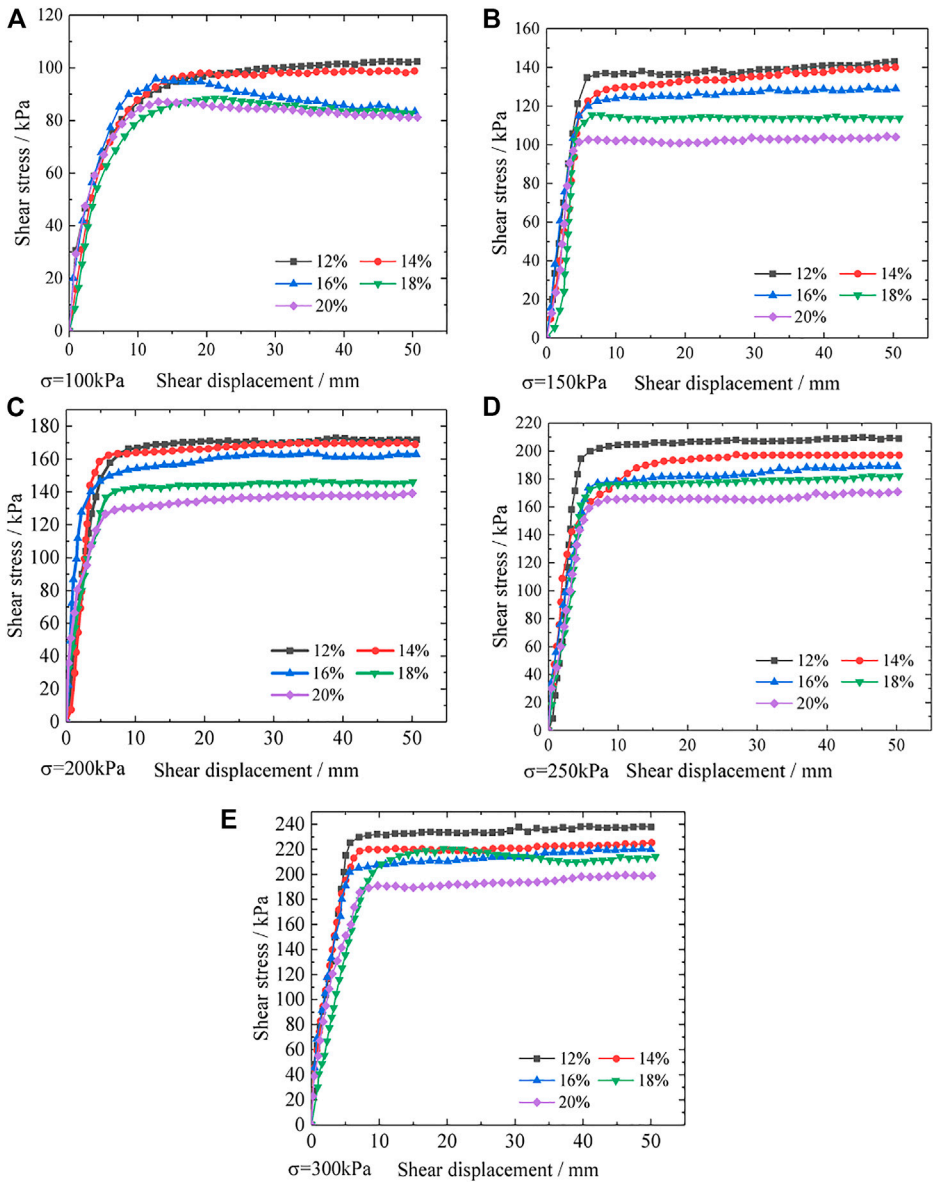

FIGURE 7 | The relationship curve of shear stress-shear displacement of sample with moisture content. **(A)** Normal stress is 100 kPa **(B)** Normal stress is 150 kPa; **(C)** Normal stress is 200 kPa; **(D)** Normal stress is 250 kPa; **(E)** Normal stress is 300 kPa.

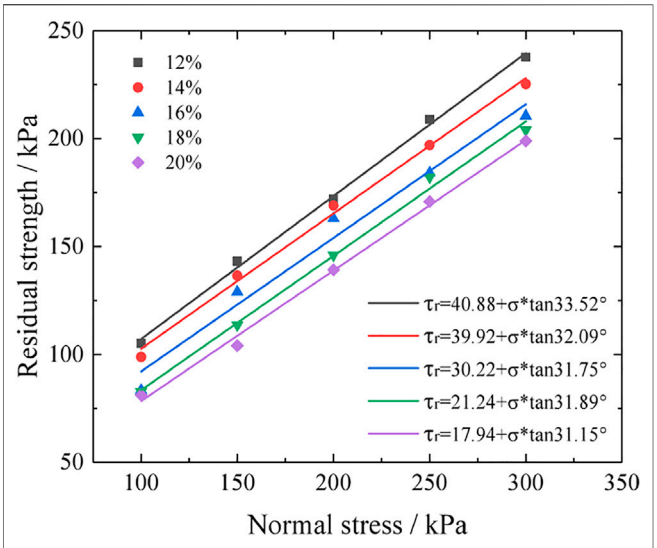

FIGURE 8 | Changes in residual strength values of specimens with different moisture content.

TABLE 3 | Residual shear strength parameters under different moisture content.

Moisture content/%	Residual cohesion/kPa	Residual internal friction angle/°
12	40.88	33.52
14	39.92	32.09
16	30.22	31.75
18	21.24	31.89
20	17.94	31.15

Additionally, it was found that the residual cohesion of loess in the ring shear test decreases with moisture content (**Figure 13**). This may be explained as follows: the increase of moisture content can thicken the bound water film attached to the surface of the soil particles (Tian et al., 2021). Furthermore, moisture will dissolve the cement and salt between the particles, causing a significant drop in cohesion (Zhang et al., 2013). With the increase of moisture content, the free water content between soil particles increases. The lubricity between particles will be enhanced, and the occlusal friction and sliding friction between particles will be significantly reduced, which causes the residual internal friction angle to be reduced. It is worth noting that with the increase of moisture content, the reduction in the residual cohesion is much greater than the reduction in the residual internal friction angle, implying that residual cohesion is more sensitive to changes of moisture content. In addition, the

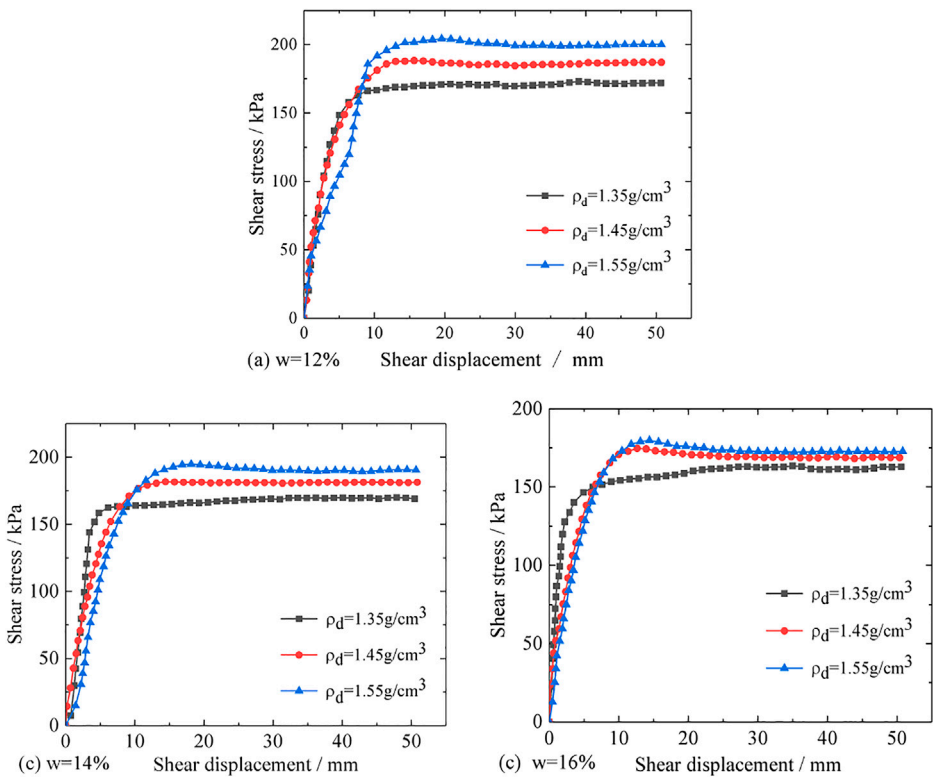

FIGURE 9 | Shear stress-shear displacement curve of specimens under different dry densities. **(A)** Moisture content is 12%; **(B)** Moisture content is 14%; **(C)** Moisture content is 16%.

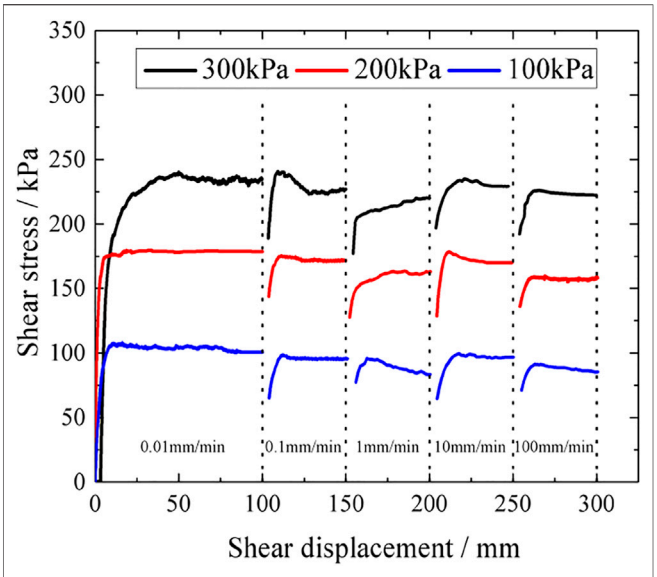

FIGURE 10 | The relationship curve of shear stress-shear displacement of specimen under different shear rates.

increased moisture content is an important factor resulting in the softening of loess. In the test, it was also found that when the moisture content of the sample is great, the soil was rotated out of the gap between the shear boxes during the shearing process (**Figure 14**). Loess is characterized by a strong water sensitivity (Dijkstra et al., 1995; Lian et al., 2020). For a slope formed in a certain geological environment, the soil in the slope has been in a balanced state of the coupling between a certain stress level and groundwater for a long time. Once water enters the slope, it would destroy the original balance system. Therefore, most unstable slopes and landslides are closely related to the action of water (Ma et al., 2019). The two slides of the Tianshuigou landslide in 2010 and 2015 occurred after summer rainfall. According to the test results and the actual situation, it can be concluded that the reduction of loess strength caused by water is the main reason for the Tianshuigou landslide.

Dry Density

The value of the dry density reflects the degree of solidity and compression of the soil, and it is manifested in the microscopic aspect as the size of the voids between soil particles and the degree of compactness of the particles (Liu et al., 2020). The results of this test revealed that the shear strength of the sample increases with the dry density at all moisture contents (**Figure 15**). The phenomenon may be explained as follows: when the dry density of the sample increases, the pores between particles decrease, which causes the particle contact to be close, the pore ratio decreases, and the cohesion between particles increases. The close contact of the particles will increase the occlusion, and the friction between the particles will also increase (Li, 2018; Xu et al., 2020). For Tianshuigou landslide, the natural dry density of the sliding zone soil is 1.35 g/cm^3. The method of improving the residual strength of soil by increasing the dry density under the natural moisture content is very impressive, which provides a way of thinking for prevention of the landslide.

For specimens with lower moisture contents, the effect of dry density on increased shear strength is more obvious (**Figure 15**). For example, when the dry density increases from 1.35 g/cm^3 to 1.55 g/cm^3 at the normal pressure of 200 kPa, the increase in the residual strength was decreased from about 29.1 kPa at the moisture content of 12% to 9.9 kPa at the moisture content of 16%. The fitting formula in the figure can describe the relationship between dry density and residual strength. For samples with lower moisture content, the larger the coefficient before dry density in the formula, it means that each unit increase in dry density contributes more to residual strength. The reason is that water in the soil sample mainly exists in the form of strongly bound water at a low moisture content, which causes the soil in relatively stable and immobile state, the shear strength can be improved to a greater extent (Lian et al., 2019). While more free water will appear on the specimen at the higher moisture content, which weaken the connection between soil particles. Thus, the influence of dry density on the increased shear strength is little.

When the shear stress of the sample is reduced from the peak strength to the residual strength, the soil particles on the shear surface are constantly adjusted and positioned along the shear direction under the action of torsion shear force to gradually form a new arrangement. Consequently, the original structure of the soil is destroyed (Sebastian and Luise, 2006). For the samples with a low dry density, the pore space of the soil particles is relatively large during the shearing process under the action of axial pressure, and the adjustment of the particle arrangement is relatively easy. Compared with samples with a lower dry density, the particles at the shear surface of the sample with a higher dry density are dense and the movable space is small, which causes the adjustment of the particles to become more difficult. Therefore, the specimen with a high dry density undergoes a greater shear displacement to reach the residual state (**Figure 9**).

Influence of Shear Behavior on Shear Strength of Loess

Shear Rate Effect on Loess Residual Shear Strength

In general, soils exhibit different shear resistance with the change of shear rate, which may show negative rate effect, positive rate effect and neutral effect (Hungr and Morgenstern, 1984; Skempton, 1985; Tika and Hutchinson, 1999; Kimura et al., 2015). The results obtained in this study show that the shear rate exhibits a negative rate effect from 0.01 mm/min to 1 mm/min, which is consistent with the conclusion reported by the Tika and Hutchinson, 1999. Additionally, it is widely acknowledged that the shear band structure changes in the ring shear test (Agung et al., 2004; Sadrekarimi and Olson, 2010). In this study, the slip surface of loess is relatively smooth when the shear rate is 1 mm/min,

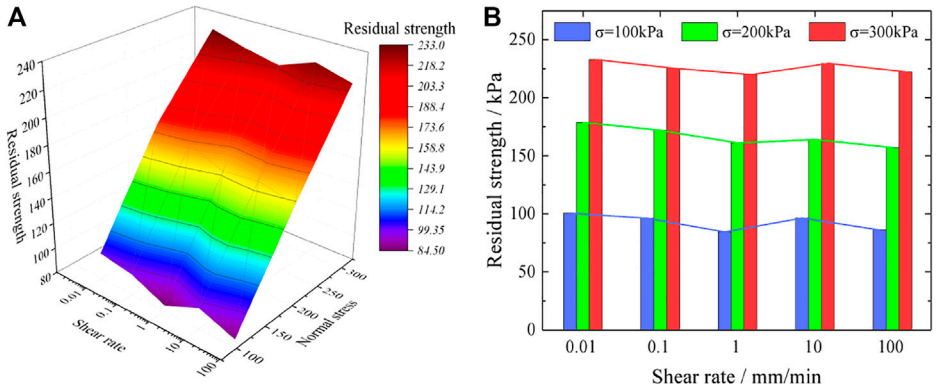

FIGURE 11 | The relationship between residual strength and shear rate. **(A)** Plot of residual strength versus shear rate and normal stress; **(B)** Plot of residual strength and shear rate.

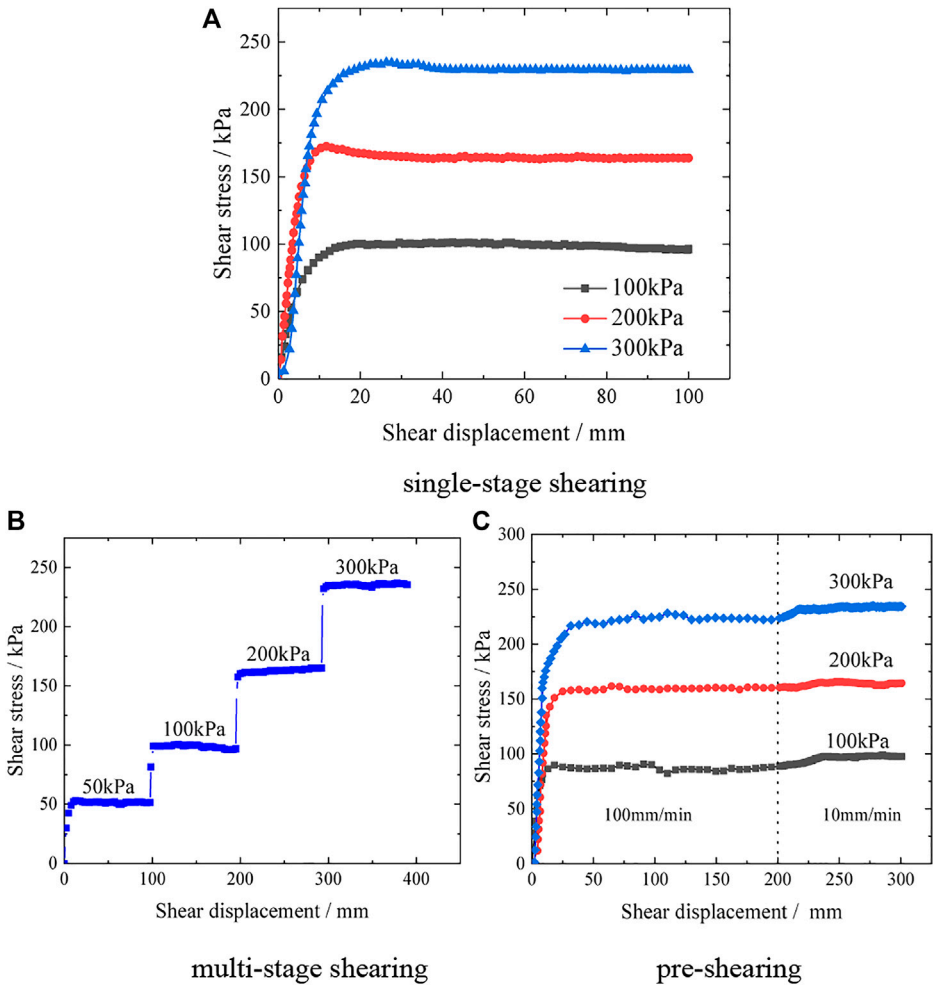

FIGURE 12 | Shear stress-shear displacement relation curve under different shear method. **(A)** single-stage shearing **(B)** multi-stage shearing **(C)** pre-shearing.

TABLE 4 | Residual strength values under different shear methods.

Shear methods	σ = 100 kPa residual strength	σ = 200 kPa residual strength	σ = 300 kPa residual strength
Single-stage shear	96.3	163.9	229.7
Multi-stage shear	96.8	165.1	235.4
Pre-shear	97.7	164.9	234.3

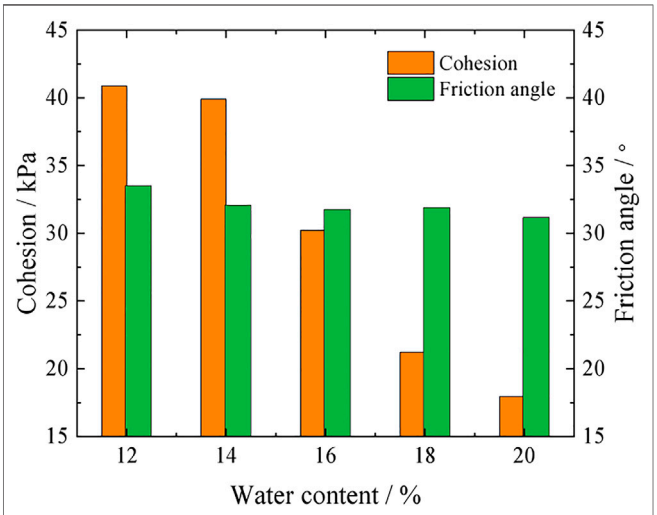

FIGURE 13 | The relationship between shear strength index and moisture content.

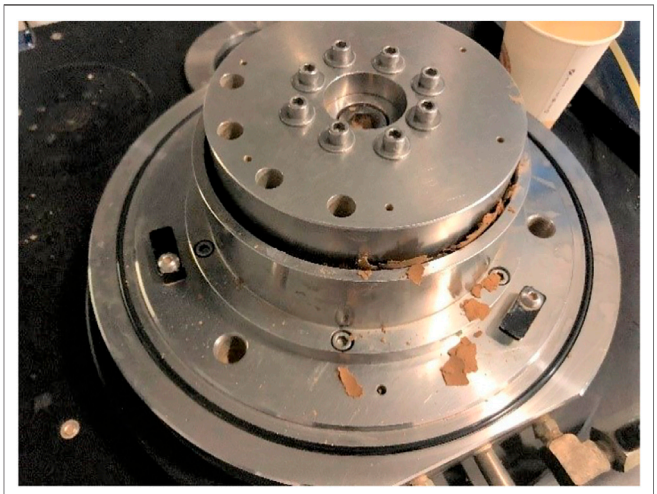

FIGURE 14 | The sample is extruded from the gap between the upper and lower shear boxes (w = 20%).

whereas a stepped slip zone which is relatively rough is formed in the slip surface when the rate increased to 10 mm/min. This may be attributed to the difficulty of the pore water pressure dissipation in time under a high shearing, resulting in a lower residual strength. In the laboratory test, it was found that the effect of shear rate on the residual strength of sliding zone soil shows a negative rate effect. when the shear rate is between 0.01 mm/min and 1 mm/min. When the Tianshuigou landslide is in instability or limit equilibrium, if a critical combination of landslide displacement and velocity is induced, the shear strength of the soil will decrease due to the negative rate effect, which will induce landslide reactivate.

When the shear rate increases up to 1 mm/min, the minimum residual strength was achieved. However, as shear rate increases from 1 mm/min to 10 mm/min, the residual strength increases. The change trend of residual strength with shear rate may be explained as follows: the increase in shear rate causes disturbances of the shear surface in a certain range, and the shear surface transitions from a single, smooth shape (**Figure 16A**) to a stepped shear zone with a certain thickness (**Figure 16B**), the residual strength is increased. As the shear rate continues to increase to 100 mm/min, the residual strength decreases, which may be attributed to the fact that the built-up pore water pressure cannot be dissipated in time under high-speed shearing and the effective residual strength decreased consequently. Additionally, the test shows that the residual strength is less affected by the shear rate at the higher normal stress level. For example, when the normal pressure is 100 kPa, the difference between the maximum and minimum residual strength of the specimen within the range of the test shear rate accounts for about 16.08%. However, when normal stress increases to 200 and 300 kPa, the difference between the maximum and minimum residual strength is roughly 12.08% and 5.58%, respectively.

Shear Method Effect on the Loess Residual Shear Strength Parameters

The residual strength obtained by different shearing methods is different (Tiwari and Marui, 2004). The test results show that the residual strength obtained by pre-shearing and multi-stage shearing are slightly larger than those obtained by single-stage shearing. Similar laws were also found in the slip zone soil of the Three Gorges Huangtupo landslide (Wang et al., 2012). The residual strength obtained by the single-stage shearing can be understood as the residual strength of the slip zone soil during the one-time sliding of the landslide. The residual strength obtained by pre-shearing is the residual strength of the slip zone soil when the sliding surface has been formed and slides again after a period of time. The residual strength obtained by multi-stage shearing can be understood as the residual strength of slip zone soil in the

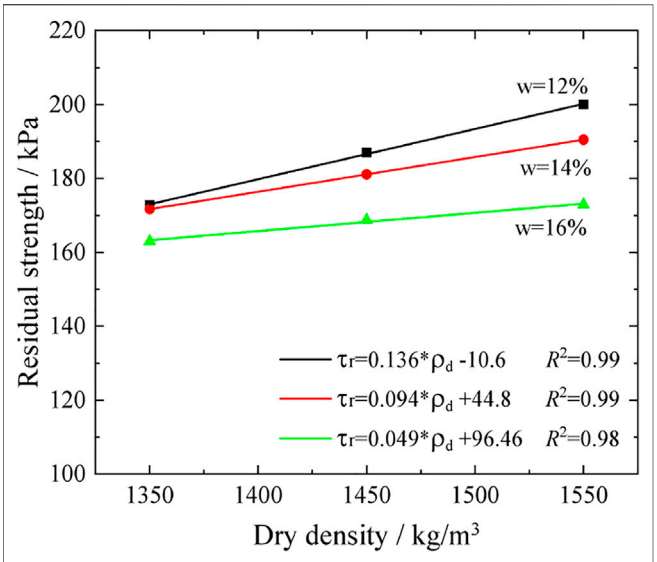

FIGURE 15 | The relationship between residual strength and dry density.

process of step-by-step penetration and sliding over time. In the early stage of the pre-shear test, the high-speed ring shear disturbed the soil particles near the shear surface greatly, which increased the thickness of the shear band, and therefore the shear strength was improved to a certain extent. In the multi-stage shear test, the slip zone soil was consolidated and sheared step by step for many times, which increased the compactness of the soil and the effective stress. In addition, it takes a relatively long time to complete a set of shear tests, and the moisture content of the sample may be reduced. Therefore, the residual strength of the soil sample under the multi-stage shear method is relatively increased. Although the single-stage shear test is more time-consuming than the other two shear methods, it is less affected by other factors and the error is relatively small.

The strain-softening phenomenon was observed when the specimen was sheared at single-stage shear method. The directional arrangement of soil particles during the shearing process is the cause of strain softening. In the multi-stage shearing and pre-shear tests, the previous shearing makes the soil particles of the shear zone basically form a directional arrangement, thus no obvious strain softening phenomenon was observed in the pre-shear tests and multi-stage shear tests.

Limitation

It is well known that the loess soil in different areas of the Loess Plateau is characterized by various geotechnical properties (Zhang and Wang, 2018). A series of ring shear tests was conducted on loess soil obtained from a loess landslide that recently occurred on the Loess Plateau in northern Shaanxi. Therefore, our experiment has certain regional limitations. In addition, the stability of slopes is significantly affected by pore water pressure generation and dissipation (Carey et al., 2017; Askarinejad et al., 2018). However, due to the fact that the equipment used in current study is not capable of recording real-time pore water pressure generated, the further investigation in the mechanical behavior of slip zone soils with a advanced apparatus which is capable of obtaining the accurate parameters such as pore water pressure is needed. Due to the large workload of the designed test, the parallel test of the ring shear test is not set up. In this experiment, it was concluded that the cohesion of the soil in the Tianshuigou landslide zone was higher at low water content, which may be related to the fine-grained composition of the soil. In view of this situation, we intend to use the X-ray diffraction method to study it in the follow-up research.

CONCLUSION

A series of drainage ring shear tests were conducted on distributed loess samples collected from a loess landslide occurred on the Loess Plateau in northern Shaanxi, China. The influence of moisture content, dry density, shear rate and

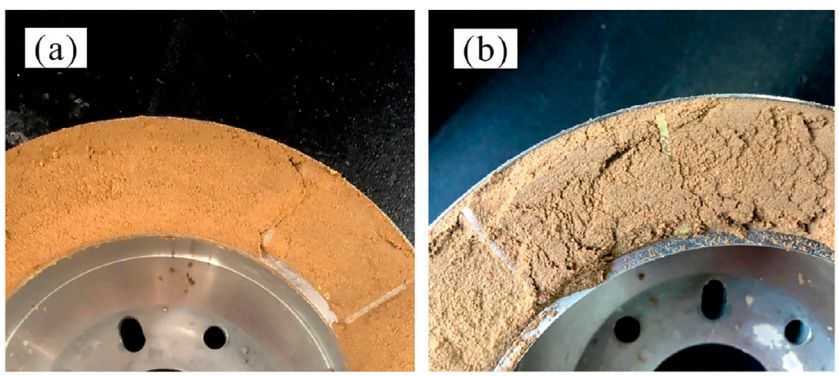

FIGURE 16 | Shear surface morphology **(A)** Smooth shear surface **(B)** Step shear zone.

shear method on the residual strength was explored. The following conclusions are obtained:

(1) The increase in moisture content causes a significant reduction in the residual strength of slip zone loess. In terms of strength parameters, the residual cohesion and residual internal friction angle decrease with the increase of moisture content. It is worth noting that the reduction in residual cohesion is much greater than that in residual internal friction angle, indicating that residual cohesion is more sensitive to changes in moisture content.
(2) Under the same conditions, the residual strength of slip zone soil increases with dry density, and the increase in the residual strength with dry density is more obvious at a lower moisture content.

(3) The residual strength shows a negative rate effect with the shear rate ranging from 0.01 mm/min to 1 mm/min. When the shear rate increased to 10 mm/min, a stepped shear band was observed and the residual strength increased. When the shear rate ranges from 10 mm/min to 100 mm/min, the decreasing tendency in residual strength was found.
(4) The residual strength obtained in the pre-shear tests and the multi-stage shear tests is slightly greater than that obtained in the single-stage shear tests. In addition, the strain-softening phenomenon was observed in single-stage shear tests, while the strain softening phenomenon was not obvious in the multi-stage shear tests and pre-shear tests.

DATA AVAILABILITY STATEMENT

The original contributions presented in the study are included in the article/Supplementary Material, further inquiries can be directed to the corresponding author.

AUTHOR CONTRIBUTIONS

KL and XW designed the experiments, analyzed data and wrote the whole paper; BL guided the writing of the paper and revised the paper; ZZ and CX designed the experiments and helped to select the experimental area. All authors have read and agreed to the published version of the manuscript.

FUNDING

The National Natural Science Foundation of China (No. 41902268), Nature Science Basic Research Plan in Shaanxi Province of China (No. 2022JQ-253) and China Postdoctoral Science Foundation (No. 2021M702648) are gratefully acknowledged.

REFERENCES

Agung, M. W., Sassa, K., Fukuoka, H., and Wang, G. (2004). Evolution of Shear-Zone Structure in Undrained Ring-Shear Tests. *Landslides* 1 (2), 101–112. doi:10.1007/s10346-004-0001-9

Askarinejad, A., Akca, D., and Springman, S. M. (2018). Precursors of Instability in a Natural Slope Due to Rainfall: a Full-Scale experiment. *Landslides* 15 (9), 1745–1759. doi:10.1007/s10346-018-0994-0

Bhat, D. R., Bhandary, N. P., and Yatabe, R. (2013). Effect of Shearing Rate on Residual Strength of Kaolin Clay. *Electron. J. Geotechnical Eng.* 18, 387–1396.

Bishop, A. W., Green, G. E., Garga, V. K., Andresen, A., and Brown, J. D. (1971). A New Ring Shear Apparatus and its Application to the Measurement of Residual Strength. *Géotechnique* 21 (4), 273–328. doi:10.1680/geot.1971.21.4.273

Carey, J. M., McSaveney, M. J., and Petley, D. N. (2017). Dynamic Liquefaction of Shear Zones in Intact Loess during Simulated Earthquake Loading. *Landslides* 14 (3), 789–804. doi:10.1007/s10346-016-0746-y

Chen, J., Dai, F., Xu, L., Chen, S., Wang, P., Long, W., et al. (2014). Properties and Microstructure of a Natural Slip Zone in Loose Deposits of Red Beds, Southwestern China. *Eng. Geology.* 183, 53–64. doi:10.1016/j.enggeo.2014.10.004

Dai, F. C., Wang, S. J., and Li, C. F. (1998). The Drained Residual Strength of Volcanics-Derived Soil Sampled on Lantau Island, Hong Kong. *J. Eng. Geology.* 6 (3), 223–229. (in Chinese).

Derbyshire, E., Dijkstra, T. A., Smalley, I. J., and Li, Y. (1994). Failure Mechanisms in Loess and the Effects of Moisture Content Changes on Remoulded Strength. *Quat. Int.* 24, 5–15. doi:10.1016/1040-6182(94)90032-9

Dijkstra, T. A., Smalley, I. J., and Rogers, C. D. F. (1995). Particle Packing in Loess Deposits and the Problem of Structure Collapse and Hydroconsolidation. *Eng. Geology.* 40 (1-2), 49–64. doi:10.1016/0013-7952(95)00022-4

Duong, N. T., and Hai, N. V. (2021). Residual Strength of Weakly Cemented Kaolin Clay in Multi-Stage Ring Shear Test. *Arabian J. Sci. Eng.* 2021, 1–15. doi:10.1007/s13369-021-06132-2

Duong, N. T., Suzuki, M., and Van Hai, N. (2018). Rate and Acceleration Effects on Residual Strength of Kaolin and Kaolin-Bentonite Mixtures in Ring Shearing. *Soils and foundations* 58 (5), 1153–1172. doi:10.1016/j.sandf.2018.05.011

Hong, Y., Ling, X. Z., and He, K. Q. (2021). Effects of Sliding Liquefaction on Homogeneous Loess Landslides in Western China. *Scientific Rep.* 11 (1), 1–14. doi:10.1038/s41598-021-91411-z

Hu, M.-j., Pan, H.-l., Zhu, C.-q., and Wang, F.-w. (2015). High-speed Ring Shear Tests to Study the Motion and Acceleration Processes of the Yingong Landslide. *J. Mt. Sci.* 12 (6), 1534–1541. doi:10.1007/s11629-014-3059-4

Hungr, O., and Morgenstern, N. R. (1984). High Velocity Ring Shear Tests on Sand. *Géotechnique* 34 (3), 415–421.

Kimura, S., Nakamura, S., and Vithana, S. B. (2015). Influence of Effective normal Stress in the Measurement of Fully Softened Strength in Different Origin Landslide Soils. *Soil Tillage Res.* 145, 47–54. doi:10.1016/j.still.2014.07.018

Kimura, S., Nakamura, S., Vithana, S. B., and Sakai, K. (2014). Shearing Rate Effect on Residual Strength of Landslide Soils in the Slow Rate Range. *Landslides* 11 (6), 969–979. doi:10.1007/s10346-013-0457-6

Labuz, J. F., and Zang, A. (2012). Mohr-Coulomb Failure Criterion. *Rock Mech. Rock Eng.* 45 (6), 975–979. doi:10.1007/s00603-012-0281-7

Lemos, L., Skempton, A. W., and Vaughan, P. R. (1985) Earthquake Loading of Shear Surfaces in Slopes. Proceedings of 11th International Conference on Soil Mechanics and Foundation Engineering 4, 1955–1958.

Leng, Y., Peng, J., Wang, Q., Meng, Z., and Huang, W. (2018). A Fluidized Landslide Occurred in the Loess Plateau: A Study on Loess Landslide in South Jingyang Tableland. *Eng. Geology.* 236, 129–136. doi:10.1016/j.enggeo.2017.05.006

Li, Y. (2018). A Review of Shear and Tensile Strengths of the Malan Loess in China. *Eng. Geology.* 236, 4–10. doi:10.1016/j.enggeo.2017.02.023

Lian, B., Peng, J., Wang, X., and Huang, Q. (2019). Moisture Content Effect on the Ring Shear Characteristics of Slip Zone Loess at High Shearing Rates. *Bull. Eng. Geol. Environ.* 79 (2), 999–1008. doi:10.1007/s10064-019-01597-w

Lian, B. Q., Wang, X. G., Liu, K., Hu, S., and Feng, X. (2021). A Mechanical Insight into the Triggering Mechanism of Frequently Occurred Landslides along the Contact between Loess and Red clay. *Scientific Rep.* 11 (1), 1–15. doi:10.1038/s41598-021-96384-7

Lian, B., Wang, X., Peng, J., and Huang, Q. (2020). Shear Rate Effect on the Residual Strength Characteristics of Saturated Loess in Naturally Drained Ring Shear Tests. *Nat. Hazards Earth Syst. Sci.* 20 (10), 2843–2856. doi:10.5194/nhess-20-2843-2020

Liu, J., Li, X. A., Xue, Q., and Guo, Z. (2020). Experimental Study on Air Permeability and Microscopic Mechanism of Intact and Remolded Malan Loess, Loess Plateau, China. *Bull. Eng. Geol. Environ.* 79 (8), 3909–3919. doi:10.1007/s10064-020-01810-1

Lupini, J. F., Skinner, A. E., and Vaughan, P. R. (1981). The Drained Residual Strength of Cohesive Soils. *Géotechnique* 31 (2), 181–213. doi:10.1680/geot.1981.31.2.181

Ma, J., Zhao, X., Li, S., and Duan, Z. (2021). Effects of High Shearing Rates on the Shear Behavior of Saturated Loess Using Ring Shear Tests. *Geofluids* 2021, 1–12. doi:10.1155/2021/6527788

Ma, P., Peng, J., Wang, Q., Zhuang, J., and Zhang, F. (2019). The Mechanisms of a Loess Landslide Triggered by Diversion-Based Irrigation: a Case Study of the South Jingyang Platform, China. *Bull. Eng. Geol. Environ.* 78 (7), 4945–4963. doi:10.1007/s10064-019-01467-5

Meehan, C. L., Brandon, T. L., and Duncan, J. M. (2007). Measuring Drained Residual Strengths in the Bromhead Ring Shear. *Geotechnical Test. J.* 30 (6), 466–473.

Nam, S., Gutierrez, M., Diplas, P., and Petrie, J. (2011). Determination of the Shear Strength of Unsaturated Soils Using the Multistage Direct Shear Test. *Eng. Geology.* 122, 272–280. doi:10.1016/j.enggeo.2011.06.003

Okada, Y., Sassa, K., and Fukuoka, H. (1998). Comparison of Shear Behaviour of sandy Soils by Ring-Shear Test with Conventional Shear Tests. *Environ. For. Sci.* 54, 623–632. doi:10.1007/978-94-011-5324-9_66

Pei, X., Zhang, X., Guo, B., Wang, G., and Zhang, F. (2017). Experimental Case Study of Seismically Induced Loess Liquefaction and Landslide. *Eng. Geology.* 223, 23–30. doi:10.1016/j.enggeo.2017.03.016

Sadrekarimi, A., and Olson, S. M. (2009). A New Ring Shear Device to Measure the Large Displacement Shearing Behavior of Sands. *Geotechnical Test. J.* 32 (3), 197–208.

Sadrekarimi, A., and Olson, S. M. (2010). Shear Band Formation Observed in Ring Shear Tests on Sandy Soils. *J. Geotech. Geoenviron. Eng.* 136 (2), 366–375. doi:10.1061/(asce)gt.1943-5606.0000220

Sassa, K., Dang, K., He, B., Takara, K., Inoue, K., and Nagai, O. (2014). A New High-Stress Undrained Ring-Shear Apparatus and its Application to the 1792 Unzen-Mayuyama Megaslide in Japan. *Landslides* 11, 827–842. doi:10.1007/s10346-014-0501-1

Sebastian, Lobo-Guerrero., and Luise, V. (2006). Modeling Granular Crushing in Ring Shear Tests: Experimental and Numerical Analyses. *Soils and Foundations* 46 (2), 147–157.

Skempton, A. W. (1985). Residual Strength of Clays in Landslides, Folded Strata and the Laboratory. *Géotechnique* 35 (1), 3–18. doi:10.1680/geot.1985.35.1.3

Sugimoto, M., Nakamura, K., Sakai, N., and Toyota, H. (2009). Ring Shear Tests to Evaluate Strength Parameters in Various Remoulded Soils. *Géotechnique* 59 (8), 649–659.

Tan, S. A., Chew, S. H., and Wong, W. K. (1998). Sand-geotextile Interface Shear Strength by Torsional Ring Shear Tests. *Geotextiles and Geomembranes* 16 (3), 161–174. doi:10.1016/s0266-1144(98)00007-7

Tian, W.-t., Dong, J.-h., Sun, J.-j., and Yang, B. (2021). Experimental Study on Main Physical Parameters Controlling Shear Strength of Unsaturated Loess. *Adv. Civil Eng.* 2021, 1–11. doi:10.1155/2021/6652210

Tika, T. E., and Hutchinson, J. N. (1999). Ring Shear Tests on Soil from the Vaiont Landslide Slip Surface. *Géotechnique* 49 (1), 59–74. doi:10.1680/geot.1999.49.1.59

Tiwari, B., and Marui, H. (2004). Objective Oriented Multistage Ring Shear Test for Shear Strength of Landslide Soil. *J. Geotech. Geoenviron. Eng.* 130 (2), 217–222. doi:10.1061/(asce)1090-0241(2004)130:2(217)

Trandafir, A. C., and Sassa, K. (2004). Undrained Cyclic Shear Response Evaluation of Sand Based on Undrained Monotonic Ring Shear Tests. *Soil Dyn. Earthquake Eng.* 24 (11), 781–787. doi:10.1016/j.soildyn.2004.06.017

Vithana, S. B., Nakamura, S., Gibo, S., Yoshinaga, A., and Kimura, S. (2012). Correlation of Large Displacement Drained Shear Strength of Landslide Soils Measured by Direct Shear and Ring Shear Devices. *Landslides* 9, 305–314. doi:10.1007/s10346-011-0301-9

Wang, G., Sassa, K., Fukuoka, H., and Tada, T. (2007). Experimental Study on the Shearing Behavior of Saturated Silty Soils Based on Ring-Shear Tests. *J. Geotech. Geoenviron. Eng.* 133 (3), 319–333. doi:10.1061/(asce)1090-0241(2007)133:3(319)

Wang, S., Wu, W., Xiang, W., and Liu, Q. (2015). Shear Behaviors of Saturated Loess in Naturally Drained Ring-Shear Tests. *Springer Ser. Geomechanics Geoengineering*, 19–27. doi:10.1007/978-3-319-11053-0_3

Wang, S., Xiang, W., Cui, D. S., Yang, J., and Huang, X. (2012). Study of Residual Strength of Slide Zone Soil under Different Ring-Shear Tests. *Rock Soil Mech.* 33 (10), 2967–2972.

Wang, X. G., Lian, B. Q., Liu, K., and Luo, L. (2021). Trigger Mechanism of Loess-Mudstone Landslides Inferred from Ring Shear Tests and Numerical Simulation. *J. Mountain Sci.* 18 (09), 2412–2426. doi:10.1007/s11629-021-6791-6

Wang, X., Wang, J., Zhan, H., Li, P., Qiu, H., and Hu, S. (2020). Moisture Content Effect on the Creep Behavior of Loess for the Catastrophic Baqiao Landslide. *CATENA* 187, 104371. doi:10.1016/j.catena.2019.104371

Wen, B. P., and Aydin, A. (2003). Microstructural Study of a Natural Slip Zone: Quantification and Deformation History. *Eng. Geology.* 68, 289–317. doi:10.1016/s0013-7952(02)00234-x

Xu, J. B., Wei, W., Bao, H., Zhang, K. K., Lan, H. X., Yan, C. G., et al. (2020). Study on Shear Strength Characteristics of Loess Dam Materials under Saturated Conditions. *Environ. Earth Sci.* 79 (13), 1–14. doi:10.1007/s12665-020-09089-x

Xu, L., Dai, F. C., Gong, Q. M., Tham, L. G., and Min, H. (2012). Irrigation-induced Loess Flow Failure in Heifangtai Platform, north-west China. *Environ. Earth Sci.* 66 (6), 1707–1713. doi:10.1007/s12665-011-0950-y

Xu, Q., Wang, W., Li, L., and Cao, Y. (2021). Failure Mechanism of Gently Inclined Shallow Landslides along the Soil-Bedrock Interface on Ring Shear Tests. *Bull. Eng. Geol. Environ.* 80 (5), 3733–3746. doi:10.1007/s10064-021-02171-z

Yuan, W., Fan, W., Jiang, C., and Peng, X. (2019). Experimental Study on the Shear Behavior of Loess and Paleosol Based on Ring Shear Tests. *Eng. Geology.* 250, 11–20. doi:10.1016/j.enggeo.2019.01.007

Zhang, F., and Wang, G. (2018). Effect of Irrigation-Induced Densification on the post-failure Behavior of Loess Flowslides Occurring on the Heifangtai Area, Gansu, China. *Eng. Geology.* 236, 111–118. doi:10.1016/j.enggeo.2017.07.010

Zhang, F., Wang, G., Kamai, T., Chen, W., Zhang, D., and Yang, J. (2013). Undrained Shear Behavior of Loess Saturated with Different Concentrations of Sodium Chloride Solution. *Eng. Geology.* 155 (6), 69–79. doi:10.1016/j.enggeo.2012.12.018

Zhang, Y., Guo, C., Lan, H., Zhou, N., and Yao, X. (2015). Reactivation Mechanism of Ancient Giant Landslides in the Tectonically Active Zone: a Case Study in Southwest China. *Environ. Earth Sci.* 74 (2), 1719–1729. doi:10.1007/s12665-015-4180-6

Zhang, Z., Wang, T., Wu, S., Tang, H., and Liang, C. (2018). Dynamics Characteristic of Red clay in a Deep-Seated Landslide, Northwest China: An experiment Study. *Eng. Geology.* 239, 254–268. doi:10.1016/j.enggeo.2018.04.005

Zou, Z., Yan, J., Tang, H., Wang, S., Xiong, C., and Hu, X. (2020). A Shear Constitutive Model for Describing the Full Process of the Deformation and Failure of Slip Zone Soil. *Eng. Geology.* 276, 105766. doi:10.1016/j.enggeo.2020.105766

Conflict of Interest: The authors declare that the research was conducted in the absence of any commercial or financial relationships that could be construed as a potential conflict of interest.

frontiers in Earth Science

ORIGINAL RESEARCH
published: 28 March 2022
doi: 10.3389/feart.2022.839073

Horizontal Compression Test: A Proposed Method for Indirect Determination of Tensile Strength of Stiff Soils and Soft Rocks

Fanfan Guan[1], Yanrong Li[1], Guohong Gao[1], Hauke Zachert[2], Gerald Eichhoff[2] and Mary Antonette Beroya-Eitner[2]*

[1]Department of Earth Sciences and Engineering, Taiyuan University of Technology, Taiyuan, China, [2]Department of Civil and Environmental Engineering, Institute of Geotechnics, Technical University of Darmstadt, Darmstadt, Germany

Tensile strength is an important parameter in many engineering applications. In loess slopes, for instance, it governs the development and propagation of tension cracks that usually ultimately lead to crack–sliding and toppling failures, which are among the most common modes of slope failure in the Loess Plateau of China. Reliable measurement of tensile strength of geomaterial is therefore a necessity. Commonly used methods for tensile strength measurement have important limitations and shortcomings, which become magnified when dealing with soil and soft rock. This study developed a new indirect tensile test, the Horizontal Compression test, for use with these materials. The proposed method not only involves simple sample preparation and test operation, it also addresses the eccentric force and stress concentration problems that are common in conventional tensile tests. To evaluate the method's validity, its performance was compared with the ISRM-suggested direct tensile test and the closely related Brazilian test. The tensile strength values from the horizontal compression test strongly correlate with those from the direct tension test, and are more stable than those obtained with either of the two conventional tests. Thus, the proposed method can be used and deemed more suitable for tensile strength determination than these conventional test methods.

Keywords: horizontal compression, tensile strength, test method, test device, soil and soft rocks

OPEN ACCESS

Edited by:
Fanyu Zhang,
Lanzhou University, China

Reviewed by:
Haijun Qiu,
Northwest University, China
Zhenguo Guo,
Tongji University, China

****Correspondence:***
Yanrong Li
li.dennis@hotmail.com

Specialty section:
This article was submitted to Geohazards and Georisks, a section of the journal Frontiers in Earth Science

Received: *19 December 2021*
Accepted: *11 March 2022*
Published: *28 March 2022*

Citation:
Guan F, Li Y, Gao G, Zachert H, Eichhoff G and Beroya-Eitner MA (2022) Horizontal Compression Test: A Proposed Method for Indirect Determination of Tensile Strength of Stiff Soils and Soft Rocks. Front. Earth Sci. 10:839073. doi: 10.3389/feart.2022.839073

INTRODUCTION

Tensile strength is one of the most important parameters in many engineering and science-based applications. In geotechnical engineering, the interest in tensile strength is on its role in crack initiation and propagation in soils and rocks (Griffith, 1921; Tapponnier and Brace, 1976; Stacey, 1981; Haimson and Cornet, 2003), and therefore in the failure of earth structures, such as slopes embankment, and dams. In loess slopes, for instance, cracking–sliding and toppling are common failure modes that are usually initiated by the development of tension cracks at the slope crown, then propagating vertically down from a few to several meters (Li, 2018). These modes of failure are a frequent occurrence in the Loess Plateau of China, causing an average of 100 deaths per year and considerable economic loss (Li et al., 2018b). Prevention and mitigation measures are therefore needed, which, for performance and cost effectiveness, require proper evaluation of the tensile strength of loess soil. To date, however, there exists no standard test for tensile strength similar to those for other geotechnical soil properties such as shear strength and compressive strength.

Tensile strength is the fracture stress under uniaxial pulling (tension) force. As such, it is ideally determined by direct tensile testing, whereby a cylindrical specimen is loaded in axial tension until failure. Tensile strength is calculated by dividing the fracture force by the cross-sectional area of the specimen under the assumption that the stress is uniform and purely uniaxial. However, as Coviello et al. (2005) pointed out, this assumption is most often invalid since anomalous stress concentration tends to occur at specimen ends, leading to early rupture in these parts. Moreover, even when the rupture occurs in the middle portion of the specimen, the stress distribution over the entire cross section may not be uniform owing to the bending moments introduced by small geometrical imperfections and/or misalignment between the specimen's axis and the machine cap axes.

Several solutions have been adopted to address the aforementioned problems, such as preparing the specimen in a dumbbell shape (e.g., Tolooiyan et al., 2014; Demirdag et al., 2019) or etching a notch on the surface to force the specimen to fracture at the middle portion, using special connectors between the specimen and the loading frame (e.g. Fairhurst, 1961; Hawkes and Mellor, 1970; Okubo and Fukui, 1996; Perras and Diederichs, 2014), and using a centering apparatus (Zhang et al., 2017). Some of these techniques are effective, but complicated and expensive (Mellor and Hawkes, 1971; Butenuth et al., 1993; Coviello et al., 2005). As a result, direct tensile test is seldom carried out in laboratories. As alternatives, several indirect test methods have been developed, including the Brazilian test (Hudson et al., 1972; ISRM, 1978), bending test (He et al., 1990), hydraulic fracturing test (Zoback et al., 1977), hoop test (Xu et al., 1988), axial fracturing test (Fang and Chen, 1972) and ring test (Hobbs, 1964).

Among the indirect tensile tests, the Brazilian test, also known as splitting tension test, is widely used due to ease of operation. In this test, tensile failure is induced in a thin, circular disc by subjecting it to diametrical compression. The principle behind the test is based on the experimental fact that most rocks in biaxial stress fields fail in tension at their uniaxial tensile strength when one principal stress is tensile and the other is compressive, where the magnitude of the latter does not exceed three times that of the former (ISRM, 1978; Li and Wong, 2013). The intermediate principal stress is assumed to have no influence on disc failure (Fairhurst, 1964). The maximum tensile stress at failure is then computed by applying the Continuum Mechanics under the assumption that the specimen is homogeneous, isotropic and linearly elastic before brittle failure occurs (Mellor and Hawkes, 1971). It is also assumed that this failure occurs at the point of maximum tensile stress, i.e. at the center of the disc. However, in many Brazilian tests, crack initiation has been observed at points away from the center of the disc and near the disc-loading platen contact where stress concentration exists (Fairhurst, 1964; Hooper, 1971; Hudson et al., 1972; Swab et al., 2011). Moreover, similar to the direct tensile test, eccentric force often appears in Brazilian test due to the difficulty of keeping the applied force along the vertical diametrical plane of the specimen throughout the test. Like most tensile tests, the main application of the Brazilian test is on rock and rock-like materials; it was recommended by the International Society for Rock Mechanics (ISRM) as the standard for determining the tensile strength of rocks (ISRM, 1978). When applied to soil and soft rocks, said test limitations can be magnified due to greater geometric tolerances that must be accepted in the specimen preparation and the difficulty of obtaining samples with smooth surfaces (Coviello et al., 2005).

Motivated by the need to understand the tensile behavior of earth materials, particularly soils and soft rocks, and realising the limitations of conventional tensile tests, we developed and proposed a new indirect tensile test called Horizontal Compression test, which is particularly suited to these materials. The proposed method is easy to use; it does not require special and expensive techniques in sample preparation and operation of the apparatus is simple. It generally operates under the same principle as the Brazilian test but improves on the latter in that the applied compressive force strictly passes through the central diametrical plane of the specimen, thereby preventing the development of eccentric forces.

In the development of the proposed method, we conducted two major laboratory test campaigns: the first was aimed at establishing the optimal parameters for use with the method, whereas the second was to evaluate the method's performance. This paper presents the proposed method and the results of the said test campaigns.

TEST METHOD AND DEVICE

The device (**Figure 1A**) developed for the proposed test method mainly comprises fracturing rods (**Figure 1B**), specimen positioning frame (**Figure 1C**), load cell, displacement sensor and data processor. A servo-controlled tension system is adopted, and a case is used to protect the tensile test frame.

Compression is carried out by the fracturing rods (**Figure 1B**), one of which is active (**Figure 1D**) and the other stationary and fixed on the frame platform (**Figure 1E**). The specimen is placed horizontally between these two rods, which are kept separated at a pre-set distance depending on the size of the specimen. Driven by the electric cylinder, the active fracturing rod then moves towards the stationary fracturing rod and fractures the specimen at a specified loading rate. The frame platform is designed to be smooth such that frictional resistance can be considered negligible.

The apparatus is equipped with a specimen positioning frame that is fitted with an operating arm and two guide columns (**Figure 1C**). The frame is manipulated through the operating arm for setting the specimen so that the active fracturing rod, the stationary fracturing rod and the central axis of the specimen are aligned in the same vertical plane. This ensures that the direction of the force strictly passes through the center of the specimen, minimizing eccentric force.

The load cell with an accuracy of 0.1 N is set up on the active fracturing rod to detect the pressure from the rod. A linear variable differential transformer with an accuracy of 0.001 mm is installed between the frame platform and the active fracturing rod to detect the displacement of the rod. The data processor then receives the data from the load cell and the displacement sensor. The load cell and the displacement sensor are easy to replace in case of malfunction.

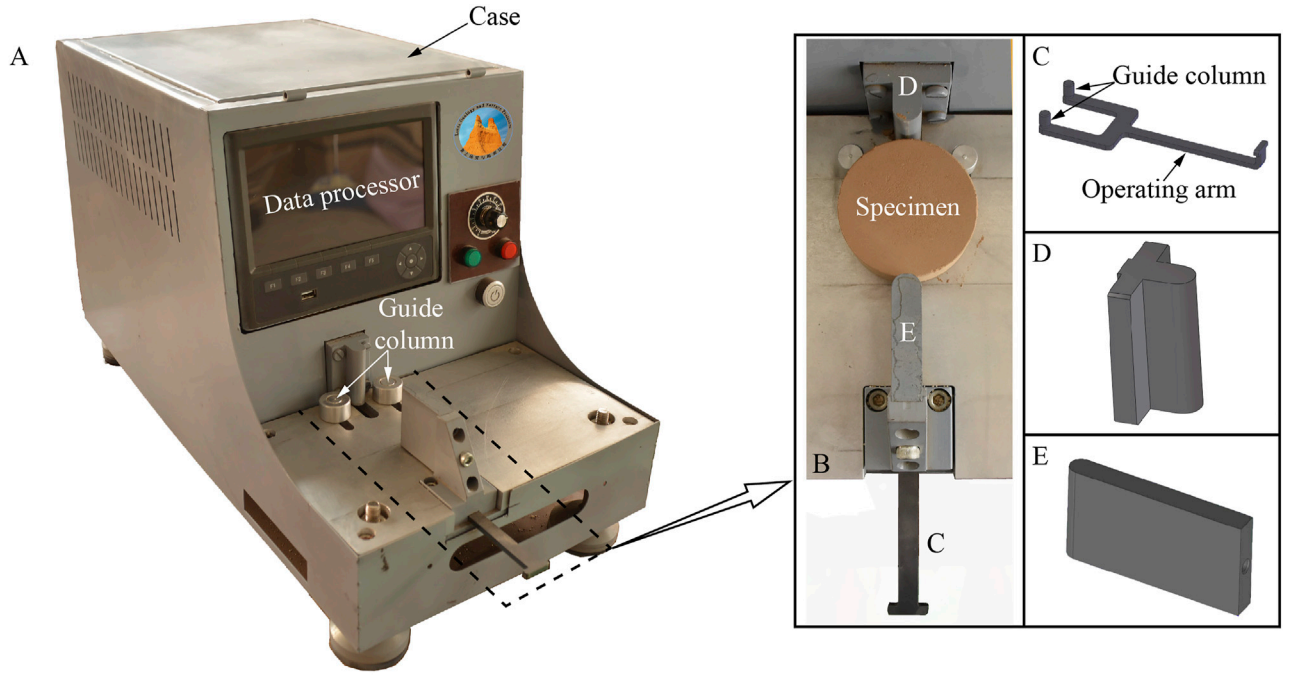

FIGURE 1 | Horizontal compression test device **(A)** overview **(B)** fracturing rods **(C)** specimen positioning frame **(D)** active fracturing rod and **(E)** stationary fracturing rod.

The tensile strength of the specimen and corresponding strain can be evaluated using the same equations for the Brazilian test (ISRM, 1978):

$$\sigma_t = \frac{2P}{\pi DT}, \quad (1)$$

$$\varepsilon_t = \delta \times \nu, \quad (2)$$

where P is the force at failure; D is the specimen diameter; T is the specimen thickness; δ is the compressive strain (equal to $\Delta d/d$, where Δd is the measured vertical displacement at failure); ν is the Poisson's ratio of the specimen.

The main procedure of the proposed horizontal compression test is in accordance with the Chinese Specification of Rock Test (GB/T 50266, 2013), ISRM Standard (ISRM, 1978) and ASTM Standard (ASTM C496/C496M-17, 2017).

A requirement of the test is the preparation of the specimen in a cylindrical form. This study utilized loess soil as test specimen, which is a strongly anisotropic geological material in its natural state (Li et al., 2018a). Thus, the soil was remolded to obtain a more homogeneous fabric than the intact specimens (Jiang et al., 2014), and thereby ensure reliable and comparable test data. The remolded specimens were prepared using a self-made mold and the universal testing frame. The stipulations of the Chinese Specification of Soil Test (GB/T 50123, 2019), British Standard (BS 1377-1, 2016) and ASTM standard (ASTM D7015-18, 2018) were strictly followed in the sampling and specimen preparation.

DETERMINATION OF OPTIMAL TEST PARAMETERS

Test Specimen

For the optimal specimen size determination, specimens with diameters of 40, 50, 60, 80, and 100 mm and respective thickness of 20, 25, 30, 40 and 50 mm (i.e., radius: thickness ratio of 1, following the 1978 ISRM recommendation for Brazilian test specimen) were prepared. For each specimen size, five specimens were tested. For the determination of loading rate, another six sets were prepared, each corresponding to different loading rates (0.05, 0.1, 0.3, 0.5, 0.7 and 0.9 mm/min) and comprising five specimens. All the remolded specimens had a dry density of 1.32 g/cm^3 and zero moisture content.

Jaw Shape

One of the most important parameters affecting the results of tensile tests is how the applied load is transferred to the specimen. In this regard, the shape of the loading jaw plays a major role. Thus, prior to starting the testing program, extensive trial tests were conducted to select the most suitable jaw shape for the proposed apparatus. Four different jaw shapes were considered (**Figure 2**). Jaws I and II (**Figures 2A,B**), which more or less represent point load contact, were found to cause initial fracture in the disc-jaw contact area and are therefore considered unsatisfactory. Jaws III and IV (**Figures 2C,D**), representing a curved contact, showed a much better performance although like Jaws I and II, Jaw III also tended to penetrate the specimen. With Jaw IV (**Figure 2D**), the initiation and propagation of cracking occurred simultaneously. No jaw penetration into the specimen was observed.

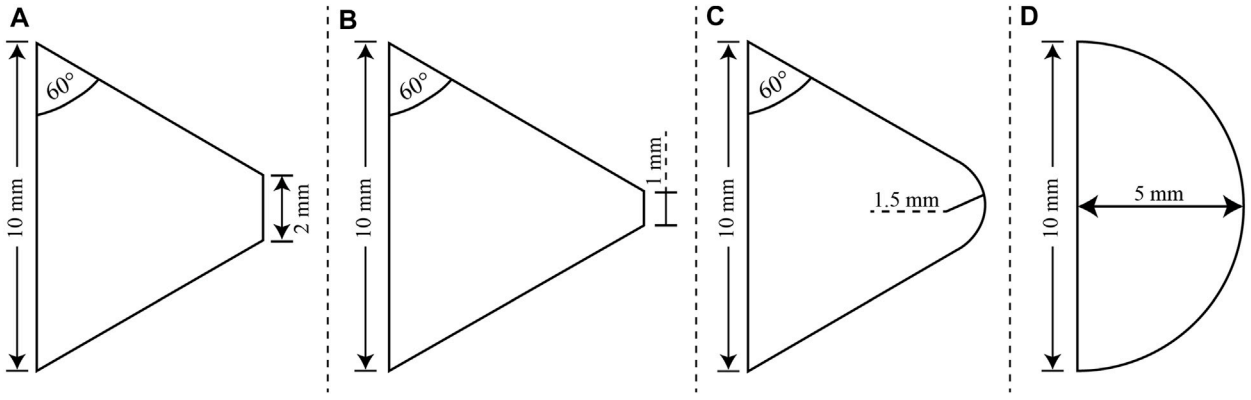

FIGURE 2 | Different jaw shapes **(A)** Jaw I **(B)** Jaw II **(C)** Jaw III and **(D)** Jaw IV.

To gain further insights into how load is transferred by the different jaw shapes, a 2D finite element simulation was conducted using Abaqus Standard 2019. The soil was modeled as a homogeneous, linearly elastic material with the following elastic constants: Young's Modulus = 15,000 kPa and Poisson's ratio = 0.23. The model was meshed with roughly 6,000 plane stress elements. The loading jaws were simulated as a rigid body, one of which was fixed whilst the other was displacement controlled and moved in the $+y$ direction. There was no bonding between the sample and the jaws. As shown in **Figure 3**, the numerical simulation results are generally consistent with the experimental results. Stress concentration, particularly at the jaw edges, is noticeable with Jaws I and II (**Figures 3A,B**), explaining the triangular fracture area that develops at the specimen-jaw contact when these jaws are used. The stress distribution with Jaws III and IV have the same pattern (**Figures 3C,D**), although stress in the former is more concentrated and higher at the disc-jaw contact. This may explain the observed penetration of the jaw into the specimen. Of all the jaws, Jaw IV gives the most homogenous stress distribution pattern, explaining the simultaneous occurrence of crack initiation and propagation. Jaw IV, therefore, was adopted for use with the proposed method.

Specimen Size

A series of tests was carried out to explore how the tensile strength obtained with the proposed method is affected by specimen size and to determine the optimal size for use with the method. To this end, specimens of different sizes with diameters of 40, 50, 60, 80 and 100 mm and respective thickness of 20, 25, 30, 40 and 50 mm were tested at a loading rate of 0.5 mm/min.

Figure 4 shows typical load-displacement curves for the different specimen sizes. Clear and sharp peaks can be observed, indicating the possibility of determining tensile strength with the horizontal compression test. The load increases with displacement until a peak is reached after which the load falls rapidly to zero. The peak load and displacement increase with increase in diameter.

The average tensile strength (σ_t) obtained for each specimen size is shown in **Figure 5**. The σ_t values decrease by 46.48% with increase in diameter from 40 to 60 mm. However, further increase in diameter did not produce significant variation in the σ_t values, indicating that the measured tensile strength is relatively stable at diameter range of 60–100 mm. Hence, the minimum specimen size requirement for the proposed method is determined to be 60 mm in diameter and 30 mm in thickness following the method used by Kuruppu and Funatsu (2012) and Hudson (1969) to determine the critical specimen size for tensile fracture toughness test and ring tensile test, respectively. With the method, the point at which the tensile strength becomes constant may be defined as the minimum specimen size that yields size-independent tensile strength. This critical or minimum specimen size is recommended for use with the proposed method, given that with larger specimens, the possibility of encountering larger and more material flaws is increased. Preparing a larger specimen without disturbance is also difficult. Thus, there exists a maximum practical size that can be tested in the proposed apparatus, which was determined to be 100 mm × 50 mm. The optimal application of the proposed method, therefore, is on fine- to medium-grained soils and rocks.

Loading Rate

Six loading rates (0.05, 0.1, 0.3, 0.5, 0.7 and 0.9 mm/min) were considered and following the test results in *Specimen Size*, specimens with a diameter of 60 mm and thickness of 30 mm were used.

As shown in **Figure 6**, the measured tensile strength gradually increases with increasing loading rate. The most stable test results, with a minimum coefficient of variation (C_v) of 3.72%, were obtained at a loading rate of 0.1 mm/min. Therefore, this loading rate can be used with the suggested method. With this low rate, problems that may arise with high loading rates (such as subcritical crack growth) can be avoided, while allowing for the test to be performed within a reasonable length of time.

PERFORMANCE EVALUATION

To evaluate the performance of the proposed method, another test campaign was conducted to compare the tensile strengths obtained with the method to those obtained with the direct tension test and the closely-related Brazilian test.

	Jaw shapes	Max vertical stress	Vertical displacement
A	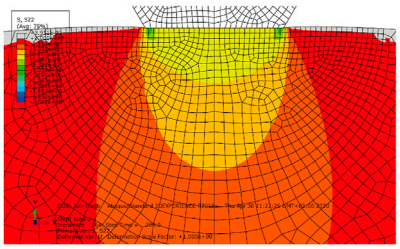	-1.15 N/mm²	0.44 mm
B	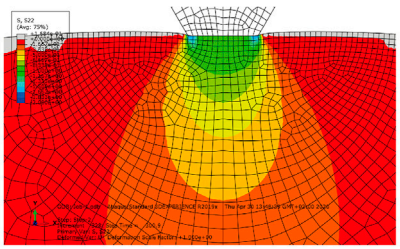	-1.72 N/mm²	0.50 mm
C	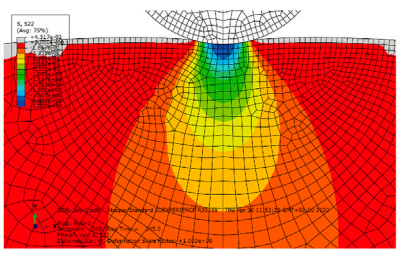	-1.95 N/mm²	0.58 mm
D	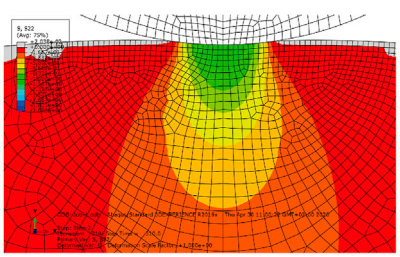	-1.16 N/mm²	0.52 mm

FIGURE 3 | Comparison of vertical stress concentration in the specimen with different shapes of jaws under a load of 40 N **(A)** Jaw I **(B)** Jaw II **(C)** Jaw III and **(D)** Jaw IV.

Test Specimen

For the direct tension test, 50 × 100 mm dumbbell-shaped specimens were prepared following the method proposed by Li et al. (2020), where a rotation grooving device was used to create a 15 mm-wide section with a reduced diameter (40 mm) in the mid-height of the specimen. For the Brazilian test, an appropriately sized (50 mm diameter and 25 mm thickness) mold was used. Each of the three test methods was carried out on seven soil specimens, all with a dry density of 1.38 g/cm^3 and zero moisture content.

Given that the direct tensile test is considered the ideal method for tensile strength determination, the performance of any indirect test method is compared and measured against this test (Liao et al., 2019). Insights from the comparison of the proposed method with the direct tension test is therefore deemed very important. Thus, to further ensure sample uniformity and data comparability, gypsum-sand specimens were additionally tested with the two test methods. Moreover, given that the artificial mixture can be prepared into stiffer and denser specimens simulating soft rock, its use allows the evaluation of the capability of the proposed method over a wider range of tensile strengths. The artificial specimen preparation followed the method proposed by Li et al. (2020). Specimens were prepared at four different densities (1.57, 1.73, 1.77 and 1.82 g/cm^3) by mixing predetermined proportions of gypsum, standard sand and

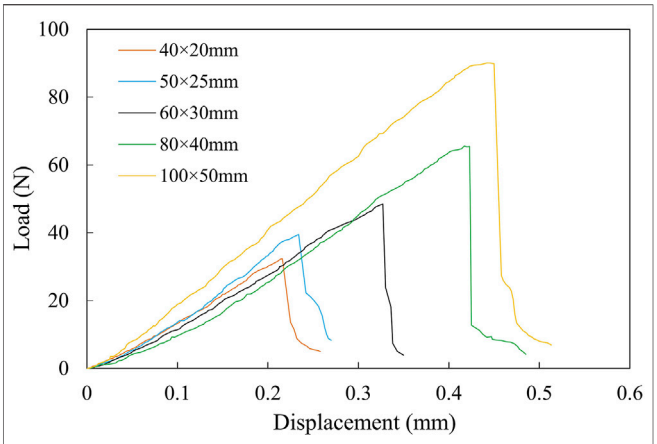

FIGURE 4 | Load vs. displacement curves for the different specimens sizes (e.g., 40 × 20 mm refers to diameter × thickness).

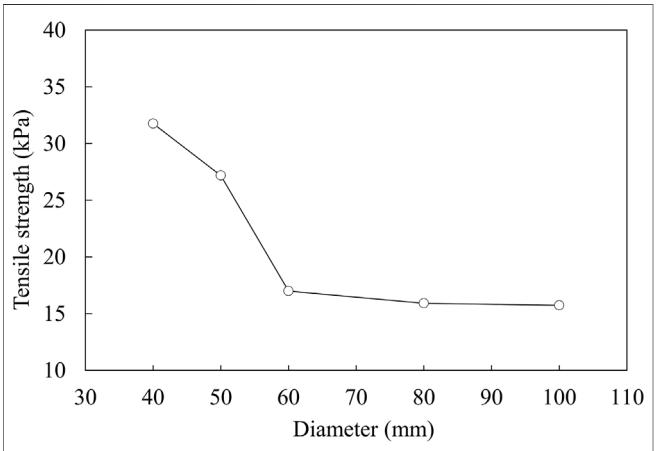

FIGURE 5 | Correlation between the measured tensile strengths and specimen diameter.

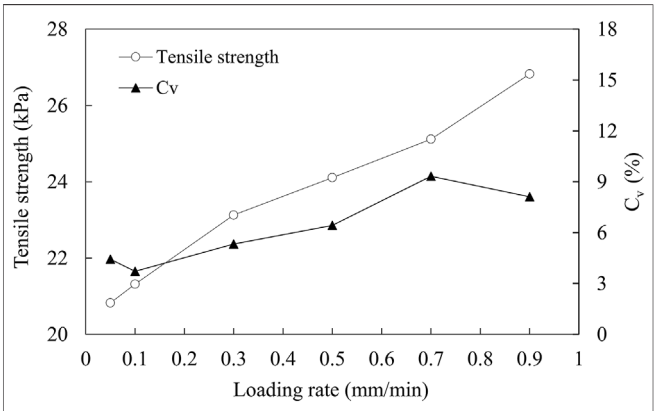

FIGURE 6 | Influences of loading rate on the measured tensile strengths (Cv is coefficient of variation, equals to the standard deviation of the tensile strength values divided by the average value).

water. This mixture was put in a container, stirred evenly and placed in a self-made mold for compaction by static pressing method. The mold was then put in an oven at 50 C for 12 h and then demolded. Finally, the specimens were put back in the oven at 50 C and dried to a constant mass. For each of the direct tension test and the proposed method, four sets of gypsum-sand specimens were prepared, each set corresponding to different densities and comprising five specimens. The properties of the gypsum, standard sand and the mixed specimen are similar to those reported in Li et al. (2020).

Direct Tension and Brazilian Tests

The direct tension and the Brazilian tests were conducted using the universal testing frame. The direct tension test (ISRM test) was performed following the procedure suggested by the International Society for Rock Mechanics (ISRM, 1978). Tensile strength and averaged tensile strain were calculated using **Eqs (3)**, **(4)** below:

$$\sigma_t = \frac{P}{A}, \tag{3}$$

$$\varepsilon_t = \frac{\delta}{H_f}, \tag{4}$$

where P is the maximum applied load, A is the original cross-sectional area of the crack plane, δ is the measured displacement and H_f is the height of the free area of the specimen (i.e. the area outside of the metal grips holding the specimen ends).

For the Brazilian test, a Chinese standard V-shaped loading strip (GB/T 23561.10, 2010) was attached to the universal testing machine (**Figure 7**). Tensile strength and corresponding critical tensile strain were respectively calculated using **Eqs 1**, **2**.

For both methods as well as the proposed method, a loading rate of 0.1 mm/min was applied following the results of *Loading Rate*.

Evaluation of Results

To investigate the specimen failure behavior under the different test methods, a high-speed camera (1,280 × 1,024 pixels) with a filming rate of 1,000 frames per second (fps) was used, allowing to record the initiation and propagation of cracks in the specimens. With this, cracks were observed to develop in the middle part of the grooved section in the ISRM, whereas in the Brazilian test, cracks were initiated in the middle and upper parts of the samples, and then extended gradually to the entire loaded diameter. Penetration of the loading jaws into the specimen was commonly observed in the latter test. The observed crack initiation in the middle and upper parts of the Brazilian test specimen was very similar to the results of Komurlu and Kesimal (2015) on testing andesitic basalt specimens. In fact, a major drawback observed by many workers with Brazilian tests is this premature failure of specimen close to the loading zone (e.g., Aonoa et al., 2012; Gutiérrez-Moizant et al., 2020), which, depending on the geometry of the loading jaw and the material tested, may lead to catastrophic failure (Erarslan et al., 2012; Komurlu and Kesimal, 2015). In the Horizontal Compression test, crack developed instantaneously along the loaded diameter of the specimen. **Figure 8** presents typical images of a specimen at various stages of loading in the proposed method: pre-loading (**Figure 8A**), crack initiation (**Figure 8B**) and post failure (**Figure 8C**). **Figures 8B,C** are consecutive images, i.e. they were taken 2/1,000 s apart, which

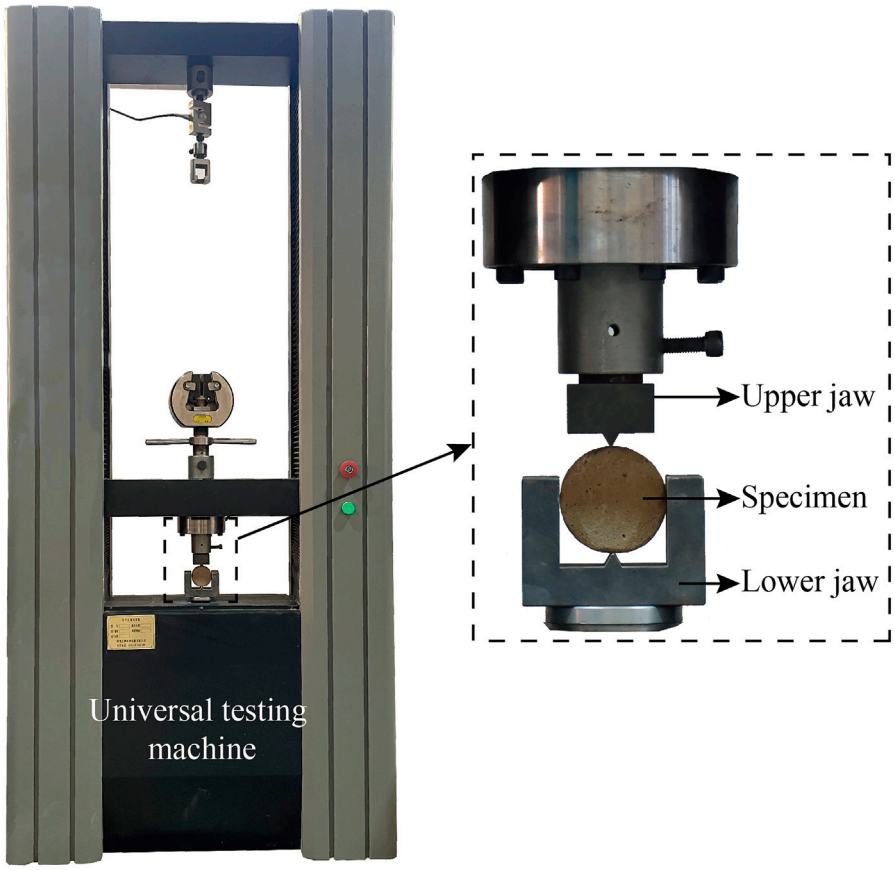

FIGURE 7 | V-shaped loading strip (GB/T 23561.10, 2010) attached to the universal testing machine.

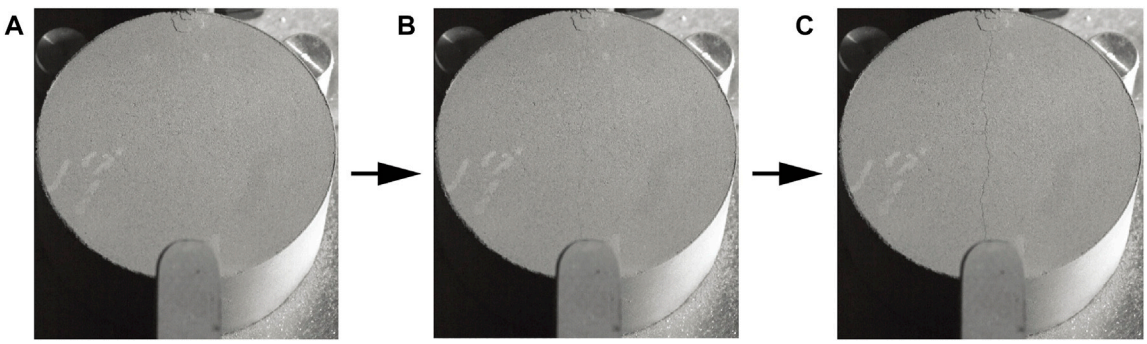

FIGURE 8 | Soil specimen at different loading stages **(A)** pre-loading **(B)** crack initiation and **(C)** post failure. Images in **(B)** and **(C)** are consecutive, showing that crack initiation and propagation happened instantaneously within 2/1,000 s.

therefore show that crack initiation and propagation occurred instantaneously along the loading axis. No measurable penetration of the fracturing rod into the specimen was observed.

Figure 9 shows the typical stress-strain curves for each test. All the curves display a similar trend of tensile stress increasing nearly linearly with strain until a peak stress is reached, after which point the stress dropped rapidly to zero, indicating the brittle nature of tensile failure. In the direct tension test, relatively bigger strain developed before failure occurred. This is ascribed to the relative slippage (roughly 0.2 mm as observed with the high-speed camera) between the fixture and the specimen (**Figure 10**), which is a common problem in direct tension test regardless of the gripping technique used (Alhussainy et al., 2019).

Figure 11 compares the tensile strengths obtained from each test, indicating that the ISRM test gave the highest value, followed by the Brazilian test then by the proposed method. This difference

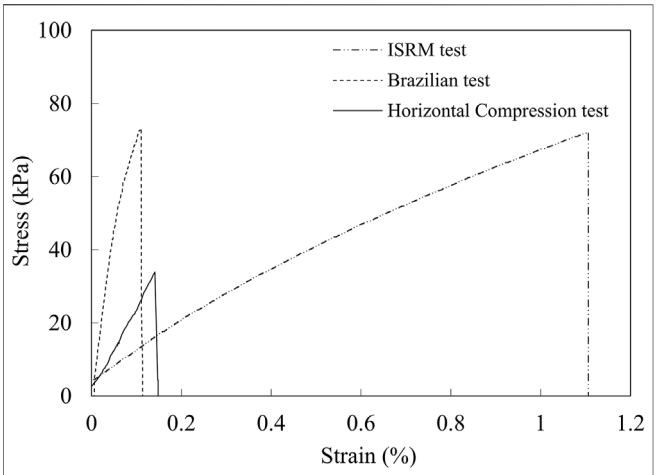

FIGURE 9 | Typical stress-strain curves for ISRM test, Brazilian test, and Horizontal Compression test.

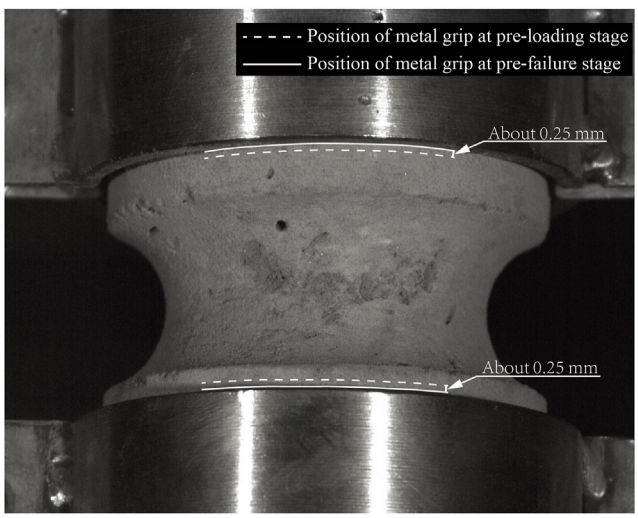

FIGURE 10 | Relative vertical slippage between the specimen and the metal grip determined by comparing the positions of metal grip at pre-loading and pre-failure stages.

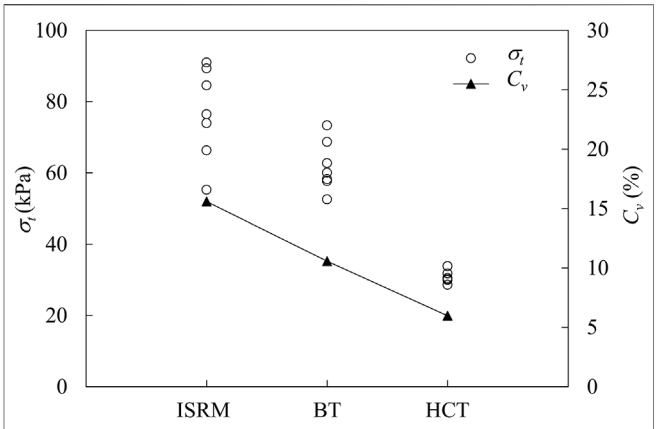

FIGURE 11 | Tensile strength obtained from ISRM test (ISRM), Brazilian test (BT) and Horizontal Compression test (HCT).

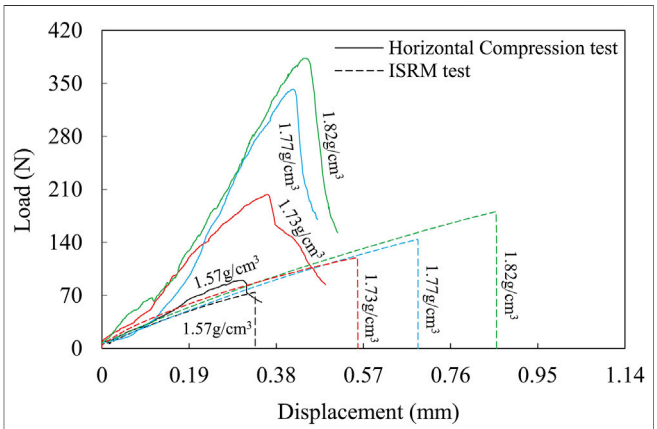

FIGURE 12 | Plot of load vs displacement for artificial specimens at different dry densities for the Horizontal Compression and ISRM tests, ISRM test data are from Li et al. (2020).

in the strength values is due to the interplay of several factors. For instance, the above-mentioned specimen-fixture connection problem in the ISRM test must have contributed to the high tensile strength obtained with this test. Meanwhile, the penetration of the loading jaws into the specimen in the Brazilian test means that the tensile fracture may be shorter than the specimen diameter. With reference to **Eq. (1)**, this may cause tensile strength underestimation. Referring to the Brazilian test and the proposed method, the scale effect may have contributed to the lower tensile strength obtained with the latter. This scale effect was originally hypothesized by Griffith (1921), positing that the bigger the specimen (such as that of the proposed method relative to that of the Brazilian Test), the higher the probability of defects. On tensile loading, stress concentration develops around these flaws, resulting in early failure at lower stress levels. The scale effect is generally validly assessed on materials of geometrically similar structure but different sizes (Biolzi et al., 2001), such as the specimens of the two tests. The tensile strength values obtained from each test and corresponding coefficient of variation (C_v) are plotted in **Figure 11**. As can be seen, the proposed method gave the most stable results of the three methods, followed by the Brazilian test and then the ISRM test.

For the comparison of the proposed method with the ISRM test using artificial specimens, **Figure 12** shows the load-displacement curves obtained from the two tests for each of the dry density considered. The following can be gleaned: 1) the shape of the curves from both tests are consistent with each other and with that obtained using soil specimens. All the curves are near-linear until the peak load is reached, after which the load sharply drops; 2) the measured peak load and the corresponding displacement increase with dry density for both tests; and 3) at the

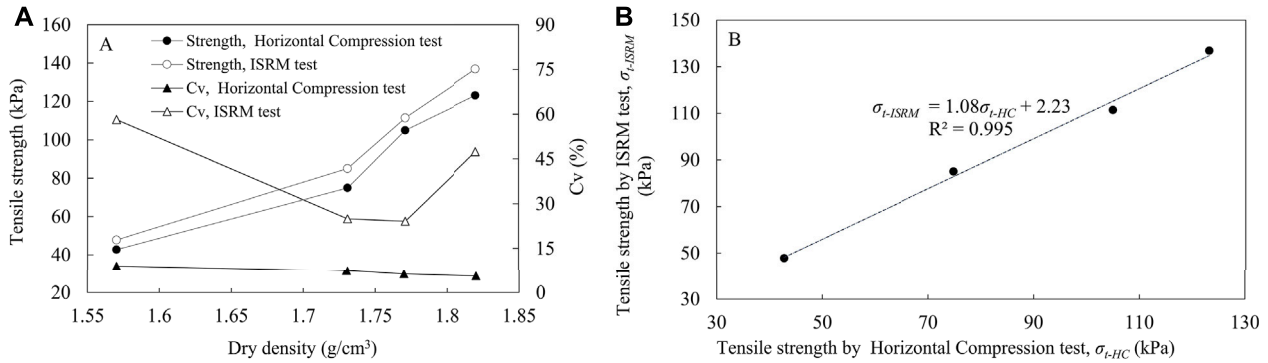

FIGURE 13 | Comparison of test results between the horizontal compression and ISRM tests **(A)** tensile strength vs dry density and **(B)** relationship of the tensile strengths obtained from both methods (Cv is coefficient of variation, and R^2 is correlation coefficient), ISRM test data are from Li et al. (2020).

same density, the peak load obtained with the Horizontal Compression test is larger than that with the ISRM test, whereas the corresponding displacement is smaller.

Results further show that in both methods, the tensile strength increases with increase in dry density, with their tensile strength–dry density plots generally following the same trend/shape (**Figure 13A**). At the same dry density, the tensile strength obtained with the Horizontal Compression test is lower than that with the ISRM test, consistent with the results using the soil specimen. Again, as in the soil specimen, the C_v of the tensile strengths obtained with the former is significantly lower than that with the latter (**Figure 13A**). For instance, at a dry density of 1.73 g/cm^3, the C_v of the former is 7%, compared with the latter's 25%, confirming that the horizontal compression test gives more stable results than the ISRM test.

In **Figure 13B**, the tensile strengths obtained from the Horizontal Compression test ($\sigma_{t\text{-}HC}$) are plotted against those obtained from the ISRM test ($\sigma_{t\text{-}ISRM}$). The $\sigma_{t\text{-}ISRM}$ values are strongly correlated with the $\sigma_{t\text{-}HC}$ values, with correlation coefficient, R^2 of 0.995.

Generally, therefore, results of the performance evaluation using natural soils and artificial mixture both indicate that the proposed method can and may even be more suitable for tensile strength determination of soil and soft rocks. Tensile strength values obtained are more stable than those obtained with either the Brazilian test or the ISRM test, which can be ascribed largely to the absence of eccentric forces in and the simplicity and ease of the proposed method's operation. Moreover, these strength values are strongly correlated with the ISRM test values.

BASIC TEST REQUIREMENTS

The basic requirements of the proposed method are outlined below on the basis of our experience in using the method and in accordance with international standards, such as the ISRM (1978), ISRM (1979) and ASTM C496/C496M (2017).

The diameter of the specimen shall be at least 10 times greater than the largest grain in the specimen (ISRM, 1978; ASTM C496/C496M-17, 2017). The end surfaces must be flat at 0.02 mm and

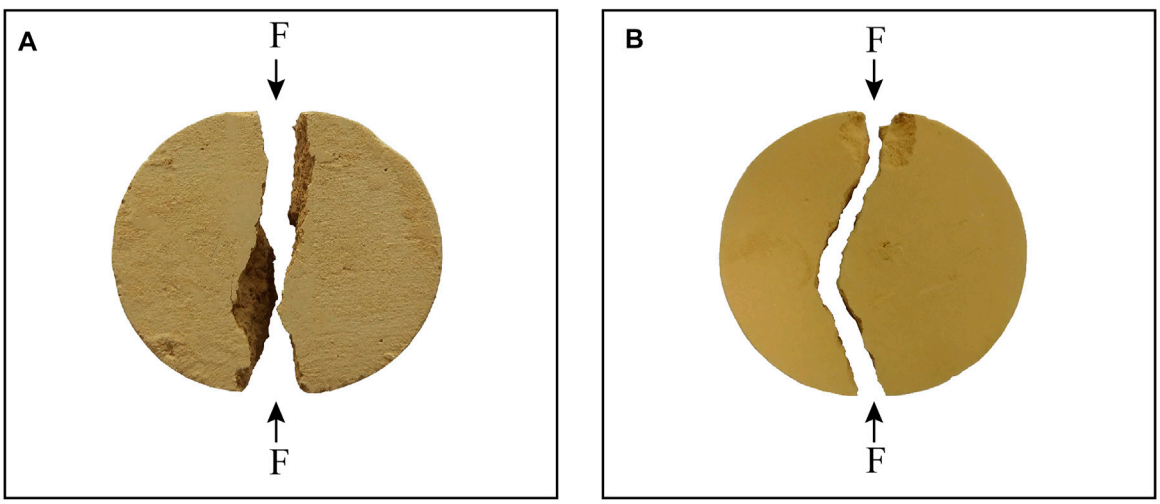

FIGURE 14 | Typical unacceptable failure modes: **(A)** Central + Twisted fracture plane mode; **(B)** Non-central mode.

should not deviate from the plane perpendicular to the longitudinal axis of the specimen by more than 0.001 radian or 0.05 mm in 50 mm (ISRM, 1979).

The sides of the specimen should be smooth, free of abrupt irregularities and straight to within 0.5 mm over the full length of the specimen (ISRM, 1978), given that unfavorable stress concentrations may occur at such irregularities.

The diameter D of the specimen should be measured to the nearest 0.1 mm by averaging three diameter measurements taken at points six0° apart from each other, one of which must be along the loading diameter. The thickness T of the specimen must be determined to the nearest 1 mm by averaging three measurements taken along the thickness of the specimen and at points 120° apart from each other. The average diameter D and thickness T should be used for calculating the cross-sectional area.

At least five specimens per sample set shall be tested to obtain a meaningful average value (ISRM, 1978). If the reproducibility of the test results is good ($C_v < 5\%$), a smaller number of specimens is acceptable. Each specimen of a set must be tested under the same conditions (ASTM C496/C496M-17, 2017).

When the test is finished, the state of the fractured specimen must be preserved for in-depth observation of the failure mode. The test should be rejected if the crack surface deviates from the loading axis by more than $0.05D$ (**Figure 14**). In our test campaign of over 120 specimens, nearly 6% were deemed unacceptable. Rough preparation, non-standard operation and inherent defects in the specimen are responsible for these failures.

Together with the tension test conditions and results, the following information must be recorded for each test: specimen storage and preparation process, moisture content and specimen size. Any macroscopic characteristics of the specimen surfaces, and any adjustment made with the specimen conditions (e.g., adjustment in moisture content) must also be reported. The surrounding environmental conditions must also be recorded, if applicable.

SUMMARY AND CONCLUSION

We developed a new indirect tensile test method, the Horizontal Compression test, which purports to address the limitations of commonly used tensile test methods. This new method involves simple specimen preparation and test operation, and therefore suitable for routine use. Moreover, it minimizes the appearance of eccentric force and the concentration of stresses that are common issues in conventional test methods. The tensile strength values from the Horizontal Compression test strongly correlate with those from the direct tension test, and are more stable than those obtained with either the direct tension test and Brazilian test. Thus, the proposed method can be used and deemed more suitable for tensile strength determination than these conventional test methods. The Horizontal Compression test was originally designed for use with soil and soft rocks. However, the technology can be easily adapted for application to other types of materials, such as hard rocks, concrete and steel.

DATA AVAILABILITY STATEMENT

The original contributions presented in the study are included in the article/Supplementary Material, further inquiries can be directed to the corresponding author.

AUTHOR CONTRIBUTIONS

YL conceived the project and designed the experiment. FG and GG carried out the laboratory tests. YL and FG jointly interpreted the test data. HZ, GE and MB-E conduced the numerical simulation. YL and FG developed the theoretical analysis. FG, YL, and MB-E wrote the paper.

FUNDING

This study was supported by the following: National Natural Science Foundation of China (No. 41877276), Key Program of National Natural Science Foundation of China (No. 41630640), Major Program of the National Natural Science Foundation of China (No. 41790445).

REFERENCES

Alhussainy, F., Hasan, H. A., Sheikh, M. N., and Hadi, M. N. S. (2019). *A New Method for Direct Tensile Testing of concrete*. Wollongong: Faculty of Engineering and Information Sciences. Papers: Part B. 1716.

Aonoa, Y., Tani, K., Okada, T., and Sakai, M. (2012). "Failure Mechanism of the Specimen in the Splitting Tensile Strength Test," in Proceedings of the 7th Asian Rock Mechanics Symposium, Seoul, South Korea, October, 2012, 615–623.

ASTM C496/C496M-17 (2017). *Standard Test Method for Splitting Tensile Strength of Cylindrical Concrete Specimens*. West Conshohocken, PA: ASTM International.

ASTM D7015-18 (2018). *Standard Practices for Obtaining Intact Block (Cubical and Cylindrical) Samples of Soils*. West Conshohocken, PA: ASTM International.

Biolzi, L., Cattaneo, S., and Rosati, G. (2001). Flexural/Tensile Strength Ratio in Rock-like Materials. *Rock Mech. Rock Eng.* 34, 217–233. doi:10.1007/s006030170010

BS 1377-1 (2016). *Methods of Test for Soils for Civil Engineering Purposes-Part 1: General Requirements and Sample Preparation*. London: British Standards Institution.

Butenuth, C., De Freitas, M. H., Al-Samahiji, D., Park, H. D., Cosgrove, J. W., and Schetelig, K. (1993). Observations on the Measurement of Tensile Strength Using the Hoop Test. *Int. J. Rock Mech. Mining Sci. Geomech. Abstr.* 30, 157–162. doi:10.1016/0148-9062(93)90708-L

Coviello, A., Lagioia, R., and Nova, R. (2005). On the Measurement of the Tensile Strength of Soft Rocks. *Rock Mech. Rock Eng.* 38, 251–273. doi:10.1007/s00603-005-0054-7

Demirdag, S., Tufekci, K., Sengun, N., Efe, T., and Altindag, R. (2019). Determination of the Direct Tensile Strength of Granite Rock by Using a New Dumbbell Shape and its Relationship with Brazilian Tensile Strength. *IOP Conf. Ser. Earth Environ. Sci.* 221, 012094. doi:10.1088/1755-1315/221/1/012094

Erarslan, N., Liang, Z. Z., and Williams, D. J. (2012). Experimental and Numerical Studies on Determination of Indirect Tensile Strength of Rocks. *Rock Mech. Rock Eng.* 45, 739–751. doi:10.1007/s00603-011-0205-y

Fairhurst, C. (1961). "Laboratory Measurement of Some Physical Properties of Rock," in Proceedings of the Fourth Symposium on Rock Mechanics, Pennsylvania, USA, March 1961.

Fairhurst, C. (1964). On the Validity of the 'Brazilian' Test for Brittle Materials. *Int. J. Rock Mech. Mining Sci. Geomech. Abstr.* 1, 535–546. doi:10.1016/0148-9062(64)90060-9

Fang, H. Y., and Chen, W. F. (1972). "Further Study of Double-Punch Test for Tensile Strength of Soils," in Proceedings of the Third Southeast Asian Conference on Soil Engineering, Hong Kong, September 1972.

GB/T 23561.10 (2010). *Methods for Determining the Physical and Mechanical Properties of Coal and Rock-Part 10: Methods for Determining Tensile Strength of Coal and Rock*. Beijing: Standards Press of China.

GB/T 50123-2019 (2019). *Standard for Soil Test Method. Ministry of Construction*. Beijing: China Planning Press.

GB/T 50266-2013 (2013). *Standard for Test Methods of Engineering Rock Mass*. Beijing: China Planning Press.

Griffith, A. A. (1921). VI. The Phenomena of Rupture and Flow in Solids. *Phil. Trans. R. Soc. Lond. A.* 221, 163–198. doi:10.1098/rsta.1921.0006

Gutiérrez-Moizant, R., Ramírez-Berasategui, M., Santos-Cuadros, S., and García-Fernández, C. C. (2020). A Novel Analytical Solution for the Brazilian Test with Loading Arcs. *Math. Probl. Eng.* 2020, 1–19. doi:10.1155/2020/2935812

Haimson, B. C., and Cornet, F. H. (2003). ISRM Suggested Methods for Rock Stress Estimation-Part 3: Hydraulic Fracturing (HF) And/or Hydraulic Testing of Pre-existing Fractures (HTPF). *Int. J. Rock Mech. Mining Sci.* 40, 1011–1020. doi:10.1016/j.ijrmms.2003.08.002

Hawkes, I., and Mellor, M. (1970). Uniaxial Testing in Rock Mechanics Laboratories. *Eng. Geol.* 4, 179–285. doi:10.1016/0013-7952(70)90034-7

He, M. Y., Cao, H. C., and Evans, A. G. (1990). Mixed-mode Fracture: the Four-point Shear Specimen. *Acta Metal. Material.* 38, 839–846. doi:10.1016/0956-7151(90)90037-h

Hobbs, D. W. (1964). The Tensile Strength of Rocks. *Int. J. Rock Mech. Mining Sci. Geomech. Abstr.* 1, 385–396. doi:10.1016/0148-9062(64)90005-1

Hooper, J. A. (1971). The Failure of Glass Cylinders in Diametral Compression. *J. Mech. Phys. Sol.* 19, 179–188. doi:10.1016/0022-5096(71)90027-5

Hudson, J. A., Brown, E. T., and Rummel, F. (1972). The Controlled Failure of Rock Discs and Rings Loaded in Diametral Compression. *Int. J. Rock Mech. Mining Sci. Geomech. Abstr.* 9, 241–248. doi:10.1016/0148-9062(72)90025-3

Hudson, J. A. (1969). Tensile Strength and the Ring Test. *Int. J. Rock Mech. Mining Sci. Geomech. Abstr.* 6, 91–97. doi:10.1016/0148-9062(69)90029-1

ISRM (1978). Suggested Methods for Determining Tensile Strength of Rock Materials. *Int. J. Rock Mech. Min. Sci. Geomech. Abstr.* 15, 99–103. doi:10.1016/0148-9062(78)90003-7

ISRM (1979). Suggested Methods for Determining the Uniaxial Compressive Strength and Deformability of Rock Materials. *Int. J. Rock Mech. Min. Sci. Geomech. Abstr.* 16, 137–140. doi:10.1016/0148-9062(79)91450-5

Jiang, M., Zhang, F., Hu, H., Cui, Y., and Peng, J. (2014). Structural Characterization of Natural Loess and Remolded Loess under Triaxial Tests. *Eng. Geol.* 181, 249–260. doi:10.1016/j.enggeo.2014.07.021

Komurlu, E., and Kesimal, A. (2015). Evaluation of Indirect Tensile Strength of Rocks Using Different Types of Jaws. *Rock Mech. Rock Eng.* 48, 1723–1730. doi:10.1007/s00603-014-0644-3

Kuruppu, M. D., and Funatsu, T. (2012). "Development of a Standard Method for Determining the Plane Strain Fracture Toughness of Rock," in Proceedings of the Seventh Australasian Congress on Applied Mechanics, Australia, December 2012.

Li, D., and Wong, L. N. Y. (2013). The Brazilian Disc Test for Rock Mechanics Applications: Review and New Insights. *Rock Mech. Rock Eng.* 46, 269–287. doi:10.1007/s00603-012-0257-7

Li, Y., He, S., Deng, X., and Xu, Y. (2018a). Characterization of Macropore Structure of Malan Loess in NW china Based on 3d Pipe Models Constructed by Using Computed Tomography Technology. *J. Asian Earth Sci.* 154, 271–279. doi:10.1016/j.jseaes.2017.12.028

Li, Y., Mao, J., Xiang, X., and Mo, P. (2018b). Factors Influencing Development of Cracking-Sliding Failures of Loess across the Eastern Huangtu Plateau of China. *Nat. Hazards Earth Syst. Sci.* 18, 1223–1231. doi:10.5194/nhess-18-1223-2018

Li, Y., Guan, F., Su, H., Aydin, A., Beroya-Eitner, M. A., and Zachert, H. (2020). A New Direct Tension Test Method for Soils and Soft Rocks. *Geotech. Test. J.* 43, 20190308–20191334. doi:10.1520/GTJ20190308

Li, Y. (2018). A Review of Shear and Tensile Strengths of the Malan Loess in China. *Eng. Geol.* 236, 4–10. doi:10.1016/j.enggeo.2017.02.023

Liao, Z. Y., Zhu, J. B., and Tang, C. A. (2019). Numerical Investigation of Rock Tensile Strength Determined by Direct Tension, Brazilian and Three-point Bending Tests. *Int. J. Rock Mech. Mining Sci.* 115, 21–32. doi:10.1016/j.ijrmms.2019.01.007

Mellor, M., and Hawkes, I. (1971). Measurement of Tensile Strength by Diametral Compression of Discs and Annuli. *Eng. Geol.* 5, 173–225. doi:10.1016/0013-7952(71)90001-9

Okubo, S., and Fukui, K. (1996). Complete Stress-Strain Curves for Various Rock Types in Uniaxial Tension. *Int. J. Rock Mech. Mining Sci. Geomech. Abstr.* 33, 549–556. doi:10.1016/0148-9062(96)00024-1

Perras, M. A., and Diederichs, M. S. (2014). A Review of the Tensile Strength of Rock: Concepts and Testing. *Geotech. Geol. Eng.* 32, 525–546. doi:10.1007/s10706-014-9732-0

Stacey, T. R. (1981). A Simple Extension Strain Criterion for Fracture of Brittle Rock. *Int. J. Rock Mech. Mining Sci. Geomech. Abstr.* 18, 469–474. doi:10.1016/0148-9062(81)90511-8

Swab, J. J., Yu, J., Gamble, R., and Kilczewski, S. (2011). Analysis of the Diametral Compression Method for Determining the Tensile Strength of Transparent Magnesium Aluminate Spinel. *Int. J. Fract.* 172, 187–192. doi:10.1007/s10704-011-9655-1

Tapponnier, P., and Brace, W. F. (1976). Development of Stress-Induced Microcracks in Westerly Granite. *Int. J. Rock Mech. Mining Sci. Geomech. Abstr.* 13, 103–112. doi:10.1016/0148-9062(76)91937-9

Tolooiyan, A., Mackay, R., and Xue, J. (2014). Measurement of the Tensile Strength of Organic Soft Rock. *Geotech. Test. J.* 37 (6), 20140028. doi:10.1520/GTJ20140028

Xu, S., De Freitas, M. H., and Clarke, B. A. (1988). "The Measurement of Tensile Strength or Rock," in Proceedings of the Symposium on Rock Mechanics and Power Plants, Spain, September, 1988, 125–132.

Zhang, Q., Duan, K., Xiang, W., Yuan, S., and Jiao, Y.-Y. (2017). Direct Tensile Test on Brittle Rocks with the Newly Developed Centering Apparatus. *Geotech. Test. J.* 41 (1), 20160301. doi:10.1520/GTJ20160301

Zoback, M. D., Rummel, F., Jung, R., and Raleigh, C. B. (1977). Laboratory Hydraulic Fracturing Experiments in Intact and Pre-fractured Rock. *Int. J. Rock Mech. Mining Sci. Geomech. Abstr.* 14, 49–58. doi:10.1016/0148-9062(77)90196-6

Conflict of Interest: The authors declare that the research was conducted in the absence of any commercial or financial relationships that could be construed as a potential conflict of interest.

Publisher's Note: All claims expressed in this article are solely those of the authors and do not necessarily represent those of their affiliated organizations, or those of the publisher, the editors, and the reviewers. Any product that may be evaluated in this article, or claim that may be made by its manufacturer, is not guaranteed or endorsed by the publisher.

frontiers in Earth Science

ORIGINAL RESEARCH
published: 31 March 2022
doi: 10.3389/feart.2022.812609

Strategies for Gully Stabilization and Highland Protection in Chinese Loess Plateau

Wanfeng Liu[1], *Huyuan Zhang*[2,3]*, *Jianghong Zhu*[2] *and Aiping Hu*[1]

[1]College of Civil Engineering, Longdong University, Qingyang, China, [2]College of Civil Engineering and Mechanics, Lanzhou University, Lanzhou, China, [3]Key Laboratory of Mechanics on Disaster and Environment in Western China, Lanzhou University, Ministry of Education, Lanzhou, China

Loess tablelands are large-scale platforms with flat top surfaces in the center of Chinese Loess Plateau, such as Dongzhiyuan, which is a ~900 km^2 loess stratum, with the thickness larger than 200 m. The break of loess tablelands is widely reported due to the retreat of gully systems, resulting in serious social problems and economic losses. The retreating rate of large gullies has been 0.5–6.6 m/year over the past 2,000 years, estimated by the calculation of erosion modulus, literature archaeology, and field monitoring. The retreating rate of a small gully can reach 7.5–27.0 m/year after a rainstorm. To protect the farmland, buildings, roads, and pipelines near to the gully head areas, a project named Gully Stabilization and Highland Protection (GSHP) was launched by the local government, including the small watershed management (SWM) around loess slopes and gully channels and sponge city construction (SCC) achieved by improving the drainage system of tableland surfaces. These efforts improve the soil and water conservations, although they contribute less to controlling gully expansion. From the perspective of mutual promotion of gravity erosion and hydraulic erosion, this paper proposes a technical framework for GSHP, focusing on the avoidance of geological disaster. This case study reports on an illustrative GSHP project, the restoration of Huoxianggou gully, including the backfilled loess embankment across the gully for convenient urban transportation, and the stabilization of unstable loess slopes. After the implementation, the retreat of the gully head has been stopped, and the soil erosion rate has been reduced by 90%.

Keywords: Chinese loess plateau, gully expansion, gully head stabilization, sponge city, soil and water conservation

OPEN ACCESS

Edited by:
Gonghui Wang,
Kyoto University, Japan

Reviewed by:
Jianqi Zhuang,
Chang'an University, China
Shenghua Cui,
Chengdu University of Technology, China

***Correspondence:**
Huyuan Zhang
zhanghuyuan@lzu.edu.cn

Specialty section:
This article was submitted to Geohazards and Georisks, a section of the journal Frontiers in Earth Science

Received: *10 November 2021*
Accepted: *21 February 2022*
Published: *31 March 2022*

Citation:
Liu W, Zhang H, Zhu J and Hu A (2022) Strategies for Gully Stabilization and Highland Protection in Chinese Loess Plateau. Front. Earth Sci. 10:812609. doi: 10.3389/feart.2022.812609

INTRODUCTION

A loess is a loose aeolian deposit of yellowish silt-sized dust, mostly formed during the Quaternary period (Liu, 1965; Liu, 1985). Loess deposits are widespread in China, which is mainly along the middle reaches of the Yellow River in central China and is called as the Chinese Loess Plateau (**Figure 1**) The thickness of loess sediments can be as large as several hundred meters. Dongzhiyuan loess tableland is an example, where there is a specific geometrographic unit with broad and flat top surfaces surrounded by deep gully systems, at Xifeng District of Qingyang, Gansu Province, China (**Figure 2**).

During the rainy season, the huge flat surface of the loess tableland receives intense precipitation, and flood water discharges into the gullies. Serious erosion is found on the gully head, bed, and side

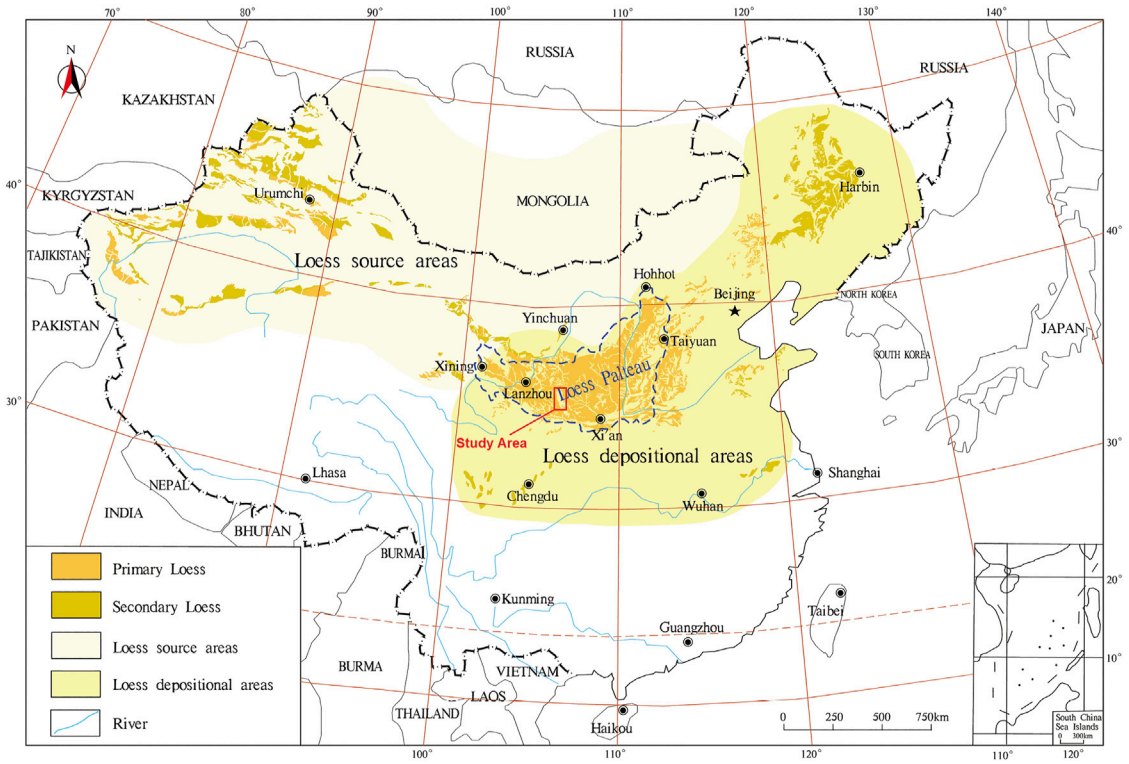

FIGURE 1 | Loess distribution and the Chinese Loess Plateau (Li et al., 2018).

slopes. Also, the gully heads have expanded quickly towards the central tableland, resulting in a shrinkage of the tableland. This process was speeded up due to the urbanization of Qingyang City at the center of the loess tableland of Dongzhiyuan. The shrinkage of the tableland limits urbanization and economic development, which is the biggest challenge for the local government.

To solve this problem, the local government consulted, with an open mind, various experts, such as experts in Quaternary geology, soil and water conservation, geological hazard prevention, meteorology, water conservancy, and urban planning. The preliminary consensus was that gully expansion is a natural process but has been speeded up by human activity in recent years. Gully heads are extremely sensitive to hydraulic scouring and piping erosion during rainfalls, which cause rapid retreat of the radial gully system on the tableland margin. Geotechnical engineering measures are recommended by experts to stabilize gully head and improve the local soil and water conservation. Geological disaster control has become a priority for reducing both gravity and hydraulic erosions. This technical idea has been summarized as Gully Stabilization and Highland Protection (GSHP), hereafter referred to as the GSHP project. Until now, the major engineering measures in the GSHP project includes backfilling, drainage, slope stabilization, and ecological slope protection (Huo et al., 2020). Based on hydrological modeling of typical watershed and field observations, the GSHP project has clearly reduced the surface runoff and sediment (Huo et al., 2021). This paper summarizes the major opinions that emerged during the initial stages of the GSHP project and proposes a technical framework for selecting effective engineering measures in practice.

BREAKING UP OF LOESS TABLELAND BY GULLY EROSION

Landforms refer to various forms of the Earth's surface that result from internal and external geological processes over time. Geomorphology divides loess landforms into three main types: the tableland, ridges, and hillocks. Loess tableland is a geomorphic unit developed at the end of the Tertiary with a large area and a flat top, which was later eroded due to uplift (Zhang, 1983). It is considered that homogenous loess deposits masked the underlying bedrocks and therefore inherited a flat top surface (Tsunekawa et al., 2014; Li et al., 2020).

The loess tableland of Dongzhiyuan is the most intact and the largest tableland in the world with a loess thickness of 150–200 m. Originally, the tableland was recorded as being more than 110 km long (north to south) and about 50 km wide (east to west). Because of the serious soil erosion, there are now just 89 km left (north–south) and 46 km east–west. Approximately 756–1,344 km^2 of the tableland retreated in the past 1,000 years, nearly 1 km^2/year (Derbyshire, 2001).

The huge tableland has a flat surface generally with 1–3° inclination, which was renowned as being a granary in the 1980s because of the abundant grain harvest in Gansu Province. There are seven large gully systems around the tableland in a radial formation

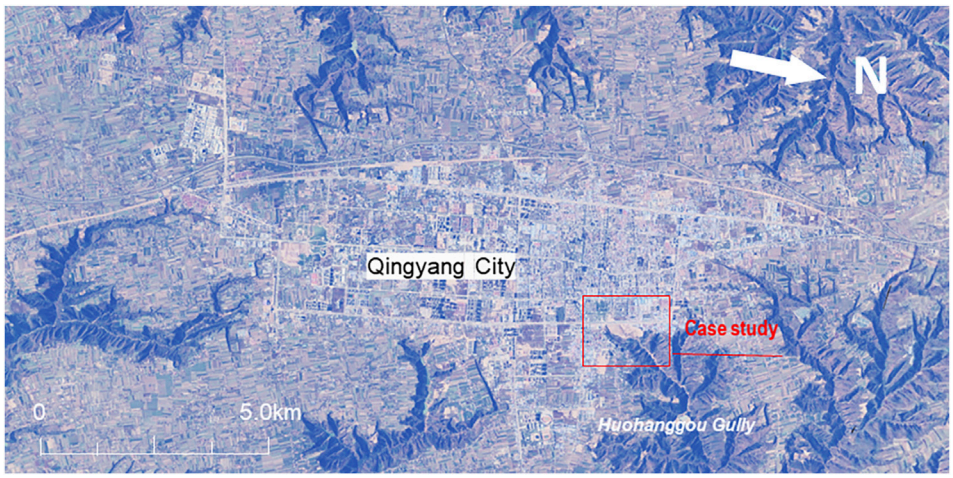

FIGURE 2 | Loess tableland of Dongzhiyuan eroded by gullies.

(**Figure 2**). The gully heads are only ~50 m apart in some locations, and they are tending to split the tableland into two parts, owing to the rapid erosion in the past few decades.

After a rainfall, flood water converges from the tableland surface and pours down with silt, washing away the fertile soil and leaving behind the barren land. The whole tableland surface is being continuously cut and shrunk year on year. The most recent investigation recorded 37 gullies of different sizes surrounding the tableland margin. On the tableland edge area 50 m away from the gully heads, there are 27 schools, 5,384 households, and more than 200 buildings, which are directly threatened by gully head expansion. Therefore, tableland protection is a huge challenge for the local government to protect both the local residents and the economic development.

Gully Expansion From a Geological View

Geologically, Loess Plateau on a regional scale inherits the basic morphological characteristics of ancient landforms because loess

TABLE 1 | Speed of gully head retreat estimated by different methods.

No	Retreat speed (m/year)	Starting time or period	Determination of gully head retreat distance	References
A1	4.21	683 B.C.	Back-calculated from erosion modulus of the gully dated by archaeology	Yao (2009)
A2	6.56	425 B.C.		
A3	2.53	226 B.C.		
A4	5.42	339 A.D.		
A5	3.13	691 A.D.		
A6	5.80	753 A.D.		
A7	2.03	1121 A.D.		
A8	4.14	1761 A.D.		
A9	0.45	1623 A.D.		
B1	0.50	Last 150 years	Estimated from historical documents	Chen et al. (2009)
B2	0.60	Last 40 years		
B3	1.50	Last 40 years		
B4	0.50	Last 30 years		
B5[a]	3.00	Last 20 years		
B6	0.80	Last 20 years		
B7	0.30	Last 20 years		
B8	1.20	Last 20 years		
B9	0.70	Last 15 years		
B10	0.58	Last 10 years		
C1	27.00	July 2006	Measured after a rainstorm event in July 2006	Chen et al. (2009)
C2	22.60	July 2006		
C3	6.60	July 2006		
C4	9.35	July 2006		
C5	7.50	July 2006		

[a]*Stands for Huohanggou Gully, the most active large gully on Dongzhiyuan loess tableland.*

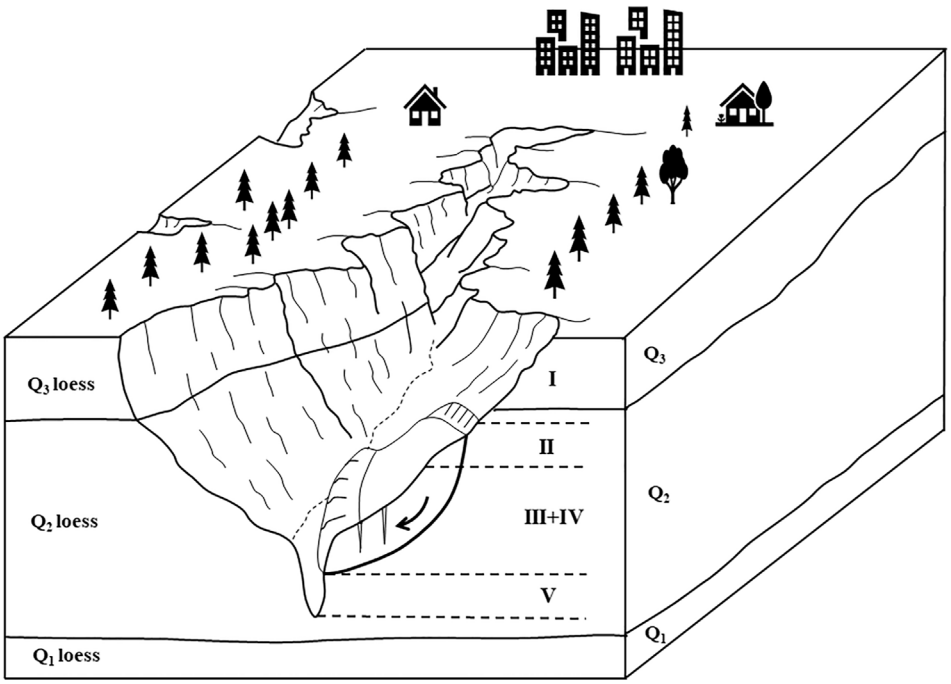

FIGURE 3 | Zonation of erosions at upstream of loess gully (modified from Zhang, 1980). I, sheet erosion zone; II, subsurface piping erosion zone; III, incising erosion zone; IV, gravitational erosion zone; V, scouring erosion zone).

has covered the underlying bedrock in geological history, but the relative height difference is smaller than that of the ancient topography (Li et al., 2018).

Geomorphology describes the evolution process of a river valley from the principle of "erosion basis." The downward erosion of a valley does not cease until the valley reaches the base level of erosion. On the loess plateau, the bed channels of the gullies are usually higher than the local erosion basis, resulting in continuous downward erosion in the last thousand years.

The gullies that formed during the geological period are referred to as ancient erosion gullies, while the gullies that have formed onto the slope of ancient erosion gullies since the Holocene are referred to as modern erosion gullies. The former gullies are mainly distributed at the lower reaches of the gully system, characterized by a wide channel and a typical U-shaped cross section. The latter are mainly distributed at the upper reaches of the gully system as the modern gully heads, characterized by a narrow and deeply grooved channel and a typical V-shaped cross section.

Statistics of Gully Head Expansion

Using the methods of archaeological investigation and historical literature research, Shi (1999) investigated the geomorphologic age of the Loess Plateau. Shi (1999) estimated that the original loess tableland began to be broken no earlier than 2,000 years ago, and the main destruction occurred in the Chinese Sui and Tang Dynasties (AD 907). This means that the river valleys and large gullies around the loess tableland have existed for at least 1,000 years. Shi (1999) mentioned that modern erosion continuously carved the tableland, resulting in longer, deeper, and wider gullies than ever before.

Based on the methodology established by Shi (2001), Yao (2009) made a new attempt to quantify the extension of gullies. Gullies are simplified as triangular pyramids, which can be enlarged equally and uniformly during historical erosion. The enlarged gullies are supposed to be originally filled by the soil eroded away, which can be calculated by the erosion modulus of the gullies. Assessment results indicated that 77 typical gullies around the Dongzhiyuan Tableland expanded their head toward the upstream direction with a rate between 0.45 and 6.56 m/year in the last 2,000 years. Typical results of the nine gullies with complete watersheds are named A series and are reported in **Table 1**.

Table 1 also lists the head retreat speed of several gullies in the recent past, as estimated by Chen et al. (2009). The gully expansion of the B series was estimated from historical records, while the gully expansion of the C series was determined by field measurement after a single rainstorm event. Small gullies of the C series retreated 7.5–27.0 m/year after a rainstorm event. In contrast, the big gullies of the B series tended to be stable over a long period if rainwater flood seldom discharged into the gullies. For example, these kinds of gullies extended 0.3–3.0 m/year during 10–150 years.

It should be noted that the retreat of gully head highly depends on the discharge of rainwater flooding. Fast retreat of a gully

TABLE 2 | Suitability of different spillways as gully head control structure (Shit et al., 2020).

Type of spillway	Overfall (m)	Peak runoff (m^3/s)	Advantages	Disadvantages
Drop spillway	<3	>2.5	Relatively stable and safe, easy to construct and maintain	Requires stable grade on either side, unsuitable for detention storage
Chute spillway	3–6	<2.5	Relatively low cost	Susceptible to failure due to seepage or rodents activity
Pipe spillway	>3	Any	Suited for upstream detention storage, road culverts, economical, stable, and safe	Sensitive to clogging by debris, requires regular inspection to avoid channeling along pipe

results from not only intensive scouring erosion but also the increasing height of the newly formed slope. The newly formed slope prompts potential gravitational erosion, such as rockfall and slope slide. Therefore, scouring erosion plays a critical role in the retreat of gullies.

Huohanggou Gully has been recognized as the number one threat to the urban safety of Qingyang City because of its fast penetration into the downtown area. In 1949, a Yellow River investigation team measured the gully expansion and reported that this gully had retreated at least 300 m from 1889 to 1949, or 5 m/year. According to the data of Chen et al. (2009) as indicated by B5 in **Table 1**, this gully has retreated 3 m/year over the last 20 years after a stormwater pond was constructed in 1952 at the gully head area.

Mechanism of Gully Head Retreat

Gully erosion is an advanced stage of rill erosion, which makes the rills wide and deep. Continuous undercut results in collapse of the gully head and triggers the upslope extension of most of the gullies. Also, the slumping and collapsing of the sidewalls contribute to a higher proportion of soil loss (Shit et al., 2020).

A headcut refers to a sudden step change in the bed elevation of a gully channel, and intense erosion occurs at this site due to the jet flow scouring from the upstream area (Bennett, et al., 2000). Gully headcut erosion is caused by a complicated process, including plunge pool erosion, headwall erosion, pore water pressure change, tension crack development, and mass failure (Vanmaercke et al., 2016). Headcut erosion mainly depends on the area of the upstream catchment and rainfall characteristics, such as the rainfall intensity and slope topography (Bennett, 1999).

The three-dimensional features of a modern erosion gully can be described simply by three geometric parameters: the length, top width, and depth of the gully. If the changes in geometric parameters are recorded, the gully expansion can be classified simply by the maximum increasing parameter. Thus, the erosion of a gully can be predominated by head retreat, widening, or deepening. Much more detailed investigations indicate that modern erosion gullies are expanded by rapid retreat of the gully head rather than widening or deepening.

For erosion gullies, five different types of loess erosion can be distinguished from a gully profile (Zhang, 1980, **Figure 3**): (I) sheet and/or rill erosion zone, (II) subsurface piping erosion zone, (III) incising erosion zone, (IV) gravitational erosion zone, and (V) scouring erosion zone. Simply speaking, sheet erosion is dominant at the upper part of the slope, while gravitational erosion occurs mainly at the middle of the slope, and underground piping erosion occurs at the toe of the slope. Vertical scouring erosion occurs mainly in the gully bed by deepening and extending the gully into the loess hillside and finally creating head cuts and steep banks.

The development of gullies has a negative impact on engineering construction, especially road construction. When a route passes through the gully area, backfilling and erecting bridges crossing deep ditches are required. Subgrades are often damaged due to the development of gullies. For example, in Northwest China, after a rainstorm, many new gullies will be formed, and the existing gullies will be lengthened for several meters, resulting in the damage of subgrades.

Generally, the development of gullies can be divided into four stages, i.e., rill and cutter stage, headcut stage, balanced section stage, and stopping development stage. It should be pointed out that the whole process of gully development is, in fact, continuous. The main significance of stage division is to choose approximate control measures.

At the first stage, local surface water is concentrated in a small concave part of the slope and begins to wash out, forming a shallow cutting ditch of about 30–50 cm. The longitudinal section of the shallow trench is roughly the same as that of the slope with a triangular cross section. At the second stage, falling water or a steep cliff is formed at a height usually of 2–10 m, sometimes up to 10–15 m. Under the wash of running water, the gully head continuously retreats in the watershed direction. At the same time, the gully bottom is rapidly incised and deepened to 25–30 m. At the third stage, the gully mouth reaches the local erosion base level, such as the river surface or terrace. The longitudinal section of the trench bottom is close to the "balance section." Before the equilibrium section is reached at the third stage, intensive erosion continues to cut down, and the slopes on both sides continue to collapse. At the fourth stage, the gully bed approaches the "equilibrium section." The undercutting stops, and the headcut becomes more and more gentle, so the gully is no longer lengthened. Sediments appear at the gully bottom, and gully slopes collapse gradually until a naturally stable condition is reached. Plants grow on to the sediments or the side slopes surface.

Suitable spillway structures are suggested by Shit et al. (2020) to control gully head (**Table 2**). It is clear that a pipe spillway has a good adaptability to different overfalls or head steps, which is characterized by low cost and less maintenance.

STRATEGIES AND MEASUREMENTS FOR THE GSHP PROJECT

The aims of the GSHP include measures to prevent the erosion of the loess highland from a practical perspective and an integrated technical system from an academic perspective for selection of effective engineering measures to prevent gully head expansion.

Various measures have been practiced for soil and water conservation in Chinese Loess Plateau, in fact, from different disciplines, such as small watershed management (SWM), geological disaster control (GDC), and sponge city construction (SCC). The different disciplines have different emphases when dealing with soil and water conservation. After 70 years of practice, several measures have been confirmed to be effective in controlling the shrinkage of Dongzhiyuan loess tableland. Strategies

TABLE 3 | Strategies and measurements of the GSHP project.

Stage	Beginning age	Leading discipline	Strategies	Key measures	Engineering location
I	1952	Small watershed management (SWM)	"Three protection belts"	1. Runoff regulation on tableland 2. Vegetation restoration of gully slopes 3. Water and sand storage in gully channels	Nanxiaohegou watershed, Qingyang, Gansu, China
II	2015	Geological disaster control (GDC)	Gully head reinforcement	4. Backfilling of gully head 5. Stabilization of unstable side slope of gully	Gully head of Huohanggou Gully, Qingyang, Gansu, China
III	2016	Sponge city construction (SCC)	Regulation and utilization of stormwater in urban area	5. Construction of water landscapes 6. Improvement of stormwater drainage systems 7. Construction of ecological parks	Urban district of Qingyang City, Gansu, China

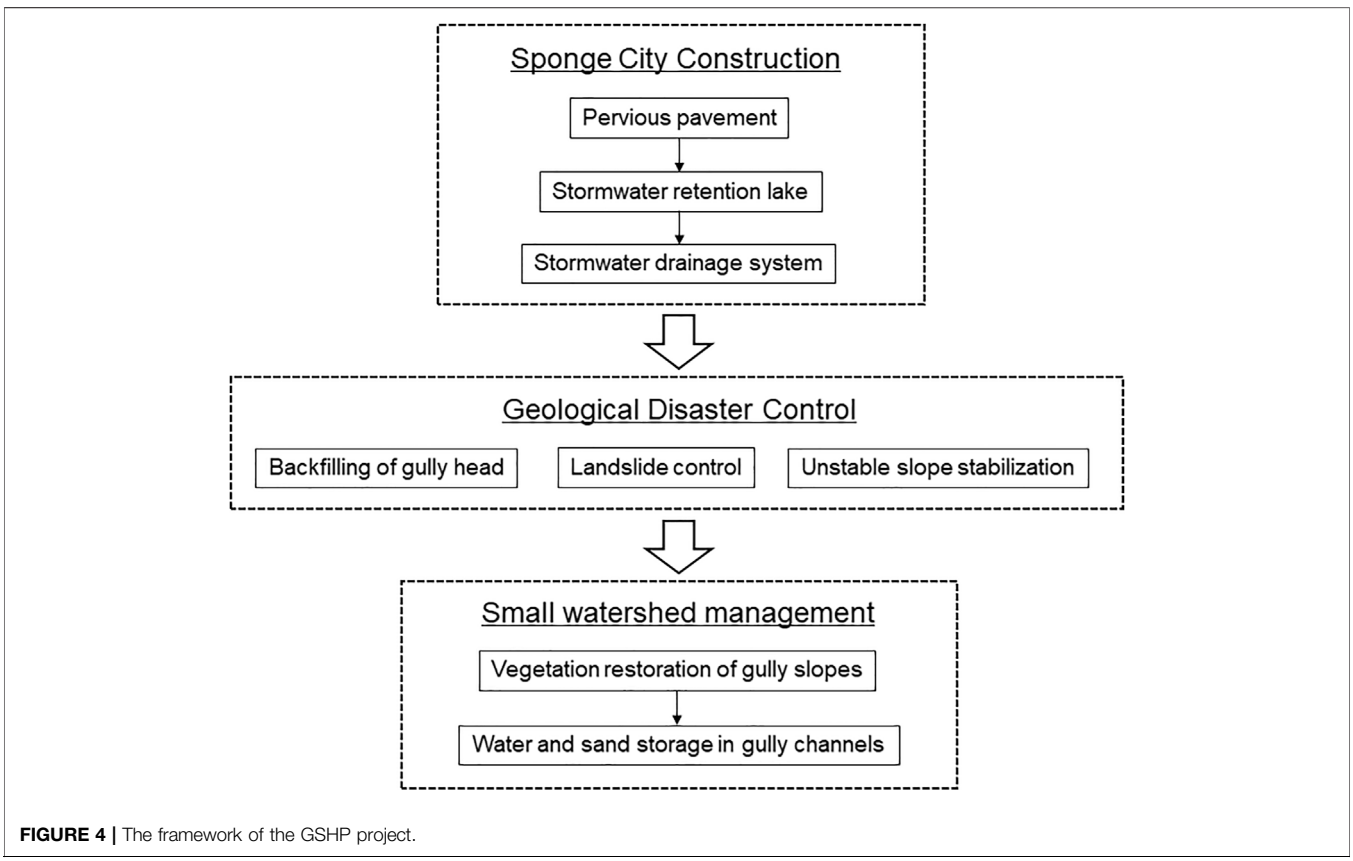

FIGURE 4 | The framework of the GSHP project.

TABLE 4 | Major hazardous events and rehabilitation of the Huohanggou Gully.

No	Date	Major events	Sources
1	618–907A.D.	Mudbrick production started in the valley.	Folk legend
2	1368–1644A.D.	It was said that landslides happened that destroyed the mudbrick factories, but no written documents were found in local official file.	Folk legend
3	1929	Permanent village and dwellings appeared nearby the gully.	Local chronicles
4	1949	For the first time, professional measurement had been carried out on gully expansion: gully head retreated at least 300 m from 1889 to 1949.	Investigation team of the Yellow River
5	1951–1952	A flood pond with 120,000 m^3 capacity was constructed at the gully head area for collection of street flood of rainstorm to be going down to the gully. From that time on, gully head retreat was almost stopped.	Local chronicles
6	1987	The flood pond was enlarged and reconstructed by concrete. The artificial lake became a famous water landscape of the Donghu Lake Park.	Local chronicles
7	1992	An old landslide was identified as 80 m long, 190 m wide, and 26 m in depth.	Geotechnical investigation records in 2017
8	2006	Big floods after rainstorms on July 2 and July 7 induced a landslide in the gully, 70 m long and 20 m wide, that destroyed the flood discharge pipeline down to the gully. Emergency repairment started in the following October.	Local residents recall
9	2013	A new landslide occurred just at the downstream side of the ancient landslides, and the displaced materials produced a small dammed lake in the gully bed.	Geotechnical investigation records in 2017
10	2017	Loess was compacted layer by layer to construct a high embankment in the gully head area, providing the foundation of a road across the gully. Stabilization of the unstable slopes began at the same time.	Local government notice
11	2019	Forest Park of Huohanggou Gully was initiated as one of three gully rehabilitation programs in Qingyang City.	Local government notice

and major measures for GSHP are listed in **Table 3**, and a framework of core technical measures is indicated in **Figure 4**. Mitigation measures are recommended to be scheduled following the steps: first stormwater regulation, then gully head stabilization, and finally the soil and water conservation on gully slopes and channels.

Practical protection of the loess tableland started in 1952, when a soil and water conservation agency was established in the central Dongzhiyuan Tableland, Qingyang City, Gansu Province, China. Therefore, early measures, at stage I, focused on passive control of soil and water in the gully channel and on the sides of the slopes. At stage II, innovation shifted to active protection—geotechnical stabilization of gully heads or side slopes. Stage III is characterized by SCC, which paid close attention to regulation and efficient utilization of rainwater on the tableland surface. Artificial lakes were constructed for stormwater retention or storage. A stormwater drainage system was specially designed to deliver the overflowing water down to gully beds.

Strategies From Small Watershed Management

Soil erosion studies have traditionally been conducted in single watersheds or at a regional scale using aerial photographs or field survey methods (Vanmaercke et al., 2016). In 1952, Xifeng Soil and Water Conservation Experimental Station was established in a watershed at Dongzhiyuan Tableland. Based on statistical data and successful erosion control on loess slopes, approximately 63% of the total runoff was generated from loess tableland, which contributed 86.3% of the total eroded sediment in watersheds (Guo et al., 2018). From successful practice in single watersheds, three "protection belts" were suggested as major reclamation areas in GSHP project. This emphasized the runoff regulation on tableland, vegetation restoration on slopes, and water and sand storage in gully channels for controlling serious erosion of the loess tableland. When the steep slope is converted into terrace forest and grassland, the erosion of coarse sediment into the Yellow River can be effectively reduced (Zhao et al., 2013). Actually, vegetation restoration plays an important role in the reformation of scattered rills, shallow gullies, or even cutter gullies on slopes because the root systems provide additional cohesion and shear and tensile strength (De Baets et al., 2008).

Strategies From Geological Disaster Control

A gully head is characterized by discrete steps, i.e., the sudden change in the elevation of a gully channel. If rainfall intensity exceeds a certain threshold, the gully head will move in upstream direction because of intense jet flow scouring, tension crack development, and mass failure. It was found that gully head retreat was caused by flow incision, headwall erosion, and gully bank collapse (Dong et al., 2019). In other words, large-scale gullying is closely related to geological disasters, such as mudflows, rockfall, and landslides. Geological disasters and gravitational erosion destroy the root systems, limiting the vegetation restoration effects. Therefore, gully head stabilization becomes a primary concern for establishing a base for further vegetation restoration.

In addition to the "three protection belts," close attention was paid to gully head stabilization, and the GSHP project was moved to its second stage. At this stage, four "protection belts" were designated as the reclamation target for the GSHP project, i.e., four landform units of tableland, gully heads, slopes, and gully channels. Specifically, reclamation included runoff regulation on the tableland, reinforcement of the gully head, vegetation restoration on slopes, and water and sand storage in the gully channels.

Geotechnical engineering plays a critical role in stabilization of landslides and unstable slopes and the backfilling of eroded sinkholes in gully head areas. Additional equipment must be provided to discharge rain flood down to the gully beds. Shit et al. (2020) analyzed the suitability of different types of spillways as gully head control structures. A pipe spillway is suitable for any gully head height and any peak flood discharge and capable of upstream detention storage or road culverts.

Strategies From Sponge City Construction

Qingyang City has suffered from limited precipitation, water resource shortage, and urban waterlogging over a long period of history. Especially in recent years, increasing rainwater is discharged down to the tableland, which has resulted in intensive erosion of gullies around the tableland due to rapid urban expansion and urban plot surface hardening.

In 2016, Qingyang City joined a demonstration program of the Sponge City project in China. Sponge City is a new design concept in China for urban planning based on the low impact development (LID) principle (US EPA, 2000). The major emphasis of the LID requirements in municipal permits is the reduction of impervious areas in order to facilitate infiltration and reduce urban runoff for specified categories of new development and redevelopment projects.

New stormwater pipelines were constructed in Qingyang City to capture rainwater from tableland surface, and artificial lakes were constructed to collect stormwater for ecological usage. As a result, both volume and peak runoff were reduced, and the intensive headcut of gullies was successfully controlled. Ecological parks were planned as recreational areas for citizens, such as the forest park in Huohanggou Gully, the wetland park in Zhangtiegou Gully, and the geological park in Xiaokongtong Gully.

SCC is characterized by practical collection and regulation of stormwater from tableland surface, improving the utilization of water resources. The implementation of the sponge city project is considered to have promoted the GSHP project into its third stage. During this stage the GSHP project has provided active measures controlling the intense erosion at the gully head by the stormwater from the tableland surface.

CASE STUDY OF GULLY HEAD STABILIZATION

Huohanggou Gully, as a natural ditch, has served as an urban drainage channel for a period of long history, discharging rain flood from the downtown area in Qingyang City to the gully bed. Since the 1940s, this gully threatened the safety of city streets.

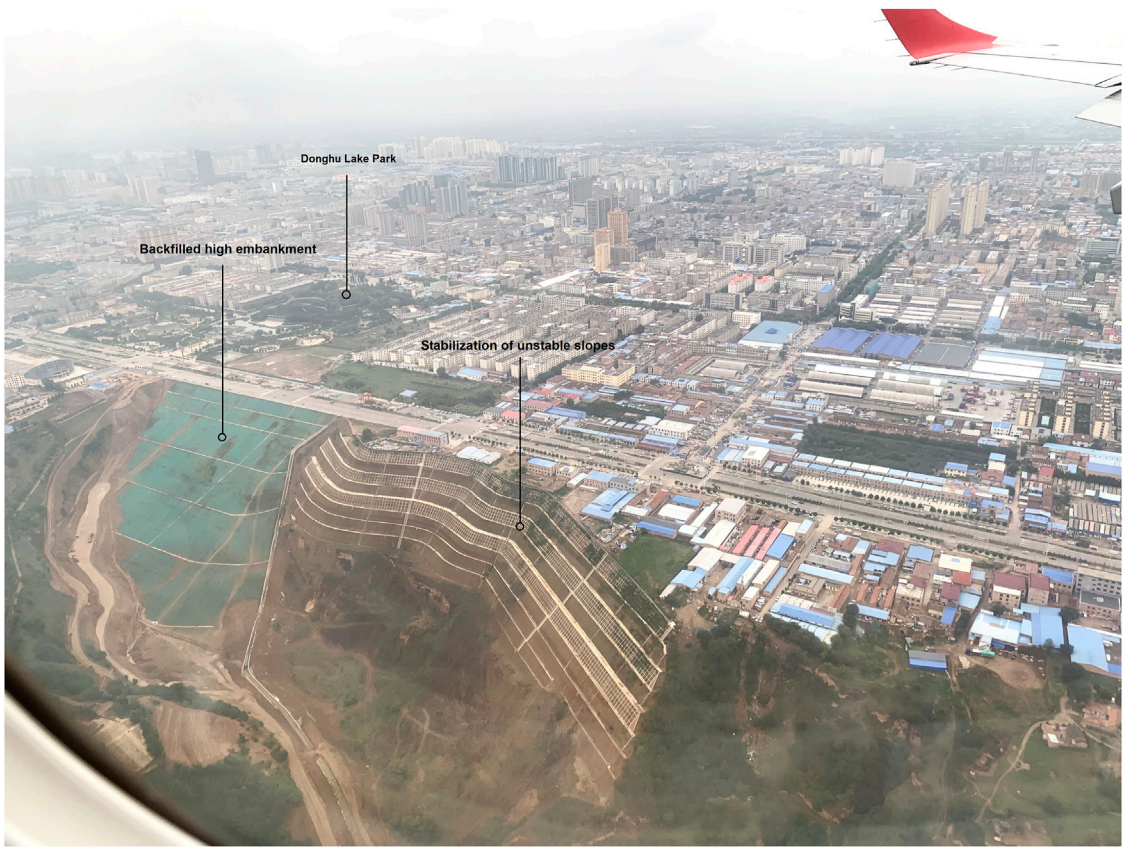

FIGURE 5 | Geohazard control engineering at Huohanggou Gully as seen from an airplane.

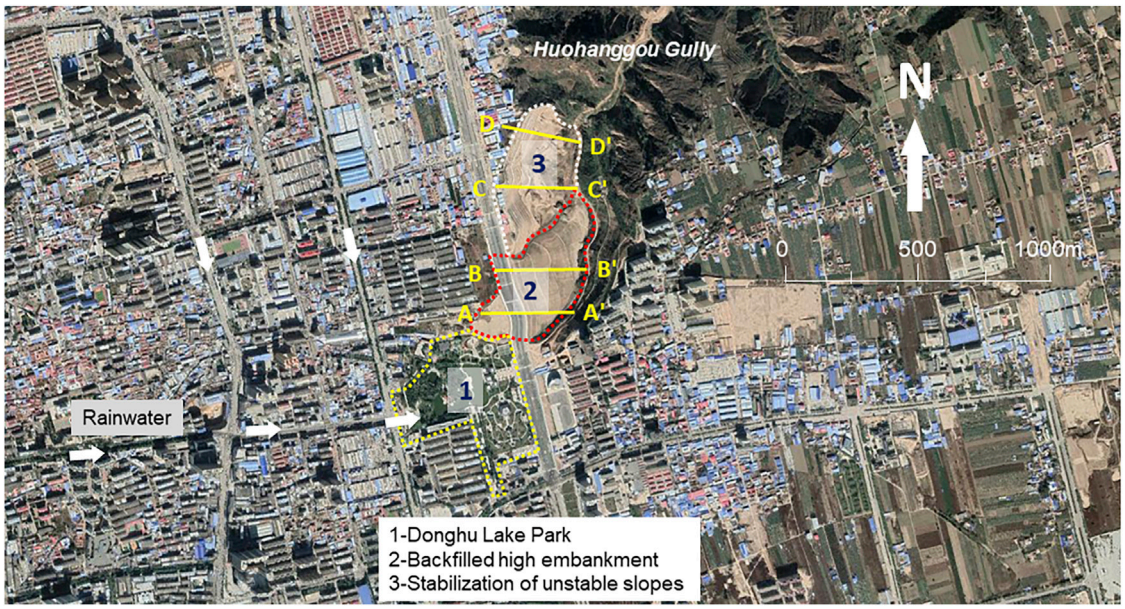

FIGURE 6 | Layout of geohazard control engineering at Huohanggou Gully. A—A', B—B', C—C', and D—D' are section lines.

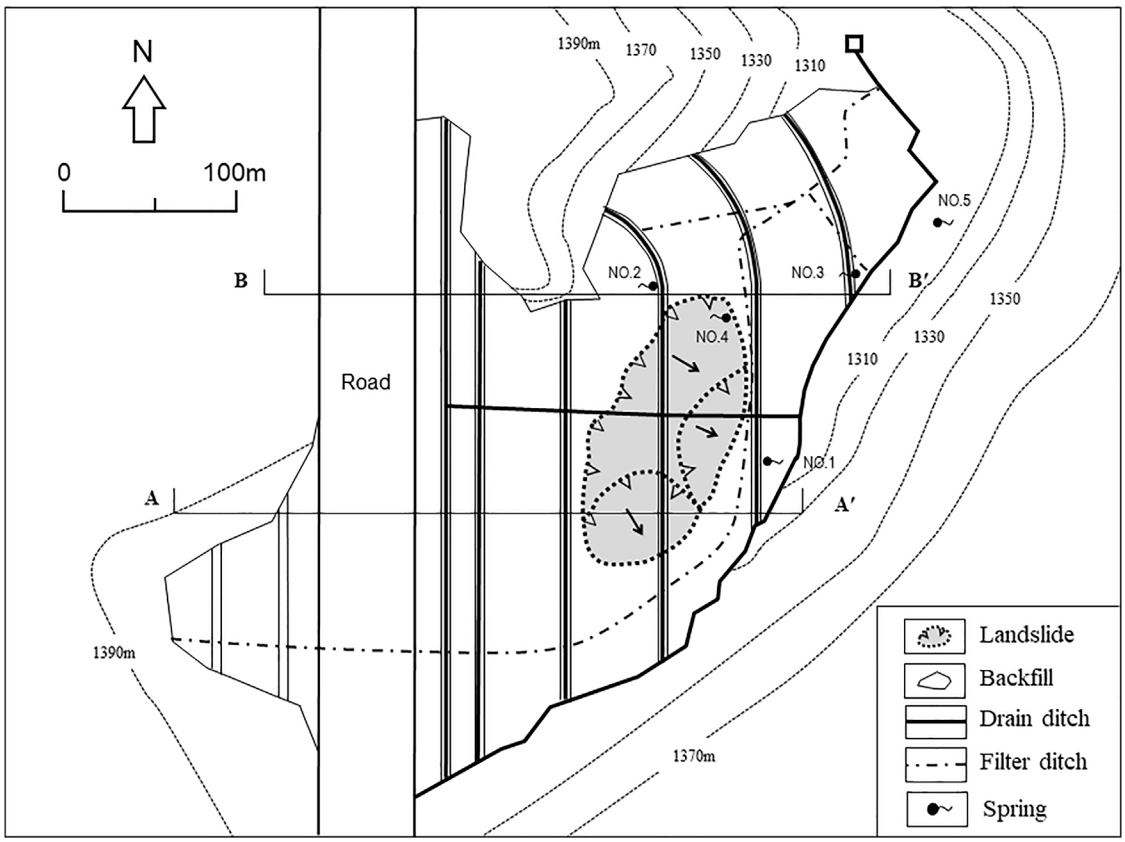

FIGURE 7 | Layout of the backfilled high embankment. A—A' and B—B' are section lines.

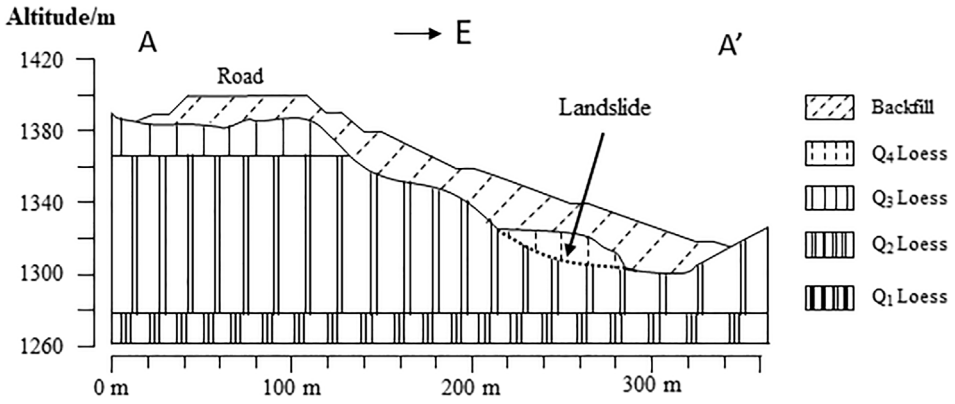

FIGURE 8 | A–A′ profile across the high backfill embankment.

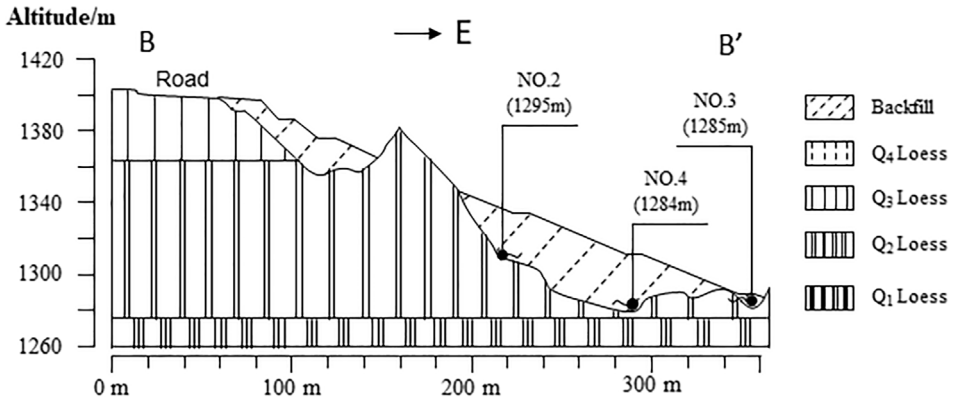

FIGURE 9 | B–B′ profile across the high backfill embankment.

Table 4 lists a brief history of the major hazardous events, such as fast head penetration into city blocks and landslide and the major mitigation measures. Since 2017, large-scale engineering has been conducted to control geological hazards in the gully head area, including both backfilling of the gully head and stabilization of unstable side slopes. No retreat of the gully head has been observed since the reclamation. This is of important academic value for the GSHP project to set up appropriate statutory mitigation measures.

The elevation of the gully head approaching loess plateau is 1,400 m, and the gully bed is 1,284 m. The 116 m difference between the elevation of the head and the bed covers 300 m of the plateau. Meteorological data show that the average annual rainfall is 540 mm, mainly occurring from July to September. The largest single rainfall event reached 200 mm, about 40% of the average annual rainfall. The maximum flood was estimated at 4,000 m^3 according to the drainage area of 20 km^2 based on local topography. The average flood flow into Huohanggou Gully was 30–50 m^3/s, and the peak flow was 500 m^3/s based on the hydrological observation. It is obvious that rain floodwater discharged into the gully without regulation possesses a huge amount of energy to intensively erode the gully bed and side slopes.

Figure 5 provides an overall impression of the GSHP conducted in Huohanggou Gully. The Donghu Lake Park is a beautiful park now, where a large flood pond was firstly dug on the tableland surface in the 1950s, and reconstructed in 1987 using concrete in the same position, for collecting stormwater from the nearby urban area as indicated by arrows in **Figure 6**. Next to the Donghu Lake Park on the east side, there is a backfilled high embankment at the gully head area as the foundation of a main street crossing the gully. Next to the north side of the backfilled embankment are the stabilized loess slopes. **Figure 7** shows the layout and the detailed structure of the embankment. Representative sections as shown in **Figure 6** will be presented subsequently.

Backfilled High Embankment

The loess strata contain horizontally continuous paleosols, which become the impermeable floor of the phreatic aquifer in the Loess Plateau area. This aquifer is generally a few meters in thickness, and widely distributed, collecting drinking water used by local

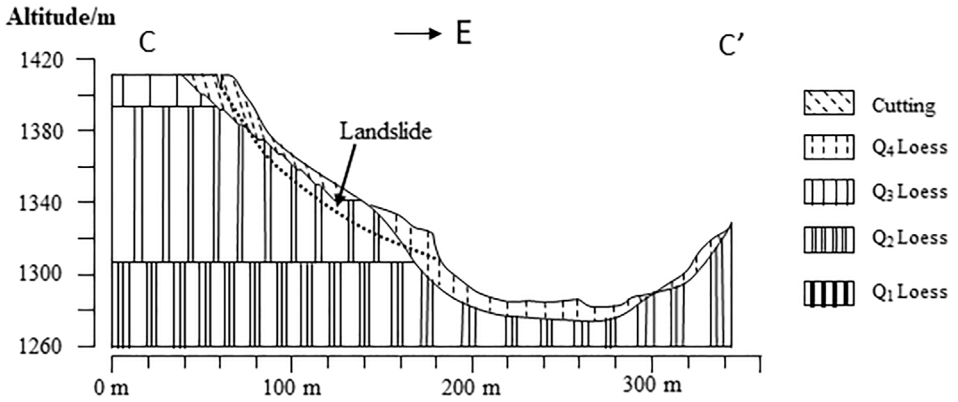

FIGURE 10 | C–C′ profile across the stabilization of unstable slope.

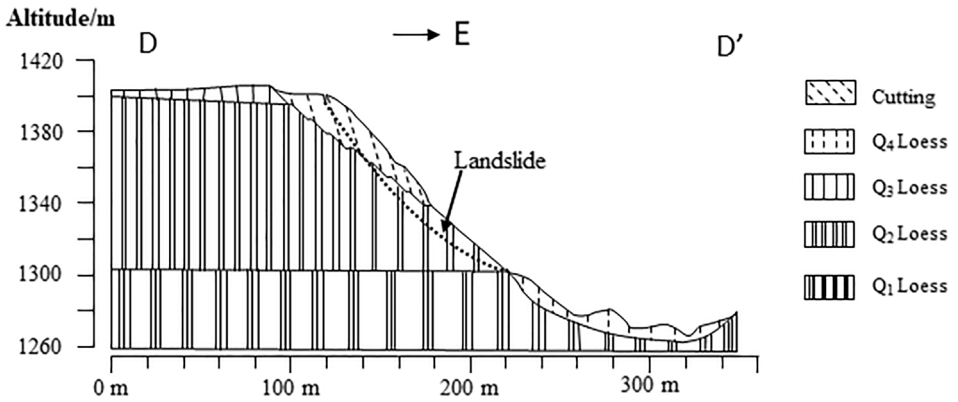

FIGURE 11 | D–D′ profile across the stabilization of unstable slope.

farmers over a long period of history. When the gully is cut down to the paleosol layer, spring water from the aquifer is exposed as four natural springs at the gully bed, which have wetted and eroded the toe of the side slopes and triggered three landslides.

Huohanggou Gully is a typical gully closely related to the disasters in the Loess Plateau: strong flood erosion coexisting with landslide at the head of the gully area. The characteristic features include the following three aspects: First, the upper reaches of the valley are rich in recharge of floodwater. With the acceleration of urbanization, especially the increase in impervious surface area, even under the same rainfall conditions, the flood peak tends to increase year on year. Second, the gullies have a larger longitudinal grade, with high potential for flood erosion and destruction. Third, the ditch slopes are steep and the foot of the slope is soaked and washed by the groundwater overflow, so landslide hazards occur.

From the perspective of traffic engineering only, it may be more economical to use a bridge to cross the gully for an urban road. If this kind of plan is adopted under a philosophy of "out of mind, out of thinking," the gully head will invade into the city, and serious urban problems will be passed on to the following generations.

The local government selected an expensive scheme, a high-fill embankment after a variety of comparisons and demonstrations. This scheme has comprehensive benefits: The backfilled embankment is arranged along the road axis to solve the traffic problem; the high embankment reinforces the steep slopes on both sides of the gully; the drainage system is set up inside the embankment to manage the flood and block the ditch head erosion. This case is not only a road promotion project but also a typical gully stabilization project. **Figures 8** and **9** give representative section profiles, indicating the backfilled area and the original landform.

The major embankment was backfilled by compacted loess soil layer by layer. It was designed according to the standard of urban main road, with a maximum width of 60 m, eight lanes in two directions, opening up a main road for this city. At the same time, the embankment was equipped with an integrated trench, in which rainwater pipes, sewage pipes, and water supply pipes were installed at the same time. As a result, dual purposes have been achieved from the backfilled embankment, gully head stabilization, and the throughput of traffic.

Stabilization of Unstable Slopes

Groundwater is the main factor affecting the landslides in Huohanggou Gully. On the one hand, groundwater has eroded the slope toe for a long time, making the gully slope steeper, and on the other hand, the existence of groundwater greatly reduces the shear strength of the soil, and these results in the reduction of effective normal stress and friction resistance due to the hydrodynamic pressure. In addition, the height difference between the slope top and ditch bed is more than 100 m, and the gradient is 30–70°. The high, steep terrain is the most vulnerable topographic condition for the formation of landslides. Buildings on the slope top have created additional load for a potential landslide. Tillage has also continuously destroyed the natural vegetation, resulting in elevated infiltration of precipitation.

Based on an analysis of the landslides, comprehensive treatment measures were proposed, including slope cutting, surface water interception and drainage, and ditch backfilling. **Figures 10** and **11** give representative profiles of the slope cut and the original landform. Firstly, the buildings on the slope top were relocated. Then, the slope was cut into eight steps, reducing the down-sliding force on the slope body, and stabilized by anchor lattice beam technology. Drainage channels were constructed on each platform to prevent the surface water from infiltrating into the slope body. The large amount of earth cut from the original slope was used for backfilling of sink holes. A concrete retaining wall was cast *in situ* at the gully bottom to ensure the stability of the backfilled slope. A blind ditch was constructed in the backfilled area to discharge water safely and smoothly.

Effectiveness and Uncertainty of GSHP Project

Dongzhiyuan loess tableland is the largest topographic platform in Chinese Loess Plateau, with unique hydrological characteristics. In the semi-arid climate, although the total annual rainfall is insufficient, the rainfall is mainly concentrated in the rainy season. Rainfall first accumulates on the huge, flat top surface to form floods, which are then discharged into the surrounding gully system. The major impact of urbanization is the rapid increase in floods because of imperviousness on surface runoff and infiltration due to urban development. On the one hand, the elevated urban floods result in serious gravity and hydraulic erosion to the gully head area, but on the other hand, the scarce rainwater resources are wasted in this process.

GSHP project emphasizes the extreme importance of geological hazard control in reducing the gully head retreat and beneficial utilization of rainwater resources. It arranges the mitigation measures in the following steps: first stormwater regulation, then gully head stabilization, and finally the soil and water conservation on gully slopes and channels.

As shown in **Figure 5**, the gully heads that invaded into the urban districts with a length of more than 500 m have been backfilled and recreated as Donghu Lake Park. The flood ponds constructed in the Park can store and adjust peak flow before discharging into the Huohanggou Gully. The drainage culvert buried in the backfilled high embankment dissipate the energy of the discharged flood and terminate the process of hydraulic erosion. The stabilization of the unstable slope gets rid of potential gravity erosion in the future. It is believed that GSHP project makes the watershed hydrology of Huohanggou Gully more eco-friendly than before. Direct evidence includes the following facts: The geological disasters that threatened the safety of urban districts in the past 50 years have been eliminated, and more than 90% of soil erosion in this gully has been effectively cut off.

Another advantage of GSHP project is the rainwater harvesting. Flood ponds create waterscape in Donghu Lake Park for leisure and entertainment. The rainwater stored in the rainy season will be transported to support the ecological restoration and improve the soil and water conservation.

As an emerging project, there is still some debate about the basic goals of GSHP project: controlling gully head expansion, eliminating geohazards, reducing soil erosion, or all. In fact, GSHP is a comprehensive project with multiple objectives and large investment. It needs to evaluate the benefits from a long-term perspective through input–output analysis. At least so far, the following technical uncertainties should be noted.

Differential settlement of backfilled loess is an important problem. Settlement cracks in a highly backfilled embankment poses a major threat to the stability of the embankment owing to the potential erosion of groundwater along the cracks, especially in a collapsible loess area. Therefore, strict quality control must be carried out to compact the loess soil as densely as possible during construction period, followed by long-term settlement monitoring. Regular inspection is necessary to check if drainage ditches have been blocked by sediments or by rodents. Emergency backfilling or grouting of the cracks is required if piping is detected.

Disturbed loess becomes more erosive than the natural loess. Rapid surface erosion usually takes place on a loess embankment. Therefore, once the loess embankment is constructed, it is necessary to carry out ecological protection or vegetation restoration of the embankment surfaces by native plants. If a loess slope is partially cut for stabilization of the slope, the freshly exposed surfaces must be covered by vegetation.

The stormwater retention pond, such as that in Donghu Lake Park, is a small reservoir that is located at a gully head that has high potential energy. Close attention must be paid to the defects such as foundation seepage and piping. Also, the risk of secondary disaster must be evaluated based on reservoir engineering principles, such as the extraordinary discharge or even collapse under extreme rainfall conditions, or the liquefaction of foundations during an earthquake.

CONCLUSION

Summarizing the historical document, this paper analyzes the environmental hazards involved in intensive soil erosion in loess tableland area so as to extract the theoretical concepts concerning

the GSHP project. The major conclusions can be drawn as follows.

1) Loess tableland is a specific landform unit with a huge and flat surface, where rainstorms are concentrated to form sudden floods. If flood water is discharged into adjacent gullies without effective control, unpredictable hazards will occur, such as intensive erosion of the gully channel, fast expansion of the gully head, or even landslides.
2) Traditional measurements for soil and water conservation can effectively control sheet erosion on side slopes in a small watershed, but they have less effect on head extension control.
3) Geotechnical stabilization of gully heads or side slopes is required as a priority to control the gully head expansion, so as to establish a base for the subsequent control of sheet erosion.
4) A systematic sewage network needs to be specially designed based on the LID idea, collecting stormwater from the huge surface of the loess tableland, regulating the discharge flow, and transporting the water to places of beneficial usage.

DATA AVAILABILITY STATEMENT

The original contributions presented in the study are included in the article/Supplementary Material, further inquiries can be directed to the corresponding author.

AUTHOR CONTRIBUTIONS

WL: Data curation, Writing—original draft. HZ: Conceptualization, Methodology, Investigation, Writing—review and editing, Funding acquisition, Project administration. JZ: Investigation. AH: Investigation.

ACKNOWLEDGMENTS

All authors are grateful for the financial support provided by the Fundamental Research Funds for the Central Universities of China (No. lzujbky-2017-ct02, lzujbky-2018-it24).

REFERENCES

Bennett, S. J., Alonso, C. V., Prasad, S. N., and Römkens, M. J. M. (2000). Experiments on Headcut Growth and Migration in Concentrated Flows Typical of upland Areas. *Water Resour. Res.* 36, 1911–1922. doi:10.1029/2000WR900067

Bennett, S. J. (1999). Effect of Slope on the Growth and Migration of Headcuts in Rills. *Geomorphology* 30 (3), 273–290. doi:10.1016/S0169-555X(99)00035-5

Chen, S. Y., Xu, J. M., Wang, W. L., Zhao, A. C., and Li, H. Y. (2009). Erosion Features of Head-Cut and its Control Measures on Dongzhiyuan of the Loess Plateau. *Bull. Soil Water Conservation* 29 (4), 37–41. (In Chinese).

De Baets, S., Poesen, J., Reubens, B., Wemans, K., De Baerdemaeker, J., and Muys, B. (2008). Root Tensile Strength and Root Distribution of Typical Mediterranean Plant Species and Their Contribution to Soil Shear Strength. *Plant Soil* 305, 207–226. doi:10.1007/s11104-008-9553-0

Derbyshire, E. (2001). Geological Hazards in Loess Terrain, with Particular Reference to the Loess Regions of china. *Earth Sci. Rev.* 54 (1-3), 231–260. doi:10.1016/s0012-8252(01)00050-2

Dong, Y., Xiong, D., Su, Z., Duan, X., Lu, X., Zhang, S., et al. (2019). The Influences of Mass Failure on the Erosion and Hydraulic Processes of Gully Headcuts Based on an *In Situ* Scouring experiment in Dry-Hot valley of China. *Catena* 176, 14–25. doi:10.1016/j.catena.2019.01.004

Guo, M., Wang, W., Kang, H., and Yang, B. (2018). Changes in Soil Properties and Erodibility of Gully Heads Induced by Vegetation Restoration on the Loess Plateau, China. *J. Arid Land* 10, 712–725. doi:10.1007/s40333-018-0121-z

Huo, A., Peng, J., Cheng, Y., Luo, P., Zhao, Z., and Zheng, C. (2020). Hydrological Analysis of Loess Plateau Highland Control Schemes in Dongzhi Plateau. *Front. Earth Sci.* 8, 528632. doi:10.3389/feart.2020.528632

Huo, A., Yang, L., Luo, P., Cheng, Y., Peng, J., and Nover, D. (2021). Influence of Landfill and Land Use Scenario on Runoff, Evapotranspiration, and Sediment Yield over the Chinese Loess Plateau. *Ecol. Indicators* 121, 107208. doi:10.1016/j.ecolind.2020.107208

Li, Y. R., Zhao, J., and Bin, L. (2018). *Loess and Loess Geohazards in China*. CRC Press.

Li, Y., Shi, W., Aydin, A., Beroya-Eitner, M. A., and Gao, G. (2020). Loess Genesis and Worldwide Distribution. *Earth-Science Rev.* doi:10.1016/j.earscirev.2019.102947

Liu, T. S. (1985). *Loess and the Environment*. Beijing: China Ocean Press. (In Chinese).

Liu, T. S. (1965). *The Deposition of Loess in China*. Beijing: Science Press. (In Chinese).

Shi, N. H. (2001). *Study on Historical Geography of the Loess Plateau*. Zhengzhou: Yellow River Water Conservancy Press. (In Chinese).

Shi, N. H. (1999). *Trifling Notes on Investigation of the Loess Plateau*, 3. Collections of Essays on Chinses Historical Geography, p1–28. (In Chinese)., NO.

Shit, P. K., Pourghasemi, H. R., and Bhunia, G. S. (2020). *Gully Erosion Studies from India and Surrounding Regions*. Springer.

Tsunekawa, A., Liu, G., Yamanaka, N., and Du, S. (2014). *Restoration and Development of the Degraded Loess Plateau*. China: Springer.

US EPA (2000). *Low Impact Development (LID): A Literature Review[R]*. United States Environmental Protection Agency. EPA-841-B-00-005.

Vanmaercke, M., Poesen, J., Van Mele, B., Demuzere, M., Bruynseels, A., Golosov, V., et al. (2016). How Fast Do Gully Headcuts Retreat? *Earth-Science Rev.* 154, 336–355. doi:10.1016/j.earscirev.2016.01.009

Yao, W. B. (2009). *The Evolution Process and Causes of Dong Zhiyuan Landform in Historical Period*. China: Doctoral thesis of Shaanxi Normal University. (In Chines).

Zhang, Z. H. (1980). Loess in China. *GeoJournal* 4, 525–540. https://www.jstor.org/stable/41142973.

Zhang, Z. H. (1983). The Compilation Principle of Landscape Type Map of Chinese Loess Plateau. *Hydrogeology Eng. Geology.* (2), 29–33. (In Chinese).

Zhao, G., Mu, X., Wen, Z., Wang, F., and Gao, P. (2013). Soil Erosion, Conservation, and Eco-Environment Changes in the Loess Plateau of China. *Land Degrad. Develop.* 24, 499–510. doi:10.1002/ldr.2246

Conflict of Interest: The authors declare that the research was conducted in the absence of any commercial or financial relationships that could be construed as a potential conflict of interest.

Publisher's Note: All claims expressed in this article are solely those of the authors and do not necessarily represent those of their affiliated organizations or those of the publisher, the editors, and the reviewers. Any product that may be evaluated in this article, or claim that may be made by its manufacturer, is not guaranteed or endorsed by the publisher.

frontiers | Frontiers in Earth Science

ORIGINAL RESEARCH
published: 04 April 2022
doi: 10.3389/feart.2022.835851

Comparison of Test Methods for Determining the Tensile Strength of Soil and Weak Rocks

Rong Wang[1], Yanrong Li[1], Dongdong Lv[1], Weichao Zhao[1], Chaobo Zhang[2], Hauke Zachert[3], Gerald Eichhoff[3] and Mary Antonette Beroya-Eitner[3]*

[1]Department of Earth Sciences and Engineering, Taiyuan University of Technology, Taiyuan, China, [2]Department of Hydraulics, Taiyuan University of Technology, Taiyuan, China, [3]Department of Civil and Environmental Engineering, Institute of Geotechnics, Technical University of Darmstadt, Darmstadt, Germany

Tensile strength is a key parameter governing tensile cracking and subsequent failure of soil or rock mass. Existing methods for measuring tensile strength are mainly designed for hard materials and come with inherent problems. As such, they are continuously being adapted and improved by the scientific community. In line with this effort, we recently developed two new tensile test methods for application to soil and weak rocks, namely, the inner hole fracturing test (IHFT) and horizontal compression test (HCT). In this study, we compared the performance of these newly developed methods and the three most commonly used approaches for tensile strength determination, namely, the uniaxial direct tensile test (UDTT), Brazilian test (BT) and three-point bending test (TPBT). Results show that IHFT and HCT exhibit distinct advantages over the three conventional methods when testing soil and weak rocks: first, IHFT and HCT can overcome the eccentric force problem that is a main challenge in UDTT and BT, and second, results obtained from these tests are highly reproducible and stable. Between IHFT and HCT, the latter is found more suitable for routine laboratory testing because of simpler and easier procedure, more stable and reliable results and uniform stress distribution within specimens.

Keywords: tensile strength, test methods, test apparatus, soil and weak rock, comparison

OPEN ACCESS

Edited by:
Fanyu Zhang,
Lanzhou University, China

Reviewed by:
Hadi Haeri,
Islamic Azad University System, Iran
Sikandar I. Mulla,
REVA University, India

****Correspondence:***
Yanrong Li
li.dennis@hotmail.com

Specialty section:
This article was submitted to Geohazards and Georisks, a section of the journal Frontiers in Earth Science

Received: *15 December 2021*
Accepted: *21 February 2022*
Published: *04 April 2022*

Citation:
Wang R, Li Y, Lv D, Zhao W, Zhang C, Zachert H, Eichhoff G and Beroya-Eitner MA (2022) Comparison of Test Methods for Determining the Tensile Strength of Soil and Weak Rocks. Front. Earth Sci. 10:835851. doi: 10.3389/feart.2022.835851

1 INTRODUCTION

Tensile strength refers to the capacity of a material to withstand forces applied in tension. It is therefore a key property influencing tensile cracking, which is known to remarkably change both the mechanical and hydraulic properties of geomaterials. The overall strength and bearing capacity of soil containing tension cracks have been found considerably less than those of intact soil (e.g., Morris et al., 1992; Lozada et al., 2015). Moreover, tension cracks can serve as preferred flow paths that can increase the hydraulic conductivity of soil and rocks, as well as increase weathering and erosion rates (Albrecht and Benson 2001). In slopes, failure is usually initiated by the development of cracks at crest area. In rocks and stiff soil like loess, these cracks may propagate vertically downwards up to several meters deep, leading to toppling and cracking–sliding failures (Li 2018). The latter causes an average of 100 deaths per year and considerable economic loss in the Loess Plateau of China (Li et al., 2018).

Compared to their compressive or shear strength, the tensile strength of soil and rocks is generally low. Because of this and the fact that there is no unity in the scientific community as to which testing

method is most suitable or satisfactory (Coviello et al., 2005; Li et al., 2018), the tensile strength of these materials is usually assumed in conventional engineering practice to be equal to zero or insignificant (Kim et al., 2012; Li et al., 2014; Yin and Vanapilli 2018). However, such an assumption may lead to conservative and cost-ineffective design. In line with the global effort towards sustainability, therefore, there is a need to give more attention to understanding the tensile characteristics of soil and rocks and the development of methods for their reliable measurement.

Methods for measuring tensile strength are generally categorised as either direct or indirect. Direct test (e.g., uniaxial direct tensile test, UDTT), where the specimen is loaded to failure in tension, is straightforward and therefore the ideal and theoretically more meaningful method. Results obtained from direct tension test is fundamentally sound because the stress field developed within the specimen depends only on the applied load and boundary conditions, and not on specimen properties (Luong 1990). However, because of the high cost and difficulties in sample preparation and test operation, direct tension method is less used in laboratories (Li et al., 2020). By contrast, specimen preparation, experimental setup and data reduction are much simpler in indirect tensile tests. The majority of indirect tests aim to induce tensile failure by subjecting the specimen to compressive loading. However, stress–strain relationship and equal moduli in tension and compression must be assumed for usability of obtained values (Luong 1990). The complexity of integral stress distributions within the sample is also increased in these tests. Moreover, like direct tests, indirect tests may also be beset with operational problems. For instance, maintaining the applied force along the vertical diametrical plane of the specimen is an outstanding challenge in the Brazilian (BT) test. Problems in both tensile test methods become more serious when dealing with soil and weak rocks (Li et al., 2020).

As emerges clearly from the foregoing, both classes of tensile tests have important advantages and disadvantages, and in recent years, there have been efforts among the scientific community to improve them and address their limitations. As such, new methods have been developed not only for testing soil and rocks (e.g., Tamrakar et al., 2007; Li et al., 2020) but also other geomaterials like concrete (e.g., Sarfarazi et al., 2015; Haeri et al., 2016; Sarfarazi et al., 2018; Liao et al., 2020; Resan et al., 2020), the validity of which was investigated both experimental and numerically (e.g., Blümel 2000; Haeri and Sarfarazi 2016). However, most of these methods, in particular those developed for concrete, require complicated specimen shapes and therefore inapplicable to soil and weak rocks. In light of this, we recently developed new direct and indirect techniques for tensile strength determination of these materials, namely, the Inner Hole Fracturing Test (IHFT) and Horizontal Compression Test (HCT), respectively (Li et al., 2020; Guan et al., 2022). In this study, a detailed comparison of these new methods and the three most commonly used tensile tests, the UDTT, BT, and TPBT (Three Point Bending Test), was conducted. The performance of each method in terms of ease of sample preparation, complexity of test operation, and stability of test results was discussed. We deem that this study can provide engineering practice with valuable insights and guidance where tensile strength determination of soil and weak rocks is a need.

2 METHOD

2.1 Test Material and Sample Preparation

The soil used in the testing programme was a greyish yellow silt that belongs to Malan loess and obtained from Jinzhong, Shanxi Province, China. Block samples were collected from trial pits at a depth of 6 m. To minimize the effect of sample heterogeneity and therefore make the comparison among test methods more meaningful, remoulded soil specimens were used in this study. Specimens were prepared as follows. First, the soil was crushed, passed through a No. 10 sieve (2 mm) and dried at 105 C. Then, water was added to obtain an initial moisture content of 7.5%. Thereafter, the soil was statically compacted using a steel pressure cylinder and a universal testing machine. Compaction was done by one-time pressing because weak layered interfaces can easily form with the traditional layered compaction method and may affect the testing result (Hu et al., 2009). Lastly, the compacted sample was dried to constant mass at 60 C. Each tensile test method was carried out on seven soil specimens, each with the same basic physical properties (**Table 1**).

Artificial gypsum–sand mixtures were additionally tested for performance comparison among IHFT, HCT and UDTT. Specimens were prepared at four different densities (1.57, 1.73, 1.77 and 1.82 g/cm^3) by mixing predetermined proportions of gypsum, sand and water. Five specimens were constituted for each density. Like the remoulded soil samples, gypsum–sand specimens were statically compacted using one-time pressing method and then dried to constant mass.

Special devices and techniques were used to comply with specific specimen size and shape requirements of each test method (**Figure 1**). A rotation grooving device (**Figure 2A**) was used to create a 15 mm-wide section with reduced diameter (40 mm) in the middle portion of the specimen to prepare a dumbbell-shaped sample for UDTT. Cylindrical moulds of appropriate sizes were used to prepare specimens for BT and HCT. A cylindrical mould with a central rounded column fixed at the base was used for the annular specimen for IHFT (**Figure 2B**). Lastly, the rectangular specimen for TPBT was prepared using a soil beam mould (**Figure 2C**).

2.2 Test Apparatus and Setup

2.2.1 Uniaxial Direct Tensile Test

As mentioned earlier, the UDTT, where the specimen is uniaxially loaded to failure in tension, is theoretically the ideal method for tensile strength determination. The test in this study was carried out according to the procedure suggested by the International Society for Rock Mechanics (ISRM 1978). Specimen ends were gripped using a metal holder (**Figure 3A**), leaving a free length of 33 mm in the middle section of the specimen. The holder was tightened with screws, the entire setup was attached to the universal testing machine (**Figure 3B**) and the tension load was applied at a constant displacement rate. This configuration ensured that the fracture occurred in the cross section through the

TABLE 1 | Basic physical parameters of the tested samples.

Soil depth, m	Dry density, g/cm^3	Specific gravity	Plastic limit, %	Liquid limit, %	Particle composition, %		
					<0.005 mm	0.005–0.05 mm	>0.05 mm
6	1.38	2.71	13.81	28.41	11.01	71.45	17.54

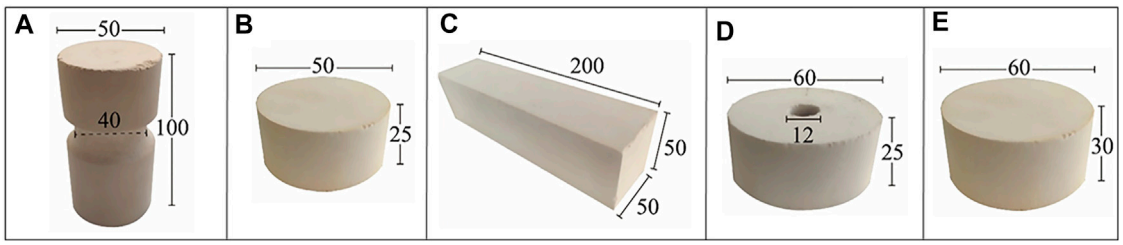

FIGURE 1 | Shapes and size requirements of specimens used in each test method **(A)** dumbbell, **(B)** solid disk, **(C)** cuboid, **(D)** hollow disk, and **(E)** solid disk, for UDTT, BT, TPBT, IHFT, and HCT, respectively. All dimensions are in mm.

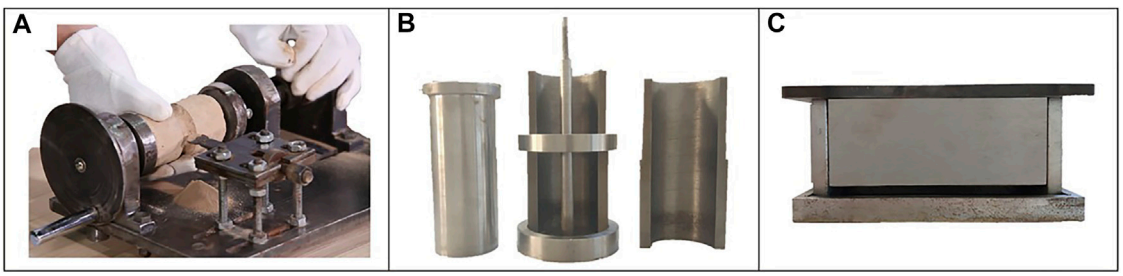

FIGURE 2 | Devices for specimen preparation **(A)** rotation grooving device (Li et al., 2020) **(B)** annular specimen mold (Li et al., 2020), and **(C)** soil beam mold.

middle of the grooved region. The stress state on the central cross-sectional plane of the specimen is assumed truly uniaxial and uniform (**Figure 4A**). Hence, tensile strength (σ_t in kPa) is the ratio between the rupture force and the central cross-sectional area of the specimen; σ_t and average strain (ε_t) can be expressed as follows:

$$\sigma_t = \frac{P}{A} \times 1000 \tag{1}$$

$$\varepsilon_t = \frac{\delta}{H_f} \tag{2}$$

where P is the maximum applied load in N, A is the original cross-sectional area of the crack plane in mm^2, δ is the measured displacement in mm and H_f is the free length of the specimen in mm.

2.2.2 Brazilian Test

Although the validity of BT has been controversial for decades, it remains the most widely used among the indirect tensile tests. BT was conducted in this study using a Chinese standard V-shaped loading strip (GB 2010) attached to the universal testing machine. The disk-shaped specimen was mounted between the upper and lower jaws (**Figure 3C**), ensuring that it does not touch the side walls of the lower jaw, and then subjected to diametrical compression. The compression induces tensile stresses normal to the vertical diameter and these stresses are assumed constant over a region around the centre (**Figure 4B**). The following are further assumed: the material is homogeneous, isotropic and linearly elastic before brittle failure (Mellor and Hawkes 1971) and failure occurs at the centre of the disk where the tensile stress is maximum (Li and Wong 2013). The maximum tensile strain of the specimen can be obtained from the measured compressive deformation and Poisson's ratio. The tensile strength (σ_t in kPa) and corresponding critical tensile strain (ε_t) are expressed as follows (ISRM 1978):

$$\sigma_t = \frac{2P}{\pi dt} \times 1000 \tag{3}$$

$$\varepsilon_t = \delta \cdot \nu \tag{4}$$

where P is the force at failure in N, d and t are the diameter and the thickness of the specimen in mm, respectively, δ is the compressive strain (equal to $\frac{\Delta d}{d}$, where Δd is the measured vertical displacement in mm at failure), and ν is the Poisson's ratio of the specimen. The usual value of Poisson's ratio is 0.25.

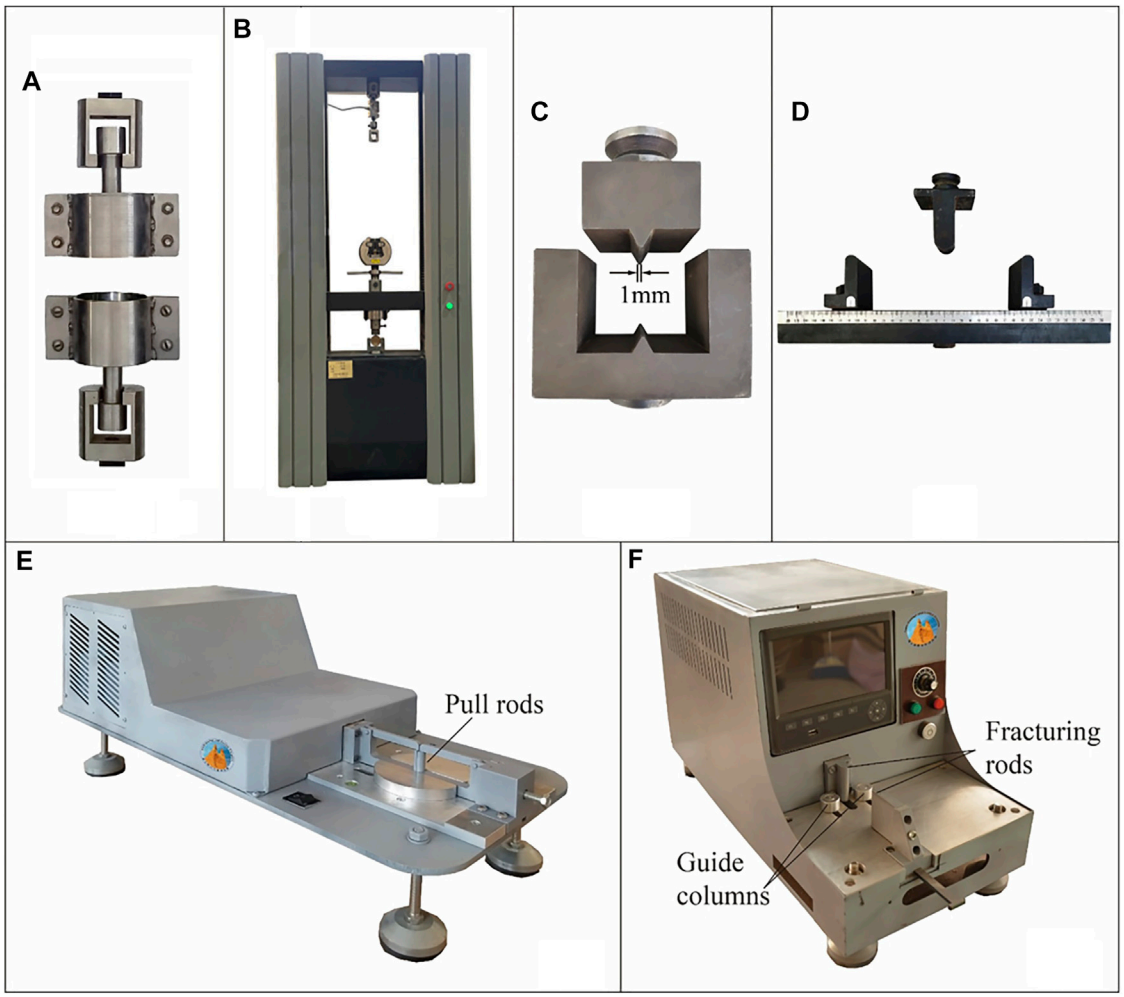

FIGURE 3 | Testing apparatuses and auxiliaries **(A)** metal holder (rigid sleeves) for UDTT, **(B)** universal testing machine, **(C)** narrow linear jaws for BT, **(D)** supporting and loading anvils for TPBT, **(E)** IHFT apparatus (Li et al., 2020), and **(F)** HCT apparatus (Guan et al., 2022).

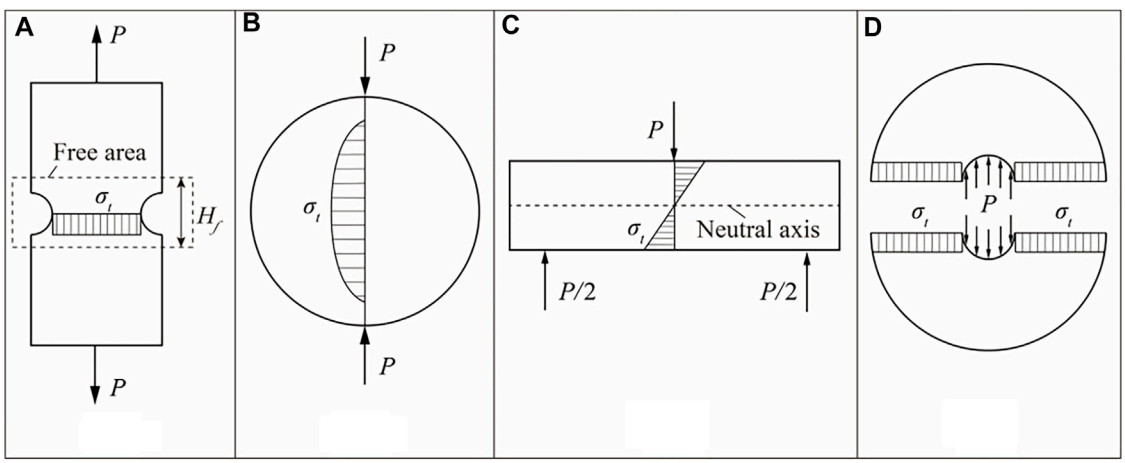

FIGURE 4 | Mechanical and kinematics models for **(A)** UDTT, **(B)** BT and HCT, **(C)** TPBT, and **(D)** IHFT.

2.2.3 Three-Point Bending Test

Flexure or bending tests are commonly used in many branches of civil engineering. In materials engineering, they are used for concrete and hard rock testing (Murray et al., 2019). The two most common flexure tests are the three-point and four-point bending tests. We used the former in this study. TPBT was performed on the universal testing machine using the fixture shown in **Figure 3D**. A rectangular soil beam was placed on two support anvils and a concentrated downward force was applied to failure at midspan through the loading anvil. As the beam is bent, tensile and compressive stresses are respectively produced in the convex (outer) and concave (inner) sides of the specimen (Murray et al., 2019). **Figure 4C** shows the expected stress distribution over the cross section of a beam, where compressive stresses act above the neutral axis whilst tensile stresses act below it. The tensile strength (σ_t in kPa) and the corresponding critical tensile strain (ε_t) at the point of maximum tensile stress (i.e., at the bottom and outermost fibre of the specimen) can be expressed as follows (ASTM 2010):

$$\sigma_t = \frac{3Pl}{2bt^2} \times 1000 \tag{5}$$

$$\varepsilon_t = \frac{6t\delta}{l^2} \tag{6}$$

where P is the force at failure in N, l is the span length or the distance between the two lower supports in mm, b and t are the width and thickness of the specimen in mm, respectively, and δ is the maximum deflection of the center of the beam in mm.

2.2.4 Inner Hole Fracturing Test

IHFT is the direct tensile test we developed as an alternative to UDTT (Li et al., 2020). **Figure 3E** shows the IHFT apparatus, of which the most important feature is the drawbar device consisting of movable and fixed pull seats. Pull seats with a half pull rod are joined to form a full cylindrical rod whose diameter is equal to the inner hole diameter of the annular specimen. The specimen was mounted on the base by letting the full cylindrical rod slip through the specimen inner hole. The left moveable pull seat was driven by a motor during loading to pull the specimen laterally apart through the half pull rod until the specimen fails. Assuming that the central diametrical plane perpendicular to the loading direction is the plane of maximum tension and the state of stress on that plane is purely tensional and generally uniaxial in the loading direction (**Figure 4D**), the tensile strength can be equated to the average tensile stress at failure on the said plane and calculated using the following equation:

$$\sigma_t = \frac{P}{T(D_o - D_i)} \times 1000 \tag{7}$$

where σ_t is the tensile strength in kPa, P is the measured peak tension force in N, D_o and D_i are outer and inner diameters of the specimen in mm, respectively, and T is the specimen thickness in mm.

The validity of the above assumptions and equation was confirmed through computational stress analysis (Li et al., 2020). The average tensile strain is simply obtained using the displacement of the active pull seat divided by the diameter of the specimen's inner hole.

2.2.5 Horizontal Compression Test

HCT, the indirect tensile test we developed is basically a modification of BT that operates in the same principle as BT (Guan et al., 2022). Unlike BT, where the specimen is mounted vertically between loading jaws, the HCT specimen is mounted horizontally. Compression is carried out via the active and stationary fracturing rods in the HCT apparatus (**Figure 3F**). The specimen was seated between these rods, then the active fracturing rod moved towards the stationary fracturing rod upon loading until the specimen failed. The compression test apparatus is equipped with a specimen positioning frame fitted with an operating arm and two guide columns to ensure that the active fracturing rod, stationary fracturing rod and centre axis of the specimen are aligned in the same vertical plane. Hence, the main advantage of HCT is that the direction of the force strictly passes through the centre of the specimen. By comparison, ensuring that the vertical load passes through the centre plane of a vertically placed circular disk specimen in BT is difficult. Both HCT and BT use **Eqs 3**, **4** to calculate the tensile strength and strain, respectively, although the compressive strain in the HCT is derived from the measured horizontal displacement instead of the vertical displacement.

A constant displacement rate of 0.1 mm/min was applied for all the above five types of tests. A high-speed camera (1280 × 1024 pixels) with a filming rate of 1000 frames per second was used to record the entire loading process.

2.3 Numerical Stress Analysis

Finite element analyses were conducted using ABAQUS/Standard 2019 to obtain new insights into the stress distribution of the specimen for each test method and setup. A 2D planar model was utilised with plane stress elements for BT, TPBT, HCT and IHFT. A 2D axisymmetric model was used with axisymmetric stress elements for UDTT. The soil was modelled as a linearly elastic material with the following elastic constants: Young's modulus = 15,000 kPa and Poisson's ratio = 0.23. Loading jaws and supports were modelled as rigid bodies. A friction coefficient of 0.1 was applied between the soil and these jaws and supports. Model data are presented in **Table 2**. For comparability, all simulations were performed in such a way that the maximum amount of tensile stress is approximately 0.025 N/mm^2.

3 RESULTS

3.1 Failure Mode

The typical failure mode for each test is shown in **Figure 5**. Cracking was initiated at peak stress, and failure usually occurred within 0.01 s for UDTT and IHFT. On the other hand, cracking began before the peak stress was reached for the three other tests. Cracks developed in the middle part of the grooved section in UDTT (**Figure 5A**). Cracks in BT initiated in the middle and upper parts of the specimens, then gradually extended to the

TABLE 2 | Model data for the numerical stress analysis.

Test Method	Model Data
UDTT	•Axisymmetric finite element model •Linear Axisymmetric Stress Elements (Type CAX4) •Number of elements Specimen - 2412 Loading jaws - about 918 each •Loading jaws as rigid body, bottom jaw fixed, upper jaw displacement controlled and moved in *Y* direction
BT	•2D finite element model •Linear plane stress elements (Type CPS4) •Number of elements Specimen - 12268 Upper jaw - 306 Bottom jaw - 2177 •Loading jaws as rigid body, bottom jaw fixed, upper jaw displacement controlled and moved in *Y* direction
TPBT	•2D finite element model •Linear Plane Stress Elements (Type CPS4) •Number of elements Specimen - 2500 Loading jaw - about 192 Fixtures - 100 each •Loading jaw and fixtures as rigid body, bottom jaw fixed, upper jaw displacement controlled and moved in *Y* direction
IHFT	•2D finite element model •Linear Plane Stress Elements (Type CPS4) Specimen - 22936 Jaws - about 2820 each •Loading jaws as rigid body, bottom jaw fixed, upper jaw displacement controlled and moved in *X* direction
HCT	•2D finite element model •Linear plane stress elements (Type CPS4) •Number of elements Specimen - 5954 Jaws - about 600 each •Loading jaws as rigid body, bottom jaw fixed, upper jaw displacement controlled and moved in *X* direction

entire central diameter (**Figure 5B**). Cracking in TPBT began in the middle-bottom part of the soil beam and extended upward with increased loading force but failed to penetrate the entire thickness of the specimen even after reaching the peak stress (**Figure 5C**). In IHFT, cracks closer to the inner hole are clearer and wider, indicating that cracking began in this inner region and then propagated outward (**Figure 5D**). Cracks in HCT developed instantaneously along the diameter of the specimen (**Figure 5E**).

3.2 Stress–Strain Curves

Figure 6 presents the typical stress–strain curve for each test method. All curves displayed a similar trend of increased tensile stress with increased strain until the peak stress is reached, after which stress rapidly dropped to zero. The stress–strain relationship is nearly linear in UDTT, BT and HCT. A large strain developed before the occurrence of failure in UDTT, but all curves clearly indicate the brittle nature of the tensile failure. **Figure 7** shows comparison of tensile strengths obtained from each test. TPBT obtained the highest value, followed by UDTT, BT, HCT and IHFT.

The difference in the stress–strain relationship and strength values obtained was a result of the interplay of a number of factors. Basic among these factors is the difference through which tensile failure is achieved (i.e., direct tension, compression and bending moment) and in assumptions each test takes. For instance, although strain is calculated directly in UDTT and IHFT, it has to be estimated from the displacement along the loading direction perpendicular to the tensile direction in the other tests. Hence, some test method particularities may considerably affect the obtained values. For example, the tensile fracture may be shorter than the specimen diameter d in BT due to loading jaw penetration into the specimen, leading to underestimation of tensile stress and critical strain by **Eqs 3**, **4**.

Although the UDTT and IHFT curves generally have the same shape, the peak stress and corresponding strain are greater in the former. A reason for this could be the specimen–fixture connection problem that is commonly encountered in UDTT. Relative vertical slippage between the fixture and the specimen can be observed from comparison of UDTT specimen images at pre-loading and pre-failure. The frictional force generated during the slip may be responsible for the large strength and deformation obtained from the test relative to those from IHFT and other tests (except the significantly larger tensile strength obtained from TPBT). Meanwhile, the stress concentration that evidently

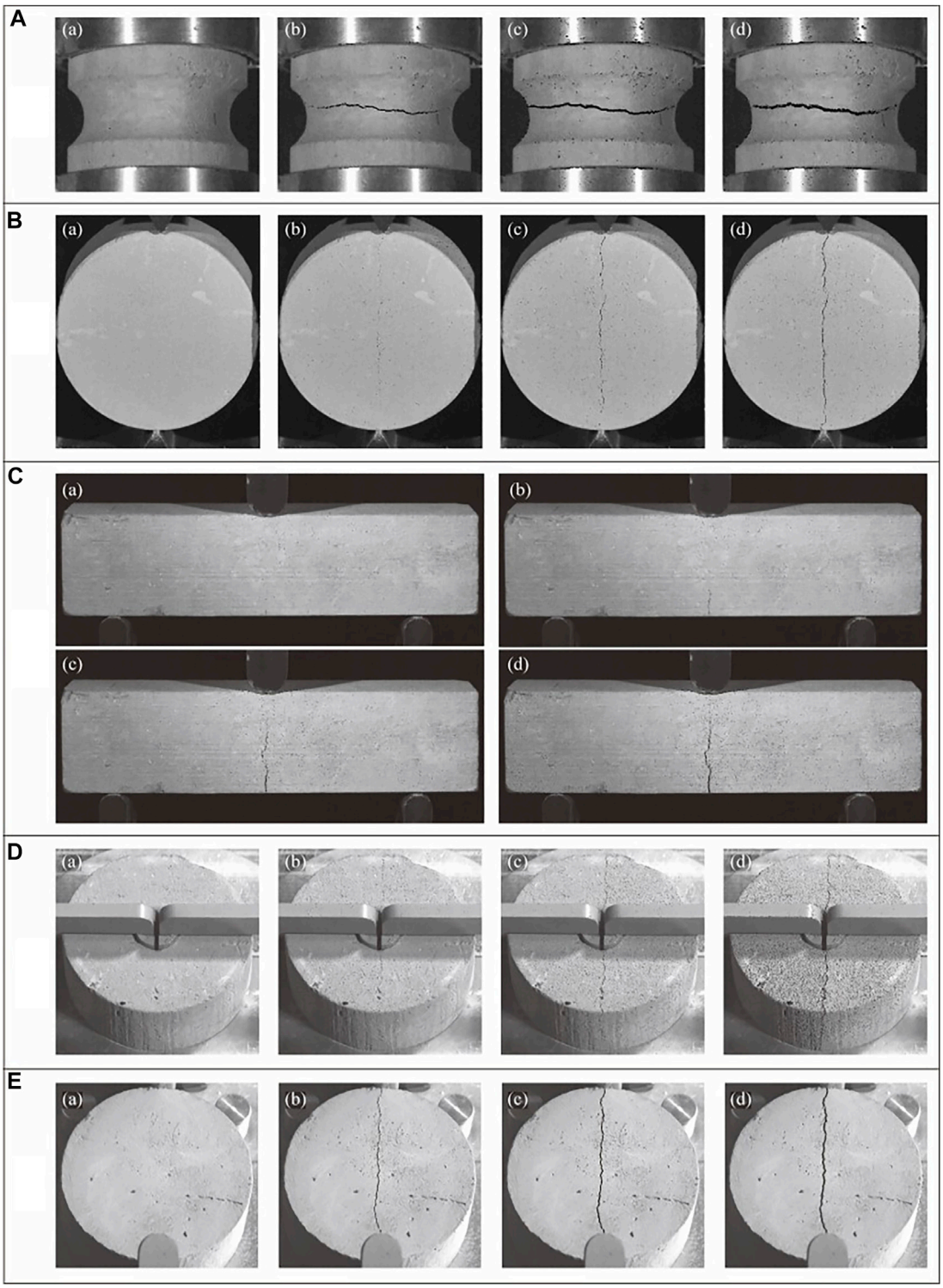

FIGURE 5 | Typical failure modes in different test methods **(A)** UDTT, **(B)** BT, **(C)** TPBT, **(D)** IHFT, and **(E)** HCT.

developed along both sides of the inner ring where the cylindrical loading rod separated likely caused premature cracking in these areas and led to a small tensile strength value in IHFT.

BT and HCT curves generally demonstrate the same shape (**Figure 6**), although the latter curve indicates lower stiffness, which may be due to the compressive deformation in the contact region between the fracturing rods and the specimen. The area

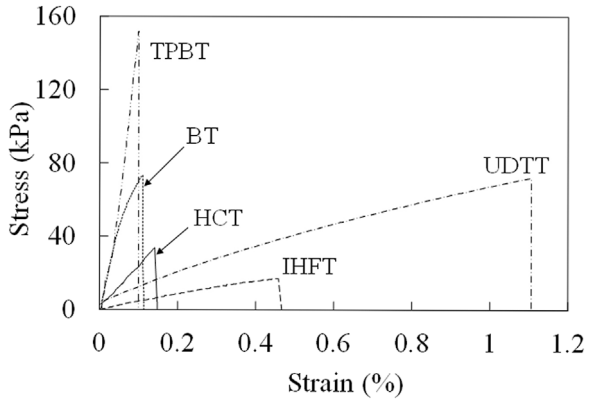

FIGURE 6 | Typical stress–strain curves from different test methods. Data sources for BT, HCT and UDTT are from Guan et al. (2022).

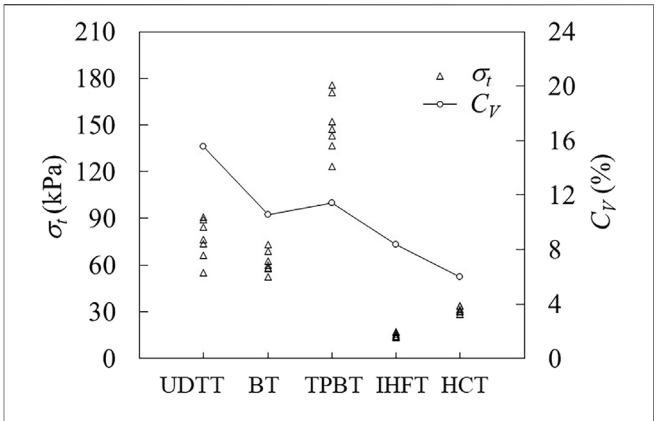

FIGURE 8 | Measured tensile strengths (σ_t) and coefficients of variation (C_V) in different test methods. C_V presents ratio of standard deviation to mean. Data sources for BT, HCT and UDTT are from Guan et al. (2022).

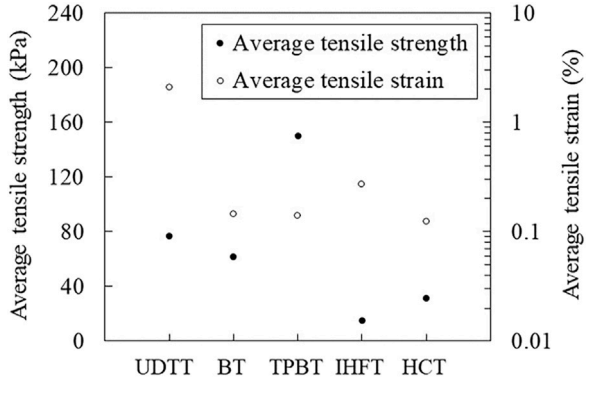

FIGURE 7 | Average tensile strengths and stains obtained from different test methods.

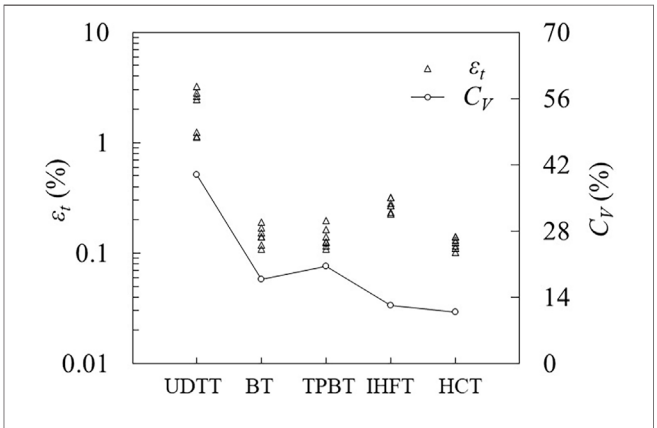

FIGURE 9 | Tensile strains (ε_t) at failure and coefficients of variation (C_V) in different test methods.

under the HCT curve is smaller, indicating that the HCT specimen behaves in a more ductile manner compared with the BT specimen. Enhanced distributed loading caused by the circular jaws in HCT and the frictional force that may have actually developed at the bottom of the HCT specimen despite the smooth design of the base of the apparatus are possible reasons for this ductile behaviour. Friction has been shown to induce ductile behaviour in composite materials (Bacarreza et al., 2017).

TPBT gave remarkably larger tensile strength values (on average greater than 100%) than the other tests. This is consistent with the findings of other workers that point bending tests (i.e. both four-point and three-point bending tests) can overestimate the tensile strength of geomaterials by as much as 100% (Biolzi et al., 2001; Coviello et al., 2005; Mardalizad et al., 2017). Various explanations have been proposed for this overestimation. For instance, Jaeger et al. (2009) attributed it to the tests' assumption of a linear stress–strain relationship throughout the critical cross section of the specimen. This may not be the main reason, however, because the other tests have the same assumption. On the basis of numerical simulation results, Namikawa and Koseki (2007) indicated that overestimation is caused by the redistribution of stresses induced by the strain-softening behaviour on the tensile side. The friction at the loading and support contacts may have also contributed to the large strength values obtained in TPBT. Fricker (1989) considered only the friction on the two fixed supports and showed that this friction can lead to a strength overestimation of approximately 5% for a prismatic square bar alumina specimen subjected to TPBT.

3.3 Evaluation of Test Performance

Tensile strength and critical tensile strain values obtained from each test and corresponding coefficient of variation (C_V) are plotted in **Figures 8**, **9**, respectively. Tests are ordered in terms of increasing C_V of strength as follows: HCT, IHFT, BT, TPBT and UDTT. The same order is observed in terms of increasing C_V of strain. Therefore, the two newly developed tensile test methods obtained the most stable results, with HCT clearly showing superiority over the other investigated methods. The low dispersion of results in HCT and IHFT may be ascribed to

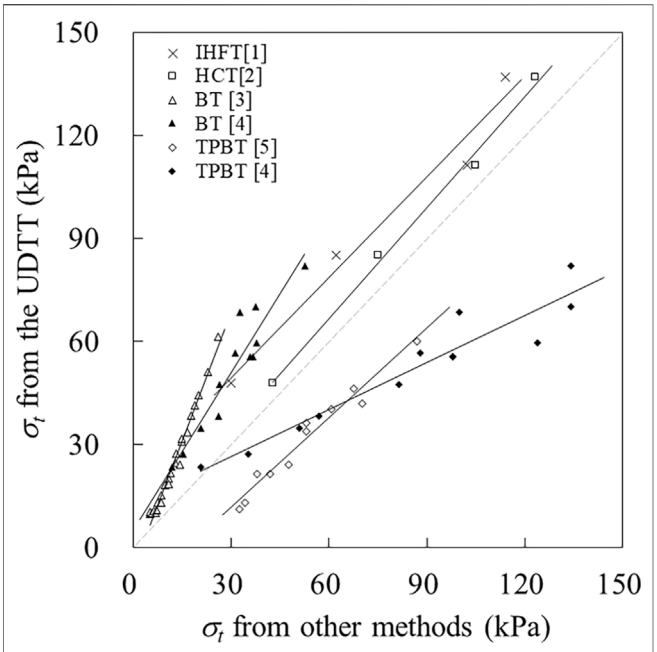

FIGURE 10 | Tensile strengths (σ_t) obtained from the UDTT vs. those obtained from other test methods. Data sources: [1] Li et al., 2020, [2] Guan et al., 2022, [3] Wang 2011, [4] Li et al., 2007, and [5] Zhu 2005.

the simplicity and high reproducibility of sample preparation and test operation. The UDTT results show the most instability and least reproducibility, which is expected given the complicated test setup, the perturbation in the uniaxial stress field introduced by even slight imperfections in specimen grips and the test's low tolerance to sample imperfections/inhomogeneity.

Despite the many limitations of the direct tensile test, it remains the basic test against which other methods are compared due to its theoretical robustness. Thus, we additionally compared the performance of the two newly developed tests against UDTT under a more controlled experiment. We used artificial gypsum–sand specimens to further minimise sample inhomogeneity. **Figure 10** shows the plot of average tensile strength values obtained with IHFT and HCT against those obtained with UDTT for the four dry densities considered, as well as the corresponding fitted lines. Fitted lines for both tests are nearly parallel to the identity line (1:1 line), with that for HCT closer to the said line. Both IHFT and HCT produce relatively lower strength values than UDTT although HCT values are closer to UDTT values. Correlation coefficients are very high for IHFT and HCT at 0.97 and 0.99, respectively.

Data from other workers were included in **Figure 10** to further compare the strength values from the direct tensile test with those obtained from other indirect test methods (Zhu 2005; Li et al., 2007; Wang 2011). All corresponding fitted lines deviate from the identity line to a larger degree than those of the IHFT and HCT, thereby indicating better performance of the proposed methods.

3.4 Stress Distribution

Figure 11 presents the numerical simulation results. Although the tensile stress is maximum in the central grooved section of the specimen in UDTT as expected, the assumption of uniformity (**Figure 4A**) does not hold since stress concentration is observed along the middle margin of the groove. Nonuniformity in the distribution of stresses is also observed along the central diametrical part perpendicular to the loading direction in IHFT. Stress concentration at the periphery of the inner hole is confirmed, explaining the initiation of failure in this area. However, Li et al. (2020) demonstrated that this phenomenon occurs only at the beginning of loading. Stresses become evenly distributed at the failure point (corresponding to the peak load). The average stress at this point can be approximated using **Eq. 7**.

Stress distribution in BT and HCT is generally the same and consistent with assumptions (**Figure 4B**) despite the difference in loading jaw shapes. However, the compressive stress that developed in areas adjacent to jaws is higher in BT than that in HCT. This is likely due to the more concentrated loading in BT, which may explain the observed penetration into the soil of jaws in this method. Stress distribution in TPBT is consistent with expectations (**Figure 4C**).

4 DISCUSSION

Although the test procedure in UDTT is intuitive and the interpretation of results is straightforward, sample preparation and actual test operation are complicated. Thus, the test results demonstrate poor repeatability. A main challenge in UDTT is the gripping of specimen ends for uniform transfer of tension load. Commonly used load transfer methods include adhesive bonding, anchoring/clamping and friction grip, each of which presents particular challenges. Zhang and Lu (2018) noted that stress concentration on specimen interfaces is unavoidable with clamping connection or adhesive bonding. Al-Hussaini and Townsend (1974) indicated that the difference in the physical properties of the adhesive and the specimen causes uneven deformation and eventual failure at the interface of these materials. Friction grip, which utilises the friction between the grip fixture and the specimen to transfer load, was used in this study. In addition, specimens were shaped into a dumbbell to reduce stress concentration on specimen interfaces. However, the simultaneous occurrence of grip slippage and breakage in the theoretical failure surface must have generated eccentric force and affected the results.

Among the indirect tests that have been developed as an alternative to UDTT, BT is the most commonly used due to the simplicity of sample preparation and testing procedure. This is reflected in the C_v of BT-obtained tensile strength values, which is the lowest among the C_v of the three conventional methods. However, cracking may occur away from the theoretical location (i.e. at the centre of the specimen where the maximum tensile stress is supposedly located). For instance, cracking occurred in the upper part of the specimen near the loading jaw in this study. The load at the lower contact point is also high due to the self-weight of the specimen. Lastly, another main challenge in BT is

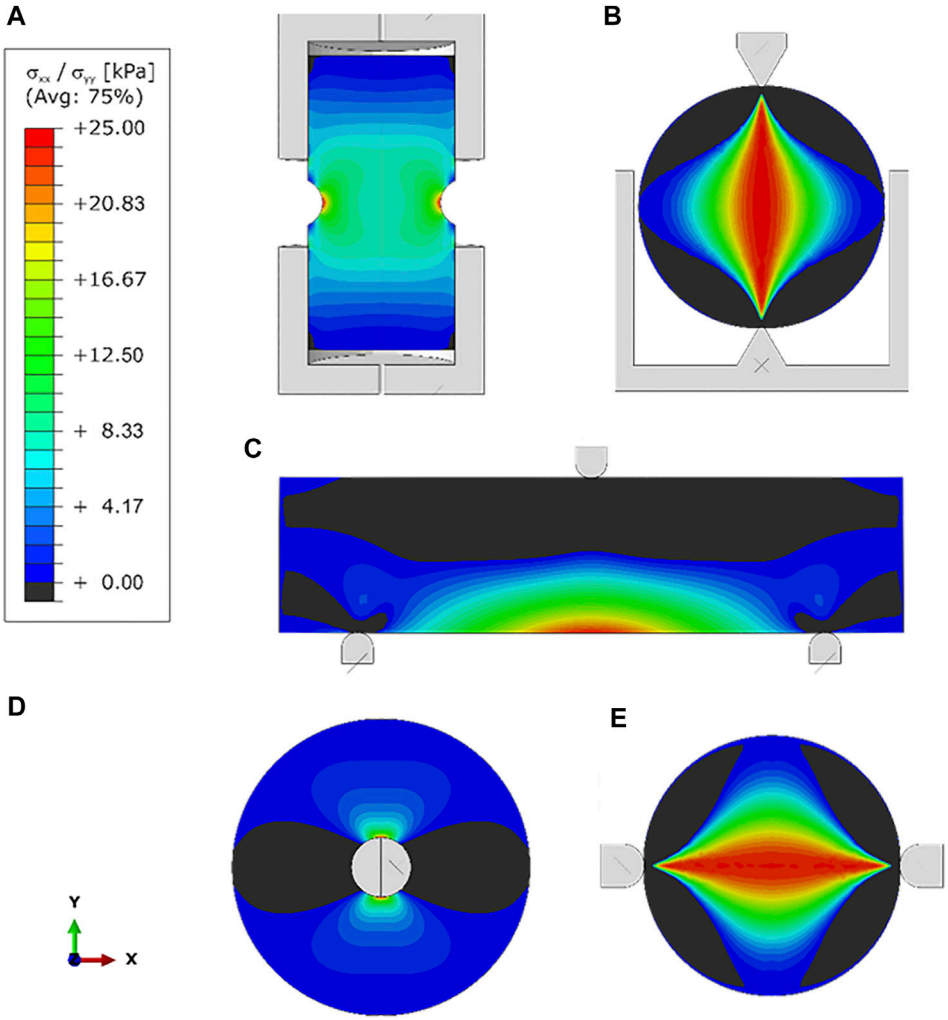

FIGURE 11 | Stress distribution of samples in different test methods **(A)** UDTT, **(B)** BT, **(C)** TPBT, **(D)** IHFT, and **(E)** HCT.

the difficulty in maintaining the applied force along the vertical diametrical plane of the specimen throughout the test and minimising the appearance of eccentric force.

The TPBT device and test procedure are likewise simple and easy to operate. However, this study confirmed the observations of many workers that the test yields unusually high values, and therefore not a recommended method for tensile strength determination.

The two newly developed methods IHFT and HCT present advantages over the three conventional methods in that sample preparation, operation procedure and test setup are even simpler. Hence, the obtained tensile strength and strain values are very stable. The strength values are consistent in trend and strongly correlated with those obtained with UDTT, implying their validity. Moreover, these tensile strength values are lower than those from UDTT, and therefore are on the safer side. The equipment for both IHFT and HCT are designed such that the force is strictly applied through the central diametrical plane to minimise the appearance of eccentric force, which is a main problem in both the UDTT and BT.

However, HCT shows a clear edge over IHFT not only in terms of simplicity of test operation but also stability and reliability of test results. At least for stiff material like the ones tested in this study, crack initiation and propagation occurred instantaneously in HCT. In contrast, tensile stress is greatest near the inner hole in IHFT; as such, cracking starts in this inner region and then propagates outward. Stress distribution in the specimen is more uniform in HCT than that in IHFT. Furthermore, where intact specimen needs to be tested, preparation of the annular specimen for IHFT presents some challenges because a hole must be drilled exactly at the centre of the specimen disk.

5 SUMMARY AND CONCLUSION

Tensile strength is a key parameter determining the stability of geomaterials and the structures. A reliable measurement of tensile

strength is of fundamental importance in geo-engineering. Existing tensile test methods come with inherent problems, which become even more serious when testing soil and weak rocks particularly since most of these methods were designed for hard material (e.g., concrete and steel). A main challenge for instance arises in specimen preparation due to the soft and brittle nature of soil and weak rocks. In light of this, we recently developed two new tensile test methods for use with the said materials. In this study, the performance of these new methods and three of the most commonly used tensile test methods was examined and compared. The results highlighted the distinct advantages of IHFT and HCT over conventional methods (UDTT, BT and TPBT): 1) sample preparation, test setup and operation procedures are easier, more convenient and flexible in IHFT and HCT; 2) IHFT and HCT minimize test errors as they can avoid the eccentric force problem, which is a main challenge in UDTT and BT; and 3) IHFT and HCT can give highly reproducible and stable tensile strength and strain values. Meanwhile, between IHFT and HCT, the latter is found more suitable for routine testing of soil and weak rocks because of the less disturbance it induces in the specimen during preparation, more uniform stress distribution in specimen, and more stable and repeatable results.

DATA AVAILABILITY STATEMENT

The original contributions presented in the study are included in the article/Supplementary Material, further inquiries can be directed to the corresponding author.

AUTHOR CONTRIBUTIONS

YL conceived and designed the project. YL, RW, DL and WZ carried out the laboratory tests. RW, YL, CZ and MB-E jointly interpreted the data. HZ, GE and MB-E. conduced the numerical simulation. RW, YL and MB-E wrote the paper.

FUNDING

This study was supported by the National Natural Science Foundation of China (No. 41877276), Key Program of National Natural Science Foundation of China (No. 41630640), and Major Program of the National Natural Science Foundation of China (No. 41790445).

REFERENCES

Al-Hussaini, M. M., and Townsend, F. C. (1974). Tensile Testing of Soils. International Journal of Rock Mechanics and Mining Sciences & Geomechanics Abstracts. *Int. J. Rock Mech. Min. Sci. Geomech. Abstr.* 11, 199. doi:10.1016/0148-9062(74)91141-3

Albrecht, B. A., and Benson, C. H. (2001). Effect of Desiccation on Compacted Natural Clays. *J. Geotech. Geoenviron. Eng.* 127, 67–75. doi:10.1061/(ASCE)1090-0241

ASTM D790-10 (2010). *Standard Test Methods for Flexural Properties of Unreinforced and Reinforced Plastics and Electrical Insulating Materials*. West Conshohocken, PA: United States. 19428-2959. doi:10.1520/D0790-10

Bacarreza, O., Maidl, S., Robinson, P., and Shaffer, M. S. P. (2017). "Exploring the Use of Friction to Introduce Ductility in Composites," in *Proceedings of the 21st International Conference on Composite Materials* (Xi'an), 20–25.

Biolzi, L., Cattaneo, S., and Rosati, G. (2001). Flexural/Tensile Strength Ratio in Rock-like Materials. *Rock Mech. Rock Eng.* 34, 217–233. doi:10.1007/s006030170010

Blümel, M. (2000). "Improved Procedures for Laboratory Testing," in *Proceedings Of the EUROCK 2000 Symposium* (Essen, Germany: Verlag Glückauf Press), 573–578.

Coviello, A., Lagioia, R., and Nova, R. (2005). On the Measurement of the Tensile Strength of Soft Rocks. *Rock Mech. Rock Engng.* 38, 251–273. doi:10.1007/s00603-005-0054-7

Fricker, D. C. (1989). *Contact Friction Effects in Flexural Strength Tests of Alumina for Orthopaedic Implants*. Manchester: Manchester University Press.

GB, T. (2010). *Methods for Determining the Physical and Mechanical Properties of Coal and Rock-Part 10: Methods for Determining Tensile Strength of Coal and Rock*. Beijing: Standards Press of China, 2356110.

Guan, F. F., Li, Y. R., Gao, G. H., Beroya-Eitner, M. A., and Zachert, H. (2022). Horizontal Compression Test: a Proposed New Method for Indirect Determination of Tensile Strength of Stiff Soils and Soft Rocks. *Front. Earth Sci.* doi:10.3389/feart.2022.839073

Haeri, H., Sarfarazi, V., and Hedayat, A. (2016). Suggesting a New Testing Device for Determination of Tensile Strength of concrete. *Struct. Eng. Mech.* 60, 939–952. doi:10.12989/SEM.2016.60.6.939

Haeri, H., and Sarfarazi, V. (2016). Numerical Simulation of Tensile Failure of concrete Using Particle Flow Code (PFC). *Comput. Concrete* 18, 39–51. doi:10.12989/CAC.2016.18.1.039

Hsieh, P. A., Cook, N. G. W., and Zimmerman, R. W. (2009). Fundamentals of Rock Mechanics. *Geofluids* 9, 251–252. doi:10.1111/j.1468-8123.2009.00251.x

Hu, H. J., Jiang, M. J., Zhao, T., Peng, J. B., and Li, H. (2009). Effects of Specimen-Preparing Methods on Tensile Strength of Remolded loess. *Rock Soil Mech.* 30 (Suppl. 2), 196–199.

ISRM (1978). Suggested Methods for Determining Tensile Strength of Rock Materials. *Int. J. Rock Mech. Min. Sci. Geomech. Abstr.* 15, 99–103. doi:10.1016/0148-9062(78)90003-7

Kim, T.-H., Kim, T.-H., Kang, G.-C., and Ge, L. (2012). Factors Influencing Crack-Induced Tensile Strength of Compacted Soil. *J. Mater. Civ. Eng.* 24, 315–320. doi:10.1061/%28ASCE%29MT.1943-5533.0000380

Li, D., and Wong, L. N. Y. (2013). The Brazilian Disc Test for Rock Mechanics Applications: Review and New Insights. *Rock Mech. Rock Eng.* 46, 269–287. doi:10.1007/s00603-012-0257-7

Li, J., Tang, C., WangPei, D. X., Pei, X., and Shi, B. (2014). Effect of Discrete Fibre Reinforcement on Soil Tensile Strength. *J. Rock Mech. Geotechnical Eng.* 6, 133–137. doi:10.1016/j.jrmge.2014.01.003

Li, J. Y., He, C. R., and Tang, H. (2007). The Comparative Study on the Tensile Strength Test of Soft clay. *Subgrade Eng.* 2, 104–105. doi:10.3969/j.issn.1003-8825.2007.02.045

Li, Y. (2018). A Review of Shear and Tensile Strengths of the Malan Loess in China. *Eng. Geology.* 236, 4–10. doi:10.1016/j.enggeo.2017.02.023

Li, Y., Guan, F., Su, H., Aydin, A., Beroya-Eitner, M. A., and Zachert, H. (2020). A New Direct Tension Test Method for Soils and Soft Rocks. *Geotech. Test. J.* 43, 20190308. doi:10.1520/GTJ20190308

Li, Y., Mao, J., Xiang, X., and Mo, P. (2018). Factors Influencing Development of Cracking-Sliding Failures of Loess across the Eastern Huangtu Plateau of China. *Nat. Hazards Earth Syst. Sci.* 18, 1223–1231. doi:10.5194/nhess-18-1223-2018

Liao, W.-C., Chen, P.-S., Hung, C.-W., and Wagh, S. K. (2020). An Innovative Test Method for Tensile Strength of Concrete by Applying the Strut-And-Tie Methodology. *Materials* 13, 2776. doi:10.3390/ma13122776

Lozada, C., Caicedo, B., and Thorel, L. (2015). Effects of Cracks and Desiccation on the Bearing Capacity of Soil Deposits. *Géotechnique Lett.* 5, 112–117. doi:10.1680/jgele.15.00021

Mardalizad, A., Manes, A., and Giglio, M. (2017). The Numerical Modelling of a Middle Strength Rock Material under Flexural Test by Finite Element Method-Coupled To-SPH. *Proced. Struct. Integrity* 3, 395–401. doi:10.1016/j.prostr.2017.04.050

Mellor, M., and Hawkes, I. (1971). Measurement of Tensile Strength by Diametral Compression of Discs and Annuli. *Eng. Geology.* 5, 173–225. doi:10.1016/0013-7952(71)90001-9

Minh Phong Luong, M. P. (1990). Tensile and Shear Strengths of concrete and Rock. *Eng. Fracture Mech.* 35, 127–135. doi:10.1016/0013-7944(90)90190-R

Morris, P. H., Graham, J., and Williams, D. J. (1992). Cracking in Drying Soils. *Can. Geotech. J.* 29, 263–277. doi:10.1139/t92-030

Murray, I., Tarantino, A., and Francescon, F. (2019). A Tensile Strength Apparatus with the Facility to Monitor Negative Pore-Water Pressure. *Geotech. Test. J.* 42, 20170354. doi:10.1520/GTJ20170354

Namikawa, T., and Koseki, J. (2007). Evaluation of Tensile Strength of Cement-Treated Sand Based on Several Types of Laboratory Tests. *Soils and Foundations* 47, 657–674. doi:10.3208/sandf.47.657

Resan, S. a. F., Chassib, S. M., Zemam, S. K., and Madhi, M. J. (2020). New Approach of concrete Tensile Strength Test. *Case Stud. Construction Mater.* 12, e00347. doi:10.1016/j.cscm.2020.e00347

Sarfarazi, V., Faridi, H. R., Haeri, H., and Schubert, W. (2015). A New Approach for Measurement of Anisotropic Tensile Strength of concrete. *Adv. concrete construction* 3, 269–282. doi:10.12989/acc.2015.3.4.269

Sarfarazi, V., Haeri, H., Ebneabbasi, P., Bagher Shemirani, A., and Hedayat, A. (2018). Determination of Tensile Strength of concrete Using a Novel Apparatus. *Construction Building Mater.* 166, 817–832. doi:10.1016/j.conbuildmat.2018.01.157

Tamrakar, S. b., Mitachi, T., and Toyosawa, Y. (2007). Measurement of Soil Tensile Strength and Factors Affecting its Measurements. *Soils and Foundations* 47 (5), 911–918. doi:10.3208/sandf.47.911

Wang, H. M. (2011). *Experimental Research on Tensile Behaviors of Cohesive Soil*. Nanjing, China: Nanjing University. [master's thesis].

Yin, P., and Vanapalli, S. K. (2018). Model for Predicting Tensile Strength of Unsaturated Cohesionless Soils. *Can. Geotech. J.* 55, 1313–1333. doi:10.1139/cgj-2017-0376

Zhang, S., and Lu, Y. (2018). Experimental and Numerical Investigation on the Dumbbell-Shaped Specimen of concrete-like Materials under Tension. *Lat. Am. J. Solids Struct.* 15, e93. doi:10.1590/1679-78254632

Zhu, A. L. (2005). *Tensile Test and Numerical Analysis on Cohesive clay*. Chengdu, China: Sichuan University. [master's thesis].

Conflict of Interest: The authors declare that the research was conducted in the absence of any commercial or financial relationships that could be construed as a potential conflict of interest.

Publisher's Note: All claims expressed in this article are solely those of the authors and do not necessarily represent those of their affiliated organizations, or those of the publisher, the editors and the reviewers. Any product that may be evaluated in this article, or claim that may be made by its manufacturer, is not guaranteed or endorsed by the publisher.

frontiers | Frontiers in Earth Science

METHODS
published: 05 April 2022
doi: 10.3389/feart.2022.884500

Deformation Feature Extraction for GNSS Landslide Monitoring Series Based on Robust Adaptive Sliding-Window Algorithm

Guanwen Huang, Duo Wang, Yuan Du, Qin Zhang, Zhengwei Bai and Chun Wang*

College of Geology Engineering and Geomatics, Chang'an University, Xi'an, China

Global navigation satellite system technology has been widely used for high-precision, real-time monitoring of landslides. To improve forecasts and early warnings, the true deformation features must be extracted from the global navigation satellite system monitoring series. However, as the deformation rate changes at different creep stages, the relationship between noise and true deformation may also change, making it difficult to accurately describe the deformation. In this study, an adaptive sliding window algorithm is proposed to account for this relationship change. First, the window was defined with an equal window width and step length, which improved the efficiency of feature extraction. Second, the median and normalized interquartile ranges were used to estimate the window samples and obtain a continuous and reliable series. Finally, the window sample breakdown point was defined to adjust the window parameter. These steps were repeated for the adjusted window to achieve adaptive processing of the monitoring series. The results based on both simulated and real landslide monitoring series demonstrated that the proposed method can provide adaptive, robust, and reliable deformation information for landslide warnings. The adaptive sliding window method also successfully assisted in the early warning of a loess landslide in Heifangtai, Gansu province, northwest of the Chinese Loess Plateau, indicating its practical application potential.

Keywords: adaptive sliding window, breakdown point, landslide monitoring, deformation feature extraction, time series, GNSS

OPEN ACCESS

Edited by:
Yueren Xu,
Institute of Earthquake Forecasting, China

Reviewed by:
Haojun Li,
Tongji University, China
Guoqiang Zhao,
Institute of Earthquake Forecasting, China

****Correspondence:***
Duo Wang
2021026014@chd.edu.cn

Specialty section:
This article was submitted to Geohazards and Georisks, a section of the journal Frontiers in Earth Science

Received: *26 February 2022*
Accepted: *11 March 2022*
Published: *05 April 2022*

Citation:
Huang G, Wang D, Du Y, Zhang Q, Bai Z and Wang C (2022) Deformation Feature Extraction for GNSS Landslide Monitoring Series Based on Robust Adaptive Sliding-Window Algorithm. Front. Earth Sci. 10:884500. doi: 10.3389/feart.2022.884500

1 INTRODUCTION

Many countries worldwide suffer from recurring geological disasters, particularly landslides, and the loss of life and property caused by landslides has increased each year (Froude and Petley, 2018). Because of the complexity of landslides, predicting the failure time of a landslide remains challenging. Previous studies showed that most landslides conform to a three-stage creep curve from the initial to final failures (Tavenas and Leroueil, 1981; Dok et al., 2011). According to the creep curve interpretation, the first stage is primary creep, in which the strain rate decreases logarithmically, followed by steady-state creep with a constant strain rate and accelerating creep with an increasing creep rate that leads to rupture (**Figure 1**). For a three-stage creep curve, time-to-failure predictions can be made using existing methods (Xu et al., 2011; Intrieri et al., 2019). The global navigation satellite system (GNSS), which captures global, continuous, and high-precision geospatial data, has

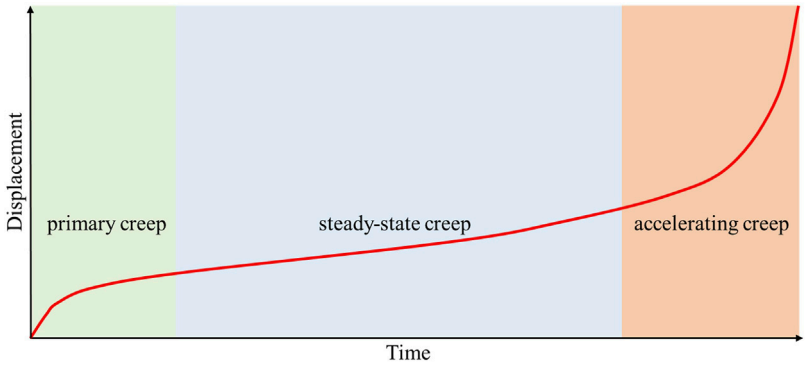

FIGURE 1 | Conventional three-state interpretation of landslide creep behavior, Shaded areas of different colors represent different stages.

been widely used for monitoring landslides and obtaining creep curves (Benoit et al., 2014; Du et al., 2020). However, GNSS positioning technology is often affected by the external environment, multipath effect, atmospheric delay, receiver noise, and other hardware influences, causing the monitoring series to create noise (Amiri-Simkooei, 2008; Li et al., 2016; Han et al., 2018).

Various methods have been applied to preprocess landslide monitoring series to reduce the effect of noise and improve prediction accuracy. Kalman filtering is a method used to describe the dynamic deformation process of a monitoring body by calculating the optimal value of the state vector. However, the GNSS monitoring series includes colored noise, which cannot satisfy the white-noise assumption of the Kalman filter (Ince and Sahin, 2000; Li and Kuhlmann, 2013; Zhao et al., 2016). The wavelet analysis method decomposes the different frequency components of the signal and extracts useful deformation information from the series. However, wavelet analysis is used for data series of equal intervals and cannot be directly used for data of non-equal intervals. Additionally, the preprocessing methods depend on the experience of those implementing the method (Yang et al., 2012). The sliding window method applies a finite time window to select the dataset for preprocessing. The window is then incrementally moved forward in time, resulting in estimates for each window (Song and Lee, 2015; Banerjee and Bansal, 2017). Based on sliding-window methods, various creep curve features, such as deformation speed, tangential angle, and acceleration, are widely used for deformation feature extraction in GNSS landslide monitoring series because of the need for a certain time interval.

The conventional sliding-window method with fixed coefficients is typically applied to extract the signal if the mean and covariance of the dataset do not change as the window moves. Inevitably, as the landslide evolves, the true deformation increases and gradually occupies the main component of the monitoring results, and the mean and covariance of the dataset constantly change. Thus, window estimation can lead to errors and reduce the real-time performance of monitoring. Therefore, as the true deformation changes, preprocessing strategies should be considered. Ren et al. evaluated the moving average method only for a slow deformation monitoring sequence (Ren and Xu, 2018). Zhu et al. proposed a self-adaptive data-acquisition method to dynamically adjust the output rate of the sensor to reduce the power consumption of the sensor node (Zhu et al., 2017). However, the crucial threshold delta of the method must be set manually and the processing window kept fixed. In this study, we present a new technology for adaptive adjustment of sliding-window coefficients based on the window sample breakdown point. This method may capture the entire displacement feature of a landslide failure in a timely manner and assist in further early warning.

We first describe the sliding-window technology; the concept of the sample breakdown point is then introduced to derive the technical process of the method. Next, the simulation experiment results are presented to demonstrate the performance of the sliding-window approach for different outliers and deformation signals. The efficiency of this approach was validated using a GNSS monitoring series, collected during displacement monitoring of the Heifangtai landslide.

2 MATERIALS AND METHODS

2.1 Fundamental Sliding-Window Parameters

The sliding window uses a time window to select the data for processing and steps forward in regular increments to obtain a series of estimates (Foster et al., 2005). Three parameters are required to define a window: 1) position of the window, 2) width of the window, and 3) the step by which the window moves forward. For a GNSS monitoring series with duration of T, the window position is defined as t, which is the central time of the window. In this case, the processing result is closest to the real deformation in that window.

The "width" of the window can be specified by the time width (W), which determines the efficiency of sample estimation in the window. A wider selected window contains more observations and gives a more reliable estimation than a narrower window. In contrast, because the position is the center of the window,

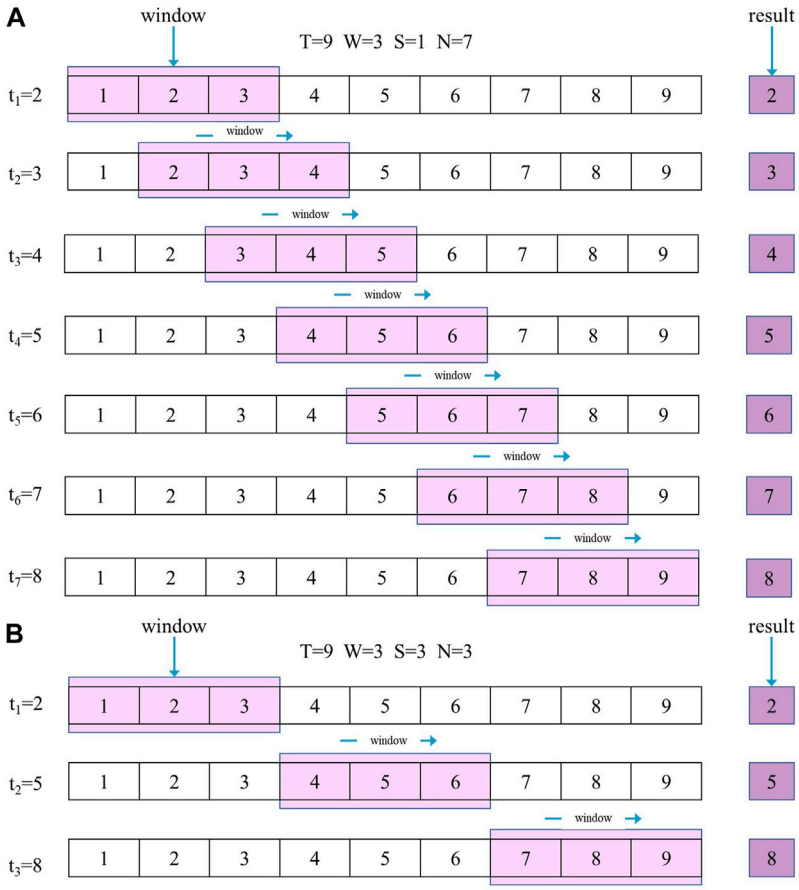

FIGURE 2 | Schematic diagram of a sliding-window process. The position of the window is the center time. **(A)** Step option 1: step by step; **(B)** Step option 2: equal with the width.

increasing the width causes a lag (τ_t) in the window position (window position later than real data time):

$$\tau_t = \frac{W}{2}, \tag{1}$$

The "step" by which the window moves forward can be specified by the time step (***S***), which determines when the window is obtained. It is possible to use either of the options: step-by-step or equal to the width. In the former option, the window is moved forward in steps, generating a full solution for each step. Since each epoch participates in the estimation of multiple windows, the option may lead to correlations between the different estimates (**Figure 2A**). In the equal option, the window moves forward in multiple steps and the estimated values are independent of each other (**Figure 2B**). The final number of estimates (N) was determined using **Eq. 2**:

$$N = floor\left(\frac{T - W}{S}\right) + 1, \tag{2}$$

where "floor" indicates that the resultant is rounded to the nearest integer. According to the equation, an increase in the step length reduces the final number of estimates, which can be used to extract more useful features from the original series. In this study, we focused on the second option, which avoids correlation and provides a regularly spaced feature series for pre-warning analysis of landslides.

2.2 Window Sample Estimation

The window sample was estimated after defining the window. The sliding window method typically uses the sample mean and standard deviation as estimators. The method can obtain an optimal estimation result only when the window sample shows a normal distribution. For real monitoring data, a window sample affected by outliers and deformation may not meet this condition. Using the median and normalized interquartile range (NIQR) is another robust method for estimating the average and standard deviation of the window sample. This method is suitable for estimating symmetric and skewed distributions (Buch, 2014). If $\boldsymbol{X}$ is a sample with values $\boldsymbol{x_1}, \boldsymbol{x_2}, \ldots, \boldsymbol{x_n}$, then the median is calculated as shown in **Eq. 3**.

$$med(X) = \begin{cases} x_{(i+1)} \, (n = 2i + 1) \\ \left(x_{(i)} + x_{(i+1)}\right)/2 \, (n = 2i) \end{cases} \tag{3}$$

,

where i is the sorted value of the dataset. NIQR can be defined as shown in **Eq. 4** (Fried and Gather, 2007).

$$NIQR = 0.7413 \times (Q_3 - Q_1) \tag{4}$$

where Q_1 (first quartile) represents the value at 25% of the window and Q_3 (third quartile) is at 75% of the window (Ismail et al., 2013). The normalization factor "0.7413" is based on the fact that, for a normal distribution, the interquartile range is approximately 1.349-fold the standard deviation.

2.3 Sample Breakdown Point

As the deformation rate increased, the proportion of outliers also increased, and the data obeyed a severely skewed distribution, whereas the NIQR method could not overcome the influence of outliers. To measure the robustness of an estimator in the presence of outliers in the data (Schmitt et al., 2014), Donoho and Huber introduced a finite sample breakdown point, which is the largest fraction of contaminated data that the method can withstand before providing estimates that are arbitrarily far off (Donoho and Huber, 1983).

If $X = (x_1, \ldots, x_n)$ is a sample of size n, the sample can be corrupted by replacing an arbitrary subset of the sample of size m with arbitrary values $y_1, \ldots, y_m$. The fraction of "bad" values in the corrupted samples X' is $\varepsilon = m/n$. This method of sample corruption is known as ε- replacement (Peter and Elvezio, 2009).

Now, let $T = (T_n)_{n=1,2,\ldots}$ be an estimator with values in Euclidean space, and let $T(X)$ be the value at sample X. The replacement breakdown point of T at X is ε^*, which is the smallest value of ε for which the estimator, when applied to the ε-corrupted sample X', can take values arbitrarily far from $T(X)$. We first define the maximum bias that can be caused by ε- corruption as

$$b(\varepsilon; X, T) = sup\left|T(X') - T(X)\right| \tag{5}$$

where "sup" means supremum, which is taken over the set of all ε-corrupted samples X'. We then define the breakdown point as **Eq. 6**, where "inf" means infimum.

$$\varepsilon^*(X, T) = inf\{\varepsilon | b(\varepsilon; X, T) = \infty\}. \tag{6}$$

For example, consider the sample mean estimator:

$$AV(X) = \frac{1}{n}\sum_{i=1}^{n} x_n \tag{7}$$

When x_i is replaced with a number close to infinity, the $AV(X)$ value becomes meaningless for the mean estimator. Therefore, this estimate has a breakdown point $\varepsilon^* = \frac{1}{n}$.

Because the window sample may reach the breakdown point, we defined a sample breakdown point for the window. In **Eq. 5**, this method uses all-window sample NIQR estimators as $T(X')$ to calculate bias rather than using arbitrary samples. $T(X)$ is the estimator of the window sample without outliers. Correspondingly, the window sample breakdown point is defined as

$$\varepsilon^*(X, T) = inf\{\varepsilon | b(\varepsilon; X, T) \geq h_0\} \tag{8}$$

For window sample estimation, h_0 is three- or four-fold of the standard deviation of $T(X)$.

2.4 Adaptive Sliding-Window Method Process

The window that reaches the breakdown point can be determined based on the definition of the sample breakdown point. In the window sample estimation problem, outliers are arranged in an increasing pattern over time, which may be much more effective at disturbing an estimator than outliers randomly placed among the data. By arranging outliers based on time, the proportion of outliers can be reduced by adjusting the window coefficients to avoid disturbing the estimators and ensure that the covariance of the dataset does not change as the window moves.

Thus, we can obtain the processing flow of the adaptive sliding window method, which includes the following steps.

- Step 1: The monitoring series was segmented with equal window widths and step lengths to divide the series into mutually independent windows.
- Step 2: For each window, the median and NIQR were estimated as the average and standard deviation of the window sample, respectively.
- Step 3: According to the estimation results, several windows with no obvious outliers were selected to calculate the average value as $T(X)$ and three-fold the standard deviation as h_0.
- Step 4: All window sample NIQR estimates were used as $T(X')$ to calculate bias, where the first window was greater than h_0 the breakdown-point window.
- Step 5: The monitoring series after the breakdown point window was segmented with a shorter window width and step length.
- Step 6: Steps two to five were repeated for adaptive processing of the monitoring series and to extract reliable deformation features.

3 SIMULATION EXPERIMENT

Window sample estimation analysis was performed in the simulation by generating outliers and deformation signals. The following situations were simulated:

Situation 1: A section of the actual GNSS monitoring dataset that was collected for 24 h at 5 min intervals and had no outliers was selected as the original signal. The window sample only contained random noise; therefore, the true deformation was the mean of the window samples (143.0 mm) (**Figure 3A**).

Situation 2: Based on the original signal, three outliers (200, 180, and 300) were added at times of 08:20:00, 14:50:00, and 20:35:00. Because the outliers did not affect the true deformation of the window, it remained unchanged at 143.0 mm (**Figure 4A**).

Situation 3: Simulated deformation was added to the original signal. Referring to the existing landslide failure data, the initial rate and acceleration of deformation were set at 2.4 mm/h and

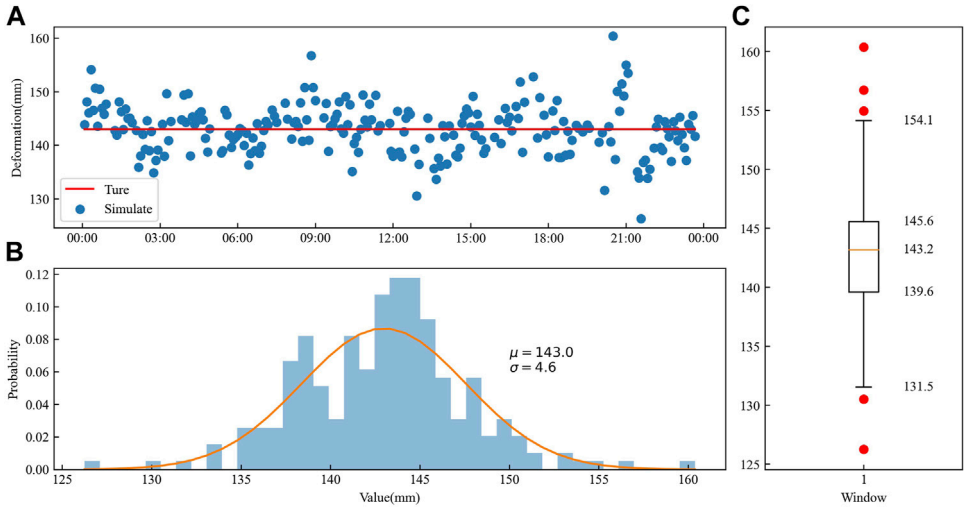

FIGURE 3 | Situation one simulation signal and estimation result. **(A)** Simulated deformation scatters plot and true value; **(B)** Frequency distribution histogram and probability distribution curve; **(C)** Boxplot of window sample.

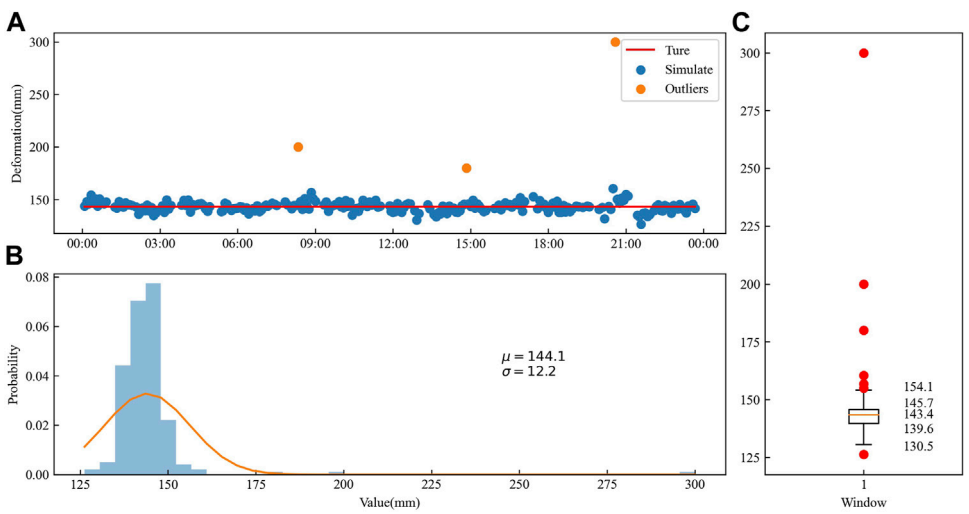

FIGURE 4 | Situation two simulation signal and estimation result. **(A)** Simulated deformation scatters plot and true value; **(B)** Frequency distribution histogram and probability distribution curve; **(C)** Boxplot of window sample.

0.024 mm/h^2. The true deformation at the center of the window (12:00:00) was 193.0 mm (**Figure 5A**).

Situation 4: Based on the simulated deformation, the window width was reduced to 4 h, and the true deformation at the center of the window (12:00:00) was still 193.0 mm (**Figure 6A**).

The frequency distribution histogram of situation 1 (**Figure 3B**) showed a normal distribution. The outliers were evenly distributed on both sides of the boxplot (**Figure 3C**), indicating that both methods yield optimal estimation results. A comparison with the conventional estimators and the NIQR estimators showed that the NIQR estimation was similar to that of conventional methods (**Table 1**).

When the outliers were added to the original signal (situation 2), the frequency distribution was asymmetrical, the peak was off-center toward the left, and the tail stretched away from the peak (**Figure 4B**). The boxplot successfully excluded these outliers (**Figure 4C**). Because it is affected by outliers, the conventional estimation method is quite different from that of situation 1, and the NIQR estimators showed little change. Therefore, the NIQR estimation method is robust.

When the simulated deformation was added to the original signal (situation 3), the series showed a gradually increasing trend, and the histogram shapes exhibited a right-skewed distribution (**Figure 5B**). The upper half of the boxplot was

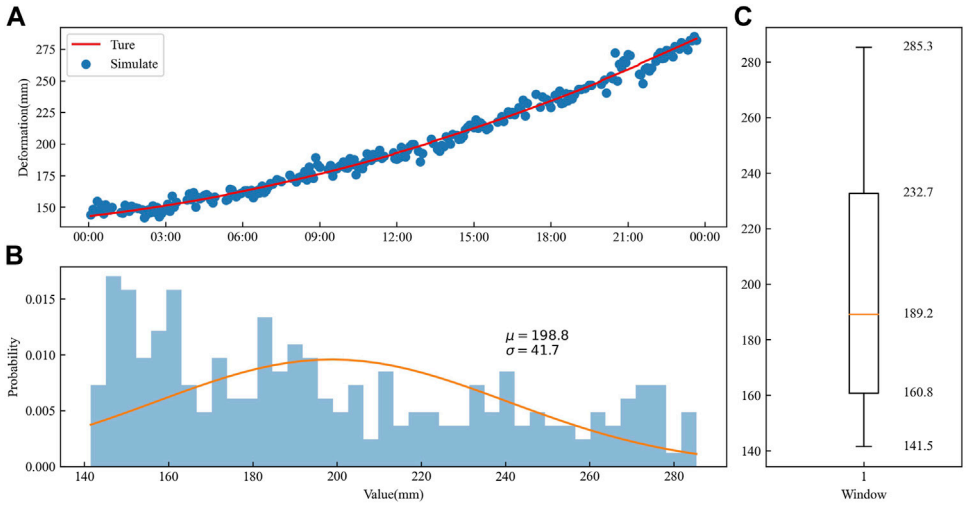

FIGURE 5 | Situation three simulation signal and estimation result. **(A)** Simulated deformation scatters plot and true value; **(B)** Frequency distribution histogram and probability distribution curve; **(C)** Boxplot of window sample.

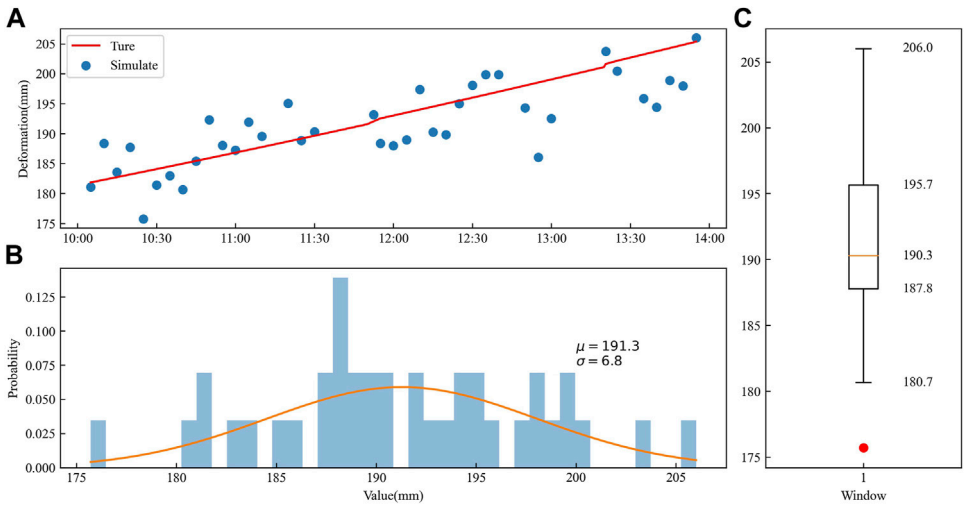

FIGURE 6 | Situation four simulation signal and estimation result. **(A)** Simulated deformation scatters plot and true value; **(B)** Frequency distribution histogram and probability distribution curve; **(C)** Boxplot of window sample.

TABLE 1 | Estimated results of the four simulated deformations.

Situations	Actual Value (mm)	Conventional Estimators (mm)		NIQR Estimators (mm)	
		Mean	STD	Median	NIQR
Situation 1	143.0	143.0	4.6	143.2	4.4
Situation 2	143.0	144.1	12.2	143.4	4.5
Situation 3	193.0	198.8	41.7	189.2	53.3
Situation 4	193.0	191.3	6.8	190.3	5.8

higher than the lower half (**Figure 5C**), and both halves showed large deviations that did not reflect the true deformation of the window because of the existence of the breakdown point.

Situation 4 reduced the window width and weakened the skewness of the frequency distribution histogram (**Figure 6B**) and window sample boxplot (**Figure 6C**). The NIQR estimated

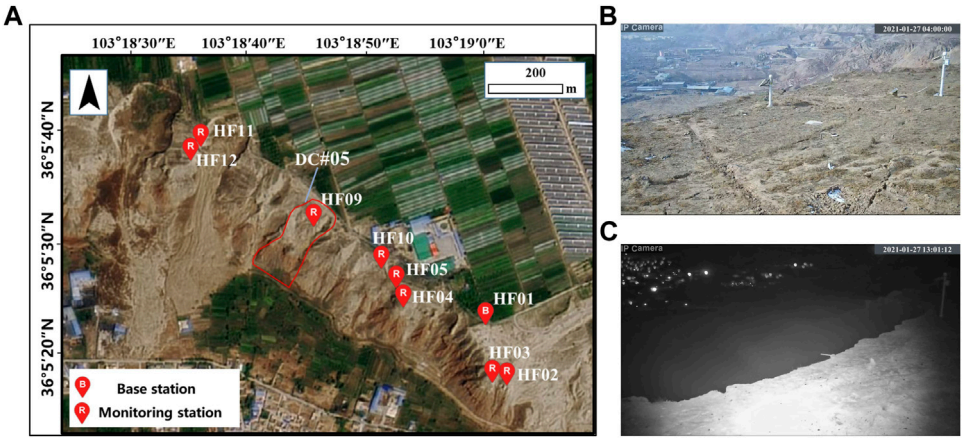

FIGURE 7 | (A) Layout of the global navigation satellite system monitoring systems at Heifangtai. And the location of DC#5 landslide occurred on 17 January 2021; **(B)** Photo of the HF09 monitoring station located at DC#5 before the landslide event; **(C)** Photo of the HF09 monitoring station after the landslide event.

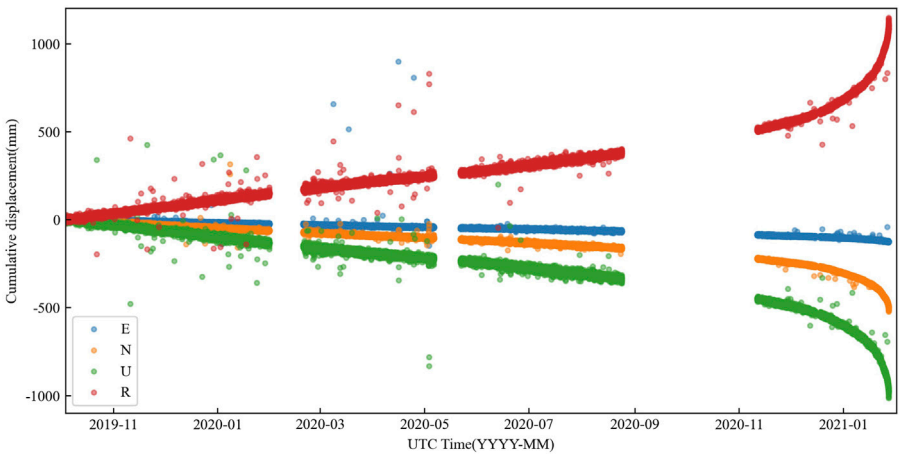

FIGURE 8 | Raw GNSS displacement time series of the HF09 monitoring station of the GNSS monitoring systems. They include east (E), north (N), upward (U), and three-dimensional (R) directions.

results were similar to the results obtained without simulated deformation; therefore, deformation in the window can be ignored.

4 RESULTS

4.1 Study Area

Heifangtai is a loess tableland located 60 km west of Lanzhou City in Gansu province, China. As this terrace was converted to agricultural land in 1968, excessive agricultural irrigation has induced more than 200 loess landslides and caused almost 40 casualties (Bai et al., 2019; Kong et al., 2021). A loess landslide (DC#5 landslide, 36°5′30.93″N, 103°18′43.6″E) occurred at 13:00 (UTC) on 27 January 2021, in the Heifangtai terrace (**Figure 7A**). Fortunately, the "High Precision Beidou System for Landslide Hazard Monitoring and Early Warning," developed at Chang'an University (China), successfully recorded the entire cumulative displacement–time data in real-time (**Figures 7B,C**). The data source for this article comes from this system. The GNSS processing software is developed by Chang'a University. The BDS/GPS relative positioning solution uses a partially ambiguity fixing method based on the data collected by the GNSS monitor station. The satellite cut-off height is 10°, and the ephemeris uses the broadcast ephemeris (Huang et al., 2018; Bai et al., 2019).

The raw GNSS displacement time series of the HF09 monitoring station located at DC#5 is presented in **Figure 8**, where R is the square root of displacements in the east (E), north (N), and upward (U) directions. The GNSS displacement time series is a typical three-stage creep curve but shows many outliers, large random noise, and inconsistent data intervals, creating difficulties in the calculation of the warning criteria. Further preprocessing of the series is required to extract accurate deformation

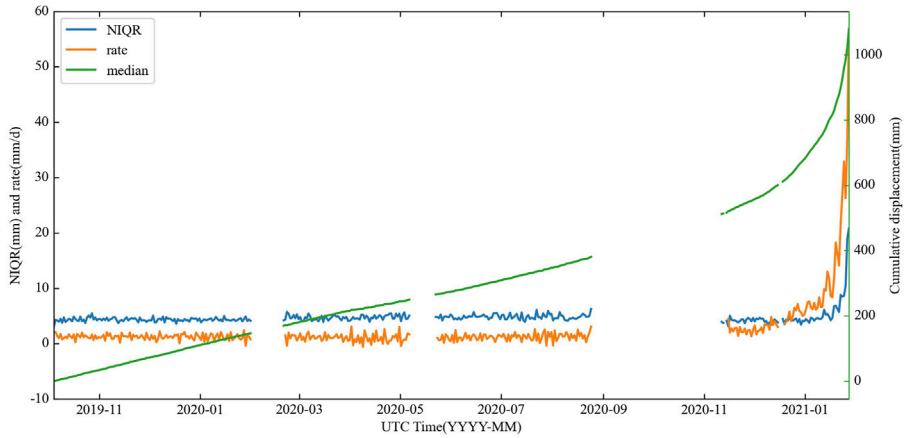

FIGURE 9 | Fixed width sliding-window estimation results and deformation rate.

TABLE 2 | Key parameters in the process of the adaptive sliding-window method.

Window Width (h)	T(X) (mm)	h_0	Breakdown Point	Adjusted Window	Rate (mm/d)
24	4.2	1.26	2021/01/18 12:00	2021/01/18 06:00	12.0
12	4.0	1.64	2021/01/24 18:00	2021/01/24 15:00	27.8
6	3.9	2.04	2021/01/26 15:00	2021/01/26 13:30	42.2
3	3.5	3.02	2021/01/27 10:30	2021/01/27 09:30	58.4
1	3.1	4.08	2021/01/27 12:30	2021/01/27 12:01	483.2

4.2 Fixed Width Sliding-Window Estimation Results

A fixed window width of 24 h was used to segment the GNSS displacement time series, and the window sample was estimated by calculating the median and NIQR. Simultaneously, the deformation rate between windows can be easily calculated, as shown in **Figure 9**. The deformation rate is relatively small in steady-state creep; thus, the GNSS positioning error is the main component of the window error, preventing the NIQR statistics from changing over time. The deformation rate tends to increase after the accelerating creep stage is reached, resulting in a gradually increasing proportion of outliers in the window. The NIQR estimators also began to rise sharply until their proportion reached a breakdown point, after which the median and NIQR estimators no longer represent the true deformation feature of the window.

4.3 Adaptive Sliding-Window Deformation Feature Results

According to the processing flow described in **Section 2.4**, the adaptive sliding window method was used to preprocess the monitoring series in the accelerating creep stage (10 November 2020 to 27 January 2021). Windows with no obvious outliers were selected from November 15, 2020 to December 15, 2020, and a width adjustment strategy was used to shorten the width by half each time until the width was less than 1 h to use real-time results. The key parameters in the adaptive sliding window method are listed in **Table 2** and are shown in **Figure 10**. The window coefficients were adjusted five times, and each adjustment caused the breakdown point to reach the same deformation rate later. This result verifies that adjusting the window coefficients can effectively reduce the number of outliers.

Figure 11 shows the deformation feature results obtained using the adaptive sliding window method after processing. Compared to the raw GNSS displacement time series, the time series after feature extraction more accurately described the creep curve during the accelerated creep stage.

4.4 Application of DC#5 Loess Landslides Early Warning

Based on the ability of the threshold definition method to suggest a probable failure, the adaptive sliding window method successfully assisted in the early warning of the DC#5 loess landslide. According to the creep curve of the loess slopes and previous findings in the Heifangtai area (Xu et al., 2020), a five-level alert criterion for the deformation rate threshold can be defined, as shown in **Table 3**. This alert was published by the local government. After receiving the warning information, the involved departments immediately launched an emergency response to evacuate people in the zone affected by the landslide. Because of this early warning, no casualties or property damage occurred.

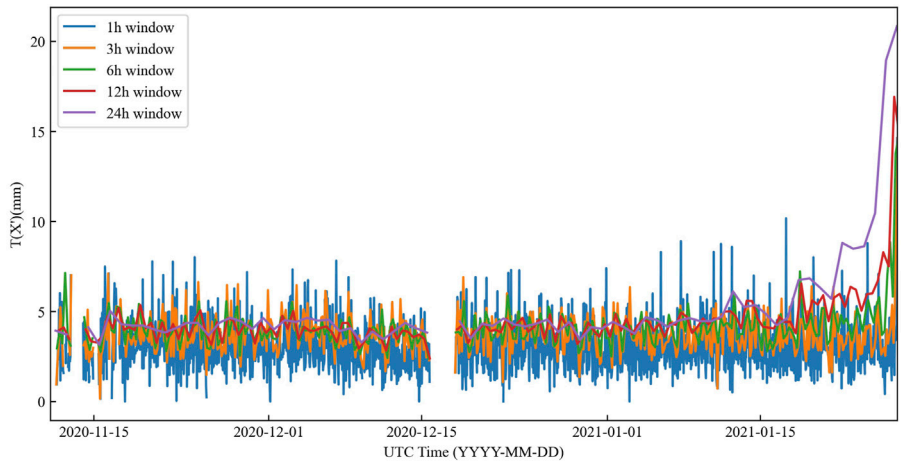

FIGURE 10 | Estimated normalized interquartile ranges of the window sample used as $T(X')$ to calculate bias in the adaptive sliding-window method.

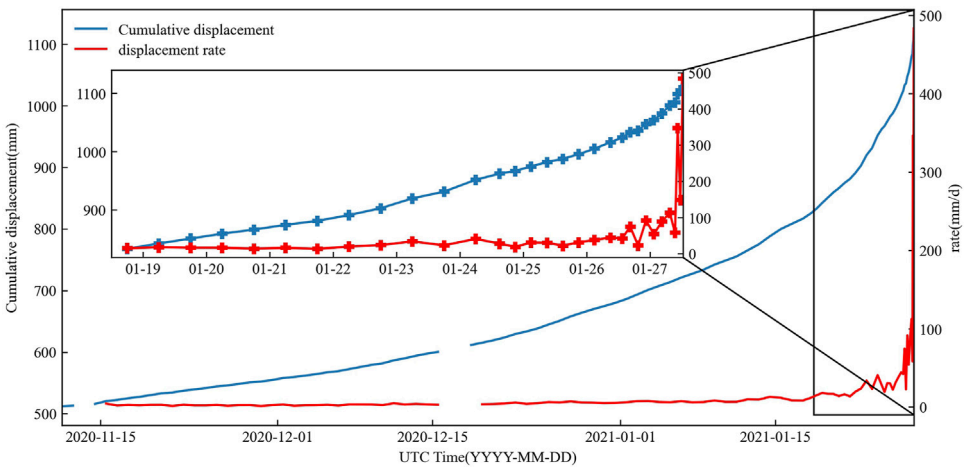

FIGURE 11 | Time series of the cumulative displacement estimation result and deformation rate of the adaptive sliding-window.

TABLE 3 | Key parameters in the process of the adaptive sliding-window method.

Threshold Level	Rate Threshold (mm/d)	Alert Time	Cumulative Displacement (mm)	Observation Rate (mm/d)
Attention	5	2020/12/22 12:00	629.4	5.8
Caution	10	2021/1/14 12:00	787.8	13.0
Vigilance	20	2021/1/22 18:00	902.8	23.7
Alarm	50	2021/1/26 16:30	1033.4	74.7
Emergency	100	2021/1/27 7:30	1079.6	112.6

5 DISCUSSION

To address the problem of the relationship between noise and true deformation changes in different creep stages, we proposed an adaptive sliding-window method for accurately extracting deformation features. Simulation experiments were conducted to evaluate the performance of the sliding window approach for different outliers and deformation signals.

According to the simulation results in the four situations, when the window sample contained only random noise, the NIQR estimation was equivalent to that of conventional methods. The NIQR estimation method is robust in the

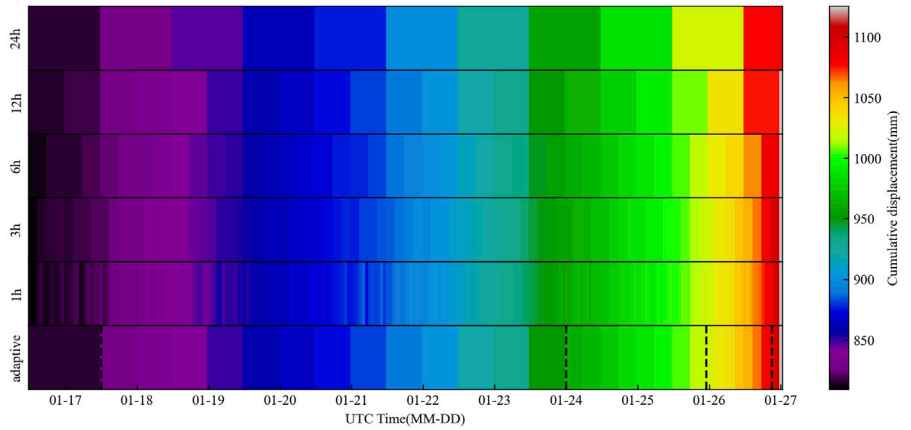

FIGURE 12 | Cumulative displacement colormap of partial adaptive sliding-window estimation results.

presence of outliers in the window sample. When window deformation occurred, both estimation methods reached their breakdown point, and the performance decreased. Reducing the width of the window can overcome this problem when the estimation method reaches the breakdown point.

A series of experiments were performed in the Heifangtai area to assess the practical application of the proposed method. The results for the time series of the cumulative displacement estimation of the adaptive sliding window showed that this method effectively reduces random noise and outliers and more accurately describes the creeping trend of the landslide. The window was used to extract the creep feature rather than a large number of unnecessary observations, which is convenient for further data analysis. Additionally, since the algorithm only works on the estimation of a single window, data interruptions have less impact on feature extraction.

Figure 12 shows a comparison of the fixed sliding window and adaptive sliding window, where the different colored blocks represent different windows and the color represents the estimated value of cumulative displacement. The window coefficient is adjusted by the black line in the figure.

In the first half of the color map, when the deformation rate was small, the deformation feature extraction results with a wider window were smoother and more reliable. Although the window lag was larger, the estimated results were close to the actual values within the window range because of the smaller deformation rate; therefore, window lag can be ignored. However, the deformation feature extraction results obtained with a shorter window showed that cumulative displacement decreased, which affected subsequent deformation analysis.

As the deformation rate increases, the lag of the window must be considered. Therefore, a shorter window width can represent a more realistic deformation feature. Our adaptive sliding-window method combines the characteristics of a wide window and a short window in different creep stages, ensuring the reliability and real-time performance of the deformation feature extraction results.

In summary, the proposed algorithm showed high reliability and practicality for obtaining creep curves and may provide support for landslide early warning. The results of the adaptive sliding-window method constantly change, which may limit the early warning method. Further studies are necessary to consider early warning methods that are more suitable for variable interval data to achieve better performance.

6 CONCLUSION

Landslide monitoring and early warnings are important in the study of landslide hazards. To obtain more accurate deformation features, raw monitoring results must be preprocessed. However, at different creep stages, the relationship between noise and deformation changes, potentially resulting in constant changes in the covariance of the dataset. This study presents an adaptive sliding-window algorithm based on the concept of the sample breakdown point.

The sliding window method is a simple and adaptable preprocessing approach for landslide monitoring. This method accurately extracts the deformation features of the window by estimating the window sample, thereby effectively reducing the influence of random noise and outliers on the results.

As the deformation rate increases, the window may reach a breakdown point. To overcome this limitation, a method based on the definition of the prior breakdown point is proposed for determining the breakdown point. The breakdown point can be postponed by adjusting the window parameters.

The processing results of the real GNSS landslide monitoring series showed that the proposed algorithm can provide reliable deformation information for landslide warnings even if the landslide is undergoing imminent failure. This algorithm could be selected as a useful reference for preprocessing methods and early warning for landslide monitoring series.

DATA AVAILABILITY STATEMENT

The original contributions presented in the study are included in the article/Supplementary Material, further inquiries can be directed to the corresponding author.

AUTHOR CONTRIBUTIONS

GH and DW designed the processing strategy and experiments, performed the experimental analyses, and wrote the manuscript. DW and YD contributed to the collection and analysis of field test data. QZ, ZB, and CW helped improve the manuscript.

FUNDING

This work was financially supported by the National Key Research and Development Plan of China (2018YFC1505105) and Program of the National Natural Science Foundation of China (42090053, 42127802, and 41941019).

ACKNOWLEDGMENTS

The authors would like to thank the reviewers and the editors for their constructive comments on this manuscript.

REFERENCES

Amiri-Simkooei, A. R. (2008). Noise in Multivariate GPS Position Time-Series. *J. Geod* 83 (2), 175–187. doi:10.1007/s00190-008-0251-8

Bai, Z., Zhang, Q., Huang, G., Jing, C., and Wang, J. (2019). Real-time BeiDou Landslide Monitoring Technology of "light Terminal Plus Industry Cloud. *Acta Geodaetica et Cartographica Sinica* 48, 1424–1429.

Banerjee, P., and Bansal, S. (2017). Revisit of Moving Average Technique for Smoothing GNSS Based Timing Data. *Mapan* 32 (1), 77–85. doi:10.1007/s12647-016-0200-6

Benoit, L., Briole, P., Martin, O., and Thom, C. (2014). Real-time Deformation Monitoring by a Wireless Network of Low-Cost GPS. *J. Appl. Geodesy* 8 (2). doi:10.1515/jag-2013-0023

Buch, K. D. (2014). "Decision Based Non-linear Filtering Using Interquartile Range Estimator for Gaussian Signals," in 2014 Annual IEEE India Conference (INDICON) (IEEE), 1–5. doi:10.1109/indicon.2014.7030658*()*

Dok, A., Fukuoka, H., Katsumi, T., and Inui, T. (2011). Tertiary Creep Reproduction in Back-Pressure-Controlled Ring Shear Test to Understand the Mechanism and Final Failure Time of Rainfall-Induced Landslides. *Kyoto Univ. Disaster Prev. Res. Inst. Annu. Rep.* 54, 263–270.

Donoho, D. L., and Huber, P. J. (1983). The Notion of Breakdown Point. in *A Festschrift for Erich L Lehmann*.

Du, Y., Huang, G., Zhang, Q., Gao, Y., and Gao, Y. (2020). Asynchronous RTK Method for Detecting the Stability of the Reference Station in GNSS Deformation Monitoring. *Sensors* 20 (5), 1320. doi:10.3390/s20051320

Foster, J., Bevis, M., and Businger, S. (2005). GPS Meteorology: Sliding-Window Analysis*. *J. Atmos. Oceanic Technology* 22 (6), 687–695. doi:10.1175/jtech1717.1

Fried, R., and Gather, U. (2007). On Rank Tests for Shift Detection in Time Series. *Comput. Stat. Data Anal.* 52 (1), 221–233. doi:10.1016/j.csda.2006.12.017

Froude, M. J., and Petley, D. N. (2018). Global Fatal Landslide Occurrence from 2004 to 2016. *Nat. Hazards Earth Syst. Sci.* 18 (8), 2161–2181. doi:10.5194/nhess-18-2161-2018

Han, J., Huang, G., Zhang, Q., Tu, R., Du, Y., and Wang, X. (2018). A New Azimuth-dependent Elevation Weight (ADEW) Model for Real-Time Deformation Monitoring in Complex Environment by Multi-GNSS. *Sensors* 18 (8), 2473. doi:10.3390/s18082473

Huang, G., Huang, G., Du, Y., Tu, R., Han, J., and Wan, L. (2018). A Lowcost Real-Time Monitoring System for Landslide Deformaion with Beidou Cloud. *J. Eng. Geology*. 26 (4), 1008–1016.

Peter, J. Huber, and Elvezio, M. Ronchetti (2009). *Robust Statistics*. 2nd ed. John Wiley & Sons

Ince, C. D., and Sahin, M. (2000). Real-time Deformation Monitoring with GPS and Kalman Filter. *Earth Planet. Sp* 52 (10), 837–840. doi:10.1186/BF03352291

Intrieri, E., Carlà, T., and Gigli, G. (2019). Forecasting the Time of Failure of Landslides at Slope-Scale: A Literature Review. *Earth-Science Rev.* 193, 333–349. doi:10.1016/j.earscirev.2019.03.019

Ismail, Z., Efendi, R., and Deris, M. M. (2013). Inter-quartile Range Approach to Length-Interval Adjustment of Enrollment Data in Fuzzy Time Series Forecasting. *Int. J. Comp. Intel. Appl.* 12 (03), 1350016. doi:10.1142/s1469026813500168

Kong, J.-x., Zhuang, J.-q., Zhan, J.-w., Bai, Z.-w., Leng, Y.-q., Ma, P.-h., et al. (2021). A Landslide in Heifangtai, Northwest of the Chinese Loess Plateau: Triggered Factors, Movement Characteristics, and Failure Mechanism. *Landslides* 18 (10), 3407–3419. doi:10.1007/s10346-021-01752-z

Li, G., Dai, W., and Zeng, F. (2016). Robust Moving Average in GPS Automatic Monitoring Data Processing Applications. *J. Geodesy Geodyn* 36 (1), 85–88.

Li, L., and Kuhlmann, H. (2013). Real-time Deformation Measurements Using Time Series of GPS Coordinates Processed by Kalman Filter with Shaping Filter. *Surv. Rev.* 44 (326), 189–197. doi:10.1179/1752270611y.0000000022

Ren, L., and Xu, T.-H. (2018). "Research on Smoothing Filtering Algorithm of BDS/GPS Slow Deformation Monitoring Sequence," in China Satellite Navigation Conference (CSNC) 2018 Proceedings, 33–44. doi:10.1007/978-981-13-0005-9_3

Schmitt, E., Öllerer, V., and Vakili, K. (2014). The Finite Sample Breakdown point of PCS. *Stat. Probab. Lett.* 94, 214–220. doi:10.1016/j.spl.2014.07.026

Song, H. Y., and Lee, J. S. (2015). Detecting Positioning Errors and Estimating Correct Positions by Moving Window. *PLoS One* 10 (12), e0143618. doi:10.1371/journal.pone.0143618

Tavenas, F., and Leroueil, S. (1981). Creep and Failure of Slopes in Clays. *Can. Geotech. J.* 18 (1), 106–120. doi:10.1139/t81-010

Xu, Q., Peng, D., Zhang, S., Zhu, X., He, C., Qi, X., et al. (2020). Successful Implementations of a Real-Time and Intelligent Early Warning System for Loess Landslides on the Heifangtai Terrace, China. *Eng. Geology*. 278, 105817. doi:10.1016/j.enggeo.2020.105817

Xu, Q., Yuan, Y., Zeng, Y., and Hack, R. (2011). Some New Pre-warning Criteria for Creep Slope Failure. *Sci. China Technol. Sci.* 54 (S1), 210–220. doi:10.1007/s11431-011-4640-5

Yang, Y. M., Wang, Z. G., Gao, Y. Y., and Gao, F. P. (2012). Deformation Monitoring Data De-noising Processing Based on Wavelet Packet. *Amm* 166-169, 1180–1186. doi:10.4028/www.scientific.net/AMM.166-169.1180

Zhao, L., Qiu, H., and Feng, Y. (2016). Analysis of a Robust Kalman Filter in Loosely Coupled GPS/INS Navigation System. *Measurement* 80, 138–147. doi:10.1016/j.measurement.2015.11.008

Zhu, X., Xu, Q., Qi, X., and Liu, H. (2017). "A Self-Adaptive Data Acquisition Technique and its Application in Landslide Monitoring," in *Advancing Culture of Living with Landslides*, 71–78. doi:10.1007/978-3-319-53487-9_7

Conflict of Interest: The authors declare that the research was conducted in the absence of any commercial or financial relationships that could be construed as a potential conflict of interest.

Publisher's Note: All claims expressed in this article are solely those of the authors and do not necessarily represent those of their affiliated organizations, or those of the publisher, the editors, and the reviewers. Any product that may be evaluated in this article, or any claim that may be made by its manufacturer, is not guaranteed or endorsed by the publisher.

frontiers | Frontiers in Earth Science

ORIGINAL RESEARCH
published: 21 April 2022
doi: 10.3389/feart.2022.814740

Failure Mechanism and Dynamic Response Characteristics of Loess Slopes Under the Effects of Earthquake and Groundwater

Shaofeng Chai[1,2,3], *Lanmin Wang*[2,3]*, *Ping Wang*[2,3]*, *Xiaowu Pu*[2,3], *Shiyang Xu*[1,2,3], *Haitao Guo*[2,3] and *Huijuan Wang*[2,3]

[1]Key Laboratory of Earthquake Engineering and Engineering Vibration of China Earthquake Agency, Institute of Engineering Mechanics, China Earthquake Agency, Harbin, China, [2]Key Laboratory of Loess Earthquake Engineering, China Earthquake Agency, Lanzhou, China, [3]Geotechnical Disaster Prevention Engineering Technology Research Center of Gansu Province, Lanzhou, China

A large-scale shaking table test was conducted with simulated earthquakes and groundwater to study the dynamic response and instability mechanism of a loess slope with a saturated bottom. By examining the acceleration, dynamic pore water pressure, corresponding soil pressure and observed macroscopic failure behaviour of the slope under different shaking intensities, the dynamic responses of acceleration and pore water pressure of the loess slope were analysed. By comparing the time history curve of acceleration with the time history curves of pore water pressure and surrounding soil pressure, we found that the instability failure of the slope was first due to the continuous vibration that caused the local structure of the slope soil to be damaged, forming locally saturated soil and the rise in the groundwater table during shaking. Then, the saturated soil liquefied under the action of strong vibration, and the liquefied soil mass slid under the action of a high-intensity earthquake force. Finally, the acceleration and spectral characteristics of the pore water pressure changed sharply with a shift in the predominant frequency at the liquefied locations under a high shaking intensity. The significant changes in dynamic pore water pressure mainly occurred when the shaking components in the low-frequency bands below 1 Hz. This implied that the shift in the frequency mainly resulted from the damage in the structure of the loess slope after high-intensity shaking. These results help us better understand the triggering mechanism and failure mechanism of saturated loess slopes during the Minxian-Zhangxian earthquake.

Keywords: shaking table test, bottom-saturated loess slope, dynamic acceleration response, dynamic pore water pressure, liquefaction sliding, failure mechanism

OPEN ACCESS

Edited by:
Fanyu Zhang,
Lanzhou University, China

Reviewed by:
Baydaa Maula,
Middle Technical University, Iraq
Ailan Che,
Shanghai Jiao Tong University, China

***Correspondence:**
Lanmin Wang
wanglm@gsdzj.gov.cn
Ping Wang
lanzhouwang_p@126.com

Specialty section:
This article was submitted to Geohazards and Georisks, a section of the journal Frontiers in Earth Science

Received: *14 November 2021*
Accepted: *28 March 2022*
Published: *21 April 2022*

Citation:
Chai S, Wang L, Wang P, Pu X, Xu S, Guo H and Wang H (2022) Failure Mechanism and Dynamic Response Characteristics of Loess Slopes Under the Effects of Earthquake and Groundwater. Front. Earth Sci. 10:814740. doi: 10.3389/feart.2022.814740

INTRODUCTION

Loess is a special soil widely distributed in northern China. Natural loess has aeolian characteristics, and the particle components are mainly powder particles; in loess, joints and large pores are visible to the naked eye, and soluble salt crystal cementation occurs between soil particles, so it has strong water sensitivity and dynamic vulnerability (Wang, 2020; Assallay et al., 1997). Documented case histories of the phenomenon of liquefaction have been useful to researchers studying the devastating

effects of loess liquefaction slipping. In the XI degree zone of the 1303 HongTong M 8.0 earthquake in Shanxi Province, China, large-scale slipping caused by liquefaction of the underlying strata occurred in the area of Huanbu on the piedmont diluvial fan with a slope of approximately 2° in northeastern HongTong County, resulting in fragmentation of the upper loess tableland (Zhao et al., 2003; Su et al., 2003). The 1811–1812 New Madrid M 8.0 earthquake in the United States caused the liquefaction of the loess stratum on the east bank of the Mississippi River, forming an irregular shallow settlement area with a length of approximately 20 km and a width of approximately 6 km, which led to the backflow of the Mississippi River and the expansion of the Reelfoot Lake area (Hwang et al., 2000; Jefferson et al., 2003). In the 1920 Haiyuan M_S 8.5 earthquake in Ningxia, the liquefaction of saturated sandy loess at the bottom of Shibeiyuan occurred approximately 14 km northwest of Yuanzhou district, Guyuan city. A large-scale liquefaction slipping area of 2.9 km^2 was formed in the X degree zone, villages were destroyed, and more than 200 people were killed (Bai and Wang, 1987). In the 1989 Dushanbe M_S 5.5 earthquake, a large amount of liquefaction was triggered on a nearly flat site below the gentle slope and hilly terrain of the Gilsa region, and a large mudflow formed, resulting in more than 200 deaths (Ishihara et al., 1990). In the 2013 Minxian-Zhangxian M_S 6.6 earthquake, Gansu Province, a large mudflow landslide was triggered by liquefaction of saturated loess in Yongguang village, located near the epicentre in the VIII degree zone; twelve people were killed, and eight houses were destroyed (Xu C. et al., 2013). The above-mentioned examples show that liquefaction can be triggered when the earthquake intensity exceeds the VIII degree, as liquefaction causes large-scale slippage of loess. The losses and impacts related to such disasters are very serious.

Prakash and Puri (1982) first proposed the liquefaction problem of saturated loess based on vibration triaxial test results of loess-like soil from the central United States under a constant amplitude cyclic load. Ishihara et al. (1990) investigated the large-scale landslides triggered by the M 5.5 earthquake in the suburb of Dushanbe, the capital of the Tajikistan Republic, and concluded that liquefaction occurred in the landslide masses due to the high collapsibility of the loess soil saturated by irrigation water. Scholars have also discovered the phenomenon of loess sliding caused by loess liquefaction in the Wenchuan earthquake (Wang et al., 2012) and Minxian-Zhangxian earthquakes (Wang and Wu, 2013) in the loess region. Studies (Zhang et al., 1995; Wang et al., 2000; Zhang et al., 2013; Wang G. et al., 2014; Wang et al., 2021; Wang, 2020) have been conducted to confirm that saturated loess, even loess with a natural moisture content higher than the plastic limit moisture content, has liquefaction potential and that liquefaction can occur in the loess layer triggered by earthquakes of a certain intensity.

The liquefaction-induced mechanism, as the dominant mechanism contributing to the slipping of saturated loess, has been widely studied. Recent research on this topic has focused on triaxial tests, ring shear tests and flume model tests to investigate the mechanism that produces the high mobility of loess landslides (Zhang et al., 1995; Zhang and Sassa, 1996; Fletcher, 2000; Wang et al., 2002; Sassa et al., 2005; Wang et al., 2007; Wang Q. et al., 2014; Zhang et al., 2014; Carey et al., 2017; Gao, 2021). Wang (2003) concluded that due to water, saturated loess causes partial or total dissolution of salt crystals and other cements, which significantly weakens its structural strength. In addition, pore water pressure is generated under the action of seismic loading, resulting in a significant decrease in the effective stress of the soil, thus causing a catastrophic flow slide. Wang et al. (2007) revealed that a significant reduction in the shear strength could result after shear failure due to the build-up of excess pore water pressure within the shear zone by performing undrained and partially drained ring-shear tests on mixtures of sandy silt with different loess contents, which agreed with the conclusions drawn by Zhang et al. (1995) and Zhang et al. (2014).

However, past studies on the behaviour of loess liquefaction have not clarified the relationship between the dynamic characteristics and macrodamage of slopes under the seismic action of saturated loess, especially loess saturated by groundwater. These include the acceleration response, surrounding-soil pressure response, and dynamic pore water pressure response. In addition, the critical ground motion acceleration and dynamic pore pressure ratio that cause loess liquefaction slipping must be further studied.

This research studied the dynamic behaviour of a loess slope model with a saturated bottom using a prototype soil profile patterned from the Yongguang Wamuchi village landslide after a past earthquake based on the shaking table test. The large-scale shaking table facility at Lanzhou Institute of Seismology, China Earthquake Administration (CEA) Key Laboratory of Loess Earthquake Engineering, CEA, was used. This experimental study provides an improved understanding of the phenomenon of liquefaction slipping of a slope in which the bottom is saturated by rising groundwater during an earthquake. In addition, the experimental data can be used as a baseline to validate numerical simulations of liquefaction-induced loess landslides and evaluate the effectiveness of different liquefaction mitigation measures, such as anti-liquefaction piles and prefabricated vertical drains.

CASE STUDY

On 22 July 2013, an M_S 6.6 earthquake occurred in the NW-trending Lintan-Tangchang fault on the northeastern edge of the Qinghai-Tibet Plateau, with the epicentre at the junction of Minxian and Zhangxian counties in Dingxi, Gansu Province. The earthquake induced at least 2330 landslides, of which 600 landslides and collapses occurred in the loess layer (Wang and Wu, 2013; Xu S. H. et al., 2013; Xu C. et al., 2013). Among these landslides, a typical loess liquefaction landslide occurred on the slope of Yongguang village, Minxian County, Gansu Province (see **Figure 1**). The landslide was approximately 45,200 m^2, and Q3 loess-induced instability almost destroyed the whole Wamuchi village, resulting in 12 deaths. The sliding distance of the landslide was approximately 1.05 km, as shown in **Figure 1B**, illustrating typical loess fluid-slip characteristics. The long-term rainfall before the earthquake increased the

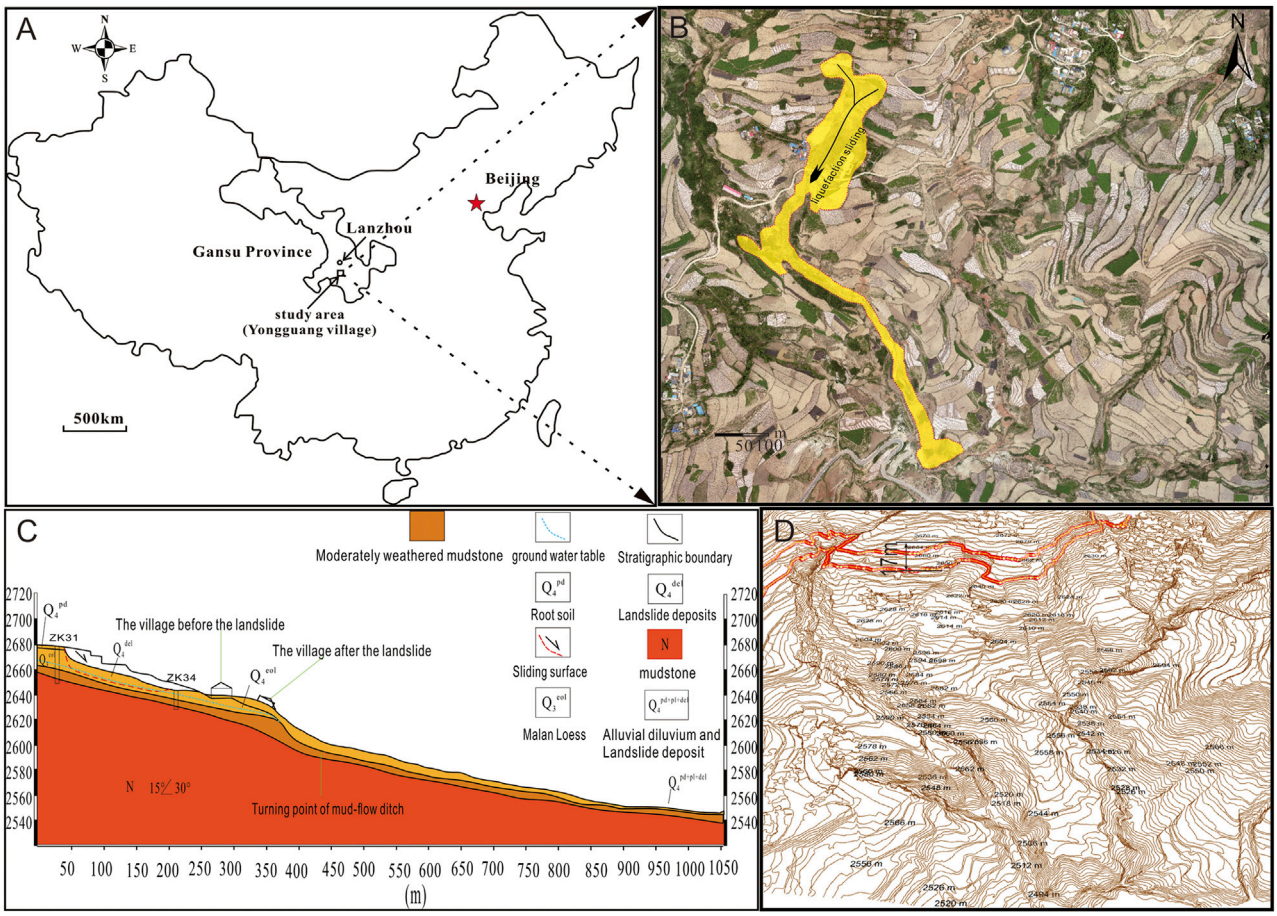

FIGURE 1 | (A) Location of the Yongguang landslide; **(B)** The landform after the landslide; **(C)** The engineering geological profile of the Yongguang village landslide; **(D)** The contour line of landslide DSM.

water content of the slope together with the groundwater. Special topographic (**Figure 1C**) and hydrological conditions provide the basic conditions for the rise in the groundwater level due to rainfall and earthquakes. Groundwater and rainfall saturated the bottom loess on the sliding surface 2–3 m above the sandstone (Liu, 2020). In addition, the moisture content of the slope surface was high due to rainfall. The high water content provides a material basis for the seismic liquefaction of loess. According to the laboratory test results, the peak acceleration of seismic ground motion caused liquefaction to be at least 122 gal (Wang et al., 2021). According to the seismic ground motion records of the Minxian seismic station (PGA is 226 gal), the peak acceleration of ground motion (PGA) on the slope of Wamuchi is more than 300 gal. During an earthquake, the excess pore water pressure of saturated loess rises due to seismic loading, which leads to slope failure. Although significant efforts have been devoted to the study of the initiation, motion, and deposition of fluidized landslides with emphasis on pore-pressure generation and dissipation, the understanding of the fluidized landslide process is limited (Wang et al., 1998). In particular, under seismic action, how excess pore pressure is generated and maintained and how the generated pore pressure affects the movement of displaced landslide material requires further scrutiny.

THE LARGE-SCALE SHAKING TABLE TEST

A large-scale shaking table test was performed to investigate the dynamic characteristics and failure mechanism of the bottom saturated loess landslide. The shaking table facility at Lanzhou Institute of Seismology, China Earthquake Administration (Key Laboratory of Loess Earthquake Engineering, CEA) was used. The shaking table size was 4 m (in width) × 6 m (in length), and the table could achieve horizontal (x), vertical (z), and horizontal-vertical (x-z) coupled loading. The shaking frequency in the x-direction was 0.1–70.0 Hz, and hat in the z-direction was 0.1–50.0 Hz. The maximum acceleration of the x-direction was 1.7 g, and that of the z-direction was 1.2 g when the loadings in the two directions were applied separately. In the combined model box used to saturate the bottom soil of the slope model, a stainless-steel sealed storage tank was embedded in the rigid

TABLE 1 | Physical properties of the tested loess.

Materials	Water content (%)	Density P (g/cm^3)	Cohesive strength C (kPa)	Friction angle φ (°)	Elastic modulus E (Pa)	Poisson's ratio μ
Prototype loess	5.0	1.35	28–51	22-35	50–80	0.3–0.35
Model loess	5.0	1.35	2.99	35	5–8	0.3

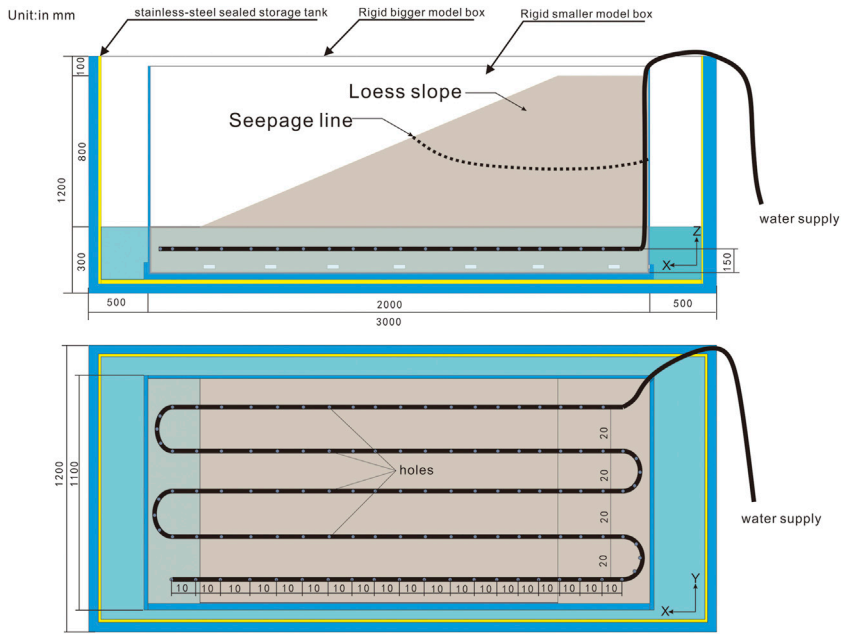

FIGURE 2 | The final loess slope model.

model box with internal dimensions of 3.0 m × 1.5 m ×1.2 m [length × width × height (L × W × H)]. In the stainless-steel tank, a smaller rigid rectangular model case was fixed on the bottom, and 18 rectangular window holes were cut on four sides around the model box. The sizes of the smaller rigid box were 2 m × 1 m × 1.1 m (L × W × H). The body and bottom plate of the smaller rigid box were separable, and water could seep into the box from the gaps around the bottom of the model case. The front and back internal faces of the smaller model box were set up with polyphenylene bubble panels to minimize possible boundary effects. Vaseline was smeared on both sidewalls along the sliding direction to reduce friction.

Similarity Relations

The physical ground model simulated prototype ground conditions representative of soil profiles with saturated bottoms observed at the Yongguang west landslide during the 2013 Minxian-Zhangxian M_S 6.6 earthquake. The designed shaking table model was expected to meet geometric, kinematic, and dynamic similarity based on similarity theory to reflect the actual dynamic response characteristics of the prototype slope. In fact, it is impossible for the parameters to meet all similarity ratios according to similarity theory. Therefore, it is necessary to control the main parameters and ignore secondary parameters according to the purpose of the test. Considering the size of the model box and the possible application to the remoulded slope model, we designed the slope model by a similarity ratio (λ) of 10 following the similarity adopted by Lin and Wang (2006). Soil density ρ, geometric length L and gravitational acceleration were selected as the fundamental parameters in this test, with values $\lambda\rho = 1$, $\lambda_L = 10$, and $\lambda a = 1$, respectively. Other similarity ratios are calculated according to Birmingham's π theorem (Birmingham, 1914).

Similarity Materials

There is a large difference in the physical and mechanical parameters between the prototype and model materials according to the similarity ratios; therefore, materials similar to natural materials must be adopted. In the modelling process, materials similar to those present in loess are loess, barite powder, fly ash, saw powder, water and glycerin, with a ratio of 0.50:0.15:0.15:0.15:0.03:0.02. Direct shear and triaxial tests on the loess samples were conducted in the laboratory, as described in previous studies (Chai et al., 2019). The basic physical and mechanical parameters of the physical model are listed in **Table 1**.

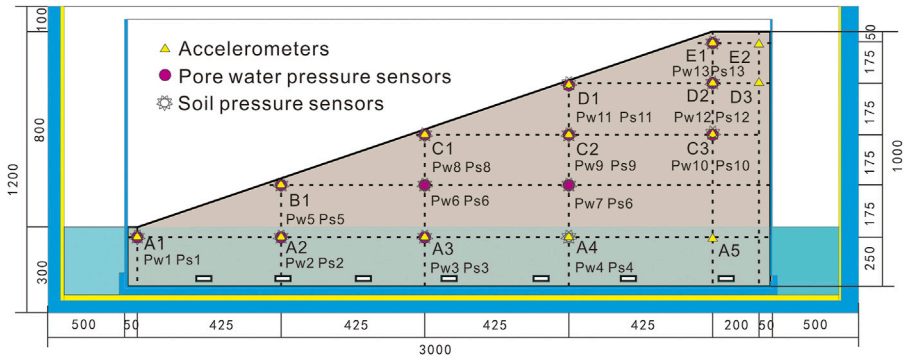

FIGURE 3 | Layout of the sensors (unit: mm).

TABLE 2 | Excitation schemes.

No.	Peak acceleration	Input wave	Loading direction	Proport ratio
Case 1	113 gal	MX wave (E-W)	X	0.5
Case 2	226 gal	MX wave (E-W)	X	1.0
Case 3	339 gal	MX wave (E-W)	X	1.5
Case 4	452 gal	MX wave (E-W)	X	2.0
Case 5	565 gal	MX wave (E-W)	X	2.5
Case 6	678 gal	MX wave (E-W)	X	3.0
Case 7	791 gal	MX wave (E-W)	X	3.5
Case 8	904 gal	MX wave (E-W)	X	4.0

The Process of Modelling

Yongguang landslide from the perspective of triggering mechanism, as **Figure 1** shown the Yongguang landslide is just a part of a mountain. The sliding body is Q3 Malan loess located on the upper part of weathered argillaceous sandstone. The weathered argillaceous sandstone is a relatively water-tight layer, the prolonged rainfall before the earthquake and the rise of the groundwater level during the earthquake caused the soil near the groundwater level was in a saturated state. The borehole data from the field survey after landslide shows that the groundwater depth at the back edge of the landslide is 16–17.8 m and the groundwater depth at slope foot position before slide is 3.2 m (Liu, 2020). According to DSM data (**Figure 1D**) of post-slide landslide, the position of the sliding surface of the trailing edge is about 17 m below the slope surface. Liquefaction of the bottom saturated loess caused by ground shaking, which leads to the occurrence of landslides (Wu et al., 2015). Through the investigation and analysis described above, the model was simplified to a single loess model slope according to the prototype. The model slope had a length of 2000 mm, height of 1000 mm, width of 1000 mm, top width of 250 mm and slope angle of 25°. The layout of the final test model is illustrated in **Figure 2**. The loess used for making the model was sifted through a sieve with a mesh diameter of 2 mm, and model material with a moisture content of 5% (natural moisture content of the loess) was prepared by spraying water, mixing, and drying. During the model-making stage, the layered tamping method was used to build it from bottom to top, and the thickness of each tamping was controlled at 10 cm. To avoid separation from other layers, the surface of each layer was especially rough to make better contact with each other layer after the tamping was completed. The density of the model was controlled at 1.35 g/cm^3.

To saturate the model slope bottom, groundwater was formed by water infiltrating through the gaps and holes around the case bottom. The water injected from the pipe with holes at equal intervals (10 cm) was buried at equal spacing distances at the bottom of the model. After the model tamping was completed, water was injected into the large model case, and the water pipe was connected to tap water (low water pressure and slow velocity) to saturate the soil at the bottom of the model. After constant injection, a water level of 30 cm was reached, and the model was steady until the water surface of the large model box did not drop within 1 h, which was necessary to form a stable groundwater level. The soil at the bottom of the model was sampled and tested; its moisture content was 33%, and its saturation was calculated to be 85.2%. According to the liquefaction standard proposed by Wang et al. (2000) and the requirements of saturation in the Standard for Building Construction in Collapsible Loess Regions (GB 50025-2018), loess was considered to be saturated when its saturation reached more than 80% after soaking and before collapsing. The completed model is shown in **Figure 2**.

Monitoring

In the test, 14 three-way capacitive acceleration sensors, 13 soil pressure sensors and 13 pore water pressure sensors were embedded in the model slope to monitor the dynamic response, as shown in **Figure 3**.

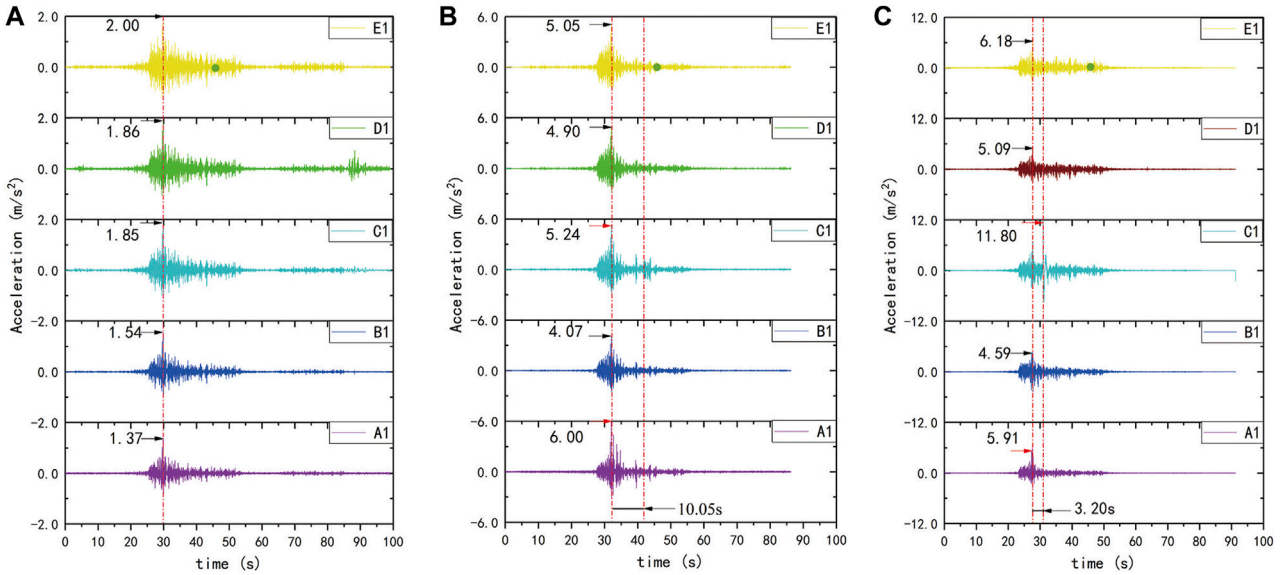

FIGURE 4 | The acceleration time history of the slope surface. **(A)** The input amplitude is 113 gal. **(B)** The input amplitude is 339 gal. **(C)** The input amplitude is 565 gal.

Shaking Sequences

The EW component of the Minxian wave (MX wave) was used in the test as the input waveform, which was recorded on 22 July 2013, at the Minxian strong motion station 18 km from the epicentre in the Minxian-Zhangxian M_S 6.6 earthquake. The peak acceleration in the EW direction was 226 gal. The EW component of the MX wave was used as the input motion proportionally scaled according to its peak wave. The EW component of the waveform had a preeminent frequency of 4.1 Hz and a duration of 70 s. The input MX wave was loaded as the excitation scheme shown in **Table 2**.

EXPERIMENTAL RESULTS

The shaking table tests provided an opportunity to further investigate the dynamic behaviour of bottom-saturated loess slopes under the action of earthquakes, which has been observed in several earthquakes. In this section, the results of the acceleration time history and acceleration amplification are evaluated thoroughly. The pore water pressure generation and its effect on observed liquefaction slipping are discussed. Additionally, the soil pressure corresponding to the pore water pressure is analysed, and the ratio of pore water pressure and corresponding soil pressure is used to identify dynamic liquefaction, combined with the slope macroscopic deformation.

Acceleration Amplification Effect of the Slope

Based on the results of the physical model, the acceleration time history of the slope surface and the inner position of the slope were obtained to analyse the peak acceleration (PGA) of each monitoring point. **Figure 4** shows the time history curves of the surface on the slope, and **Figure 5** presents the acceleration response in the slope when the acceleration amplitude of the seismic wave was 113, 339, and 565 gal. To reflect the amplification effect of acceleration, the acceleration amplification coefficient was defined at each measurement point. The peak acceleration amplification coefficient here refers to the ratio of the PGA measured at any monitoring point to the PGA measured at the shaking table (Feng et al., 2019). The relative height (h/H) was defined by the ratio of the height of any monitoring point (h, measured from the toe of the model slope) to the total height (H) of the model slope. The dynamic response acceleration reached the maximum at the same time under the action of low intensity with a peak acceleration of 113 gal. Comparing the peak acceleration amplification coefficient in **Figure 6A**, it was found that the peak acceleration of the slope surface gradually increased with increasing input ground motion and relative height (h/H). The peak acceleration increased along the slope surface (from A1 to E1) with increasing height under low intensity (see **Figure 4A**). Acceleration amplification of the slope surface showed that the closer to the shallow surface and the top of the slope, the more obvious the acceleration amplification, which is what predecessors call the surface effect (Zhang et al., 2018). However, the acceleration at the toe (A1) and the middle (C1) of the slope surface increased evidently when the input acceleration exceeded 339 gal; i.e., the accelerated response no longer increased gradually along the slope surface (**Figure 4B**). With the increase in input amplitude reaching 565 gal, the acceleration of the middle slope surface (C1) increased abnormally and reached the maximum (11.8 m/s^2) 3.20 s after the peak of input ground motion, as shown in **Figure 4C**. More interestingly, the acceleration did not have an arc attenuation

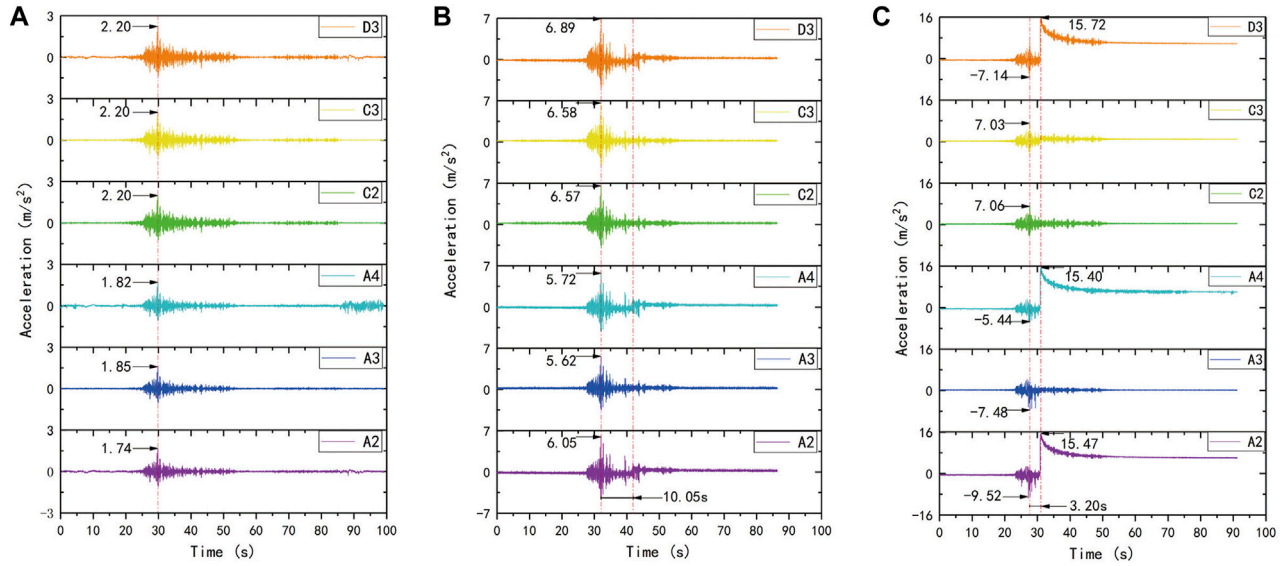

FIGURE 5 | The acceleration time history in the slope. **(A)** The input amplitude is 113 gal. **(B)** The input amplitude is 339 gal. **(C)** The input amplitude is 565 gal.

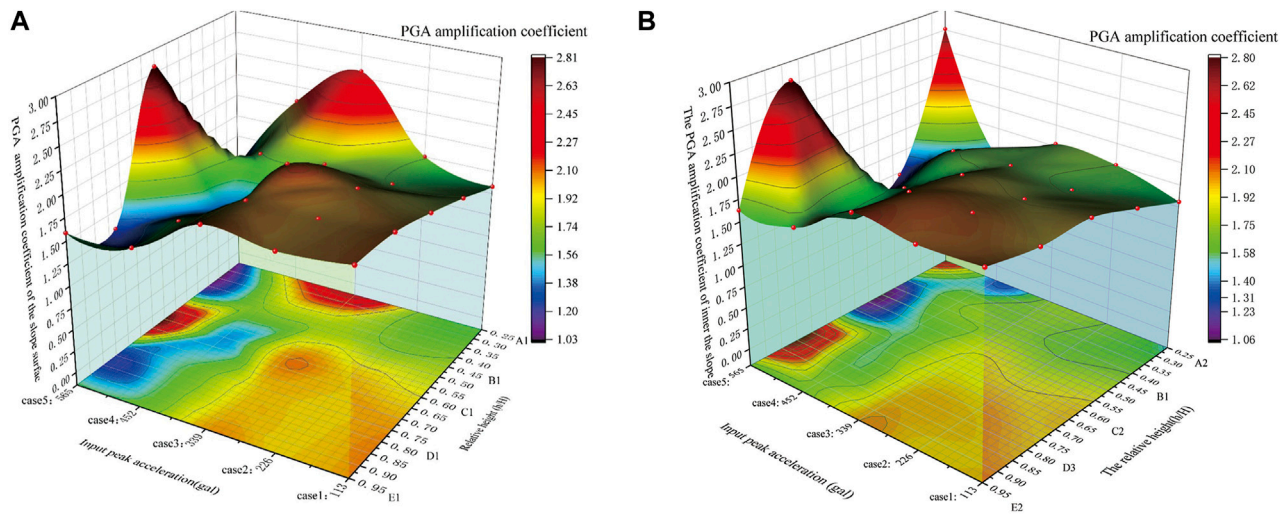

FIGURE 6 | The PGA amplification coefficient against the input peak acceleration and relative height. **(A)** The PGA amplification coefficient of the slope surface. **(B)** The PGA amplification coefficient inside the slope.

trend after a sudden increase and then slowly decreased, similar to A2/A4/D3, as shown in **Figure 5C**. Large deformations, such as cracks, probably appeared at this location, but no liquefaction slip occurred. The macroscopic deformation of the slope surface also confirms this hypothesis.

By comparing the acceleration response of different relative height monitoring points, A2, B1, C2, D3, and E2, it was found that the acceleration response gradually increased with increasing elevation of the monitoring points. However, the accelerations in the horizontal layer at the same height did not change significantly, and the peak acceleration amplification coefficient showed little difference, as shown in **Figure 6B**. Under the action of a unidirectional seismic wave, the acceleration response law inside the slope showed an elevation effect, as Zhang et al. (2018) described.

When the peak acceleration of the input vibration reached 565 gal, the acceleration of the slope bottom at A2/A4 and near the top of the slope (D3) suddenly increased and reached a maximum 3.20 s after the input shaking reached the peak value; these values slowly decreased and finally stabilized (see **Figure 5C**). However, the zeros of the stabilized acceleration deviated from the initial zeros, which indicates

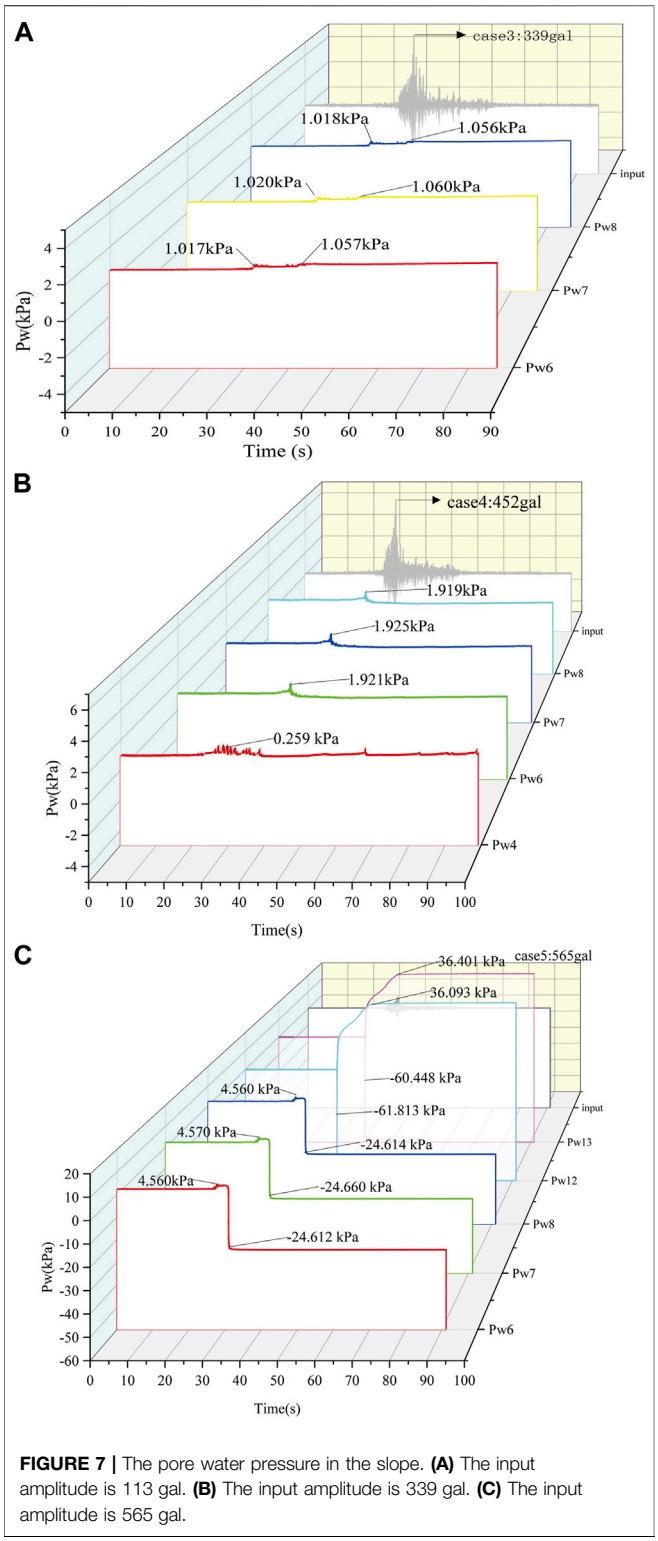

FIGURE 7 | The pore water pressure in the slope. **(A)** The input amplitude is 113 gal. **(B)** The input amplitude is 339 gal. **(C)** The input amplitude is 565 gal.

that the soil at the three points clearly migrated. The main reasons for the baseline drift of acceleration were hysteresis of the sensor, background noise of the sensor and tilt of the sensor (Zheng et al., 2010). In this study, the first two reasons were excluded because there was no drift in other channel sensors tested in the same test. The main reason for the inclination of the sensors is speculated to be the liquefaction of the soil surrounding the sensors. Moreover, the migration was in a viscous state, rather than as a landslide that broke apart. The specific explanation is that local liquefaction occurred at the monitoring points, and the liquefied soil slipped under the continuous seismic force.

Dynamic Pore Water Pressure Response

The importance of pore water pressure generation/dissipation in liquefaction mechanisms has been highlighted by numerous researchers (Major and Iverson, 1999; Wang and Sassa, 2001; Wang and Sassa, 2003). The dynamic pore water pressure of monitoring points in the slope has no significant change when a low amplitude vibration is applied. When the vibration peak reached 339 gal, the pore water pressure in the centre of the slope (P_w7) and the middle of the slope (P_w6, P_w8) suddenly increased and reached the first peak, while the input shaking reached the peak acceleration. The maxima were 1.017, 1.020, and 1.018 kPa, respectively. Then, they fluctuated and gradually decreased; 13 s later, the pore water pressure of P_w6, P_w7, and P_w8 increased again to reach the second peak, which had almost the same peak value of 1.06 kPa, and then maintained a steady state of slow increase without dissipation, as shown in **Figure 7A**.

While the peak acceleration of the input increased to 452 gal, other monitoring points in the slope body did not show significant changes, except that the pore water pressure of P_w4, P_w6, P_w7, and P_w8 suddenly increased while the peak acceleration of the input reached the maximum, but the increased amplitude was not notable; then, they decreased and remained at a stable value, as shown in **Figure 7B**. However, the pore water pressure of P_w4 began to increase and fluctuated before the input reached its peak, which was located near the bottom of the model. Moreover, the pore water pressure of P_w4 was smaller than those of P_w7 and P_w8.

When the peak acceleration of the input was 565 gal, the pore water pressure first undernote a small increase at all monitoring points. Then, 3.20 s after the peak input motion, the pore water pressure of P_w6, P_w7, and P_w8 suddenly decreased, and all pore water pressures reached their negative and smallest pore pressure values. These results indicate that tension rupture occurred at these monitoring points, resulting in the rapid dissipation of pore water pressure. However, the pore water pressure of P_w12 and P_w13 synchronously decreased to the negative and smallest values, which were −61.813 and −60.448 kPa, respectively. Then, it suddenly increased to approximately 20.00 kPa, slowly increased, and finally stabilized at 36.093 kPa (P_w12) and 36.401 kPa (P_w13) (**Figure 7C**).

Combined with the distribution of the acceleration amplification factor and the growth trend of pore water pressure (**Figure 7**), it can be noticed that with the increase in ground motion (from case 1 to case 3), the seepage line in the model gradually rose. Under the amplification of the soil in the middle of the model, the local pore water pressure of the high moisture content soil in the middle of the slope increased (P_w6/P_w7/P_w8 position), and the soil began to liquefy locally. The saturated soil at the bottom was not liquefied. Due to the weak

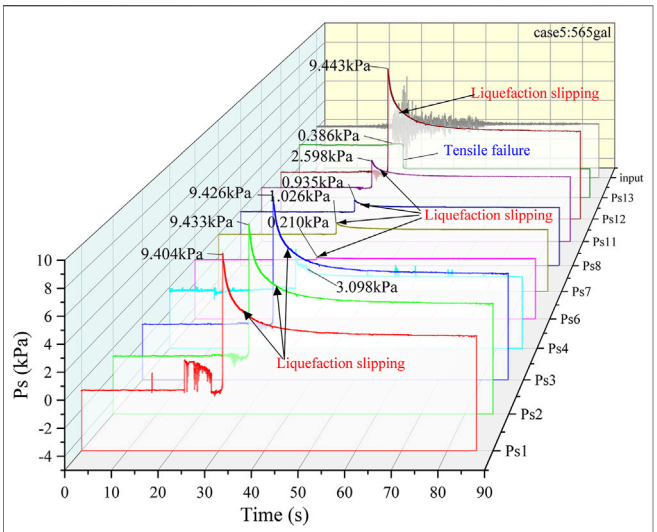

FIGURE 8 | The soil pressure in the slope when the peak acceleration of the input vibration is 565 gal.

amplification effect of ground motion at the bottom, the vibration amplitude did not reach the critical peak acceleration of liquefaction, and there was no obvious increase in pore water pressure. With a further increase in the seismic peak value, the original local liquefied soil mass was further liquefied, the liquefaction range was increased, and the saturated soil mass at the bottom also began to liquefy (A4, i.e., P_w4). When the seismic peak acceleration increased to 565 gal, the saturated loess at the bottom of the slope also began to liquefy, the middle seepage line continued to rise, and the middle and rear shoulder of the model also liquefied because the acceleration had a greater amplification effect along the elevation. The uplift of the liquefaction part proved the rise in the groundwater level under the action of earthquakes. At the same time, the liquefied soil reduced the strength of the surrounding soil. Under the action of the amplified seismic inertia force, the shear strength exceeded the shear strength of the soil, resulting in tensile failure, and the liquefied soil ejected from the tension crack (**Figure 9C**).

Soil Pressure of the Slope Model

Thirteen soil pressure transducers were arranged approximately adjacent to the pore water pressure sensors along the central line to monitor the dynamic soil pressure, as shown in **Figure 3**. When we focused on the variation tendency of the soil pressure of the slope model at the same position as the pore water pressure in the slope, the dynamic soil pressure at the bottom (Ps1, Ps2, Ps3, Ps4), in the middle (Ps6, Ps7, Ps8) and near the top of the slope (Ps11, Ps12) had the same changing tendency when the input peak shaking sequence was case 5 (PGA: 565 gal). These soil pressures built up and synchronously reached their peak 3.2 s after the input reached the peak acceleration. Furthermore, it was found that the soil pressure of Ps1, Ps2, Ps3, Ps4, Ps6, Ps7, Ps8, Ps11, and Ps12 gradually decreased in a circular tendency after the peak value, similar to the acceleration of A2, A4, and D3 mentioned previously (see **Figure 8**). This shift in soil pressure and pore water pressure can be explained by liquefaction sliding, which is directly related to the generation and dissipation of generated pore water pressure and the macroscopic deformation of damaged parts of the slope caused by earthquake forces. In the liquefaction slipping zone, the dissipation of soil pressure also presents a viscous state. The slow dissipation of soil pressure is an important reference to judge whether the measured soil is liquefied, while the soil pressure in the tensile crack zone suddenly decreases to the minimum value. Combined with the analysis of the growth and dissipation trend of pore water pressure and soil pressure in the bottom saturation zone and the middle liquefaction zone, it can be concluded that the phenomenon of mud spraying and slurry pouring occurs when the pore water pressure is greater than the surrounding earth pressure.

Failure Mode of the Slope

The deformation of the slope under separate input shaking intensities was summarized into three types, as shown in **Figure 9**. Here, we should note that the white marks are gypsum powder sprinkled for marking cracks after each test case.

1) Partial deformation and localized surface cracks. When the amplitude of the input shaking was less than 226 gal, the slope had no clear deformation. While the peak acceleration of the input vibration increased to 226 gal, three small transverse cracks and two vertical cracks appeared near the bottom on the right side of the slope surface 55 cm from the slope toe, and the spacing of the three transverse cracks was 15 and 10 cm from bottom to top, as shown in **Figure 9A**.
2) Fracture deepening and local liquefaction. When the input shaking amplitude increased to 339 gal, two transverse cracks appeared on the surface of the slope in the middle of the slope and just along the slope shoulder. With the input amplitude increased to 452 gal, these two fractures extended laterally to form penetrating fractures, and the cracks deepened. Meanwhile, new fractures appeared near the wetting front on the slope surface and were indirectly connected with the original cracks in the middle of the model. Many small tensile cracks appeared on the top of the model. However, the slope remained stable. The saturated loess at the bottom of the model was liquefied, and bubbles emerged from the front of the bottom slope foot (see **Figure 9B**).
3) Failure of slope and liquefaction sliding. When the input shaking intensity was 565 gal, liquefaction occurred at the middle surface and near the shoulder of the slope; in the bottom saturated zone, water in the soil was extruded from the soil by liquefaction and gathered at the foot of the slope. The phenomenon of mud outflow and water spraying occurred locally, and visible bubbles emerged from the liquefied soil (see **Figure 9C**). The trace of forward slippage movement appeared on the surface soil of the slope body. The whole slope

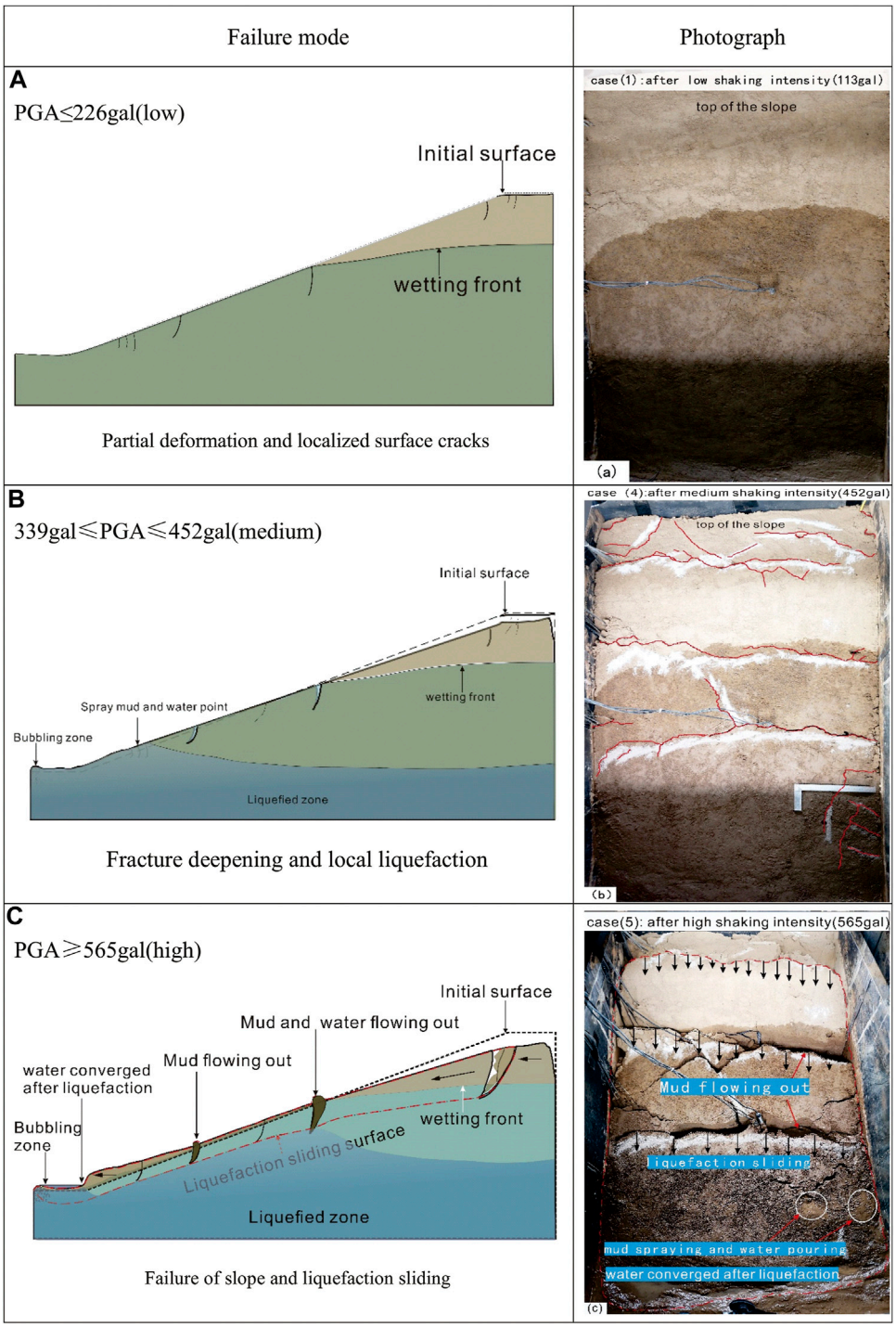

FIGURE 9 | Summarized failure modes: **(A)** low shaking intensity (113 gal); **(B)** medium shaking intensity (452 gal); **(C)** high shaking intensity (565 gal).

slid along the liquefaction surface, and the old fracture continued to grow and formed three deep fractures: one near the toes of the slope with a maximum width of 10 cm, one in the middle with a maximum width of 15 cm and one on the shoulder of the slope with a maximum width of 12 cm. The liquefied mud in the front two cracks emerged and presented the phenomenon of mud spraying. Mud spraying and water pouring, such as sand liquefaction, appeared at the foot of the model slope. The trailing edge of the model slope detached from the inner wall of the box and migrated approximately 15–20 cm along the sliding surface, resulting in significant displacement of the slope and instability failure.

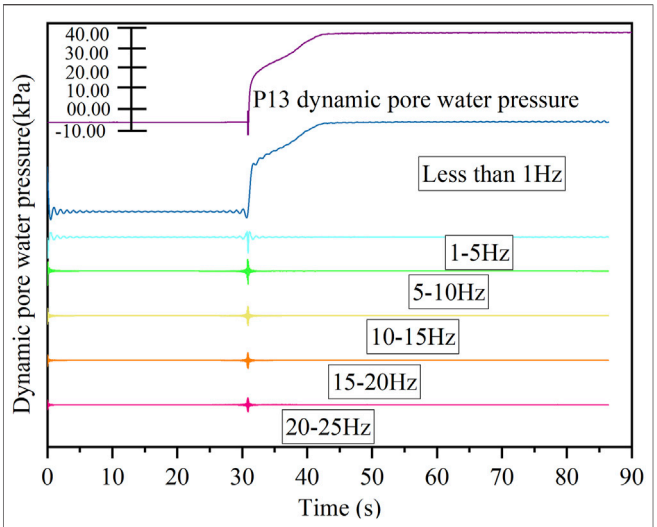

FIGURE 10 | Dynamic pore water pressure time-history curves at bandpass frequencies less than 25 Hz [curves for measurement site P_w13 of the slope model under high acceleration (case 5) are shown as an example here]. These series of subcurves are divided into six frequency bands (less than 1, 1–5, 5–10, 10–15, 15–20 and 20–25 Hz).

DISCUSSION

Variation in the Dynamic Response of Pore Water Pressure

The above analysis shows that the dynamic pore water pressure response of the model slope at each monitoring point would not change significantly under low-intensity shaking. To distinguish the main components that resulted in these sharp changes, in this study, a 4th-order Butterworth filter was adopted to decompose the recordings of dynamic pore water pressure and obtain the pore water pressure time-history curves in different frequency bands according to Ma et al. (2019). The patterns of pore water pressure time-history curves for measurement point of P_w13 for high shaking acceleration (case 5) are shown in **Figure 10**. The dynamic pore water pressure time-history curves in frequency bands less than 1, 1–5, 5–10, 10–15, 15–20, and 20–25 Hz represent the pore water pressure generated by the main energy components of the seismic wave with shaking frequencies less than 1, 1–5, 5–10, 10–15, 15–20, and 20–25 Hz. This method of decomposing the recordings of dynamic pore water pressure and obtaining the pore water pressure time-history curves in different frequency bands was used to distinguish the main components that resulted in sharp changes.

In this study, we defined a value as the ratio (hereinafter termed the peak value ratio) between the peak amplitude value for dynamic pore water pressures in different frequency bands and that obtained from the total dynamic pore water pressure time-history curve [hereinafter termed the pore water pressure peak value ratio (R_{WPV})] to evaluate the changes in dynamic pore water pressures. The peak value ratio has been written as follows:

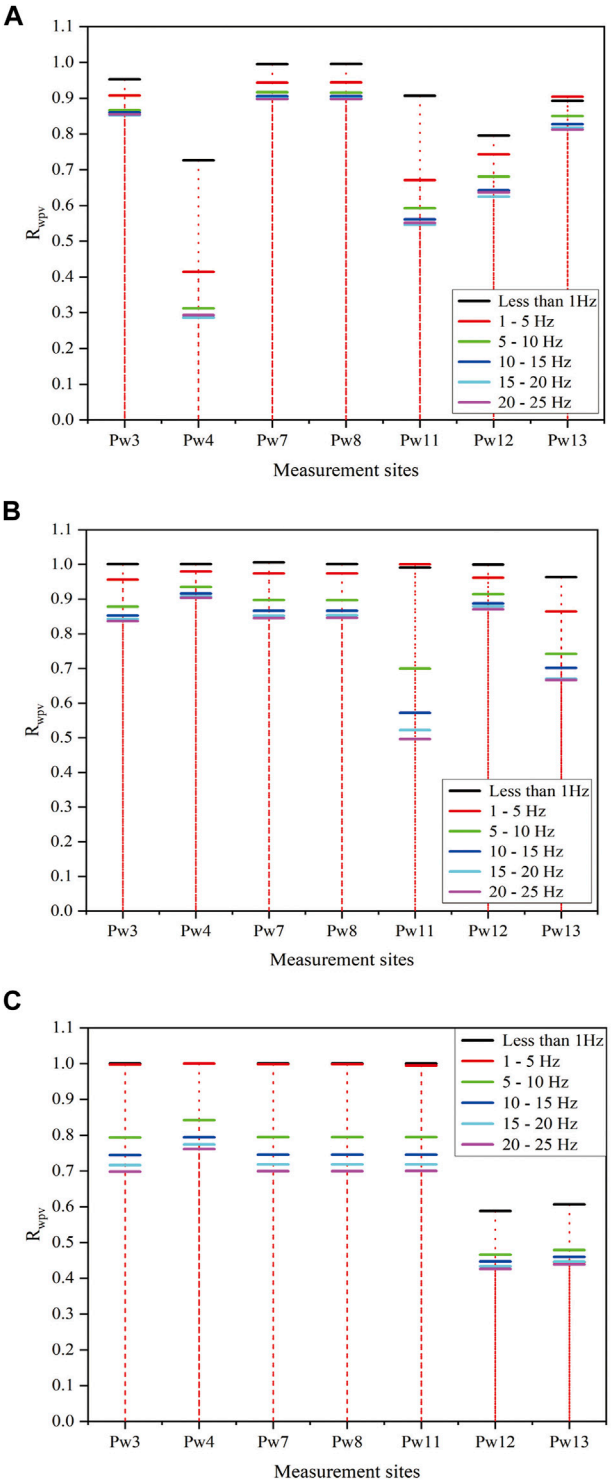

FIGURE 11 | Peak value ratios (R_{WPV}) between the pore water pressures in six frequency bands (less than 1, 1–5, 5–10, 10–15, 15–20 and 20–25 Hz) and the corresponding total dynamic pore water pressures. **(A)** Low shaking intensity (case 1: 113 gal); **(B)** medium shaking intensity (case 3: 339 gal); **(C)** high shaking intensity (case 5: 565 gal).

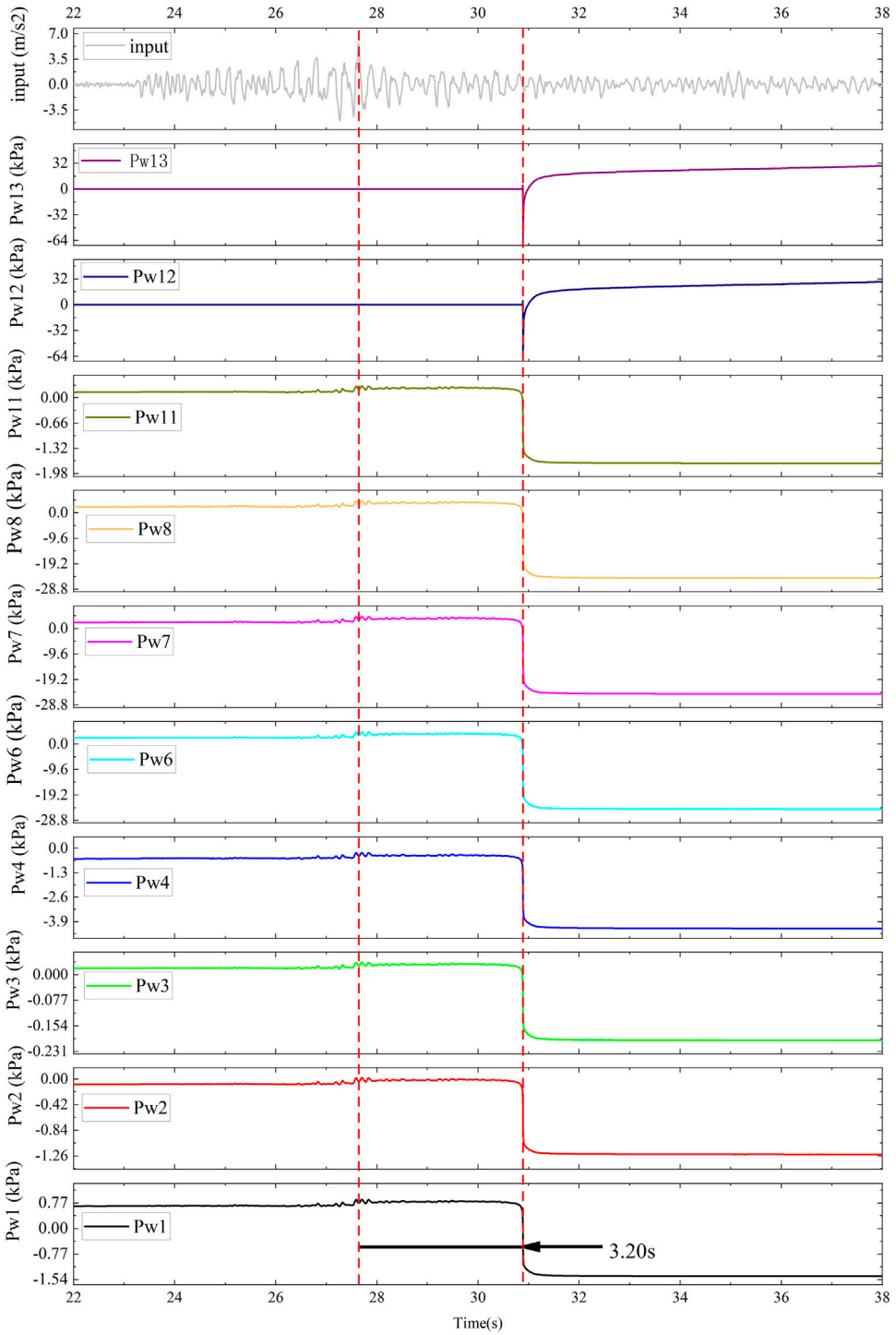

FIGURE 12 | Pore water pressure variation during high-intensity shaking (565 gal).

$$R_{WPV} = \frac{P_w^{(f_a, f_b)}}{P_{wtot}}$$

where R_{WPV} is the pore water pressure peak value ratio, P_w is the peak value of dynamic pore water pressure in measurement sites of the time-history curve, P_{wtot} is the peak value of the monitoring dynamic pore water pressure time-history curve, and (f_a, f_b) is the frequency band between a and b.

The results for the slope under three shaking intensities are presented in **Figure 11**, which shows that the values of R_{WPV} for

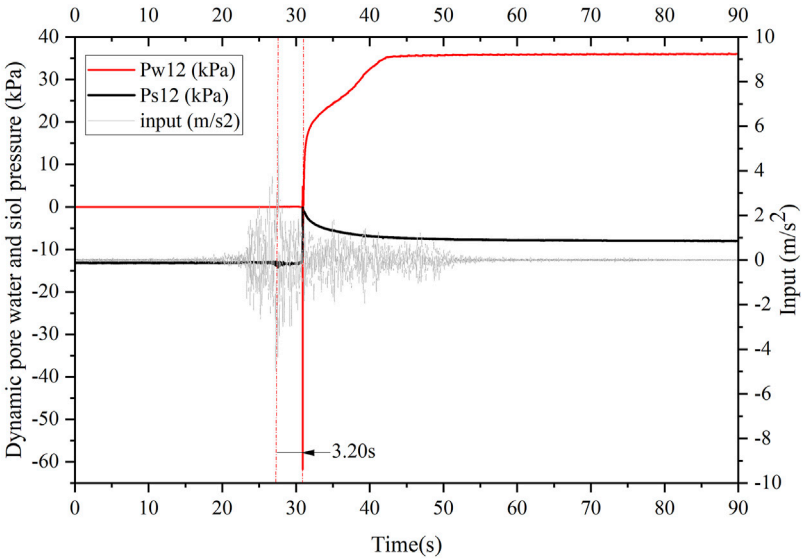

FIGURE 13 | Dynamic pore water pressure and soil pressure of P_w12 and Ps12 in the liquefied zone.

all measured points are greater in the frequency bands less than 5 Hz, and when the frequency is less than 1 Hz, R_{WPV} is greater than 0.6. R_{WPV} becomes approximately stable and shows slight differences under low and moderate shaking intensities (case 1 and case 3, respectively) (**Figures 11A,B**). However, R_{WPV} at frequencies less than 5 Hz appears to be unstable and shows clear differences in the liquefied area under the highest shaking intensity (case 5) (see **Figure 11C**). Nevertheless, the values of R_{WPV} at all measurement sites show slight changes when the frequency is greater than 5 Hz.

Generation of Negative Pore Pressure

When the peak acceleration of input shaking was 565 gal, 3.2 s after the peak acceleration, the pore water pressure at all liquefied monitoring points suddenly decreased to a negative value, as shown in **Figure 12**. The reason is that all sensor data returned to zero before the next testing in each working case, but the actual initial pore water pressure at the monitoring point was not 0 kPa. When tension was generated after sharp shaking, the pore pressure decreased below the initial pore pressure, so the recorded pore water pressure data are negative. During the extrusion deformation, the pore water pressure increased and was greater than the initial pressure as the pore water pressure time history of P_w12 and P_w13 showed, and the value of pore water pressure was positive. The difference between the maximum positive pore pressure and negative pore pressure is the increased amplitude of pore water pressure build-up under the testing case.

Flow-Sliding Motion and Liquefaction Slipping

The liquefaction-induced sliding motion presented in **Figure 9C** could be interpreted based on the monitored dynamic pore water and soil pressure behaviours as follows. In stage 1, under low shaking intensity, excess pore water pressure was not generated. The horizontal driving force generated by shaking reduced the shear resistance, which caused small tensile cracks on the shallow surface of the slope. In stage 2, as the shaking intensity increased, excess pore water pressure was first generated at the bottom of the slope and was greater than the surrounding soil, which reduced the shear resistance of the loess and caused localized liquefaction at the bottom. However, due to the constraint of a rigid baffle at the front of the slope, the liquefied soil did not slide significantly. The upper tensile cracks apparently increased because of the horizontal seismic force and the softening of the soil at the bottom. Finally, in stage 3, as the shaking intensity increased, the water table rose. The excess pore water pressure at the middle of the slope and near the shoulder increased sharply and much more than the surrounding soil pressure (see **Figure 13**). This was due to the acceleration amplification effect, as mentioned previously. The rapid increase in dynamic pore pressure resulted in the liquefaction of surrounding soil. The partial liquefaction of soil slid forward or rapid runout of tensile cracks occurred under the action of earthquake force, resulting in the destruction of the slope body. Long-distance liquefaction slipping occurs if there is no terrain ahead to prevent it or if there is a slope suitable for long-distance sliding, similar to the Yongguang landslide.

CONCLUSION

This study investigated the triggering mechanism of liquefaction-induced landslides in Yongguang village on 22 July 2013, in Minxian County, Gansu Province. A large-scale shaking table model test was conducted on a simulated slope in which the bottom was immersed in water. Based on the results presented in

this paper, the distributions of and variations in the dynamic acceleration, pore water pressure and soil pressure response of the bottom saturated loess slope under simulated earthquakes were studied, and the following conclusions were drawn:

1) The accelerations recorded in slopes increased with increasing distance from the bottom to the upper surface both along the slope surface and inside the model. The dynamic acceleration response in the slope changed markedly under high-intensity shaking, especially in the liquefied zone, which was the internal force that caused soil liquefaction. The acceleration of the liquefied zone indicated that the liquefied area first accelerated by the earthquake force, and after failure, it slid rapidly. The slope was unstable due to liquefaction and presented a liquefaction slipping phenomenon. Mud spraying and water pouring, such as sand liquefaction, appeared locally.
2) Dynamic pore water pressures build-up and fluctuation were the main causes of earthquake liquefaction slipping. As the input shaking intensity increased, the water level in the slope body increased because the permeability of the soil increased as vibration damage increased. The pore water pressure of local soil with high moisture content increased instantaneously, and the strength of the soil decreased. Under the action of continuous vibration, liquefaction occurred, and the liquefied soil was accelerated, resulting in the liquefaction slipping phenomenon.
3) The low-frequency band vibration played an important role in pore water pressure build-up and liquefaction slipping. The synchronous changes in the dynamic pore water pressure and soil pressure as well as the displacement response mainly occurred when the shaking components were in the low-frequency bands, especially below 1 Hz. This kind of resonance phenomenon occurring between the response acceleration and dynamic pore water pressure may have resulted from the change in the natural frequency of the slope after liquefaction. The vibration frequencies leading to large deformation and liquefaction of the slope soil were all below 1 Hz.
4) The mechanism of the Yongguang landslide failure was that the high-intensity earthquake vibration caused the structure of the slope soil to be damaged, and the increased permeability of the earthquake-damaged soil caused the groundwater level to rise, resulting in the liquefaction of the saturated soil. The liquefied soil slid along the long and narrow channels formed by the two sides of the mountain under the action of earthquake forces.

DATA AVAILABILITY STATEMENT

The raw data supporting the conclusions of this article will be made available by the authors, without undue reservation.

AUTHOR CONTRIBUTIONS

WL helped conceive the study and guided the writing of the thesis. WP helped conceive the study, performed the test analysis, and assisted with writing the manuscript. PX conceived the study, assisted with the shaking table data process and stability analysis, and assisted with writing the manuscript. XS and GH helped conceive the study, assisted with the model preparation and shaking tests, and wrote the manuscript. WH performed the stability analysis and field sampling and assisted with writing the manuscript. All authors contributed to the article and approved the submitted version.

FUNDING

Funding for this work was provided by the National Natural Science Foundation of China (No. U1939209), Science for Earthquake Resilience, China Earthquake Administration (XH20058Y) and Basic Scientific Research Fund, Science and Technology Innovation Base of Lanzhou, Institute of Earthquake Forecasting, China Earthquake Administration (2018IESLZ08).

ACKNOWLEDGMENTS

This research was supported by Gaofeng Che and Jinlian Ma (Key Laboratory of Loess Earthquake Engineering, CEA), and we are grateful for their help and valuable discussions on this work. Valuable English editing by AJE is appreciated. Discussions with Xiaosen Kang (ChangAn University), Ning MA (Southwest Jiaotong University), and Yanguo Zhou (Zhejiang University) greatly improved this manuscript. Two reviewers provided valuable comments, which helped us considerably improve this paper.

REFERENCES

Assallay, A. M., Rogers, C. D. F., and Smalley, I. J. (1997). Formation and Collapse of Metastable Particle Packings and Open Structures in Loess Deposits. *Eng. Geology.* 48, 101–115. doi:10.1016/S0013-7952(97)81916-3

Bai, M. X., and Wang, Z. G. (1987). *A Study Report of Low Angle Slip in the Loess Plateau of Ningxia (In Chinese) Earthquake Agency of Ningxia Hui Autonomous.*

Buckingham, E. (1914). On Physically Similar Systems; Illustrations of the Use of Dimensional Equations. *Phys. Rev.* 4, 345–376. doi:10.1103/PhysRev.4.345

Carey, J. M., McSaveney, M. J., and Petley, D. N. (2017). Dynamic Liquefaction of Shear Zones in Intact Loess during Simulated Earthquake Loading. *Landslides* 14, 789–804. doi:10.1007/s10346-016-0746-y

Chai, S. F., Wang, P., and Guo, H. T. (2019). Model Material Similarity and Associated Evaluation for Soil Slopes in A Large-Scale Shaking Table Test (In Chinese). *China Earthquake Eng. J.* 41, 1308–1315. doi:10.3969/j.issn.1000-0844.2019.05.1308

Feng, X., Jiang, Q., Zhang, X., and Zhang, H. (2019). Shaking Table Model Test on the Dynamic Response of Anti-dip Rock Slope. *Geotech Geol. Eng.* 37, 1211–1221. doi:10.1007/s10706-018-0679-4

Fletcher, L. A. (2000). Contrasting Failure Behaviour of Two Large Landslides in Clay and Silt. *Can. Geotech. J.* 39, 46–62. doi:10.14288/1.0089531

Gao, J. L. (2021). *Experimental Study on Liquefaction Slip Mechanism of Loess Low-Angle Slope:A Case Study of Shibeiyuan Landslide S (In Chinese)*. Master's thesis (Xi'an (China): Northwest university).

Hwang, H., Wang, L. M., and Yuan, Z. H. (2000). Comparison of Liquefaction Potential of Loess in Lanzhou, China, and Memphis, USA. *Soil Dyn. Earthquake Eng.* 20 (5), 389–395. doi:10.1016/S0267-7261(00)00088-9

Ishihara, K., Okusa, S., Oyagi, N., and Ischuk, A. (1990). Liquefaction-Induced Flow Slide in the Collapsible Loess Deposit in Soviet Tajik. *Soils and Foundations* 30, 73–89. doi:10.3208/sandf1972.30.4_73

Jefferson, I. F., Evstatiev, D., Karastanev, D., Mavlyanova, N. G., and Smalley, I. J. (2003). Engineering Geology of Loess and Loess-like Deposits: a Commentary on the Russian Literature. *Eng. Geology.* 68 (3/4), 333–351. doi:10.1016/S0013-7952(02)00236-3

Lin, M.-L., and Wang, K.-L. (2006). Seismic Slope Behavior in A Large-Scale Shaking Table Model Test. *Eng. Geology.* 86, 118–133. doi:10.1016/j.enggeo.2006.02.011

Liu, K. (2020). *Earthquake-Induced Failure Mechanism and Stability Evaluation of Loess Slope under Rainfall Effects (In Chinese)*. dissertation's thesis (Lanzhou (China): Lanzhou university).

Ma, N., Wu, H., Ma, H., Wu, X., and Wang, G. (2019). Examining Dynamic Soil Pressures and the Effectiveness of Different Pile Structures inside Reinforced Slopes Using Shaking Table Tests. *Soil Dyn. Earthquake Eng.* 116, 293–303. doi:10.1016/j.soildyn.2018.10.005

Major, J. J., and Iverson, R. M. (1999). Debris-flow Deposition: Effects of Pore-Fluid Pressure and Friction Concentrated at Flow Margins. *Geol. Soc. Am. Bull.* 111 (10), 1424–1434. doi:10.1130/0016-7606(1999)111<1424:dfdeop>2.3.co;2

Prakash, S., and Puri, V. K. (1982). *Liquefaction of Loessial Soils*. Seattle, Wash: Anon Proc of Third International Conference on Seismic Microzonation, 1101–1107.

Sassa, K., Wang, G., Fukuoka, H., and Vankov, D. A. (2005). Shear-Displacement-Amplitude Dependent Pore-Pressure Generation in Undrained Cyclic Loading Ring Shear Tests: an Energy Approach. *J. Geotech. Geoenviron. Eng.* 131131, 7506–7761. doi:10.1061/(ASCE)1090-024110.1061/(asce)1090-0241(2005)131:6(750)

Su, Z. Z., Yuan, Z. M., and Zhao, J. Q. (2003). A Review on Studies Concerned with the 1303 Hongtong, Shanxi, Earthquake of M8 (In Chinese). *Earthquake Res. Shanxi* (3), 4–9. doi:10.3969/j.issn.1000-6265.2003.03.009

Wang, F. W., Sassa, K., and Wang, G. (2002). Mechanism of a Long-Runout Landslide Triggered by the August 1998 Heavy Rainfall in Fukushima Prefecture, Japan. *Eng. Geology.* 63, 169–185. doi:10.1016/S0013-7952(01)00080-1

Wang, G. H., Sassa, K., Fukuoka, H., and Wang, F. W. (1998). "Study on the Excess Pore Pressure Generation in Laboratory-Induced-Landslides," in Proceedings of 8th Congress of IAEG. Editors D. P. Moore and O. Hungr (Rotterdam: Balkema), 4237–4244. Vancouver.6

Wang, G., and Sassa, K. (2001). Factors Affecting Rainfall-Induced Flowslides in Laboratory Flume Tests. *Géotechnique* 51 (7), 587–599. doi:10.1680/geot.51.7.587.51386

Wang, G., Sassa, K., Fukuoka, H., and Tada, T. (2007). Experimental Study on the Shearing Behavior of Saturated Silty Soils Based on Ring-Shear Tests. *J. Geotech. Geoenviron. Eng.* 133, 319–333. doi:10.1061/(asce)1090-0241(2007)133:3(319)

Wang, G., and Sassa, K. (2003). Pore-pressure Generation and Movement of Rainfall-Induced Landslides: Effects of Grain Size and fine-particle Content. *Eng. Geology.* 69, 109–125. doi:10.1016/S0013-7952(02)00268-5

Wang, G., Zhang, D., Furuya, G., and Yang, J. (2014). Pore-Pressure Generation and Fluidization in A Loess Landslide Triggered by the 1920 Haiyuan Earthquake, China: A Case Study. *Eng. Geology.* 174, 36–45. doi:10.1016/j.enggeo.2014.03.006

Wang, L. M., Liu, H. M., Li, L., and Sun, C. S. (2000). Laboratory Study on the Mechanism and Beheviors of Saturated Loess Liquefaction (In Chinese). *China J. Geotechnical Eng.* 22 (1), 89–94. doi:10.3321/j.issn.1000-4548.2000.01.016

Wang, L. M., and Wu, Z. J. (2013). Earthquake Damage Characteristics of the Minxian–Zhangxian Ms6.6 Earthquake and its Lessons (In Chinese). China Earthquake. *Eng. J.* 35 (3), 401–412. doi:10.3969/j.issn.1000-0844.2013.03.0401

Wang, L. M. (2003). *Loess Dynamics (In Chinese)*. Beijing: Earthquake Press.

Wang, L. M. (2020). Mechanism and Risk Evaluation of Sliding Flow Triggered by Liquefaction of Loess Deposit during Earthquakes (In Chinese). *Chin. J. Geotechn. Eng.* 42, 1–19. doi:10.11779/CJGE202001001

Wang, Q., Wang, L. M., Wang, J., Zhong, X. M., and Chai, S. F. (2014). "Research Progress of the Loess Seismic Liquefaction (In Chinese)," in , 34, 898–903.*Earthquake Eng. Eng. Dyn.*. doi:10.13197/j.eeev.2014.S0.898.wangq.141

Wang, Q., Wang, L. M., Yuan, Z. X., Wang, P., and Ding, F. M. (2012). A Study of Loess Liquefaction Induced by the Wenchuan Ms8.0 Earthquake in Tianchuan, Qingshui County, Gansu Province (In Chinese). *Hydrogeology Eng. Geology.* 37, 63–67. doi:10.16030/j.cnki.issn.1000-3665.2012.02.019

Wang, Q., Wang, Z., Su, Y., Wang, L., Ma, H., et al. (2021). Characteristics and mechanism of the landslide in Yongguang village, Minxian County, China. *Nat. Hazards* 105, 1413–1438. doi:10.1007/s11069-020-04360-7

Wu, Z. J., Sun, J. J., Chen, Y. J., Wang, Q., and Zhao, W. C. (2015). Analysis of Disaster-Causing Mechanism of Loess Landslides Induced by the Minxian-Zhangxian MS6.6 Earthquake, China. *Jpn. Geotechnical Soc. Spec. Publ.* 1 (7), 40–45. doi:10.3208/jgssp.cpn-21

Xu, C., Xu, X. W., and Zheng, W. J. (2013). Compiling Inventory of Landslides Triggered by Minxian-Zhangxian Earthquake of July 22,2013 and Their Spatial Distribution Analysis. (In Chinese). *J. Eng. Geology.* 2013 (05), 736–749. doi:10.1016/j.jseaes.2014.06.014

Xu, S. H., Wu, Z. J., Su, J. J., Yan, W. J., Su, H. J., and Su, Y. Q. (2013). Study of the Characteristics and Inducing Mechanism of Typical Earthquake Landslides of the Minxian-Zhangxian Ms6.6 Earthquake (In Chinese). *China Earthquake Eng. J.* 35, 471–476. doi:10.3969/j.issn.1000-0844.2013.03.0471

Zhang, D., Takeuchi, A., and Sassa, K. (1995). The Motion Characteristics of Loess Landslides Induced by the Haiyuan Earthquake in the Ningxua Province, China. *Landslides* 32, 12–17. doi:10.3313/jls1964.32.1_12

Zhang, D. X., and Sassa, K. (1996). A Study of the Mechanism of Loess Landslides Induced by Earthquakes (In Japanese). *J. Jpn. Soc. Erosion Control. Eng.* 49, 4–13. doi:10.11475/sabo1973.49.2_4

Zhang, F., Wang, G., Kamai, T., Chen, W., Zhang, D., and Yang, J. (2013). Undrained Shear Behavior of Loess Saturated with Different Concentrations of Sodium Chloride Solution. *Eng. Geology.* 155, 69–79. doi:10.1016/j.enggeo.2012.12.018

Zhang, X. C., Huang, R. Q., Xu, M., Pei, X. J., Han, X. S., Song, L. J., et al. (2014). Loess Liquefaction Characteristic and its Influential Factors of Shibeiyuan Landslide (In Chinese). *Rock Soil Mech.*, 801–810. doi:10.16285/j.rsm.2014.03.013

Zhang, Z. L., Wu, S. R., Wang, T., Tang, H., M., and Liangs, C. Y. (2018). Influence of Seismic Wave Amplitude on Dynamic Response of Loess-Mudstone Slope. (In Chinese). *Rock Soil Mech.* 39 (7), 2335–2349. doi:10.16285/j.rsm.2016.2335

Zhang, Z., and Wang, L. (1995). Geological Disasters in Loess Areas during the 1920 Haiyuan Earthquake, China. *GeoJournal* 36, 269–274. doi:10.1007/BF00813183

Zhao, J. Q., Zhang, D. W., and Gao, S. Y. (2003). Huanbu Ground Slide, the Relic of 1303 Hongtong, Shanxi, Earthquake of M8(in Chinese). *Earthquake Res. Shanxi* (3), 16–23. doi:10.3969/j.issn.1000-6265.2003.03.011

Zheng, S. M., Zhou, B. F., Wen, R. Z., and Wang, L. (2010). Discussion on Baseline Correction of Strong Motion Data. *J. Geodesy Geodynamics* 30 (3), 47–50. (In Chinese). doi:10.3969/j.issn.1671-5942.2010.03.011

Conflict of Interest: The authors declare that the research was conducted in the absence of any commercial or financial relationships that could be construed as a potential conflict of interest.

frontiers | Frontiers in Earth Science

ORIGINAL RESEARCH
published: 26 April 2022
doi: 10.3389/feart.2022.790882

Effect of Sulfate on the Aggregation of Clay Particles in Loess

*Liuyang Gu, Jingke Zhang, Lianxing Guo and Qingfeng Lv**

Laboratory of Mechanics on Disaster and Environment in Western China, Ministry of Education, School of Civil Engineering and Mechanics, Lanzhou University, Lanzhou, China

The type and structure of clay minerals are among the main factors affecting the physical and mechanical properties of loess, and the salt content plays a dominant role in many factors affecting aggregation. In this study, the grain size analysis, Atterberg limits tests, scanning electron microscopy (SEM), and energy spectrum analysis (EDS) were used to explore the microstructure and physicochemical mechanisms of the aggregation of clay particles. Finally, the unconfined compressive test, direct shear test, and elastic wave velocity test were conducted to explore the effect of sulfate agglomeration on loess properties. The results show that the salt-washing process leads to the loss of the original soluble salt, dispersion of the original aggregates, and increase of fine particles, such as fine silt and clay. With the increase of sulfate content, the content of fine silt and clay decreases, the liquid limit and plasticity index decrease, the plasticity limit remains unchanged, the aggregate content of fine silt and clay increases, the adsorption capacity weakens, and the diffusion layer compresses and thins. The mechanical test results show that when the sulfate content is less than 3%, the sulfate is almost completely dissolved and the aggregate is less, which increases compressive strength and the cohesion; when the sulfate content is more than 3%, too much sulfate cannot be dissolved and precipitated; hence, the aggregate increases. However, the existence of large volume mirabilite crystals reduces the cementation, which reduces the compressive strength, increases the internal friction angle, and weakens the cohesion.

Keywords: sulfate, aggregation, Atterberg limits, microstructure, macroscopic characterization

OPEN ACCESS

Edited by:
Gonghui Wang,
Kyoto University, Japan

Reviewed by:
Junhui Zhang,
Changsha University of Science and Technology, China
Xiangjun Pei,
Chengdu University of Technology, China

****Correspondence:***
Qingfeng Lv
lvqf@lzu.edu.cn

Specialty section:
This article was submitted to Geohazards and Georisks, a section of the journal Frontiers in Earth Science

Received: *07 October 2021*
Accepted: *14 March 2022*
Published: *26 April 2022*

Citation:
Gu L, Zhang J, Guo L and Lv Q (2022) Effect of Sulfate on the Aggregation of Clay Particles in Loess. Front. Earth Sci. 10:790882. doi: 10.3389/feart.2022.790882

INTRODUCTION

There have been many studies on the interaction between salt and clay minerals, and these interactions are mainly manifested in the macroscopic effect on the Atterberg limits. Some scholars have tested bentonite, kaolin, beidellite, montmorillonite, and artificial bentonite kaolin mixtures (Di Maio et al., 2004), and others have tested the consistency limits liquid limit, plastic limit, plasticity index, sediment volume, and squeezing properties) of 10 soil types with distilled water and natural seawater (Yukselen-Aksoy et al., 2008), and all of the results have indicated that salt has a greater influence on the plastic limit of montmorillonite but less on kaolinite and illite. Based on a large number of experiments, the proportion, optimum water content, liquid limit, and plastic limit of the saline soil prepared from the Luoyang loess were obtained, which decreased with the increase of chloride content, with a linear variation law; the maximum dry density of the chloride saline soil increased with the increase of salt content when the salt content was less than 8% and decreased with the increase of salt content when the salt content was more than 8% (Wang et al., 2009). (Bjerrum and Rosenqvist, 1956a) found that the shear strength of clay deposited in fresh water would be two to

three times of that deposited in brine. Using the clay consistency limits of four different salt solutions (ammonium chloride, potassium chloride, copper sulfate, and ferrous sulfate) at eight different concentrations, it was proven that the liquid limit increased with the increase of the concentration of the salt solution containing chloride ions and decreased with the increase of the concentration of the salt solution containing sulfate ions. In addition, whether it was saline soil containing chloride or sulfate ions, the plastic limit of clay decreased at a low salt concentration and increased at a high salt concentration (Arasan and Yetimoglu, 2008). By studying the effects of three different inorganic salt solutions on the mixing characteristics, liquid limits, free expansion, consolidation characteristics, and water conductivity of two clay–bentonite mixtures, it was found that the salt content of the salt solution increased the maximum dry density of the mixture and lowered the optimum moisture content and liquid limit of the mixture. The main reason for this effect was that the diffusion layer of the clay particles changed (Karimpour-Fard et al., 2011), which is consistent with the results of the study conducted by (Mishra et al., 2005). Some studies illustrated that the liquid limit of montmorillonite was significantly reduced by the influence of the salt solution (Di Maio, 1996; Gleason et al., 1997). The thickness of the diffusion layer was mainly caused by the concentration of sodium ions in pore water (Rao et al., 1993).

The aggregation of clay particles is the main microscopic mechanism of the influence of salt on Atterberg limits. From a quiescent sedimentation test of montmorillonite with different salt content, it was found that the aggregation process presented different speeds with the change of salt content, and the speed was the fastest close to 19% salt content and the slowest close to 1% salt content (Lin et al., 2013). SEM and FT-IR were applied to analyze the microstructure of aggregates, and it was found that the strength and particle size of aggregates increased with increasing salt content. The role of salt was to replenish the electrolyte, where the electric double layer adhered to form a dense aggregate (Liu et al., 2007a). In addition, a 2.25 m settling column was used to study the effect of the salt content on the aggregation velocity of fine particles, indicating that the aggregation velocity increased with the increase of salt content and that the aggregation velocity in brine was greater than that of fresh water (Portela et al., 2013). Some scholars measured the particle aggregation rate of three types of clays in the same salt solution and found that the probability of montmorillonite aggregation was higher than that of kaolin and illite, and montmorillonite was most easily aggregated (Edzwald and O'melia, 1975). However, it was found that the aggregation characteristics of different clay minerals (montmorillonite, illite, and kaolin) in still water affected by the salt content of water were different: illite and kaolin were both aggregated at a salt content of 2–3%, while the aggregation of montmorillonite did not change significantly with salt content (Whitehouse et al., 1958a).

The type and structure of clay minerals are among the main influencing factors affecting the physical and mechanical properties of the loess. There is a special soil layer called the loess salted soil distributed in Northwest China, which has the characteristics of Malan loess and saline soil. Because of the interaction of salt and clay minerals, the physical and mechanical properties of loess salted soil are complex. At present, studies on sulfate saline soil mostly focused on exploring the influence of salt change on the internal structure of single-clay minerals such as highly active bentonite and the influence of salt change on the macroscopic properties of soil (Liu et al., 2007b). Macroscopically, it is mainly manifested in the study of limit water content (Aksoy et al., 2008). Sivchantra explored the shear strength of saline soil with different water content and salt content at different temperatures. The results show that the shear strength decreases with the increase of salt content at room temperature, has the highest shear strength at zero, and 0 and 0.5% saline soil have the highest shear strength at zero (Chantra, 2019). Di Mai et al. (2004) showed that salt has a great impact on the liquid plastic limit of montmorillonite but has little impact on kaolinite and illite (Aksoy et al., 2008). However, there are few studies on the influence of salt change on the physical and mechanical properties of loess clay agglomeration.

Therefore, sulfate saline soil with different mass ratios (0, 0.3, 0.5, 3, 5.0, and 8.0%) was prepared from the soil after salt washing. In this study, based on the grain size analysis and Atterberg limits test, the aggregation of clay particles by sulfate was studied. Scanning electron microscopy (SEM) and energy spectrum analysis (EDS) were used to study the microstructure and physicochemical mechanisms of the aggregation of clay particles. Finally, through the unconfined compressive test, direct shear test and elastic wave velocity test were conducted to explore the effect of sulfate agglomeration on loess engineering properties.

MATERIALS AND EXPERIMENTAL METHODS

Materials

The original loess used in the experiment is Malan loess in Lanzhou. The natural water content is 5.89%. The basic physical parameters are shown in **Table 1**.

Anhydrous sodium sulfate is a kind of white crystalline particle or powder, the content of which is not less than 99%. The specifications are shown in **Table 2**.

TABLE 1 | Basic physical parameters of the original loess.

Plasticity index			Mass fraction (%)		
Liquid limit (%)	Plastic limit (%)	Plasticity index	2–0.075 mm	0.075–0.01 mm	<0.01 mm
27.0	15.5	11.5	10.17	73.72	16.12

TABLE 2 | Specification parameters of sodium sulfate.

Sodium sulfate	Water insoluble	Loss on ignition	Chloride	Others
≥99.0	≦0.005	≦0.2	≦0.001	≦0.121

TABLE 3 | Conductivity test results of the original loess.

Salt washing times	Conductivity (us/cm)							
1	769	774	758	765	802	795	771	757
2	319	325	322	343	324	335	319	324
3	221	220	221	220	220	219	221	222
4	159	158	164	159	169	164	158	168
5	138	138	136	136	137	136	135	136
6	135	136	133	135	136	135	134	133

Sample Preparation

To explore the nature of the fine particles and avoid the influence of larger particles on the test results, the salted soil was crushed and passed through a 2-mm sieve to remove impurities such as organic compounds or large particles. Then, the sieved soil sample and distilled water were mixed according to a volume ratio of 1:5, and the salt was sufficiently dissolved by stirring. After resting the solution until clarified, the supernatant was sucked out by a straw to leave behind a soil sample. After repeated artificial desalination of the soil samples, the desalted loess was obtained, and the process is defined as salt washing. It is necessary to test the conductivity of each soil suspension with a conductivity meter to test the desalting effect of soil samples. In addition, the temperature was controlled at 20°C during the test. Conductivity test results of original loess are shown in **Table 3**.

According to the preparation gradient, a certain amount of anhydrous sodium sulfate in powder was weighed to form the sulfate saline soil with 0, 0.3, 0.5, 3, 5, and 8% salt content. The prepared saline soil was placed for 7 days to obtain the maximum exchange adsorption of salt in the soil sample. To make the salt completely displace in the soil, the soil sample after adsorption should be added with sufficient pure water, immersed in pure water for 2 days, and then dried in a natural state so that the salt can completely displace in the soil. The air-dried samples were reground, mixed, and passed through a 2-mm sieve.

TABLE 4 | Test information.

Test	Instrument
Grain size analysis test	Mastersizer 2,000 laser particle size analyzer
Atterberg limits test	LP-100D liquid-plastic limit tester
Scanning electron microscopy	Thermoscientific Apreos scanning electron microscopy
EDS	INCA energy dispersive X-ray spectroscopy (EDS) system
Compression test	CSS-WAW300 universal material testing machine
Shear test	ZJ strain–controlled direct shear apparatus
Elastic wave velocity test	RSM-SY5 (T) non-metallic ultrasonic testing analyzer

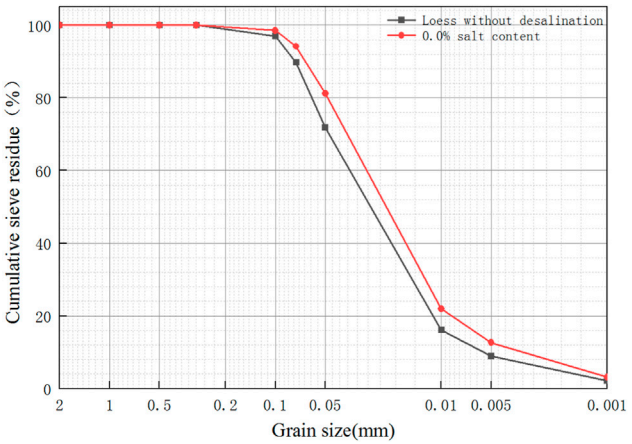

FIGURE 1 | Particle size distribution graph of loess samples before and after salt washing.

Experimental Methods

The Atterberg limits of soil reflect the difficulty with which the soil changes from one state to another. The greater the plasticity index of the soil, the stronger the plasticity is. An LP-100D liquid-plastic limit tester was used to measure the depth of the cone at different water contents. A Mastersizer 2,000 laser particle size analyzer was used to test the particle size and determine the mass fraction of each particle group. A Thermoscientific Apreos scanning electron microscope was used to characterize the micromorphology, and the chemical element analysis was analyzed by an INCA energy-dispersive X-ray spectroscopy (EDS) system. Therefore, on the basis of the aforementioned tests, the unconfined compressive strength and elastic wave velocity were studied by a CSS-WAW300 universal material testing machine and RSM-SY5 (T) non-metallic ultrasonic testing analyzer. A ZJ strain–controlled direct shear apparatus was used to explore the relationship between cohesion, internal friction angle, and salt content. The test instrument information is shown in **Table 4**.

RESULTS AND ANALYSES

Physical Index

The Results of the Grain Size Analysis Test

Figure 1 is the grain size analysis graph of loess samples before and after salt washing. The loess before salt washing is defined as the loess without desalination, and the loess after salt washing is defined as saline soil with 0% salt content. It can be seen from the figure that the particle composition of the loess without desalination and saline soil with 0% salt content is mainly powder, the content of which is more than 80%. The content of fine particles in the soil with 0% salt content increased, and the amount of fine silt and clay (<0.01 mm) increased by 6%. The results show that the salt washing process makes the larger particles finer so that the cumulative

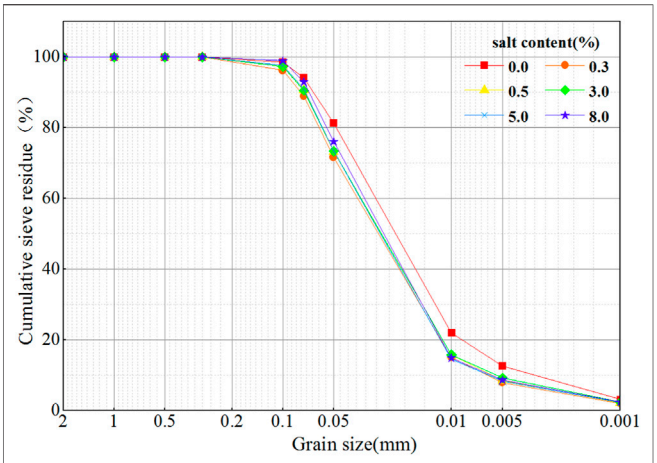

FIGURE 2 | Particle size distribution graph of different sulfate content in saline soil.

TABLE 5 | Indexes of different soils.

Sulfate content (%)	Indexes	Particle diameter (mm)
Loess without desalination	Coefficient of uniformity	6.339
	Coefficient of curvature	1.117
0	Coefficient of uniformity	8.781
	Coefficient of curvature	1.738
0.3	Coefficient of uniformity	2.364
	Coefficient of curvature	0.071
0.5	Coefficient of uniformity	6.140
	Coefficient of curvature	1.143
3.0	Coefficient of uniformity	6.426
	Coefficient of curvature	1.169
5.0	Coefficient of uniformity	5.689
	Coefficient of curvature	1.092
8.0	Coefficient of uniformity	5.690
	Coefficient of curvature	1.144

percentage content of each particle size increases compared with the loess without desalination.

Figure 2 shows the grain size analysis graph of different sulfate contents in saline soil. It can be seen that the fine silt and clay of saline soil display obvious changes. When the particle size is greater than 0.075 mm (mainly sand), the change in the particle size distribution graph is small with the change of the sulfate content, indicating that sulfate content has no effect on the particle size; when the particle size is less than 0.075 mm, there is a significant difference in the grain size analysis graph between the saline soil and desalted soil, with a maximum difference of 7.48%. With the addition of sulfate, the particle state changes, and the content of fine particles decreases.

According to the particle analysis curve, different grading parameters of all soil samples can be obtained. The results are shown in **Table 5**. It can be seen that the non-uniformity coefficient of all the samples is greater than 5, and the curvature coefficient is 1–3. Therefore, the existence of sulfate has no effect on soil gradation.

The grain composition of soil includes the particle size and proportion of each particle size in the soil, among which particle size is the main factor affecting soil properties. With the increase in sulfate concentration, the ion content increases gradually, and the thickness of the colloidal diffusion layer gradually decreases, which breaks the balance of the electrostatic force in the soil. In addition, the decrease of fine particles in soil leads to the decrease in the ability of the soil to adsorb weakly bound water and enhancing the aggregation of fine particles and clay particles. The addition of sulfate as an electrolyte reduces the proportion of fine particles and clay because of aggregation, which leads to a decrease of wet water of the cohesive soil and capillary water rising height and affects the water-physical properties of the soil, such as permeability, disintegration, and grain composition.

The Results of the Atterberg Limits Test

To ensure the reliability of the test results, three parallel tests are conducted for each sample, and the test parameters within the allowable error range are selected as the final results. That is, the double-logarithm curve of water content–cone penetration depth shall ensure that the two straight lines formed by the high water content point and the other two water content points and the difference of water content at the subsidence of 2 mm shall be less than 2%.

Table 6 shows the Atterberg limits graph of all samples. It can be seen from the table that the loss of soluble sulfate and scattering of agglomerated particles in the process of salt washing leads to the increase of clay particles, resulting in the increase of liquid limit, plastic limit, and plastic index of the test loess after salt washing. In addition, when the sulfate content is less than 3%, the liquid limit, plastic limit, and plasticity index fluctuation value fluctuate greatly; when the sulfate content is more than 3%, the liquid limit, plastic limit, and plastic index are stable. In general, with the increase of sulfate content, the liquid limit and plastic index decrease, and the plastic limit changes slightly but has a certain increasing trend.

On the one hand, the sulfate solution in soil pores gradually reaches saturation, while the excess sulfate exists in the form of crystals between the soil particles (Chen et al., 2015). The existence of sulfate crystals has a certain effect of plugging and cementation on the soil pores, which makes the pore diameter of the soil reduce, the soil more dense, and the plasticity reduce. On the other hand, as an electrolyte, sulfate changes the concentration of water and the content ratio of ions in the soil, aggregating the fine silt and clay so that the proportion is relatively increased, and the electric double-layer on the surface of the soil particles is affected. The diffusion layer is compressed, the thickness of the hydrated film is thinned, the repulsion between the soil particles is weakened, the attraction is enhanced, the spacing of the particles is reduced, and the amount of water that can be adsorbed by the particles is increasingly less (Lei et al., 2001). In general, the liquid limit and plasticity index of the soil decrease.

Microscopic Test

SEM

To clearly observe the flocculated structure of "soil particles," 1,000× electron microscopy magnification was chosen. SEM was

TABLE 6 | Atterberg limits graph of all samples.

Sulfate content (%)	Liquid limit (%)	Plastic limit (%)	Plasticity index
Loess without desalination	27.0	15.5	11.5
0.0	31.6	15.6	16.0
0.3	32.4	14.1	18.3
0.5	29.7	17.5	17.2
3.0	31.0	13.1	17.9
5.0	28.6	15.0	13.6
8.0	27.0	18.9	8.1

labeled and is shown in **Figure 4**. **Figures 3A–F** show that with the increasing sulfate content, sulfate as an electrolyte has an aggregation effect on some fine particles. According to the results of the granule analysis test, the aggregation consists of fine silt and clay. With the increase of sulfate content, the number and volume of irregular aggregates on the soil surface increase, that is, sulfate has a certain degree of elutriation on soil particles. When the sulfate content reaches 8%, a large number of sodium sulfate crystals are precipitated.

EDS

Table 7 shows the element weight percentage statistics of different sulfate contents in saline soil according to EDS. It can be seen from **Table 5** that the test soils with different sulfate contents generally comprise C, O, Na, Al, Si, etc., of which the most abundant element is O, and the content of Si is second. The composition elements and proportion of saline soil with different sulfate contents are approximately the same. For the same clay mineral, the Si/Al ratio decreases with increasing sulfate content.

Mechanical Property

The results of basic physical tests and microscopic test show that the existence of sulfate makes the clay particles agglomerate in the loess, and the change of the internal structure of loess particles will inevitably have a certain impact on the mechanical properties of the loess.

Compaction Test

Figure 4 shows the compaction curve of saline soil with different sulfate content. It can be seen from the figure that the curve change trend of different sulfate content of sulfate soil is similar. On the dry side of the compaction curve (the moisture content is

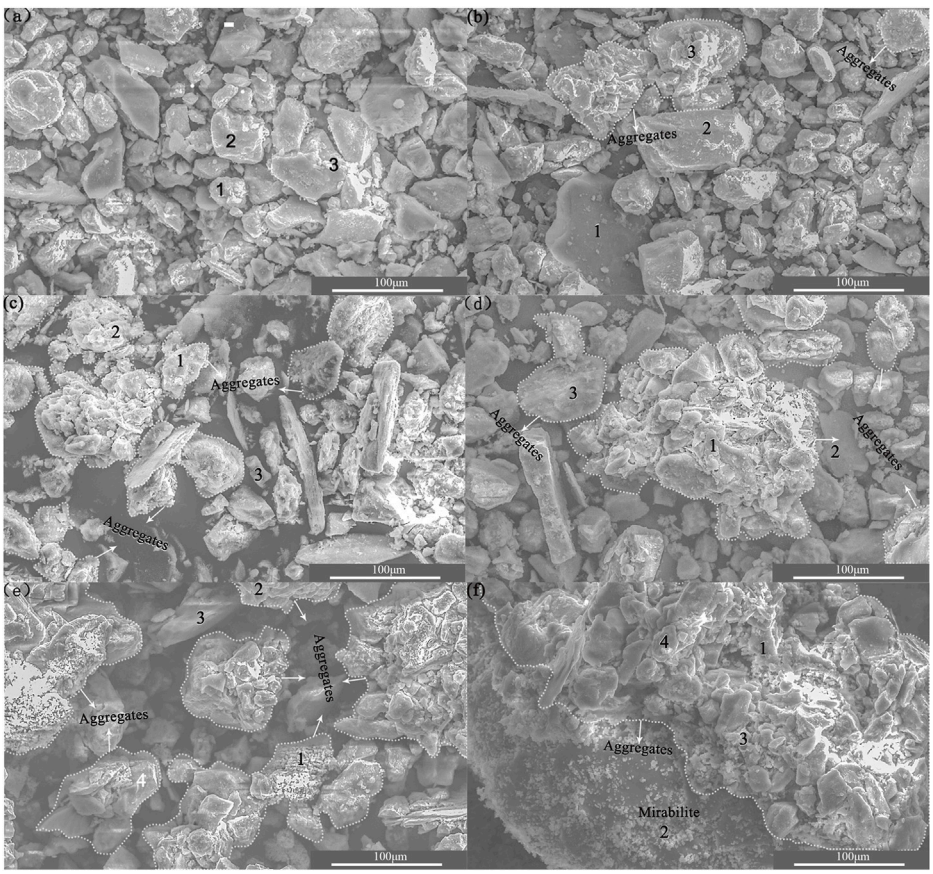

FIGURE 3 | SEM graph of different sulfate content in saline soil **(A)**: 0% salt content, **(B)**: 0.3% salt content, **(C)**: 0.5% salt content, **(D)**: 3.0% salt content, **(E)**: 5.0% salt content, and **(F)**: 8.0% salt content.

TABLE 7 | Element weight percentage statistics of different sulfate content in saline soil.

Sulfate content (%)	Spot	C	O	Na	Al	Si	Fe	Si/Al	Description
0.0	1	11.98	53.00	1.41	2.26	27.33	0.78	9.96	Montmorillonite
	2	3.53	24.74	0	9.50	29.51	4.02	2.48	Kaolinite
	3	38.66	38.12	0.80	1.98	13.94	1.41	5.03	Montmorillonite
0.3	1	12.21	44.02	1.86	4.78	27.72	0	—	Montmorillonite
	2	7.97	46.72	2.01	0	20.17	15.82	—	Illite
	3	6.21	31.11	1.90	7.75	24.19	13.74	1.62	Kaolinite
0.5	1	10.22	48.56	0.32	2.82	32.12	1.47	8.74	Montmorillonite
	2	7.32	41.63	1.17	13.94	20.58	4.12	1.24	Kaolinite
	3	1.34	6.49	0.09	4.01	17.67	0	—	Montmorillonite
3.0	1	5.85	53.20	3.10	12.15	16.12	1.89	1.19	Kaolinite
	2	7.36	41.11	10.15	10.50	27.91	0.13	2.54	Illite
	3	7.67	53.21	1.41	0	35.53	0.14	—	Montmorillonite
5.0	1	5.01	38.74	36.40	1.16	1.59	0.37	1.14	Kaolinite
	2	8.29	38.71	0	0.70	48.47	0.44	—	Montmorillonite
	3	6.59	51.03	0.65	13.21	19.33	2.15	1.30	Kaolinite
	4	4.71	41.25	19.12	6.56	7.66	1.19	1.03	Kaolinite
8.0	1	4.08	40.59	26.76	2.69	3.92	1.79	1.06	Kaolinite
	2	11.09	27.39	28.81	0	0.06	0.15	0.80	Kaolinite
	3	5.76	48.83	1.26	5.32	34.49	0.61	5.90	Montmorillonite
	4	4.45	35.80	30.66	2.27	4.72	0	—	Kaolinite

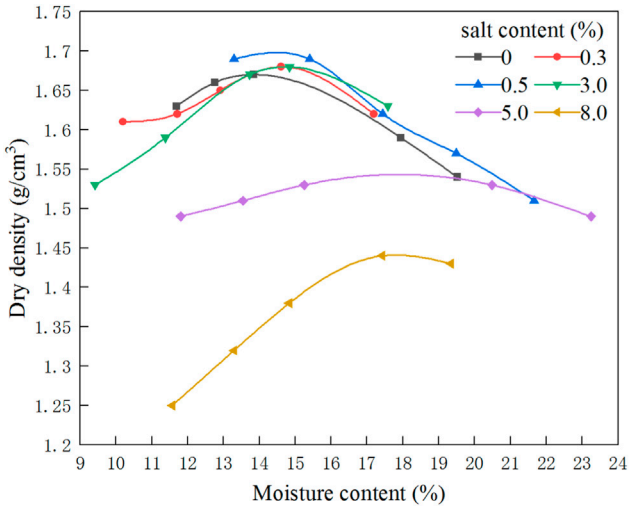

FIGURE 4 | Compaction curve of sulfate soil with different sulfate content.

lower than the optimal moisture content), the dry density increases with the increase of the moisture content and vice versa. But the peak point of the compaction curve is different. With the increase of sulfate content, the peak point shifts to the lower right, that is, with the increase of sulfate content, the optimum moisture content increases, and the maximum dry density decreases.

When the sulfate content is low, the sodium sulfate is almost completely dissolved. With the increase of the sulfate content, the precipitated sodium sulfate crystals further absorb water to form larger mirabilite crystals. The existence of crystals will increase the connection strength of soil, resulting in the decrease of the maximum dry density of saline soil. In addition, because of the strong hydration of sodium ions and existence of sodium sulfate decahydrate, the optimum moisture content increases with the increase of sulfate content (Pécsi and Bariss, 1993).

Compression Test

Figure 5 shows the relationship between compressive strength and sulfate content of sulfate saline soil. It can be seen from the figure that with the increase of sulfate content, the compressive strength increases first and then decreases, and the maximum compressive strength is obtained in this process. It shows that a certain amount of sulfate in saline soil can improve the strength of soil, but too much sulfate in saline soil is unfavorable to the soil.

The cementation of sulfate crystals has gradually developed into the main factor affecting the compression test. With the increase of sulfate content, the cementation becomes stronger, and the compressive strength reaches the peak. After the peak point, with the increase of sulfate content, excessive aggregates and larger sulfate crystals lead to the increase of soil porosity and roughness, which lead to the decrease of cementation and compressive strength.

Shear Test

Figure 6 shows the relationship between vertical pressure (100 kPa, 200 kPa, 300 kPa, and 400 kPa) and shear strength of sulfate saline soil with different sulfate content. It can be seen from the figure that with the change of sulfate content, the trend of the curve is similar, but the slope and intercept of the curve have great changes, that is, the existence of sulfate has a great influence on the shear strength of the soil.

Figure 7 shows the relationship between sulfate content and cohesion and internal friction angle. It can be seen from the **Figure 7A** that with the increase of sulfate content, the cohesion

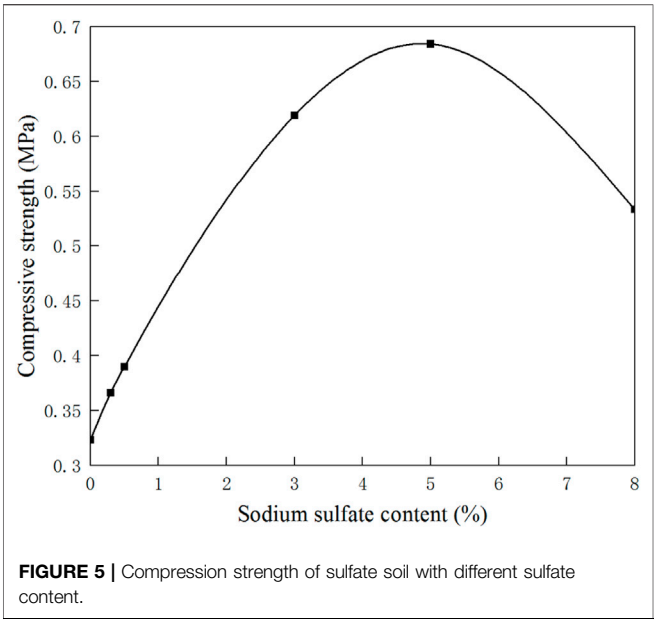

FIGURE 5 | Compression strength of sulfate soil with different sulfate content.

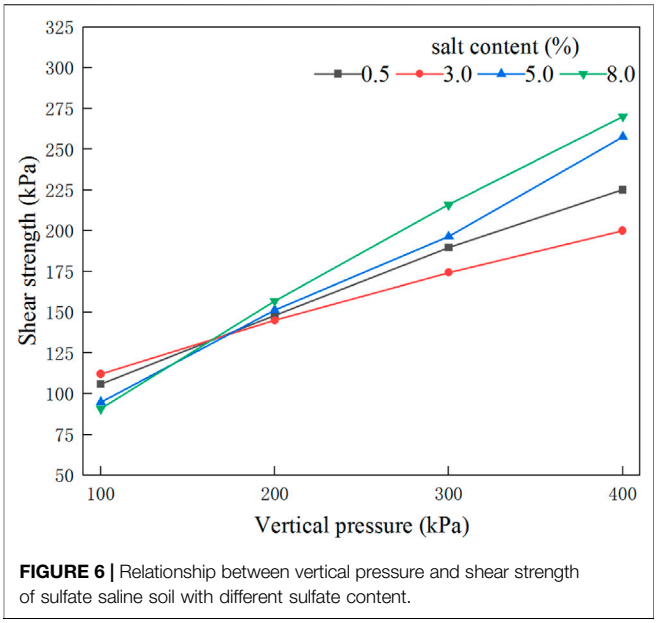

FIGURE 6 | Relationship between vertical pressure and shear strength of sulfate saline soil with different sulfate content.

of sulfate soil increases first and then decreases and changes in the range of 34.22 ~ 84.59 kPa. When the sulfate content is less than 3%, the cohesion increases with the increase of sulfate content. When the sulfate content is more than 3%, the cohesion decreases gradually. The change trend of the internal friction angle and cohesion is basically opposite, as shown in **Figure 7B**.

When the sulfate content of the soil is low, with the increase of the sulfate content, the soluble sulfate content gradually reaches saturation (Williams, 1957), and the excess sulfate in the sample precipitates in the form of sodium sulfate crystals, which act as the skeleton of the soil particles so that the cohesion between the soil particles is enhanced. The fine particles such as fine powder and clay aggregate result in the reduction of sliding friction between the particles. When the sulfate content of soil is high, more fine silt and clay aggregate together, the friction and bite force decrease, the internal friction angle of the soil increases, and cohesion decreases (Handy and Spangler, 2006).

Elastic Wave Velocity Test

Figure 8 shows the wave velocity test results of samples with different sulfate contents. The elastic wave velocity can indirectly reflect the strength of the soil. It can be seen from the figure that the elastic wave velocity of sulfate-bearing samples is generally higher than that of loess samples after salt washing; with the increase of sulfate content, the elastic wave velocity of the samples increases, indicating that the existence of sulfate plays a certain role in the solidification of soil.

DISCUSSION

(1) The results presented herein confirm that the aggregates formed by sulfate change the physical structure of the loess, resulting in changes in the physical and mechanical properties of the loess, but the mineral composition experiences no noticeable change. In the previous studies, scholars mainly explored the influence of the existence of salt on its physical and mechanical properties in the macro aspect of saline soil and did not delve into the relationship between agglomeration and property changes (Bjerrum and Rosenqvist, 1956b; Bjerrum, 1967; Chen and Anadarajah, 1998).Moreover, the research on the microscopic properties of agglomeration of saline soil mostly focuses on a single clay mineral, mainly on the boundary moisture content, and does not involve whether new substances are produced in the agglomeration process (Edzwald and O'melia, 1975; Whitehouse et al., 1958b). However, the cementation between aggregates, that is, more uniform aggregate formation have contributed to the physical structure modification, which is responsible for the changes in physicochemical and index properties (Kong et al., 2018; Kong et al., 2019). Therefore, the change of loess properties with different sulfate content is not a chemical reaction but related to the change of the physical structure caused by the formation of aggregates.

(2) In addition, scholars have studied the agglomeration of single clay minerals and found that the number and volume of aggregates increase with the increase of sulfate, but when the salt content increases to a certain extent, the agglomeration speed decreases (Liu et al., 2007b; Edzwald and O'melia, 1975). At the same time, scholars also found that with the increase of sulfate, the mechanical strength of the loess first increased and then decreased, indicating that a large salt content will inhibit the mechanical strength of the soil (Chatterj and Jensen, 1999; Aksoy et al., 2008). However, it should be noted that after the mechanical properties of the loess reached the maximum, the number of aggregates increased slowly and the volume increased significantly, mainly because the aggregates in the later stage were further agglomerated from the existing aggregates into

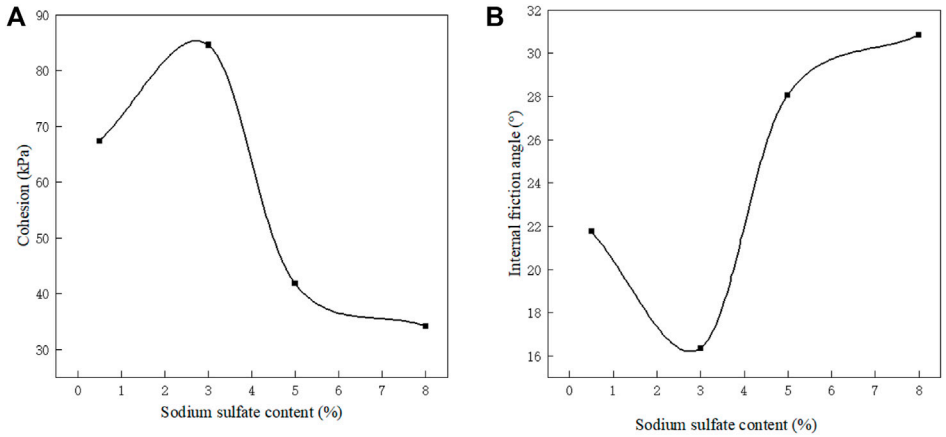

FIGURE 7 | Cohesion and internal friction angle of sulfate soil with different sulfate content.

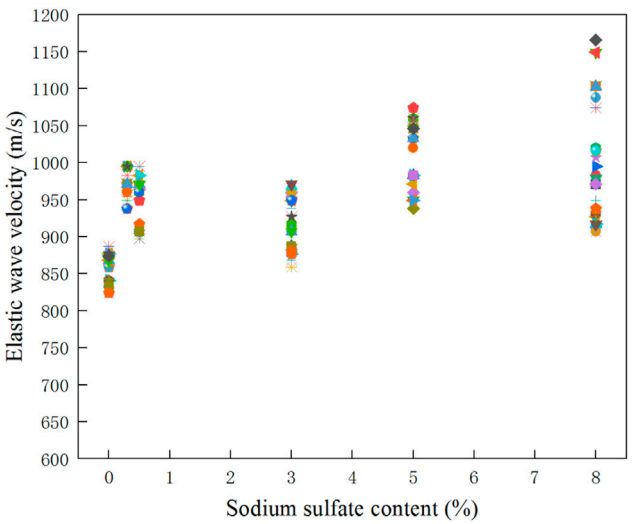

FIGURE 8 | Elastic wave velocity of sulfate soil with different sulfate content.

large particles, which affected the structure of the loess and led to the decline of mechanical strength. But, this conclusion has only been confirmed in a single sulfuric acid saline soil, and other types of saline soil and mixed saline soil still need further research. As a whole, the agglomeration of fine particles of a small amount of saline soil may facilitate improving loess performance, and thus it has potential as a new treatment technique for saline soil improvement so as to improve the resource utilization rate of saline soil in engineering construction.

(3) Finally, this study adopts a special research method of combining macro and microscopic aspects. It is found that the agglomeration in saline soil mainly concerns fine silt and clay. In the early stage, with the increase of salt content, the agglomeration speed is fast, the volume is small, and the mechanical strength of loess increases gradually. In the later stage, with the increase of sulfate, the agglomeration speed is slow, the volume increases, the mechanical strength of loess decreases, and no new substances are produced in the whole process of agglomeration (**Figures 2**, **3**, **5**, **7**). Thus, sulfate has the potential to be used as an eco-friendly additive in soil improvement.

CONCLUSION

(1) Salt washing makes the larger particles finer, and the particles which are easy to dissolve and agglomerate are washed away, resulting in the increase of clay particles, liquid limit, plastic limit, and plastic index.

(2) Aggregation occurs in the state of fine silt and clay with lower sulfate content, and as the sulfate content increases, new fine silt and clay aggregations do not occur, but the existing aggregations will further aggregate into large particles. With increasing sulfate content, the number and volume of aggregates increased, and the content of fine silt and clay decreased.

(3) With the increase in sulfate content, the aggregation particles increase, the framework grains change from point-surface contact to plane–plane contact, the adsorption capacity decreases, the compressibility increases, and the hydration film becomes thinner.

(4) When the sulfate content is low (less than 3%), the sulfate is almost completely dissolved and exists in the form of ions. The connection of soil is mainly based on the bound water, which has less influence on the limit water content. In addition, with the increase of sulfate content, the gradual precipitation of sodium sulfate crystals in the soil makes the internal cementation become stronger, the maximum dry density increase, the compressive strength increase, and the cohesion increase. When the sulfate content is large (more than 3%), excess sulfate cannot be dissolved and is precipitated in the form of crystals. The connection of the soil changes into the cementation inosculation of bound water and soluble sulfate, which has a great influence on the limit water content. With the increase of sulfate content,

because of the strong hydration of sodium ions, a large number of sodium sulfate crystals are precipitated, and the increase of aggregates leads to the maximum dry density decrease, compressive strength decrease, internal friction angle increase, and cohesion decrease.

DATA AVAILABILITY STATEMENT

The original contributions presented in the study are included in the article/Supplementary Material, further inquiries can be directed to the corresponding author.

AUTHOR CONTRIBUTIONS

All authors listed have made a substantial, direct, and intellectual contribution to the work and approved it for publication.

FUNDING

This study was supported by the National Natural Science Foundation of China (No.51878322) and Major scientific and technological projects in Gansu Province (No. 19ZD2FA001).

REFERENCES

Aksoy, Y. Y., Kaya, A., and Ören, A. H. (2008). Seawater Effect on Consistency Limits and Compressibility Characteristics of Clays[J]. *Eng. Geology*. 102 (1-2), 54–61. doi:10.1016/j.enggeo.2008.07.005

Arasan, S., and Yetimoglu, T. (2008). Effect of Inorganic Salt Solutions on the Consistency Limits of Two Clays[J]. *Turkish J. Eng. Environ. Sci.* 32, 107–115.

Bjerrum, L. (1967). Engineering Geology of Norwegian Normally-Consolidated marine Clays as Related to Settlements of Buildings [J]. *Geotechnique* 17 (02), 83–138. doi:10.1680/geot.1967.17.2.83

Bjerrum, L., and Rosenqvist, I. T. (1956). Some Experiments with Artificially Sedimented Clays. *Géotechnique* 6, 124–136. doi:10.1680/geot.1956.6.3.124

Bjerrum, L., and Rosenqvist, I. T. (1956). Some Experiments with Artificially Sedimented Clays[J]. *Geotechnique* 3 (06), 124–136. doi:10.1680/geot.1956.6.3.124

Chantra, S. I. V. (2019). *Preliminary Study of Shear Strength of Soil Containing Sodium sulfate[D]*. Beijing: Beijing Jiaotong University.

Chatterj, S., and Jensen, A. D. (1999). Efflorescence and Breakdown of Building Materials[J]. *Nordic Concrete Res.* 8, 56–61.

Chen, J., and Anadarajah, A. (1998). Influence of Pore Fluid Composition on Volume of Sediments in Kaolinite Suspensions [J]. *Clays and Clay Minerals* 2 (46), 145–152. doi:10.1346/ccmn.1998.0460204

Chen, W. W., Lv, H. M., and Cui, K. (2015). Comparative Study of the Influence of Chlorine and Sulfate Salt on Grain Size Distribution and Limit Moisture Content in Site Soils[J]. *J. Lanzhou Univ. (Natural Sciences)* 51, 334–338.

Di Maio, C. (1996). Exposure of Bentonite to Salt Solution: Osmotic and Mechanical Effects. *Géotechnique* 46, 695–707. doi:10.1680/geot.1996.46.4.695

Di Maio, C., Santoli, L., and Schiavone, P. (2004). Volume Change Behaviour of Clays: the Influence of mineral Composition, Pore Fluid Composition and Stress State. *Mech. Mater.* 36, 435–451. doi:10.1016/s0167-6636(03)00070-x

Di, M. C., Santoli, L., and Schiavone, P. (2004). Volume Change Behavior of Clays: the Influence of mineral Composition, Pore Fluid Composition and Stress State [J]. *Mech. Mater.* 36 (5-6), 435–451. doi:10.1016/s0167-6636(03)00070-x

Edzwald, J. K., and O'melia, C. R. (1975). Clay Distributions in Recent Estuarine Sediments. *Clays and Clay Minerals* 23, 39–44. doi:10.1346/ccmn.1975.0230106

Edzwald, J. K., and O'melia, C. R. (1975). Clay Distributions in Recent Estuarine Sediments [J]. *Clays and Clay Minerals* 23 (01), 39–44. doi:10.1346/ccmn.1975.0230106

Gleason, M. H., Daniel, D. E., and Eykholt, G. R. (1997). Calcium and Sodium Bentonite for Hydraulic Containment Applications. *J. Geotechnical Geoenvironmental Eng.* 123, 438–445. doi:10.1061/(asce)1090-0241(1997)123:5(438)

Handy, R. L., and Spangler, M. G. (2006). *Geotechnical Engineering [M]*. America: McGraw-Hill.

Karimpour-Fard, M., Shariatmadari, N., and Salami, M. (2011). Effect of Inorganic Salt Solutions on Some Geotechnical Properties of Soil-Bentonite Mixtures as Barriers[J]. *Int. J. Civil Eng.* 9, 103–110.

Kong, R., Yan, B., Xu, J., Shi, Z., Peng, Q., and Lin, X. (2019). Physical Homogenization and Chemical Stability of Nano-SiO2 Treated Loess. *Soil Mech. Found. Eng.* 56, 336–339. doi:10.1007/s11204-019-09611-9

Kong, R., Zhang, F., Wang, G., and Peng, J. (2018). Stabilization of Loess Using Nano-SiO2. *Materials* 11, 1014. doi:10.3390/ma11061014

Lei, H. Y., Zhang, W. S., and Zhang, X. F. (2001). Study on Engineering Property Indexes of Ultracholrine saline Soil[J]. *J. Changchun Univ. Sci. Technology* 31, 70–73.

Lin, J., Xie, D. H., and Lu, T. L. (2013). Effect of Salinity on the Flocculation of Montmorillonite Mineral[J]. *China Water Transport* 13, 121–123.

Liu, Q., Li, J., and Dai, Z. (2007). Flocculation Process of fine-grained Sediments by the Combined Effect of Salinity and Humus in the Changjiang Estuary[J]. *Acta Oceanologica Sinica* 26, 140–149.

Liu, Q. Z., Li, J. F., and Dai, Z. J. (2007). Flocculation Process of fine Grained Sediments by the Combined Effect of Salinity and Humus in the Changjiang Estuary[J]. *Acta Oceanologica Sinica* 26 (01), 1–10.

Mishra, A. K., Ohtsubo, M., Li, L., and Higashi, T. (2005). Effect of Salt Concentrations on the Permeability and Compressibility of Soil-Bentonite Mixtures. *Journal- Fac. Agric. Kyushu Univ.* 50, 837–849. doi:10.5109/4692

Pécsi, M., and Bariss, N. (1993). *Quaternary and Loess research[M]*. Hungarian: Geographical Research Institute, Hungarian Academy of Sciences.

Portela, L. I., Ramos, S., and Teixeira, A. T. (2013). Effect of Salinity on the Settling Velocity of fine Sediments of a Harbour basin. *J. Coastal Res.* 165, 1188–1193. doi:10.2112/si65-201.1

Rao, S. M., Sridharan, A., and Chandrakaran, S. (1993). Consistency Limits Behavior of Bentonites Exposed to Sea Water. *Mar. Georesources Geotechnology* 11, 213–227. doi:10.1080/10641199309379919

Wang, L., Dang, J., and Yang, X. (2009). The Research of Soil-Water Characteristic Curves of saline Soil[J]. *Geotechnical Invest. Surv.* 37, 19–23. doi:10.1109/CLEOE-EQEC.2009.5194697

Whitehouse, U. G., Jeffrey, L. M., and Debbrecht, J. D. (1958). Differential Settling Tendencies of clay Minerals in saline Waters [J]. *Clays Clay Mineral.* 7 (01), 1–79. doi:10.1346/ccmn.1958.0070102

Whitehouse, U. G., Jeffrey, L. M., and Debbrecht, J. D. (1958). Differential Settling Tendencies of Clay Minerals in Saline Waters1. *Clays and Clay Minerals* 7, 1–79. doi:10.1346/ccmn.1958.0070102

Williams, A. B. (1957). Studies of Shear Strength and Bearing Capacity of Some Partially Saturated Sands[J]. *Int. Soc. Soil Mech. Geotechnical Eng.* 2, 453–456.

Yukselen-Aksoy, Y., Kaya, A., and Ören, A. H. (2008). Seawater Effect on Consistency Limits and Compressibility Characteristics of Clays. *Eng. Geology*. 102, 54–61. doi:10.1016/j.enggeo.2008.07.005

Conflict of Interest: The authors declare that the research was conducted in the absence of any commercial or financial relationships that could be construed as a potential conflict of interest.

Publisher's Note: All claims expressed in this article are solely those of the authors and do not necessarily represent those of their affiliated organizations, or those of the publisher, the editors, and the reviewers. Any product that may be evaluated in this article, or claim that may be made by its manufacturer, is not guaranteed or endorsed by the publisher.

frontiers | Frontiers in Earth Science

ORIGINAL RESEARCH
published: 15 June 2022
doi: 10.3389/feart.2022.892179

The Piping Failure Mechanism of a Loess Dam: The 2021 Dam Break of the Yang Village Reservoir in China

Wenguo Ma[1,2], *Gang Zhang*[2]*, *Youzhen Yang*[1,2], *Ping Wang*[3], *Yishen Zhao*[1,2] *and Qingqing Lin*[1,2]

[1]School of Physics and Electronic-Electrical Engineering, Ningxia University, Yinchuan, China, [2]Institute of Solid Mechanics, Ningxia University, Yinchuan, China, [3]Key Laboratory of Loess Earthquake Engineering, China Earthquake Administration and Gansu Province, Lanzhou, China

The construction of a reservoir on a large-thickness collapsible loess cover will significantly increase the occurrence of dam break disasters. The main reason may be that although the gradation of loess particle is not uniform. The clay content is less than 10%. Piping channels easily form under the action of force and collapsibility. Near-static liquefaction of the loess in the dam body under the saturated condition will lead to piping or loss of soil strength. Therefore, it is of great significance to study the mechanical characteristics of loess in the saturated state for preventing dam break. The study investigated the 2021 dam failure of the Yang village reservoir in Ningxia, China, which resulted in millions of dollars of property damage but no casualties. The dam break is a gradual development from piping to complete dam break. This study tries to find out the real reason for dam break from the physical and mechanical properties of the foundation and the dam. We mainly carried out the research through the following three aspects: First, the dam structure was identified by using the seismograph, the compactness of the dam foundation and the dam body was determined according to the wave velocity of the soil layer, and the construction quality of the dam foundation and the dam body was comprehensively evaluated. Second, the particle size distribution confirmed the mechanism of uneven particle size distribution and clay loss. Finally, the undrained characteristics of saturated loess are tested, and the dam failure is essentially explained. The research results show that using this loess to fill the dam foundation directly and the dam body has a very high probability of piping-type dam failure. This study gives some design suggestions for using this loess for dam building, for example, through the design of the filter layer to increase the difficulty of piping occurrence.

Keywords: loess, Yang village reservoir, piping failure, dam break, near-static liquefaction

OPEN ACCESS

Edited by:
Candan Gokceoglu, Hacettepe University, Turkey

Reviewed by:
Mustafa Kanık, Firat University, Turkey
Anand Shivapur, Visvesvaraya Technological University, India

***Correspondence:**
Gang Zhang
zhanggang@nxu.edu.cn

Specialty section:
This article was submitted to Geohazards and Georisks, a section of the journal Frontiers in Earth Science

Received: *08 March 2022*
Accepted: *19 April 2022*
Published: *15 June 2022*

Citation:
Ma W, Zhang G, Yang Y, Wang P, Zhao Y and Lin Q (2022) The Piping Failure Mechanism of a Loess Dam: The 2021 Dam Break of the Yang Village Reservoir in China. Front. Earth Sci. 10:892179. doi: 10.3389/feart.2022.892179

INTRODUCTION

By the end of 2021, China has built about 100,000 reservoirs of all types, with a total storage capacity of about 9.0×10^{11} m^3 (Ministry of Water Resources of the PRC, 2021). About 280 reservoirs with a total storage capacity of 1.736×10^8 m^3 have been built in the Loess region of Ningxia. The main functions of reservoirs in Ningxia are irrigation, water supply, and aquaculture. Because of the depth and breadth of loess distribution, local materials are usually needed in the design and construction process of the dam foundation and dam body. Due to the compatibility of loess, the mechanical properties in a saturated state, and the relatively uniform gradation, there are various unpredictable

dam break factors in the design, and construction of reservoir dam failure risk is still an important problem in dam design, construction, and operation.

It is of great significance to learn lessons from the past dam break events and discuss the main rules of dam break for revealing the dam break mechanism of the reservoir and improving the safety management level of the reservoir. International Commission on Large Dams (ICOLD) Bulletin No. 175 extends the traditional method and concept to all stages before the operation stage. Many risks of dam operation come from other steps before the actual operation. This announcement is a first attempt to systematically describing the participants, roles, activities, and complex interactions involved in different stages of the dam life cycle (ICOLD, 2021) and to capture all related dam safety aspects in all preoperation stages. China, the United States, and Australia also conducted statistical analysis of the dam failure data in their own countries and summarized the causes of the dam failure. Since 2016, the average annual dam failure rate of reservoirs in China has been 0.03‰, the lowest in history, which is lower than the world-recognized standard of low dam failure rate of 0.1‰ (Ministry of Water Resources of the PRC, 2021). The United States Society on Dams (USSD) published Dams of the United States- A Pictorial Display of Landmark Dams (USSD, 2013), which introduced the concept and practical experience of dam safety management in the United States, which is worthy of reference and reference for the dam industry. The Australian National Committee on Large Dams Incorporated (ANCOLD) revised the Guidelines on the Consequence Categories for Dams (ANCOLD, 2020). The revised guide classifies potential loss of life (PLL) and the severity of damage and loss. The 6.0 m moraine core rockfill dam and the 4.5 m homogeneous earth dam with a dam height of 4.5 m are the most representative ones carried out by the EU investigation of extreme flood processes and uncertainty (IMPACT) project, the test demonstrates the whole process of dam break caused by piping (Morris et al.,2007). The Gleno dam is located in the Alps in Central Italy. A few days after the first impoundment of the reservoir it suddenly collapsed. The dam released almost 4.5 million cubic meters of water. The floods wreaked havoc in the lower valley, killing 356 people. This is the only event in Italian history when the dam collapsed due to a structural defect. The main information obtained from a large number of historical documents about the dam break of the Gleno Dam produced a dam break model, which is helpful to verify the mountain. (Pilotti et al., 2011). In the United States, the main reason for earth dam failure is flooded overtopping, followed by piping caused by seepage. For example, on 14 May 2014, the Corti-Jensen dam in Virginia had piping due to seepage, causing some dam bodies to burst, but did not cause harm to the downstream (Wu, 2020). Through a series of centrifugal model tests, the barrier lake dams failure process and mechanism due to overtopping are analyzed, and the test process of overtopping failure is simulated (Zhao et al., 2019). The Situ Gintung dam burst on 27 March 2009, according to the evaluation of the Ministry of Public Works, the main reason for the collapse of the dam body is the weakening of the dam body soil, which may be caused by the erosion and cracking of the embankment with the spillway on the left. The water in the reservoir enters the dam body through the cracks and gradually reaches a saturated state, and the shear strength of the soil body decreases (Nabilah et al., 2020). They proposed a dam risk probabilistic model (DRPM) consisting of three factors: hydrology, seepage, and slope instability, and applying this model to the Dongwushi Reservoir in Hebei Province, China, the comprehensive threshold for dam failure of the reservoir are 1.25, which indicates that the dam is in serious danger according to Guidelines On Dam Safety Evaluation of the Ministry of Water Resources of the PRC (2017). By introducing the proposed theory and method into the dam safety evaluation system, dam safety management can be carried out efficiently (Zhonget al., 2011). The BOSS-DAMBRK (this software is developed that is based on hydrodynamic flood routing) software was used to simulate the dam failure, when the entire dam collapsed at once, the extent of the downstream flood, flood propagation time, flood speed, and the impact of flood released by dam structure damage on downstream affected residents, property, and environmentally sensitive areas (Kho et al., 2009; Boss International, 1999). A total of 3,498 dam break cases in China from 1954 to 2006 are collected, and statistics are made from the historical period of a dam break, regional distribution, reservoir scale, dam height, dam type, dam break reason, dam break rate, and other aspects. The causes of the dam break and its main failure modes are preliminarily analyzed (Xie and Sun, 2009). Based on the dam break data of small reservoirs in China from 1980 to 2006, the researchers described the causes and laws of dam break of small reservoirs. They believed that the standardized management of reservoirs and the continuous promotion of reinforcement of dangerous reservoirs had laid a necessary foundation for improving the safety level of small reservoirs (Jiang and Yang, 2008).

Take the Loess dam in the Ansai area, Yan'an City, Shaanxi Province, China, as a monitoring target. The Loess dam is not fully compacted, and there may be a high permeability area in the Loess dam. Seepage channels appear in the dam body, and seepage damage occurs. These events lead to instability and damage to the dam's body. By measuring the crack, liquid level, and pore pressure, the whole life cycle of the dam is monitored. From the beginning of monitoring to the dam failure, the dam experiences three distinct types of failure, which are referred to as "internal erosion damage, slumping damage," and "slippery damage" (Xu et al., 2020a). The research object is a loess accumulation dam in Ansai Area, Yan'an City, Shaanxi Province, China. A triaxial undrained test of saturated remodeled loess was carried out on the dam body. The test shows that the deviatoric stress and pore water pressure of saturated remolded loess increase with the increase of shear strain and gradually approximated the horizontal under different cell pressure. According to on-site monitoring, it can be determined that there is more than three times the apparent damage to the dam. Through the comparison of in-site tests and indoor tests, the concept and calculation method of "inspection threshold" are put forward (Xu, et al., 2020b). Check dam system has been widely used in the Loess Plateau. However, due to the hidden danger of the dam breaking. The development of the

FIGURE 1 | Location of the Yang village reservoir.

check dam system is limited. A hydrodynamic simulation was carried out based on the failure of a typical check dam system on 15 July 2012. The simulation results show that the series fault in the tributary ditch will not lead to the stack of peak discharges. The peak flow at the catchment outlet is 20% higher than that without a dam break and 87% lower than that without a check dam (Zhang et al., 2021c). Check dam system has been widely used in the Loess Plateau. However, due to the hidden danger of the dam breaking. The development of the check dam system is limited. A hydrodynamic simulation was carried out based on the failure of a typical check dam system on 15 July 2012. The simulation results show that the series fault in the tributary ditch will not lead to the stack of peak discharges. The peak flow at the catchment outlet is 20% higher than that without a dam break and 87% lower than that without a check dam (Wang et al., 2021a). The characteristics of earth-rock dam failure research are reviewed, and the results of dam safety management (DSM) are reviewed from three aspects: disaster causes, dam failure process, and flood propagation. To improve the DSM system does not appear to be modifying the subject of the research on the change of the material properties of the dam body and its corresponding effect, the scale effect, the similarity criterion of the dam break process, and the uncertainty analysis of the commonly used models (Luo et al., 2012).

The dam break accident of the reservoir in the loess area has not been fully investigated, but there have been reports. The reasons for the dam break of reservoirs in the loess area are usually only judged based on experience. For example, causes of dam breaks are summarized into natural factors, engineering factors, and human factors, and specific mechanisms and experimental analyses are rarely carried out. This study attempts to analyze the fundamental cause of the dam break of the Yang village reservoir in the Loess Plateau, Ningxia, China, by using mechanical methods: The possibility of piping is judged according to the particle size distribution of the loess. According to the mechanical properties of remodeled saturated loess under undrained conditions, a reasonable explanation for the dam break of the reservoir may be made. The surface wave velocity test is carried out on the top of the dam to judge the compaction inside the dam body. According to the physical and mechanical properties of loess and the undrained triaxial test, the design proposal of anti-seepage and anti-filtration of a dam filled with loess material is put forward.

YANG VILLAGE DAM BREAK

Location and Introduction of Dam Break

This study investigates the failure of a loess-filled reservoir on the Loess Plateau in Ningxia, China, in the spring of 2021. The Yang village reservoir is located in the position shown in **Figure 1**. The reservoir has an area of 40,000 m^2 and a design capacity of 2.0×10^5 m^3. When the dam broke, the stored 1.4×10^5 m^3 water was washed out. The outline and breach of the reservoir are shown in

FIGURE 2 | Reservoir contour and dam break images in different directions.

FIGURE 3 | Measured length of the south slope of the dam body.

Figure 2, **Figure 2A** shows the outline of the whole reservoir, and **Figures 2B–D** show the front, side, and top views of the dam break, respectively. The breach is on the south side of the dam body, with a width of about 20 m. The sloped body on the south side of the dam body is shown in **Figure 3**, the slope length is 19 m, the inclination angle is 30 degrees, and the filling height of the dam body is 9.5 m. It can be seen from **Figures 2B,C** that the soil moisture content and layer thickness are well controlled during the construction of the dam bodies above the bottom of the breach. The damage of the dam body starts from the seepage at the bottom. It can be seen from **Figure 6** that the wave velocity at the bottom of the dam body is relatively small, corresponding to the same loess filling material, it can be considered that the compaction degree of the dam body bottom is relatively low. Therefore, under the action of the seepage force, the fine particles are gradually brought out of the dam body, and a piping channel is gradually formed at the bottom of the dam, which eventually leads to a complete dam failure. The dam breaks mainly caused nearly 0.67 km^2 of farmland to be flooded, but there were no casualties.

Geological Environment and Dam Compactness

The reservoir is located in the hinterland of the Loess Plateau the west of Hongjian Mountain. The dam foundation is directly built on the thick loess stratum, which is the Q^4 (according to the classification of stratigraphic age, the loess belongs to the sediments of Cenozoic, Quaternary, and Holocene) loess layer with a detectable depth of more than 10 m. The north and west of the reservoir depend on mountains, the south and east dams are filled with loess, and the location of the dam break is just in the dam filled in the south. As can be seen from **Figure 2C** that the

FIGURE 4 | Collection point of the test soil sample.

FIGURE 5 | Geophones arranged along the longitudinal section.

dam break started from the bottom of the dam, and there is no trace of water scouring in the middle and upper part of the dam body. The possible reason is that the compactness of the lower dam body is relatively low. After the geomembrane or geotextile blanket leakage, the water gradually infiltrates into the loess, forming a dominant channel of seepage in the dam body, resulting in the collapse of the whole dam body.

MATERIALS AND METHODS

Physical and Mechanical Properties of Loess

The filling materials in the south of the reservoir are all from the farmland in the dam's south. The farmland in the south is a slope land on the Loess Hill. As shown in **Figure 4**, the soil samples were taken from the western slope, located 3 m above the surface. The loess is massive in the dry state and muddy in the saturated state. The basic physical and mechanical properties of loess were measured in the indoor laboratory. **Table 1** gives the specific gravity, natural density, liquid limit, plastic limit, plasticity index, collapsibility coefficient, and permeability coefficient of soil samples.

Surface Wave Exploration

The Multichannel Analysis of Surface Waves (MASW) is a nondestructive method, which analyzes the dispersion characteristics of Rayleigh waves to determine how the shear wave velocity changes with depth in the layered underground. The surface wave method is widely used in seismic engineering, geotechnical engineering, and geological engineering. (Islam and Chik, 2011; Ismail et al., 2014; Harba et al., 2019). The surface wave method is also widely used in the exploration of the loose soil zone, foundation compactness, underground cavity, and complex shallow geological environment (Karray and Lefebvre, 2009; Khan and Yamin, 2019). To investigate the internal compactness of the Yang village reservoir, we conducted a surface wave test on a section of the dam (the surface wave detectors in **Figure 5** are arranged along the longitudinal section of the fracture. There are 24 detectors in total, and the 17th detector is arranged in the center of the fracture from west to east.) to obtain the details of surface wave velocity at the first 10 m below the surface. During the field investigation, we used the OYO McSEIS-SW high-precision shallow seismic instrument, 24 channels, the frequency of geophones is 4 Hz, the interval between geophones is 2 m, and the wooden hammer is used to excite the surface wave. We ensure that the surface wave excited by each hammer meets the requirements in the test. After the test, we use Seisimager software (McSEIS-SW data post-processing section) to analyze the dam body's wave velocity after filling to judge the dam body's compactness.

Triaxial Test of Loess

The dam body filled with natural loess materials may be partially saturated when the geomembrane or geotextile blanket and other impervious materials are damaged. To determine the mechanical properties of loess in a saturated state, we collected undisturbed and disturbed loess samples from the borrow pit wall on the south

TABLE 1 | Physical and mechanical property parameters of loess samples.

Specific gravity	Natural density	Liquid limit	Plastic limit	Plasticity index	Collapsibility coefficient	Permeability coefficient
G_s	ρ(g/cm^3)	w_L	w_P	I_P	δ_s	k (m/s)
2.7	1.36	27.2	18.2	9	0.056	2.5E-6

side of the reservoir. The remolded soil samples collected on-site are broken with a 2 mm sieve in the laboratory. Because the soil samples on-site are kept wet, the screening and crushing effect is perfect. The screened soil samples are used for particle size analysis and triaxial test. We used Mastersizer 3,000 laser particle sizer to test the particle size of samples by the dry method and the wet method, respectively, and each sample was tested three times. We conducted consolidated undrained (Cu) triaxial compression shear tests on loess samples under two confining pressure (100 and 200 kPa) to study the shear strength, pore water pressure development, and stress path of dam filled loess. The triaxial undrained test in this study is carried out according to ASTM standards (ASTM, 2020) are following:

1) Sample preparation: we prepare a cylindrical soil sample with a 1.5 g per cubic centimeter dry density. The height of the soil sample is 100 mm, and the diameter is 50 mm.
2) Sample installation: we protect the prepared soil sample, install the soil sample on the base of the actuator, lift the base to maintain 5N contact between the soil sample and the upper force sensor, and apply a 30 kPa confining pressure to the soil sample through the pressure–volume controller.
3) Sample saturation: we replace the saturation with carbon dioxide, and use degassed water for head saturation and back pressure saturation. We set the head pressure of 5 kPa for head saturation and keep the back pressure saturation at about 200 kPa, and the b value is more than 0.95.
4) Sample consolidation: the sample is consolidated under the confining pressure of 100 and 200 kPa, respectively. The consolidation standard is that the displacement is 0.1 ml/h, and the consolidation curve hardly changes.
5) Sample shear: we use the strain control method for consolidated undrained shear. The axial strain increases at the rate of 0.01%/min. When the axial strain is close to 20%, terminate the test.

RESULTS

Dam Compactness

Now, as a conventional geophysical exploration method. MASW has been used to determine the dam structure and compactness. MASW is favored because it can distinguish weak layers and better describe the characteristics of shallow soil. The weak penetrating layer may cause the seepage and piping of the dam body. The dam body is a uniform geological body built manually, and the hidden danger is the uneven body (weak interlayer, layered loose zone, and crack) existing in the uniform medium, which is very consistent with the research method of MASW. As we all know, surface waves mainly contain shallow strata information. Hammering waves can detect cracks near the ground, and it is indisputable that surface wave velocity changes are caused by minor faults, subsidence boundaries, cavities, etc., Therefore, in detecting the surface wave velocity changes in a shallow stratum, the surface wave has formed a meaningful primary wave, which should not be simply regarded as noise. The Rayleigh wave velocity of soil is similar to its shear wave velocity, and the shear wave velocity of soil is an important index to evaluate the strength of rock and soil, which is common knowledge. Therefore, if we carry out continuous exploration with the transient Rayleigh wave method along the strike of the earth dam, we can draw the Rayleigh wave velocity profile of the dam body by using the dispersion curve to evaluate the quality of the earth dam. **Figure 6** shows the shear wave velocity distribution on a typical longitudinal profile of the dam body. From **Figure 6**, we can find that the soil density at the dam foundation is still relatively low. In general, there is a good statistical relationship between shear wave velocity and density, for example, the experiments showed that the relationship between shear wave speed and void ratio can be expressed as follows:$V_s = 69\,(2.973 - e)^{5.5}\rho_s^{-0.5}$, where V_s, e, and ρ_s represent shear wave speed, void ratio, and soil particle density, respectively (Wang et al., 2021b).

Particle Size Distribution

The particle size grading curve of dam filling loess is measured by the dry and wet methods, respectively. **Figure 7** shows the particle size grading curve of dam filling of the Yang village reservoir. It can be seen from **Figure 7** that the mass of particles with a particle size of 5~75 um accounts for 88% of the total mass, and the plasticity index is less than 10. Therefore, the loess filling the dam body is typical silt. The non-uniformity coefficient C_u = 5.9 and curvature coefficient C_c = 1.9 of loess belong to well-graded soil, but the clay content (e.g., in silt, the part with particle size less than 0.005 mm is generally called clay.) is less than 10%. Although the gradation of loess is good, the particle size range is relatively narrow. Studies have found that liquefaction usually occurs when the clay content in silt (including loess) is less than 10% (Ministry of Housing and Urban-Rural Construction of PRC, 2016). There are also kinds of literature showing that saturated loess with a clay content of less than 12% or 15% has liquefaction behavior (Dong and Xia, 2016; He et al.,2020). The infiltration and liquefaction characteristics of loess provide favorable conditions for the occurrence of piping.

Shear Properties

In order to understand the shear characteristics of the filled loess and master the mechanical behavior of the loess comprehensively, the gradual infiltration of the dam body in the case of damage or welding gap of geomembrane or geotechnical blanket is a saturated undrained process until piping and dam break are formed. **Figure 8** compares filled loess's undrained triaxial shear test results under two different confining pressures (100–200 kPa). **Figures 8A,B** shows the variation of deviatoric stress and pore water pressure with axial strain. **Figure 8C** depicts the effective stress path. Loess samples show significant softening behavior under excess pore water pressure, and the strength decreases significantly after peak value. This deformation characteristic of loess is similar to the static liquefaction phenomenon of loose sand (He et al., 2020; Liu et al., 2020). The so-called static liquefaction refers to the apparent strain-softening phenomenon in the partial stress-strain curve of the soil sample during loading. After the peak value, the partial stress decreases sharply and approaches zero or

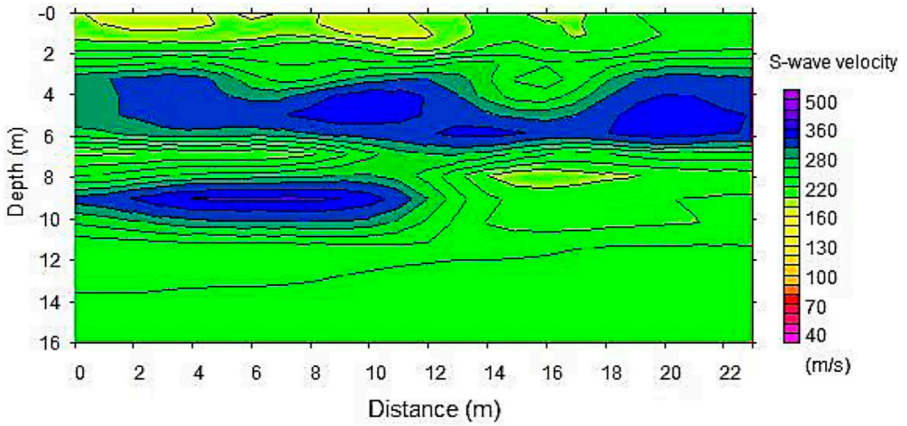

FIGURE 6 | Contour of spacing, depth, and wave velocity on longitudinal section.

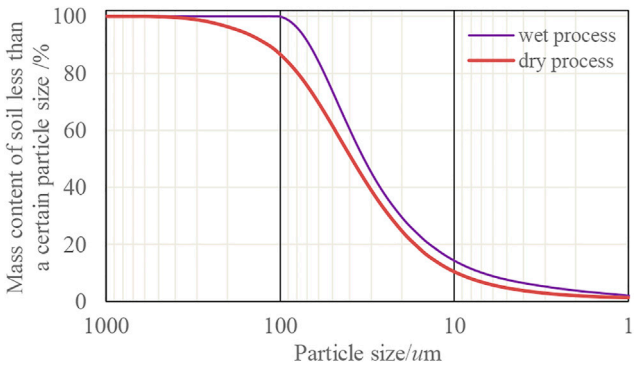

FIGURE 7 | Particle size grading curve of loess.

insufficient residual strength. The soil shows characteristics similar to fluid. **Figure 8A** is approximately consistent with the concept of static liquefaction; when the loess is saturated, the upper soil body has a loading effect on the lower soil body, and the lower saturated loess soon reaches its peak strength. When the excess pore water pressure does not increase and is almost equal to the confining pressure, the shear strength of the loess gradually decreases to the residual strength to achieve static liquefaction. These results are consistent with the Loess test results of sale mountain (Zhang et al., 2021d). Therefore, it is vital to evaluate the mechanical properties of the filled loess of the Yang village reservoir dam.

It can be seen from **Figure 8A** that the deviatoric stress peaks when the strain is minimal, and the corresponding peaks at 100 and 200 kPa are 61 and 114 kPa, respectively, and shear strength is relatively low. With the increase in the shear strain, the deviatoric stress decreases continuously from the peak value, and when the strain is significant, the deviatoric stress gradually tends to be around 25 kPa. According to the experiment, it can be seen that the residual strength of loess is deficient, showing the phenomenon of static liquefaction. The loess quickly breaks down undersaturation and deviatoric stress, further illustrating the anti-seepage arrangement's importance. It can be seen from **Figure 8B** that the development of excess static pore water pressure develops very fast at minor strains, and the development of pore water pressure begins to slow down when the strain is 3%, and finally, develops to 92 and 189 kPa. The pore water pressure and the ratios of confining pressure reached 92 and 94.5%, respectively, which were almost equal to the confining pressure, and the effective stress was already very low. From **Figure 8C**, it can be found that the effective stress path of loess has been moving towards the stress origin along with the critical state line CSL after reaching the peak value, which also reflects the same static liquefaction trend as **Figure 8A**.

DISCUSSIONS

Natural Characteristics and Approximate Static Liquefaction of Loess

The spatial variability of the Quaternary Holocene loess is enormous, and the geological environment of the Yang village reservoir is typical of silty loess with strong permeability, collapsibility, and water sensitivity. Whether it is used as an engineering foundation or dam filling material, water damage to the soil should be avoided as much as possible. As a filling material for the dam body, the management of the construction process of the dam bottom, the dam body compactness, and the construction quality of anti-seepage materials such as High-Density Polyethylene (HDPE) composite geomembrane should be strengthened, as follows:

1) The compactness of the dam bottom and the dam body should be checked layer by layer to ensure that the compactness is above 95%.
2) It is ensured that the dam bottom and body are free of unevenness, thorn particles, hard debris, etc.
3) The laying of HDPE should extend from the lowest part to the high position, do not pull too tight, to reduce the damage caused by the drag of the bentonite blanket on the foundation.

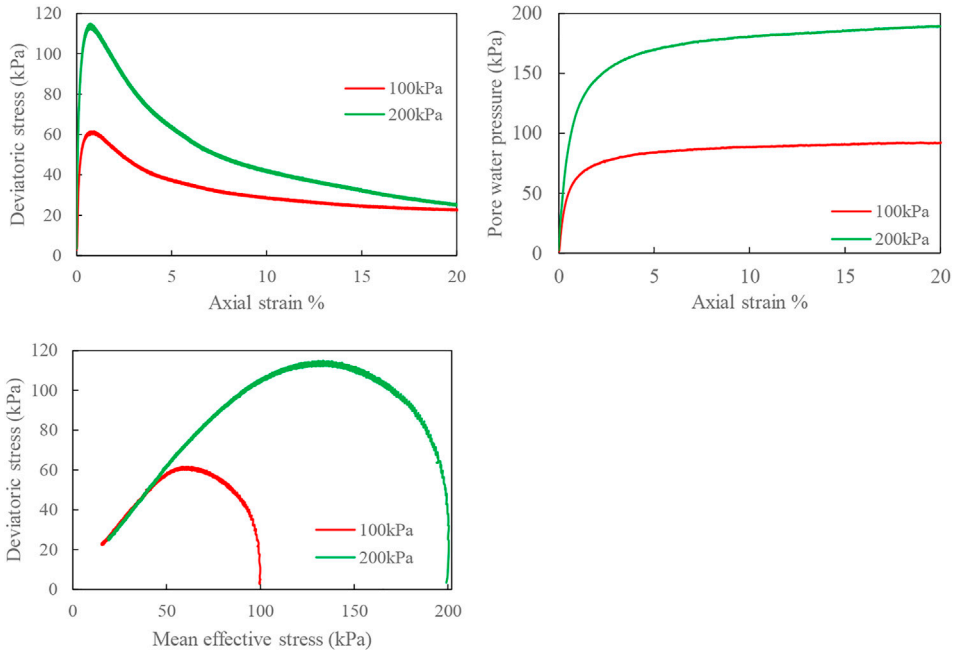

FIGURE 8 | Stress–strain relationship, pore water pressure development, and the effective stress path in loess.

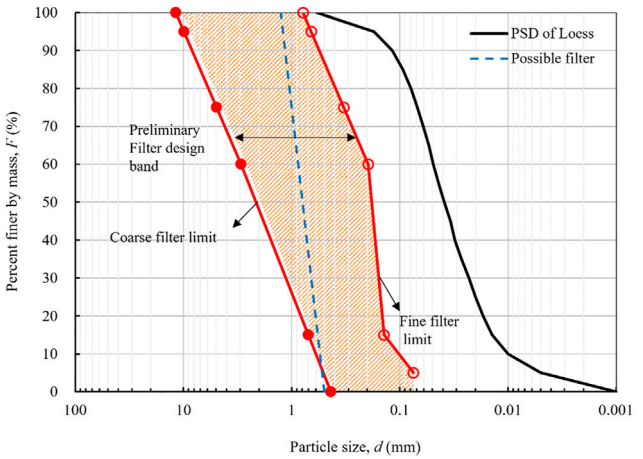

FIGURE 9 | The preliminary filter material design method.

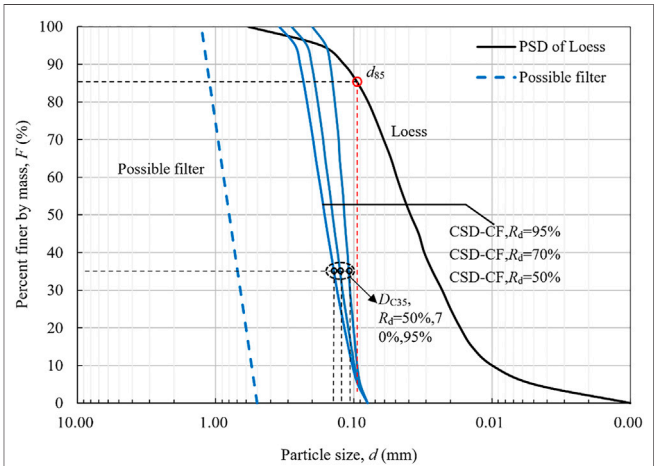

FIGURE 10 | The compaction verification of chosen filter using the CSD method.

4) Double-pass weld joints should be used in laying to reduce the number of welds, and the welding quality of the welds should be inspected in time to reduce leakage hazards. When there is a T-shaped seam, the base material is used to fill the scar, and the corners of the scar are rounded.
5) The dam body may settle under the action of the water body and its weight, and the sealing welding should also be designed to be flexible to allow vertical movement.

Suggestions on Filter Layer Design

There are three main internal erosion processes that can initiate dam failure (e.g., collapse): backward erosion, concentrated leak, and suffusion (Fell and Fry, 2007). Concentrated leakage is the main reason causing seepage failure in the embankment dams with cohesive soils, which appears in the defects (e.g., cracks, micro-fissures, and hydraulic fracture) of such structures. From the above analysis of field inspections and laboratory tests, this study concerned about the internal erosion in concentrated leaks initiated by the dam collapse. Some important physical parameters such as density, compactness, particle size distribution, fine content, and shear strength have an effect on the internal erosion properties and talked above. The most effective prevention and control measure are reasonably

installing inverted filters for the embankment dams. This study puts a particular emphasis on the design of the filter layer of loess embankment dams.

According to the characteristics of shear strength of loess in Ningxia and the potential of static liquefaction trend, a good filter design for loess will help the geotechnical and hydraulic structures in the Ningxia area maintain safety. Based on the field exploration and laboratory test results, the main reason that caused the Yang village dam break is that the internal erosion caused seepage failure because of water storage. So, the internal erosion caused potential risks should be paid special attention to this water storage structure in the loess area and filter design. Based on the current filter design theory, a well-designed filter can protect the base soil, which relates to the filter and base soil material, the hydraulic condition and the pressure acting on the base soil-filter system, shear strength of base soil, and filter soil (Zhang et al., 2021a). However, there is no filter design method related to loess. The loess soil is a kind of cohesive soil, and the cohesive soil has the ability of self-filtration (Locke and Indraratna, 2002), an improved design method of filter gradation band curves are chosen for the preliminary design of filter soils. In addition, there is an excellent possibility of dispersion for loess (Vakili et al., 2015), so the compaction of filter and base soil and other special measures should be considered for the filter design of loess.

Based on the above-mentioned analysis, a coupled design method is proposed, containing two parts. First, a filter gradation band curves design method is introduced considering the self-filtration index of loess (Zhang et al., 2021b), The preliminary filter band can be designed for the chosen filter soil; Second, a constriction size distribution (CSD) based method (Vakili et al., 2015) is chosen considering the compaction of loess and the chosen filter and the potential characteristic of dispersion. (Vakili et al., 2015), and can be used for dispersive cohesive soils, which shows as follows: $D_{15f} \leq 0.28mm$, when fine content F = 40~85%, with dispersive percent larger than 65%; $D_{c35}/d_{85}^{*} \leq 1.0$, when fine content F = 40~85%, with no dispersion; $D_{c35}/d_{85}^{*} \leq 1.25$, when fine content F ≥ 85%, with no dispersion, where, D_{15f} means the size of filter material of which 15% mass passes; D_{c35} constriction size whereby 35% of filter constriction is finer than this; d_{85}^{*} means d85 size calculated using modified PSD curve by neglecting base soil particles larger than D_{c95}; D_{c95} has the similar meaning as D_{c35}.

The coupled filter design method for loess is used in the Yang village dam, where the particle size distribution (PSD) of loess (**Figure 7**) is chosen as an example to verify the proposed method. The process of the proposed method is divided into two steps. First, the possible filter design band curves are designed using the Zhang et al. method (**Figure 9**). Second, determine the compaction and dispersive condition by choosing a possible filter in the design band curves (**Figure 10**). **Figure 9**, possible filter material chosen band intuitively displayed in **Figure 9**, we can choose one filter PSD for further compaction and dispersion verification. Finally, the chosen possible filter PSD in **Figure 8** works well when its compaction exceeds 50% (relative density greater than 50%). **Figure 10**. The above-mentioned analysis shows that the proposed filter design method for loess can work well, which can be a reference for the study of internal erosion caused failure problems in loess areas.

CONCLUSION

When the silty loess leaks in the anti-seepage materials such as the dam body's composite geomembrane, water forms the most explicit infiltration path in the silty loess, and the strength of loess is almost entirely lost, causing rapid dam failure and vast loss of life and property. We investigated a small reservoir in a typical silty loess area in Ningxia, China. The dam failure accident of this reservoir formed a typical case study of silty loess filling dam materials. In addition, the MASW survey confirmed that it could be used as a dam bottom and method for the detection of dam compactness.

Our triaxial shear tests show that the loess exhibits a near-static liquefaction phenomenon under undrained conditions, and the strength of silty loess quickly peaks with increasing strain and then gradually softens, forming a mud-like non-Newtonian fluid. Among them, the excess static pore water pressure and the effective stress path directly indicate the poor engineering properties of saturated loess (U.S. National Committee of ICOLD, 2013).

DATA AVAILABILITY STATEMENT

The original contributions presented in the study are included in the article/Supplementary Materials, further inquiries can be directed to the corresponding author.

AUTHOR CONTRIBUTIONS

GZ provided a scientific design of an inverted filter for filling materials of loess dam. The authors express their sincere gratitude to YZ and QL of Ningxia University for invaluable assistance in the field investigation.

FUNDING

This work was supported by the National Natural Science Foundation of China (NSFC), Grant/Award Nos: 51768059 and 11662015, and the Natural Science Foundation of Ningxia Province, Grant/Award No: 2022AAC03106.

ACKNOWLEDGMENTS

The first author's special thanks go to Lei Wang, Earth Products China Limited (EPC), who actively carried out surface wave tests on site. This company was not involved in the study design, collection, analysis, interpretation of data, the writing of this article or the decision to submit it for publication. The first author is particularly grateful to PW and YY for giving helpful guidance in surface wave measurement, triaxial test, and particle size analysis.

REFERENCES

ASTM. (2020). Standard Test Method for Consolidated Undrained Triaxial Compression Test for Cohesive Soils. Available at: https://www.astm.org/standards/d4767, pp.1–14. doi:10.1520/D4767-11R20

Boss International (1999). *BOSS DAMBRK Hydrodynamics Flooding Routing User's Manual*. Madison, USA: Wiscosin.

Dong, L. L. M., and Xia, K. (2016). Two Discoveries in the Liquefaction Evaluation Method of Saturated Loess. *China Earthq. Eng. J.* 38 (5), 770–774. doi:10.3969/j.issn.1000-0844.2016.05.0770

Fell, R., and Fry, J. J. (2007). *Internal Erosion of Dams and Their Foundations: Selected Papers from the Workshop on Internal Erosion and Piping of Dams and Their Foundations*. London: Taylor & Francis.

Harba, P., Pilecki, Z., and Krawiec, K. (2019). Comparison of MASW and Seismic Interferometry with Use of Ambient Noise for Estimation of S-Wave Velocity Field in Landslide Subsurface. *Acta Geophys.* 67 (6), 1875–1883. doi:10.1007/s11600-019-00344-9

He, S., Wang, X., Fan, H., Wang, H., Ren, R., and Guo, C. (2020). The Study on Loess Liquefaction in China: a Systematic Review. *Nat. Hazards* 103, 1639–1669. doi:10.1007/s11069-020-04085-7

International Commission on Large Dams (ICOLD) (2021). Dam Safety Management: Pre-operational Phases of the Dam Life Cycle. *Bulletin* 175. London: CRC Press. doi:10.1201/9781003169482

Islam, T., and Chik, Z. (2011). Advanced Performance in Geotechnical Engineering Using Tomography Analysis. *Environ. Earth Sci.* 63 (2), 291–296. doi:10.1007/s12665-010-0702-4

Ismail, A., Brett Denny, F., and Metwaly, M. (2014). Comparing Continuous Profiles from MASW and Shear-Wave Reflection Seismic Methods. *J. Appl. Geophys.* 105, 67–77. doi:10.1016/j.jappgeo.2014.03.007

Jiang, J., and Yang, Z. (2008). Laws of Dam Failures of Small-Sized Reservoirs and Countermeasures. *Chin. J. Geotechnical Eng.* 30(11),1626–1631.

Karray, M., and Lefebvre, G. (2009). Détection des cavités sous les pavages par l'analyse modal des ondes de Rayleigh (MASW). *Can. Geotech. J.* 46 (4), 424–437. doi:10.1139/T09-009

Khan, Z., and Yamin, M. (2019). Evaluation of Shear Geophones in MASW Testing. *Int. J. Geotechnical Eng.* 13 (2), 184–190. doi:10.1080/19386362.2017.1329260

Kho, F. W., Law, P. L., Lai, S. H., Oon, Y. W., Ngu, L. H., and Ting, H. S. (2009). Quantitative Dam Break Analysis on a Reservoir Earth Dam. *Int. J. Environ. Sci. Technol.* 6 (2), 203–210. doi:10.1007/bf03327623

Liu, W., Chen, W., Wang, Q., Wang, J., and Lin, G. (2020). Effect of Pre-dynamic Loading on Static Liquefaction of Undisturbed Loess. *Soil Dyn. Earthq. Eng.* 130. 105915. doi:10.1016/j.soildyn.2019.105915

Locke, M., and Indraratna, B. (2002). Filtration of Broadly Graded Soils: the Reduced PSD Method. *Géotechnique* 52 (4), 285–287. doi:10.1680/geot.2002.52.4.285

Luo, Y, Chen, L., Xu, M., and Tong, X. (2012). Review of Dam-Break Research of Earth-Rock Dam Combining with Dam Safety Management. *Procedia Eng.* 28, 382–388. doi:10.1016/j.proeng.2012.01.737

Ministry of Housing and Urban-Rural Construction of PRC (2016). *GB 50011-2010, Code for Seismic Design of Buildings*. Edition. China: China Architecture & Building Press, 23–25.

Ministry of Water Resources of PRC (2021). *River Management in the Chinese Water Statistical Yearbook*. Beijing: China Water & Power Press, 30–52.

Ministry of Water Resources of PRC (2017). *SL258-2017, Guidelines on Dam Safety Evaluation*, 37–42. Beijing: China Water & Power Press.

Morris, M. W., Hassan, M. A. A. M., and Vaskinn, K. A. (2007). Breach Formation: Field Test and Laboratory Experiments. *J. Hydraulic Res.* 45 (2S), 9–17. doi:10.1080/00221686.2007.9521828

Nabilah, R. A., Sutjiningsih, D., Sutjiningsih, D., Anggraheni, E., and Murniningsih, S. 2020). Dam Break Analysis of Situ Gintung Dam Collapse Reconstruction, *IOP Conf. Ser. Earth Environ. Sci.*, 599, 012064. doi:10.1088/1755-1315/599/1/012064

Pilotti, M. A., Maranzoni, A., Tomirotti, M., and Valerio, G. (2011). 1923 Gleno Dam Break: Case Study and Numerical Modeling. *J. Hydraul. Eng.* 137 (4), 480–492. doi:10.1061/(asce)hy.1943-7900.0000327

The Australian National Committee on Large Dams Incorporated (2020). *Guidelines on the Consequence Categories for Dams (Reprint with Amendments)*. Tasmania: Hobart.

U.S. National Committee of ICOLD (2013). *Dams of the United States-A Pictorial Display of Landmark Dams*. Colorado: U.S. Society of Dams.

Vakili, A. H., Bin Selamat, M. R., and Abdul Aziz, H. bin. (2015). Filtration of Broadly Graded Cohesive Dispersive Base Soils. *J. Geotechnical Geoenvironmental Eng.* 141 (5), 1–12. doi:10.1061/(asce)gt.1943-5606.0001280

Wang, Z. Y., Chen, Z. Y., Yu, S., Zhang, Q., Wang, Y., and Hao, J. W. (2021a). Erosion-control Mechanism of Sediment Check Dams on the Loess Plateau. *Int. J. Sediment Res.* 36 (5), 668–677. doi:10.1016/j.ijsrc.2021.02.002

Wang, H., Wang, Y. Z., Tang, Z. G., Yuan, X. M., and Duan, X. F. (2021b). Shear Wave Velocity-Relative Density United Tests and Verification of Empirical Formula. *Chin. J. Undergr. Space Eng.* 17 (6), 1881–1887.

Wu, S. (2020). Statistics and Analysis of Dam Failures in United States since 2010. *Dam Saf.* 5, 61–65. doi:10.3969/j.issn.1671-1092.2020.05.017

Xie, J. B., and Sun, D. Y. (2009). Statistics of Dam Failures in China and Analysis on Failure Causations. *Water Resour. Hydropower Eng.* 40 (12), 124–128. doi:10.3969/j.issn.1000-0860.2009.12.032

Xu, J., Wei, W., Bao, H., Zhang, K., Lan, H., Yan, C., et al. (2020). Failure Models of a Loess Stacked Dam: a Case Study in the Ansai Area (China). *Bull. Eng. Geol. Environ.* 79 (2), 1009–1021. doi:10.1007/s10064-019-01605-z

Xu, J., Wei, W., Bao, H., Zhang, K., Lan, H., Yan, C., et al. (2020). Study on Shear Strength Characteristics of Loess Dam Materials under Saturated Conditions. *Environ. Earth Sci.* 79 (13). doi:10.1007/s12665-020-09089-x

Zhang, Z., Chai, J., Li, Z., Xu, Z., and Yuan, S. (2021a). Reconstruction and Effects of a Failure of a Typical Check Dam System under an Extreme Rainstorm on the Loess Plateau, China. *Nat. Hazards* 111, 1401–1419. doi:10.1007/s11069-021-05101-0

Zhang, G., Wang, H. Y., and Jahanzaib, I. (2021b). Improved Design Method of Gradation Band Curves for Granular Filters. *Shuili Fadian Xuebao/Journal Hydroelectr. Eng.* 40 (4), 73–83. doi:10.11660/slfdxb.20210408

Zhang, G., Israr, J., Ma, W., and Wang, H. (2021c). Modeling Water-Induced Base Particle Migration in Loaded Granular Filters Using Discrete Element Method. *Water* 13 (14), 1976. doi:10.3390/w13141976

Zhang, F., Peng, J., Wu, X., Pan, F., Jiang, C., et al. (2021d). A Catastrophic Flowslide that Overrides a Liquefied Substrate: the 1983 Saleshan Landslide in China. *Earth Surf. Process. Landforms* 46 (10), 2060–2078. doi:10.1002/esp.5144

Zhao, T. L., Chen, S. S., Fu, C. J., and Zhong, Q. M. (2019). Centrifugal Model Tests and Numerical Simulations for Barrier Dam Break Due to Overtopping. *J. Mt. Sci.* 16 (3), 630–640. doi:10.1007/s11629-018-5024-0

Zhong, D., Sun, Y., and Li, M. (2011). Dam Break Threshold Value and Risk Probability Assessment for an Earth Dam. *Nat. Hazards* 59 (1), 129–147. doi:10.1007/s11069-011-9743-6

Conflict of Interest: The authors declare that the research was conducted in the absence of any commercial or financial relationships that could be construed as a potential conflict of interest.

Advantages of publishing in Frontiers

OPEN ACCESS
Articles are free to read for greatest visibility and readership

FAST PUBLICATION
Around 90 days from submission to decision

HIGH QUALITY PEER-REVIEW
Rigorous, collaborative, and constructive peer-review

TRANSPARENT PEER-REVIEW
Editors and reviewers acknowledged by name on published articles

Frontiers
Avenue du Tribunal-Fédéral 34
1005 Lausanne | Switzerland

Visit us: www.frontiersin.org
Contact us: frontiersin.org/about/contact

REPRODUCIBILITY OF RESEARCH
Support open data and methods to enhance research reproducibility

DIGITAL PUBLISHING
Articles designed for optimal readership across devices

FOLLOW US
@frontiersin

IMPACT METRICS
Advanced article metrics track visibility across digital media

EXTENSIVE PROMOTION
Marketing and promotion of impactful research

LOOP RESEARCH NETWORK
Our network increases your article's readership